
TARGETING HEAVY RARE EARTH ELEMENTS IN CARBONATITE COMPLEXES

SUBMITTED BY SAM BROOM-FENDLEY TO THE UNIVERSITY OF
EXETER AS A THESIS FOR THE DEGREE OF DOCTOR OF
PHILOSOPHY IN GEOLOGY IN MAY, 2015

This thesis is available for Library use on the understanding that it is copyright material and that no quotation from the thesis may be published without proper acknowledgement.

I certify that all material in this thesis which is not my own work has been identified and that no material has previously been submitted and approved for the award of a degree by this or any other University.

SIGNED _____



Targeting Heavy Rare Earth Elements in Carbonatite Complexes
Sam Broom-Fendley

Cover image: View looking north from Songwe Hill, over lake Mpoto

Abstract

The HREE¹ are generally considered to be the most critical of the REE², indispensable for many high-tech applications such as smart-phones and electric vehicles. Currently, carbonatites are the main source of REE due to their high REE grade; most carbonatites, however, are HREE-poor.

This thesis presents the findings on HREE mineralisation at the Songwe Hill carbonatite, in the CAP³ of south-eastern Malawi. Across all carbonatite types at Songwe, whole-rock Y and P₂O₅ concentrations correlate positively, indicating that phosphate minerals have a strong control over the HREE contents. This is confirmed through textural and geochemical analyses (LA ICP-MS⁴ and EPMA⁵) of apatite, which show that it can be subdivided into 5 different types (Ap-0–4), found at different stages of the paragenetic sequence. The chemistry of each of these apatite types becomes progressively more HREE-enriched, up to 3 wt. % Y₂O₃, and ultimately culminating in xenotime crystallisation.

Cross-cutting relationships indicate that HREE-enriched apatite formed as an early crystallisation product from a late-stage, carbonatite-derived hydrothermal fluid. It is evident that LREE⁶-fluorocarbonate mineralisation occurred after apatite crystallisation and it is assumed that crystallisation of all hydrothermal phases was through the evolution of a single fluid, rather than several different fluids.

The apatite composition is compared to a compilation of analyses of apatite from other carbonatites and granitoids, as well as new analyses of late-stage apatite from the Kangankunde and Tundulu carbonatites, Malawi. Based on these analyses, it is concluded that apatite from Songwe has the highest HREE-concentration compared to apatite from any previously analysed carbonatite. However, apatite from the Tundulu carbonatite has a similar geochemistry and paragenesis to the HREE-rich apatite from Songwe, suggesting that late-stage HREE enrichment may be a common process in carbonatites.

In order to elucidate the fluid conditions which led to HREE mineralisation, new fluid inclusion and stable isotope data are presented to complement the mineralogical data. The fluid inclusions constrain the minimum temperature of apatite crystallisation of 160 °C, and most homogenisation temperatures in apatite are between 160–360 °C. Inclusions from apatite are CO₂-rich, and it is suggested that transport of the REE occurred in carbonate complexes. Stable isotope data were obtained from both conventional C and O analyses of carbonates and from a novel method developed for acquiring $\delta^{18}\text{O}_{\text{PO}_4}$ from apatite. A conceptual model involving the simultaneous cooling and mixing of magmatically-derived and meteoric fluids is suggested.

Two possible causes of REE fractionation are suggested: (1) a crystal-chemical control and (2) control through preferential stability of LREE and HREE complexes. However, neither mechanism is equivocal and further work on the stability of carbonate complexes is suggested in order to better understand REE mineralisation at carbonatites.

¹heavy rare earth elements

²rare earth elements

³Chilwa Alkaline Province

⁴laser ablation inductively coupled plasma mass spectrometry

⁵electron probe micro-analyser

⁶light rare earth elements

In addition to results on the HREE mineralisation in carbonatites, new data on the mineralogy, geochemistry and age of the Songwe Hill carbonatite and the closely-associated Mauze nepheline syenite intrusion are presented. Songwe comprises three stages of intrusion (C1–3): (C1) sövitic calcite carbonatite, (C2) alvikitic calcite-carbonatite and (C3) Fe-rich carbonatite. The LREE grade increases with the increasing Fe-content of the intrusion, as is common at many REE-rich carbonatites. Later-stages of the intrusion include apatite-fluorite veins (C4) and Mn-Fe-veins. The former is a volumetrically minor stage, but can contain up to 1 wt. % Y_2O_3 , and the latter is formed through oxidation of carbonatite by supergene fluids. Samples analysed from Mauze show that it is REE- and P_2O_5 -poor, with MREE⁷-depleted REE distributions. U-Pb dating of zircons from Songwe and Mauze show that they are 131.5 ± 1.3 and 133.1 ± 2.0 Ma, respectively. The close temporal association of each intrusion suggests that Mauze could be a 'heat-engine' for hydrothermal mineralisation at Songwe.

⁷mid rare earth elements

Acknowledgements

I would like to thank my supervisors Frances Wall, Gus Gunn, Jens Anderson, Aoife Brady and Will Dawes for supporting my ideas, applications and analyses. My thanks also go out to Aoife Brady, Will Dawes, Alex Lemon, James Mtegha, Paul Armitage and Chikondi Mcheka of Mkango resources who provided financial and logistical field support, access to drillcore and whole-rock analyses, as well as interesting and enthusiastic discussions in the Malawian sun. Steve Pendray is thanked for rapidly producing thin sections of excellent quality, and for helping to develop the production of polished wafers. I am grateful to Lorraine Field, Jeremy Rushton, and Toni Milodowski for support using the BGS⁸ SEM⁹, to Simon Chenery for assistance using the LA ICP-MS and to John Naden for training on the use of fluid inclusion stages. Don Appleton and Mike Styles are kindly thanked for providing additional material and unpublished results from Tundulu, as well as for stimulating discussions. Dave Smith is thanked for provision of Kangankunde samples from the NHM¹⁰. Tim Heaton and Hilary Sloane facilitated or carried out stable isotope analyses and Matt Horstwood supported the acquisition of radiogenic isotope data at NIGL¹¹. Funding from the Geological Society and the Society of Economic Geologists is gratefully acknowledged for a secondment to Quebec. My thanks are extend to Volker Möller and Willy Williams-Jones (McGill), who hosted me during this time, and to Alex Néron and Paul Bédard who accommodated me in Chicoutimi. Niobec are thanked for providing access to the St Honoré mine and for permission to take samples.

Gus Gunn, Frances Wall, Aoife Brady, Tim Heaton, Jens Anderson, Ryan Langdon and Janet Fendley diligently reviewed chapters, and Gus is particularly thanked for his rapid turnaround and critical eye.

Kate Littler is thanked for her continued patience and support, and for listening to me talk about carbonatites and rare earths for the last 4 years.

The project was funded by NERC, through a BGS funding scheme with case support from Mkango Resources Ltd.

⁸British Geological Survey

⁹scanning electron microscope

¹⁰Natural History Museum

¹¹NERC¹² Isotope Geosciences Laboratory

Contents

1	Introduction	1
1.1	Significance of the study	1
1.2	Aims and objectives	2
1.3	Approach	3
1.4	Study Area	3
1.5	Thesis structure	3
2	Literature review	5
2.1	Carbonatites	5
2.1.1	Classification	6
2.1.2	Composition	6
2.1.3	Occurrence	7
2.1.4	Petrogenesis	8
2.2	Rare earth elements	9
2.2.1	Definition	9
2.2.2	Chemical characteristics	11
2.2.3	Abundance	12
2.2.4	Mineralogy	13
2.2.5	Importance of the REE	14
2.2.6	Importance of the HREE	15
2.3	REE deposits	16
2.3.1	Carbonatites	17
2.3.2	Alkaline Rocks	17
2.3.3	Placer deposits	19
2.3.4	Ion-adsorption deposits	20
2.3.5	Other deposit types	20
2.4	REE in the mantle	21
2.5	Magmatic enrichment of REE	22
2.6	REE transport	23
2.6.1	Stability of different aqueous REE complexes	23
2.6.2	Solubility of REE minerals	29
2.6.3	Y/Ho fractionation and the tetrad effect	34
2.6.4	The chemistry of REE-bearing fluids	35
2.6.5	Current REE deposit models	46
2.7	Supergene REE enrichment	50
2.8	Summary	50
3	Geological setting	53
3.1	Review of the CAP	53
3.2	CAP carbonatites	57

3.3	Study area	58
3.4	Techniques	60
3.4.1	Basic mapping	60
3.4.2	Portable XRF ¹³	60
3.5	Songwe Hill	62
3.5.1	Exploration history	65
3.5.2	Current exploration	65
3.5.3	Geology	66
3.5.4	Sample collection	78
3.5.5	Interpretation and discussion	80
3.6	Conclusions	81
4	Geochemistry	83
4.1	Previous data	84
4.2	Methods	87
4.2.1	Sample selection	87
4.2.2	Whole-rock analyses	91
4.2.3	Mineralogy and micro analysis	94
4.3	Results	100
4.3.1	Petrography	100
4.3.2	EPMA analyses of carbonate	112
4.3.3	Whole-rock data — Mauze	117
4.3.4	Whole rock data — Songwe drillcore	120
4.3.5	Nomenclature and carbonatite classification for Songwe Hill	124
4.3.6	Trends in the Songwe whole-rock data	125
4.3.7	Calcite-carbonatite at Songwe: sövite or alvikite?	128
4.3.8	Rare earth distribution of the Songwe carbonatite	128
4.4	Mauze WR discussion	132
4.4.1	Comparison of Mauze with other silicate rocks of the CAP	132
4.5	Songwe discussion	133
4.5.1	Stages of intrusion of the Songwe carbonatite	133
4.5.2	Y anomaly: a significant result or an analytical artefact?	136
4.5.3	Controls on the REE distribution at Songwe	137
4.5.4	Comparison of Songwe with other CAP carbonatites	138
4.6	Conclusions	140
5	HREE minerals	143
5.1	Apatite in carbonatite	144
5.2	Methods	145
5.2.1	Petrography	145
5.2.2	Quantitative electron microscopy (EPMA)	145
5.2.3	Laser ablation ICP-MS	146
5.3	Songwe apatite	148
5.3.1	Textural variations between apatite types	148
5.3.2	Chemical variation between the apatite types at Songwe	155
5.3.3	Fluorite from C4 apatite-fluorite veins	165
5.3.4	Interpretation	169
5.4	Kangankunde and Tundulu	182
5.4.1	Kangankunde	183

¹³X-ray fluorescence

5.4.2	Tundulu	184
5.4.3	Laser ablation analyses	189
5.4.4	Interpretation and comparison with previously published data	191
5.5	Discussion	199
5.5.1	Comparison between apatite from Songwe, Tundulu and Kangankunde	199
5.5.2	Comparison with apatite from other localities	200
5.5.3	What can the changing apatite composition tell us about the nature of late-stage fluids in carbonatites?	205
5.5.4	Reconciling apatite REE distributions with whole-rock distributions	207
5.6	Conclusions	207
6	Fluids in carbonatite	211
6.1	Methodology	211
6.1.1	Sample selection	211
6.1.2	Wafer preparation	212
6.1.3	Microthermometry	212
6.2	Results	213
6.2.1	Petrography	213
6.2.2	Microthermometry	214
6.3	Interpretation	219
6.3.1	Salinity	219
6.3.2	Temperature	220
6.3.3	Changes in composition and temperature with paragenesis	220
6.4	Discussion	221
6.4.1	Composition of HREE-bearing fluids	223
6.4.2	HREE enrichment of apatite	223
6.5	Conclusions	227
7	Stable Isotopes	229
7.1	Isotope compositions	230
7.1.1	General principals of temperature control on stable isotope ratios	230
7.1.2	Isotopic composition of crystallising fluid	232
7.2	Experiment rationale	238
7.2.1	Advantages and disadvantages of bulk-carbonate analyses in carbonatite	239
7.2.2	Apatite stable isotope analyses	240
7.2.3	Previous work	241
7.3	Sample selection	242
7.3.1	Worldwide carbonatites	242
7.3.2	Songwe carbonatites	243
7.4	Methodology	247
7.4.1	Carbonates	247
7.4.2	Apatite	247
7.5	Results	251
7.5.1	Worldwide carbonatites	251
7.6	Results	253
7.6.1	Songwe samples	253

7.7	Discussion	256
7.7.1	Comparison of apatite preparation techniques	256
7.7.2	Primary igneous apatite	258
7.7.3	Comparison of $\delta^{18}\text{O}_{\text{PO}_4}$ and $\delta^{18}\text{O}_{\text{whole-apatite}}$ data	259
7.7.4	Isotopic diffusion in apatite	260
7.7.5	Songwe carbonate isotopes	261
7.7.6	Songwe apatite isotopes	267
7.7.7	Compositional estimates for mineralising water	271
7.7.8	Reconciling calcite $\delta^{18}\text{O}$ and apatite $\delta^{18}\text{O}_{\text{PO}_4}$ data	271
7.7.9	A model for the mineralising fluid	273
7.8	Conclusions	274
8	U-Pb dating	279
8.1	Introduction	279
8.2	Methodology	280
8.3	Results	284
8.3.1	Zircon petrography	285
8.3.2	U-Pb dates	290
8.4	Discussion	292
8.4.1	Age interpretation	292
8.4.2	REE implications	300
8.4.3	Songwe and Mauze ages in the context of the CAP	302
8.5	Conclusions	307
9	Conclusions	309
A	“Mantrap”	353
A.1	Geology	356
A.1.1	Basement	356
A.1.2	Syenite	357
A.1.3	Phonolite	357
A.1.4	Trachyte/trachytic breccia	359
A.1.5	HREE-rich veins	359
A.2	Portable XRF results	360
A.3	Sampling	360
A.4	Interpretation and discussion	360
A.4.1	Order of emplacement	360
A.4.2	Trachyte or pseudotrachyte?	363
A.4.3	REE mineralisation	365
B	Supplementary analytical methods	367
B.1	EPMA	367
B.1.1	Standard selection	367
B.1.2	interference	369
B.1.3	Detector artefacts	370
B.2	LA ICP-MS	372
C	Sample list	379

D Supplementary analytical data	385
D.1 Whole-rock	385
D.2 Laser-ablation	396

List of Figures

1.1	The criticality matrix evaluated by the European Commission (2014).	2
2.1	Le Bas carbonatite model	10
2.2	Concentration of the REE in the continental crust	13
2.3	Prices of the REE	16
2.4	Spatial distribution and REE tonnages of the different types of REE-deposit	18
2.5	Schematic of different types of carbonatite-related ore deposit	22
2.6	First formation constants of different REE ligands at ambient temperature	26
2.7	First formation constants of different REE ligands extrapolated to 300 °C	27
2.8	Experimentally-derived first formation constants for REE complexes between 100 and 300 °C	30
2.9	Experimentally-derived equilibrium constants for dissolution of NdPO ₄ and REEF ₃	32
2.10	REE concentrations in natural fluids normalised to chondrite.	38
2.11	REE concentrations from fumarolic encrustations at Oldionyo Lengai	40
2.12	Temperature and pressure ranges of common REE-bearing minerals found in carbonatites.	45
2.13	Schematic of REE speciation in a hypothetical hydrothermal fluid	48
3.1	Geological map of the CAP	54
3.2	Map of the study area	61
3.3	Comparison between data from handheld XRF analyses and ICP-MS ¹⁴ analyses	63
3.4	View of Songwe and Mauze during the wet season	63
3.5	Geological map of Mauze and Songwe and geological map of carbonatite types at Songwe	64
3.6	Photograph of Chenga Breccia in the field	66
3.7	Examples of float samples from Mauze	67
3.8	Example of fenite from Songwe Hill	68
3.9	Example of grey C2 calcite-carbonatite in the field	71
3.10	Example of a pebble dyke in the field	71
3.11	Schematic diagram and photographs of calcite carbonatite sawn section	72
3.12	Example of Fe-rich carbonatite from drillcore	73
3.13	Schematic diagram and photographs of a Fe-rich carbonatite sawn section	74

¹⁴inductively coupled plasma mass spectrometry

3.14	Photograph and schematic diagram of Fe-rich carbonatite breccia in the field	77
3.15	Example of a road-cut with extensive alteration of Fe-rich rock . . .	78
3.16	Example of an apatite-fluorite vein in the matrix of the contact breccia on Chenga Hill.	79
4.1	Review of whole-rock data from Songwe analysed by the JICA ¹⁵ /MMAJ ¹⁶ .	86
4.2	Chondrite-normalised REE plot using whole-rock data from the JICA/MMAJ	88
4.3	Calcite-fenite mixing model	95
4.4	Fenite in thin section	102
4.5	C1 calcite-carbonatite in thin section	103
4.6	C2 calcite-carbonatite in thin section	105
4.7	C2 calcite-carbonatite in thin section	106
4.9	QEMSCAN image of C3 carbonatite	109
4.12	Ternary plot of carbonate compositions from Songwe	115
4.13	Major-element variations in Songwe carbonates	116
4.14	XRD trace of Fe-bearing carbonatite	116
4.15	Major element concentrations, from Mauze samples, against SiO ₂	119
4.16	Chondrite-normalised REE distribution of samples from Mauze . .	120
4.17	Ternary plot of carbonatite compositions from Songwe	126
4.18	Binary plots of whole-rock data from carbonatite, Mn-Fe- veins and apatite-fluorite veins from Songwe.	129
4.19	Average Songwe calcite-carbonatite values compared with median sövite and alvikite values from Le Bas (1999)	130
4.20	Average distribution of the REE in Songwe carbonatites, Mn-Fe- veins and Apatite-fluorite veins	130
4.21	Whole-rock REE distributions of the different Songwe carbonatite types	131
4.22	Comparison of whole-rock data for Mauze with data from Woolley and Jones (1987)	134
4.23	Y/Ho and Zr/Hf compared to the CHARAC field, and chondrite-normalised distributions plotted against ionic radii.	137
4.24	Binary plots of whole-rock data from carbonatite and Mn-Fe- veins from Songwe.	139
4.25	Comparison between Songwe and other CAP whole-rock data . .	140
5.1	Analyses of SRM 612 check-standard, for Y and Ce, compared with published concentrations	147
5.2	CL ¹⁷ and BSE ¹⁸ images of Ap-0 in sample T0134.	149
5.3	CL, BSE and X-ray count images of Ap-1, 2 and 3 from C1 calcite carbonatite.	151
5.4	CL, BSE and X-ray count images of Ap-3 from C2 calcite carbonatite and C3 Fe-rich carbonatite	152
5.5	CL and BSE images of Ap-4 from C4 apatite-fluorite veins.	153
5.6	CL and BSE images of xenotime from Chenga Hill C4 carbonatite	154

¹⁵Japan International Co-operation Agency

¹⁶Metal Mining Agency of Japan

¹⁷cathodoluminescence

¹⁸back-scattered electron

5.7	Variations in major element concentration of Songwe apatite from EPMA data	156
5.8	Variation in REE and trace element concentrations in Songwe apatite from LA ICP-MS data.	157
5.9	Variation in REE and trace element concentrations in Songwe apatite from LA ICP-MS data	158
5.10	Distribution of the REE + Y in apatite samples from fenite, calcite carbonatite, Fe-rich carbonatite, Mn-Fe-veins and apatite-fluorite veins.	159
5.11	Binary plots of minor elements and REE distribution of Songwe xenotime	166
5.12	Example of fluorite under CL in a C4 carbonatite	167
5.13	Chondrite-normalised REE distribution of fluorite from C4 calcite carbonatite. Chondrite values from McDonough and Sun (1995)	169
5.14	Cathodoluminescence spectra from apatite representative of the different rock types at Songwe.	171
5.15	Paragenetic diagram of the different carbonatite stages and apatite types at Songwe.	172
5.16	Schematic representation of different apatite generations at Songwe.	173
5.17	PPL ¹⁹ and XPL ²⁰ images showing an example of early, primary ovoid apatite from Jacupiranga.	174
5.18	Apatite-fluid K_D values for the REE	179
5.19	Composition of Songwe fluorite compared to other carbonatite fluorites	182
5.20	CL and BSE images of turbid apatite cores and clear rims in Kangankunde sample BM 1962 73 (131)	185
5.21	PPL, CL and BSE images of apatite from Nathace Hill sample T160	186
5.22	CL and BSE images of silicified apatite carbonatite from Nathace Hill, Tundulu	187
5.23	EDS ²¹ maps of early turbid apatite and late apatite overgrowths from Tundulu	188
5.24	Binary plots of REE and Na data from the cores and rims of apatites from Kangankunde and Tundulu	192
5.25	Binary plots of Sr, U, Th and Na data from the cores and rims of apatite from Kangankunde and Tundulu	193
5.26	Chondrite-normalised REE distributions for turbid cores from Kangankunde and Tundulu	194
5.27	Chondrite-normalised REE distributions for euhedral apatite rims from Kangankunde and Tundulu	195
5.28	Interpretation of the paragenetic sequence at Tundulu	197
5.29	Comparison of LA ICP-MS data from late-stage apatite from Songwe (Ap-3 and Ap-4)	201
5.30	Comparison of apatite from Songwe, Tundulu and Kankankunde with published carbonatite and granitoid analyses	203
6.1	Images of fluid inclusions in apatite, fluorite and quartz	215

¹⁹plane-polarised light

²⁰cross-polarised light

²¹electron dispersive spectroscopy

6.2	Histogram of homogenisation temperatures of fluid inclusions in apatite and fluorite	217
6.3	Plot of homogenisation temperature and ice melting temperature for fluorite	219
6.4	Schematic diagram of changing fluid inclusion compositions and temperatures	222
7.1	Compilation of published O-isotope fractionation factors for apatite–calcite and apatite–water.	232
7.2	Schematic diagram of the controls on carbonatite isotopic composition	233
7.3	Arrhenius plot of diffusion coefficients versus reciprocal temperatures for minerals of importance in carbonatites.	238
7.4	Compilation of previous analyses of apatite from Oka, Jacupiranga, Tikshezero, and Siilinjärvi	242
7.5	Compilation of previous analyses of calcite-carbonatite from Oka, St Honoré, Jacupiranga, Fen and Kaiserstuhl	244
7.6	CL and PPL images of recrystallisation of calcite in the St Honoré carbonatite	245
7.7	Paragenetic diagram of the Songwe Hill carbonatite, with approximate position of the samples selected for isotope analysis.	246
7.8	Example of glassy, hand-picked apatite from sample Jac-12	248
7.9	Photos of the different stages of preparation of AgPO ₄	250
7.10	Comparison of $\delta^{18}\text{O}$ results from analysis as a bulk powder and from picked apatite analysis	253
7.11	$\delta^{18}\text{O}$ and $\delta^{13}\text{C}$ results for bulk carbonates from Songwe, plotted against the PIC ²² field	254
7.12	Songwe $\delta^{18}\text{O}$ results from calcite and $\delta^{18}\text{O}$ results from apatite, arranged in approximate paragenetic order	255
7.13	Calculated equilibrium temperatures between calcite and apatite	260
7.14	Songwe stable isotope values compared with models for fluid-rock interaction	265
7.15	Palaeomap reconstruction of the world at 130 Ma with the approximate position of Malawi indicated	266
7.16	Examples of ‘tiger-stripe’ weathering and dissolution cavities in outcrop and under CL	268
7.17	Conceptual model of mixing between meteoric water and deuterium water	273
7.18	Schematic representation of each apatite type and the isotopic conditions of formation	275
7.19	Schematic model for fluid transport around a carbonatite	276
8.1	Systematic variance in zircon standards	284
8.2	BSE images of different zircon habits found in samples from Mauze	286
8.3	Cold-CL images of hydrothermal zircon in samples from Mauze	289
8.4	BSE images of zircon habits found in carbonatite from Songwe.	291
8.5	Tera-Wasserburg and equivalent Wetherill plots of Mauze zircons	293
8.6	Tera-Wasserburg concordia ages of Mauze zircons with discordant data points excluded	297

²²‘Primary Igneous Carbonatite’

8.7	Tera-Wasserburg and equivalent Wetherill plots of calzirtite rims from Mauze	299
8.8	Tera-Wasserburg and equivalent Wetherill plots of Songwe zircons	301
8.9	New Songwe and Mauze U-Pb zircon ages compared with published age data	305
A.1	Photo of Mantrap Hill looking from the north.	354
A.2	Sketch map of the vents to the south of Mauze, including Mantrap	355
A.3	Example of folded calc-silicate-bearing gniess.	356
A.4	Typical syenite from the south-west flank of Mantrap Hill.	357
A.5	Example photographs of trachyte breccia from Mantrap	358
A.6	Examples of HREE-rich veins from near Mantrap	361
A.7	Geological sketch map of Mantrap and the surrounding area, including spot analyses of Y using a portable XRF.	362
B.1	Mount map of new Smithsonian REE standards	368
B.2	Areas of approximate equal BSE intensity in the Zagi mountain xenotime check-standard.	371

List of Tables

2.1	Atomic number, radii, symbol and abundance of the REE	11
2.2	Definitions of the LREE ²³ , MREE ²⁴ and HREE ²⁵ used in the literature an this thesis	12
2.3	Some common REE minerals	14
2.4	Uses of the REE	15
2.5	Advantages and disadvantages of different REE-deposits	19
2.6	Anion concentrations of carbonatite- and granite-derived REE-bearing fluids	37
2.7	Summary of the mineralogy and fluid-inclusion data from hydrothermal REE deposits.	43
3.1	Sequence of geological emplacement in the CAP	55
3.2	List of carbonatites in Malawi	59
3.3	Multiple analyses of a sample using the Niton handheld XRF	62
3.4	Mineralogy of the different carbonatite types found at Songwe.	69
4.2	Standard and black concentrations in the whole-rock data	96
4.3	List of minerals which can luminesce, their luminescence colours and, where documented, known activator elements	98
4.4	Probe conditions for carbonate analyses	99
4.5	Composition of carbonates from different generations of Songwe carbonatite, analysed by EPMA.	114
4.6	Whole-rock data from Mauze nepheline syenites and dyke rocks.	118
4.7	Summary of the Mkango drillcore data, sorted into fenite, calcite-carbonatite, Fe-rich carbonatite and Mn-Fe- veins	121
4.8	Whole-rock major and trace data from Apatite-fluorite veins (C4) found in drillcore and from Chenga Hill	123
4.9	Nomenclature of the carbonatite types at Songwe Hill.	125
5.1	Standards used, and beam conditions for calibration.	146
5.2	Laser conditions for the different minerals analysed.	147
5.3	Elements and isotopes analysed by laser-ablation	148
5.4	Summary of the textural differences between the apatite at the Songwe Hill carbonatite.	149
5.5	Representative and average EPMA analyses of apatite from Songwe (part 1)	160
5.6	Representative and average EPMA analyses of apatite from Songwe (part 2)	161

²³light rare earth elements

²⁴mid rare earth elements

²⁵heavy rare earth elements

5.7	Average LA ICP-MS data for apatite from Songwe fenite and calcite-carbonatite samples.	162
5.8	Average LA ICP-MS data for apatite from Songwe Fe-rich carbonatite, Mn-Fe veins and apatite-fluorite vein samples	163
5.9	Composition of xenotime associated with zircon, Fe-oxides and rutile	167
5.10	Composition of xenotime associated with apatite in the apatite-fluorite veins	168
5.11	Composition of fluorite from C4 apatite-fluorite veins	170
5.12	Late-apatite-bearing samples analysed from Kangankunde and Tundulu.	183
5.13	Compiled sources of REE data from apatite.	202
6.1	Microthermometric fluid inclusion data from Ap-3.	216
6.2	Microthermometric fluid inclusion data from Ap-4	217
6.3	Microthermometric fluid inclusion data from C4 fluorite	218
7.1	Summary of different methods applied for deriving O-isotope values from the PO ₄ site in apatite	241
7.2	Sample details from worldwide carbonatites selected for stable isotope analysis.	244
7.3	Sample details and mineralogy of carbonatite samples from Songwe selected for stable isotope analysis	248
7.4	Stable isotope results for carbonates and apatite from Songwe and other carbonatites.	252
8.1	Metadata for laser-ablation MC-ICP-MS ²⁶ U-Pb dating.	282
8.2	Sample selection for zircon U-Pb dating and number of analysed zircons from each sample.	285
8.3	Laser-ablation U-Pb dating results	296
8.4	Published intrusion ages from other intrusions of the CAP	306
B.1	Standards used, and beam conditions for calibration.	368
B.2	Table of analysis conditions for EPMA analyses of xenotime.	370
C.1	Samples from drillcore	381
C.2	List of samples from outcrop	384
D.1	All whole-rock geochemistry data for each rock type.	395
D.2	Laser-ablation data for apatite from Kangankunde and Tundulu	397
D.3	Laser-ablation data for apatite from Kangankunde and Tundulu	399
D.4	Laser-ablation data for apatite from Kangankunde and Tundulu	401
D.5	Laser-ablation data for apatite from Kangankunde and Tundulu	403
D.6	Laser-ablation data for apatite from Kangankunde and Tundulu	405

²⁶multi-collector inductively coupled plasma mass spectrometer

List of Acronyms

Ap-0 Anhedral apatite grains hosted in fenite

Ap-1 Early ovoid apatite hosted in sövite

Ap-2 Apatite overgrowth on Ap-1

Ap-3 Anhedral stringers of HREE-rich apatite

Ap-4 Anhedral apatite with xenotime overgrowths

BGS British Geological Survey

BRGM Bureau de recherches géologiques et minières (French Geological Survey)

BSE back-scattered electron

C1 Sövitic calcite carbonatite

C2 Alvikitic calcite carbonatite

C3 REE-rich ferruginous calciocarbonatite

C4 Apatite-fluorite veins

CAP Chilwa Alkaline Province

CL cathodoluminescence

CRM Certified Reference Material

CSM Camborne School of Mines

DIW deionised water

EDS electron dispersive spectroscopy

EPMA electron probe micro-analyser

FT fission-track

FTIR Fourier Transform Infra-Red spectroscopy

HFSE high field strength elements

HREE heavy rare earth elements

HSAB Hard-Soft-Acid-Base

ICP-MS inductively coupled plasma mass spectrometry

ICP-OES inductively coupled plasma optical emission spectrometry

IOCG iron-ore-copper-gold

IC ion-counter

- IUGS** International Union of Geological Sciences
- IUPAC** International Union of Pure and Applied Chemists
- JICA** Japan International Co-operation Agency
- LA ICP-MS** laser ablation inductively coupled plasma mass spectrometry
- LIP** large igneous province
- LOD** limit of detection
- LOI** loss on ignition
- LREE** light rare earth elements
- MC-ICP-MS** multi-collector inductively coupled plasma mass spectrometer
- MORB** mid ocean ridge basalt
- MMAJ** Metal Mining Agency of Japan
- MREE** mid rare earth elements
- MS** mass spectrometry
- MSWD** Mean Square of Weighted Deviates
- NERC** Natural Environment Research Council
- NIGL** NERC Isotope Geosciences Laboratory
- OES** optical emission spectrometry
- OIB** ocean island basalt
- PGE** platinum group element
- PPL** plane-polarised light
- PIA** primary igneous apatite
- PIC** 'Primary Igneous Carbonatite'
- QEMSCAN** Quantitative Evaluation of Minerals by Scanning electron microscopy
- REE** rare earth elements
- REO** rare earth oxide
- SEM** scanning electron microscope
- SIP** species identification protocol
- SIMS** Secondary Ionisation Mass Spectrometry
- SRM** Standard Reference Material
- TC/EA** thermal conversion elemental analyser

TIMS thermal ionisation mass-spectrometry

TREE total REE

TREO Total Rare Earth Oxide

VPDB Vienna Pee Dee Belemnite

VSMOW Vienna standard mean ocean water

WDS wavelength dispersive spectrometry

XPL cross-polarised light

XRD X-ray diffraction

XRF X-ray fluorescence

Chapter 1

Introduction

1.1 Significance of the study

The REE¹ are a geochemically-similar group of elements composed of the lanthanoids (excluding scandium) and yttrium. They are considered by many to be among the most 'critical metals'. These are metals which are of growing economic importance but for which there is a risk of supply disruption (e.g. Fig. 1.1). The production of critical metals is generally restricted to a few countries and they are not readily substituted in many of their applications. Furthermore, global recycling rates are low.

More than 90 % of the global REE production is from China (Humphries, 2013). In recent years there have been several changes in China's REE export policies such that the long-term future of supplies to the West is uncertain. As a result there has been a surge in exploration for new deposits and a move to re-open old REE mines.

Most REE mines and many exploration projects exploit carbonatites or carbonatite-related deposits. Carbonatites are igneous rocks comprising greater than 50 % carbonate minerals. They are very high grade and high tonnage REE sources, but most are typically LREE²-rich and relatively HREE³-poor (chapter 2; Wall, 2014). Most analyses of future REE availability suggest that there will be no problem in meeting demand for LREE, whereas shortages of HREE are possible in the short- and medium-term (Bauer et al., 2011; Hatch, 2012). Indeed, the European Commission (2014) consider the HREE to be more critical than the LREE due to their higher supply risk (Fig. 1.1), and Hatch (2012) considers only Nd, Eu, Tb, Dy and Y, as critical due to their crucial use in high-strength permanent magnets and phosphors. Of these five elements, four are HREE.

Some REE deposits in carbonatites meet the grade and tonnage requirements

¹rare earth elements

²light rare earth elements

³heavy rare earth elements

for mining and they also have low U and Th contents, such that radioactivity does not constitute a significant problem for extraction. HREE enrichment is rare, but is currently of particular interest because of their critical status and prevailing high prices. Examples of HREE-bearing carbonatites include Lofdal, Namibia (Wall et al., 2008), and Khibina, Kola Peninsula, Russia (Zaitsev et al., 1998). These are characterised by post-intrusion hydrothermal fluids. However, our knowledge of the nature of these fluids, and the processes leading to HREE enrichment, is low. Furthermore, it is not known if some degree of HREE enrichment is a common process in carbonatites, which could potentially be exploited to account for the shortfall in HREE at carbonatite-hosted, LREE mines.

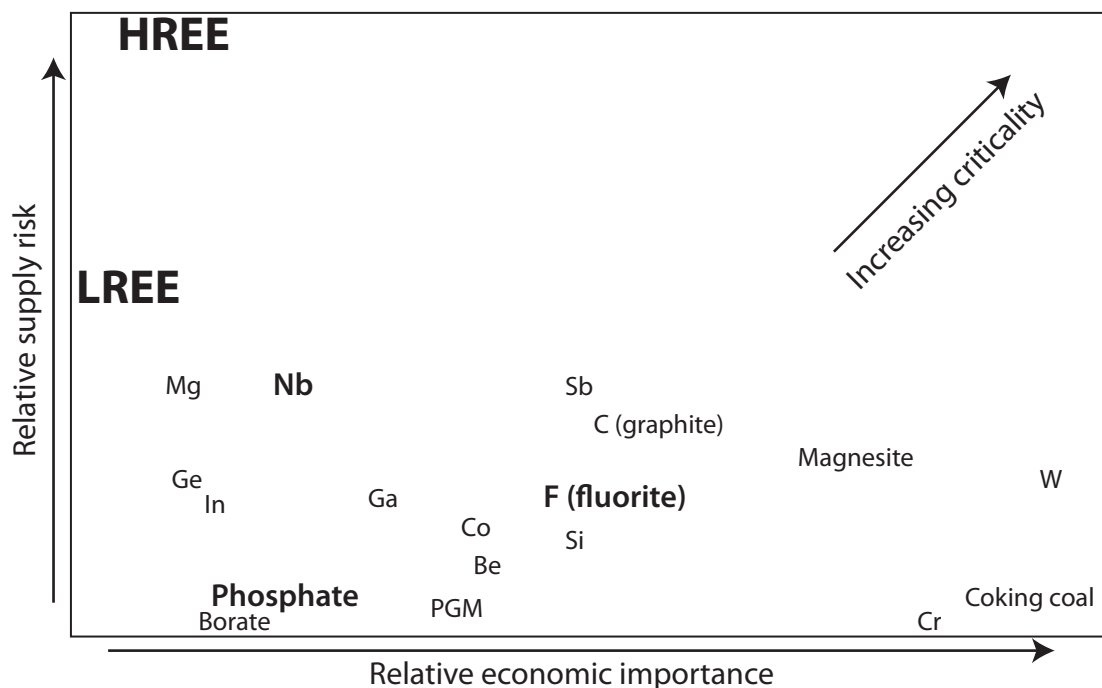


Figure 1.1: The criticality matrix evaluated by the European Commission (2014), modified to show only the elements in the arbitrarily defined 'critical' part of the graph, with relatively high risk of supply disruption and economic importance. NB, scales are relative, criticality increases toward the top-right. PGM: platinum group metals. The REE are highlighted, as are Nb, phosphate and F which are found in abundance in many carbonatites, but are not the subject of this study.

1.2 Aims and objectives

Accordingly, the objectives of this study are to:

- Identify the potential HREE-enriched phases in carbonatite
- Elucidate the conditions that led to HREE enrichment
- Develop a model for HREE enrichment in carbonatites

1.3 Approach

To carry out these aims, this thesis presents a detailed mineralogical, petrological, geochemical and isotopic study of the Songwe Hill carbonatite, Malawi. This carbonatite was chosen because it is a LREE deposit under active exploration, with early indications indicating that it was anomalously HREE-enriched. Furthermore, it is part of the well-known CAP⁴, and access to comparison carbonatites was relatively simple (Chapter 3).

The mineral hosts for the HREE, the mineral paragenesis, and the source and nature of the fluids involved in forming the minerals are constrained. Apatite is shown to be important in controlling the HREE at Songwe, so apatite from two further carbonatite examples was analysed for comparison. Some samples from the neighbouring Mauze nepheline syenite were also dated and analysed since very few data are available for this intrusion.

This work was mostly carried out at CSM⁵ and the BGS⁶. Isotopic analyses were carried out at NIGL⁷ and fluid inclusion work was undertaken during a short visit to McGill University.

1.4 Study Area

Work at the Songwe Hill carbonatite was carried out in collaboration with the exploration company Mkango Resources Ltd. Few geological data have been previously presented on Songwe. Therefore, a further objective of this thesis is to understand more about the geochemistry and mineralogy of the different intrusion stages of the carbonatite in the context of the CAP. Two field seasons were spent at Songwe, with logistical support and training from Mkango. Access to core samples and geochemical data were also generously provided.

1.5 Structure of the thesis

Chapter 2 introduces the reader to carbonatite-hosted REE-deposits and the known controls on their formation. Subsequent chapters present data, with each being broadly split into different analytical techniques, and including a detailed mineralogy. The data chapters are split into three overarching themes: the first two (chapters 3 and 4) document the general geology of Songwe, incorporating new mapping work, geochemistry, petrography and mineralogy; the following

⁴Chilwa Alkaline Province

⁵Camborne School of Mines

⁶British Geological Survey

⁷NERC⁸ Isotope Geosciences Laboratory

chapter (chapter 5) explores potential host minerals for the HREE in carbonatites, focussing on xenotime and apatite; chapters 6, 7 and 8 explore the role of hydrothermal fluids in mobilising the HREE. Fluid inclusions are used to constrain temperature and composition, and an isotope study attempts to constrain the source of the fluids. Using these data, a model is suggested for the transport, fractionation and precipitation of the HREE.

Chapter 2

A review of carbonatites and rare earth elements: definition, genesis, and formation of ore-deposits

This chapter reviews the classification, composition, occurrence and genesis of carbonatites; the properties and uses of the REE; the different types of REE deposit; and the current state of knowledge of the transport and enrichment of the REE from the mantle through to hydrothermal ore deposits.

2.1 Carbonatites

More than 500 occurrences of the igneous carbonate rocks, carbonatites, are known. They are distributed globally, but often concentrated in stable, Precambrian, intra-plate cratons, along lineaments related to rifting (Woolley, 1989; Woolley and Kjarsgaard, 2008a). They are emplaced both intrusively and extrusively and can be temporally and spatially associated with a diverse range of (typically alkaline) silicate rocks (e.g. Woolley, 2001). The source region of carbonatites is debated, with some researchers favouring a lithospheric-mantle source on the basis of continued carbonatite and alkaline volcanism at the same site over geological time (e.g. Woolley and Bailey, 2012), while others favour an asthenospheric-mantle source based on isotopic data (e.g. Bell and Simonetti, 2010). Petrogenetic models for carbonatites are also diverse, with three different proposed mechanisms for carbonatite formation: (1) direct mantle melts, (2) liquid immiscibility from CO₂ saturated silicate melts, and (3) residual melts of fractionated carbonated nephelinite or melilitite; combinations of these theories are also common (Jones et al., 2013). Once formed, carbonatites commonly evolve to higher Fe, REE and Sr contents (Le Bas, 1989). From an economic perspective, carbonatites can host several critical materials, such as the REE, niobium and fluorite as well as iron, copper, apatite and vermiculite and by-products such as barite,

baddelyite, tantalum and uranium. The Phalaborwa carbonatite in south Africa also hosts significant PGEs¹, gold and silver (Mariano, 1989).

2.1.1 Classification

The IUGS² defines carbonatite as an igneous rock containing at least 50 % modal carbonate and less than 20 % silica (Le Maitre, 2002). This has been questioned on the grounds that it groups all rocks with more than 50 % carbonate together, despite an apparent diversity of origin. An alternative has been proposed where the system is split between igneous and “carbothermal” carbonatite (Mitchell, 2005). In this system igneous carbonatite is defined as > 30 % carbonate, with no silica limit, with principal minerals prefixed in ascending order, while carbothermal residua should include a description of not only the rock, but also the antecedent. In this thesis the IUGS definition is used because of the igneous origin of the carbonatites studied.

Following the IUGS system, carbonatites are named first on the dominant carbonate mineral in the rock (Woolley and Kempe, 1989). These are as follows:

Calcite-carbonatite where the main carbonate is calcite, subdivided into:

- alvikite: medium–fine-grained calcite carbonatite
- sövite : coarse-grained calcite carbonatite

Dolomite-carbonatite (Beforsite) where the main carbonate is dolomite

Ankerite-carbonatite where the main carbonate is iron rich

Natrocronatite composed of sodium, potassium and calcium carbonate, and only found at Oldoinyo Lengai, Tanzania

Failing mineralogical identification, similar nomenclature bands can be assigned based on whole rock modal CaO, MgO and (FeO + MnO) concentrations (Woolley and Kempe, 1989) or on calculated cation concentrations (Gittins and Harmer, 1997). These groups are calciocarbonatite, magnesiocarbonatite, ferrous calciocarbonatite and ferrocarbonatite, respectively.

2.1.2 Composition

The major minerals in carbonatites are dominantly carbonates: calcite, dolomite and ankerite. The alkali carbonates, gregoryite and nyerereite, are limited to natrocronatites from Oldoinyo Lengai. Other minerals commonly present are

¹platinum group elements

²International Union of Geological Sciences

apatite, magnetite, olivine, phlogopite, diopside and accessory pyrochlore, periclase, spinel, baddeleyite, fluorite, monazite and REE-fluorcarbonates.

The major elements in carbonatites are CaO, MgO, FeO, P₂O₅ and CO₂, with variable concentrations of, SiO₂, SrO, BaO, MnO and low concentrations of TiO₂, Al₂O₃, K₂O and Na₂O. The trace elements REE, U, Pb, Th, Nb, Sr and Ba are typically enriched, relative to primitive mantle. REE profiles of carbonatites, relative to chondrite, show strong enrichment in all the REE, especially the LREE, and display no Eu anomaly.

There is a general trend, in carbonatite composition, from early calcite-carbonatites through dolomite carbonatite to later ankerite carbonatite (Le Bas, 1989). With this evolution the REE concentration increases, though it is not observed in all REE-rich carbonatite (e.g. Mountain Pass; Castor, 2008). During the later stage of carbonatite emplacement, as carbonatites transition from a magmatic to a hydrothermal regime, fluids are expelled from carbonatite (Rankin, 2005). These fluids lead to REE, barite, strontianite and fluorite mineralisation and carbonate veins.

2.1.3 Occurrence

Carbonatites can be emplaced both intrusively and extrusively. Intrusive carbonatites are the most common occurrence, found as dykes, ring dykes, cone sheets, diatremes and subvolcanic pipes and plugs (Barker, 1989).

Extrusive carbonatites, first discovered in the 1960s (Dawson, 1962), are less well known. Only 10 % of carbonatites contain an extrusive component (Woolley and Church, 2005), although research into new extrusive carbonatite occurrences is expanding (Bailey and Kearns, 2012). Most of these are pyroclastic, with lava flows known at only a few sites. The most famous carbonatite volcano is Oldoinyo Lengai in Tanzania. This is the only active carbonatite volcano and the only known locality where natrocarbonatite is found.

Most carbonatites occur surrounded by an alkali metasomatic aureole composed of fenite. Fenite is split into sodic and potassic varieties, both formed from fluids sourced from the intrusion. Potassic fenite comprises K-feldspar, while sodic fenite comprises Na-rich amphibole with albite and K-feldspar. Younger carbonatite intrusions, with a shallow depth of erosion, are usually accompanied by potassic fenite, with a high degree of brecciation, while older intrusions, with a deeper erosion depth, generally are accompanied by sodic fenite, with much less brecciation (Le Bas, 2008).

Many carbonatites are intruded after various accompanying silicate rocks. These are commonly alkali-silicate rocks such as nephelinite-ijolite, nepheline syenite and syenite but carbonatites are also common accompanying kimberlite, lamprophyre and phoscorite (Krasnova et al., 2004; Woolley and Kjarsgaard,

2008b). Carbonatites with no accompanying silicate rocks are also known, and the carbonatite–silicate connection is not well understood (Harmer and Gittins, 1997).

2.1.4 Petrogenesis

Source

Radiogenic isotope ratios for $^{87}\text{Sr}/^{86}\text{Sr}$ and $^{143}\text{Nd}/^{144}\text{Nd}$ from carbonatites plot in a similar field to OIB³, being more enriched (higher $^{87}\text{Sr}/^{86}\text{Sr}$, lower $^{143}\text{Nd}/^{144}\text{Nd}$) than MORB⁴, spanning a range between HIMU (mantle with a high mu value) and EM1 (enriched mantle). The close similarity between carbonatites and OIB suggests the parental magmas are derived from a long-lived depleted mantle source, either from the lithosphere or sub-lithosphere (Bell et al., 1998; Bell and Tilton, 2001). Near-linear $^{143}\text{Nd}/^{144}\text{Nd}$ ratios with time suggest that enrichment in the LREE must have occurred at the time of magma genesis, either by immiscibility, vapour phase transfer or low degrees of partial melting in a garnet-rich source (Bell and Blenkinsop, 1989). Stable O, C and S isotopes are also indicative of a mantle source region (Deines, 1989).

The processes of carbonatite emplacement between the mantle and the surface are the subject of debate with two main causes of partial melting commonly invoked. Isotopic signatures of carbonatite suggest a mantle plume component (Bell and Simonetti, 2010), while repeated intrusions at the same, cratonic, locations over large spans of geological time suggest a control within the lithosphere (Woolley and Bailey, 2012).

Genesis

Once a carbonate, or siliciocarbonate, melt has begun to form, there are three main theories regarding the genesis of a carbonatite magma:

1. Residual melts of the fractional crystallisation products of a carbonatite melilite or nephelinite magma (Gittins, 1989).
2. Liquid immiscibility between carbonate and silicate melts (Lee and Wyllie, 1997, 1998).
3. Direct formation of carbonatite in the mantle through partial melting of a CO₂-bearing peridotite, and rapid ascent (Harmer and Gittins, 1997, 1998).

³ocean island basalt

⁴mid ocean ridge basalt

In the first two models, a carbonated-silicate melt forms in the mantle, or at depth in the lithosphere, and ascends to the surface with little chemical reaction. This liquid may then separate into silicate and carbonate portions, either by fractional crystallisation or by liquid immiscibility. Alternatively, carbonate fluids can be produced by partially melting carbonated mantle peridotite at depth, forming magnesian carbonate. Upon ascent this would react with orthopyroxene present in Iherzolite and harzburgite and undergo 'chemical death'. However, it may be possible for a melt to avoid this by rapid ascent before equilibrium can be established or by forming and travelling through a metasomatic wehrlite conduit (Harmer and Gittins, 1997, 1998). Various combinations of these models have also been proposed.

Evolution

Le Bas (1977, 1981, 1987) devised a general petrogenetic model relating the nephelinite group of rocks to associated carbonatites, based predominantly on carbonatites from the East African Province (Fig. 2.1). This model has become the generally accepted carbonatite model. It suggests that carbonatites and associated nepheline-bearing rocks are the eroded cores of extinct nephelinite volcanoes. The model favours the intrusion of a carbonated nephelinite magma into the lower crust which undergoes immiscible separation into a volatile-rich liquid and a silicate liquid. Importantly, the volatile-rich fluid evolves, fractionates apatite and mafic silicates, and exolves Na- and K-bearing fluids to fenitise the country rock. This fluid rapidly ascends to the surface and produces carbonatite lavas and pyroclastics. If the carbonatite continues to evolve, it becomes more Fe-, REE-, Sr- and Ba-rich, evolving from sövite, through alvikite, towards ferrocarnatite. Mineralising fluids can cause successive deposits of the REE, fluorite, quartz veining and, lastly, U-Th deposition.

2.2 Rare earth elements

2.2.1 Definition

The REE comprise the 15 elements of the lanthanoid series of the Periodic Table, plus yttrium and scandium. In geochemical and mineralogical studies, promethium and scandium are excluded from this group as, respectively, they have no stable isotopes or behave markedly differently; leaving a total of 15 elements (Table 2.1). The REE are grouped together because they exhibit similar geochemical characteristics and are difficult to separate from each other chemically. Such was the difficulty in separating them that it took approximately 150 years from the first

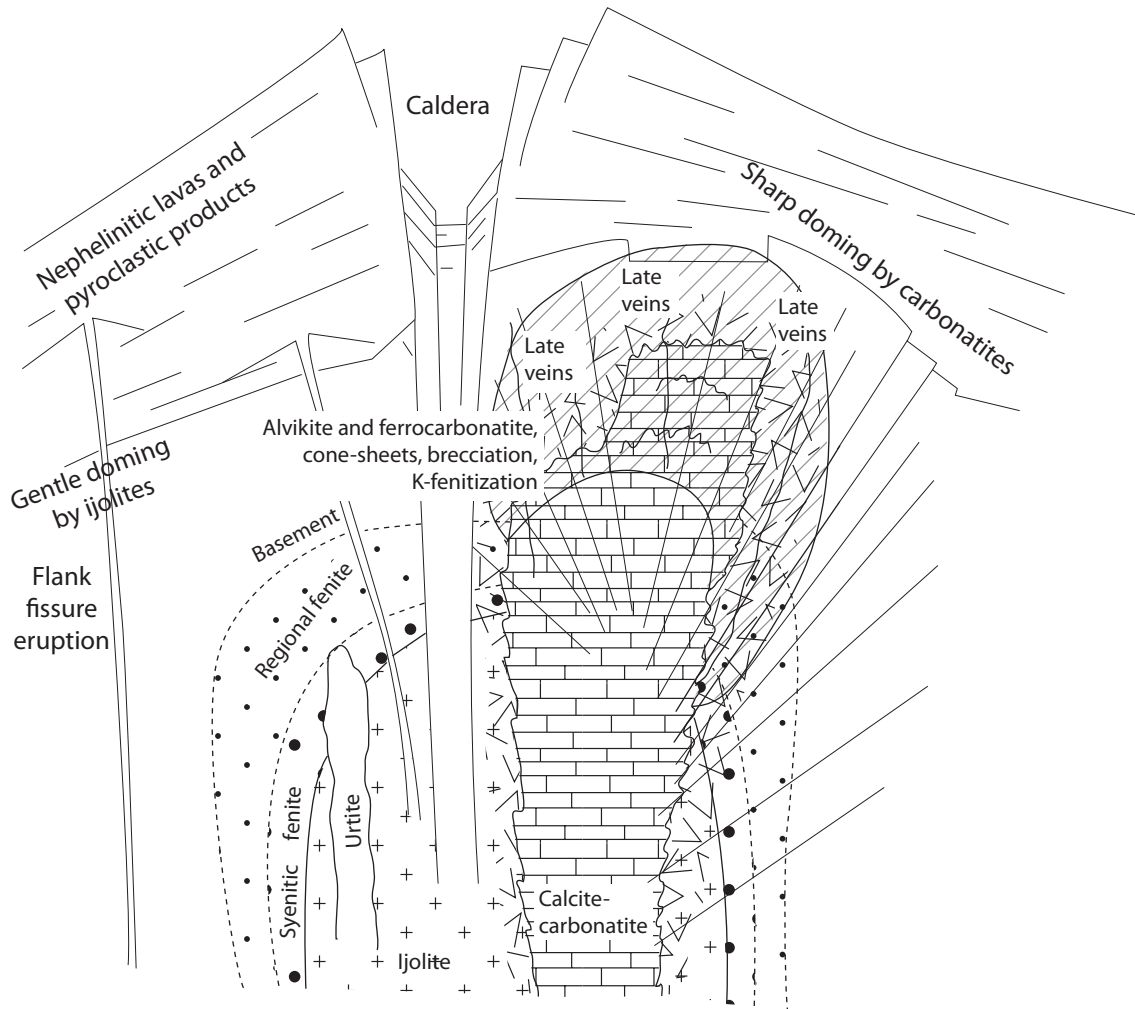


Figure 2.1: Petrogenetic model relating carbonatites to nephelinites, redrawn after Le Bas, 1987.

isolation of 'Yttria' (itself a mix of Y, Tb and Er) to the isolation of all the individual REE, including Pm (Wall, 2014).

A_N	Symbol	Name	Radii (nm)	Abundance (ppm)
39	Y	Yttrium	9.00	21.00
57	La	Lanthanum	10.32	31.00
58	Ce	Cerium	10.10	63.00
59	Pr	Praseodymium	9.90	7.10
60	Nd	Neodymium	9.83	27.00
61	(Pm)			
62	Sm	Samarium	9.58	4.70
63	Eu	Europium	9.47	1.00
64	Gd	Gadolinium	9.38	4.00
65	Tb	Terbium	9.23	0.70
66	Dy	Dysprosium	9.12	3.9
67	Ho	Holmium	9.01	0.83
68	Er	Erbium	8.90	2.30
69	Tm	Thulium	8.80	0.30
70	Yb	Ytterbium	8.68	2.00
71	Lu	Lutetium	8.61	0.31

Table 2.1: Names and symbols of the REE (after Henderson, 1996). Radii are for REE with an VI coordination number; abundance is the concentration in the upper continental crust (after Rudnick and Gao, 2003). Promethium has no natural long-lived nuclei and, therefore, no natural abundance.

2.2.2 Chemical characteristics

The REE share similar geochemical characteristics because additional electrons are accommodated into the inner 4f shell, with the exception of Gd, La and Lu which are able to accommodate 1 electron into the 5d shell. As a result the REE, with two exceptions, maintain the same 3+ oxidation state. The two exceptions are Eu^{2+} and Ce^{4+} which can form under reducing and oxidising conditions, respectively. Different oxidation states of the some of the other REE are known, but seldom occur in nature.

The major difference between the properties of the REE is the systematic decrease in atomic radii across the group, known as the lanthanide contraction. This is caused by the positive charge of the nucleus increasing with atomic number (and weight) while electrons added in the f orbital do not screen the other electrons from the positive pull. This contraction varies the size of the 3+ ion from 10.32 nm for La to 8.61 nm in Lu (Henderson, 1996). Yttrium has a similar 3+ charge and a cation radius of 9 nm and, thus, fits in the sequence between Dy and Ho (Table 2.1). This variation in ionic radius leads to the differentiation of the

REE, by weight, into the LREE⁵ and HREE⁶, with some also favouring an extra group, the MREE⁷. There is some variation in the definitions of each group (Table 2.2). Conventionally, the LREE include La–Eu, and the HREE include Gd–Lu + Y, although Eu is often included as a HREE by, for example, the IUPAC⁸. Often economic geologists also favour the IUPAC definition because it is the approximate division between the REE of low and high value. Mineralogists prefer a boundary between Gd and Tb, where REE phosphates switch from a monoclinic (monazite) to a tetragonal (xenotime) structure. This is also the point where the REE switch from partially filled $4f$ orbitals to full $4f$ orbitals. Process engineers separate the REE into three groups based on the behaviour of the REE during chemical separation. The term ‘critical’ REE is occasionally used to denote REE with the highest risk of supply disruption.

Grouping basis	LREE	MREE	HREE	Example reference
‘Conventional’	La–Eu		Gd–Lu + Y	Chakhmouradian and Wall (2012)
Economic/IUPAC^a	La–Sm		Eu–Lu + Y	Wall (2014)
Mineralogical	La–Gd		Tb–Lu + Y	Mariano and Mariano (2012)
Process engineering	La–Nd	Sm–Gd	Tb–Lu + Y	Hatch (2012)
‘Critical’	(Nd)		(Eu, Tb, Dy, Y)	Hatch (2011)

Table 2.2: Different definitions of the LREE^b, MREE^c and HREE^d used in the literature, with the definition used in this thesis in bold. Also included are the ‘critical’ REE, which are so-called because these elements are predicted to be at the highest risk of supply disruption.

^aInternational Union of Pure and Applied Chemists

^blight rare earth elements

^cmid rare earth elements

^dheavy rare earth elements

2.2.3 Abundance

The abundance of the REE in the continental crust decreases with increasing atomic number but the notion that the ‘rare’ earths are rare is false. The most abundant REE, Ce, is more abundant than copper and the least abundant REE, Lu, is more abundant than gold (Fig. 2.2). What makes the REE ‘rare’ is that chemical and geological separation of individual REE is difficult. This causes two problems: first, they are not easily concentrated into rich deposits, and the

⁵light rare earth elements

⁶heavy rare earth elements

⁷mid rare earth elements

⁸International Union of Pure and Applied Chemists

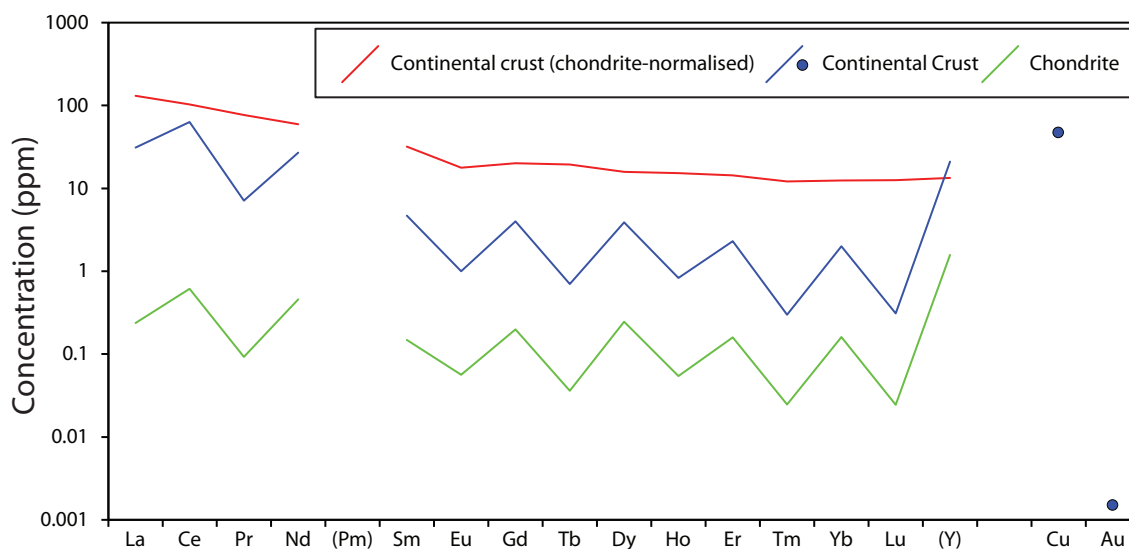


Figure 2.2: Abundances (ppm) of the REE in the continental crust, chondrite and the same continental-crust concentrations normalised to chondrite. Values from Rudnick and Gao (2003); McDonough and Sun (1995).

abundance is spread out across all of the continental crust; and, second, some of the REE are rarer than others meaning demand for a less-abundant REE will cause a more-abundant REE to be over-supplied.

Variation in the abundance of the REE is due to nucleosynthetic processes and the incompatibility of the LREE in the mantle during partial melting. The results of nucleosynthesis are best observed in the REE concentration of a C1 chondrite (Fig. 2.2). Looking at the even-atomic-numbered REE (e.g. Ce, Gd, Yb) it is clear that the concentration of these elements decreases with increasing atomic number. However, it is also clear that the concentration of these is much greater than the odd-atomic-numbered REE. This is due to the Oddo-Harkins effect, where odd-numbered nucleides are less stable than even-numbered ones, leading to a 'zig-zag' variation in abundance. Because of these effects it is common to normalise REE plots to chondritic meteorites (Fig. 2.2).

Chondrite-normalised REE distributions for the continental crust are LREE enriched. This is due to partial melting of the mantle and the varying cation size of the REE. During low-degree partial melting the larger LREE are much more incompatible in mantle minerals than the smaller HREE. Therefore the HREE are retained in the source residue, while the LREEs enter the melt and ascend, becoming enriched in the crust.

2.2.4 Mineralogy

The REE are not found as native metals. They occur either as trace or minor constituents of other minerals or as REE minerals. Over 200 REE-bearing minerals are known. These occur as a wide range of types including borates, carbonates,

oxides, halides, silicates, phosphates, arsenates, sulphates, vanadates, uranyl-carbonates and uranyl-silicates. The most common and important of these are listed in Table 2.3. The most abundant REE in each mineral is indicated in parentheses e.g. xenotime-(Y), although the REE site will accommodate all of the REE to a low concentration. REE can also reach high concentrations in minerals where they easily substitute into other cation sites (e.g. Ca^{2+} in apatite and calcite) and these minerals can accommodate the bulk of the REE in rocks where REE minerals are not found.

Mineral	Formula
Carbonates/Fluorcarbonate	
ancylite-(Ce)	$\text{SrCe}(\text{CO}_3)_2(\text{OH}) \text{H}_2\text{O}$
bastnäsite-(Ce)	CeCO_3F
parisite-(Ce)	$\text{CaCe}_2(\text{CO}_3)_3\text{F}_2$
synchysite-(Ce)	$\text{CaCe}(\text{CO}_3)_2\text{F}$
Phosphates	
monazite-(Ce)	CePO_4
xenotime-(Y)	YPO_4
florencite-(Ce)	$(\text{Ce})\text{Al}_3(\text{PO}_4)_2(\text{OH})_6$
fluorapatite	$\text{Ca}_5(\text{PO}_4)_3\text{F}$
Oxides	
cerianite	CeO_2
Silicates	
allanite-(Ce)	$\text{CaNdAl}_2\text{Fe}^{2+}(\text{SiO}_4)(\text{Si}_2\text{O}_7)\text{O}(\text{OH})$
britholite-(Ce)	$(\text{Ce,Ca,Sr})_2(\text{Ce,Ca})_3(\text{SiO}_2,\text{PO}_4)_3(\text{O,OH,F})$

Table 2.3: Some common REE minerals after Wall (2014)

2.2.5 Importance of the REE

The REE are important both academically and economically. In geochemistry, the lanthanide contraction causes the REE to have smooth, systematic distribution coefficients with atomic number. This can be useful for modelling mineral or rock genesis. The presence and magnitude of Ce and Eu anomalies in the REE distribution can also be used to infer redox conditions during rock formation and, in the case of Eu, processes in the presence of plagioclase. The REE are also used in isotope geoscience for dating of rocks, modelling magma mixing and as an indicator of provenance.

Economically, the REE are used in a wide variety of high-tech applications, although often in small amounts; the total consumption of REE, worldwide, was

115,000 tonnes in 2012 (Wall, 2014). Demand for the REE has generally increased since the 1950s, but levelled-off between 2008–2011 due to the volatility in REE price (Table 2.4). Projected REE requirements in the future, however, are set to increase, especially due to demand from REE permanent magnets for clean energy technology (Hatch, 2012; Alonso et al., 2012). In 2012 production of these magnets uses 20 % of the REE supply (Wall, 2014). Other uses for the REE include metal alloys, catalysts, polishing powders, phosphors, glass additives and ceramics (Table 2.4).

The REE are considered by many organisations to be a ‘critical metal’ e.g. the UK (Lusty and Walters, 2011), the EU (European Commission, 2014; Buchert et al., 2009), the USA (Long et al., 2010), and Australia (Hoatson et al., 2011). In the case of the REE the main factor affecting its ‘criticality’ is the concentration of production in China. In 2010, about 97 % of global production was in China, although this fell to less than 90 % in 2014 as new mines came on stream (Henderson et al., 2011; Long et al., 2010). This is compounded by the difficulties of substituting the REE with other elements and the low REE recycling rates.

Use	Consumption (kt)		Forecast 2016	Elements used
	2008	2011		
Catalysts	25	20	25	La, Ce (Pr, Nd)
Glass	12	8	10	Ce, La, Pr, Nd, Gd, Er, Ho
Polishing	15	14	18	Ce, La, Pr, Nd, Gd, Er, Ho
Alloys	22.25	21	30	La, Ce, Pr, Nd, Y
Magnets	26.25	21	36	Nd, Pr, (Tb, Dy)
Phosphors	9	8	12	Eu, Y, Tb, Nd, Er, Gd, (Ce, Pr)
Ceramics	7	7	10	La, Ce, Pr, Nd, Y, Eu, Gd, Lu, Dy
Other	7.5	6	19	All

Table 2.4: Uses and consumption of the REO^a (kt) in 2008, 2011 and forecast for 2016. 2008 data from Lusty and Walters (2011), 2011 and forecast data from Hatch (2012).

^arare earth oxide

2.2.6 Importance of the HREE

The HREE can be considered as more ‘critical’ than most of the LREE because of their lower abundance (Fig. 2.2) and greater economic value. Specifically, all of the critical REE (Table 2.2), except Nd, are HREE. The high criticality of these elements is chiefly driven by demand in REE permanent magnets and phosphors.

The economic value of the REE is strongly influenced by their supply. There is an over supply of the LREE (except Nd) and shortage of the HREE because of the LREE-rich nature of the upper crust and the rarity of geological separation of

the REE. It is, therefore, predicted that the LREE will be oversupplied in the near future but the HREE will be under-supplied. These, unlike the LREE, will maintain a high demand for at least 4 years (Hatch, 2011, 2012). The price difference between the REE reflects this factor: Ce oxide, for example, has a price of $< \$ 20 \text{ kg}^{-1}$ while Eu oxide has a price of $> \$ 500 \text{ kg}^{-1}$ (Metal-pages, 2014) (Fig. 2.3). The low consumption of the HREE, however, can cause these prices to fluctuate rapidly over a wide range.

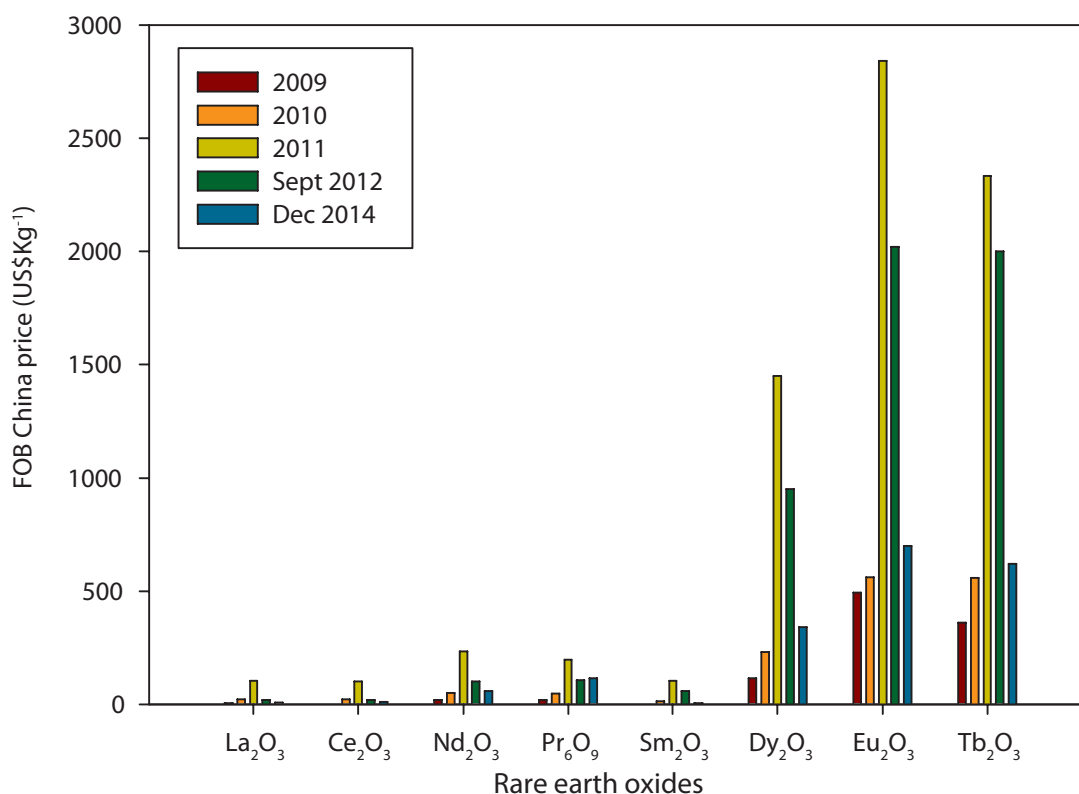


Figure 2.3: Variations in the REE prices between the HREE and LREE since 2009. Data from Metal-pages (2014). FOB, Free On Board price, indicating the price of the oxide, plus transport and loading onto a ship for export.

2.3 REE deposits

Demand for the REE, driven by the use of Nd-magnets and REE-phosphors, combined with a restriction in exports from China, has caused a resurgence in exploration for REE deposits. As previously mentioned, the REE are not particularly rare, and this is reflected in the abundance of potential REE-deposits. Figure 2.4 demonstrates the worldwide distribution of REE exploration projects at the 'advanced stage' (those with a formally defined mineral resource or reserve), and the total tonnage of REO available to be mined at these deposits. Also included are the locations of some of the major active and historic REE producing regions and, where possible, an indication of the amount of REO extractable from these

deposits. It is clear from this figure that REE deposits are globally distributed and, considering that annual demand for the REE is approximately 150–170 kty⁻¹ (Hatch, 2012), potential supply could far outweigh demand.

There are several different types of REE deposits, each with different characteristics. The main types are: carbonatite, alkaline rock, placer deposits and ion-adsorption deposits. Minor and un-utilised sources include hydrothermal deposits, IOCG⁹ deposits, mine waste and, looking into the future, sea floor and extra-terrestrial deposits (Kato et al., 2011; Taylor and Martel, 2003). There are many deposits worldwide, the main characteristics which vary between them are grade, tonnage, REE distribution, environmental impacts, mineralogy, metallurgy, location, proportion of radioactive minerals, other environmental implications and economic factors, such as vertical supply chain integration, available workforce, etc (Table 2.5).

2.3.1 Carbonatites

REE deposits in carbonatites are typically high grade and high tonnage deposits and the largest working (and worked) REE-deposits are all carbonatite related (Bayan Obo, China; Mountain Pass, USA; Mt Weld, Australia). The REE mineralogy varies between relatively simple, well-understood, minerals such as monazite and bastnäsite, to much more complex and difficult to process minerals such as those of the crandallite group. Carbonatite-derived monazite is ubiquitously low in Th which is advantageous for transport and processing (Weng et al., 2013). Carbonatites can also be major Nb and F sources, and, because of the ease of chemical weathering of carbonates, deep weathering profiles can form above carbonatites, causing residual enrichment in Nb and REE-minerals. The major disadvantage of carbonatite-hosted REE-deposits is their low HREE concentration and lack of an extractable HREE-bearing phase.

2.3.2 Alkaline Rocks

In this thesis the term 'alkaline rock' is applied *sensu lato* and covers all forms of Na- and K-rich and Si- and Al-poor intrusions. In these rock types the REE are enriched through a combination of low-degree partial melts and an extremely high degree of crystal fractionation. Furthermore, the most REE-rich alkaline intrusions usually feature autometasomatism, where intrusion-derived fluids react with the rock and further upgrade the REE concentration.

Alkaline igneous intrusion-related REE deposits are notable for having a high concentration of the HREE, large tonnages and commonly an abundance of Zr,

⁹iron-ore-copper-gold

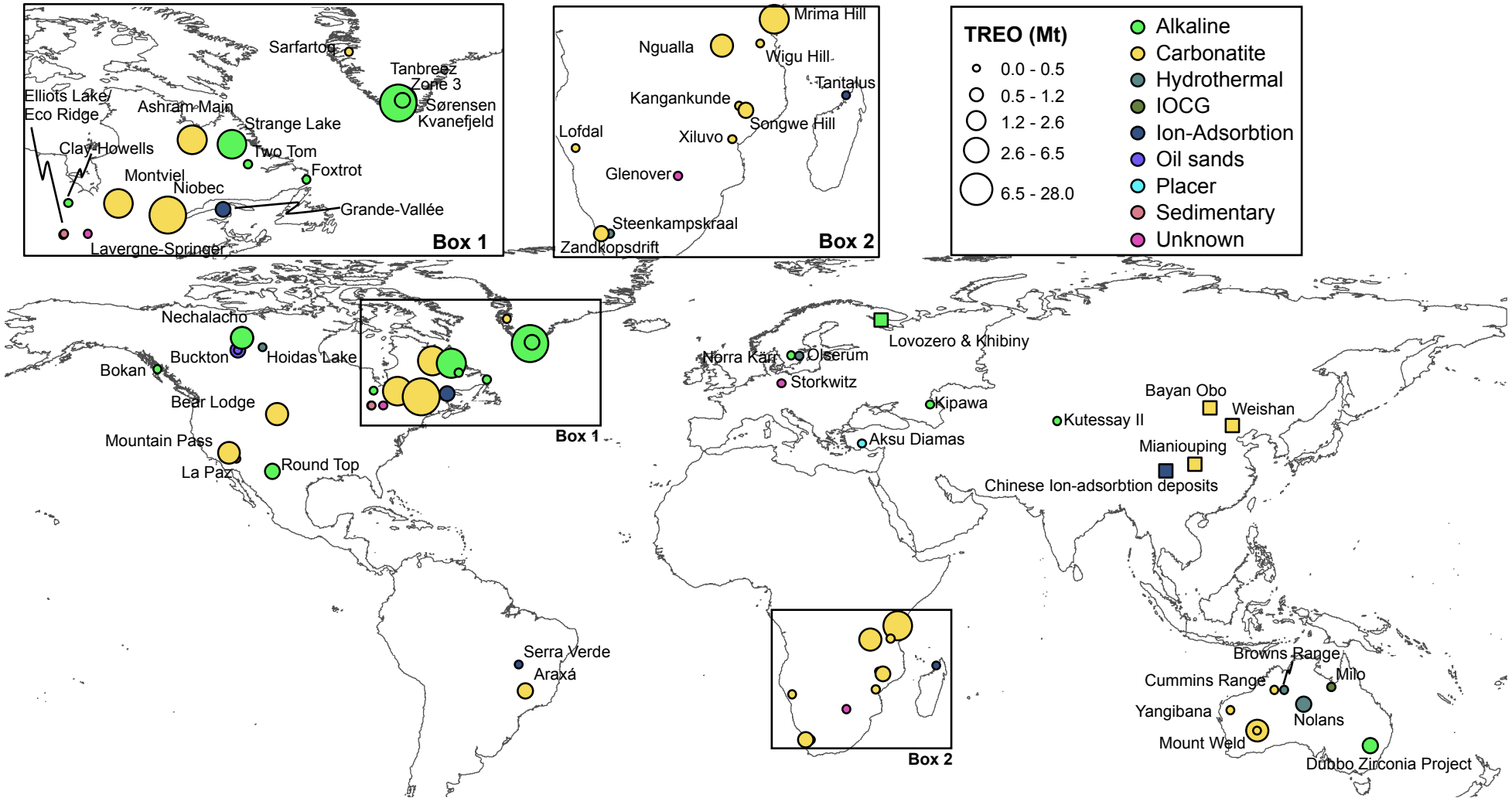


Figure 2.4: Spatial distribution and REE tonnages (both resources and reserves) of the different types of REE-deposit at an advanced stage. Also included are the locations of important REE-deposits without tonnage data. Data sourced from Technology Metals Research (2015).

Criteria	Carbonatite	Alkaline rocks	Placer	Ion-adsorption
Grade:	High	Low	Mid/Low	v. Low
Tonnage:	High	High	High	Low
HREE proportion:	LREE	HREE	LREE	L/HREE
Mineralogy:	Constrained/ Understood	Varied	Constrained/ Understood	N/A
Radioactive issues:	Low	High	High	Low
Ease of extraction:	Mid-hard	Hard	Easy	Easy
Other issues:				Illegal mining, environmental problems

Table 2.5: Advantages and disadvantages of the major REE-deposit classes.

Nb, and U. Grades of the TREE¹⁰ are typically low, although they may still be economically favourable owing to the high-very high HREE contents. Mineralogically, alkaline intrusions can be very complex, often deceptively so, such that minerals which are, in theory, easy to process, such as eudialyte, are often pseudomorphed by much more complicated mineral assemblages (e.g. Coulson, 1997; Mitchell and Liferovich, 2006; Sheard et al., 2012). Furthermore, Th and U levels may be high in this deposit type, although this is not a universal feature. Other factors influencing the viability of an alkaline intrusion REE-deposit include the 'hard-rock' nature of the host intrusions, which would require extensive blasting and crushing, and the location. Some of the largest alkaline intrusions are in northern Canada, Alaska and Greenland. Access would require extensive road building or the construction of a deep-water port.

2.3.3 Placer deposits

Placer deposits include modern and palaeo heavy mineral sands. Historically, Indian beach sands were the main source of global REE supply prior to the development of Mountain Pass, in the USA, in the 1960s. The REE are found in the heavy minerals monazite and xenotime, which are commonly associated with ilmenite, rutile and zircon.

These deposits are low grade, generally large in volume, and the REE minerals can be extracted as a by-product of Ti and Zr. They are easy to work, requiring little to no crushing. Currently, however, at active mineral sand extraction operations, REE-bearing minerals are not extracted or stockpiled, and are re-buried in-situ. This is because of the high Th concentration in monazite which means any stockpiled monazite concentrate would be too radioactive to transport or process.

¹⁰total REE

2.3.4 Ion-adsorption deposits

In this thesis, the term 'ion-adsorption' denotes any deposit where the REE are found in the weathered horizon of a rock, adsorbed on clay minerals. It does not include deposits where the REE have been upgraded through weathering and removal of gangue minerals, such as at laterites above a carbonatite.

Ion-adsorption type deposits, mostly found in southern China, supply a large proportion of the global HREE demand. This deposit type, however, is one of the most enigmatic REE sources and is not well understood. Two factors are known to be required:

1. A deep, tropical weathering profile with low erosion rates
2. A readily-leachable REE mineral phase in the weathered host rock

Breakdown of REE-minerals in the parent rock releases REE, which adsorb via cation-exchange or chemisorption onto clay minerals such as kaolinite, halloysite and smectites in the deeply weathered zone. This process can enrich the weathered horizon in REE up to five times relative to the parent rock (Kynicky et al., 2012).

The grades and tonnages of ion-adsorption deposits are very low (0.05–0.2 wt. % REO; Kynicky et al., 2012). However, the deposits are easy to mine and in some cases can be mined in-situ with little need for heavy machinery. Their U and Th contents are also low. However, their exploitation in numerous small-scale pits over extensive areas and associated groundwater pollution has caused serious environmental damage. Ion-adsorption deposits are typically HREE rich but the REE distribution varies from LREE-enriched deposits to HREE-enriched deposits. This is likely to be controlled by the REE distribution of the protolith (Sanematsu et al., 2013).

2.3.5 Other deposit types

Other potential REE sources include hydrothermal veins of unknown provenance (i.e. not related to a known intrusion; e.g. Steenkampskraal, South Africa, Andreoli et al., 1994), IOCG deposits (e.g. Olympic Dam, Australia), and by-products, co-products and waste sources.

The potential to extract REE as a co-product, a by-product, or from waste are particularly attractive. A co-product is defined as being of equal importance to the main product and intentionally produced as part of the same mineral-processing flowsheet. A by-product is a secondary or incidental product which can be refined after processing if it is technically feasible to do so and under favourable economic conditions. Waste is what remains when the commodities of interest have been

removed. It can be, therefore, enriched in other metals which were not targets of the primary extraction.

Phosphate extraction is a favourable source for REE co- or by-product extraction (Emsbo et al., 2015). It is extracted from both sedimentary and igneous sources for use in fertiliser, and extraction of the REE could take place during processing of these rock types. For example, Simandl (2014) calculated that 70 kt of REE could be extracted annually from worked sedimentary phosphorite deposits. Apatite could also be a potential by-product from Kiruna-type iron-ore deposits, the Khibiny apatite mine, and from apatite waste from Mineville, USA (Ihlen et al., 2014; Mariano and Mariano, 2012).

Other potential by-product REE sources include extraction during Nb production from loparite at Lovozero, Russia (Wall, 2014); and as a by-product of uranium mining (Simandl, 2014). Other potential waste sources include red muds from aluminium production, xenotime from tin production at Pitinga, Brazil, U-ore tailings in Kazakhstan (Wall, 2014), and possibly from coal ash (Seredin and Dai, 2012).

2.4 REE from the mantle to a carbonatite-hosted ore deposit— sources of REE in the mantle

In the following sections the processes that lead to the formation of REE ore deposits in carbonatites are discussed. Schematically, the subdivisions of each stage are shown in Figure 2.5. The sources of REE in the mantle, and the effects of magmatic processes on the REE are covered. Most REE-deposits are either hydrothermally derived, or have a strong hydrothermal overprint, and, therefore, this section is most thoroughly reviewed. Finally, the formation of supergene deposits is briefly covered.

Mantle metasomatism, where materials are added to the mantle by either diffusion or through the infiltration of another phase, is widely acknowledged as a requirement in enriching the mantle in the REE and other incompatible elements (Chakhmouradian and Zaitsev, 2012). This can occur through transport in CO₂-bearing fluids, supercritical aqueous fluids or in hydrated silicate melts (Meen et al., 1989).

As previously discussed, LREE-enrichment in melts is largely due to the incompatibility of the LREE in mantle minerals, and thus these metals will preferentially be incorporated into the melt during partial melting. Candidate minerals for providing the majority of the REE into the melt include silicates, such as clinopyroxene, amphibole and phlogopite, or less common minerals, such as apatite or titanate minerals of the chrichtonite series (Jones and Ekambaram, 1985; Jones,

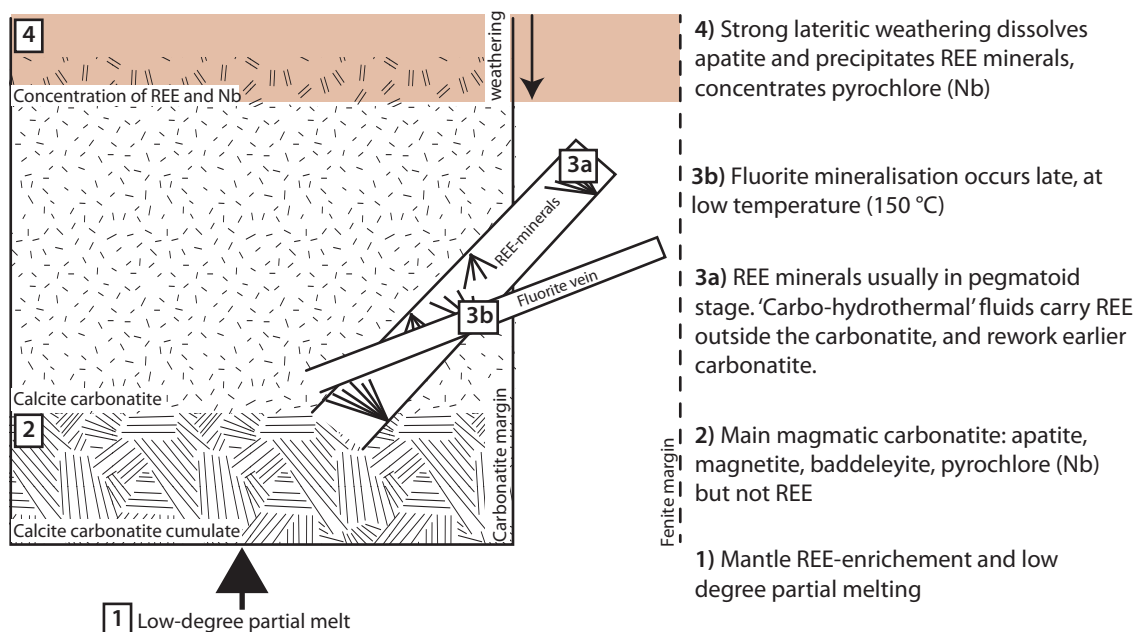


Figure 2.5: Schematic of different types of carbonatite-related ore deposit, caused by mantle (1), magmatic (2), hydrothermal (3) and supergene (4) processes.

1989; Wyllie et al., 1996; Hammouda et al., 2010).

2.5 REE from the mantle to a carbonatite-hosted ore deposit— magmatic processes

Low degree partial melts from a metasomatised mantle are commonly emplaced in intracontinental, anorogenic, extensional settings. Fractionation of REE-poor minerals is required to enrich the melt, as direct mantle melts do not have sufficiently high REE concentrations to produce an ore deposit outright. In carbonatites, the common association of these rocks with clinopyroxene-magnetite and olivine-magnetite rocks supports the hypothesis that enrichment of the REE in a carbonatite melt can occur through simple fractionation of silicate phases. However, the presence of apatite as early ovoid grains and the occurrence of phoscorites (magnetite-olivine-apatite rocks; Krasnova et al., 2004) with some carbonatites demonstrates that apatite can also fractionate from a carbonatite. The REE readily substitute into apatite, and fractionation of apatite from a carbonatite melt is likely to lead to a REE-poor carbonatite.

An alternative means of REE enrichment, if the carbonatite formed through liquid-immiscibility from a carbonated silicate melt, is through preferential partitioning of the REE into a carbonatite melt. However, experimental work shows that this does not occur and, upon silicate and carbonatite melt separation, the REE preferentially partition into the silicate phase (Veksler et al., 2012).

Carbonatite enriched in the REE can produce primary magmatic REE min-

erals. Primary magmatic mineralisation is rare, but a notable example is crystallisation of bastnäsite-(Ce) at Mountain Pass, California (Mariano and Mariano, 2012). Experimental work on the system $\text{CaCO}_3\text{--Ca(OH)}_2\text{--La(OH)}_3$ and $\text{CaO--La}_2\text{O}_3\text{--CO}_2\text{--H}_2\text{O}$ shows that bastnäsite can crystallise at shallow crustal depths to temperatures as low as 550 °C (Wyllie et al., 1996). Another example of a magmatic REE mineral, supported by isotopic data, is burbankite-(Ce) (Zaitsev et al., 2002). This can form crystals up to several cm in size in pegmatites or small drop-like inclusions in carbonates. Burbankite is thought to commonly form in carbonatites, but is commonly pseudomorphed to strontianite, barite and REE-fluorcarbonates by hydrothermal fluids.

2.6 REE from the mantle to a carbonatite-hosted ore deposit— REE transport in hydrothermal fluids

Most REE mineralisation in carbonatites occurs as a result of transport and deposition of the REE in a hydrothermal fluid at a late stage in the evolution of a carbonatite. Understanding of the behaviour of the REE in hydrothermal solution (i.e. conditions which make hydrothermal ore deposits) has improved considerably in the past 25 years. Far from being elements which are immobile in solution, it is now understood that, under some conditions, these elements are highly mobile and can lead to the formation of large REE ore deposits (e.g. Bayan Obo, China; Smith et al., 2014).

Mobility of the REE is a function of the stability of the possible aqueous complexes, the availability of ligands to form complexes, the solubility of REE minerals, and the temperature, pH and redox conditions of the fluid (e.g. Lottermoser, 1992; Gieré, 1996). Understanding the theoretical constraints of REE mobility and the composition of geological fluids where REE mobility has taken place is important to the understanding of how REE ore deposits form. Herein, the thermodynamic data and current knowledge of REE-bearing fluids are reviewed with respect to current REE ore deposit models.

2.6.1 Stability of different aqueous REE complexes

REE in solution invariably form complexes with anions; even when no anion is present the REE are surrounded by water molecules. The number of surrounding molecules (coordination number) of the HREE is 8, while for the LREE the number may be slightly higher (8–9) (Wood, 2003). The strength of the interaction between the REE in solution and available anions can be compared for different

anions by measuring the formation constant (*syn*: stability constant, binding constant). This is the equilibrium constant for the formation of a complex in solution, denoted as β and is a function of the ratio of the concentrations of the ligands and metals in isolation and the concentration of combined ligands:

$$\beta = \frac{[ML]}{[M][L]} \quad (2.1)$$

Where $[M]$ and $[L]$ denote the concentrations of the metal and ligands, respectively, and $[ML]$ denotes the combined concentration. Thus, the higher the value of β , the more stable the aqueous complex. In reality, more than one ligand can often bind to a metal, and, as such, the denotation β_n^L is more valid where:



Where, M^x , L^y and $ML_n^{x-(ny)}$ represent the metallic cation, ligand and complex respectively, where x and y are the respective charges of each and n represents the number of ligands of superscript L in the complex. Thus, the formation constant of a first-order complex of the REE and Cl ($REECl^{2+}$) would be denoted as β_1^{Cl} , while a second-order complex ($REECl_2^+$) would be denoted as β_2^{Cl} . These values are typically measured experimentally in a certain concentration of an acid, but to make the formation constants comparable between different solutions, they are, where possible, referenced to conditions of infinite molar dilution. Formation constants for the REE have been sourced by three techniques:

1. Ambient temperature stability experiments
2. Extrapolation of ambient temperature thermodynamic data to high ($> 100^\circ\text{C}$) temperature
3. Experimental measurements of thermodynamic properties at high temperature

Stability of aqueous REE complexes at ambient temperature

Thermodynamic data from ambient temperature analyses of the REE prior to 1990 were summarised by Brookins (1989); Wood (1990a) and Millero (1992). These papers included stability constants for the REE with SO_4^{2-} , F^- , Cl^- , OH^- , NO_3^- , CO_3^{2-} and HCO_3^- . Subsequent papers have refined the values for sulphate (Schijf and Byrne, 2004), fluoride (Schijf and Byrne, 1999; Luo and Byrne, 2000), chloride (Luo and Byrne, 2001), hydroxide (Klungness and Byrne, 2000), carbonate (Liu and Byrne, 1998; Luo and Byrne, 2004), and bicarbonate (Luo and Byrne, 2004) and new data for complexation by phosphate has been acquired (Byrne et al., 1991). The updated ambient temperature data are shown in Figure 2.6.

The analyses of complexation at ambient temperature show that the 'hard' (not polarisable), trivalent, REE cations preferentially bond with 'hard' (ionic) anions, in accordance with Pearson's HSAB¹¹ theory (Pearson, 1963; Brookins, 1989). Thus, according to Williams-Jones et al. (2012), and the data shown in Figure 2.6, the REE will form complexes with the following orders of stability:

Monovalent anions $F^- > OH^- > NO_3^- > (?) H_2PO_4^- > Cl^- > Br^-$

Divalent anions $CO_3^{2-} > (?) HPO_4^{2-} > SO_4^{2-} > P_2O_5^{2-}$

The hardness of the REE increases with atomic number, at ambient temperature, because of the greater charge density of the HREE and thus an assumed stronger ligand-interaction (Lottermoser, 1992). In other words, at ambient temperature the stability of the LREE-bound ligands is less than that of the same ligand bound with the HREE. This is best shown by F^- and CO_3^{2-} in Figure 2.6. This does not appear to occur for SO_4^{2-} , which maintains a relatively similar stability for all the REE. Divalent (Eu^{2+}) and tetravalent (Ce^{4+}) are, respectively, softer and harder cations than REE^{3+} . Thus, the stability of complexes with these cations will be decreased for Eu^{2+} and increased for Ce^{4+} , relative to complexes with REE^{3+} (Sverjensky, 1984; Bau, 1991; Wood, 2003).

Extrapolation of ambient temperature data to high temperature

The stability of REE complexes at higher temperature can be extrapolated from ambient temperature experiments (Wood, 1990b; Haas et al., 1995). A critical review of the different techniques used is beyond the scope of this thesis, but an example of extrapolated data to 300 °C is shown in Figure 2.7. These higher-temperature estimates broadly mimic the order of stability seen in the lower temperature experiments. The REE preferentially complex in the following order:

Monovalent anions $OH^- > F^- \gg Cl^- \approx H_2PO_4^- > HCO_3^-$

Divalent anions $CO_3^{2-} > SO_4^{2-}$

This trend is expected following the results of ambient temperature experiments where REE complexes with harder anions, such as OH^- , F^- and CO_3^{2-} , are more stable than complexes with softer anions such as Cl^- and HCO_3^- . A notable discrepancy between ambient temperature and extrapolated high temperature formation constants is the seemingly greater stability of OH^- compared to F^- (i.e. two log units greater on Figure 2.7). This discrepancy may be a function of the input parameters for the model. Ambient temperature stability constants used in the Haas et al. (1995) model for OH^- (sourced from Millero, 1992) are higher

¹¹Hard-Soft-Acid-Base

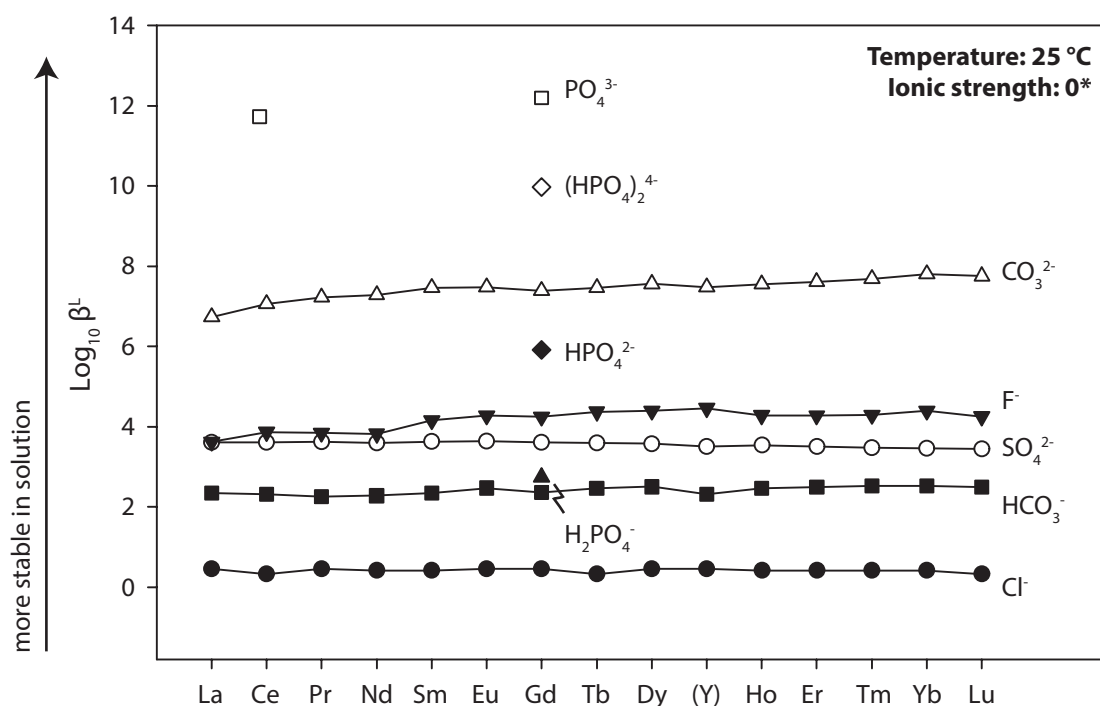


Figure 2.6: First formation constants ($\text{Log}_{10} \beta_1^L$) for different ligands (L) at ambient temperature and at zero* ionic strength, with the exception of Cl, where data are presented for 0.7 molar ionic strength. Note the increases in stability with atomic number for F^- and CO_3^{2-} . Data sources: sulphate (Schijf and Byrne, 2004), fluoride (Luo and Byrne, 2000), chloride (Luo and Byrne, 2001), carbonate (Luo and Byrne, 2004), and bicarbonate (Luo and Byrne, 2004), and phosphate (Byrne et al., 1991). Data for hydroxide are not presented as they are reported as $\beta^*(m)$ and are not directly comparable (Klungness and Byrne, 2000).

than that of F^- . However, these may be unreliable as, according to Klungness and Byrne (2000) they “do not provide a coherent representation of YREE hydrolysis behaviour... [and] exhibit an overall range of approximately two orders of magnitude”.

Importantly, in the extrapolated data, the trend of increased ligand stability with higher atomic number is preserved, especially for fluoride complexes, and the HREE appear to form stronger complexes than the LREE. This trend has influenced the interpretation of REE distributions in hydrothermal minerals where HREE-enrichment is observed, and has led to a widespread assumption that F^- is predominantly responsible for REE transport and distribution (e.g. Williams-Jones et al., 2000; Salvi et al., 2000; Jiang et al., 2003; Holtstam and Andersson, 2007). As will be shown in the following sections (2.6.5), new high-temperature experiments and an improved understanding of the solubility of REE minerals indicate that this may not be the case.

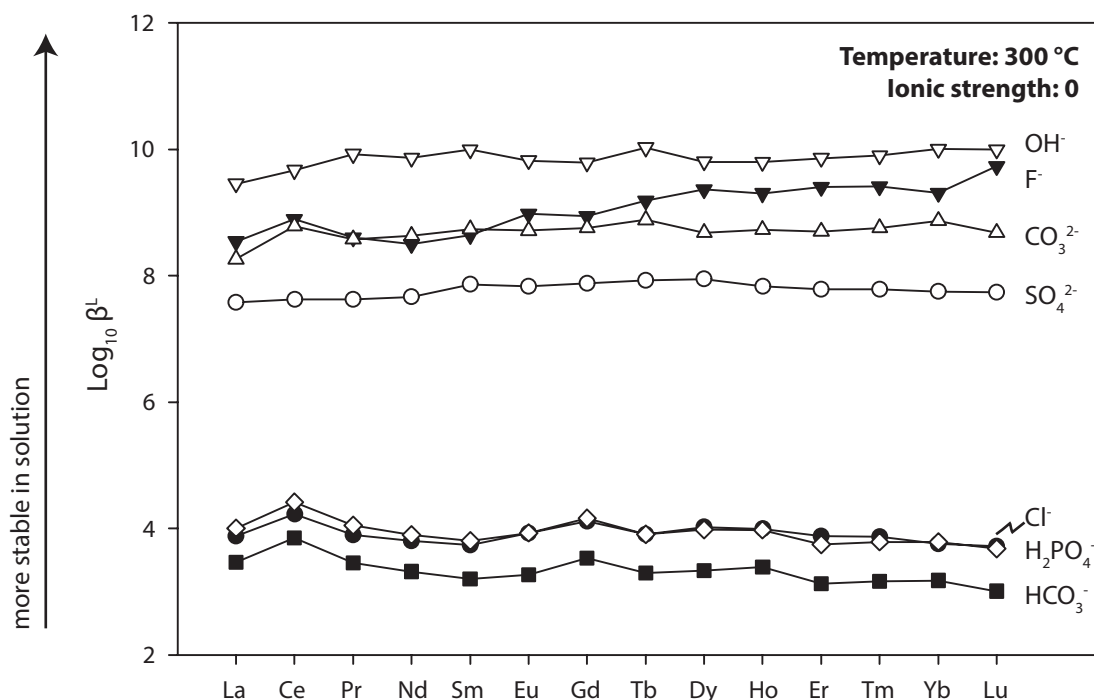


Figure 2.7: First formation constants ($\text{Log}_{10}\beta_1^L$) for different ligands (L) at 300 °C and at zero ionic strength based on extrapolation of formation constants at ambient temperature (Haas et al., 1995). Note the overall increase in stability compared to 25 °C, and the increase in stability with atomic number for F^- , similar to Figure 2.6.

Experimental measurements of thermodynamic properties at high temperature

Analyses of the complexation of the REE at higher temperature, up to 300 °C, has been carried out for F^- , Cl^- , OH^- and SO_4^{2-} (Gammons et al., 1996, 2002; Wood

et al., 2002; Migdisov and Williams-Jones, 2002, 2006; Migdisov et al., 2006; Migdisov and Williams-Jones, 2007, 2008; Migdisov et al., 2008, 2009; Loges et al., 2013) as well as complementary studies on the ligand numbers (number of occupied coordination sites around the REE) for aqueous solutions (Anderson et al., 2002) and chloride-bearing aqueous solutions (Ragnarsdottir et al., 1998; Mayanovic et al., 2002, 2007, 2009a). The results of these experiments are summarised by Wood (2003); Mayanovic et al. (2009b); Williams-Jones et al. (2012) and Migdisov and Williams-Jones (2014) and are illustrated in Figure 2.8. Notably absent from Figure 2.8 are data for REE complexation with PO_4^{3-} , HPO_4^{3-} , CO_3^{2-} and HCO_3^- , as no high-temperature complexation experiments have yet been carried out for these anions. Equilibrium constants for OH^- have been derived, but these are reported as molal equilibrium quotients (Wood et al., 2002). Experiments to determine formation constants for CO_3^{2-} and HCO_3^- at high temperature are currently in progress (Williams-Jones, *pers comm*).

The data derived from high-temperature experiments show that Pearson's HSAB theory still holds when comparing the average formation constants of Cl^- and F^- . For F^- these are approximately 3 log units higher than Cl^- and, thus, the REE form more stable complexes in solution with F^- . The data from OH^- complexation show that the theoretical estimates of REE-hydroxide complexes were several orders of magnitude higher than the experimental results (Wood et al., 2002). The higher formation constants, observed at low-temperature, for the HREE compared to the LREE (Fig. 2.6) and, importantly, extrapolated to higher temperature (Fig. 2.7) are not observed. Instead, the LREE are more stable than the HREE in both Cl^- - and F^- -bearing solutions (Fig. 2.8).

Two reasons have been suggested for this contrast, (1) increased steric hindrance at higher temperature, where the larger size of LREE ions allows a greater degree of complexation than the HREE (Mayanovic et al., 2009b), or (2) the increased dielectric constant of water at higher temperature, and thus shielding of the ligand through hydrogen bonding (Migdisov et al., 2009; Williams-Jones et al., 2012). Evaluating the cause of the enhanced LREE stability is beyond the scope of this work, but it is important to note that the same degree of enhanced stability has been observed independently, by two different research groups in two different laboratories through different techniques. Evidence for this decreased HREE mobility and enhanced LREE mobility in solution represents a paradigm shift from the ambient temperature projections and fundamentally changes our understanding of the causes of fractionation in REE-bearing hydrothermal fluids.

Nevertheless, the extrapolated data from Haas et al. (1995) is included in this thesis as, for SO_4^{2-} , the experimental data and the theoretical projections are broadly similar. Both sets of formation constants show that there is little offset between the LREE and the HREE at elevated temperature. Furthermore, experi-

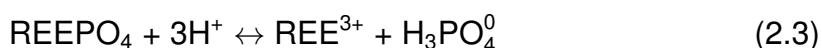
mental data are limited to Nd, Sm and Er, while data for all the REE, including Y, are available from the projected ambient-temperature data (Wood, 1990b; Haas et al., 1995). Additionally, no experimental formation constants currently exist for PO_4^{3-} , HPO_4^{3-} , CO_3^{2-} , HCO_3^- and OH^- (with the exception of ligand-number data for LaOH^x), and thus the theoretical projections are the only available data source for the stability of REE complexes with these ligands.

2.6.2 Solubility of REE minerals

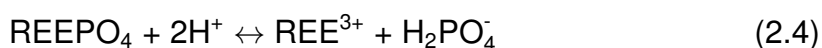
Experimental data on the solubility of REE minerals are lacking, yet knowledge of the solubility of REE minerals is necessary to understand the capacity of a solution to transport the REE. No data exist regarding the solubility of the following important REE-minerals: synchysite, ancylite, burbankite, allanite, and florencite, while limited data are available for the britholite group and for loparite. Extensive work has been carried out only for the REE phosphates (monazite and, to a lesser extent, xenotime), and for REE fluorides (fluorcerite). Recent work on the thermodynamic properties of bastnäsite and parisite has been published which will underpin modelling work in the future (Gysi and Williams-Jones, 2014).

Solubility of REE-phosphates

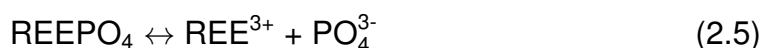
Solubility controlling reactions of phosphates at conditions relevant to hydrothermal deposits have mostly been carried out at low pH. Under these conditions, the solubility of REE phosphates is controlled by the reaction between the phosphate and an acid:



or



The equilibrium constant for this reaction is often converted to conventional solubility products (K_{SP}), which is the equilibrium constant for the following reaction:



Solubility products reported in the literature are limited to a range from ambient temperature up to 300 °C and, as mentioned above, low pH (Fig. 2.9). At conditions relevant to ore deposit formation, pH and temperature exhibit a strong control on REE-phosphate solubility. With increasing pH, the solubility of REE phosphates decreases considerably, shown both in theoretical calculations (Wood and

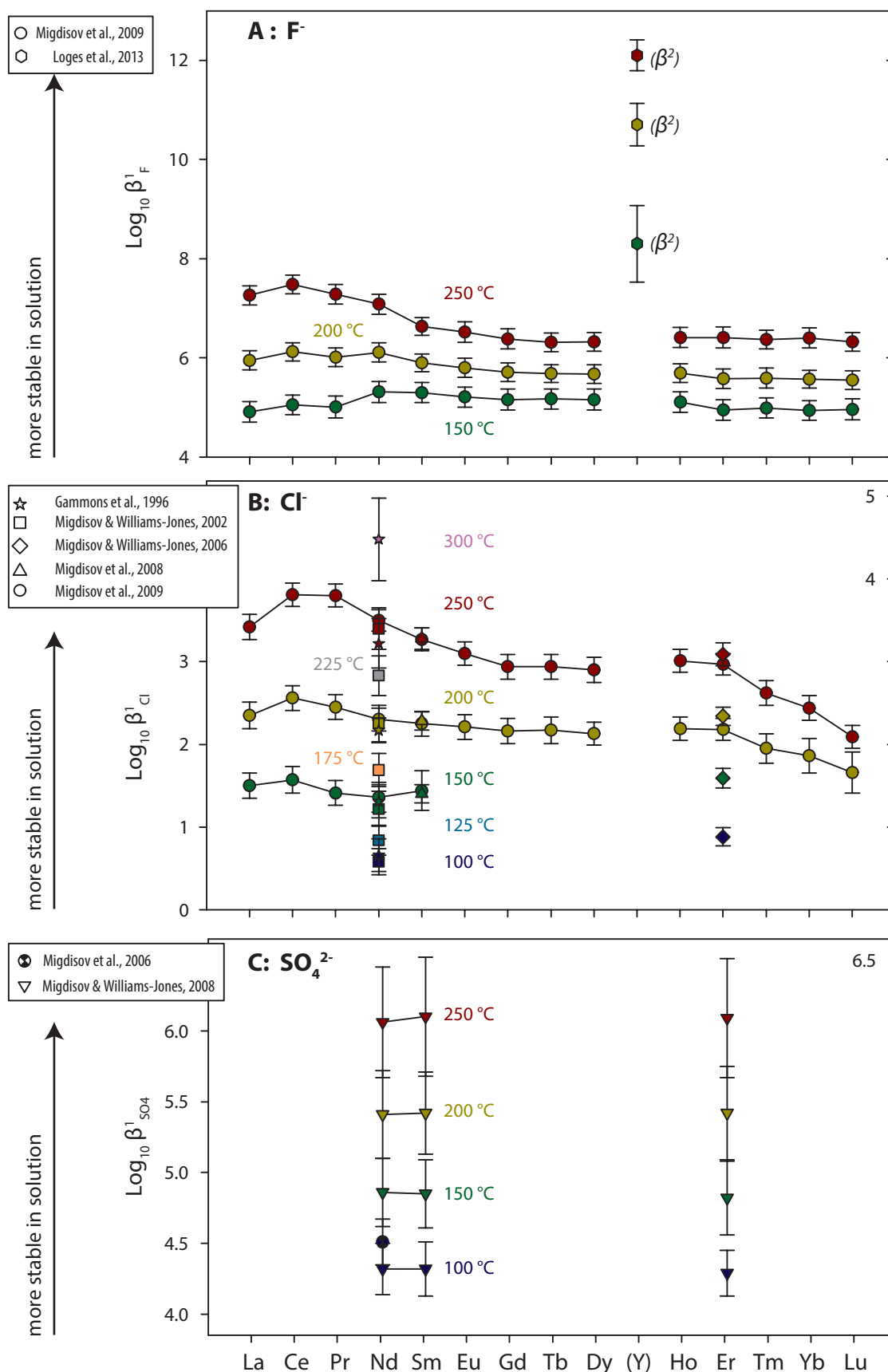


Figure 2.8: First formation constants ($\text{Log}_{10} \beta_1^L$) for (A) fluorine, (B) chlorine and (C) sulphate between 100 °C and 300 °C. YF_2^{2+} could not be detected by Loges et al. (2013), and thus the second formation constant (YF_2^+) is illustrated for reference. Note the increase of stability for the (LREE)F-complex with increasing T, in contrast to Figure 2.7. Data sources are listed in the legends. Note the different scales on the Y axes.

Williams-Jones, 1994) and under experimental conditions (Cetiner et al., 2005; Schmidt et al., 2007; Pourtier et al., 2010; Tropper et al., 2011).

As can be seen from Figure 2.9, the effect of temperature on the solubility of REE phosphates is retrograde (i.e. it decreases with increasing temperature), up to 300 °C (Poitrasson et al., 2004), a conclusion which is supported by theoretical calculations (Wood and Williams-Jones, 1994). Above 300 °C, Wood and Williams-Jones (1994) suggest that the solubility of REE phosphates may become prograde (i.e. it increases with increasing temperature). This is supported by experimental measurement of REE concentrations in acidic hydrothermal solutions up to 800 °C (Schmidt et al., 2007; Pourtier et al., 2010; Tanis et al., 2012). However, the experimental results of Schmidt et al. (2007) show that prograde solubility, of both monazite and xenotime, starts to occur from much lower temperatures which are approximately 100 °C, 200 °C lower than the theoretical and low-temperature experimental estimates. Increased pressure also increases the solubility of REE phosphates (Ayers and Watson, 1991; Tanis et al., 2012).

In the results of most of the solubility studies, little difference is observable between the solubility of LREE phosphates (monazite) and HREE phosphates (xenotime). Slightly higher solubility in HREE phosphates can be observed in data acquired at ambient temperature, where LuPO_4 is two log-units (K_{SP}) more soluble than PrPO_4 (Liu and Byrne, 1997). At very high temperature and pressure (800 °C, 1 GPa), Tropper et al. (2011) observed that with increasing NaCl concentration (increasing pH) the solubility of CePO_4 and YPO_4 increase to a point, until increasing NaCl concentration has a greatly reduced effect on the increase in YPO_4 concentration, while the solubility of CePO_4 continues to increase. The opposite effect is observed in the presence of NaF where increasing the concentration of NaF increases the solubility of YPO_4 over CePO_4 (Keppler, 1993; Tropper et al., 2013). Furthermore, Tropper et al. (2013) showed that at high temperature and pressure, the solubility of both CePO_4 and YPO_4 are much higher in the presence of F than Cl. Given the role of F in these experiments, it seems that further experiments on the solubility of REE phosphates in the presence of F are required at lower temperature; especially given the decreasing dissociation constant of HF with increased temperature (see Migdisov and Williams-Jones, 2014 and section 2.6.5).

Solubility of REE fluorides

The solubility of REE fluorides (fluorcerite) has been determined between 150 °C and 250 °C for all the REE and Y (Migdisov et al., 2009; Loges et al., 2013). K_{SP} values were experimentally determined for the reaction:



The solubility of REE-fluorides is greater than that of REE phosphates. At all temperatures, the HREE are more soluble than the LREE, and, as is the case for REE phosphates, solubility is retrograde (Fig. 2.9).

Solubility of other REE minerals

Limited solubility data are available for other REE minerals. Migdisov and Williams-Jones (2014) suggest that, given bastnäsite is more common than fluorcerite in nature and precipitation of minerals from a solution is controlled by the least soluble component, bastnäsite probably has a lower solubility than fluorcerite. This similarity can probably be extended to the rest of the REE-fluorcarbonate group.

Mitchell (1997) carried out solubility experiments between 600–750 °C on a simplified analogue of loparite ($\text{NaLaTi}_2\text{O}_6$) in the system CaCO_3 – CaOH , used as an analogue of natural carbonatite magma. It was found that loparite crystallises in grain boundaries, after the formation of carbonates and it was speculated that the loparite could crystallise from quite low-temperature fluids after the formation of carbonatite, although no specific temperatures or other conditions are specified (Mitchell, 1997).

Solubility of apatite

Although not a REE mineral *sensu stricto*, apatite is an important host for the REE in the mantle and many rocks, including, granite, alkaline rocks and in carbonatites (Hogarth, 1989; Ayers and Watson, 1991; Piccoli and Candela, 2002). Many experiments have been performed on the solubility of apatite in fluids, although most of the work has focussed on the solubility of apatite in silicate melts (e.g. Wolf and London, 1995).

The solubility of apatite in silicate melts increases with increasing temperature, decreasing melt-polymerisation and decreasing SiO_2 (Piccoli and Candela, 2002). Under these conditions apatite is more soluble than monazite, and REE enrichment in apatite can only occur if monazite saturation in a liquid is low enough (50–100 ppm) that it is avoided (Wolf and London, 1995). Much less work has been carried out on the solubility of apatite in hydrothermal fluids. Ayers and Watson (1991) show that at high temperatures (between 800–1200 °C) and in pure H_2O , apatite has a low solubility, but with the addition of NaCl , and thus the decrease of pH, the solubility of apatite increases. Interestingly, Krenn et al. (2012) show that in alkali, Cl- or F-bearing fluids, the solubility of monazite can be greater than that of apatite. In these situations, apatite has a great capacity to incorporate high concentrations (up to 23 wt. %) of the REE.

2.6.3 Y/Ho fractionation and the tetrad effect

In magmatic systems, the lanthanide contraction gives rise to regular CHARAC¹² behaviour of the REE+Y and smooth, chondrite-normalised distributions, with the well-understood exceptions of Ce⁴⁺ and Eu²⁺ (Henderson, 1996). In aqueous fluids, however, there are two additionally known aberrations from the lanthanide contraction: Y/Ho fractionation, and the tetrad effect.

Y/Ho fractionation

In most geological materials, including chondrites, basalts, shales, and most granites, the ratio between Y and Ho is constant, at a value of approximately 26 (Bau, 1996; Pack et al., 2007). Fractionation between Y and Ho, and deviation from this value, has been observed in hydrothermal fluorite (Bau and Dulski, 1995; Bau et al., 2003; Schwinn and Markl, 2005), allanite and titanite from Kiruna (Smith et al., 2009), in highly evolved granites and pegmatites (Bau, 1996), and in deep-sea ferromanganese crusts (Bau et al., 1996). The exact cause of this fractionation is unknown. Bau (1996) and Bau et al. (1996) suggest that it is due to sorption of Y and the REE onto hydrous Fe-Mn-oxides, or through F forming more stable complexes with Y than Ho. The latter suggestion is supported by experimental stability constants. These show that YF₂⁺ complexes are more stable than HoF²⁺ complexes (Fig. 2.8) and that, at a given temperature and F activity, YF₃ and HoF₃ have different solubilities (Loges et al., 2013). Thus, Y/Ho fractionation in a mineral is often interpreted as being indicative of crystallisation in a hydrothermal environment with a high F-activity. Nevertheless, Pack et al. (2007) suggest, based on a similar hypothesis for Zr/Hf fractionation, that fractionation need not be an aqueous effect and that non-ideal activity coefficients of Ho and Y could cause fractionation in Si-rich polymerised melt environments. However, this hypothesis is not explained in great detail, and more thermodynamic data are needed to evaluate whether (anhydrous) non-ideal behaviour could cause fractionation in magmatic systems.

The tetrad effect

The tetrad effect refers to the subdivision of the REE into four groups: La–Nd, Pm–Gd, Gd–Ho and Er–Lu. These groups correspond to $\frac{1}{4}$ -, $\frac{1}{2}$ -, and $\frac{3}{4}$ -filled $4f$ electron-shells where changes in REE-ligand stability occur due to repulsion between electrons within the f orbital (Bau, 1996). This can give rise to anomalous breaks in the otherwise smooth chondrite-normalised REE-distribution patterns, with breaks at Pm, Gd and Ho. Such breaks may be observable in complexation experiments, especially in older literature (see, for example, the anomalous

¹²Charge and Radius controlled

kinks in the distributions, especially at Gd, in Figure 2.7), where the tetrad effect causes changes in the stability of REE complexes. However, newer and more precise complexation experiments (e.g. Fig. 2.6) have much smoother REE stabilities with increasing atomic number, leading Wood (2003) to question whether complexation with geologically-relevant ligands could cause the tetrad effect in nature.

Numerous geological examples exist where the tetrad effect has been interpreted, predominantly in highly evolved systems where aqueous fluids play a role in petrogenesis, such as pegmatites (Masau et al., 2000; Liu and Zhang, 2005), granites (Monecke et al., 2002; Wu et al., 2004), albitized rocks (Monecke et al., 2007) and in tin-bearing systems (Monecke et al., 2011). Given the irregular pattern of the tetrad effect, it is absolutely crucial to ensure that the analytical procedure used is precise, and preferably ratified through multiple techniques (Bau, 1996). Furthermore, analytical artefacts may occur when using solvent extraction or ion-exchange columns which may be difficult to mitigate (Wood, 2003). These problems aside, it has been argued by McLennan (1994) and Pan (1997) that fractionation of certain minerals, such as apatite or monazite, could lead to similar REE distributions in geological samples. It is important to rule-out before interpreting an irregular REE-distribution as the result of the effects of a hydrothermal fluid.

2.6.4 The chemistry of REE-bearing fluids

The availability of ligands with which the REE can complex, and the temperature, pH and redox properties of the fluid, can be ascertained by two different methods:

1. Direct measurements of fluids from, for example:
 - (a) Fluid inclusions of REE-bearing fluids
 - (b) Solutions from deep-sea hydrothermal vents
 - (c) Solutions from geothermal fields
 - (d) Encrustations from fumaroles
2. Indirect inferences of fluid chemistry from minerals, for example:
 - (a) Mineralogy of REE-bearing deposits
 - (b) Derivation of fluid chemistry from daughter minerals in fluid inclusions from REE deposits

Direct measurements of REE-ore forming fluids

The most direct method of understanding how HREE ore deposits form is to study the chemistry of fluids which have led to REE deposits. This is, however, challenging because of the lack of modern analogues. The closest available proxy is through analysis of fluid inclusions where a REE-bearing fluid has been trapped *prior* to forming an ore deposit. Analysis of fluid inclusions from an ore deposit where the REE have already precipitated will only provide information on the conditions following REE transport. Furthermore, the fluid inclusions must be in minerals which do not readily exchange many elements with a fluid and, for crush-leach analysis, must be predominantly primary inclusions of one assemblage.

There are only two published comprehensive studies of the REE chemistry of fluid inclusions from a magmatic source: a granite and a carbonatite, respectively. Granite-derived orthomagmatic fluid inclusions from the Capitain pluton, New Mexico, were analysed by crush-leach analysis by Banks et al. (1994) and Campbell et al. (1995). Fluid inclusion assemblages were hosted in quartz in two samples each of granophyre and aplite. Granophyre-hosted inclusions represent a fluid which has not precipitated REE minerals, while aplite-hosted inclusions may have formed after crystallisation of allanite and/or titanite. Fluids from both samples were shown to be rich in the REE, and LREE enriched relative to chondrite (Fig. 2.10 A). Concentrations of Cl, SO₄ and F, were 40 wt. %, 20 wt. % and 500–5,000 ppm, respectively. Other anions analysed included B, Br and I (Table 2.6). Homogenisation temperatures for all the inclusions were approximately 500 °C (Campbell et al., 1995). Thus, the results of this study indicate that appreciable REE concentrations, and LREE-enrichment, can be caused by a hot, Cl-, S-, and, to a lesser extent, F-rich acidic brine.

Carbonatite-derived fluid inclusions, trapped in country rock quartz, were analysed from the Kalkfeld carbonatite complex, Namibia (Bühn and Rankin, 1999). These were analysed by two techniques: in-situ synchrotron XRF¹³ and a bulk-analysis of crushed and cleaned quartz by ICP-MS¹⁴. Both techniques gave similar results, with very high REE concentrations in the fluid, up to several wt. % (Fig. 2.10 A). As with the fluids from the Capitain Pluton, the Kalkfeld fluids are LREE-rich, and have a slight Eu anomaly. In contrast to the Capitain Pluton, however, the anion content of the fluids is Cl-poor and CO₂-rich (Table 2.6). Fluorine concentrations are slightly higher than the Capitain Pluton, between 5000 and 12,000 ppm. Sulphate concentration was not analysed. Homogenisation temperatures of these fluids were greater than 250 °C, at which point the inclusions decrepitated. The results of this study suggest that a CO₂-, Cl-, and F-bearing carbonatite-derived fluid is capable of transporting high REE concentrations.

¹³X-ray fluorescence

¹⁴inductively coupled plasma mass spectrometry

Some authors have alluded to, but not fully discussed, analyses of REE in fluid inclusions from other localities. For example, Dostal et al. (2011) mention Y and Ce concentrations of over 10 ppm and up to 10 ppm, respectively, from the Bokan Mountain complex, USA. Interestingly, this difference in concentration probably equates to a HREE-enriched fluid, with a salinity (5–12.4 NaCl eq. wt. %) significantly lower than the inclusions from the Capitain pluton.

The dearth of studies on the chemistry of REE fluids, especially the lack of analyses of inclusions from carbonatites and alkaline igneous rocks, means that the analyses from the Capitain Pluton are often used as an example of a REE ore-forming fluid where analyses of fluids from other, not yet analysed, rocks may be better suited for modelling.

	Carbonatite-derived fluid			Aplite		Granophyre	
	KF113	KF153	KF155	MTE	W3-3	CPU-2	CMX
Σ REE	10,244	40,097	12,334	193	251	1,290	466
CO ₂ (%)	20±8	20±8	20±8				
B				214	220	438	157
SO ₄				21,472	20,773	24,210	21,137
F (%)	0.6±0.1	1.2±0.3	0.5±0.1	0.035	0.044	0.17	0.05
Cl (%)	5.0±1.3	0.7±0.2	6.7±1.8	42.95	44.34	39.89	42.82
Br				250	220	146	235
I				0.54	0.8	0.91	1.17

Table 2.6: Anion concentrations of carbonatite- and granite-derived REE-bearing fluids from the Kalkfeld carbonatite and Capitain Pluton, (Bühn and Rankin, 1999; Campbell et al., 1995). Concentrations in ppm except where otherwise labelled. CO₂ concentration is estimated.

REE-bearing solutions from deep-sea hydrothermal fluids

The concentrations of the REE and other elements, including important anions, have been studied in deep-sea hydrothermal vents (Michard et al., 1983, 1984; Michard and Albarède, 1986; Michard, 1989; Klinkhammer et al., 1994; Douville et al., 1999, 2002; Allen and Seyfried Jr, 2005; Cole et al., 2014). Clearly, these systems are not perfect analogues for REE ore-forming fluids, but they do provide an insight into REE mobility at higher temperatures.

Hydrothermal fluids in deep sea hydrothermal vents can range in temperature between approximately 150 °C to supercritical fluids over 400 °C. Values for pH are typically low. The predominant anions in the fluid, in terms of concentration, are Cl⁻ and SO₄²⁻, of which Cl⁻ is significantly more abundant. The REE concentration in hydrothermal vent fluids is low relative to that of orthomagmatic fluids, but is approximately two orders of magnitude higher than seawater (Fig. 2.10B).

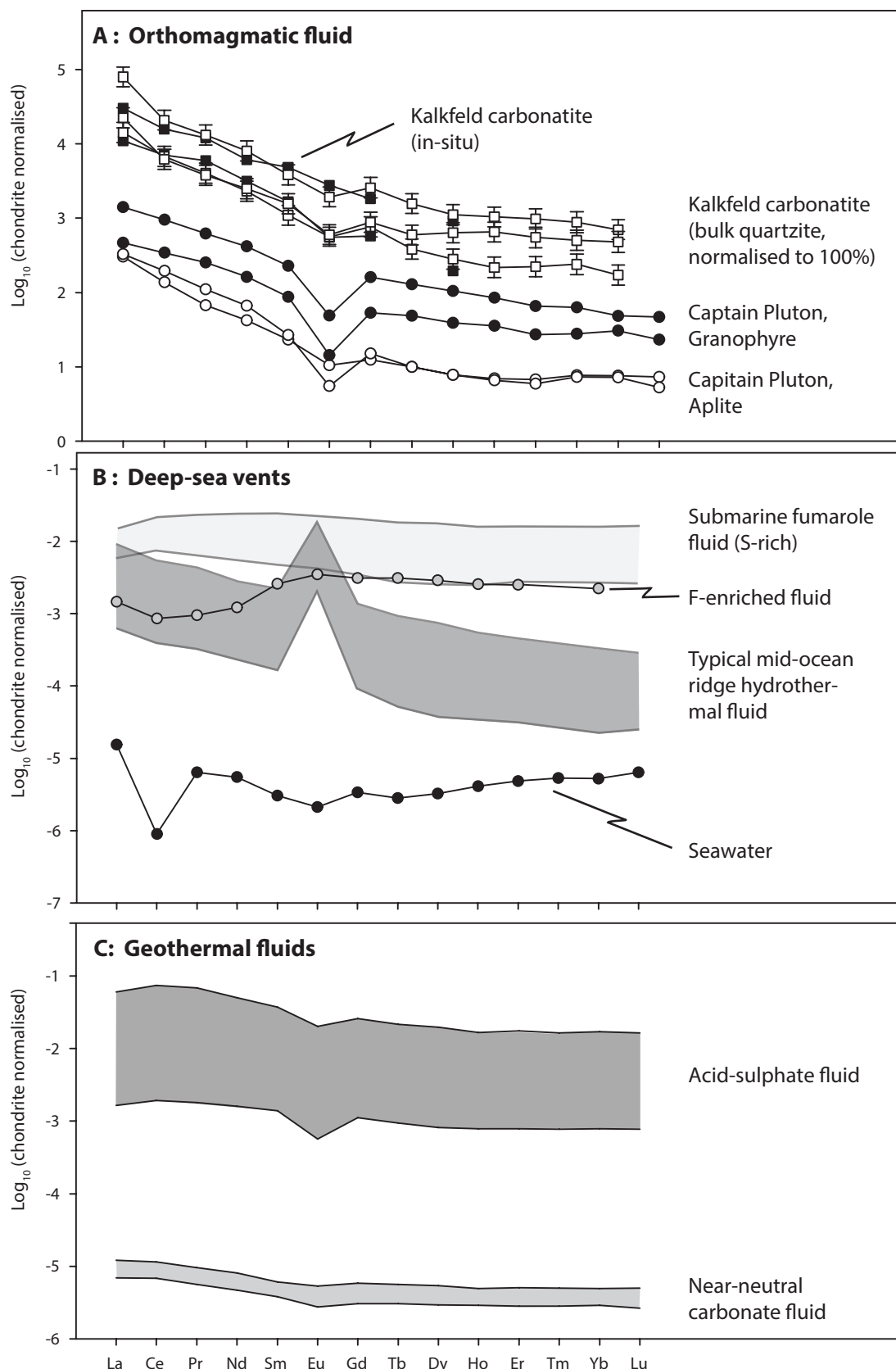


Figure 2.10: REE concentrations in natural fluids normalised to chondrite. Fluids are: (A) Igneous-derived fluids from the Captain Pluton (Banks et al., 1994), and from carbonatite-derived inclusions in quartzite (Bühn and Rankin, 1999) (B) compiled Mid-ocean-ridge-fluid, (Klinkhammer et al., 1994; Douville et al., 1999; Bau and Dulski, 1999; Douville et al., 2002; Schmidt et al., 2010; Craddock et al., 2010); Seawater: (Cole et al., 2014); Fumarole and F-enriched fluid: (Craddock et al., 2010) (C) Acid-sulphate fluids from Waiotapu, near-neutral fluids from Waimangu, New-Zealand (Wood, 2003)

Chondrite-normalised REE distributions are typically LREE-enriched, and often have a prominent Eu anomaly. The most likely cause of this distribution is through REE exchange between the fluid during plagioclase recrystallisation (Klinkhammer et al., 1994; Bau and Dulski, 1999; Douville et al., 1999). However, preferential mobility by Cl^- has also been suggested as causing fractionation due to preferential mobility of the LREE and Eu^{2+} in Cl^- -rich brines (Sverjensky, 1984; Bau, 1991; Wood, 2003; Craddock et al., 2010). The concept of anion-controlled REE-distribution is further reinforced by the finding of similar LREE-rich, chondrite-normalised patterns from fluids sourced from ultramafic rocks with no plagioclase contribution (Douville et al., 2002), from experimental studies of interaction of Cl^- -bearing fluid with peridotite (Allen and Seyfried Jr, 2005), and from vents where fluid may have mixed with magmatic volatiles (Cole et al., 2014). In the cases where mixing with magmatic volatiles are suggested as a control on the REE distribution, the chondrite-normalised REE plots deviate from the typical LREE-enriched, Eu-depleted pattern (Craddock et al., 2010; Cole et al., 2014). HREE enrichment in these fluids correlates with higher F^- concentration in more acidic fluids, which cannot currently be reconciled with the high-temperature thermodynamic data from Williams-Jones et al. (2012). Craddock et al. (2010) also sampled fluids considered to be submarine equivalents of fumaroles. These fluids had relatively flat REE patterns attributed to low pH and high sulphate concentrations, but the stability of the REE did not seem to be greatly influenced by temperature.

REE-bearing solutions from geothermal fields

REE distributions from continental geothermal fluids are much more varied than submarine hydrothermal fluids (Fig. 2.10 C). Geothermal fluids include both crustal and volcanic fluids, studied from a variety of locations, including: Bulgaria, Tibet, (Michard et al., 1987; Michard, 1989), Yellowstone (Lewis et al., 1997, 1998), Western USA (van Middlesworth and Wood, 1998; Wood and Shannon, 2003; Wood, 2003), New Zealand (Wood, 2003, 2006), Italy, Turkey, Germany and Jordan (Möller et al., 2003, 2004, 2005, 2006). REE distributions of the fluids are variable. Möller (2002) and Möller et al. (2003, 2004, 2005, 2006) argue that the distribution is dependent on the REE distribution of the minerals which dissolved into the fluid at depth. Little evidence of preferential fractionation of the REE into solution is observable when comparing chondrite-normalised patterns of host-rocks and fluids. Broadly speaking, however, Wood (2003) suggests that geothermal fluids can be divided into acid-sulphate fluids (Lewis et al., 1997, 1998; Wood, 2003, 2006) and near-neutral carbonate fluids (Michard and Albarède, 1986; Johannesson et al., 1996; van Middlesworth and Wood, 1998; Wood, 2003; Wood and Shannon, 2003). An example of each is shown in Figure 2.10C. Acid-sulphate fluids have much higher REE concentrations than the

near-neutral carbonate fluids, suggesting the pH has a strong control over REE mobility. It is possible that ligands have a subtle control over the REE distribution of the fluid, but any effect is masked by the REE distribution of the source minerals. Carbonate-rich fluids from New Zealand might be expected show HREE enrichment based on the high stability of HREE-carbonate complexes, but this is not observed in the data (Wood, 2003, 2006).

REE-bearing vapours from Oldoinyo Lengai

Low-density, vapour-like fluids from volcanic vents can be an important ore-fluid carrier (Williams-Jones and Heinrich, 2005). Analyses of these vapours from fumarolic encrustations at Oldoinyo Lengai provide the only example of hydrothermal fluids from an active carbonatite (Gilbert and Williams-Jones, 2008; Teague et al., 2011). These studies show that the vapour phase is LREE-enriched, and it is likely that higher concentrations of the REE are deposited at hotter fumaroles (Fig. 2.11). Concentrations of the REE can reach similar levels to those seen in orthomagmatic fluids from granites (Banks et al., 1994). Analysis of a gas sample from one of these fumarolic vents shows that it is CO₂-dominated, with an order of magnitude lower concentrations of HCl and S, and two orders of magnitude lower HF concentration (Fig. 2.11). These data suggest carbonate complexation may be able to transport the REE in the vapour phase (Gilbert and Williams-Jones, 2008).

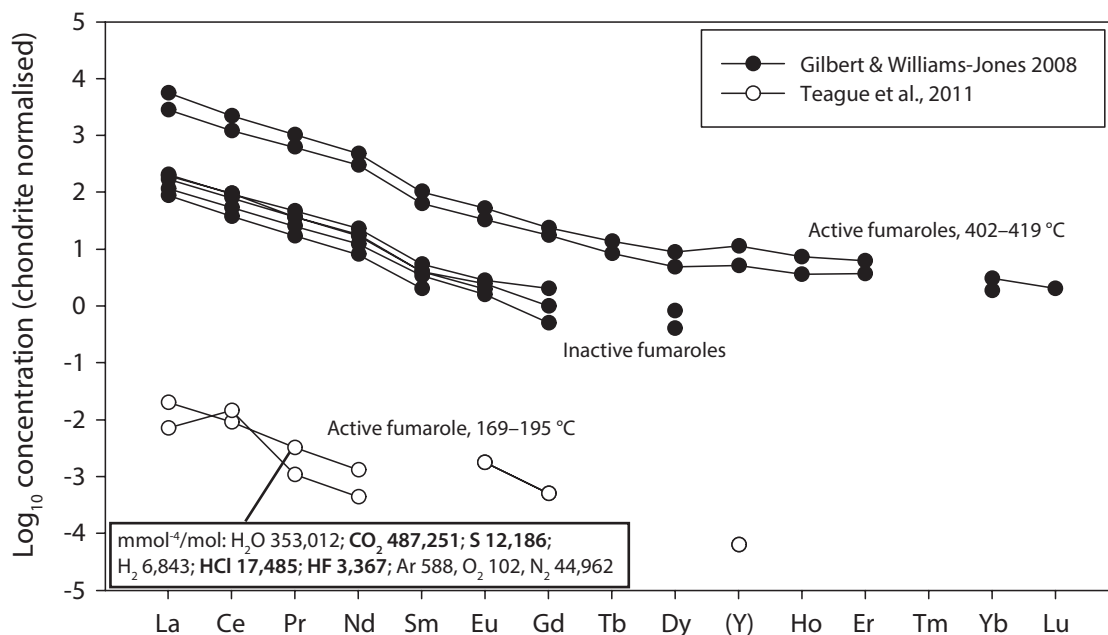


Figure 2.11: Chondrite-normalised REE concentrations from fumarolic encrustations from Oldoinyo Lengai and a single bulk-gas analysis from an active fumarole (inset box). Data from Gilbert and Williams-Jones (2008) and Teague et al. (2011).

Inferences from the mineralogy of hydrothermal REE deposits

The mineralogy of a rock crystallised from a hydrothermal fluid can be used to infer the composition of the fluid. This is especially true for major elements, but the composition must be interpreted with caution. For example, the absence of a mineral does not necessarily mean that certain elements were not present in the system: water-ice is not required to infer the presence of water, and soluble minerals, such as NaCl, may not remain stable. In addition, minerals can crystallise through reaction with a host-rock (e.g. limestone, or equivalent, in the case of a skarn), and thus, in this example, the presence of Ca-bearing minerals does not mean that Ca was present, or indeed absent, in the fluid. Furthermore, the behaviour of trace elements in a fluid will be dictated by, not only the availability and stability of transporting ligands, but also the partition coefficients of the mineral into which they substitute. Recent advances have expanded these parameters to multiple elements under particular experimental conditions (van Hinsberg et al., 2010), but experimental work for many fluids and compositions is still lacking.

Despite the difficulties in inferring fluid composition from mineralogy, some of the best evidence of REE speciation in hydrothermal solutions is derived this way. For example, the first discoveries of REE minerals were from skarn environments at the Bastnäs-type deposits, Sweden. Here, clear textural evidence indicates that the REE were mobilised into the skarn, and deposited during reaction with the carbonate minerals, although the source of the fluid is still not understood (Holtstam and Andersson, 2007; Holtstam et al., 2014).

The mineralogy of hydrothermal REE ore deposits are quite similar, suggesting a common link between some of the elements in the gangue mineralogy and the REE. REE-bearing and gangue minerals from different hydrothermal deposit types are listed in Table 2.7. Common gangue minerals from hydrothermal REE mineralisation include fluorite, barite and calcite, as well as other F-bearing phases such as apatite, F-bearing amphibole and phlogopite. This association indicates that fluoride and sulphate anions are commonly associated with REE deposits while phosphate and carbonate are occasionally associated. The common association of F-bearing minerals with REE deposits means that F is often interpreted to be a major contributor to REE mobility in hydrothermal REE ore deposits.

Careful interpretation of the paragenesis of a REE mineral deposit can also provide information on the mobility of the REE in solution. Paragenetic sequences can be interpreted as evidence for preferential mobilisation of the LREE or the HREE. For example, at the Thor Lake intrusion, Canada, Sheard et al. (2012) interpreted that primary eudialyte had been altered, in-situ, to a mixture of zirconium- and REE-bearing minerals which were preferentially enriched in the HREE, while the LREE are transported away from the area of alteration. This is interpreted as

Table 2.7

Deposit type and location	REE-bearing minerals	Gangue minerals	Fl types	T _n (°C)	Salinity (NaCl eq.)	Daughter minerals	Trapped minerals	References
Bastnäs-type								
Type-1	Cerite-(Ce), Ferriallanite-(Ce), bastnasite-(Ce)	Tremolite-actinolite, sulphide phases	LLV (bast) LV (fl)	310 ±20 (bast), 100-150 (fl)	6-29 % eq CaCl ₂ (bast), 0-16 (fl)		Calcite (fl)	(Holtstam and Andersson, 2007; Holtstam et al., 2014)
Type-2	Fluorbritholite-(Ce), Y-dominant species	Tremolite-actinolite, norbergite, chondroite, fluorphlogopite, <i>fluorite</i>	As above	As above	As above			
Carbonatite-derived								
Amba Dongbar, India	REE-fluorcarbonates, florencite	Quartz, <i>fluorite</i> , <i>barite</i> , strontianite, columbite						(Doroshkevich et al., 2009)
Maoniuping, China	Bastnäsite	<i>Calcite</i> , <i>fluorite</i> , <i>barite</i> , aegerine, arfvedsonite, microcline, biotite	Melt (M), Melt and liquid (ML), CO ₂ -rich (AC, ADC, C), Aqueous assemblage (AV, ADV)	(M) >737–850, (ML) 600–850, (CO ₂ -rich) 194–453, (aqueous) 224–477	N/A ¹⁵	CO ₂ -rich and aqueous sulphate minerals		(Hou et al., 2009; Xie et al., 2009)
Barro do Itapirapua, Brazil	REE-fluorcarbonates	Ankerite, quartz, apatite, <i>barite</i> , galena						(Andrade et al., 1999b,a; Ruberti et al., 2002, 2008)
Tundulu, Malawi	REE-fluorcarbonates	Quartz, <i>barite</i> , apatite						(Ngwenya, 1994)
Kangankunde, Malawi	Monazite-(Ce), bastnäsite-(Ce), florencite	Ferroan-dolomite, strontianite, <i>barite</i> , quartz, iron-oxides, <i>calcite</i> , apatite						(Wall and Mariano, 1996)
Oka, Canada	(Study not related to mineralisation)		LV, LVS (ap, mont, cal)	(mont) 300–450, (ap) 200–400, (cal) 100–200	4.2–49	Halite, nahcolite	Apatite, strontianite, calcite, mirabilite, magnetite	(Samson et al., 1995a,b)
Arshan, Russia	Bastnasite	<i>Calcite</i> , phlogopite, sulphates, strontianite, <i>fluorite</i>		>480				(Doroshkevich et al., 2008)
Bear Lodge, Wyoming	REE-fluorcarbonates, ancylite, monazite, cerianite	<i>Calcite</i> , <i>fluorite</i> , <i>barite</i> , strontianite, pyrite, ankerite						(Moore et al., 2014)
Wigu Hill, Tanzania	Bastnäsite	Quartz, strontianite, <i>barite</i>						referenced in (Wall and Mariano, 1996)
Fen, Norway	Monazite, parisite, bastnäsite, (allanite?)	<i>Calcite</i> , dolomite, haematite, ankerite, quartz, pyrite						(Andersen, 1986a)
Khibina, Russia	Burbankite, synchysite	<i>Calcite</i> , dolomite, <i>barite</i> , strontianite						(Zaitsev et al., 1998, 2002)
Nkombwa, Zambia	Bastnäsite, monazite, daqingshanite	<i>Barite</i> , dolomite						(Zambezi et al., 1997)
Alkaline-intrusion-derived								
Strange Lake, Canada	Fluorcerite-(Ce), bastnäsite-(Ce), kainosite-(Y), gagarinite-(Y), monazite	Phyllosilicates, quartz, <i>fluorite</i> , secondary zircon, zirconosilicates, haematization, Ca-metasomatism	LLV (early), LV(±S) (late)	300–360 (early), 150–200 (late)	23–27 (early), 12–25 (late)	Bastnäsite (late)	Haematite (late)	(Salvi and Williams-Jones, 1990, 1992, 1996, 2006; Gysi and Williams-Jones, 2013)
Tamazeght, Morocco	Bastnäsite, parisite	Cancrinite, nepheline, <i>fluorite</i> , Fe-Mn-hydroxides, orthoclase, albite, aegerine-augite, amphibole	LVS	300	24–27	Parisite, zircon(?)		(Salvi et al., 2000)
Thor Lake, Nechalacho, Canada	Fergusonite-(Y), (zircon), monazite-(Ce), allanite-(Ce), REE-fluorcarbonates	albite, quartz, biotite, <i>fluorite</i> , kutnohorite, haematite						(Sheard et al., 2012)
Thor Lake, T-zone, Canada	Bastnäsite, xenotime,	Quartz, aegerine, K-feldspar, albite, polyolithonite, biotite, chlorite, magnetite, <i>fluorite</i> , thorite	LLV	140–420	2–17	Halite, minor sylvite, rare parisite		(Taylor and Pollard, 1996)
Bokan Mountain, USA	Britholite, xenotime, allanite, bastnäsite, iimorite, monazite	<i>Fluorite</i> , thorite, uranothorite, aegerine, amphibole	(1) LLV, (2) LV	(1) 178–296, (2) 140–345	(1) 5-12.4 (2) 2.8–20.3		(2) Y-HREE-minerals	(Dostal et al., 2011, 2014)

Continued on next page ...

¹⁵abundance of SO₄ led the authors to conclude that salinity could not be determined

Table 2.7 – continued from previous page

Deposit type and location	REE-bearing minerals	Gangue minerals	FI types	T _h (°C)	Salinity (NaCl eq.)	Daughter minerals	Trapped minerals	References
Loch Loyal	Allanite, (titanite), (apatite)	Biotite, magnetite, pyroxene, amphibole, <i>barite</i>						(Walters et al., 2013)
Khalzan Buregte and Tsakhir, Mongolia	Allanite-(Ce), fergusonite, bastnäsité	Quartz, albite, microcline, amphibole, aegerine, zirconium minerals, <i>fluorite</i> , <i>calcite</i>						(Kempe et al., 2014)
Shuiquangou (China)	Allanite	Quartz, biotite, zircon, ilmenite, titanite						(Jiang et al., 2003)
Misery Lake, Canada	(apatite), britholite, fergusonite, bastnäsité, monazite	Pyroxene, fayalite, amphibole, zircon, magnetite, <i>fluorite</i>						(Petrella et al., 2014)
Other Hydrothermal Galinas Mountains, USA	Bastnäsité, (parisite, xenotime)	<i>Fluorite</i> , <i>barite</i> , quartz, <i>calcite</i> , pyrite, haematite	LV, LVS, LLV	300 (LVS, bast, qrtz), 100–150 (LV, LVS, flr)	12–18			(Williams-Jones et al., 2000)
Snowbird deposit, USA Kizilcaören, Turkey	Parisite Bastnäsité	Quartz, <i>calcite</i> , <i>fluorite</i> , ankerite <i>Fluorite</i> , <i>barite</i> , quartz, <i>calcite</i> , phlogopite, pyrolusite, haematite	LLVS (1) LV, (2) LV, (3) LV	400–500 (1)250–450, (2) 200–300, (3) 100–200	33–50 (1) 10–25, (2, 3) 0–10	Halite		(Samson et al., 2004) (Gültekin et al., 2003)
Bayan Obo ¹⁶ , China	Monazite, bastnäsité, parisite, huanghoite	Apatite, magnetite, haematite, zircon, aegerine, <i>calcite</i> , <i>fluorite</i> , amphibole, phlogopite, <i>barite</i>	(1 ¹⁷) LLV ;(2) LV, LLV ;(3) LV, LCS ;(4) LLV, LVS;(5) LV(S)	(1) 280–360; (2) 300–400, (3) 430–360 ¹⁸ ; (4) 350–278; (5) 250–150	1.3–5 (1); 1.6–10.1 (2); 6–15 (3); 1–20.2; 26.9–60 (4); 0–18.9, 26.5–32.3 (5)	halite (3, 4, 5); bastnäsité(?)		(Smith and Henderson, 2000; Fan et al., 2004)

Table 2.7: Summary of the mineralogy and fluid-inclusion data from hydrothermal REE deposits. Common gangue minerals are italicized for emphasis. Abbreviations: L- liquid, V- vapour, S- solid, M- melt; LL denotes an inclusion assemblage with two liquid phases, usually an aqueous and carbonic phase.

¹⁶Although Bayan Obo was probably originally carbonatite derived, it has a complex genesis, with multiple stages of deformation, and thus is included as 'other hydrothermal'

¹⁷Bayan Obo paragenetic stages: (1) - early disseminated monazite; (2) banded ores; (3) aegerine alteration; (4) aegerine vein fill; (5) fluorite–barite mineralisation

¹⁸estimated

evidence for greater mobility of the LREE in hydrothermal fluids, consistent with experimental work from the same research group. In contrast, multiple stages of mineralisation at Khibina, Russia, indicate that later-stage carbonatites have higher HREE concentrations than earlier hydrothermal stages, and are HREE-mineral bearing which suggests that, in some carbonatites, hydrothermal conditions can preferentially mobilise the HREE (Zaitsev et al., 1998).

Mineralogy can also be used to infer temperature and pressure ranges, based on theoretical and experimental mineral stabilities. The P-T ranges of some common REE-minerals found in carbonatites has been reviewed by Wall et al. (2004) (Fig. 2.12). This review compiles the work of Williams-Jones and Wood (1992) who first built a petrogenetic grid based on observational and thermodynamic data in the $\text{REE}(\text{CO}_3)\text{F}-\text{CaCO}_3-\text{F}_2(\text{CO}_3)_{-1}-\text{H}_2\text{O}$ system, adding additional constraints from subsequent experimental work on bastnäsité and observational constraints for cerianite, florencite, pyrochlore, monazite, allanite, burbankite and ancylite.

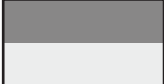
Inferences from fluid inclusions

The temperature, salinity and limited compositional data of REE-bearing hydrothermal fluids can be inferred from fluid inclusions. To date, few studies have been carried out on fluid inclusions from hydrothermal REE deposits, and the data are typically restricted to inclusions in fluorite, quartz, barite, and apatite, with limited additional data from REE-phases, such as bastnäsité. Analysis of fluid inclusions has been carried out on samples from carbonatites (Samson et al., 1995a,b; Böhn and Rankin, 1999; Costanzo et al., 2006), fluorite deposits related to carbonatites (Palmer and Williams-Jones, 1996; Böhn et al., 2002; Xie et al., 2009), at the carbonatite-related Bayan Obo REE deposit (Smith and Henderson, 2000; Fan et al., 2004), alkaline-rock related REE deposits (Taylor and Pollard, 1996; Salvi and Williams-Jones, 1996, 1997), hydrothermal REE deposits (Williams-Jones et al., 2000; Samson et al., 2004), and at the Bastnäs-type skarn deposits (Holtstam et al., 2014). A summary of the homogenisation temperature, composition and salinity of inclusions from these locations is included in Table 2.7.

Direct evidence for REE mobility is found where REE-bearing daughter minerals are present in fluid inclusions. For example, burbankite has been found as a daughter mineral in fluid inclusions from carbonatites (Böhn et al., 1999), and fluorocarbonate minerals have been interpreted as daughter minerals at Bayan Obo, China; Tamazeght, Morocco; Strange Lake and Thor Lake, Canada (Fan et al., 2004; Salvi et al., 2000; Salvi and Williams-Jones, 1990; Taylor and Pollard, 1996). In these cases the salinity of the fluid ranges from 6 to 29 wt. % NaCl eq. and the homogenisation temperatures are 300–360 °C.

The temperature of REE-bearing fluids can be inferred from the homogenisa-

	Temp.	Pressure	REE fluorcarbonates			carbonates		phosphates		oxides	silicates
Magmatic	> 750°C	>0.1 GPa	REE substitute at low levels into dolomite and calcite			REE in Sr-rich carbonate		REE substitute into apatite; rare monazite		accessory pyrochlore, perovskite	
Transition	750°C	0.1 GPa						monazite			allanite?
	650°C		bastnäsite	synchysite		burbankite					
	550°C				parisite		carbocernaite				
Hydro-thermal	450°C										
	350°C					ancylite					
	250°C								florencite-goyazite		
	150°C										
Weathering	25°C	Atmospheric						monazite rhabdophane	crandallite-group	cerio-pyrochlore	cerianite



 Common temperature range
 Less common or uncertain temperature range

Figure 2.12: Temperature and pressure ranges of common REE-bearing minerals found in carbonatites. From Wall et al. (2004).

tion temperature of fluid inclusions. In this case the homogenisation temperature provides a constraint on the minimum temperature of the fluid, due to the effects of pressure. The homogenisation temperature of inclusions in REE minerals, or in phases paragenetically related to the formation of REE minerals, generally fall between 200–400 °C (Table 2.7). The salinity of inclusions is very variable, with a median of approximately 10 wt.% NaCl eq. but inclusions can range in salinity from near 0 wt.% NaCl eq. to halite-bearing inclusions with up to 60 wt.% NaCl eq. Similarly, there is a wide range of fluid inclusion types, from simple liquid-vapour inclusions to multi-phase and CO₂-rich inclusions.

Where inclusion data are available from both REE-bearing minerals and gangue minerals, the gangue minerals typically have fluid inclusions with a lower homogenisation temperature than those from the REE-bearing phase. For example, fluorite often contains inclusions, typically simple LV¹⁹ inclusions, with homogenisation temperatures between 100–200 °C (e.g. Bayan Obo, Kizilçaören and Bastnäs; Smith and Henderson, 2000; Gültekin et al., 2003; Holtstam et al., 2014). A similar observation is noted from carbonatite-derived fluorite deposits such as Okorusu, Namibia, and Amba Dongar, India, where the homogenisation temperature of fluorite is typically less than 160 °C (Palmer and Williams-Jones, 1996; Bühn et al., 2002). These observations potentially indicate that F can remain in solution to relatively low temperatures, and after formation of REE-minerals.

2.6.5 Current REE deposit models

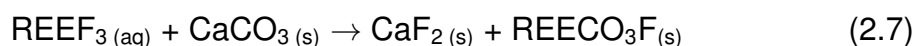
It has been established that the mobility of the REE is a function of the stability of different complexes, the solubility of REE-minerals, the availability of anions to complex with and the P, T, pH and redox conditions of the fluid. The key points are:

- At high temperature, F⁻, CO₃²⁻ and SO₄²⁻ form the most stable complexes with the REE
- With increasing temperature, the solubility of REE phosphates, fluorides and probably fluorcarbonates (although not proven) decreases.
- Fluids transporting the REE are known from limited fluid inclusion experiments and from natural analogues and these:
 - are often between 200–400 °C,
 - are typically acidic,
 - are generally NaCl-bearing, and sometimes NaCl-rich,

¹⁹liquid-vapour

- can also be sulphate- and/or CO₂-rich,
- Commonly have low F concentrations relative to Cl, CO₂ and S.

As previously discussed, the abundance of F-bearing minerals, such as fluorite, associated with REE deposits has led many researchers to interpret REE deposition as due to reaction of acidic REE-fluoride complexes with a neutralising substance, such as calcite:



This is supported by the strong ability of the REE to form complexes with fluorine, and the common association of bastnäsite with fluorite. However, Williams-Jones et al. (2012) and Migdisov and Williams-Jones (2014) raise some issues with this model:

1. Based on inclusions from the Capitan Pluton (Banks et al., 1994; Campbell et al., 1995), the fluorine concentration in REE-bearing fluids is low. Most other natural analogues support this.
2. The solubility of REEF₃ is low, and very acidic (pH < 3) conditions are required to keep it in solution.
3. Hydrofluoric acid is a strong acid and, at low pH conditions, HF doesn't readily dissociate, so the amount of free F⁻ available for the REE to complex with is low.

Thus, on the basis of combined experimental work and theoretical estimates, Williams-Jones et al. (2012) and Migdisov and Williams-Jones (2014) advocate that fluorine alone is unlikely to complex and transport the REE. In acidic conditions it will remain as HF and, at less acidic conditions, the REE will precipitate out of solution forming REE-fluoride minerals (e.g. Fig. 2.13). The scenario is most applicable at temperatures between 200–400 °C. At lower temperatures the stability of REE-fluoride minerals and the dissociation constant of HF increases and, thus, F may be able to complex the REE in low temperature fluids. Nevertheless, as Table 2.7 shows, evidence from fluid inclusions indicates that the most common conditions under which REE minerals are formed is around 300 °C.

Instead of fluorine as the complexing anion, Williams-Jones et al. (2012) and Migdisov and Williams-Jones (2014) propose SO₄²⁻ and/or Cl⁻ as alternative complexing anions, favouring Cl. This is because Cl⁻ is abundant in fluids and, at elevated temperatures, forms relatively stable complexes with the REE. Furthermore, HCl is a weak acid, and thus, at low pH, many Cl⁻ anions would be available to complex with the REE. At conditions with higher pH and temperature (increasing in significance from around 300 °C), sulphate could also contribute to the mobility of the REE (Fig. 2.13).

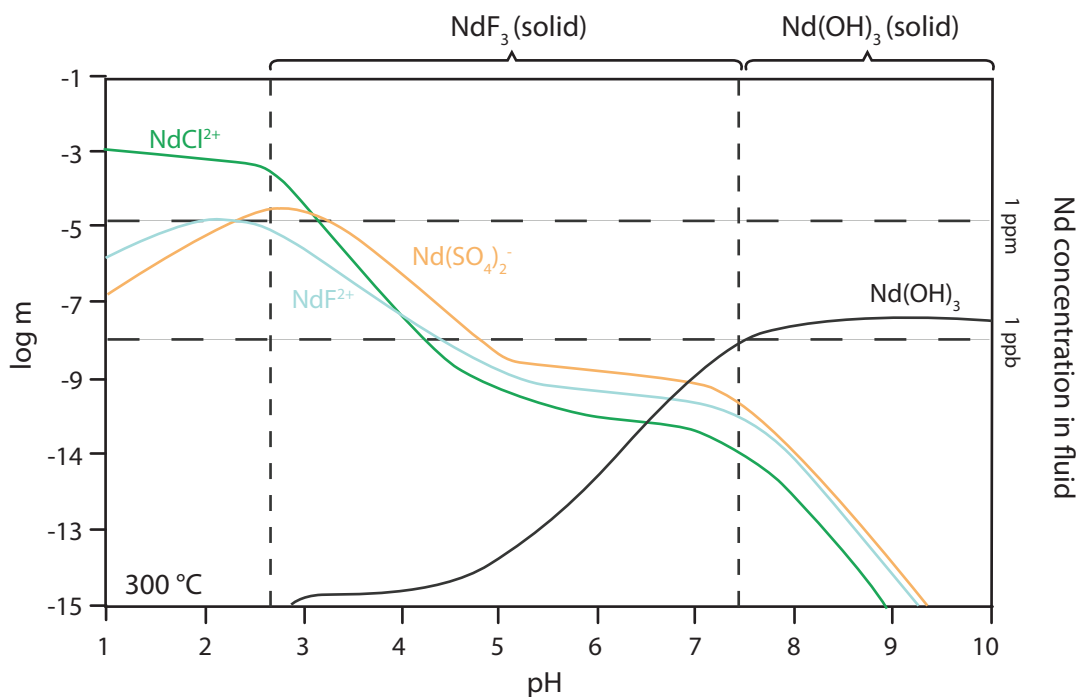


Figure 2.13: Simplified speciation diagram of Nd as a function of pH in a 300 °C hydrothermal solution at 100 MPa. The initial composition of the fluid is 10 wt.% NaCl, 2 wt.% Na₂SO₄, 500 ppm HF and 200 ppm Nd, based on the composition of inclusions from the Capitan Pluton (Banks et al., 1994). Diagram simplified after Migdisov and Williams-Jones (2014)

Fluorine is considered by Williams-Jones et al. (2012) and Migdisov and Williams-Jones (2014) to act not as a transporting complex, but as a binding ligand, causing precipitation of REE-bearing minerals. An example would be a re-interpretation of reaction 2.7, where a REE-Cl species, in the presence of HF, reacts with a carbonate-bearing rock:



In this example, the introduction of calcite increases the pH of the solution, precipitating bastnäsite and any excess fluorine is precipitated as fluorite. Other suggested depositional mechanisms include increasing the pH through mixing with higher pH fluids, boiling/degassing or cooling. Other, non-pH related, mechanisms include removing S from solution through precipitation of barite or introduction of P into the solution. As REE-phosphate minerals have a lower solubility than REE-fluoride minerals, introduction of P by, for example, reaction with apatite, would cause precipitation of monazite or xenotime.

Separation of the LREE from the HREE can potentially be achieved using this model. At temperatures of around 300 °C, the LREE form complexes which are more stable than complexes with the HREE in both F-bearing and Cl-bearing solu-

tions (Migdisov et al., 2009; Fig. 2.8). In a model fluid, where successive amounts of REE-bearing fluid are fluxed through a P-bearing sample, the pH buffering capacity of the rock is decreased due to consumption of P to form monazite. As more REE-bearing fluid is fluxed through, the LREE are preferentially dissolved from the monazite and re-precipitated further from the source at a lower temperature. Thus, fluxing of fluids multiple times through a rock can cause the LREE to be transported further from the REE source than the HREE (Sheard et al., 2012; Williams-Jones et al., 2012).

The model fluid compositions used by Migdisov and Williams-Jones (2014) are close to that of the composition of fluid inclusions from the Capitain Pluton (Banks et al., 1994; Campbell et al., 1995). While the model presented by Migdisov and Williams-Jones (2014) is a good general model for many hydrothermal fluids, it may not be directly applicable for *all* fluids, especially those derived from carbonatite. For example, the high-temperature, high-CO₂, high-SO₄ fluids from Maoniuping, China, are considerably different than the fluids from the Capitain Pluton, and may be an example of where sulphate- and/or CO₂-rich fluids are responsible for the complexation of the REE (Xie et al., 2009). Furthermore, the model does not consider the transport of REE in low salinity fluids. Salinity in fluid inclusions from hydrothermal ore deposits may be lower than 10 wt.% NaCl, and thus the amount of Cl in solution could significantly reduce the amount of REE complexed by Cl. It is also possible that, especially in carbonatites, F concentrations could be higher than 500 ppm used in the model solution. Indeed, even at the Capitain Pluton, the concentration of F in solution can reach 5000 ppm (Campbell et al., 1995). Fluorine concentrations in fluids from carbonatites are not readily available, but fumarole vapours have an HF concentration of over 3000 mmol/mol (Teague et al., 2011) and fresh natrocarbonatite, although perhaps not the best analogue, can have F concentrations up to 3.6 wt. % (Mangler et al., 2014).

It is possible that carbonate could be a significant transporting ligand for the REE. Carbonate complexes are not considered in the calculations of Migdisov and Williams-Jones (2014) as no speciation data is available for these phases. For REE depositional models from alkaline rocks, the exclusion of CO₂ from the model may be acceptable as high CO₂ concentrations in fluid inclusions from these rocks are less common (Table 2.7). In carbonatites, however, CO₂ may be an important complexing agent. It forms strong complexes with the REE, and the concentration of CO₂ in solution can be high, up to 50 molar % in vapours from Oldionyo Lengai (Teague et al., 2011). Migdisov and Williams-Jones (2014) predict that the solubility of REE carbonates would be low, given the low solubility of calcite and dolomite, but no experimental work has yet demonstrated this.

2.7 REE from the mantle to a carbonatite-hosted ore deposit— supergene processes

The final process which can enrich the REE in a carbonatite-hosted ore deposit is through supergene alteration and breakdown of carbonates, leading to residual enrichment of the REE into the regolith, such as laterite (Fig. 2.5). The REE are retained in the laterite due to their limited mobility in low-temperature fluids (Fig. 2.6). REE concentrations in the laterite can show as much as an order of magnitude greater REE concentration than the host carbonatite. Ores are typically a fine grained mixture of secondary REE phosphates such as churchite-(Y) and rhabdophane-(Ce), with clays and crandallite-group minerals. The most well-known REE deposit associated with a laterite is Mt Weld, Australia (Lottermoser, 1990). However, similar deposits also occur at Araxá and Catalão Brazil (Morteani and Preinfalk, 1996); Dong Pao, Vietnam; and Tomtor, Russia (Kravchenko and Pokrovsky, 1995).

2.8 Summary

In this review, carbonatites and the REE²⁰ were defined. Carbonatites are igneous rocks with greater than 50 % carbonate minerals. The REE are the 15 elements of the lanthanoid series, plus Y, but excluding Pm. The REE are subdivided into the HREE²¹ and the LREE²² comprising La–Sm and Eu–Lu+Y, respectively.

Carbonatites are sourced from the mantle and are distributed worldwide, typically in intracratonic rift zones. They form from low-degree partial melts of a metasomatised mantle. Commonly, carbonatites are associated with alkaline silicate rocks. Genetic models account for this association through formation via liquid immiscibility from a carbonated silicate magma, or through fractional crystallisation of a nephelinite magma. Alternatively, they could form directly from the mantle and not be genetically associated with silicate rocks. Geochemically, carbonatites are enriched in the REE, Nb, Sr, Ba, P, Ca, Mg and Fe and are major economic hosts for the REE, fluorite, and Nb.

The REE are an economically and geochemically important group of elements. They share similar geochemical characteristics but behave subtly, but consistently, different from each other due to the lanthanide contraction. They all form 3⁺ ions, with the exceptions of Ce⁴⁺ and Eu²⁺ which form under oxidising and reducing conditions, respectively. The LREE are much more abundant than the HREE, but many of the elements of the latter group are considered as critical

²⁰rare earth elements

²¹heavy rare earth elements

²²light rare earth elements

metals. This is due partly to their lower abundance, but is also driven by economic demand for REE permanent magnets and phosphors. Most of the REE are actually quite geologically common, and this is reflected in the wide range and large number of potential ore deposits worldwide. Major REE hosting environments include carbonatite, alkaline rocks, placer deposits and ion-adsorption deposits. The importance of by-products and co-products such as apatite, which can host significant concentrations of the REE, remains to be demonstrated. Carbonatite-hosted deposits are considered to be attractive targets as they can be high grade and high tonnage, with low U and Th concentrations (both of which are problematic for the transport and processing of the REE). Furthermore, the mineralogy of these deposits is relatively simple to process.

There are four major stages in the formation of a carbonatite-associated REE deposit: mantle processes, including metasomatism and melting; magmatic differentiation; hydrothermal transport and fractionation; and supergene enrichment. This thesis focusses mostly on the hydrothermal evolution of the REE from carbonatites.

The ability of hydrothermal fluids to transport and fractionate the REE is dependent on the solubility of REE minerals, the stability of REE complexes and the availability of different anions for the REE to complex with. Other factors also include the temperature, pH, and redox conditions of the fluid. The stability of different REE complexes is known from ambient-temperature experiments, theoretical extrapolations and high-temperature experiments. These have shown that F^- , Cl^- , CO_3^{2-} and SO_4^{2-} form stable complexes with the REE. The stability of LREEF and LREECl complexes is higher than their HREE counterparts, while the stability of REE complexes with CO_3^{2-} and SO_4^{2-} is relatively similar for the different REE. Solubility information on the REE minerals is scarce, but some data are available for the REE phosphates. These are shown to be highly insoluble, with decreasing solubility with increasing T, although this trend may be reversed at higher temperatures (above 300 °C).

There is little data on the composition of REE-bearing hydrothermal fluids and, therefore, little is known about what are the prevailing REE complexes in nature. From limited measurements of the REE in fluid inclusions, Cl^- , SO_4^{2-} , and F^- are known to be present in fluids from granitic sources, and the LREE are more abundant. Similar results were obtained from the measurement of fluids from carbonatitic sources, although these have much higher REE contents, and also a significant component of CO_2 . Other sources of data to infer the composition of a REE-mobilising fluid include deep-sea hydrothermal fluids, geothermal fluids and vapours from Oldoinyo Lengai. These are almost all LREE-enriched, but the concentrations of the REE vary substantially. S- and F-rich fluids carry the highest concentrations of the REE, and F-enriched fluid from deep-sea vents are slightly

LREE-depleted. Carbonate fluids carry the lowest concentrations of the REE, but high temperature CO₂-dominated vapours from Oldoinyo Lengai can have high REE concentrations similar to those in granitic derived fluids.

Where direct measurements of REE fluid are not obtainable, the composition of a REE-bearing fluid is often derived from the mineralogy of a REE-ore deposit. Common gangue minerals in these deposits include barite, calcite, fluorite and apatite. These minerals indicate that SO₄²⁻, CO₃²⁻/HCO₃⁻, and F⁻ are present in the precipitating fluid. Information about the nature of the fluid can also be obtained from REE patterns, as Y/Ho ratios are typically strong indicators of F complexation. Measurements of the homogenisation temperature of fluid inclusions related to these deposits shows that the REE minerals typically form between 200–400 °C. The salinity and composition of the inclusions is variable, with 0–60 wt. % NaCl eq. and variable CO₂ contents.

A general deposit model for hydrothermal REE complexation and formation has been suggested by Williams-Jones et al. (2012) and Migdisov and Williams-Jones (2014). This model proposes that the main ligands transporting the REE are Cl⁻ and SO₄²⁻. The common occurrence of F⁻ with REE deposits is attributed to the role of F⁻ as a binding ligand. REECl- and HF-bearing fluids are transported until the fluid reacts with a carbonate- or apatite-bearing rock. The model works well for alkaline rock- and granite-related REE deposits, as the model is based upon the composition of REE-bearing fluids from a granite. The model does not consider, however, the role of CO₂ in transporting the REE. This ligand is likely to be important in transporting the REE in carbonatites, as demonstrated by the high concentration in fluids from carbonatites at Oldoinyo Lengai and from fluid inclusions.

Chapter 3

Geology of the Songwe Hill carbonatite and its surroundings

The main carbonatite studied in this thesis is the Songwe Hill carbonatite, located in south-eastern Malawi, in the CAP¹. In this chapter, the CAP is reviewed, with a focus on the CAP carbonatites, to put the Songwe Hill carbonatite into context. Subsequently, the geology of Songwe Hill is summarised, with a focus on the carbonatite types and field relationships of the different geological units. These descriptions incorporate both a literature review and new observations made during fieldwork in 2011 and 2012.

3.1 Review of the Chilwa Alkaline Province

The CAP, originally named the Chilwa Series (Dixey et al., 1955), is a mostly intrusive suite of Early Cretaceous alkaline rocks, ranging from carbonatites through nephelinites, ijolites (essential nepheline and augite), nepheline-syenites, syenites, quartz-syenites and granites (Woolley and Garson, 1970; Woolley, 2001). It is a region approximately 300–400 km in diameter extending from the southern end of Malawi into Mozambique (Fig. 3.1). The intrusions of the CAP were emplaced into an area of crustal weakness possibly associated with rifting (Woolley and Garson, 1970).

There are four main geological units in southern Malawi, where most of the CAP is located. A summary of the geological succession, after Garson and Walshaw (1969), is given in Table 3.1.

The regional basement in south-eastern Malawi consists of Precambrian quartzofeldspathic granulites and gneiss, with varying amounts of biotite, pyroxene, hornblende, garnet and, locally, marble (Bloomfield, 1968). This is intruded by the Stormberg series, a suite of Jurassic dolerite dykes trending NE–SW. The Storm-

¹Chilwa Alkaline Province

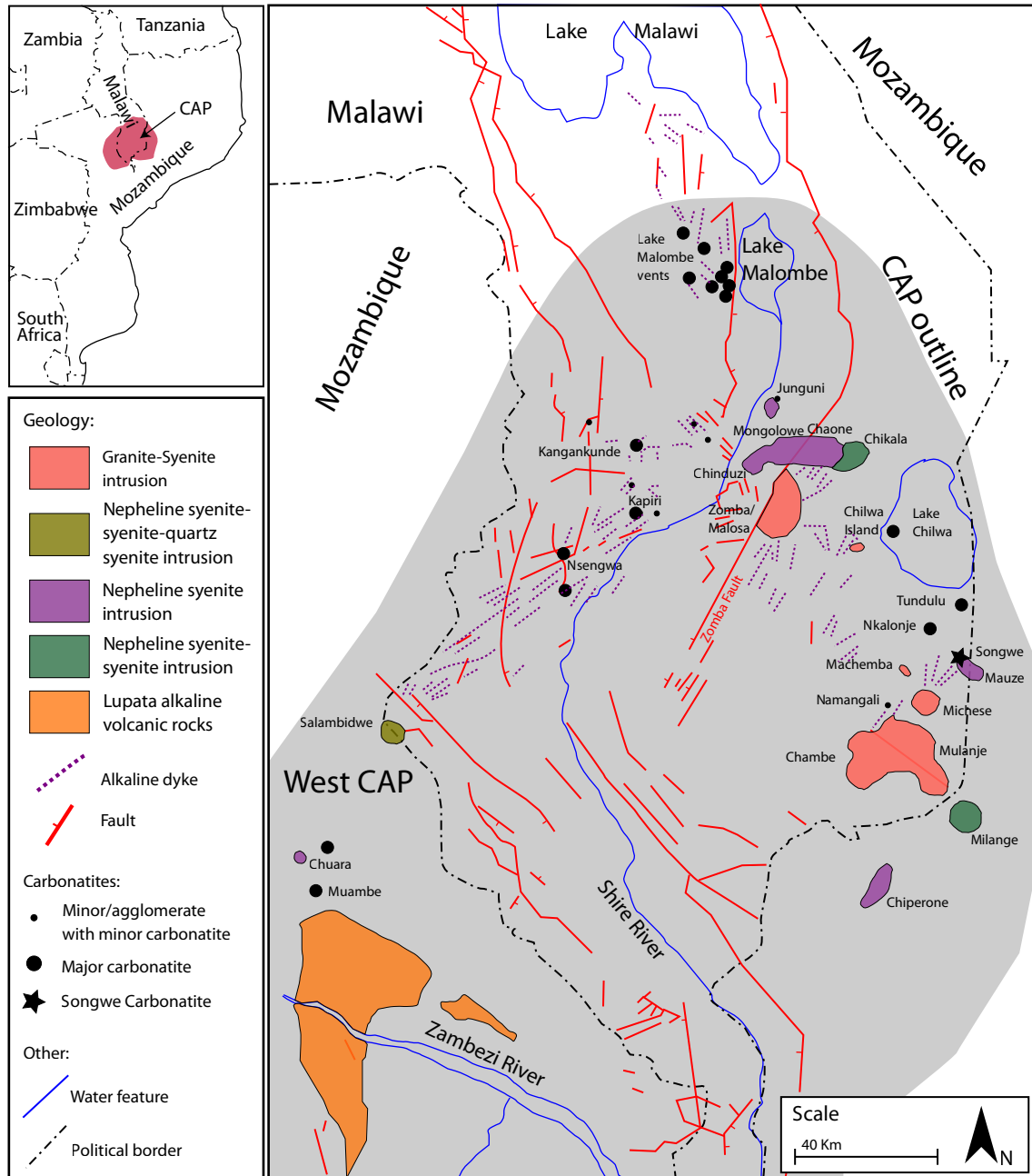


Figure 3.1: The geology of the CAP showing the carbonatite centres and tectonic setting. Adapted from Woolley (2001) and Garson and Smith (1965)

Age	Geology
4 Cenozoic–Recent	Lacustrine and alluvial sediments
3 Upper Jurassic–Lower Cretaceous	Chilwa Alkaline Province
~~~~~ unconformity ~~~~~	
2 Lower Jurassic	Stormberg Series
~~~~~ unconformity ~~~~~	
1 Precambrian	Basement complex

Table 3.1: Regional geological sequence, after Garson and Walshaw (1969)

berg series pre-dates the CAP by approximately 30 Ma, and is petrologically unrelated to it (Macdonald et al., 1983). A petrogenetic link between large igneous provinces and carbonatites, however, has been suggested (Ernst and Bell, 2010), and it is possible that the Stormberg series may be a result of the early stages of rifting in East Africa, at the close of regional Karroo sedimentation but prior to the CAP (Woolley and Garson, 1970).

The CAP intrudes the basement in a variety of styles, ranging from large mountainous plutons to smaller alkaline dyke swarms. The largest features are the mountainous granites and peralkaline syenites such as those at Zomba-Malosa, Mulanje and Michese in Malawi and Morrumbala in Mozambique (Table 3.2). Large nepheline syenites occur at Junguni, Mongolowe, Chaone in Malawi, Mauze in Malawi/ Mozambique, Chiperone and Chuara in Mozambique. Nepheline-syenite–syenite intrusions occur at Chikala in Malawi and Milange in Mozambique and nepheline-syenite–syenite–quartz-syenite intrusions occur at Salambidwe in Malawi/Mozambique and at Gorongosa in Mozambique. These intrusions are mineralogically diverse, and are host to numerous REE- and HFSE²-rich minerals (Platt et al., 1987; Woolley and Platt, 1988; Woolley and Jones, 1992). The depth of these intrusions is generally considered to be shallow, and the level of erosion low (Eby et al., 1995). Numerous alkaline dykes are present in the region, following NE–SW lines of crustal weakness, and there are also many small nephelinite and phonolite plugs and small breccia vents (Woolley, 2001) (Fig. 3.1). Volcanic rocks of the Lupata-Lembombo area in Mozambique are comprised of phonolites,

²high field strength elements

kenytes (a variety of porphyritic phonolite or trachyte with rhomb-shaped anorthoclase, variable olivine and augite in a glassy matrix) and blairmorites (porphyritic phonolite with analcime). These rocks are considered to be potentially related to the CAP, possibly representing an early rift stage (Woolley and Garson, 1970).

Post-CAP volcanism, the region was eroded, possibly more deeply in the east than in the west (Eby et al., 1995). Cenozoic lacustrine and alluvial sediments cover much of the eastern part of the region forming a flat plain, with sporadic inselbergs where the lesser eroded CAP intrusions and basement are often found.

The intrusions of the northern and western parts of the CAP have been well studied and, because the southern and eastern CAP has the same rock types, these can broadly be considered as representative of the whole province. The igneous rocks of the CAP can be divided into three groups based on geochemistry (Woolley and Jones, 1987), field relations (Woolley, 1987) and geochronology (Eby et al., 1995):

1. The earliest phase (*ca.* 133 Ma) of nephelinite, basanite and sodalite-rich nepheline syenite. This is suggested to be associated with carbonatite activity at Chilwa Island.
2. A later phase of nepheline syenite and syenite plutons (*ca.* 126 Ma.).
3. The latest phase of syenites and granites (*ca.* 113 Ma). These syenites differ from earlier syenites in having a larger volume, and lower CaO and MgO with greater SiO₂.

In the CAP, there is a notable abundance of felsic rocks relative to mafic intrusions. A common trend of the intrusions is increasing size of the intrusion and total SiO₂ content with time. Woolley (1987) interprets these three suites as coming from three different parental magmas of deep nephelinitic/carbonatitic, intermediate phonolitic and shallow trachytic composition. A model has been proposed involving focussed metasomatism of the lithosphere migrating upwards toward the lower crust, causing processes akin to fenitisation and a zoned mineralogy with depth (Woolley, 1987). This led to uplifting and faulting due to the lower densities of the metasomatised rocks, facilitating further metasomatism. As the faulting progressed, the pressure release caused partial melting over a range of depths resulting in a range of different magma compositions. In contrast, Burke et al. (2003) suggest that the source of the alkaline and carbonatite magmatism could be from previously-subducted deformed alkaline and carbonatite rocks, emplaced as part of the Mozambique belt (*ca.* 550 Ma). It is proposed that remelting of this alkaline source at *ca.* 100 km depth could have been caused by early rifting. While evidence for such deformed alkaline rocks exists (e.g. Bloomfield, 1965b; Ashwal et al., 2007), a problem with the hypothesis is that it does not identify the

source of the alkaline melts; it merely pushes back the timing of alkaline activity to the Precambrian.

3.2 Carbonatites of the Chilwa Alkaline Province

The carbonatites of the CAP were the first to be recognised in Africa (Dixey et al. 1937, reprinted as Dixey et al., 1955). They were extensively studied in the 1950s and 1960s and reviews of the carbonatites can be found in Garson (1965), with a modern update in Woolley (2001). They are documented in Table 3.2. Garson (1965) describes 17 occurrences of carbonatite in Malawi, with 6 occurring as larger ring structures, 4 occurring as dykes or infilled fissures, 3 major areas of carbonatitized vent-agglomerates and numerous smaller agglomerate-choked vents, thought to be associated with carbonatite. Woolley (2001) documents 4 areas containing carbonatite in the Mozambique sector of the CAP, with 1 major ring structure, 2 minor occurrences and 1 which is listed as possibly erroneous.

The major intrusions in the CAP occur as ring structures. These have arcuate structural forms, with features younging progressively towards the centre of the intrusion. The first and outermost stage of an intrusion is a zone of contact breccia above the carbonatite pluton. This is formed of angular, fragmented country rock, infilled with comminuted and fenitised country-rock and, locally, igneous or hydrothermal rocks. This zone of brecciation is fenitised to a varying degree, producing rocks consisting of aegerine, orthoclase–microperthite or anorthoclase, and albite. During the latter stages of magmatic activity, contact breccia is increasingly altered to feldspathic breccia. The degree of feldspathisation increases towards the main carbonatite intrusion. The igneous stage of the intrusion is typically comprises three types of carbonatite: the earliest is calcite carbonatite (sövite), followed by magnesiocarbonatite and ferrocarbonatite (e.g. Chilwa Island, Garson and Smith, 1958). This pattern is common worldwide for carbonatite associated with nepheline-bearing rocks (Le Bas, 1981), but is not always the case. At Tundulu, for example, magnesio- and ferro carbonatites are not a major phase, but apatite carbonatite is abundant (Garson, 1962). At Kangankunde, magnesio- and ferro carbonatites are the only observed carbonatites and 'earlier' calcite carbonatite is absent (Garson and Smith, 1965; Wall, 2000).

The minor carbonatite occurrences do not form ring structures, and are either carbonatitized agglomerate vents, dykes, veins or infilled fissures. Carbonatitized agglomerates are normally composed of small, roughly circular vents filled with fenitised agglomerate with areas where the matrix is partly, or fully, replaced with carbonate. These vents may have an associated area of fenitization and brecciation. Dykes, veins and in-filled fissures are usually small and often not laterally extensive.

Silicate rocks are commonly associated with both major and minor carbonatite intrusions. Silicate rocks preceding the carbonatite are not common, but when present they are usually nephelinitic (e.g., Chilwa Island, Garson and Smith, 1958). Trachytes are often listed as preceding the carbonatite intrusions (Garson, 1965) but these are often 'ultra-fenites' where fenite has been remobilised into a highly alkaline siliceous rock (see Le Bas, 2008; and section A.4.2). Alkaline dykes, including phonolite and sölvbergite (a variety of peralkaline microsyenite or peralkaline trachyte; Le Maitre, 2002), often post-date the carbonatite intrusions, but these could be part of regional dyke swarms, rather than directly related to the intrusion of individual carbonatites.

Chilwa Island and Kangankunde have been isotopically studied to investigate the source region of the CAP (Simonetti and Bell, 1994; Ziegler, 1992). These studies found that the mantle source has depleted Rb/Sr and Sm/Nd and enriched Th/Pb and U/Pb, relative to bulk-earth, suggesting that it is part of the ancient depleted sub-continental lithospheric mantle, similar to most of the other carbonatites in East Africa, extending as far north as Uganda (Bell and Tilton, 2001).

Carbonatites in the CAP have been investigated as a potential target for a variety of mineral resources over the past 60 years. The main minerals and metals of interest have been apatite (P), the REE, strontianite (Sr), pyrochlore (Nb) and, to a lesser extent, barite (Ba) and Mn and Fe oxide minerals (Garson, 1965). The main intrusions of interest have been the larger carbonatite complexes: Chilwa Island, Tundulu, Kangankunde and Songwe. These have been historically investigated by BRGM³, MMAJ⁴ and JICA⁵, and the BGS⁶, principally for niobium, REE and phosphate. There is currently a great deal of renewed interest in CAP carbonatites due to the recent (2011) REE boom, and many are being explored for the REE.

3.3 Study area

The area studied in this research is located in the east CAP in the Phalombe district of south-east Malawi (Fig. 3.2). Fieldwork was carried out in collaboration with Mkango Resources in their Phalombe exclusive prospectivity licence area. The main focus was the Songwe Hill (*syn.* Songwe) carbonatite. Limited investigations were also carried out at the Tundulu and Nkalonje carbonatites, and at two breccia cones: Sombani, and 'Mantrap' - a previously un-described breccia cone on the southern flanks of Mauze (Appendix A). Reasonable all-weather

³Bureau de recherches géologiques et minières

⁴Metal Mining Agency of Japan

⁵Japan International Co-operation Agency

⁶British Geological Survey

Name	Geographical features	Geological features		
		Pre-carbonatite	Carbonatite	Post-carbonatite
Chilwa Island	Rings of low, broken hills surrounding a central conical hill.	Fenitised and brecciated basement.	4 igneous centres of (1) acmite-sövite, (2) olivine-nephelinite, alnoite, pyrochlore-sövite, phonoite and aegirine-biotite-sövite, (3) dykes of foyaite, juvite, phonolite, ijolite and silicate-sövites and (4) ankerite-sövite, manganiferous and sideritic carbonatite.	Hydrothermal activity, dykes of sölvbergite, olivine nephelinite and dolerite, lamprophyre plug.
Tundulu	Steep arcuate ridges (300 m) around a central conical hill.	Fenitised and brecciated basement with early nephelinite and melanephelinite dykes.	3 rings structures of (1) sövite and agglomerate, (2) apatite-rock, apatite-sövite and agglomerate and (3) carbonate-silicate rocks in a foyaite ring dyke.	Alkaline dykes, dykes and plugs of melanephelinite, and beforosite.
Songwe	Steep, conical hill rising 300 m on the NW of Mauze.	Fenitisation, intrusion of melanephelinite and foyaite, brecciation.	Lobes of fine grained, calcite carbonatite with dark streaks or veins of Fe and Mn oxides, and entrained fenite clasts	Alkaline dykes, related to local dyke swarm in the area from Lake Chilwa to Mlanje.
Kangankunde		Potassic and sodi-potassic fenite with phlogopitisation.	Apatite rich dolomite, ferroan dolomite and ankerite carbonatites with Mn rich varieties in arcuate dykes. Cross-cutting ferrocarbonatite	Biotite alnöite and sölvbergite.
Nkalonje	Low, joined hills rising about 150 m.	Fenitization, updoming and intrusion of early melanephelinite. Followed by remobilisation of fenite and brecciation, nepheline syenite and phonolite intrusion	Two dykes of medium to coarse grained calcite carbonatite and siderite carbonatite	Bands of quartz-fluorite rocks and lamprophyre dykes
Namangali	Steep hill, rising about 150 m from the plain.	Brecciation, fenitisation and reworking of fenitised material. Intrusion of phonolite and microfoyaite dykes.	Small carbonatite veins in breccia associated with sodalite. Slightly carbonatitic matrix.	
Nsengwa	Steep 350 m hill, amongst rolling rills.	Microsyenite, breccia and fenite.	Veins and small dykes of ankerite carbonatite agglomerate and quartz carbonatite.	Monchiquite, and sölvbergite and bostonite dykes.
Kapiri	Long, low ridge	Carbonatized nephelinite and fenitised basement.	Quartz-carbonatite agglomerate with marble xenoliths, central carbonatite and carbonatite dykes.	Phonolite and monchiquite dykes.
Lake Malombe vents	Steep sided hills, rising to 350 m, with the larger vents having crater-like hollows.	Brecciation and infilling of vents with nephelinitic agglomerate. Fenitisation and feldspathic agglomerate.	Carbonate replacement of agglomerate, infilling extensive parts of the matrix of some vents.	Microfoyaite, phonolite and carbonate-feldspathoidal plugs. Alkaline dykes.
Caumbwi		Brecciation and fenitisation.	Partial carbonatization of the matrix.	
Western Shire valley vents (4)			Thin veins of carbonatite and carbonatite agglomerate with calcite and siderite matrix.	
Bangala			Small calcite carbonatite dyke	Phonolite(?).
Tumbine			Carbonatite, shown to the SW of Tumbine, possibly erroneous.	
Chandava	Small hill, 1.2 km long	Ordering of other deposits unknown	Carbonatite dyke, trending E-W.	
Buzimuana	Hill, W of Chandava.	Ordering of other deposits unknown.	Fine grained carbonatite, with calcite, limonite, quartz, orthoclase and chlorite.	
Muambe	5 km ring, around a ridge 400 m high.	Ordering of other deposits unknown.	Calcite carbonatite plug, with potential high abundance of silicates and fluorite.	

Table 3.2: List of carbonatites in Malawi, based upon Garson (1965), excluding minor vents around Chilwa Island, the Chimbiri hills and Liwonde. Carbonatite complexes from Mozambique are after Woolley (2001)

roads extend as far as Phalombe, while the last 15 km beyond Phalombe is an unmade track. As of 2011, some lengths of this track are being upgraded. The climate varies between a wet season (November–April) and a dry season. April–November is the most comfortable time to work, with vegetation levels decreasing towards November.

The field area is a flat alluvial plain, centred around Lake Mpoto and the Sombani river (Fig. 3.2). The population density is quite high, with much of the flat ground cultivated and some of the hills terraced, leaving only the tops of hills covered with thick undergrowth. On hills, exposure is often good, although soil cover is substantially thicker over weaker lithologies (e.g. some carbonatite types) and the degree of weathering in these areas is quite high. Weathering can extend locally to several metres deep, but it is patchy and often preferentially follows fractures in rock. Cavities and caves are commonly found in the carbonatites.

3.4 Field techniques and sampling

Fieldwork was undertaken in Malawi in October/November 2011 and November 2012. Each field seasons consisted of approximately 3 weeks of fieldwork and incorporated regional exploration, mapping, geochemical analyses and sampling. The initial field season was based at the Mkango field camp at Songwe, while the 2012 field season was based in Zomba.

3.4.1 Basic mapping

The geological mapping of Songwe Hill, carried out by James Mtegha (Mkango) and Alan Woolley (NHM⁷), was completed during late 2011/early 2012, with final publication in Croll et al. (2014). Additional reconnaissance mapping (3 days) was carried out at “Mantrap” (see Appendix A), with the assistance of James Mtegha and Chikondi Mcheka (Mkango), to a scale of 1:160.

3.4.2 Portable XRF⁸

In the field a handheld XRF analyser was extensively used to guide sampling. The instrument used was a Thermo-Scientific Niton[®] XLP hand-held XRF analyser, which was calibrated for the semi-quantitative analysis of the REE. This instrument was not used for accurate analyses, but to obtain an approximate ratio between the LREE and the HREE. Ce and Y were taken as proxies for the

⁷Natural History Museum

⁸X-ray fluorescence

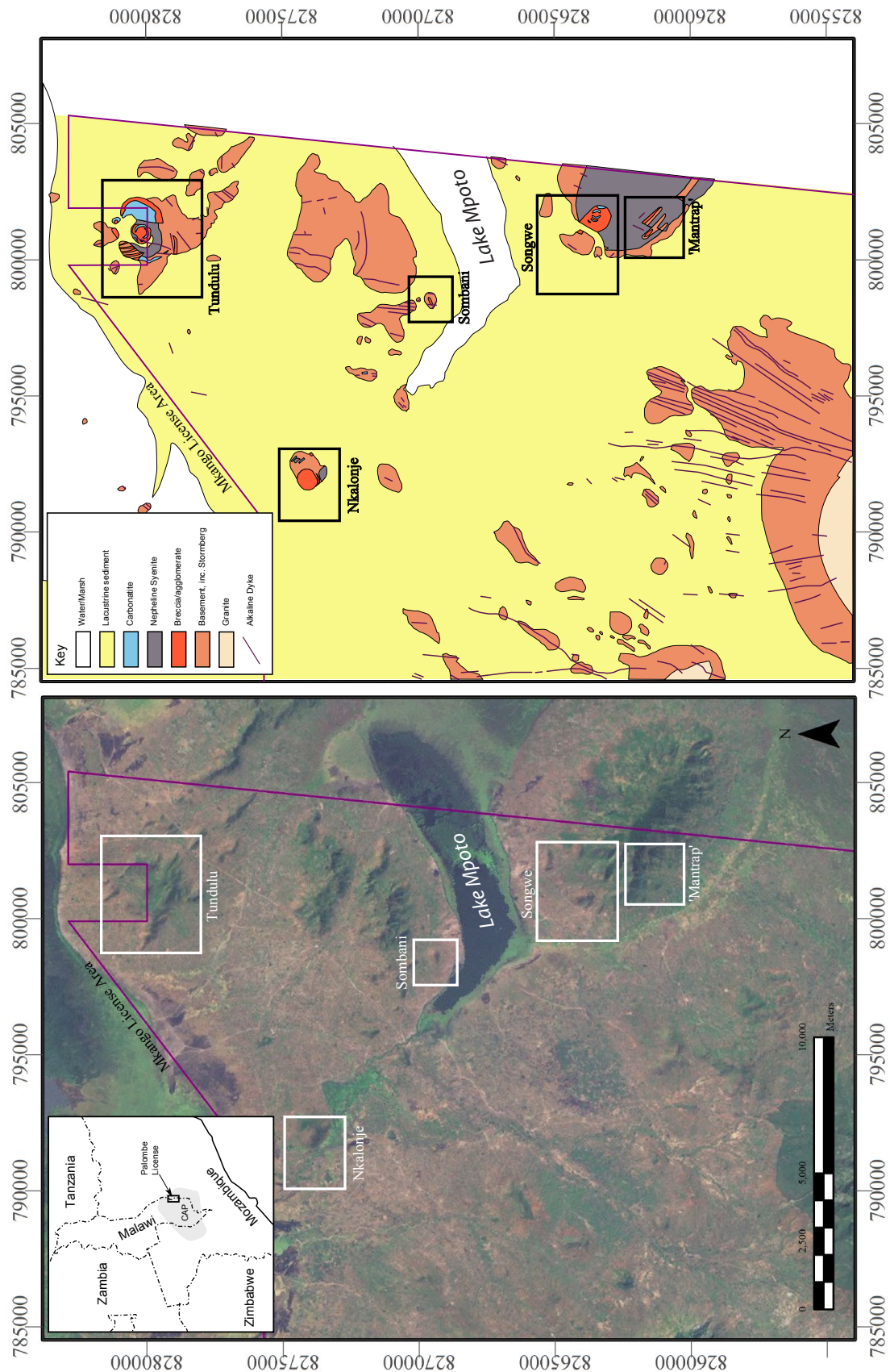


Figure 3.2: Landsat imagery and simplified geological map of study area. Grid system is UTM 36°S. Geological map after Garson and Walshaw (1969)

LREE and the HREE, respectively, as these elements often have the highest natural concentrations, and are subject to the fewest X-ray line overlaps.

An approximate assessment of precision was acquired by determining repeat analyses on sample T0106C (Table 3.3). These repeat analyses provided an assessment of analytical uncertainty due to sample heterogeneity and random machine error. Six repeat analyses were taken, and the concentrations of Y, La, Ce and Th between each analysis was within the reported error from the instrument (Table 3.3). All of the other elements analysed were less precise, and these data were generally not used to aid geological interpretation.

Where analyses were acquired from both the portable XRF analyser and whole-rock ICP-MS⁹, the data show a reasonable correlation, indicating that the accuracy of Y and Ce determined by the portable XRF analyser is good, and provides a very useful field guide (Fig. 3.3). Notable, however, are the effects of sampling bias in the field-analysis, where the REE concentration is over-estimated through the targeting of REE-rich domains within a sample. These effects are shown in the higher REE concentration of some samples analysed by XRF, when compared to the whole-rock analyses.

	1	2	3	4	5	6
Y	1282±140	1190±145	1169±797	1306±164	1182±159	1318±167
La	3963±714	4294±817	4289±1709	4245±849	4390±892	3641±810
Ce	7912±1525	8341±1719	8628±943	7577±1675	9192±1918	8285±1842
Nd	3590±866	3675±890	3545±943	2904±948	2692±828	2560±957
Dy	1997±927	1485±1017	1367±963	1856±1108	2473±1253	
Zr	395±105	265±110	182±109	238±126		213±125
Nb	195±47.7	172±49	254±54	318±64	497±79	377±68
Ba	12.6K±1.4	16.1K±1.8	16.5K±1.8	23.9K±2.5	22.9K±2.5	31.4K±3.3
Sr	4166±303	4394±345	5376±402	6259±507	6971±578	5885±484
Th	1044±172	903±176	1064±186	1146±211	974±202	1225±220
Zn	1244±320	918±324	1218±340	1158±366	1437±398	1576±399
Fe	241.1K±10.6	244.8K±12	275.4K±12.8	294.2K±15.3	286.3K±15.4	288K±15.4
Mn			4705±2126	4406±2336	8411±2366	4356±2697

Table 3.3: Multiple analyses of sample T0106C using the Niton handheld XRF

3.5 The Songwe Hill carbonatite

Songwe is a steep-sided conical hill rising from the north-west side of Mauze. It is approximately 800 m in diameter rising about 230 m from the surrounding plain and partially enclosed by Chenga and Pindani hills to the north (Figs. 3.4 and 3.5A).

⁹inductively coupled plasma mass spectrometry

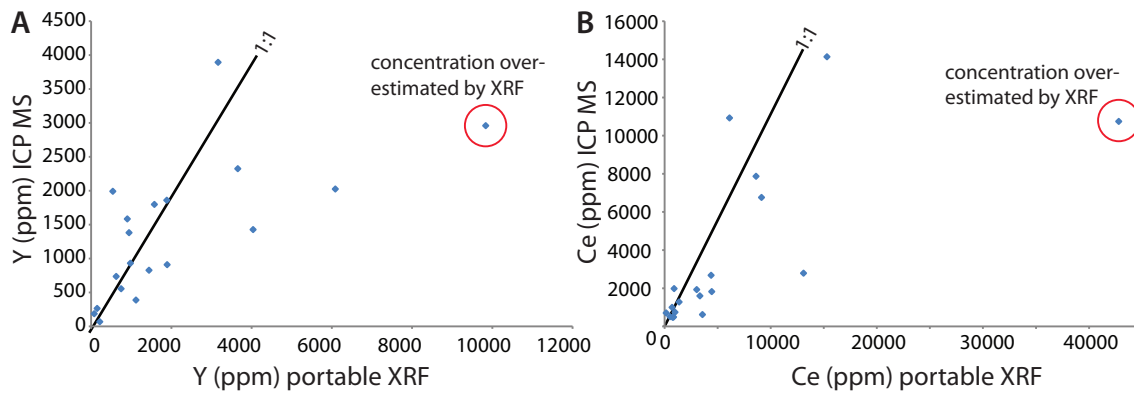


Figure 3.3: Comparison of Y (A) and Ce (B) data from the hand-held XRF and from whole-rock ICP-MS. Data broadly follow the 1:1 line (black), but some analyses from the portable XRF can give significantly higher values than the whole-rock analyses. This is a result of sample heterogeneity and the small area sampled by the XRF.

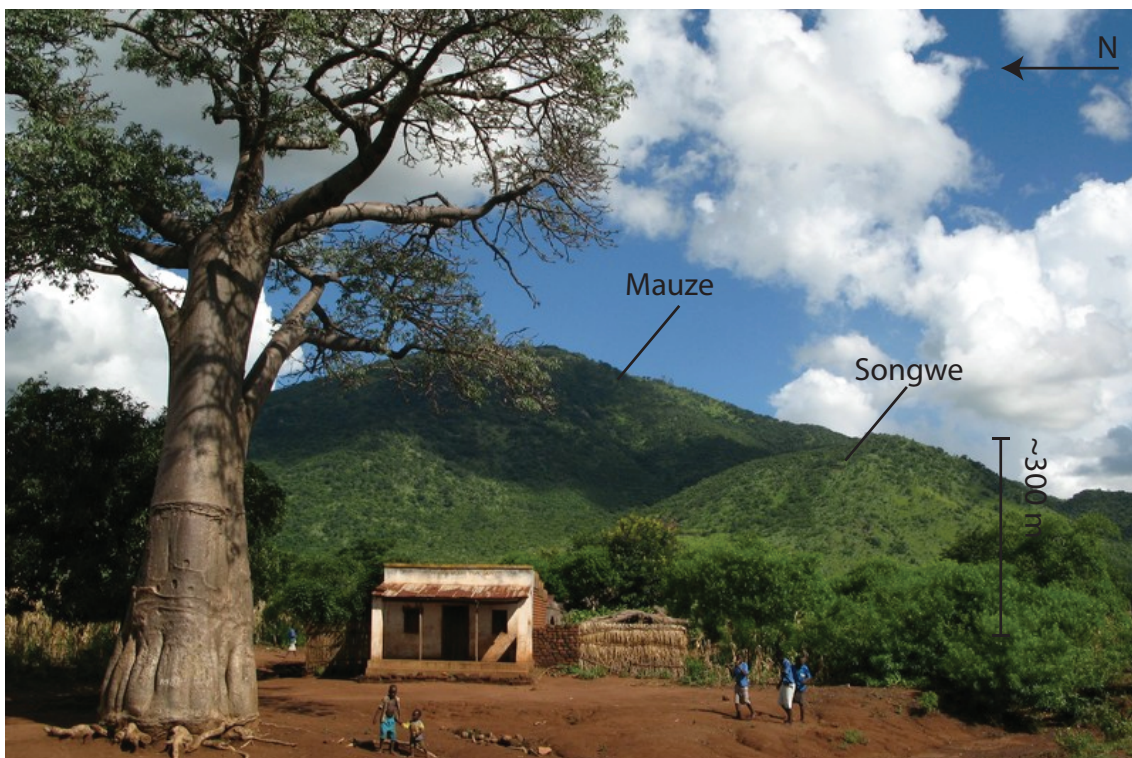


Figure 3.4: View of Songwe (midground) and Mauze (background) during wet season. Photo credit: Will Dawes, Alexander Lemon.

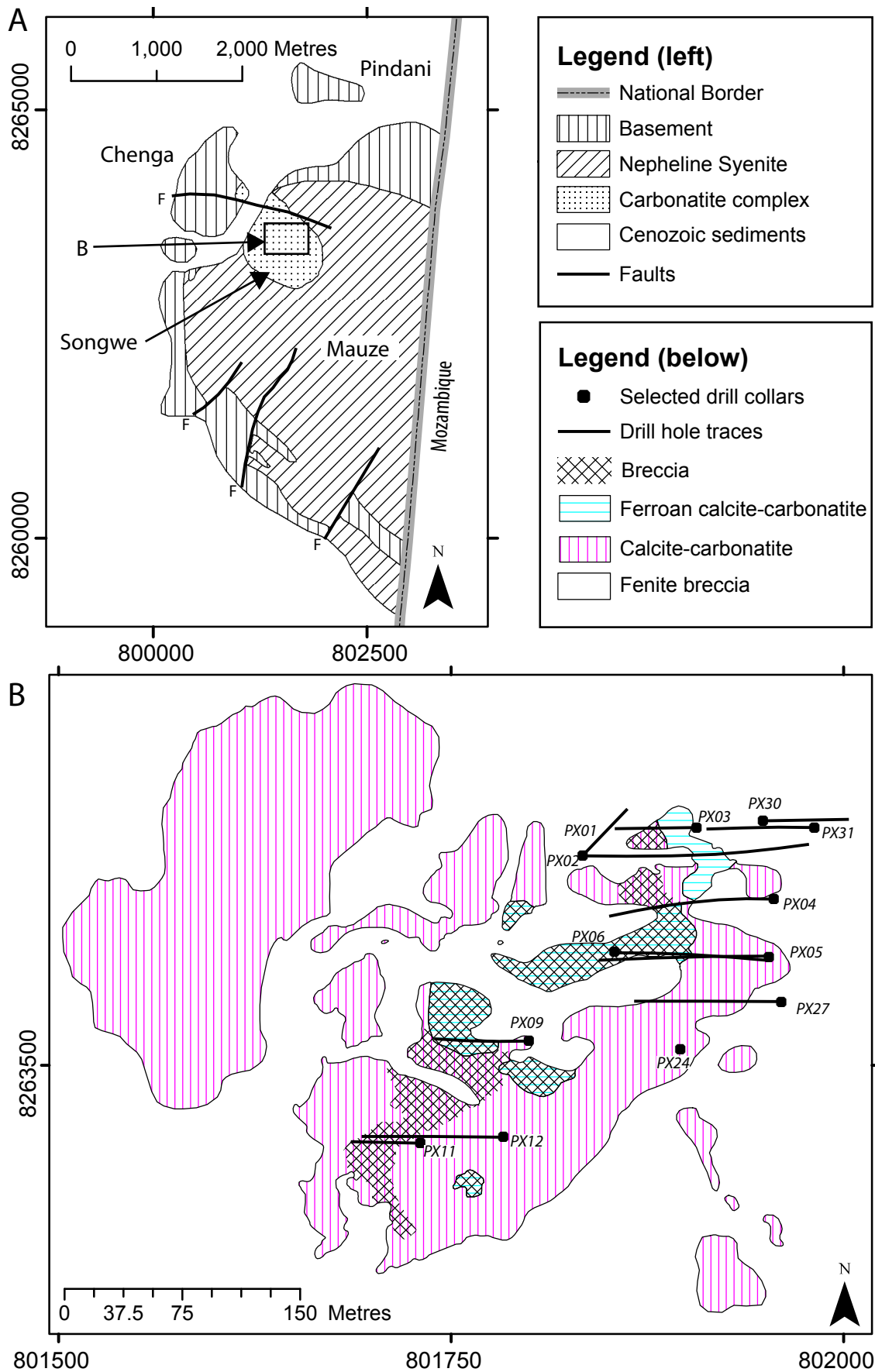


Figure 3.5: Geological map of Mauze and Songwe (A) and of carbonatite types at Songwe (B). Drill holes from which samples were taken are included. For the complete geological map, and all drill hole collars, see Croll et al. (2014). Grid system is UTM 36S, WGS1984 datum. Maps redrawn after Garson and Walshaw (1969) and Croll et al. (2014)

3.5.1 Exploration history

Before 1981, Malawi was explored mostly by the British Overseas Geological Survey and the Geological Survey of Malawi. Songwe was amongst the first carbonatite occurrences to be identified in Africa. Dixey et al. (1955) included a sketch map and a brief description of the hill, noting the range in colours, fine grain size, dark areas containing manganese and iron, and a preponderance of “*red feldspar rock*” as an agglomerate in the main vent, and concluded Songwe had a magmatic origin. Garson (1965) mapped and gave a full geological account of Songwe (Table 3.2). Mineralogical descriptions describe the carbonatite as consisting of mainly calcite with iron oxides, possibly after siderite with accessory apatite, pyrochlore, pyrite and REE fluorcarbonates. Darker carbonatite was also described, containing broken iron and manganese oxides, partly replaced by calcite and fluorite with leucocratic drusy areas of calcite, quartz, apatite and REE fluorcarbonates.

After 1981 work was undertaken mostly by private and contracted organisations. National aeromagnetic, gravity, radiometric and topographic data was acquired under contract to the United Nations. Exploration took place at Songwe between 1986 and 1988 by the JICA and the MMAJ, targeting REE (JICA and MMAJ, 1989a). Geochemical sampling, thin section studies, trenching and drilling to 55 m took place at Songwe, across three different field campaigns (‘phases’ using JICA/MMAJ nomenclature). At the end of the exploration it was concluded that it was possible to exploit Songwe for REE, especially given the enrichment in the mid REEs, but that the current market conditions were not favourable.

3.5.2 Current exploration

Currently Songwe Hill is under licence to Mkango Resources Ltd (March 2015). Mkango has carried out high-resolution mapping of the carbonatite (Fig. 3.5 B). Two stages of drilling (Phase I and Phase II) have also been completed in 2011 and 2012 respectively, totalling 4864.9 m. In addition, 424 m of channel samples were cut using a rock saw. Using these data, Mkango has established a (NI 43-101 compliant) mineral resource estimate, comprising indicated and inferred components of 13.2 million tonnes (grading 1.62 % TREO¹⁰) and 18.6 million tons (grading 1.38 % TREO) respectively, using a cut-off grade of 1 % TREO (Swinden and Hall, 2012). Subsequent work has upgraded the certainty associated with the estimate, and Mkango reports that the deposit comprises a probable mineral reserve of 8.4 million tonnes at 1.6 % TREO, which equates to approximately 136 kt TREO content (Croll et al., 2014).

¹⁰Total Rare Earth Oxide

3.5.3 Geology

The following geological descriptions represent a compilation of the authors observations, those of Mkango geologists (Croll et al., 2014) and descriptions from Garson (1965). Observations are based on outcrop, as well as samples from drill-core and channel sampling. The geological units below are listed in order of geological emplacement. The main carbonatite units are mapped in Figure 3.5 B.

Basement

The country rock around Songwe Hill is divided between regional metamorphic basement to the north and west, found on Chenga and Pindani, and nepheline syenite to the south and east, on the flanks of Mauze (Fig. 3.5A).



Figure 3.6: Contact breccia from the eastern edge of Chenga Hill, showing partially fenitised gneiss and dolerite fragments from the country rock.

Basement rocks around Songwe Hill are fenitised to varying degrees, and commonly brecciated. A particularly striking example crops out on the eastern edge of Chenga Hill. This outcrop comprises large clasts of brecciated basement gneiss and Stormberg dolerite, fenitised to varying degrees (Fig. 3.6). Similar rocks are found around the edges of other carbonatites in the CAP and are termed contact breccias (Garson and Smith, 1958). The contact between Songwe and the country rock is not observed at the surface, and is covered by eluvial deposits.

It is unclear whether brecciated outcrops such as those found on Chenga represent the margin of the Songwe carbonatite, or whether they are small separate vents, connected to the main carbonatite at depth.

Mauze

Little work has been undertaken on Mauze owing to the difficulty in accessing the mountain. The exact position of the contact between Mauze and Songwe is not known, and is largely covered by boulders eroded from Mauze. The contact has not been encountered during drilling (Croll et al., 2014). Boulders of material from Mauze comprise relatively homogenous, equigranular nepheline-syenite, with perthitic K-feldspar, albite and nepheline and accessory aegerine–augite and cancrinite visible in hand specimen (Fig. 3.7 A). Garson (1965) and Garson and Walshaw (1969) give similar descriptions from reconnaissance mapping of Mauze. Additionally, fine-grained phonolite veins/dykes cross-cut the nepheline-syenite and late-stage pegmatoidal veins of amphibole and feldspar cross-cut both the equigranular nepheline syenite and the phonolite dykes (Fig. 3.7 B).

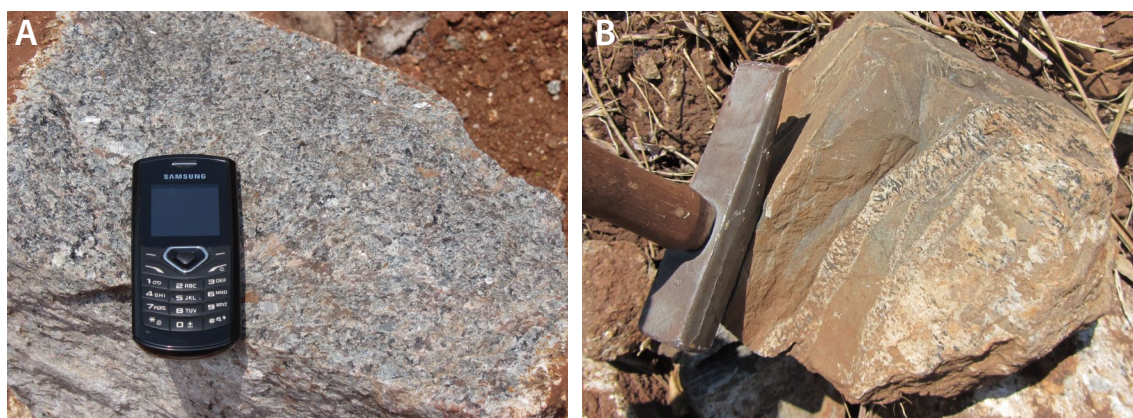


Figure 3.7: Equigranular nepheline syenite from Mauze (A) and pegmatoidal amphibole-rich veins cross-cutting a late phonolite dyke (B). Samples F03 (A) and F01 (B). Both samples from float. Hammer-head is approximately 10 cm, phone is approximately 8 cm.

Fenite

Fenite is found both within and around Songwe Hill, and fenitisation extends an unknown distance from the intrusion. Fenitisation is exclusively potassic, and where rocks have been completely fenitised they are composed almost entirely of K-feldspar, most likely orthoclase, although structurally-maximum microcline has been suggested for some fenites in other complexes (Le Bas, 2008).

Within the intrusion, fenite is invariably found in all rock-types. It is found as large blocks/boulders (> 10 m) through to small, angular, clasts (< 1 mm)

in carbonatite. Both large blocks and the clasts of fenite extend to depth in the drill-holes (e.g. fenitised phonolite at 302 m depth, PX001).

The fenite within the intrusion is light-pink–buff, with visible K-feldspar apparent (sanidine or orthoclase; Garson, 1965, although orthoclase is most likely). In many an equigranular igneous texture is preserved, suggesting that the clasts are of fenitised nepheline syenite. Other clasts are fine grained, which could be altered phonolite. Little evidence of banding, as seen in the country rock around Songwe, is observed in the fenite clasts, indicating either that it has been completely lost, or that fenitised gneiss clasts are uncommon.

Large blocks of fenite appear to be in-situ, or have had a very short transport distance. Contacts with the host carbonatite are typically sharp, although it is evident from reaction with dilute HCl that some degree of carbonatisation has occurred in many of the smaller clasts. Given the large size of the fenite blocks within the carbonatite, these are interpreted as stoped blocks from the roof zone of the carbonatite. The abundance of these blocks indicates that the exposed section of Songwe Hill is probably towards the top of the intrusion.

Around the intrusion, fenitisation is most prominent on Chenga Hill in the contact breccia (Fig. 3.6). Basement clasts are present with varying degrees of fenitisation from edge to core. Garson (1965) reports alteration of biotite and hornblende in these rocks to aegirine–augite.



Figure 3.8: Example of fenite from Songwe Hill, with K-feldspar grains. Sample T0185, hole PX003, depth 89.1 m. Thin-section image in Figure 4.4 A, Chapter 4, page 102.

Carbonatite

Songwe Hill comprises many different stages of carbonatite intrusion (Table 3.4), but essentially comprises two main carbonatite types, both of which are fine-

grained and incorporate varying proportions of brecciated fenite. The first stage is a fresh, light grey, calcite carbonatite and the latter is a darker Fe-rich carbonatite, termed ferroan calcite-carbonatite (*sensu* Gittins and Harmer, 1997) or ankerite carbonatite (*sensu* Woolley, 1989). The carbonatite is cross-cut by numerous, laterally discontinuous, REE-bearing Mn-Fe- veins, varying in width between 1 cm and approximately 1 m, but reaching up to 10s of metres in isolated pockets.

The terms C1–C4 are used here to distinguish different rock types (Table 3.4). This is the first use of this classification, and it is not used by Mkango. The terms are chosen to overlap with the terminology used by Le Bas (1981, 1987, 1999), where C1 represents sövitic calcite carbonatite; C2, alvikite; C3, ferrocronatite; and C4, late-stage carbonate veins (see also section 4.5.1).

Rock type	Major minerals	Minor minerals
Fenite	Kfs, Fe-oxides, Mn-oxides,	Ap, Zrn, Rt, Ilm, Hem
Calcite carbonatite (C1)	Cal, Ap	Ank, Pcl, Py, Zrn, Kfs
Calcite carbonatite (C2)	Cal, Ank, Ap, Fe-oxides, Mn-oxides	Fl, Py, Zrn, Kfs
Fe-rich carbonatite (C3)	Ank, Cal, Ap, Fe-oxides, Mn-oxides	Syn, Qtz, Brt, Str, Flo
Apatite-Fluorite veins (C4)	Ap, Flr, Cal	Bar, Qtz, Kfs, Str, Syn, Flo, Hem, Xtm, Rt, Zrn, Mn-oxides
Mn-Fe veins	Fe-oxides, Mn-oxides	Ap, Fl, Syn, Hem, Py, Sp, Gn

Table 3.4: Mineralogy of the different carbonatite types found at Songwe. Mineral abbreviations: Kfs, K-feldspar; Ap, apatite; Zrn, zircon; Rt, rutile; Ilm, ilmentite; Hem, hematite; Cal, calcite; Ank, ankerite; Pcl, pyrochlore; Py, pyrite; Fl, fluorite; Qtz, quartz; Bar, barite; Xtm, xenotime; Sp, sphalerite; Gn, galena; Syn, synchysite; and Flo, florencite.

The carbonatite at Songwe is commonly part of a feldspathic-rich breccia (*syn.* agglomerate). Because of this heterogeneity, separation of the two lithologies on a map can be difficult. Areas mapped in Figure 3.5 represent areas which comprise over 70 % of one carbonatite type. Consequently, minor veins and areas of alteration were not mapped. As a result of this limitation, the shape, and therefore the inferred structure, of the carbonatite shown in Figure 3.5 is inevitably subjective. Areas of extensive brecciation are also mapped, with the host carbonatite indicated.

Calcite-carbonatite (C1 and C2)

Calcite-carbonatite is the earliest carbonatite stage at Songwe Hill. It forms two approximately arcuate lobes aligned approximately north-east–south-west

(Fig. 3.5). Calcite carbonatite has a light grey weathered surface with karstic weathering textures. Karstic features continue to depth, with large cavities encountered during drilling (up to 200 m, hole PX005). Acacia trees are common on calcite-carbonatite -rich areas. On a fresh surface the rock is creamy white and homogenous. From a larger scale the homogeneity of the calcite carbonatite is less apparent as it is frequently cross cut by darker grey Fe-rich carbonatite and entrained fenite. Because of these cross cutting relationships it is inferred to be one of the earliest carbonatite stages at Songwe. This calcite-carbonatite commonly contains entrained clasts of fenite (Fig. 3.9).

At least two calcite-carbonatite stages can be observed in the field; with intrusion features such as calcite-carbonatite pebble dykes incorporating clasts of older calcite carbonatite (Fig. 3.10). These calcite carbonatite stages are subdivided into C1 calcite-carbonatite and C2 calcite carbonatite. C1 carbonatite is very uncommon at Songwe, and is only found as a clast in other carbonatite types. It typically comprises medium-grained calcite with few other phases readily observable in hand specimen. C2 carbonatite is much more abundant and is a cover-all term for any fine-grained white–grey calcite-carbonatite at Songwe. By definition, it is fine-grained and, as well as calcite, minor pyrite cubes can be identified in hand specimen. Banding and streaks are common, with some bands in the carbonatite having a more rose-pink hue, while other sections are dull grey. Macroscopic magnetite is conspicuously absent from both C1 and C2 carbonatite.

Channel sampling and core samples provide a good example of the small-scale heterogeneity in the C2 calcite carbonatite. For example, the channel sample in Figure 3.11 shows areas of the creamy-white C2 calcite carbonatite, incorporating fenite clasts, areas of alteration where iron-bearing minerals have broken down to goethite, and streaky-pink sections which are relatively rich in Y and apatite (as determined by portable XRF).

Fe-rich carbonatite (C3)

Fe-rich carbonatite is a term applied in the field to any carbonatite with a dark weathering texture and abundant Fe. In this thesis it is classified as C3 carbonatite. The fine-grained nature of the rock type makes it difficult to classify. Fe-rich carbonatite can occur as veins in the calcite carbonatite, as breccia clasts and as larger discreet individual masses. It is found throughout the intrusion, but is most common towards the centre (Fig. 3.5). It contains frequent clasts of fenite and calcite-carbonatite. It is dark-black on a weathering surface, hard, and has a knobby surface texture. On a fresh surface it is dark, fine grained and often banded. The nature of the contact between Fe-rich carbonatite and C2 calcite carbonatite is typically sharp. It is often made up of two distinct components: a

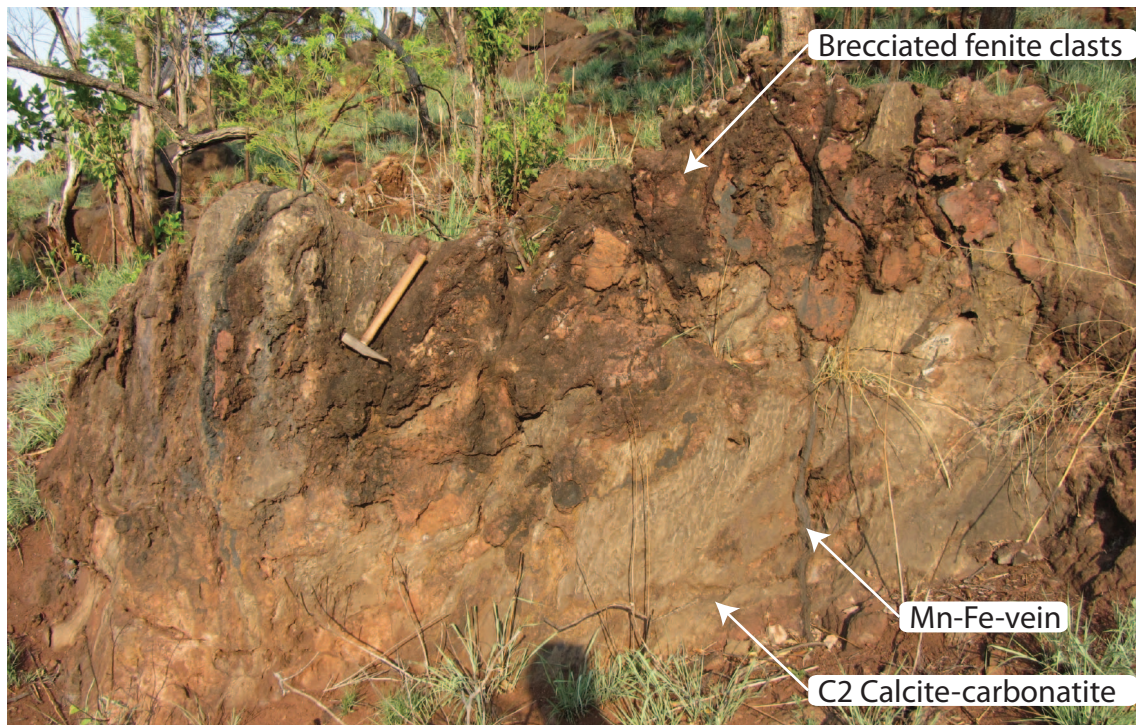


Figure 3.9: Grey C2 calcite-carbonatite with distinctive rough karstic weathering surface. The carbonatite incorporates clasts of fenite and is cross-cut by a small Mn-Fe-vein. Photo taken on the south-western flank of Songwe. Hammer is 30 cm long.

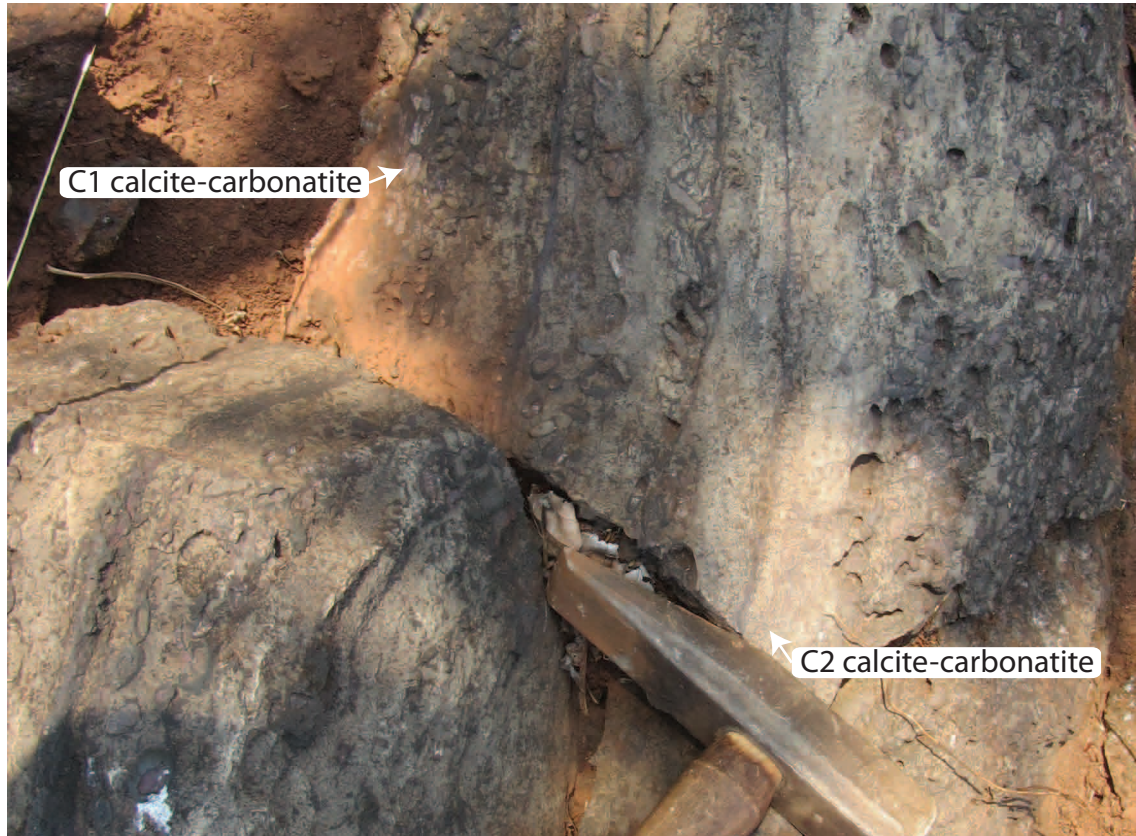
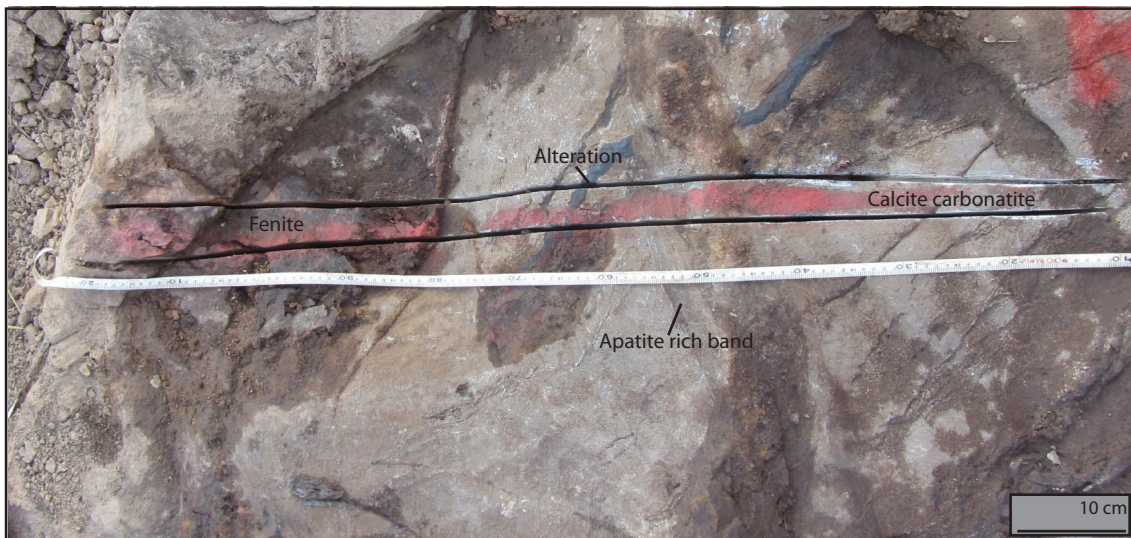


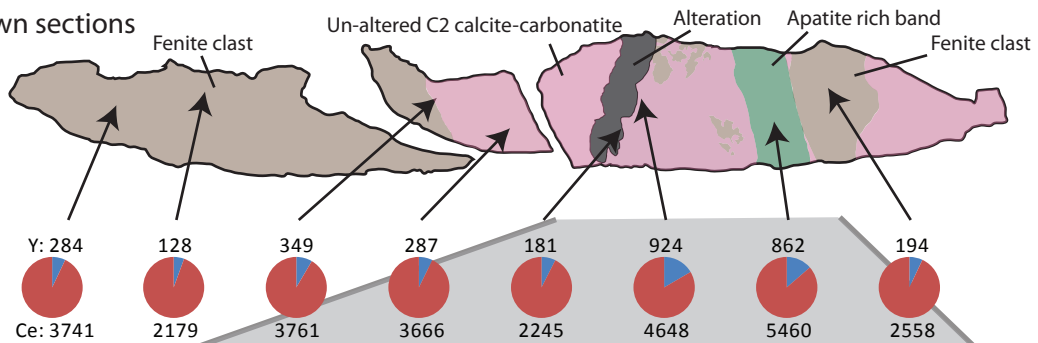
Figure 3.10: 'Pebble-dyke' including two different types of calcite carbonatite: earlier C1 calcite carbonatite, and later C2 calcite-carbonatite. Photo taken on western flank of Songwe. Hammer head is approximately 10 cm.



Outcrop section



Sawn sections



REE concentrations - from portable XRF



Sawn sections - area of interest

Alteration Un-altered C2 calcite-carbonatite Apatite rich band Fenite clast

Figure 3.11: Sawn section through calcite-carbonatite showing small-scale heterogeneity, alteration, fenite clasts and spot REE concentrations from a portable XRF. Black rectangles correspond to areas where thin-sections have been taken (Chapter 4, Figures 4.6 and 4.11, pages 105 and 113, respectively).

dark, carbonate-rich component, and a white-pink component. The dark matrix is a mix of calcite, due to its effervescent reaction with acid, ankerite and Fe-oxides. Areas of alteration are often rust-yellow due to alteration of Fe-phases to limonite. Subhedral rhombs of dark carbonates are often visible. Small blebs of a white mineral and pink minerals are also observable, these typically are around 1–5 mm, and clearly crystallised after the carbonate (Fig. 3.12). These are an assemblage of synchysite, barite and strontianite, and apatite (see Chapter 4). In places, the ‘blebby’ nature of these rocks is lost and the mixed white–pink and darker parts of the carbonatite have a banded texture.

Spot analyses of the Fe-rich carbonatite by portable XRF indicate that it typically has higher REE concentrations than the calcite-carbonatite. As for calcite-carbonatite, however, the distribution of REE-rich areas is irregular, and does not always correlate with areas with a high abundance of pink-white blebs.



Figure 3.12: Contact between (C3) Fe-rich carbonatite and C2 calcite carbonate in drill core (PX03, 16 m depth). Note the juxtaposition between the banded white and dark carbonatite with the creamy calcite carbonatite (far left).

Breccia

Almost all parts of Songwe Hill contain some clasts of fenite. Clasts of earlier calcite-carbonatite are also present in some breccias, particularly in Fe-carbonatite-rich breccias, but also less commonly in calcite-carbonatite (e.g. Figure 3.10). These are subdivided by Croll et al. (2014) into feldspathic-rich breccias (agglomerate using the terminology of Garson and Smith, 1958) and carbonatite-rich breccias (which include the ‘pebble-dykes’).

In areas of the intrusion where breccia is the dominant phase at an outcrop (i.e. it is more clast than matrix), the area is mapped as brecciated carbonatite, with the matrix carbonatite indicated. The areas mapped are invariably feldspathic-rich breccias (e.g. Figure 3.14). Breccia-rich areas form a band from

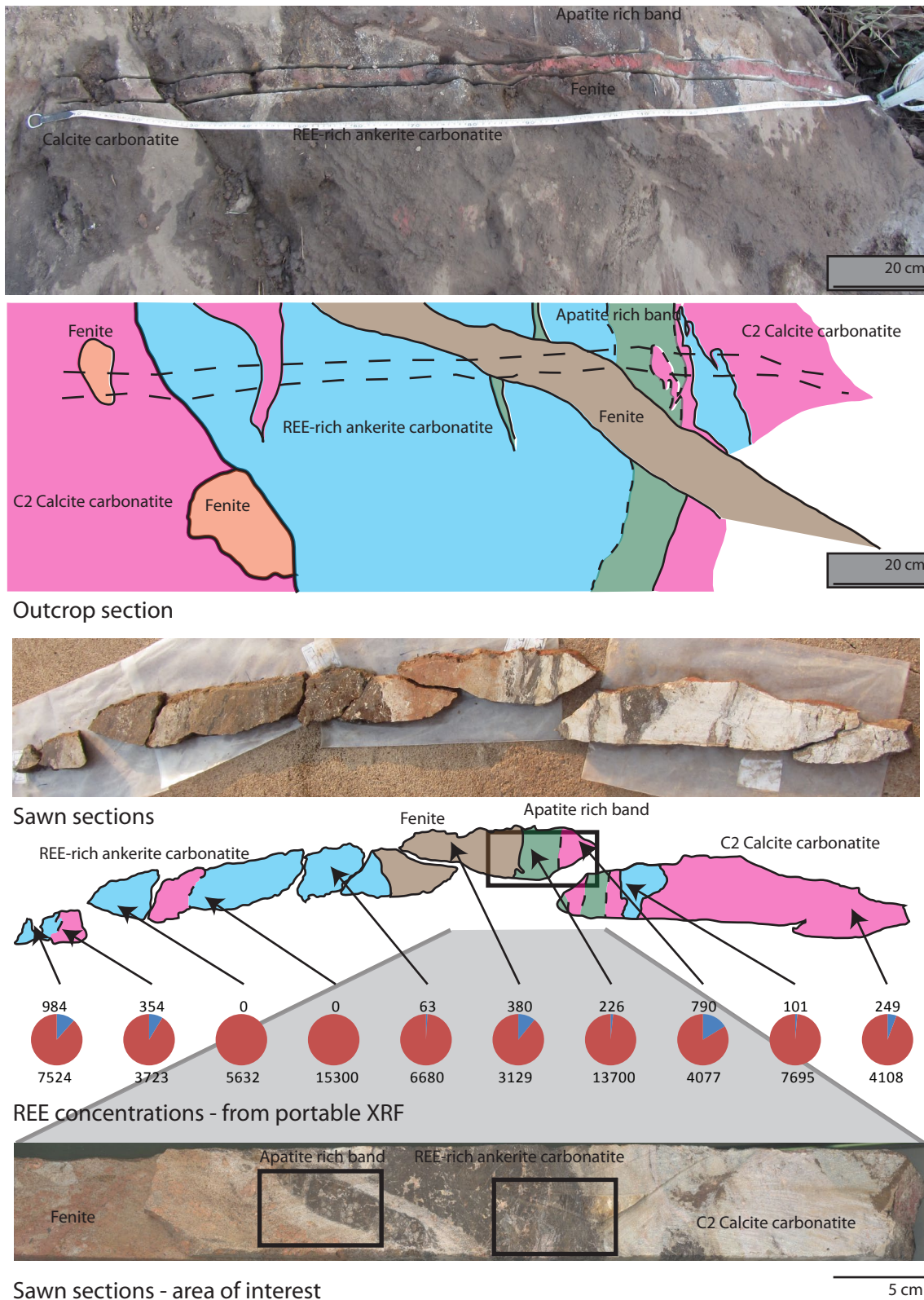


Figure 3.13: Sawn section through calcite-carbonatite, Fe-rich carbonatite and fenite. Spot REE concentrations are from a portable XRF. Black rectangles correspond to areas where thin-sections have been taken (Chapter 4, Figure 4.4, page 102)

the north-east to the south-west of the intrusion, occurring in both Fe-rich carbonatite and calcite-carbonatite (Fig. 3.5).

In the feldspathic-rich breccias, fenite clasts are typically angular, and can range in size from a few mm, through to metre-sized blocks (Fig. 3.14). Clasts have a high relief against the matrix and show varying degrees of fenitisation: some are weakly fenitised and original feldspar crystals can be seen, while other clasts have been completely altered. Commonly, clasts which have fragmented into multiple pieces can be visually 're-assembled' indicating that transport distance of fenite clasts was low.

Calcite-carbonatite clasts in the feldspathic-rich breccia are rounded, and range from a few mm to less than a metre in size. The clasts are typically composed of creamy-white, medium–coarse-grained C1 calcite-carbonatite. The rounding in the clasts indicates a greater transport distance, and in some instances the clasts are found as 'pebble-dykes' with calcite carbonatite grains rounded and aligned in the direction of flow.

The pebble-dykes (carbonate-rich breccias) are not mapped in Figure 3.5, but they are found in calcite-carbonatite, most prominently on the western side of the intrusion. The breccias form thin dykes comprised of calcite-carbonatite clasts and, less-commonly, small rounded fenite clasts (Fig. 3.10). Similarly to clasts in the feldspathic-rich breccias, the carbonatite clasts in the carbonatite-breccia are rounded but to a greater degree. They are also typically smaller and more uniform in size, typically a few cm across.

The abundance of breccia at Songwe is interpreted as being due to three factors:

1. Rapid, forceful emplacement of the carbonatite into the country rock. This is indicated by the presence of contact breccias around the carbonatite and by the abundance of large, relatively un-rounded, blocks of fenite within the carbonatite. The blocks are thought to have stopped into the magma upon ascent.
2. Explosive degassing/de-volatilisation of the carbonatite — possibly at multiple different times during emplacement. The most likely timing of this is after emplacement of C1 carbonatite, but prior to intrusion of C2 carbonatite due to the presence of rounded calcite-carbonatite clasts in a matrix of C2 carbonatite in pebble dykes.
3. A relatively shallow depth of erosion. Although speculative, it is possible that the abundance of breccia and the structure suggest a degassing magma with a shallow depth of emplacement. Thus, the part of the carbonatite currently exposed could be the shallow sub-volcanic section of a carbonatite

volcano. It has been suggested (Woolley, 2012, *pers comm*) that Songwe may not have erupted.

Hydrothermal overprinting

Throughout the carbonatite several stages of overprinting and later cross-cutting veins are evident. These can essentially be subdivided into Mn-Fe-veins and fluorite/apatite–fluorite mineralisation.

Apatite-fluorite veins (C4) Fluorite mineralisation is cryptically distributed in different stages of the carbonatite. Small veins rich in fluorite and apatite form a volumetrically minor part of the carbonatite and are most conspicuous in breccia outside of the main intrusion. The breccia at Chenga hosts some of the largest and most distinct apatite-fluorite veins that are known (Fig. 3.16). While only a volumetrically small part of the carbonatites, they are important as they are strongly HREE-enriched and can contain up to 1 % Y_2O_3 . As such, in this thesis, these veins are referred to as C4. Similar fluorite-rich areas are also found in drill core, most prominently in core PX016 where they are mis-logged as ‘phonolite’ (Brady, 2014, *pers comm*). In addition, in early descriptions of Songwe Hill, Garson (1965) identified an apatite-fluorite rock in boulders approximately half a mile north-east of Songwe. The description of this rock is similar to the apatite-fluorite veins found on Chenga Hill and in drill-core.

Mn-Fe-veins vary from a few cm to a few metres across. They are composed of a mixture of Fe-bearing carbonates, Fe- and Mn-oxides (hematite and wad), often hydrated to limonite. The ratio of Fe-carbonate to oxides varies in different veins. On the small scale they follow straight fractures cross-cutting carbonatite and fenite (e.g. Figures 3.9 and 3.11). These have distinct alteration halos around them, where Fe-bearing carbonates in the carbonatite have begun to break down to Fe-oxides. A good example of this is shown in Figure 3.11, where creamy-white calcite carbonatite is altered to grey-carbonatite around a central alteration zone of Mn- and Fe-oxides. In areas of larger scale alteration, the relationship between the Mn-Fe-veins and the host-rock is difficult to establish. Often these areas are deeply weathered and have only been revealed by bulldozed road-cuts (Fig. 3.15). Here the unit is composed of massive Mn- and Fe-oxides, with little evidence of minerals other than weathering products. This rock type is not limited to surface weathering, and is found in pockets at depth, often associated with cavities. At the edge, and towards the top of the intrusion, similar Mn- and Fe-rich rocks form the matrix of fenite-rich breccia.

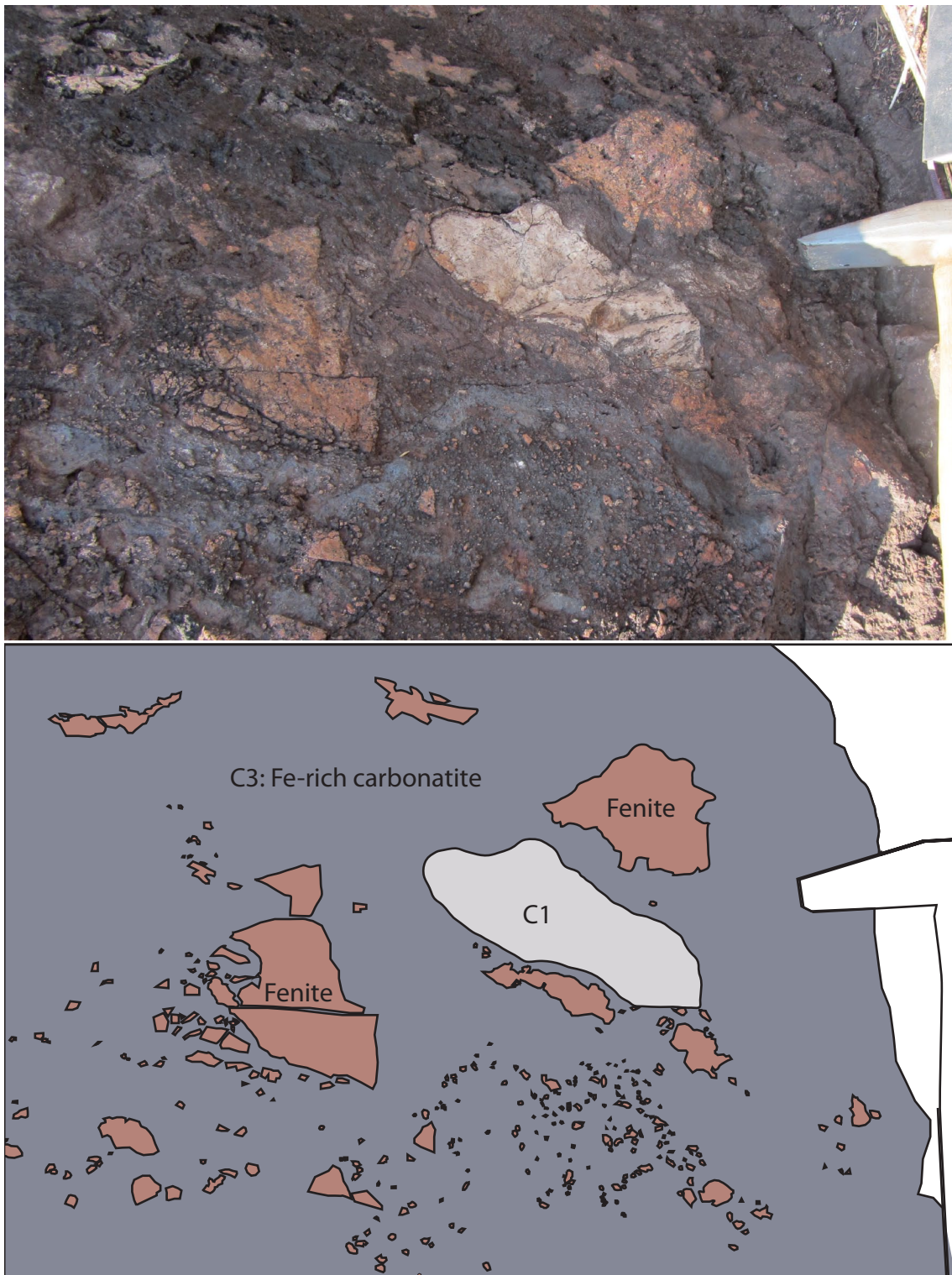


Figure 3.14: Fe-rich carbonatite breccia with C1 calcite carbonatite clast and fenite clasts.

Similar rock types have been described from other locations, summarised as hematite-carbonatites by Andersen (1987b). Examples include: Fen, Norway; Lueshe, DR-Congo; and several locations in Kenya (Andersen, 1984, 1987b). Intrusion styles include veins, dykes and stocks, and hematite-rich breccias. These rocks are interpreted as the products of post-magmatic dissolution of Fe-rich carbonatite under oxidising conditions, where Fe is immobile (Andersen, 1987b). Based on O isotope analyses, Andersen (1987a) interprets the alteration to have been caused by meteoric water, after the last stages of intrusion.



Figure 3.15: Example of a road-cut with extensive alteration of Fe-rich rock to hematite, goethite, wad and limonite.

Post-carbonatite activity

Locally and regionally Garson and Walshaw (1969) report phonolite and solvsbergite (peralkaline microsyenite or peralkaline trachyte; Le Maitre, 2002) dykes. These are not seen at the surface of Songwe, but have been found at depth in the drill-core. These units mark the cessation of CAP activity at Songwe.

3.5.4 Sample collection

A mixture of grab-samples from outcrop and float were collected, as well as samples from drill-core and channel samples. Drill core samples were typically 5–15 cm in length, while sawn sections were up to 1.5 m long. Samples are listed in appendix C. In total, 52 grab samples, 74 core samples, and 6 sawn sections were collected from Songwe.



Figure 3.16: Example of an apatite-fluorite vein in the matrix of the contact breccia on Chenga Hill.

3.5.5 Interpretation and discussion

The order of intrusion and a model for REE-mineralisation at Songwe Hill has been developed in conjunction with Aoife Brady (Mkango), James Mtegha (Mkango) and Alan Woolley (NHM). This was published in the 2012 43-101 mineral resource estimate (Croll et al., 2014). A generalised model for the intrusion based on field relationships, is shown below. Modifications made since the 43-101 report are shown in italics.

1. Intrusion of the Mauze nepheline syenites and phonolites
2. Fenitisation of the host nepheline syenites
3. *Intrusion, at depth, of sövitic C1 calcite-carbonatite*
4. Intrusion(s) of calcite carbonatite (C2) in a ring type structure and concomitant incorporation/stopping of fenite blocks
5. *Degassing and formation of pebble dykes*
6. Pulses of Fe-bearing carbonatite magma emplacement and replacement of calcite carbonatite
7. Intrusion of thin Fe-rich carbonatite dykes/veins in the calcite and Fe-bearing carbonatites
8. Multiple later stage episodes of brecciation
9. Extensive hydrothermal/carbohydrothermal activity resulting in REE enrichment of the various carbonatite and related lithologies
10. *Widespread alteration and hematization of the carbonatite by low-temperature meteoric fluids*

This interpretation is based largely on cross-cutting relationships observed in the field and is consistent with a general model for the formation of many REE-rich carbonatites, where initial calcite-carbonatite is followed by carbonatites with progressively increasing Fe, Sr and REE concentration, culminating in hydrothermal mineralisation (Le Bas, 1989; Gittins, 1989). Given the high degree of brecciation and incorporation of stoped fenite blocks, the intrusion is interpreted as the roof-zone of a sub-volcanic vent. The abundance of hydrothermal overprinting, and retention of stoped fenite in the carbonatite suggests that the intrusion never reached the surface, and remained under pressure. Syn-intrusion and post-intrusion faulting is evident across Songwe Hill although displacements appear to be relatively small. Hydrothermal fluids utilised these planes of weakness which led to widespread alteration of Fe-rich carbonatite to Mn- and Fe-oxides.

Comparison with other CAP carbonatites

Parallels can be drawn between Songwe and the other large carbonatite complexes in the CAP. Tundulu and Chilwa Island are also multiphase intrusions with associated nepheline-syenite intrusions and multiple injections of carbonatite, with progressively increasing Fe and REE concentrations (Garson and Smith, 1958; Garson, 1962). Brecciation of country rock around the intrusion is common to all of the intrusions, with feldspathic breccia and agglomerate common at each locality.

There are, however, significant differences between Songwe and other CAP carbonatites. While many other intrusions in the CAP are associated with nepheline-syenite, the volume of nepheline-syenite exposed is much lower, relative to the volume of nepheline-syenite at Mauze. In addition, the degree of brecciation is generally lower than that observed at Songwe. Major intrusions in the CAP form ring complexes, and typically young towards the centre of the intrusion, while a broadly similar pattern is observed at Songwe, it is poorly developed.

3.6 Summary and conclusions

In this chapter, an overview of the regional geology of the CAP¹¹ has been described in the context of the work at Songwe Hill and related intrusions. A detailed evaluation of the field relationships at Songwe Hill has been provided, and an intrusion order suggested. The sequence of events is:

1. Intrusion of the Mauze nepheline syenites and phonolites
2. Fenitisation of the host nepheline syenites
3. Intrusion at depth of sövitic C1 calcite-carbonatite
4. Intrusion(s) of calcite carbonatite (C2) in a ring type structure and concomitant incorporation/stopping of fenite blocks
5. Degassing and formation of pebble dykes
6. Pulses of Fe-bearing carbonatite magma emplacement and replacement of calcite carbonatite
7. Intrusion of thin Fe-rich carbonatite dykes/veins in the calcite and Fe-bearing carbonatites
8. Multiple later stage episodes of brecciation

¹¹Chilwa Alkaline Province

9. Extensive hydrothermal/carbohydrothermal activity resulting in REE enrichment of the various carbonatite and related lithologies
10. Widespread alteration and hematization of the carbonatite by low-T meteoric fluids

REE mineralisation is found throughout Songwe Hill, but is particularly abundant in the later stages of the intrusion. Songwe shares many similar features with other intrusions in the CAP, including a high degree of brecciation, shallow intrusion level, extensive potassic fenitisation and evolution of carbonatite types from an initial sövitic carbonatite, through to later-stage REE-rich carbonatites.

Chapter 4

Geochemistry, petrography and mineralogy of the Songwe Hill carbonatite

Since the discovery of carbonatites in Africa (Dixey et al. 1937, reprinted as Dixey et al., 1955), most of the major carbonatite complexes of the CAP¹, southern Malawi, have been subject to extensive field and petrographic studies, resulting in excellent memoirs on Chilwa Island (Garson and Smith, 1958), Tundulu (Garson, 1962) and Kangankunde (Garson and Smith, 1965), as well as importantly accessible collections. These have since formed the basis for subsequent further geochemical, mineralogical and isotopic investigations of these intrusions (e.g. Woolley, 1969; Ngwenya, 1991, 1994; Simonetti and Bell, 1994; Wall and Mariano, 1996; Wall, 2000; Duraiswami and Shaikh, 2014; Dowman, 2014). However, the Songwe Hill carbonatite was not subject to the same extensive surveying and mapping as the nearby complexes (e.g. Garson and Walshaw, 1969) and only short descriptive summaries have been published (Garson, 1965; Woolley, 2001). There are no published studies on the geochemistry and mineralogy of the Songwe Hill carbonatite.

In this chapter the principal objective is to build upon the new geological observations outlined in chapter 3, presenting new whole-rock, major and trace-element data from Songwe drillcore, petrographic observations and mineral analyses using EPMA². These data will help to answer the following questions:

1. How do the different petrogenetic stages of the Songwe-Hill carbonatite differ mineralogically and geochemically?
2. At which stage is REE mineralisation abundant?
3. What are the principal controls on REE and HREE mineralisation at Songwe?

¹Chilwa Alkaline Province

²electron probe micro-analyser

New geochemical data from Mauze are also presented here, although the limited number of analyses precludes the development of a detailed evolutionary model. This is recommended for further work. However, the data are combined with previously analysed major element data for comparison with the other nepheline syenite intrusions of the northern part of the CAP.

With the results from this chapter, an understanding of the genesis of the Songwe Hill carbonatite can be developed. From this basis, our understanding of REE mineralisation can be expanded, and investigated in subsequent chapters.

4.1 Background— previously published (pre-2010) geochemical data from Songwe Hill

While there have been geochemical studies on the intrusions from the northern part of the CAP (e.g. Woolley and Jones, 1987), very few geochemical data are available from Songwe, Mauze or the other intrusions in the southern part of the CAP. Dixey et al. (1955) described several samples from Songwe and Mauze and included major element analyses of three dyke-rocks and one nepheline syenite sample from Mauze. The dykes were described as: N1122a, phonolite; N1122b, microfoyaite; and N1122c, microfoyaite rich in cancrinite, while the nepheline syenite sample was described as a biotite-bearing aegerine-augite-foyaite (where foyaite is equivalent to hypersolvus nepheline syenite; Mitchell, 1996). The analyses of these samples are listed in Table 4.6 and will be discussed, in combination with the new data, in section 4.4.

Garson (1965) includes an analysis of a composite sample of carbonatite from Songwe, but this is from chip samples derived from multiple locations across the hill, and is not useful for petrological interpretation. The JICA³/MMAJ⁴ phase I work involved more extensive geochemistry, with the analysis of 89 samples. These were analysed using ICP-MS⁵ for 60 elements (JICA and MMAJ, 1987). The data are not peer reviewed, lacks a full methodology and records some elements (e.g. sulphur) that are susceptible to interference using ICP-MS. It is, however, the only comprehensive source of geochemical data prior to recent exploration work. Other whole rock geochemical data have been presented, but this was limited to select REE, P and Sr data (JICA and MMAJ, 1988, 1989b).

The JICA/MMAJ phase I data provide a guide to the carbonatite types at Songwe and include some data for elements that were not analysed in the current assay results. In the original publication the data were used primarily for quantifying concentrations of elements, and was not used to analyse or classify

³Japan International Co-operation Agency

⁴Metal Mining Agency of Japan

⁵inductively coupled plasma mass spectrometry

the carbonatites in detail. Nevertheless, on the basis of field observations of the 89 rocks analysed, 66 were classed as sövite, 10 were unclassified carbonatite, 1 was classed as siderite carbonatite and 12 were alkali rocks (undefined). In the field, sövite was a white/grey, medium/fine grained rock with a strong reaction to HCl and siderite carbonatite was a brown/dark rock with coarse siderite in leached or mineral form.

The results of the JICA/MMAJ geochemical survey all have low totals. This could be due to various factors, including: abundance of hydrous phases; failure to correct FeO as Fe₂O₃; dissimilar concentrations in standards and samples; and incomplete digestion of refractory minerals. As the analytical methodology is not included with the data it is difficult to comment on the importance of these factors. However, the reported low Zr concentrations (most below LOD⁶, max 164 ppm) compared to other carbonatites (e.g. Kangankunde 0–1349 ppm Wall, 2000) suggests incomplete digestion. Data for the elements Ba, Nb and Sr are interpreted with caution as low concentrations could be due to these elements being retained in refractory barite, pyrochlore and strontianite, respectively.

The JICA/MMAJ data show that at Songwe there is a general increase in TREE⁷ with increasing Fe and Mn and decreasing Ca and CO₂ (Figs. 4.1A and 4.1B). Because of the falling CO₂ concentrations with increasing iron, the increase is probably due to an increase in Fe and Mn oxides rather than Fe/Mn carbonate minerals. In the alkali rocks, the converse is true, and Fe drops while Ca increases with increasing TREE. This is most likely due to the increasing proportion of carbonatite in the alkali rock increasing the REE grade and is also shown by decreasing Si with increasing TREE.

As might be expected with carbonatites, there is an increase in F content with increasing TREE (Fig. 4.1C). This is probably controlled by increasing content of REE fluorcarbonates, such as synchysite, as there is no enrichment of F with Ca or P, which would be observed if fluorite or fluorapatite were controlling the distribution. There is also a weak positive correlation between Ba and TREE. This is most likely due to the increased content of barite which is often found in association with REE fluorcarbonates.

P and Sr exhibit two trends with increasing TREE (Figs. 4.1D–E). In some samples Sr and P increase very little with increasing TREE while in others these elements correlate with TREE. The correlation between Sr and P could be because of the substitution of Ca with Sr in apatite, implying that apatite is a major control on the phosphate distribution in these rocks and when it is Sr-rich it has a strong control on the TREE content. Phosphorus may also increase with REE due to increases in REE phosphate minerals, such as monazite-(Ce), florencite-(Ce) and xenotime-(Y). Little correlation between Nb and TREE is observed indicating

⁶limit of detection

⁷total REE

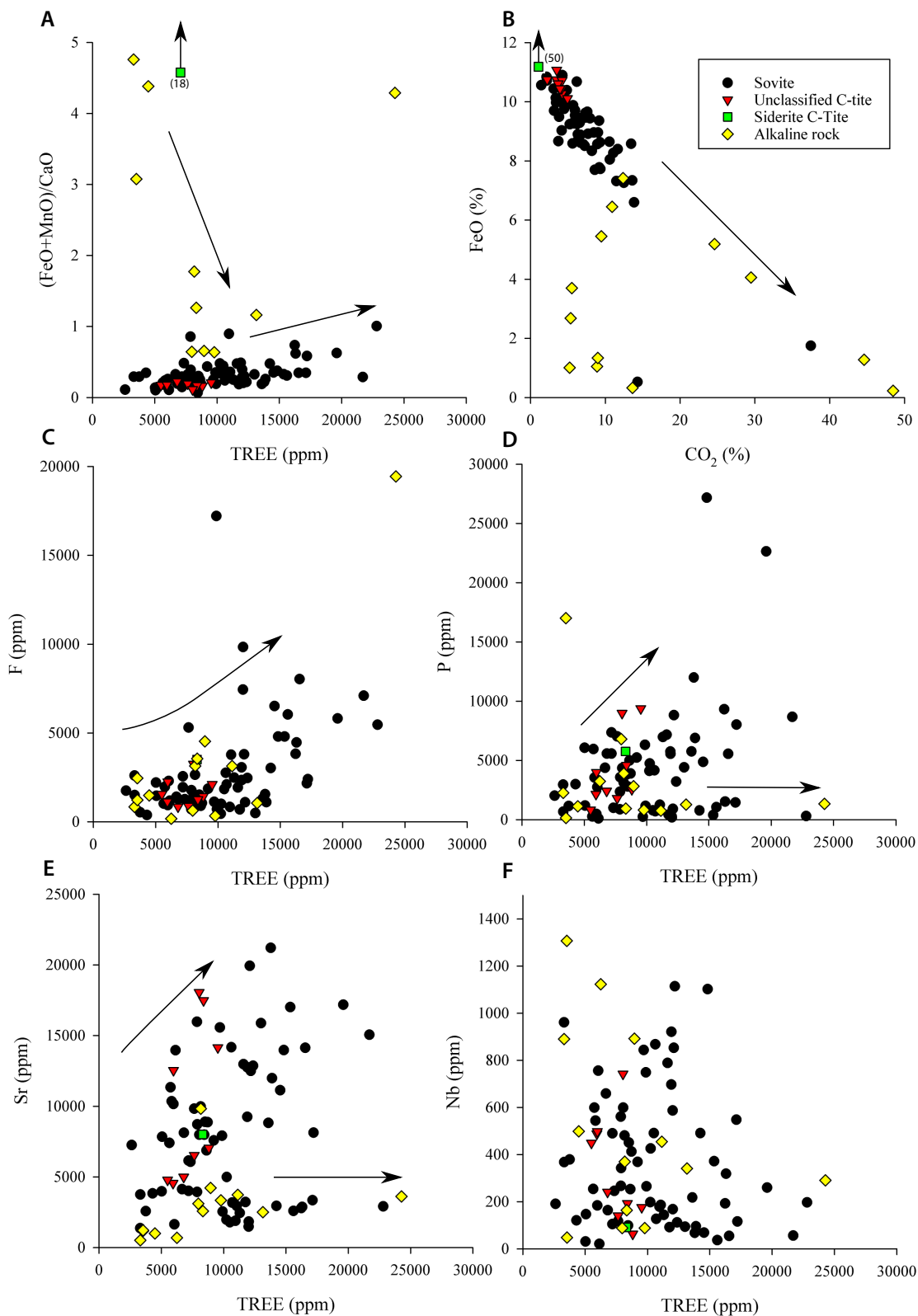


Figure 4.1: Review of whole-rock data from Songwe analysed by the JICA/MMAJ showing relationships between selected minor and major elements. Data source: JICA and MMAJ (1987). Rocks are classified according to JICA field identifications. TREE in these graphs is the sum of La, Ce, Nd, Sm, Eu, Tb, Dy and Yb. FeO is total FeO. Arrows represent broad trends in the data.

a minor role for pyrochlore in hosting the REE.

The relationships between the REE and F, P and Sr suggest that all the carbonatite samples contain a certain amount of REE fluorcarbonates. Samples enriched in TREE with P and Sr are likely to have the REE hosted in both fluorcarbonates and phosphate minerals, while the samples which do not show increasing TREE with P and Sr are likely to have the REE hosted in only fluorcarbonates.

Chondrite-normalised REE distributions for the JICA samples are plotted in Figure 4.2. The large degree of scatter in the data and the many 'anomalous' data points, mean that the data should be interpreted with caution. It is clear, however, that all the samples are LREE enriched, rising approximately two orders of magnitude higher than the bulk continental crust. This is the same for both the alkaline rocks and the Songwe carbonatites. Many of the anomalous data points are not easily explained; La, Sm, Tb and Dy do not readily form ions other than 3⁺ and as such are unlikely to become anomalously enriched or depleted compared to their geochemical neighbours. These data are, therefore, considered erroneous and are due to analytical artefacts. While Ce and Eu are known to be able to form different oxidation states in nature, the wide scatter in the data and abundance of spurious data points means that these data can be afforded little weight in contributing to a model for the development of the observed REE distribution at Songwe.

4.2 Methods

In order to improve upon the previous published analyses, whole-rock data from the Mkango drillcore have been re-assessed. Furthermore, samples from the core, grab samples collected by the author, and channel samples have been petrographically investigated.

4.2.1 Sample selection

Whole-rock data for fenite, carbonatite, apatite-fluorite veins and Mn-Fe- veins were available from Songwe drillcore analysed by Mkango Resources (for the analytical method see Section 4.2.2). In addition, grab-samples of apatite-fluorite veins from Chenga Hill and of nepheline syenite from Mauze were selected for geochemical analysis. These samples consisted of about 1–2 kg blocks hammered out of veins from a breccia, with weathered surfaces removed. Sawn channel samples from Songwe were also petrographically investigated to look at small-scale heterogeneity in the carbonatites (see Chapter 3 for the nature of these samples).

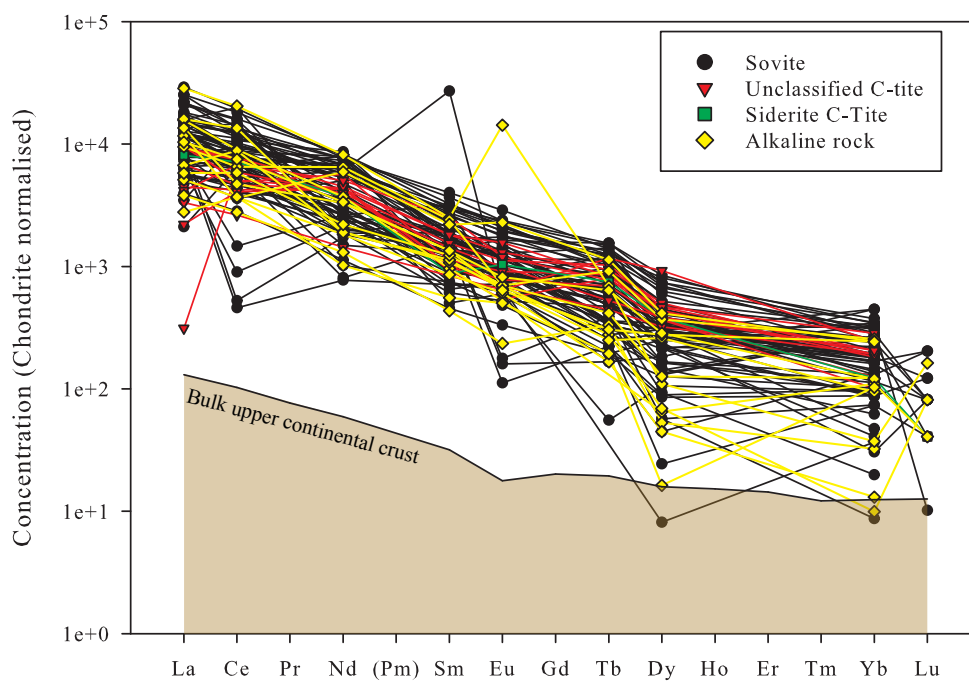


Figure 4.2: REE distribution diagram for Songwe carbonatites and alkaline rocks normalised to chondrite after McDonough and Sun (1995). Included for reference is the bulk upper continental crust after Rudnick and Gao (2003). Data from JICA and MMAJ (1987).

Mauze grab-samples

Four grab samples were analysed from Mauze (see Chapter 3 for the nature of these samples). These can be separated into two groups: equigranular nepheline syenite (U4913, F03) and pegmatoidal amphibole-rich syenite (U4914, F01). No dyke-rocks were sampled, but analyses of the dyke-rocks are available from Dixey et al. (1955). The equigranular samples were selected to be representative of the bulk Mauze composition, while the pegmatoidal samples were sawn to be representative of later, cross-cutting stages (see Figure 3.7, page 67, chapter 3).

Samples from Mkango drillcore

While a small number of representative carbonatite grab samples were acquired, the much greater quantity of data from the Mkango drillcore samples permits more detailed and rigorous data analysis.

Drillcore was initially logged by Mkango geologists, mostly by eye, but also using a Niton portable XRF⁸ analyser as a guide for mineralised areas. The fine grain size of many of the rocks means that the mineralogical classifications of Woolley and Kempe (1989) cannot be easily applied by visual examination and, therefore, a generic field classification was used. This subdivided the carbonatite into calcite-carbonatite, Fe-bearing 'dark' carbonatite and unclassified carbonatite, Fe-bearing veins and fenite. It is important to note that coarse-grained sövitic carbonatite (C1) and fine grained carbonatite (C2) (identified in Chapter 3) were not differentiated during core logging by the company geologists. Some of the groups recognised by Mkango have been merged in this thesis, highlighted in italics:

- Calcite-carbonatite
- Black carbonatite (Fe-rich carbonatite)
- Mn-Fe- veins, incorporating:
 - *Mn/Fe carbonatitic vein*
 - *Fragmental carbonatite (Brown)*
 - *Mn/Fe carbonatite*
- Fenite, incorporating:
 - *feldspathic breccia*
 - *feldspathic fenite*
 - *fenitised nepheline syenite*

⁸X-ray fluorescence

- *fenitised phonolite*
- *fenitised syenite*

Additionally, the following carbonatite types have not been included in the geochemical analyses presented due to their high degree of heterogeneity and uncertain affinities:

- Core-loss
- Pebble dyke
- Carbonatite breccia
- Carbonatite (undefined)
- Breccia

Some silicate rocks (other than fenite) were encountered during drilling, these were logged as:

- Phonolite
- Calc-silicate
- Syenite
- Nepheline syenite

Because of the lack of Na data available by the analytical route utilised, these company data are not useful for interpretation of the silicate rocks and are therefore not used. Additionally, some of these rocks were incorrectly logged, with most of the 'calc-silicate' rock later identified as Fe-rich carbonatite, and some phonolite identified as apatite-fluorite veins (Brady 2015, *pers comm.*). The data for the phonolite, later shown to be apatite-fluorite veins, are utilised in this thesis due to the dearth of analyses of this rock type.

Chenga grab-samples

In addition to samples available from the drillcore, two grab samples of apatite-fluorite veins from Chenga hill (T0134, T0178) were also analysed, complementing the data for the apatite-fluorite veins ('phonolite') from the drillcore. T0178 was cut with a rock saw to remove as much fenite material as possible. T0134, however, was effectively a bulk sample, comprising the veins and the fenite breccia country rock, as the veins were too small to separate from their host.

4.2.2 Whole-rock analyses

Whole-rock major and trace element data from over 12,000 drillcore samples, made available by Mkango Resources, were analysed (Table. 4.1). These samples were prepared and analysed commercially by Intertek-Genalysis. A full methodology is presented in Croll et al. (2014) and a summary of the methodology is presented below. Additionally, 11 grab samples collected in 2011 were analysed by the same techniques as the drillcore samples, and 14 grab samples collected in 2012 were prepared at CSM⁹ and analysed at Intertek-Genalysis using a Li metaborate flux for dissolution (Table. 4.1).

Data type	Preparation	Major elements (OES ^a)	Trace elements (MS ^b)	# of samples
Drillcore assay data (1)	FP6 (Na ₂ O ₂ fusion)	Al ₂ O ₃ , CaO, FeO, K ₂ O, (LOI), MgO, MnO, P ₂ O ₅ , SO ₃ , SiO ₂ , TiO ₂	B, Be, Cr, Ga, Hf, Li, Nb, REE, Sc, Sn, Sr, Th, U, V, W, Y, Zr	816
Drillcore assay data (2)	FP6 (Na ₂ O ₂ fusion)	Al ₂ O ₃ , CaO, FeO, K ₂ O, MgO, MnO, P ₂ O ₅ , SO ₃ , SiO ₂ , TiO ₂	Ga, Hf, Nb, REE, Sr, Th, U, Y, Zr	11340
Grab samples (2011)	FP6 (Na ₂ O ₂ fusion)		As above	11
Grab samples (2012)	FB6 (Li ₂ B ₄ O ₇ fusion)	Al ₂ O ₃ , CaO, FeO, K ₂ O, (LOI), MgO, MnO, Na ₂ O, P ₂ O ₅ , SO ₃ , SiO ₂ , TiO ₂	Ba, Cr, Ga, Hf, Rb, Sr, Ta, Th, U, Y, Zr	14

Table 4.1: Whole rock geochemistry preparation techniques and elements analysed. Preparation codes refer to Intertek-Genalysis product codes.

^aoptical emission spectrometry

^bmass spectrometry

Preparation — crushing and grinding

Drillcore samples and grab samples collected in 2011 were prepared for analysis by Intertek-Genalysis in South Africa. Of the samples sent 5 % were blanks (REE-barren Magaliesberg quartzite chips) and 5 % were certified reference samples (carbonatites: AMIS 0185, SARM 40 and GRE-04). These were prepared and

⁹Camborne School of Mines

analysed in exactly the same way as all the other samples. Samples were dried for 8 hours at 110 °C, crushed in a jaw crusher to <1 cm and then milled to 85 % < 75 µm using a swing mill. Grab samples collected in 2012 were prepared at CSM, using a jaw crusher to < 1 cm chips and tungsten-carbide TEMA mill to 90 % <63 µm. Between each sample, both the crusher and mill were thoroughly cleaned. Furthermore a blank of quartz chips was milled between each sample, cleaned again, followed by a small amount of sample, which was disposed of, and cleaned again.

Analysis

Powders were analysed by Intertek-Genalysis in Australia. Samples from the drill-core and grab samples collected in 2011 were prepared using Intertek-Genalysis technique FP6 (Intertek-Genalysis internal catalogue number). This technique involves digestion using a sodium peroxide fusion to dissolve refractory minerals. This took place in a muffle to retain sulphur. Grab samples from 2012 were prepared using Intertek-Genalysis technique FB6 which uses a lithium borate fusion to dissolve refractory minerals, but otherwise they were prepared in the same way as the 2011 samples. This different technique was used to obtain Na concentrations in silicate rocks. Major and trace elements were analysed using ICP-OES¹⁰ and ICP-MS, respectively. The fusion products were dissolved in HCl and diluted for analysis. The results were corrected for the dilution and amount of flux used for digestion. Internal standards were used to correct for drift, viscosity effects and plasma fluctuations.

Data quality

While a large volume of data are available, many of the data have relatively low totals due to the lack of LOI¹¹ data. Of the available drillcore data, 816 samples include LOI data and have totals close to 100 %. These data are those that have been most used in this thesis. The data for other samples are useful for examining trace element and REE distributions but are less reliable for the major elements. The use of these data without LOI is almost exclusively limited to analyses of the apatite-fluorite veins due to the abundance of data with LOI for the other rock types. Where data without LOI are used it will be highlighted to clarify the potentially reduced reliability.

As a Na-bearing flux was used to aid dissolution of most of the samples, data for Na are absent for almost all samples. In addition, the 14 samples collected in 2012 lack Li and B data due to the use of a Li-metaborate flux. For most

¹⁰inductively coupled plasma optical emission spectrometry

¹¹loss on ignition

samples this is not an issue as Na concentrations in carbonatites are usually low (excluding natrocarbonatite). However, the Na contents of fenite, and any other rock types with Na-feldspar, can be high and consequently the lack of Na data is problematic for interpretation of these rocks.

Blank analyses show occasional spikes in the REE concentrations, reaching up to 680 ppm from a typical background of 43 ppm (Table. 4.2). A possible cause, which cannot be excluded, is analysis of small grains of monazite in the quartzite blank. Another possible cause is contamination during sample crushing and grinding. Spikes appear typically after preparation of particularly REE-rich samples and, although the sample crushing chamber is vacuumed after each use, a small amount of residual material can remain. Potential contamination is exacerbated by the large degree of volume change between the blanks and the samples (up to 1 m of drillcore compared with a few grams of blank) and the large difference between the REE concentration in samples and blanks (3–4 orders of magnitude). This contamination implies that when samples with greatly differing concentrations are milled sequentially, the second sample is contaminated by the first. Despite these issues, the relative differences in REE concentration between blank samples and REE-bearing samples means that any contamination would have a negligible effect on the REE concentration and REE distribution of almost all carbonatite samples. Only in samples with a very low REE concentration should the issues with occasional REE spikes arise, and these samples are uncommon in carbonatites.

The carbonatite CRMs¹² were used as a check on the accuracy and precision of the analytical data. The CRMs used were SARM 40 from a carbonatite in the Brits area of the Transvaal, South Africa, GRE-04 from an un-referenced carbonatite in Tanzania and AMIS 0185 from Wigu Hill carbonatite in Tanzania. The availability of different carbonatite standards was limited with each having positive and negative traits: SARM 40 has a similar composition to the Songwe carbonatite but has been analysed in a limited number of laboratories and certified values are not available for some elements; AMIS 0185 has been analysed in a large number of laboratories, but has very high concentrations of the REE and is not of a similar composition to the Songwe carbonatite; and GRE-04 is not certified for the major elements and most trace elements, except the REE. Analyses of AMIS 0185 and GRE-04 in this study gave similar results to published values (McWha and Smee, 2011; Geostats, 2015), indicating that the data are accurate (Table. 4.2). Analyses of Sr, Zr, Fe, S and Th from the SARM 40 standard departed significantly from published values (Potts et al., 1992; Table. 4.2). An investigation of the particle size of the SARM 40 powder showed that this was above the required minimum of 75 μm , which had led to incomplete diges-

¹²Certified Reference Materials

tion of refractory minerals during preparation. Consequently, the SARM 40 was not extensively used and most standard data are obtained from AMIS 0185 and GRE-04. These standards provide good data with which to evaluate the quality of the unknown data. Precision of the reported values was determined by the magnitude of two standard deviations of analyses of the AMIS 0185 or the GRE-04 standards, whichever is larger. These were consistently lower than the ranges of uncertainty quoted in the standard reference data.

Sampling and heterogeneity issues

As demonstrated in Chapter 3, the carbonatite at Songwe is heterogenous at both the small and large scale. In addition, fenite is found as large blocks and as small fragments within the carbonatite. This heterogeneity makes it difficult to effectively separate the fenite from carbonatite. Sampling of the drillcore attempted to alleviate this. The drillcore was typically sampled in 1 metre long intervals. Where a change of lithology occurred within the sampling interval, then each lithology was sampled separately, using a minimum and maximum drillcore length of 20 cm and 130 cm, respectively (Croll et al., 2014). However, some carbonatite analyses incorporate a significant (up to 90 vol. %!) proportion of fenite (Fig. 4.3). This is demonstrated by the negative correlation between CaO and Al₂O₃, SiO₂, K₂O and Sc. A plot of Al₂O₃ against CaO was used to discriminate between fenite and carbonatite. This is because the Al₂O₃ concentration is high in K-feldspar, a major mineral in fenite, but it is only a trace element in carbonatite, where it is found in minor florencite-(Ce). SiO₂, while not common in Songwe carbonatite, can be found in late quartz, and was therefore not used to discriminate between fenite and carbonatite. An arbitrary cut-off of 2 wt. % Al₂O₃ was used to discriminate between fenite-rich and fenite-poor carbonatite. Carbonatites with greater than 2 % Al₂O₃ are considered too heterogeneous and are therefore excluded from interpretation. These samples are not plotted on any subsequent graphs.

4.2.3 Mineralogy and micro analysis

Polished thin sections (30 µm) were prepared for petrography using the usual techniques in the CSM preparation laboratory. Most samples were investigated using a polarising microscope, but for many samples optical petrography proved to be a poor technique to identify minerals due to staining from Fe-oxides which rendered some minerals opaque under transmitted light. Cold-CL¹³, however, was a very effective technique for mineral identification in carbonatites as the luminescence was not affected by the presence of iron-oxides. Analysis by CL

¹³cathodoluminescence

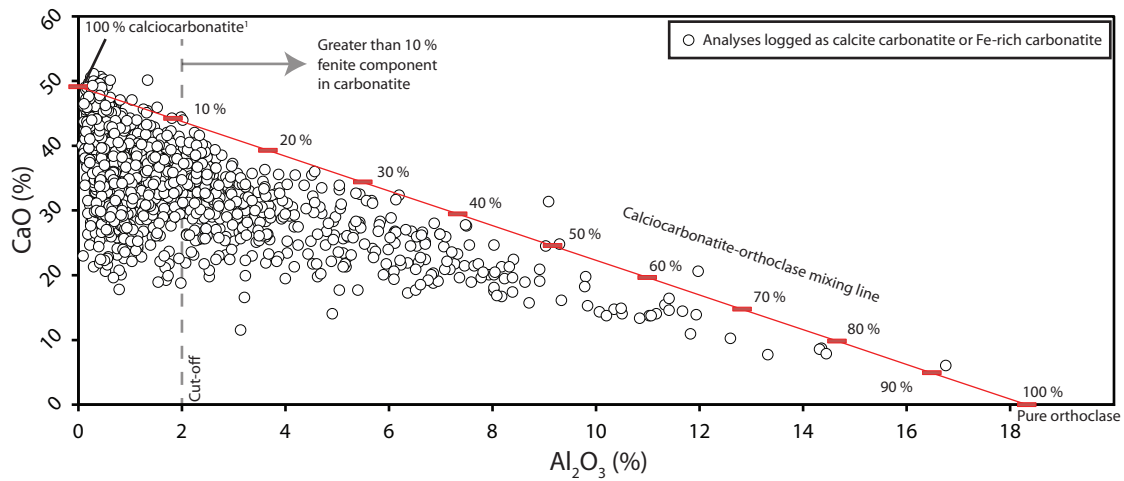


Figure 4.3: CaO and Al_2O_3 in all carbonatite (Fe-rich and calcite carbonatite) compared to a simple binary mixing model between calciocarbonatite and orthoclase. The ¹calciocarbonatite value is the average CaO concentration from Woolley and Kempe (1989), while the value for 100 % orthoclase represents a fenite. A conservative cut-off of 2 % Al_2O_3 is indicated; values with greater than 2 % Al_2O_3 are considered to contain at least 10 % fenite and are not used for geochemical plots of carbonatite.

Element	Blank (Magaliesberg quartzite)				SARM 40					AMIS 0185					GRE-04						
	Max	Min	Avg (n=114)	2SD	Published Conc	Max	Min	Avg (n=19)	2SD	Published Conc	2SD	Max	Min	Avg (n=91)	2SD	Published Conc	2SD	Max	Min	Avg (n=105)	2SD
Al ₂ O ₃	0.77	0.34	0.47	0.01	0.41	0.47	0.32	0.41	0.02	2.22	0.12	2.51	2.14	2.36	0.02	-	-	8.52	5.90	6.44	0.66
CaO	2.66	0.14	0.31	0.06	49.77	52.19	48.27	50.06	0.57	11.48	0.36	12.31	10.21	11.43	0.08	-	-	1.26	0.84	1.01	0.28
Fe ₂ O ₃	1.13	0.28	0.65	0.04	2.75	3.09	2.43	2.66	0.07	5.29	0.28	6.98	5.08	6.14	0.10	-	-	61.45	48.17	54.47	4.09
K ₂ O	0.78	0.14	0.37	0.02	0.03	0.19	0.07	0.12	0.02	0.10	0.02	0.36	0.07	0.18	0.01	-	-	0.51	0.06	0.15	0.16
LOI	6.55	-0.48	0.21	0.30	-	42.39	39.07	39.29	0.35	20.69	0.64	22.31	20.03	20.70	0.15	-	-	-	-	-	-
MgO	0.10	0.02	0.03	0.00	1.97	1.92	1.81	1.89	0.02	4.65	0.20	4.96	4.23	4.66	0.03	-	-	0.65	0.05	0.14	0.12
MnO	0.26	0.26	0.26	0.00	0.18	0.39	0.26	0.32	0.03	1.09	0.16	1.42	0.77	1.17	0.02	-	-	2.71	2.07	2.44	0.22
P ₂ O ₅	0.11	0.02	0.04	0.01	2.05	2.09	1.83	1.98	0.03	1.74	0.10	1.97	1.40	1.75	0.02	6.20	0.10	6.71	5.09	5.99	0.55
SO ₃	0.27	0.12	0.20	0.01	0.05	0.95	0.20	0.54	0.14	0.24	0.35	5.77	2.45	3.95	0.14	-	-	1.90	1.37	1.68	0.19
SiO ₂	107.82	81.29	96.63	1.03	3.08	3.64	2.99	3.39	0.10	21.53	0.82	24.39	18.40	22.28	0.19	-	-	6.85	1.07	3.50	1.36
TiO ₂	-	-	-	-	0.05	0.17	0.08	0.11	0.01	0.08	0.02	0.18	0.08	0.12	0.01	2.77	0.08	3.15	2.20	2.71	0.24
ppm																					
B	70.00	52.00	59.40	2.45	-	-	-	-	-	-	-	-	-	-	-	-	-	-	-	-	-
Be	-	-	-	-	-	-	-	-	-	3.59	2.02	5	3	4	0.2	-	-	-	-	-	-
Ce	679	14	44	15	160	170	144	154	3	40750	4610.00	45205	38227	41351	336	6127.0	146.0	6746.8	5437.8	6085.3	481.2
Cr	1094	349	803	56	35	131	51	77	12	48	22	86	50	65	4	-	-	-	-	-	-
Dy	10	1	1	0.20	-	7	6	6	0.16	27	5	36	23	27	0.45	96.5	6.8	101.5	82.7	92.3	7.2
Er	3.1	0.2	0.6	0.1	-	3.5	2.8	3.0	0.1	4.2	1.7	7.9	1.2	3.5	0.3	28.6	1.8	29.5	22.4	26.1	2.5
Eu	8.1	0.1	0.5	0.2	-	3.8	3.1	3.4	0.1	94.2	12.1	101.2	79.0	91.0	0.9	100.6	9.2	104.6	84.7	93.3	8.3
Ga	4.0	1.0	2.0	0.1	-	3.0	1.0	2.4	0.3	183.0	155.0	514.0	1.0	73.8	23.9	-	-	58.0	14.0	28.8	14.6
Gd	19.6	0.8	1.6	0.4	-	10.7	8.1	9.2	0.3	244.0	90.2	159.0	113.8	141.0	1.7	232.8	15.1	240.0	182.0	214.6	20.0
Hf	2.0	1.0	1.5	0.0	-	2.0	1.4	1.6	0.1	1.4	1.1	4.1	1.2	1.6	0.1	-	-	46.5	18.4	22.5	6.0
Ho	1.5	0.1	0.2	0.0	-	1.3	1.1	1.2	0.0	3.2	0.5	3.3	2.7	3.0	0.03	13.5	1.0	14.7	11.6	12.9	1.0
La	381	7	24	9	-	83	66	71	2	30030	1710	36595	30332	33895	309	2735.5	53.2	2955.6	2416.4	2671.7	232.2
Li	4.0	1.0	1.6	0.3	-	6.0	1.0	2.4	0.7	18.5	11.1	24.0	17.0	20.3	0.8	-	-	-	-	-	-
Lu	0.3	0.1	0.1	0.0	-	0.7	0.3	0.4	0.0	0.6	0.3	0.8	0.2	0.4	0.02	1.8	0.2	2.1	1.5	1.8	0.2
Nb	189.0	10.0	34.8	7.5	10.0	17.0	10.0	12.3	1.8	72.6	88.3	131.0	99.0	113.1	1.4	3553.0	308.0	3956.0	1133.0	3250.8	747.4
Nd	230	5	15	5	-	78	63	70	2	9238	1033	10554	8343	9254	99	2702.0	133.0	2973.1	2405.4	2721.0	237.0
Pr	71	1	4	2	-	20	17	18	0	3471	343	3908	3250	3529	30	721.1	46.0	825.3	650.5	728.2	66.1
Sc	-	-	-	-	-	-	-	-	-	15.4	3.5	87.0	21.0	79.4	6.9	88.4	4.2	-	-	-	-
Sm	32	1	2	1	-	13	10	12	0.34	556	48	585	488	546	5	390.4	18.0	424.3	337.5	375.5	30.4
Sn	10.0	2.0	3.9	0.8	-	6.0	2.0	3.4	0.7	1.1	0.2	-	-	-	-	-	-	-	-	-	-
Sr	1263	20	91	36	1353	1836	1513	1648	40	53344	3848	61449	50244	57015	587	-	-	3270.0	50.0	2892.6	840.1
Ta	1.7	0.1	0.3	0.1	-	1.1	0.5	0.6	0.1	0.2	0.1	0.9	0.1	0.3	0.1	122.1	14.0	-	-	-	-
Tb	2.3	0.1	0.2	0.0	-	1.4	1.1	1.2	0.0	15.3	5.2	12.4	5.3	8.3	0.3	24.5	1.6	25.8	19.4	22.5	2.3
Th	24.8	2.3	3.7	0.5	12.0	7.1	5.4	5.8	0.2	237.0	42.3	260.9	213.3	238.1	1.8	-	-	160.1	123.8	138.6	11.5
Tm	0.4	0.1	0.1	0.0	-	0.5	0.4	0.4	0.0	0.4	0.1	0.5	0.3	0.4	0.01	3.0	0.2	3.3	2.4	2.8	0.3
U	5.5	0.6	1.0	0.1	-	2.1	0.2	0.4	0.2	46.3	9.3	58.9	41.2	46.5	0.6	-	-	144.0	116.3	127.5	9.3
V	-	-	-	-	27.0	-	-	-	-	54.2	22.0	116.0	71.0	96.6	5.6	-	-	-	-	-	-
W	5.0	1.0	3.0	0.2	-	-	-	-	-	1.3	2.1	-	-	-	-	-	-	-	-	-	-
Y	35.2	3.9	5.8	0.8	33.0	31.7	27.6	29.9	0.5	62.0	7.7	69.3	53.1	60.4	0.6	319.4	14.8	339.1	268.1	302.3	26.7
Yb	2.5	0.2	0.5	0.1	-	2.8	2.2	2.5	0.1	2.8	1.3	2.3	0.1	1.0	0.1	15.0	0.7	15.1	11.6	13.6	1.2
Zr	82.0	35.0	55.2	1.5	87.0	123.0	82.0	97.5	4.9	57.5	45.2	158.0	56.0	69.1	2.8	948.0	128.0	3009.0	738.0	960.4	440.2

Table 4.2: Results for REE blank analyses, and carbonatite standard analyses, including published standard values from drillcore assay data (Potts et al., 1992; McWha and Smee, 2011; Geostats, 2015). Values indicated by a hyphen (-) were not analysed. Standard values in italic are not certified, but recommended values for guidance.

was typically followed-up with SEM¹⁴ analysis to confirm phase identification.

Cold-cathodoluminescence (CL)

CL can be a powerful tool for mineral identification in carbonatites. Samples are loaded into a vacuum chamber, attached to a standard petrographic microscope, and are bombarded by electrons. Defects and impurities in various minerals emit different colours depending on the CL activator. For different minerals, several different activators and, thus, several different luminescence colours are possible. Based upon observations by Marshall (1988), Mariano and Mariano (2014) and the authors own observations, these are summarised in Table 4.3. Not all minerals optically luminesce and elements such as Fe in some minerals are considered to 'quench' CL. Furthermore, at high concentrations, elements which are considered as activators, such as the REE, may self-quench, and thus not luminesce; a good example which demonstrates self-quenching is the REE-mineral, monazite. In some minerals, such as in carbonates, the approximate brightness of the luminescence can give a rough indication of the ratio of activators to quenchers, commonly Fe:Mn and, thus, an indication of the Fe content of a carbonate (Hiatt and Pufahl, 2014). This technique, however, is not quantitative and needs to be interpreted carefully as exsolution of Fe from carbonate alteration can give a falsely bright CL image, indicating lower Fe than may be present.

Petrography using CL was performed using an electron beam from a Citl Mk 3a electron source, operated at approximately 300–450 μA and 3–13 kV. The sample was observed through a Nikon digital camera at 2 \times magnification with a 2–4 second exposure time. At high voltages, long exposures of the sample to the electron gun can cause damage and thus exposure times were kept short.

Qualitative electron microscopy

Further petrography and confirmation of CL mineral identification was carried out by BSE¹⁵ imagery and qualitative EDS¹⁶ analysis on a SEM. Petrography using a SEM was carried out using a Jeol JSM-5400LV SEM with an electron beam set to 25 kV and a spot size of 1 μm . Samples were carbon-coated (approximately 25 nm) prior to analysis. EDS spectra were processed using the attached Oxford Instruments ISIS package. Back-scattered electron images are generated by the return of electrons to a detector as an incident electron beam scans across a sample. The brightness of a point on the generated image is a function of the average atomic number at that point, with higher atomic number areas backscattering more electrons and thus producing brighter points. This technique is very

¹⁴scanning electron microscope

¹⁵back-scattered electron

¹⁶electron dispersive spectroscopy

Mineral	Colours	Activators
Feldspar	Bright Blue Greenish-Yellow Red	Ti ⁴⁺ , Cu ²⁺ Fe ²⁺ , Mn Fe ³⁺
Quartz	Red Blue Brown Non-luminescent	
Calcite	Bright orange	Mn
Dolomite	Orange/Red	Mn
Strontianite	Blue	
Apatite	Violet Blue Red-orange Yellow	Ce ³⁺ Eu ²⁺ Sm ³⁺ Mn ²⁺ , Dy ³⁺
Fluorite	Electric blue	
Zircon	Bright Violet Yellow	
Xenotime	Muted blue Apple green	

Table 4.3: List of minerals which can luminesce, their luminescence colours and, where documented, known activator elements. Compiled from Marshall (1988); Mariano and Mariano (2014) and this study.

effective for finding minerals with a high atomic number, such as barite and REE-fluorocarbonate minerals. As neither of these minerals luminesce under CL, BSE proved to be a useful complementary imaging technique for petrography. Mineral identification using the SEM was confirmed using EDS. This technique measures the photon energy of X-rays generated when incident electrons interact with an element in the sample. Different elements produce characteristic X-rays, and the ratios between X-ray intensity of different elements in a mineral can be compared to published spectra (e.g. Reed, 2005). When interpreting the spectra it is important to be cautious with regards to unanalysed elements such as C and OH and assumptions of mineral structure.

Quantitative electron microscopy (EPMA)

Quantitative carbonate compositions were acquired at CSM using a Jeol JXA 8200 EPMA with 4 WDS¹⁷ detectors equipped with a range of crystals, operated at varying beam conditions and spot sizes over three different analytical sessions (Table 4.4). Analyses were corrected for atomic number, absorption and fluorescence effects using the in-built ZAF correction programme. A variety of metal, sulphide and oxide standards was used (Table 4.4). Standards were measured with the same beam conditions as the sample.

Element	Standard	Count time	Crystal	DL (%)
Sessions 1 and 2				
<i>Spot size: 50 (1) and 30 (2) μm; voltage: 10 KeV; current: 5 nA</i>				
Ca	Apatite	10	Pet K α	0.06
Mg	Olivine	10	Tap K α	0.17
Fe	Olivine	10	LifH K α	0.12
Mn	Rhodonite	10	LifH K α	0.12
Sr	Celestite	10	Tap L α	0.12
Ba	Barite	10	Pet L α	0.06
Session 3				
<i>Spot size: 15 μm; voltage: 20 KeV; current: 5 nA</i>				
Ca	Calcite	10	PetH K α	0.08
Mg	Dolomite	30	Tap K α	0.30
Fe	Olivine	30	LifH K α	2.60
Mn	Rhodonite	40	Lif K α	2.30
Sr	Celestite	40	Tap L α	0.89
Ba	Barite	60	PetH L α	0.20

Table 4.4: Probe conditions for carbonate analyses on the Jeol JXA 8200 EPMA at CSM. Background times are half peak count times.

¹⁷wavelength dispersive spectrometry

QEMSCAN® analyses

QEMSCAN (Quantitative Evaluation of Minerals by Scanning electron microscopy) is an SEM-EDS based technique where EDS spectra are generated from pixels (varying from 1 μm –10 μm) across a thin section. The EDS spectra are processed using a SIP¹⁸ which compares the spectra to a known database. This generates a mineral map of a sample, and additional data on mineral abundance, size and relative positions.

QEMSCAN was not extensively used in this thesis, but three field-scans (X-ray maps of a whole thin section) are included. These were generated using the QEMSCAN 4300 at CSM. The analytical set-up of this instrument is outlined by Andersen et al. (2009) and Rollinson et al. (2011). Spectra were collected with 1000 total X-ray counts at a 10 μm grid spacing, and compared to the LCU-5 SIP, heavily modified to include REE minerals. All minerals identified using the QEMSCAN were checked using optical microscopy and BSE imagery.

4.3 Results

4.3.1 Petrography

To identify the mineralogy of each carbonatite generation, and to identify the major REE-bearing minerals in the carbonatite, petrographic analyses were carried out. Representative samples of all of the carbonatite types identified in chapter 3 were selected. These are described below in paragenetic order.

Mauze

Thin sections were prepared from three Mauze samples. These can be divided into equigranular (U4913) and pegmatoidal (U4914, F01) samples. Equigranular sample F03 was examined only in hand specimen.

The equigranular sample (U4913) is composed of rounded large (5 mm) xenocrystic perthite (20 %) in a groundmass of smaller (0.5 mm) orthoclase (60 %) with biotite (15 %), minor nepheline (5 %) and trace zircon (<1 %) and rutile (<1 %). Under CL the groundmass orthoclase displays intense blue luminescence compared to blue-brown luminescence in the perthite. This description differs somewhat from the samples described by Dixey et al. (1955), who identified much more nepheline, and aegirine, which were not identified in this sample. In hand specimen, sample F03 appears to be much more similar to the description of N1121 described by Dixey et al. (1955), with more abundant nepheline and small pyroxene grains.

¹⁸species identification protocol

Pegmatoidal samples U4914 and F01 contain large (50 mm) albite and amphibole (arfvedsonite?) grains, crystallising unidirectionally from the edge to the centre of a vein. Additionally, in U4914, rounded xenocrystic perthite is present and appears broken-down with respect to the later albite and amphibole. Some amphiboles show oscillatory zoning, and some cores are partially corroded and altered to opaque phases. Minor titanite(?) and zircon were observed.

Fenite

Thin sections of fenite were prepared from: Chenga Hill (T0134), drillcore (T0185, T0201, T0235, T0248) and a channel sample (T3A). In addition, fenite clasts are present in many of the carbonatite samples.

In large fenite blocks, and in fenite outside the carbonatite, fenite is composed largely of coarse- and fine-grained K-feldspar (>90 %) (Fig. 4.4 A). Minor phases include apatite, zircon, rutile, ilmenite and hematite. Thin, cross-cutting quartz veins are uncommon. Alteration of Fe-phases to goethite is common.

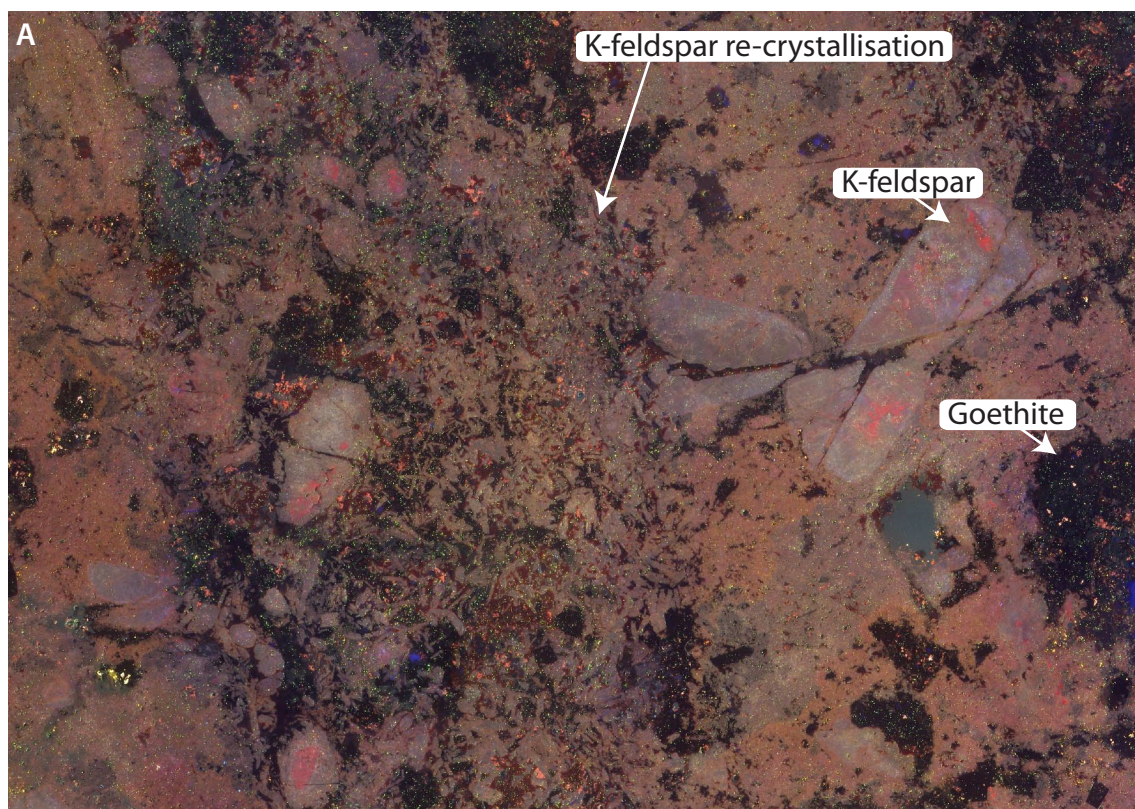
In small clasts within the carbonatite, fenite commonly shows carbonatisation. In hand specimen, the boundary between carbonatite and fenite is well defined (Fig. 3.13, chapter 3, page 74). However, in thin section, the boundary is much more diffuse and the area near the boundary is composed of a groundmass of fine-grained calcite with K-feldspar-rich fenite clasts occurring as rounded grains (Fig. 4.4 B). Apatite and florencite are more commonly found in these areas.

C1 calcite-carbonatite

C1 carbonatite is uncommon, and it was only found in two samples of calcite-carbonatite from the drillcore (T0206, T0218). It is composed of medium-grained anhedral calcite (90 %), minor anhedral ankerite (5 %) and an assemblage of ovoid apatite, subhedral zircon, euhedral pyrite, anhedral pyrochlore and anhedral K-feldspar (in total comprising the remaining 5 %) which displays large-scale flow-banding in hand specimen. Some calcite appears re-crystallised under CL, luminescing a brighter yellow colour than the majority of the groundmass calcite (Fig. 4.5). Zoning is present in apatite (see chapter 5) and zircon (see chapter 8).

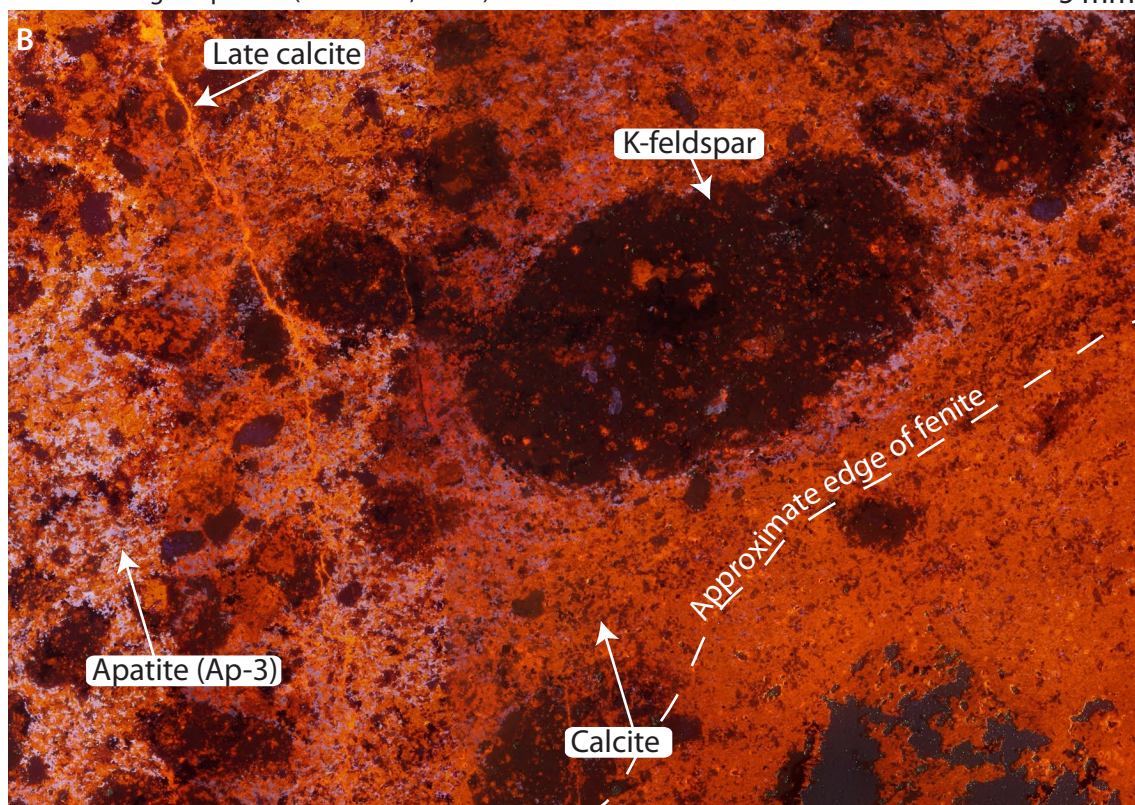
C2 calcite-carbonatite

C2 calcite-carbonatite is the most abundant and the most texturally complex carbonatite at Songwe. It ranges from simple, fine-grained calcite-rich rocks, through to complex, multi-phase samples. It is most commonly composed of fine-grained calcite with minor ankerite (Figures 4.6 and 4.8 A). Apatite-rich bands cross-cut earlier calcite-rich phase and in these bands, apatite is anhedral and can



T0185: CL high exposure (4 seconds, 10 kV)

5 mm



T3A: CL high exposure (4 seconds, 10 kV)

5 mm

Figure 4.4: CL images of fenite from a large fenite block (A) and from a fenite clast next to carbonatite (B). Fenite in A is composed almost entirely of K-feldspar of different sizes. Alteration of Fe-phases to goethite is common. Fenite in B is carbonatised, and the edge of the original fenite block is not recognisable. Most K-feldspar is altered, and only small rounded grains remain. Apatite (as Ap-3, see Chapter 5) is common, and florencite is common near the remaining K-feldspar grains. Images correspond to hand specimen Figures 3.8 and 3.13, on pages 68 and 74, for A and B, respectively.

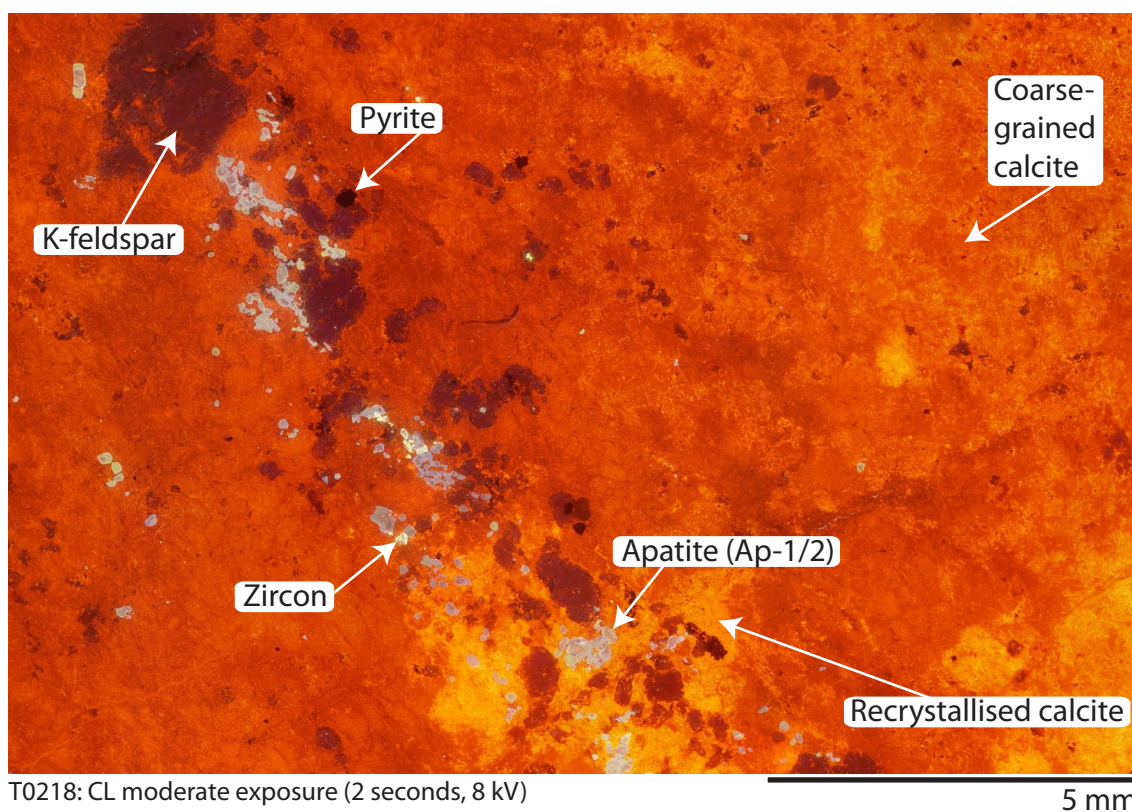


Figure 4.5: CL image of C1 calcite carbonatite, showing zircon, apatite, pyrite and K-feldspar. Most calcite is coarse-grained, orange-luminescent and is interpreted as magmatic. Some recrystallised, bright-yellow luminescent calcite is also present.

form stringers (e.g. Fig. 4.7 A). Calcite in association with this later, apatite-bearing, stage luminesces brighter under CL than earlier calcite. In some samples xenocrysts of zircon, pyrochlore, pyrite and K-feldspar are present which show varying degrees of rounding and alteration (Fig. 4.7 B). Pyrite, zircon and K-feldspar show little rounding, and are found in bands, while pyrochlore is often rounded and partially broken-down.

Small vugs are disseminated throughout C2 carbonatite and these often contain an assemblage of euhedral synchysite-(Ce), barite, and anhedral strontianite (Fig. 4.8 C). This mineral assemblage is mineralogically similar to mineral assemblages in C3 carbonatite. The relationship between the LREE-bearing mineral assemblage and the crystallisation of anhedral apatite stringers is not apparent in C2 calcite-carbonatite, but can be observed in C3 Fe-carbonatite.

C3 Fe-rich carbonatite

Fe-rich carbonatite has been identified in drillcore samples (T0250, U4904, U4921) channel samples (T3B, T3C) and in grab samples (T0167). It has a banded appearance in hand specimen, and the cross-cutting relationships of these bands indicate that it formed over three stages (e.g. Fig. 4.9). In paragenetic order, these are:

1. Groundmass
2. Apatite-bearing band
3. A band of a LREE-fluorcarbonate-bearing assemblage

The groundmass is predominantly (95 %) composed of a dark-brown/opaque carbonate phase which luminesces rusty-orange under CL. Under BSE this phase shows exsolution textures between calcite and Fe-oxides and is interpreted to be altered ankerite (see Fig. 4.8 B, and EPMA analyses, section 4.3.2). Minor hematite (4 %) and zircon (1 %) are also present in the groundmass. These phases are approximately 10–100 μm in size and are euhedral, except where zircon is in contact with the LREE-fluorcarbonate-bearing assemblage. Where this is the case, the zircons are subhedral and show resorption textures (see Chapter 8).

Apatite bands are monominerallic. The apatite is anhedral, very fine grained and is similar to the apatite bands found in the C2 calcite carbonatite. The bands are typically thin, up to 1 mm wide, but up to 1 cm in length. They are often aligned parallel to one another and parallel to the later LREE-fluorcarbonate-bearing assemblage.

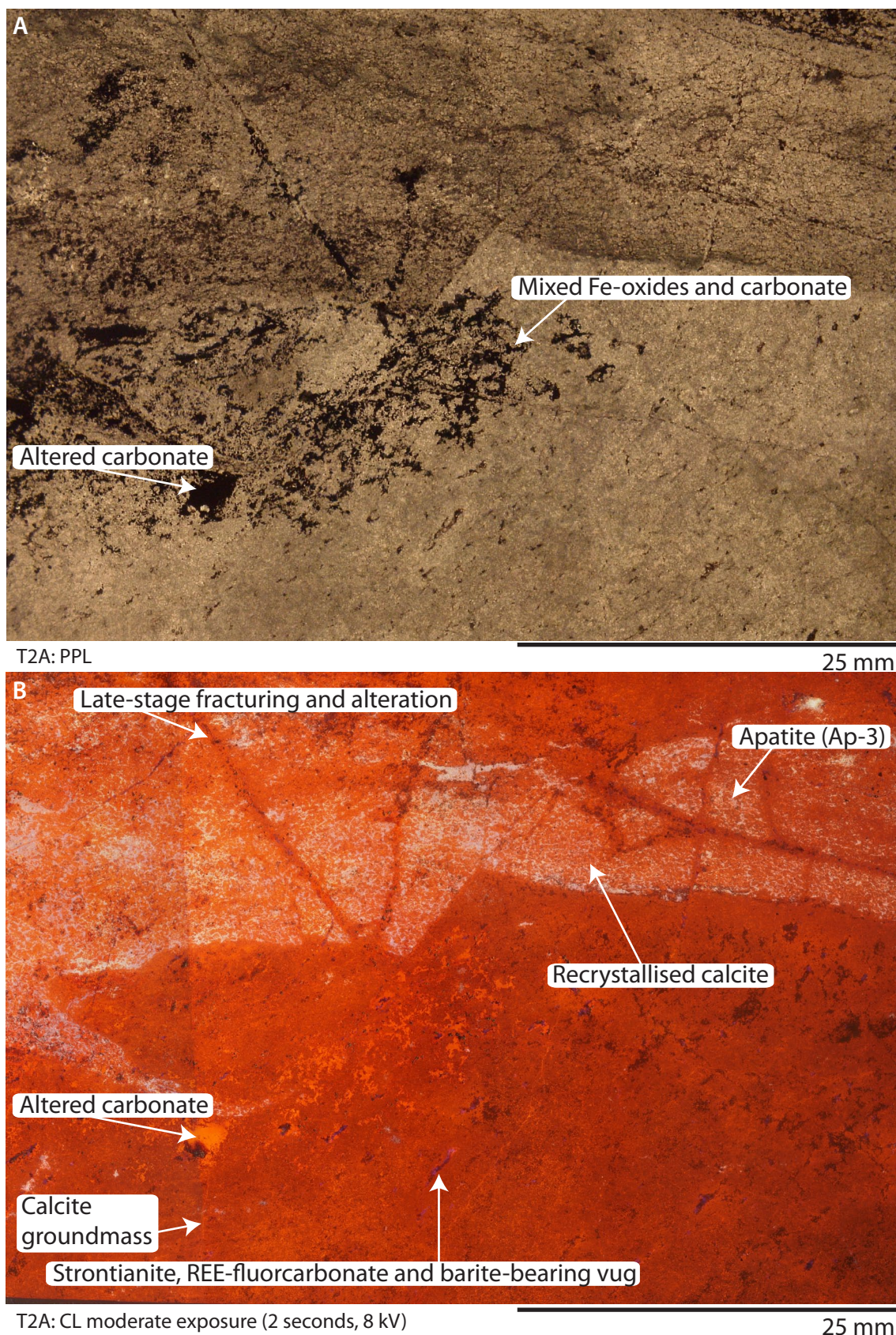
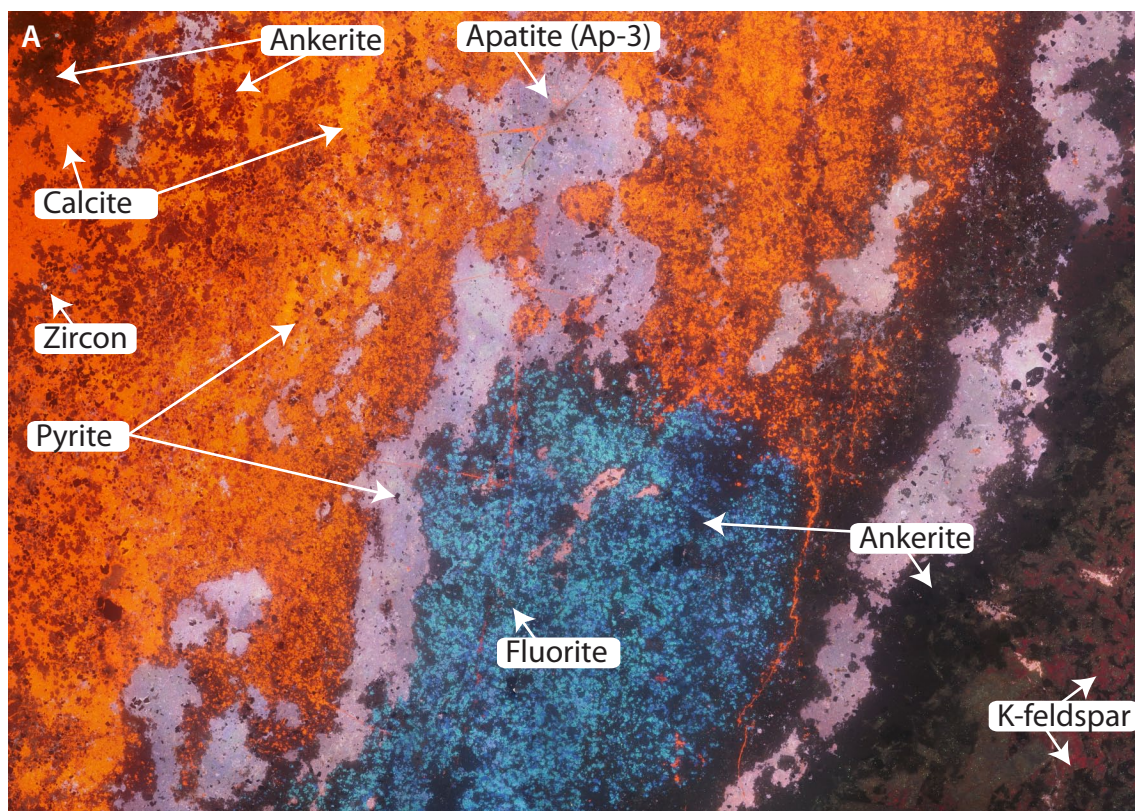


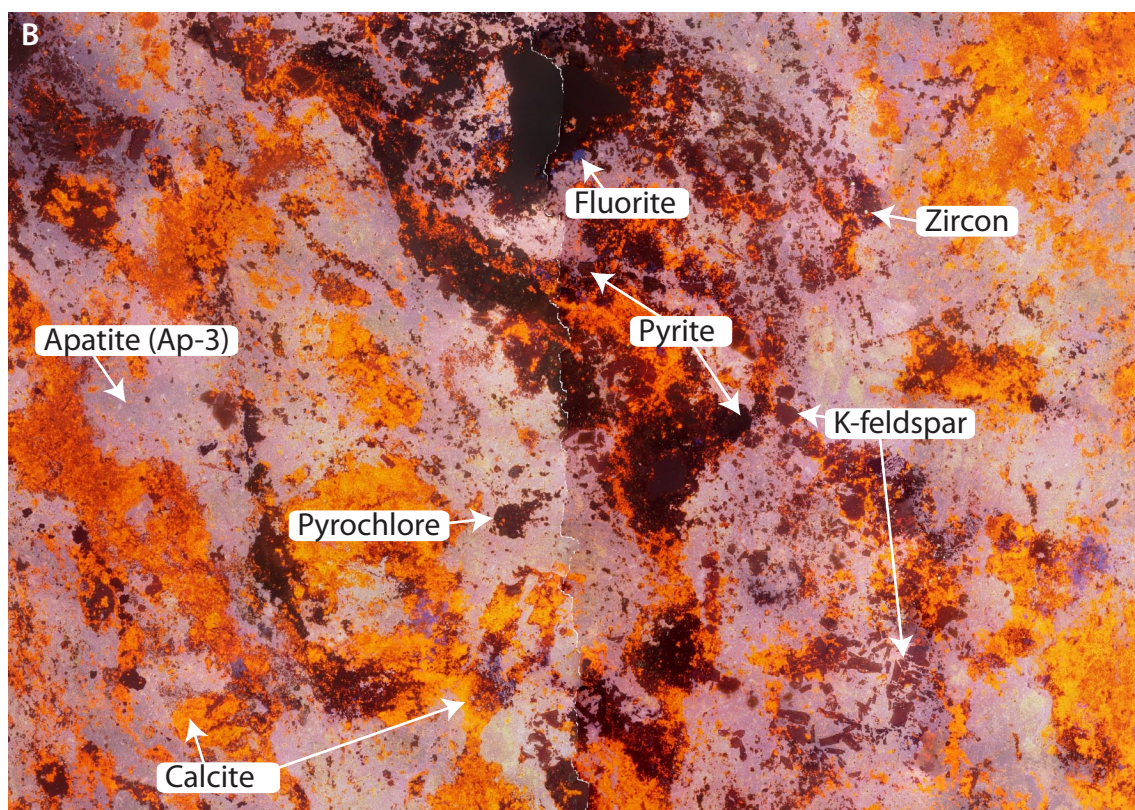
Figure 4.6: PPL^a (A) and CL (B) images of a C2 calcite-carbonatite thin section. Note the contrast between the earlier, fine-grained, calcite in the lower part of the image and later, brighter-luminescent, calcite associated with apatite in the upper part of the image. Subsequent alteration of carbonate to calcite and Fe-oxides occurs afterwards, either synchronously with, or post-dating, brittle fracturing of the rock. Images correspond to hand specimen Figure 3.11, on page 72.

^aplane-polarised light



T0225: CL composite, 8 kV, 4 s

20 mm



T0262: CL composite, 8 kV, 4 s

15 mm

Figure 4.7: CL images of C2 calcite-carbonatite showing varying proportions of modal apatite concentration. The upper image is interpreted to have formed paragenetically earlier and the lower image, later. The apatite content progressively increases combined with calcite recrystallisation and incorporation of earlier calcite-carbonatite minerals such as pyrite, zircon and pyrochlore.

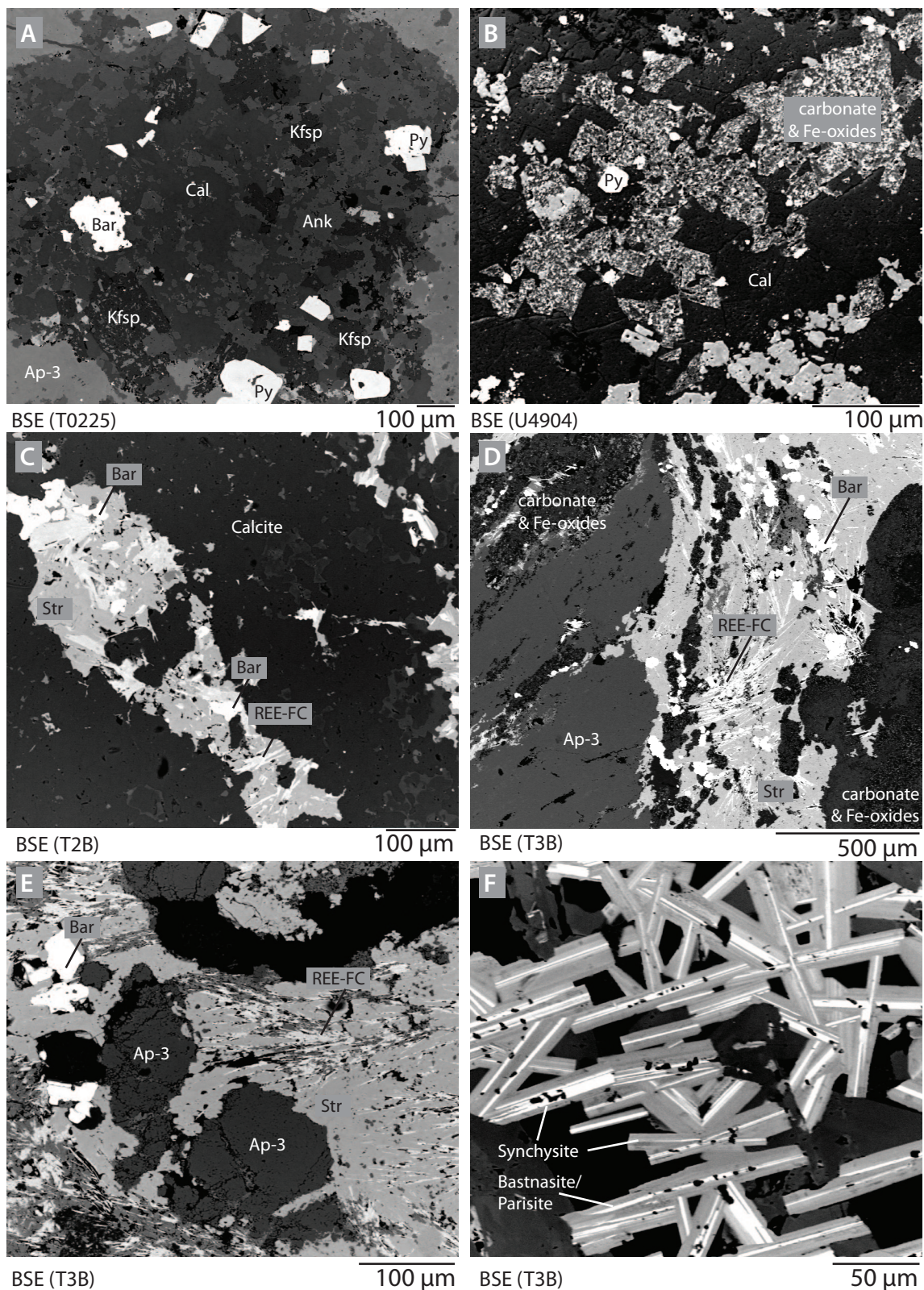


Figure 4.8: BSE images of C2 and C3 carbonatite showing the different carbonate phases present (A, B, D); the relationship between carbonatite, apatite and the barite–strontianite–REE–fluorcarbonate assemblage (C–E); and syntaxial intergrowths of synchysite and bastnäsite/parisite (F). Abbreviations: Bar, barite; Str, strontianite; Ap, apatite; Kfsp, K-feldspar; Py, pyrite; REE-FC, REE-fluorcarbonates. Ap-3 refers to the apatite type, discussed in chapter 5.

The LREE-fluorcarbonate-bearing assemblage is similar to the LREE-bearing assemblage found in vugs in the C2 calcite-carbonate, and is composed of syntaxial intergrowths of euhedral synchysite and parisite/bastnäsite, euhedral barite and anhedral strontianite or calcite (Fig. 4.8 F). The cross-cutting relationships between the various stages are evident from the truncation of an apatite stringer by a REE-fluorcarbonate-bearing assemblage (Figures 4.8 C–D), and from the presence of partially fragmented apatite in a matrix of strontianite and fluorcarbonates (Fig. 4.8 E).

Apatite-fluorite veins

Seven thin sections were prepared from the apatite-fluorite vein samples from Chenga Hill, and 2 samples were prepared from the drillcore. As the mineral assemblages of the drillcore and Chenga samples are very similar only samples from Chenga are described.

Major minerals in the apatite-fluorite veins include calcite/ferroan-calcite, fluorite, apatite, quartz and barite (Fig. 4.10). Minor minerals include xenotime, zircon, rutile/anatase, Mn-oxides, hematite, and synchysite/parisite. Trace minerals include florencite, britholite, goyazite and allanite.

A substantial component of the apatite-fluorite rock is carbonate. Two types of carbonate are observed: brown–rusty-orange luminescent carbonate which is opaque under PPL and bright yellow–orange luminescent carbonate which is clear under PPL. The former type is predominant, comprising >95 % of the carbonate and typically forming large, anhedral masses. The variation in CL luminescence colour and intensity between brown and rusty-orange typically forms a ‘tiger-stripe’ pattern, similar to alteration seen in outcrop. Under the SEM the carbonate displays similar exsolution textures to carbonate seen in other samples at Songwe, with intermixed calcite and Fe-oxide/hydroxide minerals (Fig. 4.8 B). The other carbonate present in these samples is small anhedral calcite associated with fluorite. This calcite is bright yellow–orange under CL and forms small patches or veins typically a few tens of μm across. It is relatively featureless under the SEM.

Fluorite is sub–anhedral and typically occurs in elongate stringers and in discrete patches. Individual grains vary in size from 20–200 μm , with most typically around 20–50 μm . Under CL the fluorite shows excitation colours of bright electric-blue and muted electric-blue, possibly associated with zoning. Under the SEM the fluorite is porous and shows no variation in brightness. Under PPL the fluorite has many simple liquid-vapour fluid inclusions, varying from 5 μm to 20 μm (see Chapter 6).

Apatite is subhedral and typically forms aggregates in veins formed of equigranular crystals approximately 150–200 μm in size. It exhibits varied CL activation

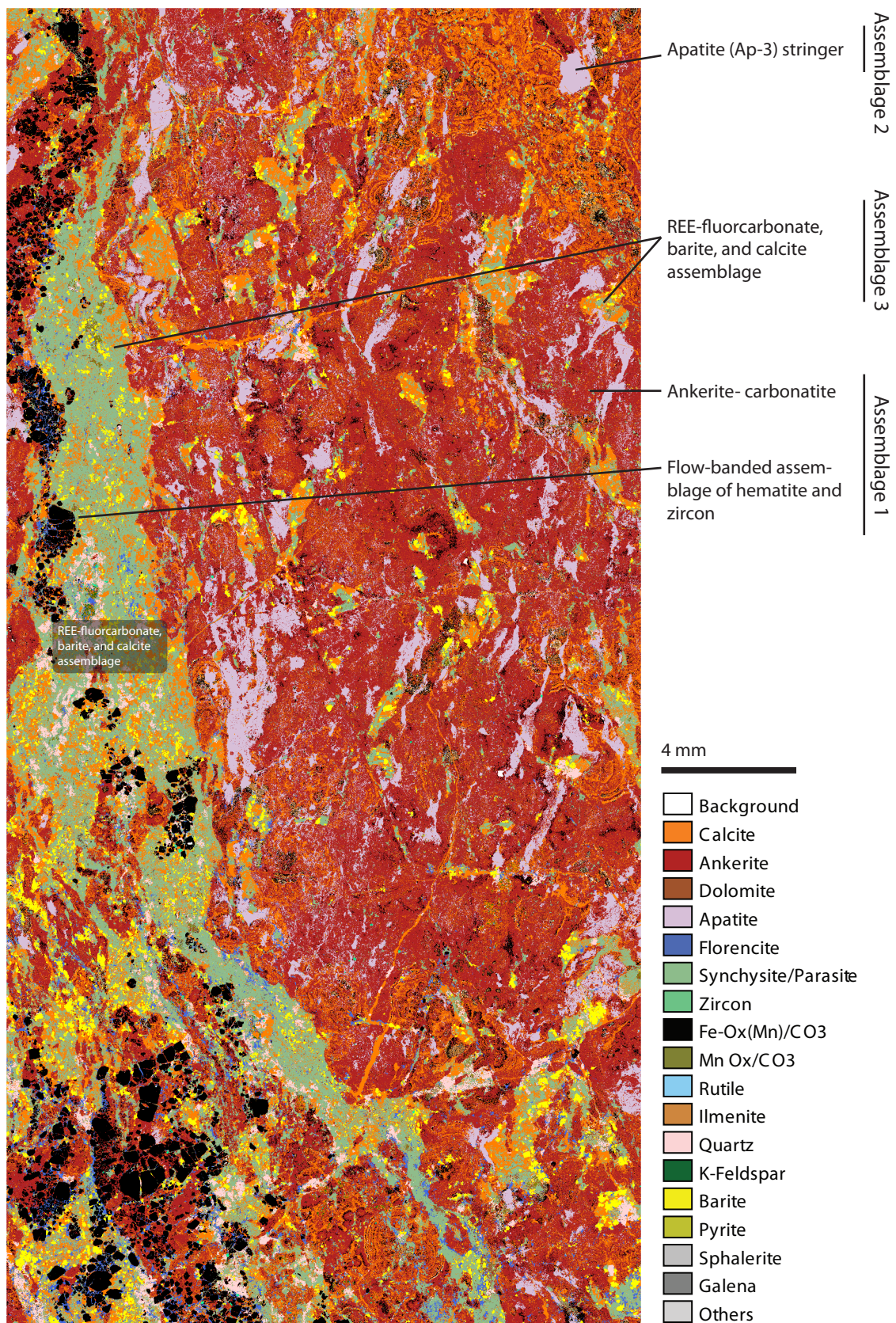


Figure 4.9: QEMSCAN image of C3 Fe-carbonatite, showing banding of apatite (mauve) and REE-fluorcarbonate assemblages (green and yellow). Sample U4904.

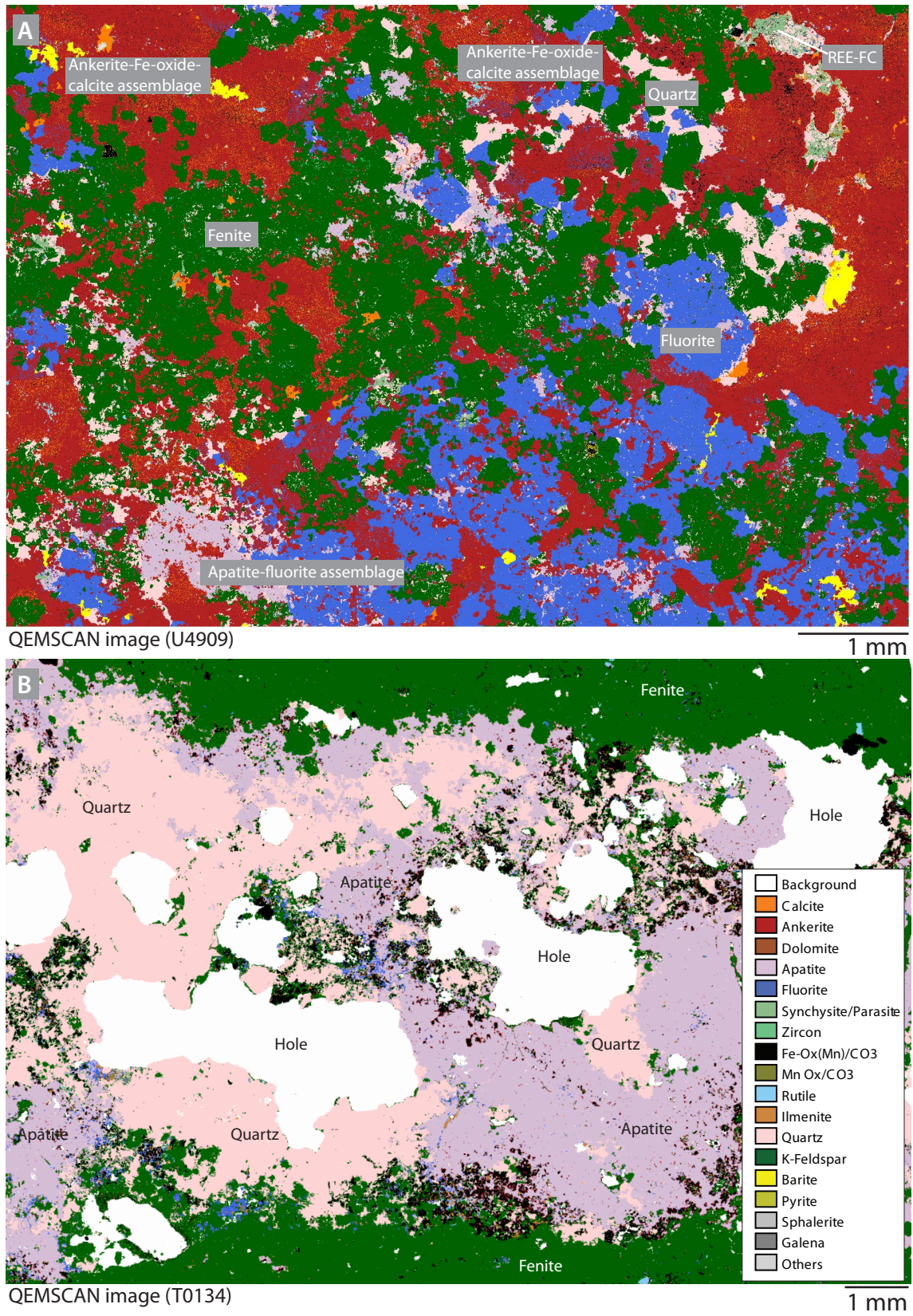


Figure 4.10: QEMSCAN images of apatite-fluorite veins showing a carbonate-rich example (A) and an apatite- and quartz-rich example (B).

colours including bright white, violet, earthy-green and dark green/brown. When viewed under BSE on the SEM the apatite shows variations in brightness and texture. Areas corresponding to brighter CL luminescence colours (e.g. white and violet) are typically brighter under BSE while areas corresponding to darker and greener CL colours are typically darker. All of the apatite has a spongy texture. Within the holes in the apatite small (10 μm) inclusions of Fe-oxide, xenotime, zircon, Mn-oxides, britholite, goyazite and allanite(?) are locally found. Apatite may also have small overgrowths of xenotime.

An assemblage of hematite, rutile, zircon and xenotime locally forms bands associated with the contact between apatite-fluorite veins and fenite. Hematite forms large (approx. 100 μm), euhedral crystals which display a variety of brightness levels and small fractures under BSE. Zircon forms aggregates of small anhedral crystals up to 5 μm which often surround rutile. Rutile/anatase is sub-anhedral and ranges in size between 1 and 25 μm .

Two crystallisation habits of xenotime are present in the apatite-fluorite veins: (1) xenotime associated with apatite and (2) xenotime associated with rutile and zircon (see Chapter 5). In both the grain size is small: type 1 is typically 10–25 μm and type 2 is typically 1–10 μm . Type 1 xenotime is the most common, accounting for approximately 80 % of all the xenotime in the veins. It forms eu-subhedral overgrowths on apatite, sometimes with a Ti- or Zr-rich core identifiable under BSE. Type 2 xenotime is much less abundant, and is commonly associated with large rutile and micro-zircons. It forms euhedral crystals near zircon, and locally forms small overgrowths on zircon or rutile.

Fragments of broken K-feldspar are common in the apatite-fluorite rock, ranging in size from 100 μm –2 mm. The pieces are angular and show little evidence of alteration or reaction with the host rock. In sample T0134, there appears to be an increase in the frequency of these K-feldspar fragments closer to the edge of the vein suggesting that the veins were forcefully emplaced.

Late-stage minerals include anhedral barite and quartz. Barite forms anhedral, 100–200 μm crystals. Quartz is euhedral and is typically around 500 μm across the c-axis. It displays sector zoning under XPL¹⁹ and concentric zoning under PPL. Radial zoning is manifested as variations in the size and density of mineral and fluid inclusions. The core of the quartz is typically clear, and the density of mineral and fluid inclusions increases towards the edge of the grain with a distinct inclusion-rich rim. Concentric zoning is also visible under CL. The core of the quartz is non-luminescent, but the inclusion-rich rims show slight brown/purple CL activation. SEM analyses shows that most of the mineral inclusions are Fe-oxides or carbonates.

Mn-oxides are present as an infilling phase in vugs and along fractures in the

¹⁹cross-polarised light

apatite-fluorite veins. The Mn-oxides form small (typically 10 μm or less), thin crystals, radiating from the edge of the vug/fracture towards the centre. Some of the vugs are completely infilled with Mn-oxides.

Mn-Fe- veins

Mn-Fe- veins are not composed of any specific mineral assemblage, rather they represent an area of intense alteration of carbonate phases. These comprise mainly Fe-oxides, with subordinate Mn-oxides, derived from the alteration of Fe-bearing carbonates and sulphides. Under PPL these veins are opaque. Under CL, however, it is evident that carbonate is present, but that Fe-oxides have exsolved out of the carbonate structure (Fig. 4.11). Complex exsolution textures between carbonate and Fe-oxides are shown under BSE (Fig. 4.8 B). Around the Mn-Fe- veins alteration can continue for several cm. The extent of the alteration typically depends on the size of the Mn-Fe-vein, but this can be very difficult to identify in the field except on a very smooth clean rock surface. This pervasive alteration may explain the prevalence of altered ankerite in many of the carbonatite types without obvious veining.

4.3.2 EPMA analyses of carbonate

EPMA analyses of carbonates were obtained from C1–C4 carbonatites, from 13 thin sections in three different analytical sessions (Table 4.5). These data were used to identify the principal carbonate minerals present in each carbonatite generation. In general, calcite and ankerite are found in all carbonatite types, with calcite predominantly found in the earlier carbonatite generations but with increasing proportions of ankerite found in the later carbonatite generations.

Complete analytical totals to 100 %, for carbonate analyses, are difficult to obtain because of the difficulties involved in analysing CO_2 using an EPMA. In general, however, all of the totals are below the ideal stoichiometric composition for each end-member composition (e.g. 56.03 % for calcite). This is, in part, due to the substitution of other elements into the main cation site. However, there are subtle, systematic variations between the totals acquired over different analytical sessions which precludes a detailed comparison of the composition of the carbonates from different carbonatite generations. As such, these EPMA data are used only for carbonate identification and for comparison of the different generations.

On a ternary plot of Ca, Mg and Fe+Mn, most analyses fall in three areas: high Ca; Ca and Fe-rich; and Mg-bearing, Fe-rich (Fig. 4.12). The high-Ca analyses represent calcite, and the Mg-bearing, Fe-rich analyses plot near the ankerite end of the dolomite–ankerite solid-solution. Some C2 analyses plot below the most

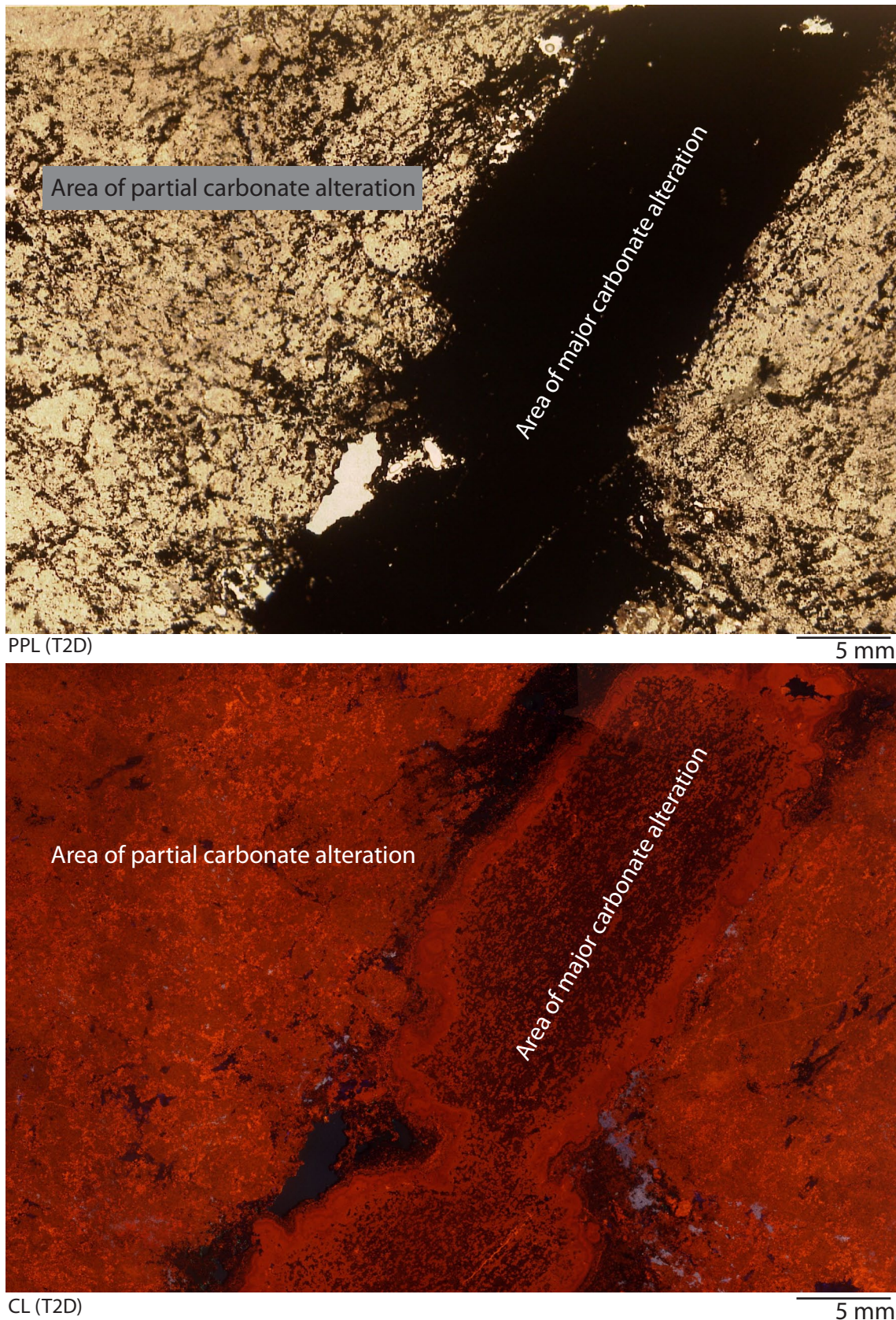


Figure 4.11: PPL (A) and CL (B) images of an Mn-Fe-vein cross-cutting and altering a C2 calcite-carbonatite. The vein is composed of Mn- and Fe-oxides and carbonate, but the carbonate is only visible under CL. Alteration extends out from the vein, and partial breakdown of Fe-bearing carbonates to Fe-oxides and calcite is visible in the C2 carbonatite around the vein. Images correspond to hand specimen figure 3.11, on page 72.

Sample	T0206				T0218				T0202				T0210				T0225				T0232				T0234			
Rock type	C1		C1		C1		C1		C2		C2		C2		C2		C2		C2		C2		C2		C2			
Mineral	Cal		Ank		Cal		Ank		Cal		Ank		Cal		Ank		Cal		Ank		Cal		Ank		Cal			
n=	30		10		40		13		6		12		37		125		58		9		29		29		29			
	Avg	2SD	Avg	2SD	Avg	2SD	Avg	2SD	Avg	2SD	Avg	2SD	Avg	2SD	Avg	2SD	Avg	2SD	Avg	2SD	Avg	2SD	Avg	2SD	Avg	2SD		
Wt. % oxide																												
CaO	51.38	1.13	27.97	0.62	52.46	1.39	28.69	2.91	50.03	0.38	50.48	2.68	47.87	7.88	25.57	1.74	46.40	5.91	30.31	7.90	21.39	0.76	21.39	0.76	21.39	0.76		
MgO	0.20	0.11	6.81	0.81	0.12	0.21	5.83	2.94	0.09	0.16	0.23	0.42	0.30	2.26	5.24	1.84	0.46	0.86	0.80	0.24	7.25	0.94	7.25	0.94	7.25	0.94		
FeO	1.14	0.39	19.02	1.33	0.75	0.53	18.85	3.81	1.34	0.47	2.00	1.62	1.39	4.72	19.41	3.03	1.37	6.88	18.53	6.07	20.84	2.00	20.84	2.00	20.84	2.00		
MnO	0.46	0.46	1.43	0.31	0.76	0.77	2.58	1.41	0.53	0.16	1.03	0.50	1.10	1.65	3.24	1.91	0.59	1.19	2.89	4.57	1.65	0.60	1.65	0.60	1.65	0.60		
SrO	0.70	0.37	0.38	0.17	0.40	0.28	0.48	0.39	0.55	0.19	0.57	0.27	0.20	0.20	0.25	0.29	0.27	0.46	0.07	0.21	0.34	0.25	0.34	0.25	0.34	0.25		
BaO	0.02	0.21	0.00	0.00	0.00	0.00	0.00	0.00	0.00	0.00	0.00	0.00	0.06	0.20	0.06	0.27	0.08	0.26	0.16	0.68	0.06	0.21	0.06	0.21	0.06	0.21		
Total	53.95	0.62	55.62	1.37	54.51	0.86	56.43	1.13	52.53	0.82	54.35	0.89	50.91	1.29	53.74	2.67	49.16	3.35	52.72	4.96	51.53	2.20	51.53	2.20	51.53	2.20		
Atoms per 3 oxygens																												
Ca	0.902	0.021	0.503	0.014	0.925	0.028	0.521	0.056	0.867	0.012	0.890	0.047	0.817	0.131	0.454	0.035	0.779	0.094	0.538	0.140	0.371	0.017	0.371	0.017	0.371	0.017		
Mg	0.005	0.003	0.170	0.021	0.003	0.005	0.147	0.072	0.002	0.004	0.006	0.010	0.007	0.055	0.130	0.045	0.011	0.020	0.020	0.006	0.175	0.022	0.175	0.022	0.175	0.022		
Fe	0.016	0.005	0.267	0.021	0.010	0.007	0.268	0.058	0.018	0.006	0.028	0.022	0.019	0.065	0.269	0.046	0.019	0.101	0.257	0.090	0.282	0.033	0.282	0.033	0.282	0.033		
Mn	0.006	0.006	0.020	0.004	0.011	0.011	0.037	0.020	0.007	0.002	0.014	0.007	0.015	0.023	0.045	0.027	0.008	0.016	0.041	0.068	0.023	0.009	0.023	0.009	0.023	0.009		
Sr	0.007	0.004	0.004	0.002	0.004	0.003	0.005	0.004	0.005	0.002	0.005	0.003	0.002	0.002	0.002	0.003	0.002	0.004	0.001	0.002	0.003	0.002	0.003	0.002	0.003	0.002		
Ba	0.000	0.001	0.000	0.000	0.000	0.000	0.000	0.000	0.000	0.000	0.000	0.000	0.000	0.001	0.000	0.002	0.001	0.002	0.001	0.005	0.000	0.001	0.000	0.001	0.000	0.001		
Sample	T0262				T0282				T0167				U4904				T0178				U4909							
Rock type	C2		C2		C2		C2		C3		C3		C3		C4		C4		C4		C4		C4					
Mineral	Cal		Ank		Cal		Ank		Cal		Ank		Cal		Ank		Cal		Ank		Cal		Ank					
n=	16		3		21		9		36		48		14		27		11		13		13		13					
	Avg	2SD	Avg	2SD	Avg	2SD	Avg	2SD	Avg	2SD	Avg	2SD	Avg	2SD	Avg	2SD	Avg	2SD	Avg	2SD	Avg	2SD	Avg	2SD				
Wt. % oxide																												
CaO	52.83	1.80	37.78	4.17	42.37	6.24	30.91	4.75	48.30	7.53	34.84	2.47	52.38	3.07	27.98	6.68	51.89	3.25	32.44	4.73	32.44	4.73	32.44	4.73				
MgO	0.22	0.33	0.51	0.27	0.32	0.25	0.41	0.13	0.35	0.38	0.45	0.20	0.86	2.68	2.86	0.92	1.37	3.51	4.00	0.88	4.00	0.88	4.00	0.88				
FeO	0.10	0.27	19.39	7.05	2.74	8.04	18.88	5.40	1.99	8.19	17.27	2.44	0.58	1.22	18.47	4.77	0.24	0.50	19.79	5.22	19.79	5.22	19.79	5.22				
MnO	1.00	1.27	1.01	0.56	0.59	1.22	1.80	2.37	0.34	1.64	3.43	1.45	0.33	0.23	3.42	3.84	0.54	0.73	4.48	1.76	4.48	1.76	4.48	1.76				
SrO	0.26	0.13	0.17	0.07	0.12	0.14	-0.05	0.20	0.16	0.24	0.05	0.17	0.56	0.41	0.46	0.44	0.50	0.49	0.48	0.45	0.48	0.45	0.48	0.45				
BaO	0.00	0.00	0.00	0.00	0.10	0.22	0.08	0.31	0.09	0.29	0.15	0.33	0.00	0.00	0.21	0.60	0.00	0.00	0.01	0.06	0.01	0.06	0.01	0.06				
Total	54.41	0.62	58.87	3.33	46.23	3.10	52.03	2.58	51.22	3.63	56.19	2.25	54.71	1.39	53.39	6.30	54.55	0.49	61.21	2.28	61.21	2.28	61.21	2.28				
Atoms per 3 oxygens																												
Ca	0.929	0.035	0.710	0.051	0.695	0.086	0.545	0.074	0.826	0.114	0.639	0.049	0.923	0.052	0.500	0.133	0.912	0.064	0.622	0.075	0.622	0.075	0.622	0.075				
Mg	0.005	0.008	0.013	0.007	0.007	0.006	0.010	0.003	0.008	0.009	0.012	0.005	0.021	0.066	0.071	0.020	0.033	0.085	0.107	0.025	0.107	0.025	0.107	0.025				
Fe	0.001	0.004	0.285	0.116	0.036	0.108	0.260	0.081	0.028	0.115	0.247	0.039	0.008	0.017	0.258	0.077	0.003	0.007	0.297	0.084	0.297	0.084	0.297	0.084				
Mn	0.014	0.018	0.015	0.009	0.008	0.016	0.025	0.034	0.005	0.023	0.050	0.021	0.005	0.003	0.049	0.057	0.007	0.010	0.068	0.028	0.068	0.028	0.068	0.028				
Sr	0.003	0.001	0.002	0.001	0.001	0.001	0.000	0.002	0.001	0.002	0.000	0.002	0.005	0.004	0.004	0.004	0.005	0.005	0.005	0.005	0.005	0.005	0.005	0.005				
Ba	0.000	0.000	0.000	0.000	0.001	0.001	0.001	0.002	0.001	0.002	0.001	0.002	0.000	0.000	0.001	0.004	0.000	0.000	0.000	0.000	0.000	0.000	0.000	0.000				

Table 4.5: Composition of carbonates from different generations of Songwe carbonatite, analysed by EPMA.

prominent data cluster due to a higher Fe concentration. Many analyses from C3 Fe-carbonatite are Fe- and Ca-rich. This composition does not represent a stable carbonate composition at temperatures which are reasonable for a carbonatite (Anovitz and Essene, 1987) and it is interpreted to represent a mixture of calcite and exsolved Fe-oxides, as indicated by the complex exsolution textures seen in thin section (Fig. 4.8 B). The interpretation is clearly shown in on binary plots of CaO against FeO+MnO and MgO against FeO+MnO (Fig. 4.13). These diagrams show the high CaO and low MgO concentration of the mixed calcite and Fe-oxides. Furthermore, a qualitative XRD²⁰ trace on a bulk-powder analysis of T0167 indicates that the main peaks are calcite, and goethite, despite the sample displaying many characteristics of an Fe-bearing carbonatite (Fig. 4.14).

There is little difference in the concentration of other analytes, such as SrO and BaO, between the different carbonates. The only exception to this is the SrO concentration of the mixed calcite and Fe-oxides, which are typically lower.

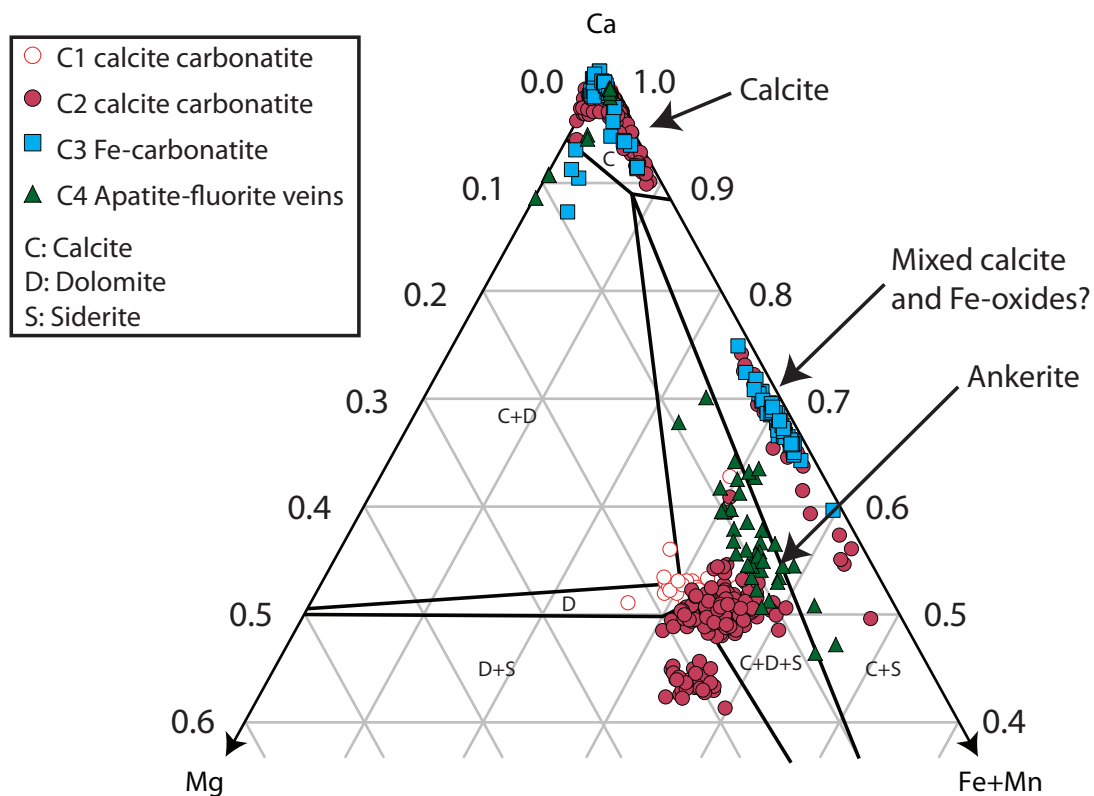


Figure 4.12: Ternary plot of carbonate compositions. Data plotted as atoms per formula unit (to 3 oxygens). The sub-solidus carbonate phase relations at 550 °C after Anovitz and Essene (1987) are also shown, indicating the lack of pure ankerite stability.

²⁰X-ray diffraction

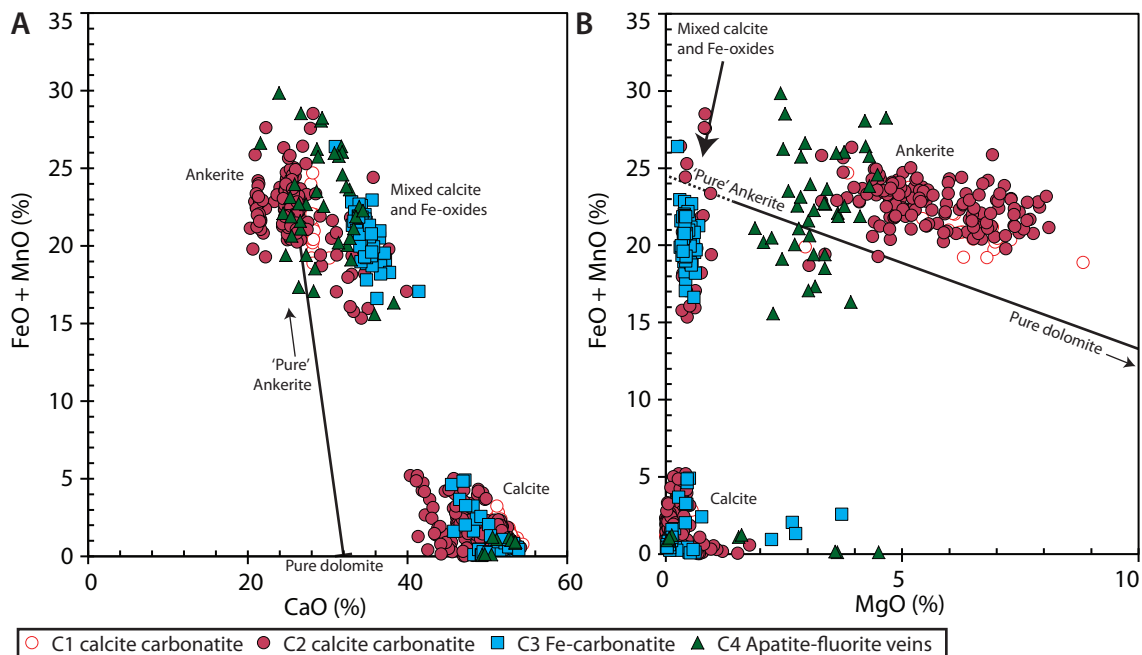


Figure 4.13: Major element compositions of Songwe carbonates from EPMA data. Solid-solution compositions between pure dolomite–ankerite are plotted for reference. ‘Pure’ ankerite (i.e. $\text{CaFe}(\text{CO}_3)_2$) is not stable in nature and is therefore indicated with a dashed line.

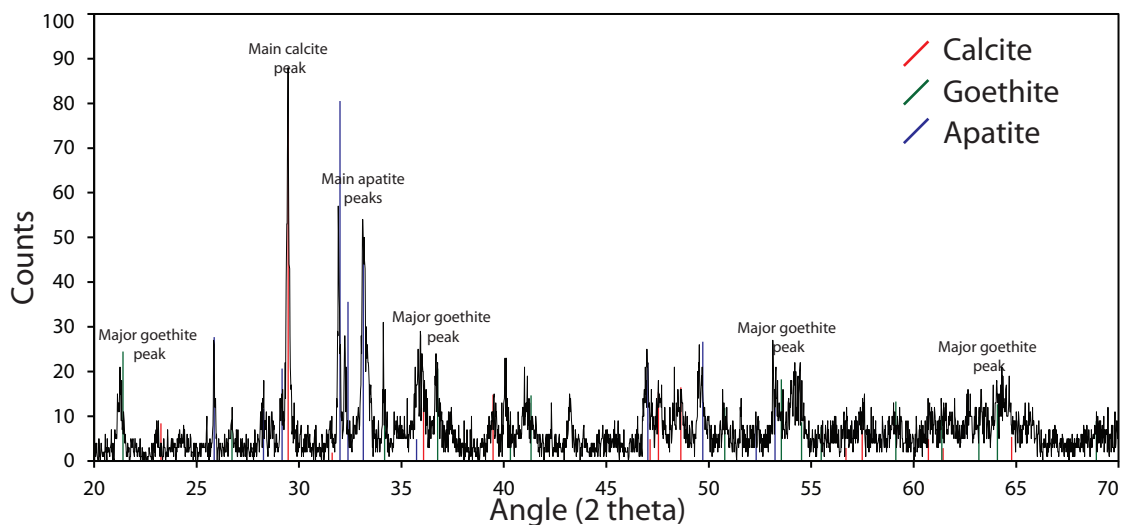


Figure 4.14: Qualitative XRD trace of a powder from Fe-carbonatite sample T0167 showing major peaks for calcite, apatite and goethite.

4.3.3 Whole-rock data — Mauze

Major and trace-element data of the four Mauze samples are shown in Table 4.6. Also included, because of the lack of available data, are the four previously published major-element analyses of Dixey et al. (1955), for comparison. Weight % oxide data for Sr, Ba, Zr, Cl and F has been converted to trace element concentrations and Fe_2O_3 data from the new dataset are converted to FeO_t to facilitate comparison of data between the two sets of results.

Texturally, the samples can be broadly subdivided into three groups: equigranular, pegmatoidal and dyke-rocks. SiO_2 concentrations range between 52–57 wt. %, with the pegmatoidal samples typically having the highest SiO_2 concentrations. Most elements are present in similar concentration in all samples, with the exception of U4913 which has distinctly higher K_2O and lower Na_2O (13.85 and 2.24 wt. %, respectively, compared with 4.8–7.35 and 8.21–10.73 wt. %). The low P_2O_5 concentrations are notable, they average 0.037 wt. %, compared with 0.149 wt. % for nepheline syenites from intrusions in the northern CAP (Woolley and Jones, 1987).

Classification of Mauze

Sensu lato, Mauze is classified as a hypersolvus-nepheline syenite (foyaite) because of the presence of nepheline and perthitic alkali feldspar (Mitchell, 1996). All of the rocks analysed are peraluminous (i.e. Al_2O_3 is greater than the sum of CaO, Na_2O and K_2O). Furthermore, the early, equigranular rocks are more potassic (especially U4913) than the later, pegmatoidal rocks, which have higher concentrations of sodium.

Trends in the Mauze whole-rock data

Both MgO and SiO_2 are suitable indices of fractionation in the Mauze whole-rock data. Elements which positively correlate with MgO negatively correlate with SiO_2 . CaO, TiO_2 and P_2O_5 negatively correlate with SiO_2 , while K_2O negatively correlates and Na_2O positively correlates with SiO_2 if the high K_2O sample (U4913) is excluded (Fig. 4.15). Zr and SiO_2 also show a broadly positive correlation in all samples. Interestingly, P_2O_5 , CaO and TiO_2 values are lowest, while Zr and Na_2O are relatively high, in the late pegmatoidal vein samples (U4914 and F01).

Although there is a limited amount of trace element data, there appears to be no correlation between indices of fractionation and the REE. Pegmatoidal vein samples typically have lower REE concentrations than the equigranular samples.

Symbol (wt. %)	Nepheline-syenites				□ N1121 ²	◇ N1122a ²	Dykes	
	■ U4913	● U4914 ¹	● F01 ¹	■ F03			◇ N1122b ²	◇ N1122c ²
SiO ₂	56.66	56.98	56.84	53.57	54.37	56.83	55.3	52.78
TiO ₂	0.42	0.19	0.12	0.59	0.77	0.12	0.61	1.01
Al ₂ O ₃	20.12	16.91	18.71	20.67	23.22	20.78	20.56	20.55
Fe ₂ O ₃	3.07	6.88	5.41	3.87	1.62	3.57	3.56	4.39
FeO					0.32	0.41	1.9	1.06
FeO _t	2.76	6.19	4.86	3.48	0.64	1.12	2.61	1.93
MnO	0.12	0.23	0.21	0.29	0.07	0.4	0.11	0.19
MgO	0.13	0.03	0.04	0.44	0.57	0.02	0.45	0.43
CaO	0.57	0.53	0.76	2.37	1.6	0.65	1.01	1.48
Na ₂ O	2.24	9.5	9.42	8.21	8.25	10.73	8.32	8.26
K ₂ O	13.85	4.8	5.39	6.97	7.35	4.72	6.99	7.14
P ₂ O ₅	0.02	-	-	0.02	0.08	0.001	0.09	0.09
SO ₃	0.07	0.07	0.05	0.07	0	0.1	0.1	0.03
LOI (105 °C)	0.2	0.27	0.19	0.2	0.5	0.32	0.12	1.21
LOI (1000 °C)	0.75	0.84	0.59	0.53	0.28	0.57	0.26	1.77
(ppm)								
F					-	-	-	1000
Cl					700	400	200	1500
Ba	3396	342	161	4182	1075	179	717	1433
Cr	-	-	-	-	-	-	-	-
Ga	23	38.8	31.6	23	-	-	-	-
Hf	12.1	46.8	45.3	6.7	-	-	-	-
Nb	144.2	333.8	76.4	121.4	-	-	-	-
Rb	582	167.8	228.7	155	-	-	-	-
Sr	1701.6	214.8	186.7	914.8	-	592	-	-
Ta	4.6	13.6	3.9	7.6	-	-	-	-
Th	10.2	16.9	3.3	6.3	-	-	-	-
U	2.4	20	1.6	1.2	-	-	-	-
Zr	691	1646	1386	266	74	2961	1110	222
La	40.5	55.6	19.9	62.3	-	-	-	-
Ce	59.6	78.3	25	110.2	-	-	-	-
Pr	5.8	6.9	2.4	11.4	-	-	-	-
Nd	18.7	18.3	6.6	34.8	-	-	-	-
Sm	2.7	2.2	0.7	4.5	-	-	-	-
Eu	0.9	0.6	0.3	1.2	-	-	-	-
Gd	2.07	1.36	0.4	3.09	-	-	-	-
Tb	0.5	0.4	0.1	0.6	-	-	-	-
Dy	2.6	2.2	0.7	3.2	-	-	-	-
Ho	0.7	0.7	0.3	0.8	-	-	-	-
Er	2	2.3	1	2.1	-	-	-	-
Tm	0.4	0.5	0.3	0.3	-	-	-	-
Yb	2.4	4	2.5	2.6	-	-	-	-
Lu	0.3	0.7	0.5	0.5	-	-	-	-
Y	17	17.5	7.9	17.3	-	-	-	-
Subtotal	98.59	96.84	97.40	98.01	99.83	100.75	102.19	102.74
O ≡ Cl, F, S	0.01	0.01	0.01	0.01	0.02	0.03	0.02	0.08
Total	98.57	96.83	97.39	97.99	99.81	100.73	102.17	102.66

¹ Coarse-grained unidirectional solidification texture samples.

² Data from Dixey et al. (1955)

Table 4.6: Whole-rock data from Mauze nepheline syenites and dyke rocks. Analyses denoted with a hyphen (-) were below detection, blank cells represent elements not analysed. The symbol represents the icon assigned to this sample in Figures 4.15 and 4.16.

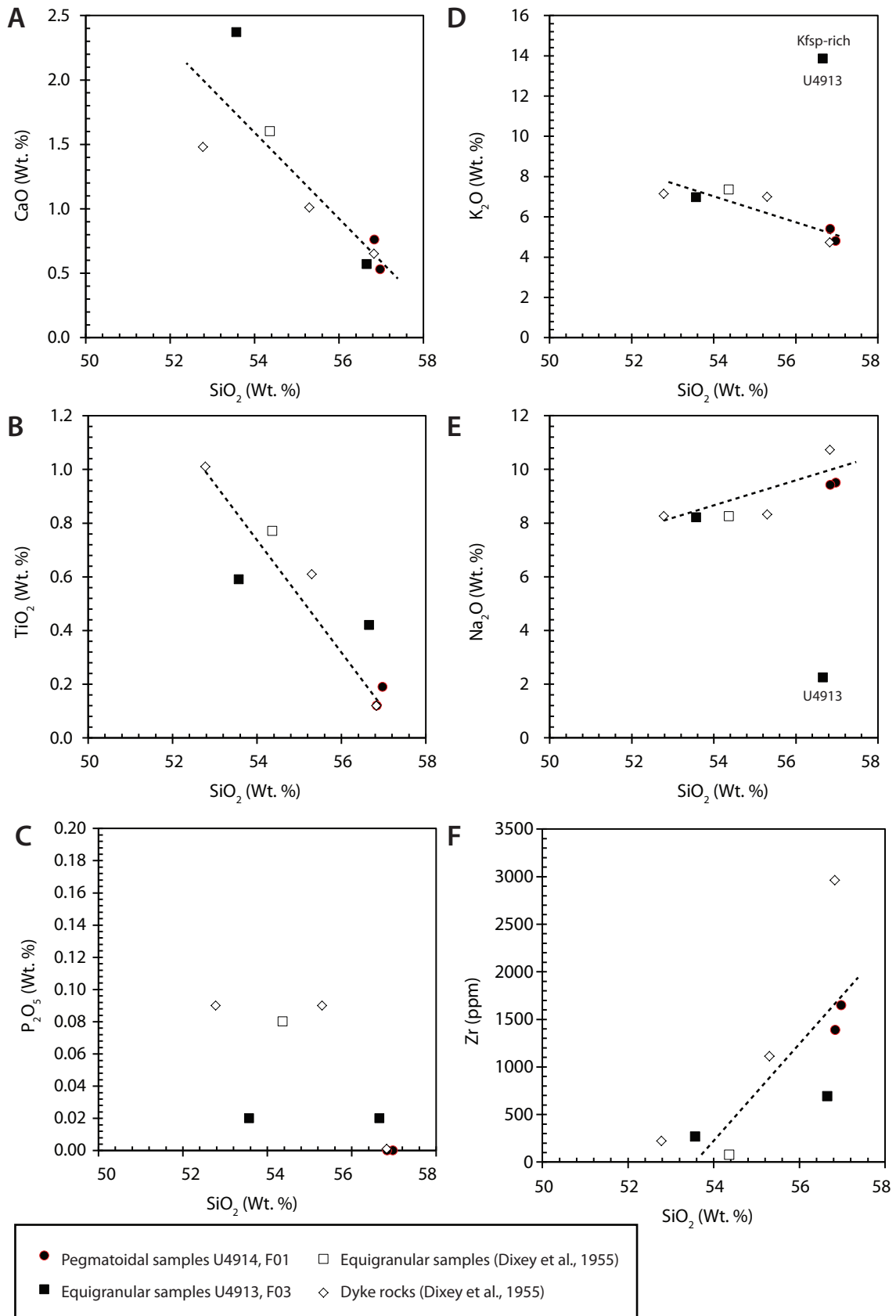


Figure 4.15: Major element concentrations against SiO₂, where SiO₂ is an index of fractionation. Filled symbols represent data from this study, hollow symbols from Dixey et al. (1955). Dashed lines are possible fractionation trends.

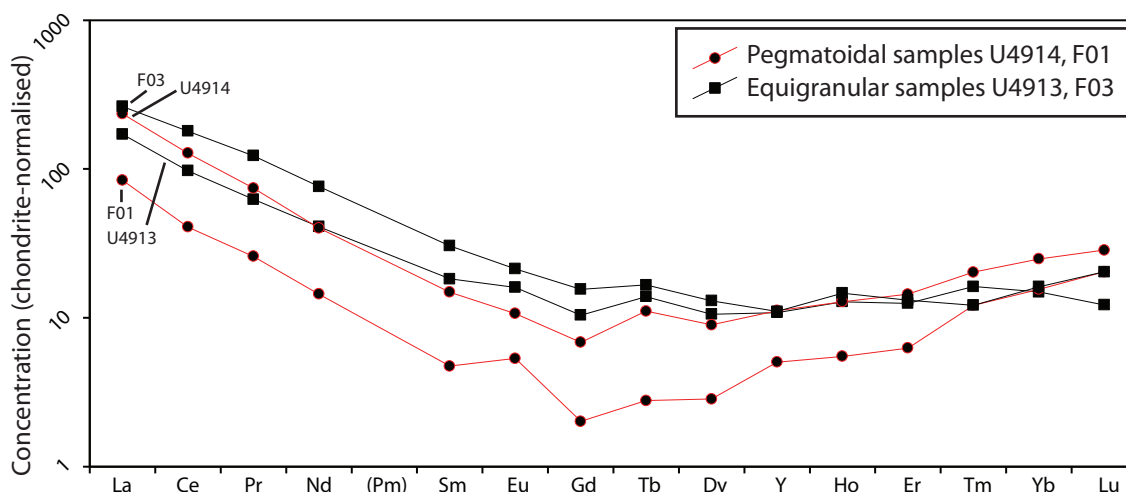


Figure 4.16: Chondrite-normalised REE distribution of samples from Mauze. Chondrite values from McDonough and Sun (1995).

Rare earth distribution

Chondrite-normalised REE plots of all samples display LREE-enrichment, but the HREE patterns of the two sub-groups differ slightly (Fig. 4.16). Equigranular samples display relatively flat MREE and HREE patterns, with little variation in the chondrite-normalised values, while the pegmatoidal samples are more depleted in MREE values, relative to the equigranular samples, but have slightly enriched in HREE values. Samples F03 and U4914 display a slight positive Eu anomaly, possibly related to accumulation of feldspar.

4.3.4 Whole rock data — Songwe drillcore

Simple univariate statistics for major and trace-elements determined in fenite, calcite-carbonatite, Fe-bearing carbonatite and Mn-Fe veins from drillcore samples are presented in Table 4.7. A full dataset of the analyses used is available in appendix D.1. Carbonatite and Mn-Fe- vein data are presented with Al_2O_3 values greater than 2 % removed (see Section 4.2.2 and Fig. 4.3).

Due to the occurrence of Nb, Sr and the LREE in major/minor minerals, these elements are recalculated as wt. % oxide to provide a more representative total. Nevertheless, the totals for these analyses are typically less than 98 %, averaging 97 %, after calculating equivalent O for S. This probably reflects the absence of F, Na and Ba from the elements analysed. Fluorite, REE-fluorcarbonates and fluorapatite are present in almost all samples from Songwe and barite is common in late-stage carbonatites.

The missing contribution from F can be partially re-calculated by assuming that all P_2O_5 is hosted in fluorapatite. Therefore, for every 1 wt. % P_2O_5 , 0.0516 % F is present in the sample. This includes a correction for O by difference. Such an addition of F has little effect on the totals, adding an average of only 0.14 %.

This does not, however, account for additional fluorine from fluorite and REE-fluorocarbonates which is more difficult to calculate. No major or minor minerals in the carbonatite, except orthoclase in fenite clasts, contain abundant Na₂O and typical carbonatites average only 0.26–0.39 wt. % (calciocarbonatite–ferrocarbonatite, respectively; Woolley and Kempe, 1989). Therefore, the missing Na data are expected to only contribute a small amount to the reduced total values. BaO could contribute a significant proportion of the missing total as it can range between 0.34–3.25 wt. % (calciocarbonatite–ferrocarbonatite, respectively; Woolley and Kempe, 1989). However, it is difficult to back-calculate and therefore BaO is probably a major cause of the low totals in the analyses. In the Fe-carbonatite and the Mn-Fe- veins, most of the Fe-bearing minerals are goethite. In these rocks recalculating ferrous for ferric iron significantly increases the totals for these rocks, from 95.4 to 97.8 %.

Sample Symbol (Wt. %)	Fenite			Calcite-carbonatite			Fe-rich carbonatite			Mn-Fe- veins		
	Avg.	2SD	n=	Avg.	2SD	n=	Avg.	2SD	n=	Avg.	2SD	n=
SiO ₂	29.92	24.43	421	1.53	2.61	145	1.03	1.61	30	1.98	3.06	34
TiO ₂	0.66	0.81	421	0.19	0.31	145	0.15	0.18	30	0.17	0.34	34
Al ₂ O ₃	10.89	8.80	421	0.70	0.87	145	0.73	0.60	30	0.98	0.93	34
FeO	11.20	12.89	421	10.81	9.04	145	15.58	7.34	30	22.95	17.57	34
MnO	1.48	1.43	421	1.93	1.47	145	3.35	1.15	30	4.69	5.64	34
MgO	1.51	2.06	421	1.96	2.75	145	2.73	3.00	30	0.39	0.44	34
CaO	14.69	16.38	421	37.15	13.88	145	31.10	9.25	30	30.52	16.09	34
Na ₂ O												
K ₂ O	6.65	5.35	421	0.43	0.60	145	0.19	0.34	30	0.38	0.62	34
P ₂ O ₅	1.19	2.27	421	2.43	4.98	145	3.85	2.55	30	2.95	4.95	34
SrO	0.75	1.36	421	2.07	1.88	145	2.78	2.18	30	0.55	0.87	34
Nb ₂ O ₅	0.14	0.15	421	0.19	0.40	145	0.21	0.23	30	0.13	0.27	34
LOI (1000 °C)	15.49	13.82	421	34.87	6.80	145	28.73	6.03	30	25.28	9.95	34
Total ¹	94.99	5.46	421	94.85	5.49	145	91.21	5.12	30	91.09	7.01	34
ppm												
Ba												
Be	13.0	32.1	421	2.7	5.5	145	4.1	4.6	30	4.4	7.5	34
Cr	5.5	35.2	421	0.7	12.2	145	5.6	34.4	30	3.6	29.6	34
Ga	5.8	14.0	421	11.5	7.6	145	0.3	2.9	30	9.3	13.8	34
Hf	5.8	14.0	421	0.8	1.5	145	2.0	2.8	30	1.7	4.1	34
Li	8.5	12.8	421	3.4	5.1	145	5.4	4.8	30	4.2	8.3	34
Sc	0.2	3.7	421	2.0	14.8	145	19.7	27.8	30	13.9	32.5	34
Sn	6.5	6.0	421	2.7	5.3	145	3.9	2.3	30	2.6	4.5	34
Ta	19.4	24.7	421	1.3	2.1	145	0.8	1.0	30	1.4	3.2	34
Th	272.3	237.7	421	283.0	263.9	145	367.2	185.4	30	421.5	418.5	34
U	18.7	23.9	421	11.0	15.5	145	7.7	15.3	30	11.3	22.2	34
V	113.8	142.5	421	136.2	148.7	145	143.2	61.6	30	203.1	399.8	34
W	13.9	16.4	421	8.6	12.9	145	15.1	13.3	30	9.1	13.9	34
Zr	361.1	958.7	421	37.3	75.0	145	101.1	143.4	30	87.8	205.7	34
La	1616	2547	421	3489	4500	145	9223	7380	30	5324	8747	34
Ce	2817	3967	421	6714	6362	145	13439	8288	30	9073	11717	34
Pr	291	373	421	719	553	145	1358	661	30	941	1105	34
Nd	966	1133	421	2429	1585	145	4108	1664	30	2948	3049	34
Sm	147	143	421	342	212	145	479	161	30	378	320	34
Eu	43.7	40.1	421	94.8	64.4	145	119.4	39.4	30	100.4	89.2	34
Gd	109	100	421	223	139	145	279	93	30	244	236	34
Tb	13.6	13.1	421	28.8	19.5	145	34.0	12.3	30	31.1	34.5	34
Dy	62	67	421	137	93	145	153	62	30	146	173	34
Ho	9.9	12.2	421	24.3	19.4	145	23.9	11.6	30	23.5	27.8	34
Er	23	31	421	57	49	145	54	31	30	54	61	34
Tm	2.8	4.1	421	7.3	6.7	145	6.6	4.1	30	6.7	7.6	34
Yb	17	25	421	41	38	145	35	22	30	38	41	34
Lu	2.2	3.1	421	5.2	4.5	145	4.5	2.9	30	5.0	5.3	34
Y	245	320	421	605	527	145	591	328	30	589	697	34
Total ²	96.44	5.30	421	96.63	4.85	145	97.11	4.59	30	93.94	5.28	34

Table 4.7: Summary of the Mkango drillcore data, sorted into fenite, calcite-carbonatite, Fe-rich carbonatite and Mn-Fe- veins. Carbonatite data with more than 2 % Al₂O₃ are considered to be contaminated with fenite and are not presented. Total¹ refers to totals of major element data only, while Total² includes light rare earth oxides (La–Nd) and trace elements, including the remainder of the REE. Full dataset presented in appendix D.1.

Fenite

Despite the absence of Na₂O data from the analyses, the fenite data have totals close to 100 %, reflecting the K-feldspar-rich nature of these samples. Average LOI values are 15.5 % suggesting mixing with carbonatite is common in most samples. SrO, MgO, S, CaO and the REE correlate positively with LOI, while SiO₂ and Al₂O₃ and K₂O correlate negatively with the LOI concentration, reflecting the association of these elements with carbonatite.

The abundance of carbonatite in most fenite analyses makes it difficult to deduce the concentration of trace elements of interest. Given the dominance even small amounts of carbonatite have on the TREO²¹ concentration, the TREO content of fenite is likely to be very low. However, because of the large carbonatite component to fenite, it is included in the deposit model at Songwe as it includes an average of 1 % TREO (Croll et al., 2014).

Songwe carbonatite intrusion

Average concentrations for most major elements are similar for both calcite-carbonatite and Fe-rich carbonatite, reflecting subtle mixing between these two carbonatite types which is hard to discriminate. CaO, FeO, MnO and MgO concentrations respectively average 37.2, 10.8, 1.9 and 2.0 wt. % oxide for calcite carbonatite, and 31.1, 15.6, 3.4 and 2.7 wt. % oxide for Fe-rich carbonatite. Average P₂O₅, SrO, Th and REE concentrations are slightly higher in Fe-rich carbonatite than calcite-carbonatite.

Mn-Fe- veins

Mn-Fe- veins have much higher average FeO and MnO concentrations than both carbonatite types, with approximately 23.0 and 4.7 wt. % oxide respectively. CaO concentrations are similar to the carbonatites, but MgO and SrO are much lower, averaging 0.4 and 0.6 wt. % oxide, respectively. The average LOI for the Mn-Fe-veins is also lower than for carbonatites, averaging 25.3 wt. %.

Apatite-fluorite veins

Data from apatite-fluorite veins are presented in Table 4.8. Analyses were available from both drillcore and grab samples. All analyses have low totals because not all significant elements were analysed and should therefore be interpreted with caution. A charge-balance calculation to calculate the missing CO₂ and F, and therefore evaluate the data quality, is not possible due to the variable ratio

²¹Total Rare Earth Oxide

Location Drill hole Sample #	PX016 E1120	PX016 E1122	PX016 E1123	PX016 E1124	PX016 E1125	PX016 E1126	PX016 E1127	PX016 E1128	PX016 E1130	PX016 E1131	PX016 E1132	PX016 E1133	PX016 E1134	PX016 E1135	PX016 E1137	PX016 E1138	PX016 E1139	PX016 E1140	PX016 E1142	PX016 E1143	PX016 E1144	Chenga T0178	Chenga T0134
SiO ₂	0.64	0.64	0.86	1.28	2.99	38.08	2.99	5.99	0.86	1.28	0.43	0.86	0.43	0.64	0.86	0.86	2.14	0.43	1.71	1.50	1.93	22.68	47.70
TiO ₂	-	0.08	0.17	0.35	0.47	0.63	0.45	0.45	0.63	0.30	0.43	0.53	0.48	0.72	0.68	0.62	0.53	0.32	0.47	0.08	-	0.82	1.63
Al ₂ O ₃	1.34	0.91	1.08	1.51	2.15	11.68	1.57	2.32	1.00	1.32	0.94	0.98	0.76	0.81	0.98	1.42	1.30	1.10	2.36	1.81	3.48	4.29	14.19
FeO	11.93	13.34	15.49	16.57	24.06	10.06	22.33	18.71	24.01	14.38	13.80	22.59	23.26	23.63	18.22	16.39	16.29	13.34	13.64	12.58	14.22	7.35	8.71
MnO	2.71	2.32	2.45	2.32	3.10	1.16	1.94	2.07	2.84	2.20	2.32	2.84	2.97	2.71	2.45	2.97	2.71	2.58	2.84	2.84	2.97	1.29	1.03
MgO	3.83	3.75	4.46	3.93	3.47	1.49	3.03	2.98	4.94	3.78	3.81	4.28	4.81	4.86	4.41	4.26	4.16	4.81	4.69	4.10	4.13	1.13	0.17
CaO	34.98	32.74	33.72	28.96	23.37	10.35	26.03	26.58	27.70	26.44	31.76	25.05	21.97	24.21	26.72	28.12	28.12	31.62	30.50	33.16	28.54	28.40	3.64
K ₂ O	0.22	0.24	0.13	0.23	0.61	8.72	0.71	1.25	0.14	0.33	0.22	0.23	0.13	0.12	-	0.16	0.51	0.14	0.36	0.40	0.40	2.75	9.20
P ₂ O ₅	8.52	10.72	10.11	7.08	1.99	1.95	7.72	5.94	6.37	6.94	9.85	5.13	3.02	4.03	7.01	6.58	6.67	9.60	6.46	7.29	5.48	9.17	3.05
S	0.38	0.93	0.69	0.77	0.79	0.44	0.79	0.61	1.85	0.83	0.63	0.83	1.2	0.96	0.62	0.79	0.66	0.58	0.48	0.53	0.54	0.13	-
Total	64.55	65.68	69.15	63.01	63.00	84.57	67.57	66.90	70.35	57.81	64.21	63.32	59.03	62.69	61.96	62.16	63.10	64.52	63.52	64.29	61.67	77.99	89.33
Ga	-	-	-	-	-	15	-	-	-	-	-	-	-	-	-	-	-	-	-	-	-	10	38
Hf	6.1	3.6	5.1	5.2	2.3	1.6	3.4	3.3	5	5.5	3.5	6.5	3.4	5	3.5	2.9	3.8	3	4.3	3.2	2.5	24	15.1
Nb	301	746	1474	1046	1668	964	3799	3239	2445	1353	1568	757	869	2437	1608	1513	2277	1070	572	369	281	602	518
Sr	5904	5739	7138	7912	7969	4573	5183	6688	5705	5642	6266	4747	4559	4051	5178	6339	4902	6615	7184	7154	13313	5712	1582
Th	315	484.6	332.5	367.3	296.6	265	331.3	327.5	305.2	266.3	585.3	315.1	306	246	254.6	442.1	359.5	430.2	393.1	422.4	535	381.7	347.2
U	6.4	11.3	12.1	14.5	11.5	16.8	13.4	11.2	10	10.3	12.6	5.5	6.9	12	9.9	10.1	12.7	13.5	4.5	4.1	4.1	27.8	11.4
Zr	266	206	263	296	169	105	212	193	254	263	201	314	179	244	190	174	231	191	264	204	157	1293	819
La	3883	3313	3415	3083	1856	761	2636	2582	2438	2532	3087	2416	4229	2875	2685	4020	3405	2968	3442	3460	4822	856	1284
Ce	8174	7090	7411	6768	3918	1776	5797	5534	5274	5457	6765	5119	7965	5698	5757	8291	6930	6327	7225	7271	9667	1275	1925
Pr	977	812	860	792	450	221	675	632	610	623	803	583	799	602	652	969	788	717	865	831	1147	123	190
Nd	3358	3076	3215	3007	1697	881	2541	2398	2277	2308	3125	2144	2520	2086	2375	3244	2727	2735	2922	3085	3839	416	621
Sm	461	481	498	459	268	168	390	370	327	346	531	314	282	264	347	457	391	431	414	434	528	101	100
Eu	131	145	148	134	73	53	116	113	94	102	162	89	71	72	101	132	113	128	118	122	146	55	37
Gd	315	367	362	317	164	133	284	276	228	252	402	215	161	170	245	316	272	331	274	295	349	252	128
Tb	42.7	53.1	51.2	42.8	18.8	17.6	39.5	39.1	31.7	36.0	57.9	28.8	20.6	22.3	35.1	43.3	38.2	49.2	38.1	41.2	47.8	79.3	26.3
Dy	230	297	278	226	88	89	216	210	175	196	322	165	108	122	191	239	217	294	216	234	264	557	153
Ho	40.9	53.4	49.9	39.6	14.9	15.3	38.7	36.7	32.9	36.0	58.5	30.3	20.1	22.5	34.3	43.9	39.7	54.6	40.2	43.7	49.1	104.4	27.5
Er	118	158	143	115	43	44	117	110	102	109	172	90	61	65	95	124	114	155	118	129	140	258	66
Tm	16.5	22.2	19.2	15.6	6.1	6.0	16.5	15.1	14.4	15.2	22.2	12.0	8.0	8.4	11.9	15.9	14.3	18.7	15.2	16.5	18.2	30.9	8.0
Yb	96	128	110	90	37	35	95	87	82	88	124	69	46	46	64	84	77	98	83	92	103	173	45
Lu	12.7	16.7	14.1	11.4	5.0	4.8	12.5	11.2	10.5	11.4	15.5	8.6	6.0	6.0	8.0	10.4	9.6	11.9	10.3	11.9	13.0	21.3	5.5
Y	1096	1531	1410	1050	390	420	1056	1033	908	995	1646	830	555	620	908	1257	1165	1591	1209	1299	1437	2959	736

All data represented in figures by this symbol: ▲

Table 4.8: Whole-rock major and trace element data from Apatite-fluorite veins (C4) found in drillcore and from Chenga Hill. Note the lack of LOI, Na, F and Ba data and, therefore, the low totals. Analyses denoted with a hyphen (-) were below detection of the analytical technique used, blank cells represent elements not analysed.

of calcite to fluorite. Similarly a comparison of normative mineralogy with modal mineralogy cannot be carried out for the same reasons.

It is evident, from the elevated levels of SiO_2 , Al_2O_3 , Ga, K_2O , TiO_2 and Zr, that the grab samples from Chenga Hill contain large volumes of entrained fenite. Despite being termed apatite-fluorite veins, these rocks are also rich in both CaO, MgO and FeO with ranges of 10–35, 1.1–4.9 and 7–24 wt. %, respectively. Given the low totals of these samples (which is assumed to be caused by the lack of LOI and F data; Table 4.8), these elements are most likely to be hosted in carbonates, although fluorite and apatite are likely to host some Ca. P_2O_5 concentrations range from 1.95–10.72 wt. %, reflecting the apatite-rich nature of these rocks. Unfortunately, no F data are available so it is not possible to comment on the fluorite content of these samples. TREO concentrations are similar to those of calcite-carbonatite, with an average value of approximately 17,000 ppm TREO. Y concentrations, however, are high relative to carbonatite, averaging 1135 ppm, approximately double the carbonatite average (Table 4.7).

4.3.5 Nomenclature and carbonatite classification for Songwe Hill

As the grain-size of the carbonatites is too small for mineral identification, the carbonatites have been divided, initially, on the basis of their appearance in the field. This is summarised in Table 4.9. EPMA analyses of the different carbonatites indicate that both generations contain calcite and ankerite, although the proportion of ankerite is greater in the Fe-rich carbonatite. In many samples, however, the presence of ankerite is assumed on the basis of the presence of calcite with exsolved Fe-oxides (e.g. Fig. 4.8 B). Analyses of these carbonates with a defocused electron beam on the EPMA gives similar results to that of an ankerite, but with notably lower MgO concentration (Fig. 4.13). Given that ankerite is assumed to be present in many samples, it was decided that the best means of classification for the carbonatites would be to use whole-rock geochemistry.

The IUGS²² classification of carbonatites, where minerals cannot be identified, is a ternary plot of CaO, MgO and $\text{FeO}_t + \text{MnO}$ wt. % oxides at respective anti-clockwise points from the top (Woolley and Kempe, 1989; Le Maitre, 2002). Subdivisions are made between carbonatites using fields for calciocarbonatite, magnesiocarbonatite and ferrocyanatite at 20 % CaO, and 50 % MgO concentration. Gittins and Harmer (1997) recommended re-plotting these data as molar proportions because on a wt. % oxide diagram the calciocarbonatite boundary requires a greater modal proportion of calcite on the Mg-side than the Fe-side. Additionally, the field of 'ferruginous-calciocarbonatite' is added, to emphasise

²²International Union of Geological Sciences

the calcitic nature of most ferrocarnatites. This diagram is considered to be a better representation of the carbonatite subdivisions but both are plotted in Figure 4.17 for comparison.

Group	Field ID	Drillcore identification	Geochemical name ¹	Mineralogical name ²	Other names	Symbol used
C1	Calcite-carbonatite	N/A	Calcio-carbonatite	Calcite-carbonatite	Sövite	●
C2	Calcite-carbonatite	Calcite-carbonatite	Calcio-carbonatite	Calcite-carbonatite	Alvikite	●
C3	Fe-rich carbonatite	Fe-rich carbonatite	Ferruginous calcio-carbonatite	Ankerite-carbonatite	Ferro-carbonatite	■
C4	Apatite-fluorite veins	'phonolite'	N/A	N/A	N/A	▲
N/A	Mn-Fe- veins	Mn-Fe- veins	N/A	Hematite-carbonatite/ Hematite-rock	Rødberg	▲

¹after Gittins and Harmer (1997)

²after Woolley and Kempe (1989)

Table 4.9: Nomenclature of the carbonatite types at Songwe Hill.

When plotted on a ternary plot the carbonatite types spread over the different boundaries (Fig. 4.17). Typically calcite-carbonatite spreads between the calcio-carbonatite and ferruginous calcio-carbonatite fields of Gittins and Harmer (1997). Fe-rich carbonatite forms a small cluster on the ferruginous calcio-carbonatite and ferro-carbonatite boundary while the Mn-Fe- veins form a continuum between calcite-carbonatite and ferro-carbonatite. The Mn-Fe- veins differ from the other carbonatites in having much lower MgO concentrations, typically not reaching above 1 %. Based on this diagram, calcite-carbonate is best defined as a calcio-carbonatite, Fe-rich carbonatite is a ferruginous calcite carbonatite, and the Mn-Fe- veins are difficult to classify.

4.3.6 Trends in the Songwe whole-rock data

The chemistry of the samples broadly follows the field identification scheme but there is a large degree of overlap between the analyses. This is probably a reflection of the heterogeneity of the carbonatite, rather than any petrological relationship between the different carbonatites. For instance, on a plot of CaO against MnO+FeO (Fig. 4.18 A), calcite-carbonatite spans a continuum of values along a line from high CaO and low MnO+FeO through to low CaO and moderate MnO+FeO. As CaO concentration decreases and MnO+FeO concentration increases, along this line, the proportion of samples logged as Fe-rich carbonatite increases. This carbonatite type clusters around 30 wt. % MnO+FeO and 20 wt. % CaO. Analyses of Mn-Fe- veins follow a distinctly different trend, plotting

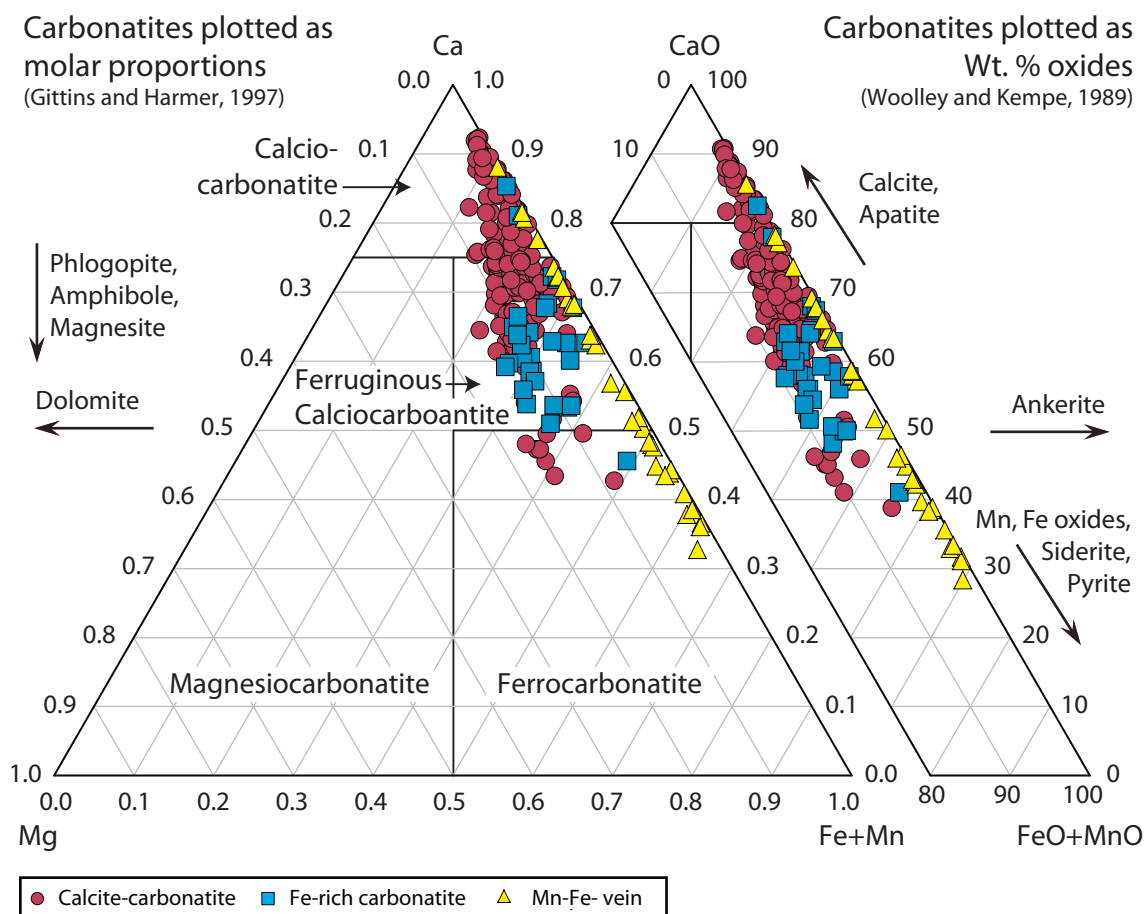


Figure 4.17: Songwe carbonatite ternary plot with data presented as molar proportions, after Gittins and Harmer (1997), and as wt. % oxides, after Woolley and Kempe (1989). Minerals which can effect the carbonatite composition on this diagram are illustrated.

on a straight line from high CaO concentrations through to very high MnO+FeO, reaching a maximum of approximately 50 wt. % (Fig. 4.18 A).

Divergence of Mn-Fe- veins from calcite-carbonatite and Fe-rich carbonatite is also observed on plots of MnO+FeO against MgO and SrO (Figures 4.18 B–C). In both cases, the Mn-Fe- veins have distinctly lower MgO and SrO than the calcite- and Fe-rich carbonatite, typically not reaching above 1 wt. % or 1.5 wt. %, respectively. The carbonatite analyses show a positive correlation between MnO+FeO against MgO and SrO (Figures 4.18 B–C). The correlation with MgO is most likely due to increasing proportions of ankerite/ferroan-dolomite in the more Fe-rich samples, while increasing SrO concentration is a common feature of more Fe-rich carbonatites (Le Bas, 1989).

Minerals controlling the FeO concentration in a carbonatite are varied, and can include ankerite, siderite, hematite, goethite, magnetite and pyrite. The role of these different Fe-phases can be evaluated on a plot of CO₂ against total Fe (Fig. 4.18 D). On this plot LOI is assumed to be directly proportional to CO₂ concentration, although this is not strictly correct as it will include other volatile phases such as H₂O. On Figure 4.18 D, mixing lines between 100 % calcite and various Fe-bearing phases have been plotted. It is clear that, for calcite-carbonatite and Fe-bearing carbonatite, the range in data is best explained by varying proportion of calcite and pyrite (or an alternative low LOI, moderate Fe phase). However, there is a large degree of scatter in the data along this line. This may be caused by various mechanisms, including varying proportions of calcite and ankerite, as indicated by the correlation between MgO and FeO (Fig. 4.18 B), or by a small variations in the proportion of pyrite and goethite, related to alteration. A large contribution from siderite can be excluded as this would result in a high FeO concentration whilst retaining a high LOI, a trend not shown in the data. Data from the Mn-Fe- veins plot above the calcite–pyrite mixing line, suggesting that these samples are combinations of carbonates and an Fe-rich phase, such as hematite or goethite. Breakdown of an Fe-bearing carbonate, such as ankerite, would result in a decrease in CO₂ (and consequently LOI), leaving an Fe-rich residuum.

REE concentrations in the carbonatites ranges from approximately 5000–60000 ppm TREO (Figure 4.18 E). As also shown in the JICA/ MMAJ data (Fig. 4.1 A), there is a general positive trend in the carbonatite samples of higher TREO concentrations with increasing FeO and MnO. Calcite carbonatite typically has TREO concentrations in the range of 5,000–25,000 ppm, while the Fe-rich carbonatite is usually between 25,000 and 60,000 ppm REE, with some overlap between the two groups. Mn-Fe- veins do not show any relationship between TREO and MnO+FeO values. TREO concentrations span the same range of values as samples from both calcite-carbonatite and Fe-rich carbonatite. As is common in REE-rich carbonatites, the SrO and REE contents are positively correlated

(Fig. 4.18 F). As for other analytes, there is a continuum between the calcite carbonatite and Fe-rich carbonatite. As in the JICA/MMAJ data (Fig. 4.1 E), there appear to be two trends in the SrO and REE data with the Mn-Fe- veins typically having low SrO contents that are not correlated with TREO.

4.3.7 Calcite-carbonatite at Songwe: sövite or alvikite?

Sövite and alvikite are commonly considered as textural terms for calcite-carbonatite, representing coarse-grained and fine-grained varieties, respectively (Woolley and Kempe, 1989). Based on these terms, calcite-carbonatite from Songwe is almost entirely alvikite, excluding the clasts of sövite found in breccias. Le Bas (1999) also distinguishes sövite and alvikite geochemically, with elevated Ba, Th, Pb, Nb, La, Ce, Nd and V concentrations in sövite, relative to alvikite. Furthermore, compared to bulk silicate earth (pyrolite; after McDonough and Sun, 1995) Sr, in alvikite, is anomalously negative, relative to sövite. Le Bas (1999) classes sövite and alvikite, when defined geochemically, as C1 and C2 carbonatites, respectively.

On a plot of median sövite and alvikite concentrations, normalised to pyrolite, values from Songwe are elevated compared to both the sövite and alvikite (Fig. 4.19). It is difficult, therefore, to use the criterion of elevated trace-element concentrations in sövite to classify these samples. However, a distinct depletion in Sr, relative to the REE, is evident, as well as a possible depletion in Nb, relative to La and Th. On these bases, and because of the fine grain-size of most carbonatite at Songwe, calcite-carbonatite is considered to be alvikite (C2 carbonatite).

4.3.8 Rare earth distribution of the Songwe carbonatite

Average chondrite normalised REE distributions of the different carbonatites types are shown in Figure 4.20. Plots of the average values with a standard deviation for each carbonatite type are shown in Figure 4.21. These plots show that all rock types found at Songwe are LREE enriched (Fig. 4.20), common to most carbonatites, but that the absolute concentration of the REE at Songwe is higher than the average carbonatite composition (Woolley and Kempe, 1989). Comparison of average values of the Fe-rich carbonatites and the calcite-carbonatites shows that the Fe-rich carbonatites are slightly more enriched in the LREE than the calcite-carbonatites, as is reflected in Figure 4.20 and as is common to most carbonatites. There is some spread in HREE contents as indicated by the increased standard deviations on the average values, especially in the Mn-Fe veins, suggesting that some fractionation of the HREE may be taking place (Fig. 4.21). This is most clearly illustrated by the higher HREE values of the apatite-fluorite veins, which display a prominent bulge, relative to the other carbonatites. Fe-rich car-

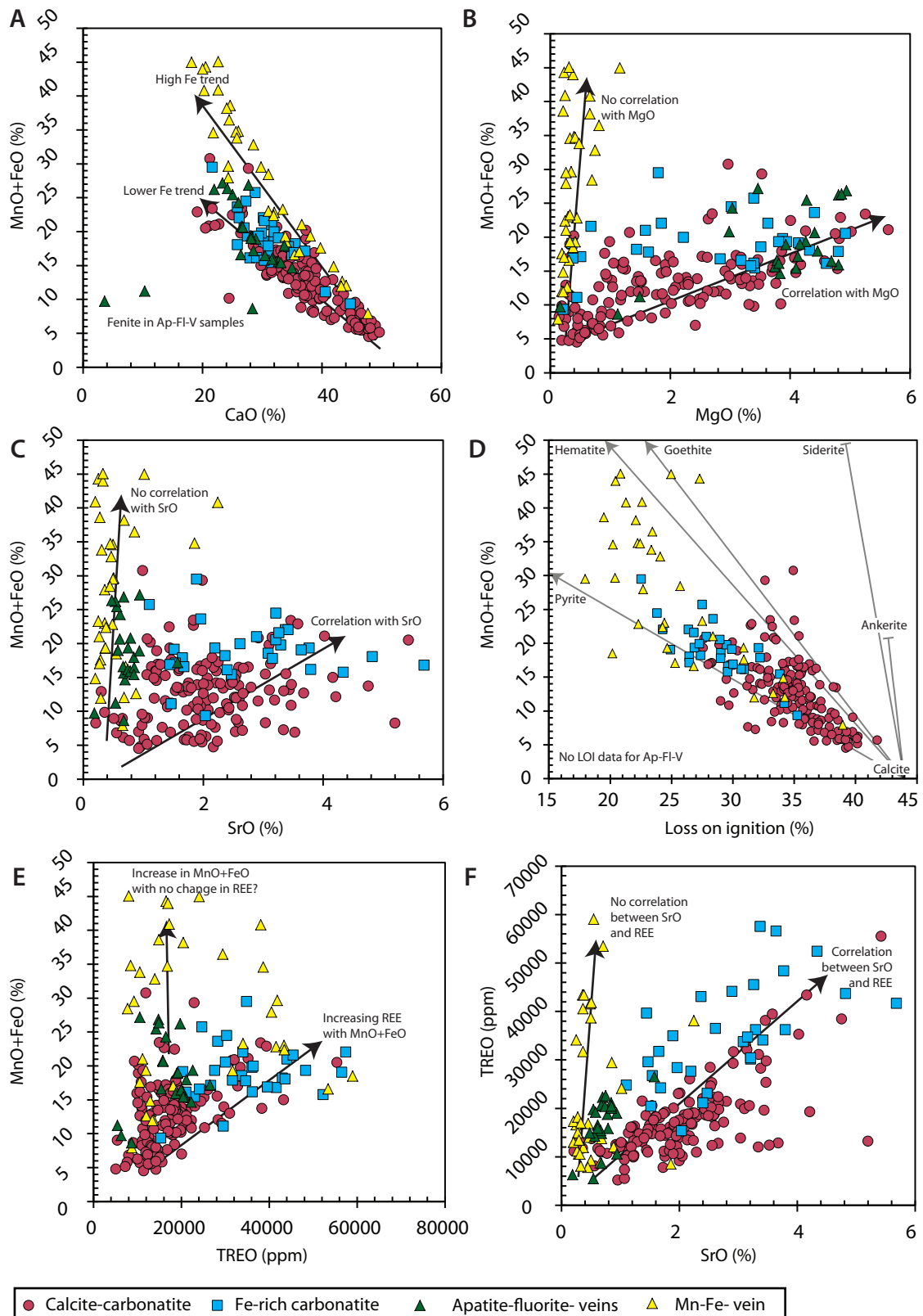


Figure 4.18: Binary plots of whole-rock data from carbonatite, Mn-Fe-veins and apatite-fluorite veins from Songwe. (D) LOI represents a close approximation of CO_2 . Grey lines in equate to mixing lines between pure calcite (bottom-right) and various Fe-phases indicated on the graph. These are simple plots of binary mixing and are not intended to be wholly representative of the composition of the samples. Lines in all other figures are to indicate the main trends in the data.

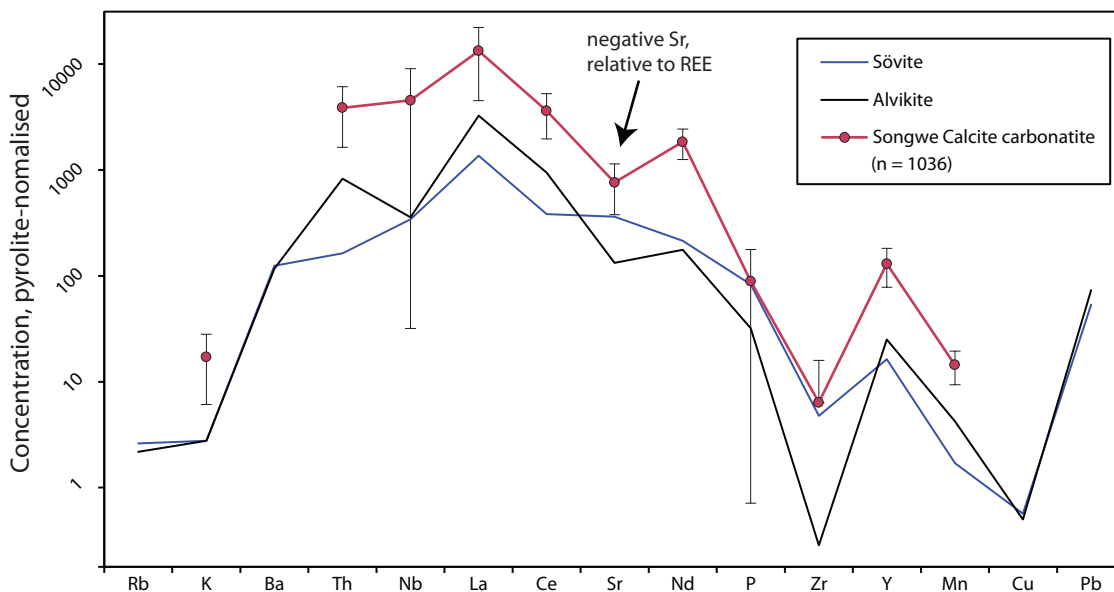


Figure 4.19: Average Songwe calcite-carbonatite values compared with median sövite and alvikite values from Le Bas (1999). Error bars on the Songwe values equate to 1 standard deviation from the mean. Note the elevated concentrations of the Songwe analyses, and the relative depletion in Sr, relative to the REE. Values normalised to pyrolite values from McDonough and Sun (1995).

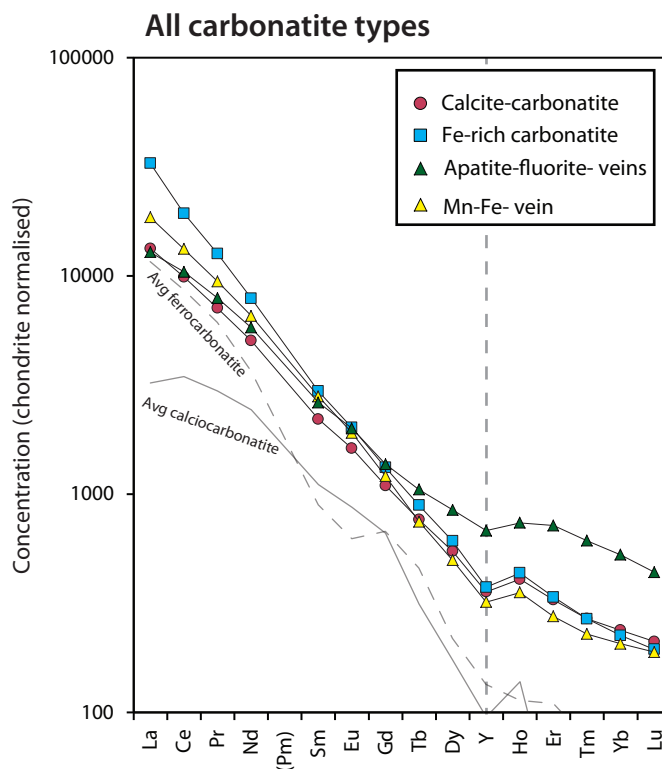


Figure 4.20: Average distribution of the REE in Songwe carbonatites, Mn-Fe-veins and Apatite-fluorite veins. Also included are the average calcio- and ferro-carbonatite compositions (Woolley and Kempe, 1989). The position of Y is highlighted for easy reference. Data are normalised to chondrite after McDonough and Sun (1995).

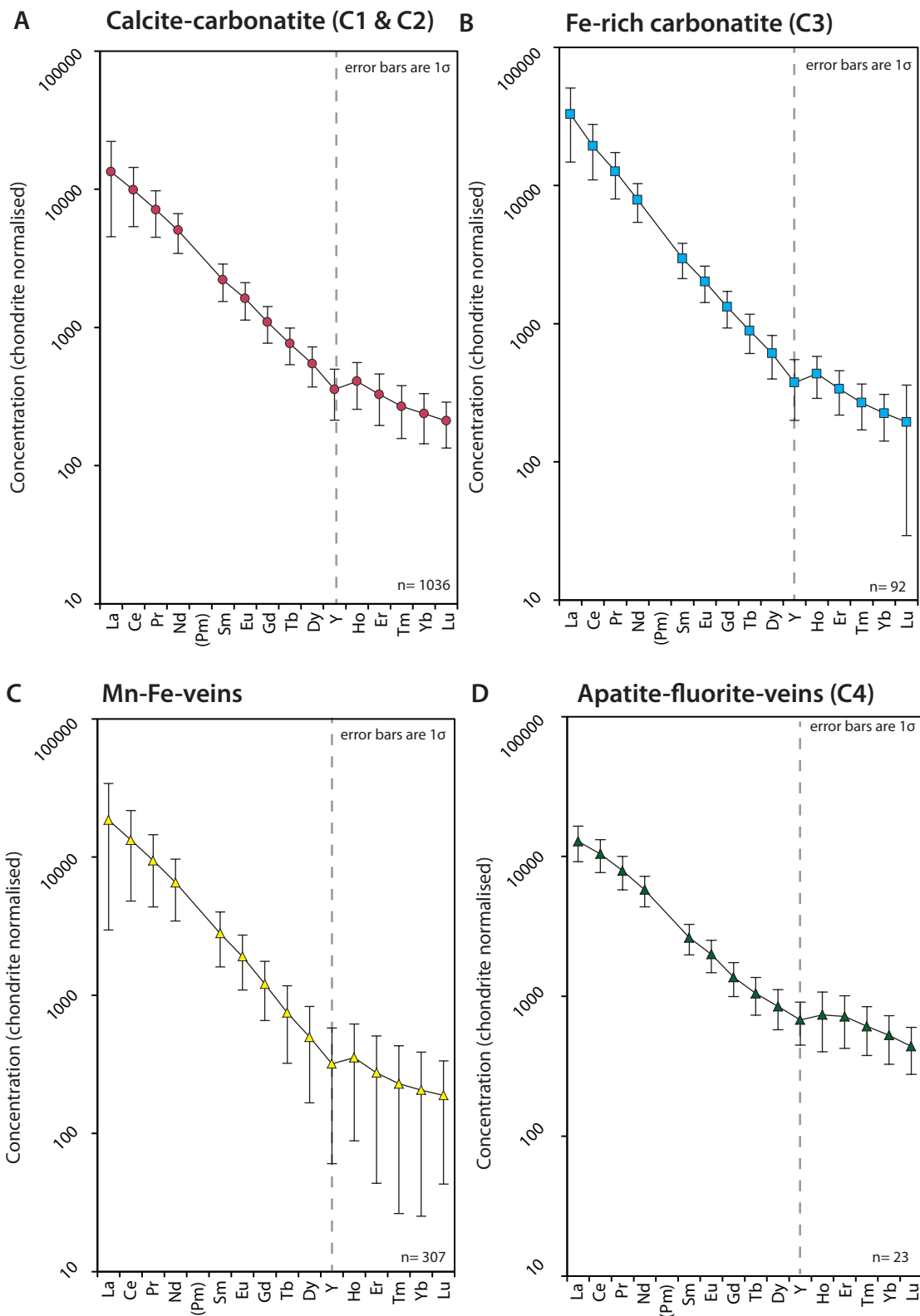


Figure 4.21: REE distributions of individual carbonatite types with 1 standard deviation error bars. The position of Y is highlighted for reference. Data are normalised to chondrite after McDonough and Sun (1995).

bonatite does not show a spread at the HREE end of the diagram, but this may be a function of the lower number of analyses of this type (n= 92). Apparent in the REE distribution in all of the carbonatite types (including the average calcio-carbonatite) is a negative Y anomaly.

4.4 Discussion—Mauze

4.4.1 Comparison of Mauze with other silicate rocks of the CAP

In their study of bulk-rock compositions of the intrusions in the northern part of the CAP, Woolley and Jones (1987) subdivided the intrusions of the province into three suites, interpreted to be derived from three different parental magma compositions. These are:

1. Syenite–quartz-syenite–granite, derived from a trachyte parental magma.
2. Syenite–nepheline syenite, derived from a phonolite parental magma.
3. Nephelinite–nepheline syenite series, derived from a nephelinite parental magma.

It is therefore evident that rocks classed mineralogically as nepheline syenites may be potentially derived from two differing parental magmas, phonolite and nephelinite.

Using the major element data of Dixey et al. (1955), Woolley and Jones (1987) considered that the carbonatite-associated silicate rocks of the southern part of the CAP, such as those from Tundulu and Nkalonje, fell into the nephelinite trend, similar to the silicate intrusions at Chilwa Island. The available datum utilised from Mauze, however, was ambiguous, but, because of low CaO concentrations relative to other data from carbonatite-associated intrusions, Woolley and Jones (1987) suggested that it was more geochemically similar to phonolite-derived nepheline syenite (2) than nephelinite-derived nepheline syenite (3). They concluded that this feature suggested that Mauze may be unique among the carbonatite-associated silicate rocks of the CAP. This is consistent with the larger size of Mauze compared to the other carbonatite-associated silicate rocks in the province.

The addition of four new whole-rock analyses for Mauze permits a greater understanding of which trend (after Woolley and Jones, 1987), and therefore which postulated parental magma, this intrusion belongs to. The most useful plot used by Woolley and Jones (1987) to differentiate the intrusions was a binary plot of

SiO₂ against CaO (Fig. 4.22). On this plot, trachyte-derived intrusions plot bimodally, but on a general negative trend from approximately 60 % to 75 % SiO₂, with CaO concentration decreasing from 4–0 %. Nephelinite-derived intrusions plot along a steep negative trend from approximately 40 % to 60 % SiO₂, with corresponding CaO concentrations of 14–1 %. Phonolite-derived intrusions do not show a clear correlation between CaO and SiO₂, and the data are clustered around 55 % SiO₂ and 1.5 % CaO. The new data from Mauze plot towards the low SiO₂ end of the data-cluster for phonolite-derived intrusions (Fig. 4.22). This is in accordance with the suggestion that Mauze is unique among the carbonatite-associated nepheline syenites (e.g. those from Tundulu and Chilwa Island) and more comparable to the large nepheline syenites of the northern part of the CAP (Woolley and Jones, 1987). However, the new data also clearly display a negative correlation between CaO and SiO₂, and the trend of this negative correlation is approximately equivalent to the rocks of the nephelinite-derived intrusions (Fig. 4.22). It is, therefore, suggested that Mauze *may* be a SiO₂-rich member of the nephelinite series, thus implying that Mauze may not be unique in the CAP. Binary plots of other elements support this interpretation, with Mauze data generally clustering with phonolite-derived intrusions, but also correlating with the nephelinite-series and potentially representing the SiO₂-rich end of nephelinite-derived differentiation. The paucity of data makes it difficult to define unequivocally the nature of the source for Mauze. A detailed investigation of the geochemical evolution of Mauze is beyond the scope of this thesis. Further mapping, mineralogical and geochemical studies are required to understand Mauze's potentially unique place in the CAP.

4.5 Discussion—Songwe

4.5.1 Stages of intrusion of the Songwe carbonatite

Carbonatites have been classified by Le Bas (1977, 1981, 1989, 1999) as intruded in a series, C1 through to C4, of calcite-carbonatite (C1), alvikite-carbonatite (C2), ferro-carbonatite (C3) and back to late stage calcite-carbonatite (C4). The terminology used to describe the carbonatites at Songwe is based on these (Tables 3.4 and 4.9). The series is envisaged, by Le Bas, as a fractional crystallisation trend, from calcite-rich to iron-rich carbonatites with decreasing Ca, P, Zr, Nb and increasing LREE and F. These trends are broadly supported by the carbonatite compositions at Songwe.

Based on field observations at Songwe the early coarse-grained C1 carbonatite probably belongs to the C1 group. This is supported by mineralogical criteria, such as its platy, coarse-grained carbonates and flow-banded apatite, py-

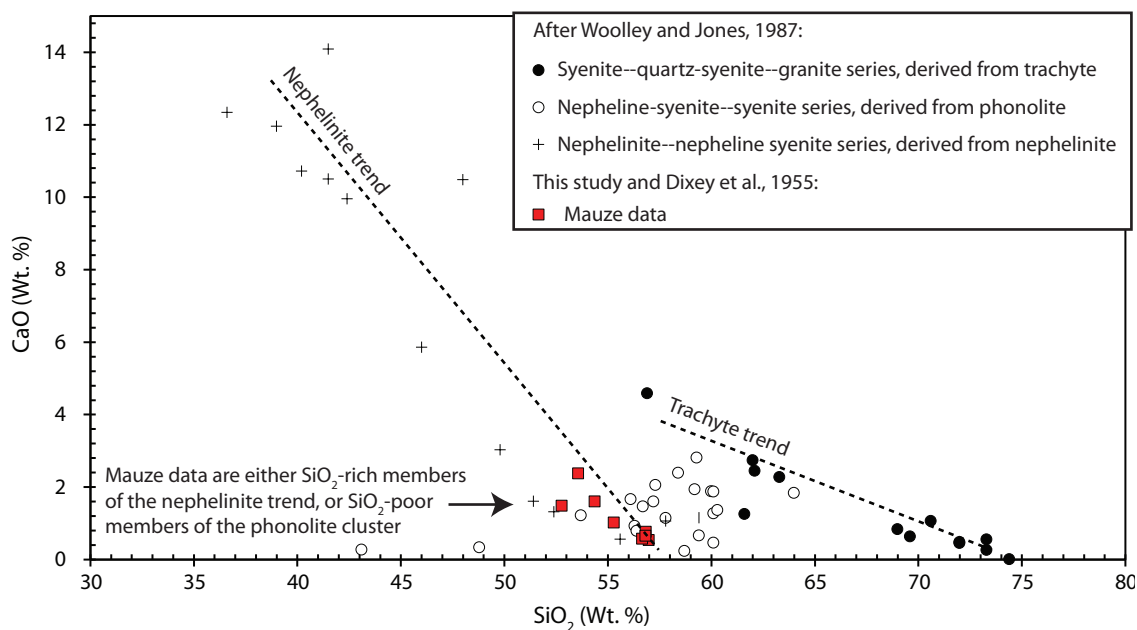


Figure 4.22: Comparison of data from Mauze, including new data and data from Dixey et al. (1955), with data from other intrusions of the CAP (Woolley and Jones, 1987). Data from other intrusions of the CAP are divided into the syenite–quartz-syenite–granite series, nepheline syenite–syenite series and nephelinite–nepheline syenite series. These are postulated to be derived from trachyte, phonolite and nephelinite, respectively. Symbols are the same as from Woolley and Jones (1987), while the analyses from different rock types from Mauze are grouped together for clarity. The relationship between Mauze and these trends is suggested to be either a SiO₂-rich member of the nephelinite series, or a SiO₂-poor member of the phonolite series.

rochlore and zircon. Other criteria, such as diffuse boundaries with the country rock and geochemical distinctions cannot be made due to the paucity of samples and therefore lack of geochemical data. However, contact relations with later stages are clear, through the presence of C1 clasts in C2 calcite-carbonatite (Chapter 3).

Justification for considering most calcite-carbonatite at Songwe as C2 carbonatite was made in the previous section (4.3.7). This carbonatite type is inferred to be the most abundant at Songwe, and is notable for containing xenoliths of C1 carbonatite, as well as extensive brecciation and flow structures such as pebble dykes (Chapter 3). This stage is also notable for its low MgO concentration.

Fe-rich carbonatite is interpreted as being equivalent to the C3 ferrocarbonatite using the nomenclature of Le Bas (1989) (c.f. Gittins and Harmer, 1997). This is based mostly on the increasing abundance of ankerite, and the increased concentration of the LREE and Sr in this rock type, relative to the preceding stages and the prevalence of REE mineralisation. No siderite is observed in this carbonatite type. The definition of a ferrocarbonatite, however, remains unclear (Gittins and Harmer, 1997). Descriptions of individual complexes vary from those containing siderite (e.g. Garson and Smith, 1958; Buckley and Woolley, 1990; Thompson et al., 2002; Zaitsev et al., 2004) and those which appear to be composed almost entirely of hematite (e.g. Andersen, 1984, 1986b, 1987b).

Fe-rich carbonatite and Mn-Fe- veins were distinguished in the field on the basis of reaction to HCl and through field relationships. Fe-rich carbonatite reacts to HCl and Mn-Fe- veins do not, and Mn-Fe- veins typically form thin veins, while Fe-rich carbonatite can intrude in a multitude of different ways. It is notable that geochemically, these two carbonatite generations are considerably different, with Mn-Fe- veins displaying much lower MgO and SrO concentrations. Furthermore, Fe-rich carbonatite typically hosts the majority of the LREE mineralisation at Songwe, while Mn-Fe veins host highly variable amounts. It is, therefore suggested, that C3 Fe-rich carbonatite and Mn-Fe- veins at Songwe are different rock types, and that the Mn-Fe veins represent deuteric or meteoric alteration products (Barker, 1989). This is in accordance with how the Mn-Fe- veins appear to follow late-stage fractures in the carbonatite, and that the degree of breakdown and alteration of Fe-bearing carbonates decreases away from these veins (Chapter 5).

Late mineralisation in carbonatites commonly consists of LREE, fluorite, barite, quartz and rarely U and Th mineralisation. Late-stage apatite-fluorite veins, as identified at Songwe, appear to be an uncommon component of most carbonatites. These will be discussed extensively in Chapter 5.

4.5.2 Y anomaly: a significant result or an analytical artefact?

Unlike fractionation of Eu and Ce, which is caused by changes in the oxidation state (and therefore the valence state) of these elements, fractionation of Y is generally considered to be caused by the different behaviour of Y in aqueous fluids (Bau, 1996; and see Chapter 2). Complexation with fluoride complexes is thought, from both theoretical and laboratory experiments, to preferentially transport Y over the other HREE (Bau and Dulski, 1995; Loges et al., 2013). Complexation with carbonate, however, has been suggested to cause Y to behave more like LREE complexes (Bau and Dulski, 1995). Changes in the chondrite-normalised Y position is, therefore, a powerful indicator for hydrothermal activity and can potentially be used to investigate the complexing anion in an REE-bearing fluid.

Although a negative Y anomaly is consistently observed in all the whole-rock analyses, it is subtle and therefore worth investigating to find out if it is an analytical artefact. The low magnitude of the anomaly is emphasised by how most of the Y/Ho ratios of the analysed samples lay within, or on the edge of, the CHARAC²³ field (arbitrarily defined by Bau, 1996). This field represents analyses of igneous rocks considered to have their REE distribution controlled by igneous, rather than hydrothermal, processes (Fig. 4.23 A). The scatter in the Zr/Hf data on this diagram is likely to be due to the low concentration of these elements in the analysed samples and, therefore, increased uncertainty. The concentration of both Y and Ho, however, are both high and the ratios are, therefore, accurate.

One potential cause of an apparent Y anomaly is the positioning of Y on a chondrite normalised diagram. On Figures 4.20 and 4.21, Y is placed exactly half way between Dy and Ho. The effective ionic radii of Y, however, is much closer to that of Ho than Dy, with radii of 9.0, 9.01 and 9.12 nm for Y, Ho and Dy, in the VI coordination state, respectively (Shannon, 1976). Therefore the position of Y on Figures 4.20 and 4.21 is artificially to the left of where it should be and this could cause subtle 'kinks' in the distribution. However, on Figure 4.23 B, the average chondrite-normalised distribution for calcite-carbonatite is re-plotted with the REE arranged by ionic radii, and the anomalously negative position of Y, relative to Ho, is confirmed.

Another potential cause of an apparent Y anomaly is a, hitherto unforeseen, methodological issue with the Y analyses. However, comparison of the carbonatite standard data (Table 4.2) and the 105 analyses of this standard show that an Y anomaly is present in both the published data for the standard and the new analyses (Fig. 4.23 B). With these potential artificial sources excluded, the Y anomaly is considered to be related to a natural process and to have some significance regarding the evolution of carbonatites.

²³Charge and Radius controlled

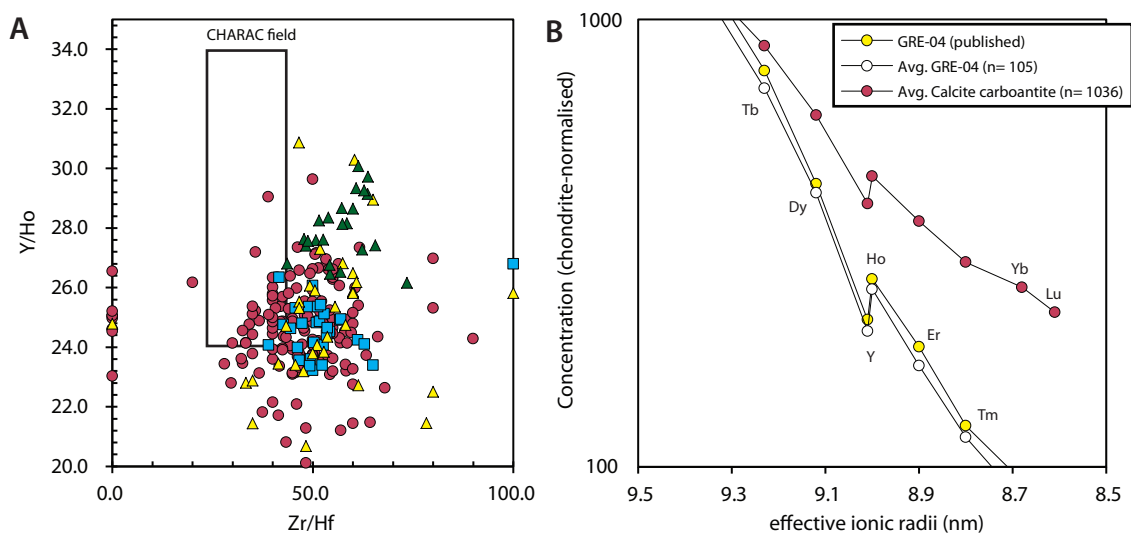


Figure 4.23: Plot A compares the geochemical twins Y/Ho and Zr/Hf for the whole-rock data of the different carbonatite generations at Songwe Hill. Data points are the same as Figure 4.21. Also illustrated is the CHARAC field after Bau (1996), illustrating the arbitrary field within which 73 % of the ratios of 48 igneous standards, and a chondrite data-point, plot. Note that most of the data plot on the edge of this field. Plot B illustrates the chondrite-normalised distribution of the GRE-04 carbonatite standard, the average results of 105 analyses of this standard (see Table 4.2), and the average of 1036 analyses of calcite-carbonatite from Songwe. These data are plotted against effective ionic radii with coordination number VI, illustrating the closer relationship of Y to Ho than Dy.

A negative whole-rock Y anomaly may be a common feature in carbonatites as it is also present in the published compilation of 16 analyses of ‘average’ calcite-carbonatite (Fig. 4.21, Woolley and Kempe, 1989). A compilation of published whole-rock REE+Y data was beyond the scope of this study, but is recommended for future work. Bühn (2008) demonstrated that, for the Namibian Ondurakorume and Kalkfeld carbonatites, an increasingly negative Y anomaly correlated with decreasing MgO, P₂O₅ and Y concentrations. Such a correlation could not be attributed to the fractionation of a mineral phase, and was suggested by Bühn (2008) to be due to the expulsion of an HREE-bearing, fluoride-complexed, fluid phase. This hypothesis is supported by the increased stability of Y-fluoride complexes over other HREE-fluoride complexes (Loges et al., 2013) and by the high F activity in carbonatite magmas (Gittins et al., 1990; Jago and Gittins, 1991; Mitchell and Kjarsgaard, 2004; Mangler et al., 2014). It is therefore suggested that the negative Y anomaly in the whole-rock data from Songwe may be caused by a similar process of HREE-bearing fluid expulsion.

4.5.3 Controls on the REE distribution at Songwe

Despite the low magnitude Y anomaly, Y concentrations can be used as a proxy for total HREE concentration as its chondrite-normalised values are broadly sim-

ilar to the other HREE. In the Songwe carbonatites, whole-rock Y concentrations can reach up to 3000 ppm, but are typically in the range of 250–1250 ppm. Unlike values for TREO (Fig. 4.18 E), Y and MnO+FeO do not correlate.

In all samples, Y (and therefore the HREE) shows a strong positive correlation with P₂O₅ (Fig. 4.24 A–B). This relationship is clearly demonstrated on a diagram of all carbonatite analyses (including those with no LOI data), where the R² value (measure of the goodness of fit of a straight line, up to 1) between Y and P₂O₅ is 0.434 (Fig. 4.24 A). Minor variations in the data can be seen when data from the different carbonatite types are highlighted. In the case of Fe-rich carbonatite, Y contents are similar to those of calcite-carbonatite, while apatite-fluorite veins have a slightly higher Y concentration. These are both enriched in P₂O₅ relative to calcite-carbonatite.

Correlations between P₂O₅ and other elements are less clear (Figures 4.24 C–D). There is a subtle weak correlation between P₂O₅ and TREO, but it is much less distinct than that of P₂O₅ and Y. This indicates that the LREE are controlled less by P₂O₅ concentration than the HREE and that the HREE are preferentially partitioning into phosphate minerals. While SrO commonly substitutes into apatite in carbonatites, there is little correlation between the two elements in the whole-rock data for calcite-carbonatite and Fe-rich carbonatite. This is probably due to formation of strontianite in these rocks. In the apatite-fluorite- and Mn-Fe- veins, however, SrO and P₂O₅ show a positive correlation, indicating that strontianite is not present in these samples and that Sr is incorporated in apatite.

In all samples there is a variable but weak correlation of Y with Th and U concentrations (Figures 4.24 E–F). This indicates that these are being controlled by similar processes. P₂O₅, however, shows a weak correlation with U and Th, indicating that the abundance of P₂O₅ is not the dominant control.

4.5.4 Comparison of Songwe with other CAP carbonatites

REE data from other carbonatites in the CAP are limited. REE data are available from Tundulu (Ngwenya, 1991, 1994; Appleton and Styles, *unpublished*, and this study), and from Kangankunde (Wall, 2000). No published REE analyses are available for Chilwa Island, but major and some minor element data, including Y, are available (Simonetti and Bell, 1994).

Comparison of REE concentrations and the relationship between Y and P₂O₅ are shown in Figure 4.25. Data for the REE are limited to Y and La due to the dearth of analyses of other elements.

The positive correlation between P₂O₅ and Y observed in the Songwe carbonatites is also observed in carbonatites from Tundulu and Kangankunde but is not seen in the data from Chilwa Island (Fig. 4.25 A). Samples from Kangankunde, however, are very Y-poor and LREE-rich and any correlation between Y and P₂O₅

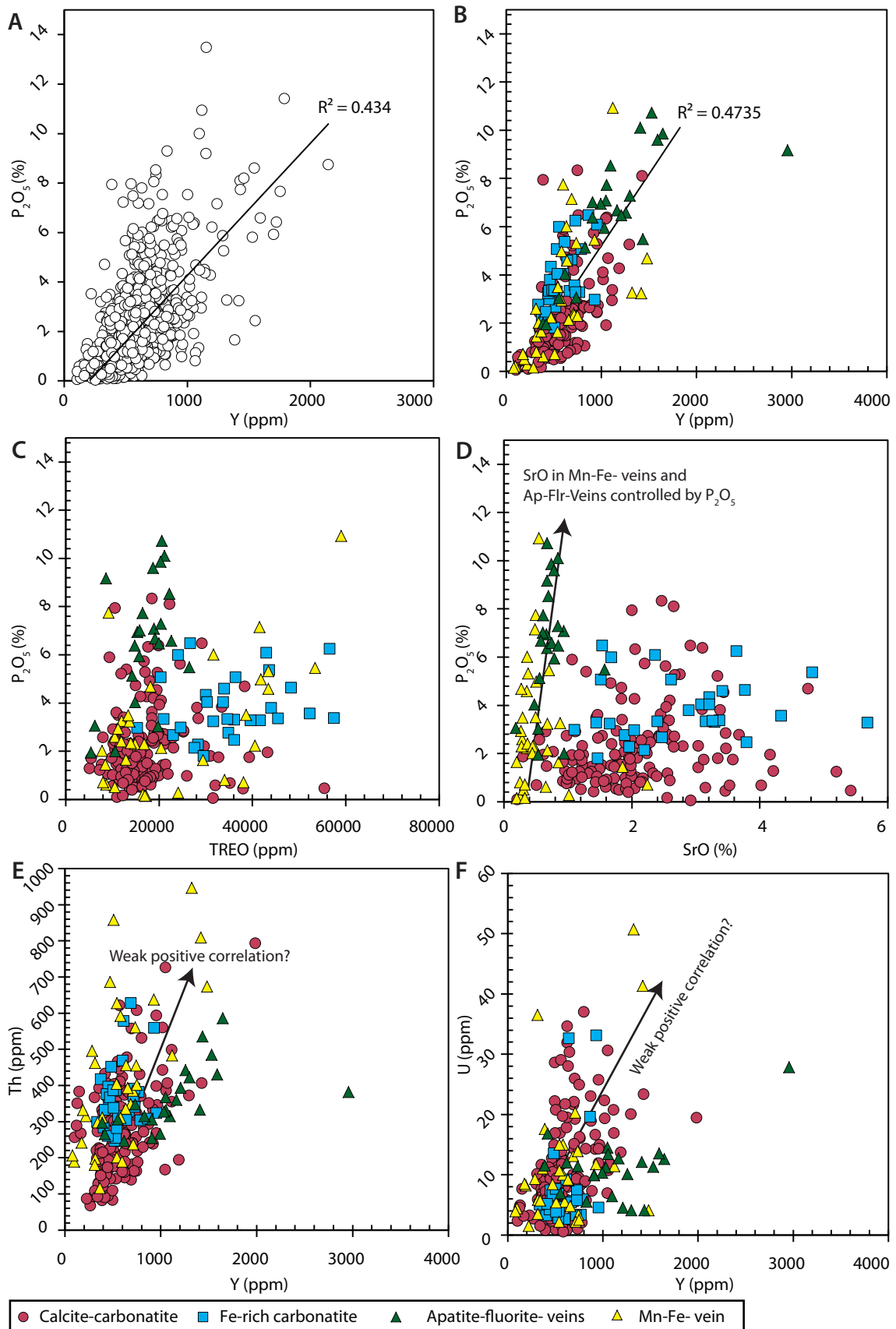


Figure 4.24: Binary plots of whole-rock data from carbonatite and Mn-Fe-veins from Songwe. Data in Figure A includes all analyses from carbonatite derived from this study, including analyses with no LOI data. Symbols same as Figure 4.18.

in these samples is most probably due to trace Y substitution into monazite, rather than apatite. Analyses of apatite from Tundulu include many samples of silicified apatite-carbonatite from Nathace Hill, which are apatite-rich, hence the high P_2O_5 concentrations. These samples are considered, from field-relationships, to be formed during the late stages of carbonatite emplacement (Ngwenya, 1994). Y and P_2O_5 show a strong positive correlation in these samples suggesting that apatite at Tundulu is hosting the HREE and that it is similar to that found at Songwe. Y concentrations in the two deposits, however, are similar, despite the higher P_2O_5 concentrations at Tundulu, and it is possible that the HREE are more concentrated in apatite from Songwe than from Tundulu. However, La (representing the LREE) concentrations are lowest in the Tundulu samples, suggesting that LREE-minerals are scarce in these samples. La concentrations are highest in samples from Kangankunde as a result of the high monazite-(Ce) content of these carbonatites.

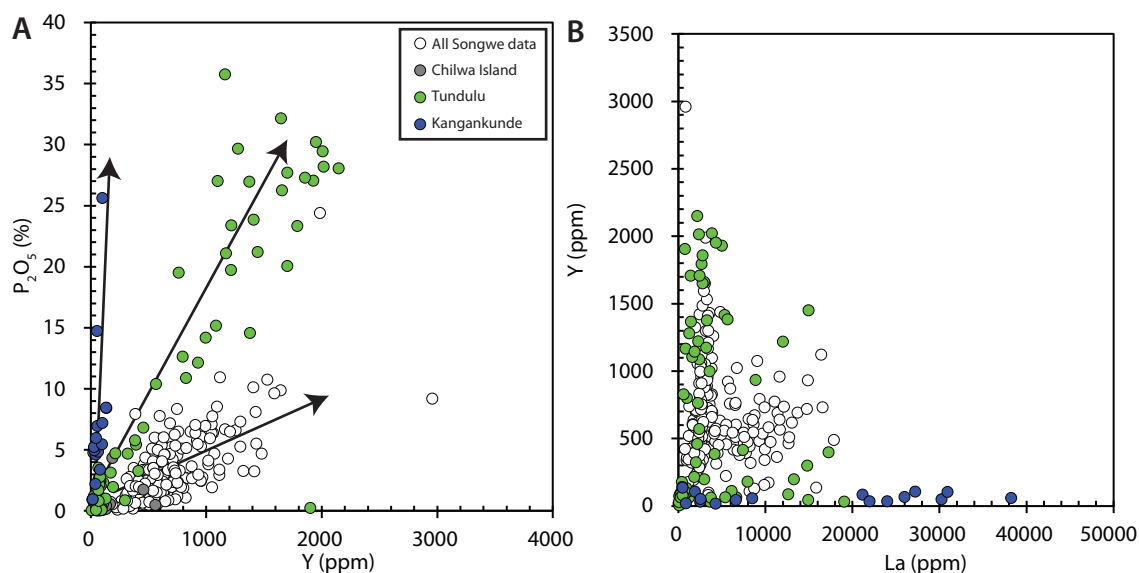


Figure 4.25: Comparison of whole-rock P_2O_5 , Y and La data from from Songwe and other CAP carbonatites. Note that the correlation between Y and P_2O_5 at Kangankunde is not observable on this graph.

4.6 Conclusions

In this chapter, new geochemical and petrographic data have been presented for the Songwe Hill carbonatite and the associated Mauze nepheline-syenite intrusion.

The new data from Mauze show that it is more geochemically and mineralogically variable than previously thought, with a wide range in K_2O and Na_2O concentrations. It is uniformly P_2O_5 -poor, with decreasing P_2O_5 with increasing SiO_2 .

New analyses of late-stage pegmatoidal samples have the lowest P_2O_5 concentrations. All analysed samples are MREE depleted, with the degree of depletion increasing towards the later stages of the intrusion.

Comparison of the new geochemical data from Mauze with published data from intrusion in the northern part of the CAP suggests that Mauze could be related to two different nepheline syenites with contrasting parental melts (Woolley and Jones, 1987). It is suggested that Mauze may be related to the carbonatite-associated nephelinite-series, and not a uniquely carbonatite-associated member of the phonolite series as suggested by Woolley and Jones (1987). The paucity of data, however, make it difficult to establish reliable conclusions. Further field and laboratory investigations are required to substantiate the origin of Mauze.

The new geochemical data from Songwe show that the different intrusion stages are mineralogically and geochemically distinct. These can be summarised as follows:

C1 calcite carbonatite Petrographic analysis shows that it is composed of medium-coarse grained calcite, with flow-banded ovoid apatite and euhedral pyrite, zircon and pyrochlore. Whole rock data are not available due to the rarity of this rock type.

C2 calcite carbonatite is the most abundant carbonatite type and is mostly composed of fine-grained calcite with minor ankerite. It is geochemically and texturally similar to alvikites (*sensu* Le Bas, 1999) and is therefore classified as such. Apatite mineralisation occurs towards the late stages of this carbonatite type, and forms anastomosing stringers or anhedral pods.

C3 Fe-rich carbonatite is ankerite rich, but is frequently altered to Fe-oxides and calcite. This carbonatite type contains abundant REE mineralisation, and has the highest REE and SrO concentrations

C4 Apatite-fluorite veins are volumetrically relatively minor, but they contain a high proportion of apatite and HREE. The exact temporal relationship with the other intrusion stages is unknown. They are assumed to be late stage based on the common occurrence of fluorite late in carbonatite emplacement.

Mn-Fe- veins occur towards the end of the intrusion at Songwe, and are considered to be representative of a stage of extensive hydrothermal alteration. These veins follow fractures in the carbonatite and are represented by alteration products of Fe-bearing carbonates, chiefly to Fe-oxides and calcite. They are geochemically distinct from the other carbonatite stages in having much lower MgO and SrO concentrations.

LREE mineralisation is predominantly found in bands in the Fe-rich carbonatite, as is reflected by the relatively high TREO concentration in whole-rock analyses of this carbonatite. The LREE are associated with barite, strontianite and late-stage calcite. It is also found in small vugs in the C2 calcite carbonatite. Cross-cutting relationships show that it occurred after widespread apatite crystallisation.

A prominent Y anomaly is present in all the whole-rock chondrite-normalised REE distributions. This is considered to be related to a natural process, possibly the expulsion of a HREE-bearing, fluoride-complexed, fluid phase.

A strong positive correlation between P_2O_5 and Y is prominent in all the carbonatite stages at Songwe. This suggests that the HREE are hosted in apatite, as the few other phosphate phases are present only in very small quantities in any of the carbonatites. A similar correlation is observed between P_2O_5 and Y in the Tundulu carbonatites.

Chapter 5

Trace-element analyses of HREE-bearing minerals in carbonatites from Malawi: fluorapatite and xenotime-(Y)

In this chapter, petrographic, LA ICP-MS¹ and EPMA² data are presented for fluorapatite and xenotime-(Y) from the Songwe Hill carbonatite intrusion, Malawi. These data are used to test the hypotheses that carbonatites can host HREE and that phosphate minerals can preferentially incorporate and enrich the HREE, relative to whole-rock compositions, during carbonatite evolution.

Apatite is found throughout the paragenesis at the Songwe Hill intrusion, and another hypothesis examined in this chapter is whether apatite can be used to trace carbonatite, or a carbonatite-derived fluid, throughout its evolution. To aid this interpretation, trace-element data for fluorite are also presented.

Data for late-stage apatite from the Tundulu and Kangankunde carbonatites (Malawi) are also presented for comparison to test if the processes leading to HREE-enrichment at Songwe are unique. The paragenesis of each deposit is re-evaluated with the aid of CL³ petrography.

Apatite from each carbonatite is interpreted with respect to the causes of its luminescence, element substitutions and REE distribution. The abundances of the 'penalty' (i.e. bad for processing and extracting) elements U and Th are highlighted due to the issues in concentrating these elements when extracting the HREE. Additionally, some of the first analyses of As in apatite from carbonatite are presented in the data from Songwe.

Data for apatite at Songwe are compared to a comprehensive compilation of

¹laser ablation inductively coupled plasma mass spectrometry

²electron probe micro-analyser

³cathodoluminescence

literature data from other carbonatites and granitoids, as well as the supporting data acquired from the Tundulu and Kangankunde carbonatites. New diagrams for apatite classification are proposed. It is also shown that apatite from Songwe has some of the highest concentrations of HREE yet reported.

5.1 Why analyse apatite in carbonatite?

REE-minerals currently extracted from carbonatites (REE-fluorcarbonates, monazite) are typically LREE-rich and HREE-poor (Wall, 2014). Only a few examples of HREE enrichment in carbonatites have been described. For example, Zaitsev et al. (1998) showed that the Khibiny complex in Russia evolves from a LREE-rich system towards HREE-enriched mckelveyite-(Y) group minerals at the late stages of its paragenesis. Magmatic and hydrothermal xenotime-(Y) is known from the Lofdal carbonatite complex in Namibia, and is currently being explored (Wall et al., 2008). Xenotime-(Y) and other HREE-rich phases are also found at the Huanglongpu and Huayangchuan carbonatites, China (Xu et al., 2007; Kynicky et al., 2012). Low-tenor HREE enrichment has been found in apatite from the carbonatites at Tundulu, Malawi; Sukulu, Uganda; and Juquiá, Brazil, where HREE-enrichment is observed in very late-stage apatite (Ngwenya, 1994; Ting et al., 1994; Walter et al., 1995).

A relationship between P_2O_5 and the HREE was demonstrated in the whole-rock geochemical data (Chapter 4), with P_2O_5 and Y concentrations attaining maximum values of 10 % and 3000 ppm, respectively. It was suggested that this correlation results from the presence of these elements in the phosphates apatite and/or xenotime.

Fluorapatite ($Ca_5(PO_4)_3F$) is ubiquitous in carbonatites, usually comprising 2–5 modal % of the rock, and it can be the main REE host (Hogarth, 1989). It is typically a liquidus phase, but can occur throughout emplacement, from early magmatic to late hydrothermal stages (Eby, 1975; Kapustin, 1980; Hogarth, 1989). It is a remarkably tolerant mineral to structural distortion and chemical substitution, being able to accept many different elements into its structure, particularly the REE (Pan and Fleet, 2002). Concentrations of up to 5 wt % REE in apatite have led to the suggestion that it may be a viable by-product or co-product of phosphate extraction, although the REE distribution is commonly LREE enriched (Mariano and Mariano, 2012; Ihlen et al., 2014).

In addition to its potential as a REE co-product, apatite can be used to track petrological processes in igneous rocks. This is facilitated by the common occurrence of apatite in many rock types and its structural flexibility. For example, apatite has been used for this purpose in granitoid rocks where apatite chemistry has been related to host-rock composition (Belousova et al., 2002; Macdonald

et al., 2013), and using apatite to trace differentiation in granites (Sha and Chappell, 1999; Chu et al., 2009). In carbonatites, apatite has been used to elucidate the relationship between carbonatites and associated alkaline rocks (Le Bas and Handley, 1979; Stoppa and Liu, 1995; Wang et al., 2014), to trace carbonatite evolution (Walter et al., 1995) and to study the process of REE mineralisation (Campbell and Henderson, 1997).

5.2 Methods

5.2.1 Petrography

CL and BSE⁴ petrography were carried out using the methods described in Chapter 4. Additionally, some CL spectra were generated to quantify the luminescence colours from apatite. The instrumentation used was an ELM-3R Luminoscope with a grating-type H-20 Jobin-Yvon spectrometer equipped with an R-928 photomultiplier detector. Spectra were acquired in a dark-room at McGill University. The results were compared to reference values from Marshall (1988) and Mitchell (2014).

5.2.2 Quantitative electron microscopy (EPMA)

Major elements in apatite were analysed at the BGS⁵ using a FEI-Quanta 600 SEM⁶. Analyses of xenotime-(Y) were carried out at CSM⁷ using a Jeol JXA 8200 EPMA.

The analyses of apatite were carried out using EDS⁸, with beam conditions and count times (20 kV, 3 nA and 60 s) kept low to avoid issues with fluorine diffusion (Stormer et al., 1993). Dead-time was typically around 25 %. Quantitative analyses were calibrated using a combination of pure element and mineral standards using the method detailed in Walters et al. (2013). The elements Y and Si were measured on the attached WDS⁹ to avoid peak overlaps. Counting times were 60 s and 40 s for Y and Si respectively. Background counts were half peak counts. A British Museum apatite was used as a quality control standard and the results were within a 2 % variation, which was deemed acceptable for quantitative analyses.

Xenotime-(Y) had not been previously run using the EPMA at CSM. Therefore, a protocol was set up to obtain reproducible analyses (appendix B). Beam

⁴back-scattered electron

⁵British Geological Survey

⁶scanning electron microscope

⁷Camborne School of Mines

⁸electron dispersive spectroscopy

⁹wavelength dispersive spectrometry

conditions varied, with a spot size of 1–10 μm , a voltage of 20 kV, and a current of 5–30 nA. Counting times were typically high, up to a maximum of 60 s, to reduce the LOD¹⁰ of low concentration REE. Background times were half the duration of peak analysis times. Beam conditions were matched for standard and sample analyses, with the exception of Ho, Tm and Lu standards, which were analysed with a larger spot-size and reduced current due to their high volatility (Table 5.1).

Element	Standards	Spot size (μm)	Current (nA)	Voltage (kV)	count time (s)	LOD (% oxide)
Nd	Sm_Nd	2	30	20	60	0.10
Sm	Sm_Sm	2	30	20	40	0.07
Eu	Sm_Eu	2	30	20	40	0.10
Gd	Sm_Gd	2	30	20	20	0.14
Tb	Sm_Tb	2	30	20	40	0.11
Dy	Sm_Dy	2	30	20	40	0.10
Ho	Ast_Ho	10	5	20	20	0.24
Er	Sm_Er	2	30	20	40	0.13
Tm	Ast_Tm	10	5	20	40	0.12
Yb	Sm_Yb	2	30	20	40	0.10
Lu	Ast_Lu	10	5	20	40	0.11
Y	Sm_Y	2	30	20	120	0.04
Th	AST-M-Th	2	30	20	40	0.04
U	AST-M-U	2	30	20	60	0.04
Pb	AST-M-Pb	2	30	20	80	0.01
Si	MkII-olivine	2	30	20	60	0.07
Fe	MkII-olivine	2	30	20	20	0.06
Ca	AST-Apatite	2	30	20	20	0.03
P	AST-Apatite	2	30	20	20	0.46

Table 5.1: Standards used, and beam conditions for calibration.

5.2.3 Laser ablation ICP-MS

In-situ trace element analyses using LA ICP-MS were carried out on apatite and fluorite. This work was undertaken at the BGS, utilising a New Wave Research Quintupled Nd-YAG 193 nm laser attached to an Agilent-7500 ICP-MS¹¹.

A mixture of 30 μm and >100 μm -thick sections were used for analysis and, to avoid ablating through the thin sections, different laser conditions were utilised (Table 5.2). For 30 μm sections, the minerals were ablated with a small spot size and a moving raster pattern, while for thick sections a single large spot was

¹⁰limit of detection

¹¹inductively coupled plasma mass spectrometry

used. Different laser conditions were used for different minerals to ensure the best ablation conditions, maintaining a fluence of approximately 3.5 J/cm^2 and also to maintain sufficient sample ablation volumes for ICP-MS analysis (Table 5.2).

Elements analysed for each mineral are shown in Table 5.3. Data were processed using Iolite software (Paton et al., 2011). Results were calibrated using NIST SRM 610 as an external standard and checked using SRM 612. Ca was used as an internal standard, for which values were measured using SEM-EDS or EPMA analyses, with the exception of fluorite, where stoichiometric values were used. The positioning of the laser spots was checked on the SEM after ablation to ensure the electron beam and laser spot had analysed the same area.

Owing to high blank concentrations in the check-standard, Na, Mg, K, Si, As, Mn, Zr and Pb data were removed from raster data points. All check-standard data are within 5 % of published values, with the exception of Th, which is within 10 % of the published concentration. An example of repeat analyses of SRM 612 is shown in Figure 5.1. All other SRM¹² repeat analyses are shown in appendix B.2.

	Apatite (2012)	Apatite (2013)	Fluorite
Ablation type	Raster	Spot	Spot
Spot size (μm)	15	50	
Spacing (μm)	15	-	-
Repetition rate (Hz)	10	10	10
Intensity (%)	60	60	60
Dwell time (s)	30	30	30
Radiance (GW/cm^2)	1.05	0.97	1.15
Fluence (J/cm^2)	5.14	2.69	3.09

Table 5.2: Laser conditions for the different minerals analysed.

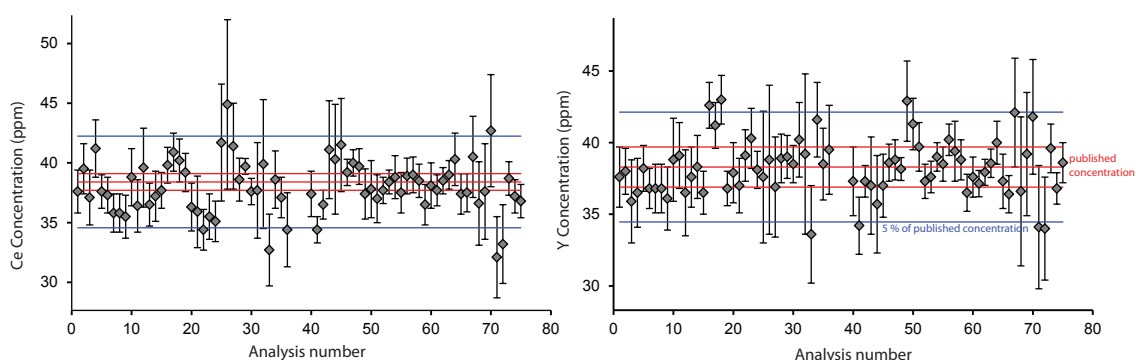


Figure 5.1: Analyses of SRM 612 check-standard, for Y and Ce, with published concentrations marked in red (plus upper and lower uncertainties at 95 % confidence) and 5 % of published concentrations marked in blue. Error bars represent uncertainty in the integration of the raw data and are generated by Iolite. Graphs of the analyses of other elements are shown in appendix B.2.

¹²Standard Reference Material

	Apatite ¹	Apatite ²	Fluorite		Apatite ¹	Apatite ²	Fluorite
²³ Na	✓	✓	✓	¹³⁷ Ba	✓	✓	✓
²⁴ Mg	✓	✓	✓	¹³⁹ La	✓	✓	✓
²⁷ Al			✓	¹⁴⁰ Ce	✓	✓	✓
²⁸ Si	✓			¹⁴¹ Pr	✓	✓	✓
³¹ P	✓	✓		¹⁴⁶ Nd	✓	✓	✓
³⁹ K		✓	✓	¹⁴⁷ Sm	✓	✓	✓
⁴² Ca	✓	✓	✓	¹⁵³ Eu	✓	✓	✓
⁴⁴ Ca	✓	✓	✓	¹⁵⁷ Gd	✓	✓	✓
⁴⁷ Ti	✓			¹⁵⁹ Tb	✓	✓	✓
⁵⁵ Mn	✓	✓	✓	¹⁶³ Dy	✓	✓	✓
⁵⁶ Fe	✓	✓	✓	¹⁶⁵ Ho	✓	✓	✓
⁵⁹ Co			✓	¹⁶⁶ Er	✓	✓	✓
⁷⁵ As		✓		¹⁶⁹ Tm	✓	✓	✓
⁸⁵ Rb			✓	¹⁷² Yb	✓	✓	✓
⁸⁸ Sr	✓	✓	✓	¹⁷⁵ Lu	✓	✓	✓
⁸⁹ Y	✓	✓	✓	²⁰⁸ Pb	✓	✓	✓
⁹⁰ Zr		✓	✓	²³² Th	✓	✓	✓
¹¹¹ Cd		✓		²³⁸ U	✓	✓	✓

Table 5.3: Elements and isotopes analysed for different minerals during LA ICP-MS. Apatite¹ and Apatite² denote apatite analyses in 2012 and 2013, respectively.

5.3 HREE-bearing minerals associated with carbonatite (1): apatite and xenotime from Songwe

Apatite occurs in all the rock types found at Songwe. It varies in its habit, CL colour and trace element content.

5.3.1 Textural variations between apatite types

The different types of apatite from the carbonatite have been divided on the basis of their texture into five groups (Table 5.4). One apatite type is found in fenite outside the main carbonatite body (Ap-0). Within the main carbonatite, three apatite types have been distinguished on the basis of textural relations (Ap-1, Ap-2 and Ap-3). Another type is present in the apatite-fluorite veins predominantly found outside the main carbonatite intrusion (Ap-4).

Ap-0 (Fenite)

Ap-0 is characterised by large (typically greater than 0.1 mm), partially fragmented anhedral grains (Fig. 5.2). It is found in association with altered K-feldspar and locally minor zircon grains. Under CL it luminesces purple–mauve, and is compositionally homogeneous under BSE.

Apatite type	Rock types present	Texture	CL colour	BSE features
Ap-0	Fenite	anhedral, fragmented	purple-mauve	featureless
Ap-1	Calcite-carbonatite (C1)	ovoid - core	purple	zoning, spongy and fractured
Ap-2	Calcite-carbonatite (C1)	ovoid - rim	blue-green	zoning and fractures
Ap-3	Calcite-carbonatite (C2) and Fe-rich carbonatite (C3)	anhedral, stringers	white-purple, uncommon yellow	dark, spongy, ovoid patches
Ap-4	Ap-Flr veins (C4)	anhedral, occasional euhedral overgrowths	tan-green, purple-white overgrowths	spongy, with xenotime-(Y) overgrowths

Table 5.4: Summary of the textural differences between the apatite at the Songwe Hill carbonatite.

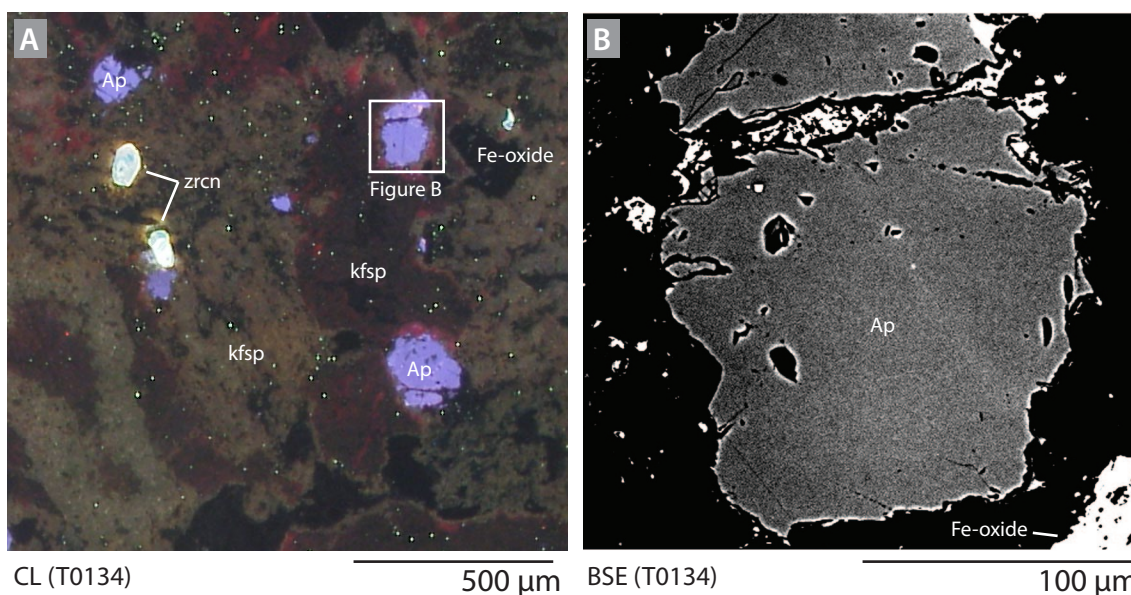


Figure 5.2: CL (A) and BSE (B) images of Ap-0 in sample T0134. Note the partial fragmentation, anhedral shape and compositional homogeneity. Abbreviations: zrcn, zircon; ap, apatite; kfsp, K-feldspar.

Ap-1, Ap-2, (C1—Early igneous carbonatite)

Cores of ovoid grains in C1 calcite carbonatite are termed Ap-1. The rims of these grains are called Ap-2. Ovoid grains are uncommon, and have been identified in only 2 of the samples analysed. The apatite is associated with large (>100 µm) eu-subhedral calcite, eu-subhedral zircon and broken laths of K-feldspar. Cores (Ap-1) and rims (Ap-2) are evident under CL and BSE. Ap-1 is ovoid in shape (Figures 5.3 A–D) and forms grains approximately 50–250 µm in length. Ap-2 forms a 10–75 µm thick overgrowth which partially resorbs Ap-1. Ap-1 luminesces violet and is typically dark under BSE relative to Ap-2 which is lighter under BSE and luminesces light blue under CL.

X-ray maps of Ce and Y counts for Ap-1 and Ap-2 reveal little difference in the chemistry of the two apatite types (Fig. 5.3). They do, however, reveal a clear compositional contrast between Ap-1 and Ap-2 with Ap-3 (see next subsection).

Ap-3 (C2, C3 —Main Songwe apatite)

Ap-3 occurs as an anhedral groundmass and as stringers (Figure 5.4) in calcite-carbonatite (C2), late-stage Fe-rich carbonatite (C3) and in Mn-Fe-veins. In one example (T0206) Ap-3 can be found as an overgrowth on Ap-1/Ap-2 grains (Figures 5.3 B, D–F). As it is found throughout the different carbonatite stages, Ap-3 represents the most volumetrically abundant apatite type found at Songwe. It is associated with a wide range of mineral phases, including fluorite, sulphides (predominantly pyrite, but also rare sphalerite and galena), anhedral calcite, ankerite and broken K-feldspar. Ankerite, in many samples, shows evidence of supergene alteration to calcite and Fe-oxides (e.g. Fig. 5.4 B–C). Ap-3 is texturally complex, but has a similar habit and complexity in all of the carbonatite types. Under CL it commonly luminesces bright white–purple, but some areas luminesce darker purple or greenish-yellow (Fig. 5.4 A–B).

In Fe-rich carbonatite (C3), Ap-3 is cross cut by a LREE-bearing mineral assemblage. This assemblage includes euhedral synchysite-(Ce), barite and strontianite in an anhedral calcite groundmass (e.g. Figures 5.4 C and 4.8 D–E). Vugs, infilled with these minerals, are also found in calcite-carbonatite (C2) and Fe-rich carbonatite (C3), indicating replacement or infilling of the earlier carbonatite.

Ovoid, or pseudo-ovoid, areas are dispersed randomly throughout Ap-3. These features are conspicuous in X-ray count maps (e.g. Fig 5.4 E–F), where the ovoid areas have lower REE concentration than the rest of the Ap-3. These areas are darker under BSE and appear spongy.

Variations in the Ap-3 composition are clearly distinguished by X-ray count maps for Y and Ce. Brighter areas, under both CL and BSE, have higher X-ray counts for Y than the darker ovoid patches (Figures 5.3 D–F and 5.4 D–F). Ce

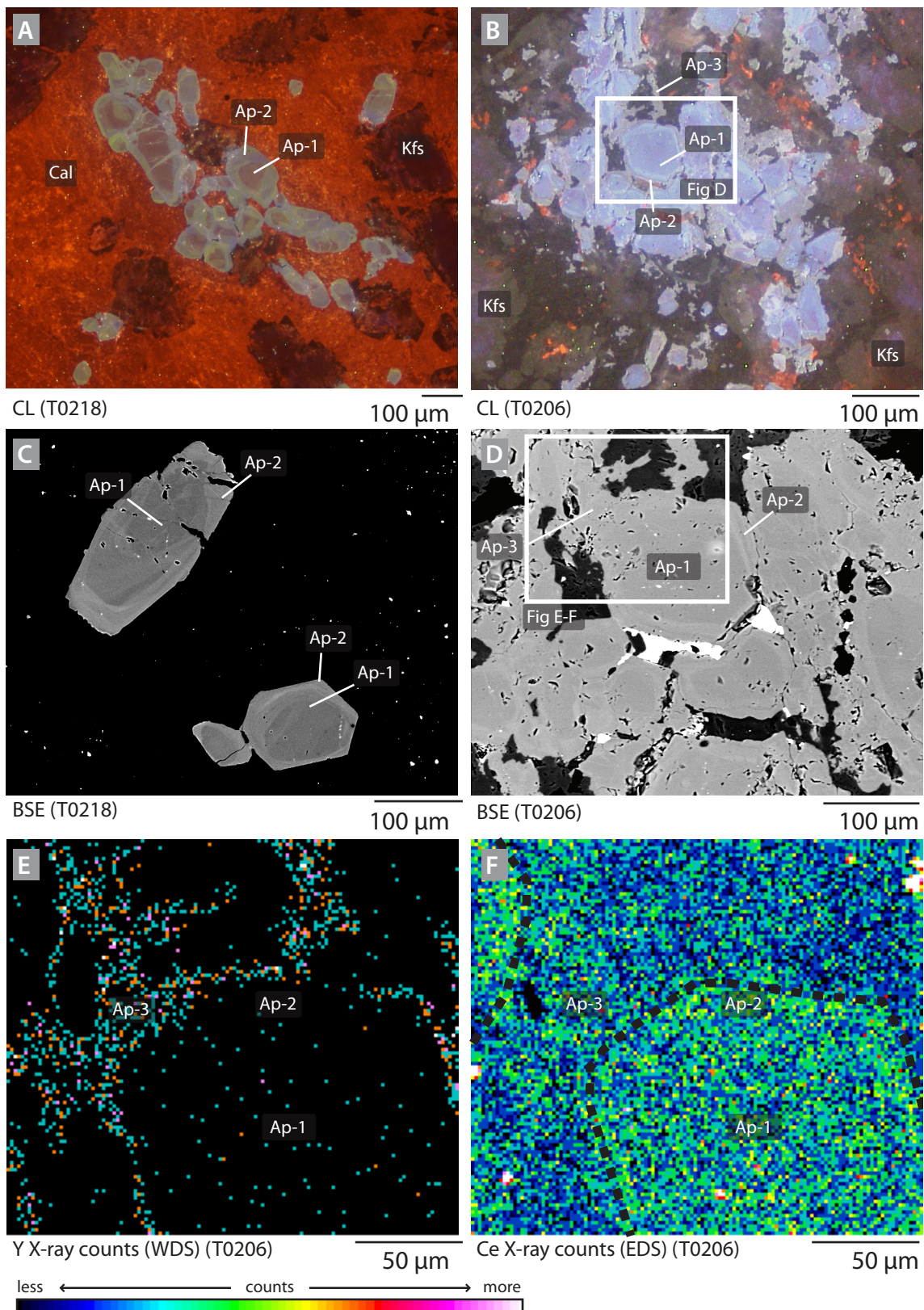


Figure 5.3: CL (A–B), BSE (C–D) and X-ray count (E–F) images of Ap-1, 2 and 3 from C1 calcite carbonatite. Note the rounded/euhedral shape, zoning between Ap-1 and Ap-2, and juxtaposition with Ap-3. X-ray count maps show that Ap-1 and Ap-2 have a lower Y concentration, but greater Ce concentration than Ap-3. X-ray count maps are from WDS and EDS spectrometers for Y and Ce, respectively, and thus the intensities of the colour scales are not comparable and no meaning can be attributed to concentration. Abbreviations: ap, apatite; kfs, K-feldspar; cal, calcite.

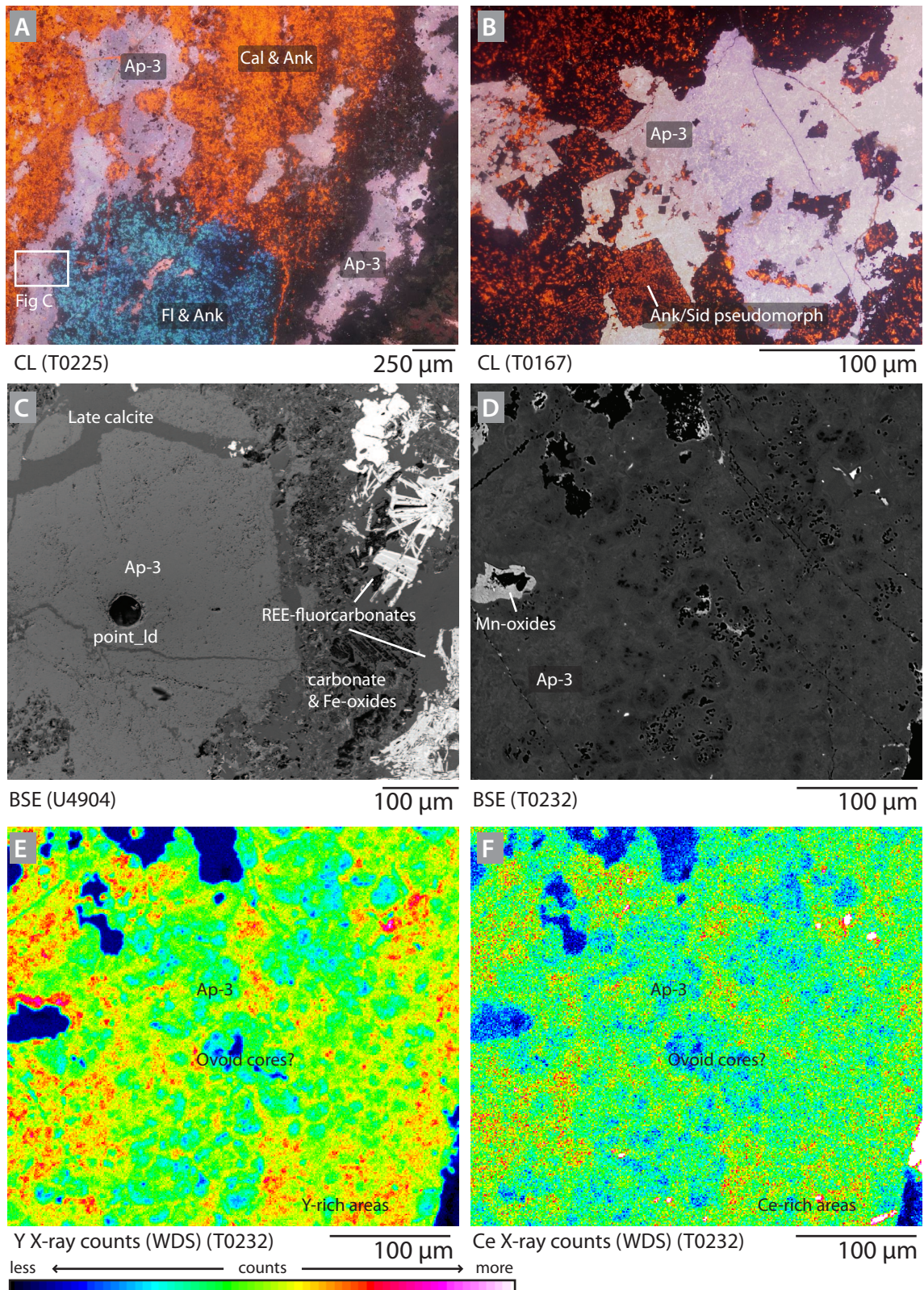


Figure 5.4: CL (A–B), BSE (C–D) and X-ray count (E–F) images of Ap-3 from C2 calcite carbonatite (A, D–F) and C3 Fe-rich carbonatite (B–C). Hotter colours in E–F correspond to areas with higher X-ray counts for Y (E) and Ce (F). Note the variation in the REE concentrations in different parts of the apatite, and that the areas with lower REE intensity correspond to spongy pseudo-ovoid regions.

counts, in Figure 5.4 F, also appear higher where Y counts are high. This is not seen in Figure 5.3 F, but this may be due to the higher LOD of EDS detectors.

Ap-4 (C4 — apatite-fluorite veins)

Ap-4 occurs in apatite-fluorite veins found outside the main carbonatite intrusion at Chenga Hill, as well as at depth in drill hole PX016 (Chapters 3 and 4). It is texturally similar to Ap-3, being composed of an aggregation of eu-subhedral grains, each with a resorbed core and a recrystallised overgrowth (Fig. 5.5). This apatite type is associated with fluorite (see section 5.3.3), calcite, barite, quartz and xenotime-(Y). It displays tan-green and purple-white luminescence, similar to Ap-3 (Fig. 5.4) but has a considerably more complex texture under BSE than under CL (Fig. 5.5). The apatite comprises intergrown eu-subhedral crystals with complex zoning. Earlier remnant dark cores are largely overgrown by bright, spongy apatite. This is commonly overgrown by xenotime-(Y).

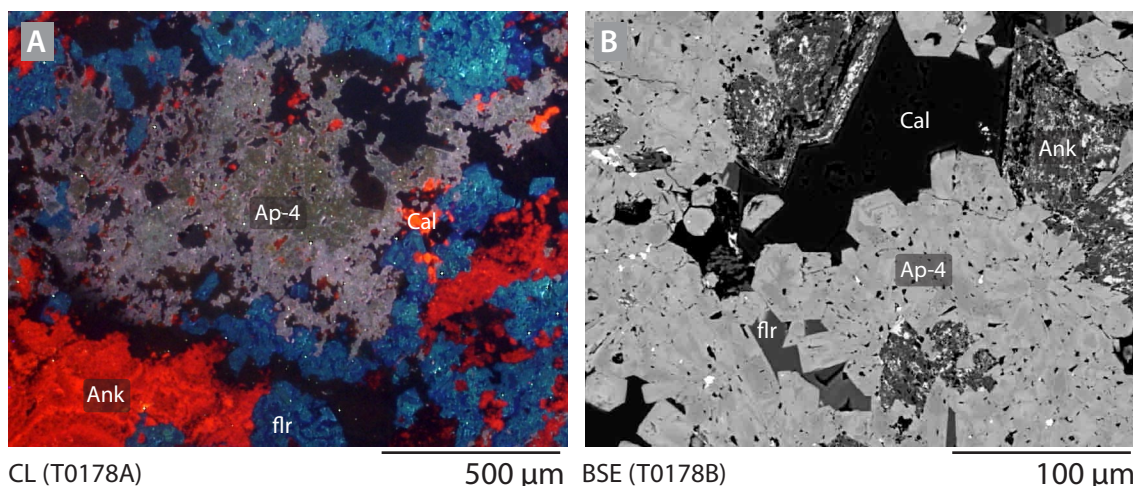


Figure 5.5: CL (A) and BSE (B) images of Ap-4 from C4 apatite-fluorite veins.

Xenotime-(Y) from C4 apatite-fluorite veins

Minor xenotime-(Y) crystallisation follows the formation of apatite and carbonate in the apatite-fluorite veins (C4) at Chenga Hill. This xenotime-(Y) occurs in two habits in the C4 apatite-fluorite veins:

1. Xenotime-(Y) associated with rutile, zircon and Fe-oxides (Fig. 5.6 A–C): this xenotime type is uncommon and accounts for approximately 5 modal % of the xenotime present. It is associated with euhedral Fe-oxides (possibly after magnetite?), subhedral rutile and disseminated small zircon crystals. The xenotime commonly overgrows zircon/rutile grains, but also forms euhedral crystals without a zircon/rutile core. Grains typically reach a maximum of 10 μm across. It can be observed and distinguished from the zircon under CL and BSE: zircon luminesces muted blue, while the xenotime

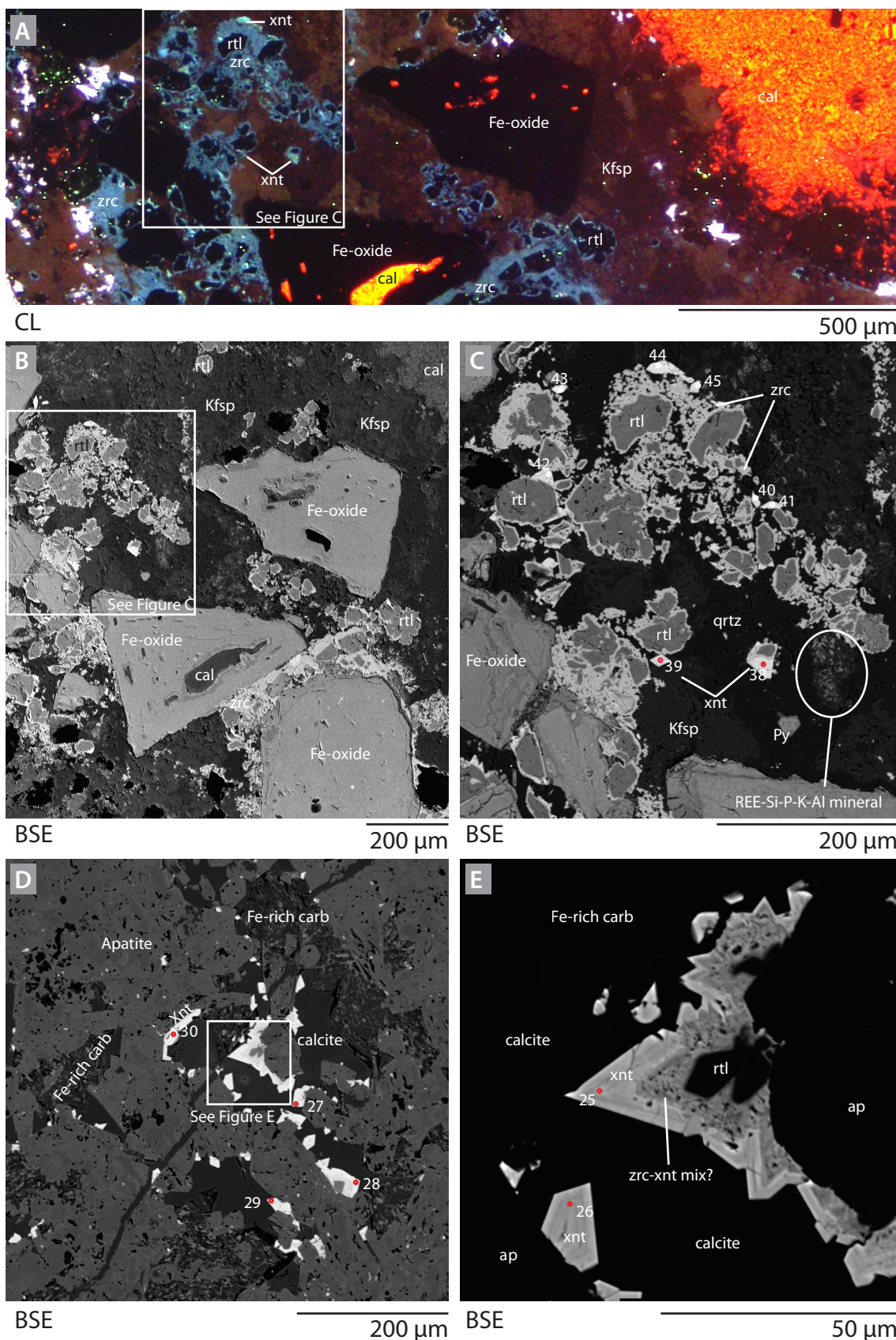


Figure 5.6: CL (A) and BSE (B–E) images of xenotime from Chenga Hill C4 carbonatite samples T0178B and T0178C. Xenotime mineralisation is divided into two types: (A–C) associated with schlieren of Fe-oxides, rutile and zircon; and (D–E) overgrowths on apatite in late calcite, with associated rutile and possible zircon growth. Xenotime displays blue luminescence under CL. Numbers refer to analyses in Tables 5.9 and 5.10.

luminesces a teal colour, and is brighter under BSE (Fig. 5.6 A–C). The Fe-oxide–rutile–zircon–xenotime assemblage forms schlieren, associated with fenite clasts in the apatite-fluorite veins.

2. Xenotime-(Y) overgrowing apatite (Fig. 5.6 D–E): this xenotime type is the most abundant (approximately 95 modal % of the xenotime present). It forms overgrowths on apatite in recrystallised calcite, which can reach up to 50 μm across. No luminescence was observed in this xenotime type, although it may be obscured by luminescence from the neighbouring apatite. The xenotime is finely zoned, and many grains have a small rutile core, and a spongy Zr-rich phase, similar to the zircon associated with the zircon, rutile and Fe-oxide schlieren. It is associated with late fluorite and recrystallised calcite.

5.3.2 Chemical variation between the apatite types at Songwe

Representative and average major element analyses of apatite by EPMA for apatite are presented in Tables 5.5 and 5.6. Average trace element results by LA ICP-MS for each apatite type are shown in Tables 5.7 and 5.8.

There are some similarities between all the apatite types at Songwe. All the apatite is fluorapatite. F concentrations are greater than 2 %, and F does not correlate with any other analysed element. In all samples apatite has low MnO, SO₃ and SiO₂ concentrations, typically below the LOD on the EPMA. SrO and Na₂O concentrations are typically between 1 and 4 wt. %, and 0.1 and 1.4 wt. %, respectively. REE concentrations are variable, with Ce₂O₃ ranging from below the EPMA detection limit of 0.1 wt. % to 1.5 wt. % and Y₂O₃ from below detection (approximately 0.1 %) to 3.5 wt. %.

The texturally-different apatite types from the various carbonatite generations are compositionally varied but few distinctive differences are notable. There are commonly overlaps between the chemistry of each apatite type, and for Ap-3 there is little systematic variation between apatite from the different carbonatite types (C1–3). Analyses from each apatite generation have been assigned a particular symbol, while analyses from different carbonatite types have been assigned different colours (Figures 5.7, 5.8 and 5.9). The general patterns in the data fall into three groups: fenite (Ap-0, ×); early apatite (Ap-1 and -2, ● and ○ respectively); and later apatite (Ap-3 and -4, ■, ■, ■, and ▲).

Ap-0 (fenite)

Ap-0 has the highest SiO₂ concentration of all the analysed apatite types. It also has higher SO₃ concentrations than apatite from the carbonatite, but lower U, Th and Na. It is strongly enriched in the LREE, and has a near-linear, with a

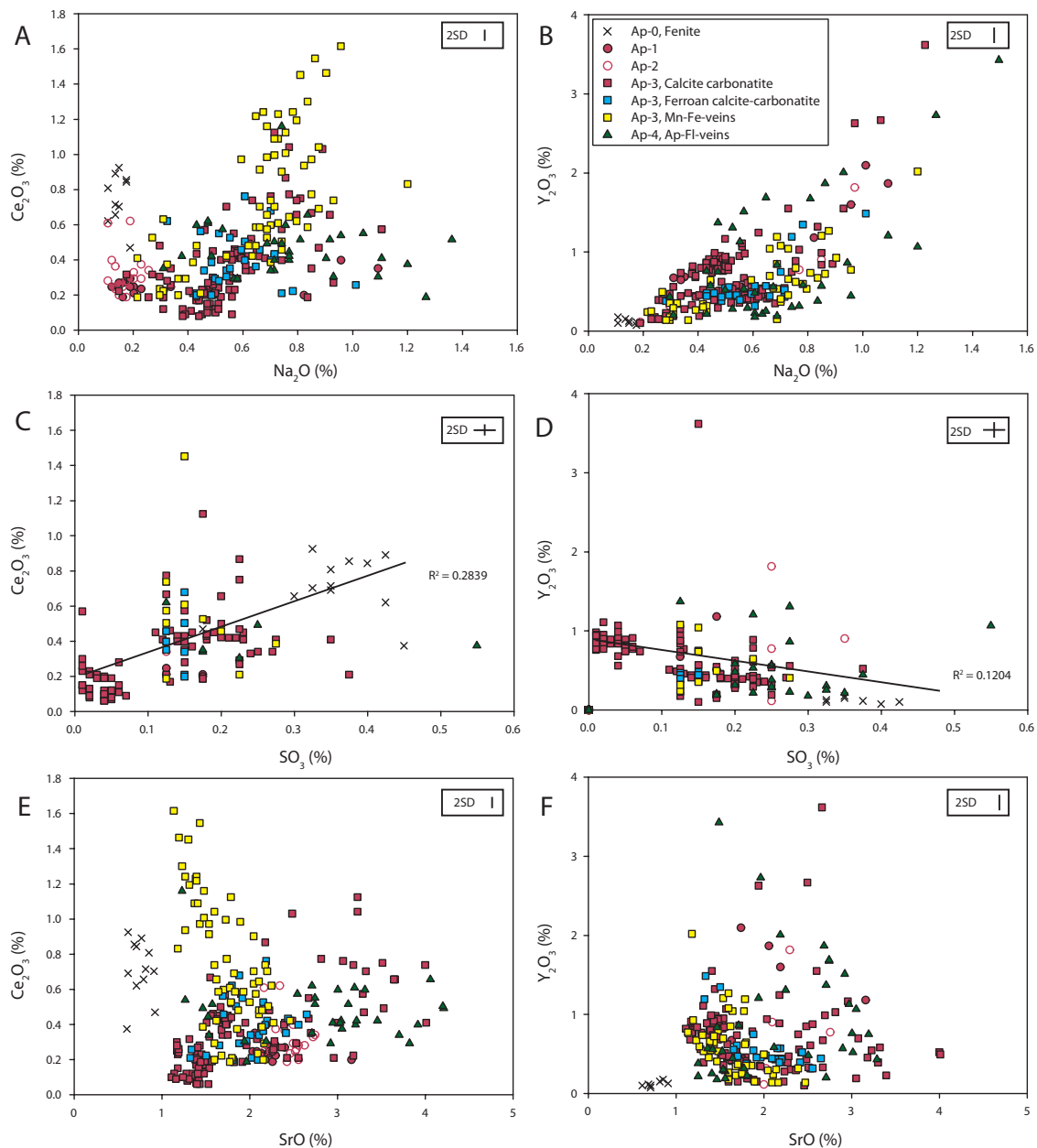


Figure 5.7: Variations in major element concentration of Songwe apatite from EPMA data. Individual carbonatite types are depicted by the colour of the symbols used, while the shape of the symbol indicates the different types of apatite. Typical error from two standard deviations of repeat analyses of an internal standard are shown in a separate box. Analyses below the LOD have been removed for clarity.

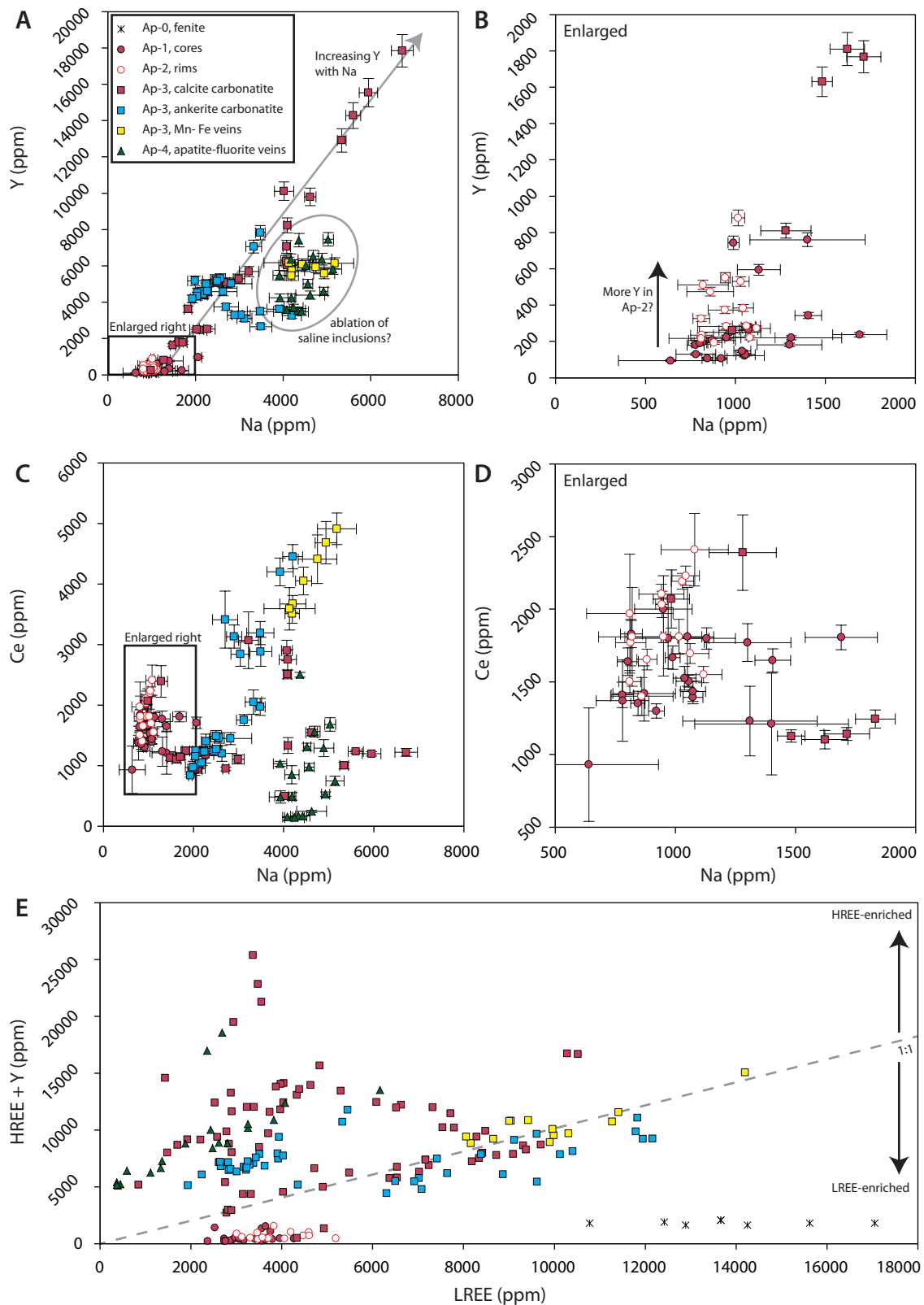


Figure 5.8: Variation in REE and trace element concentrations in Songwe apatite from LA ICP-MS data. Individual carbonatite types are depicted by the colour of the symbols used, while the shape of the symbol indicates the different types of apatite. Error bars represent 2 standard errors derived for each integration.

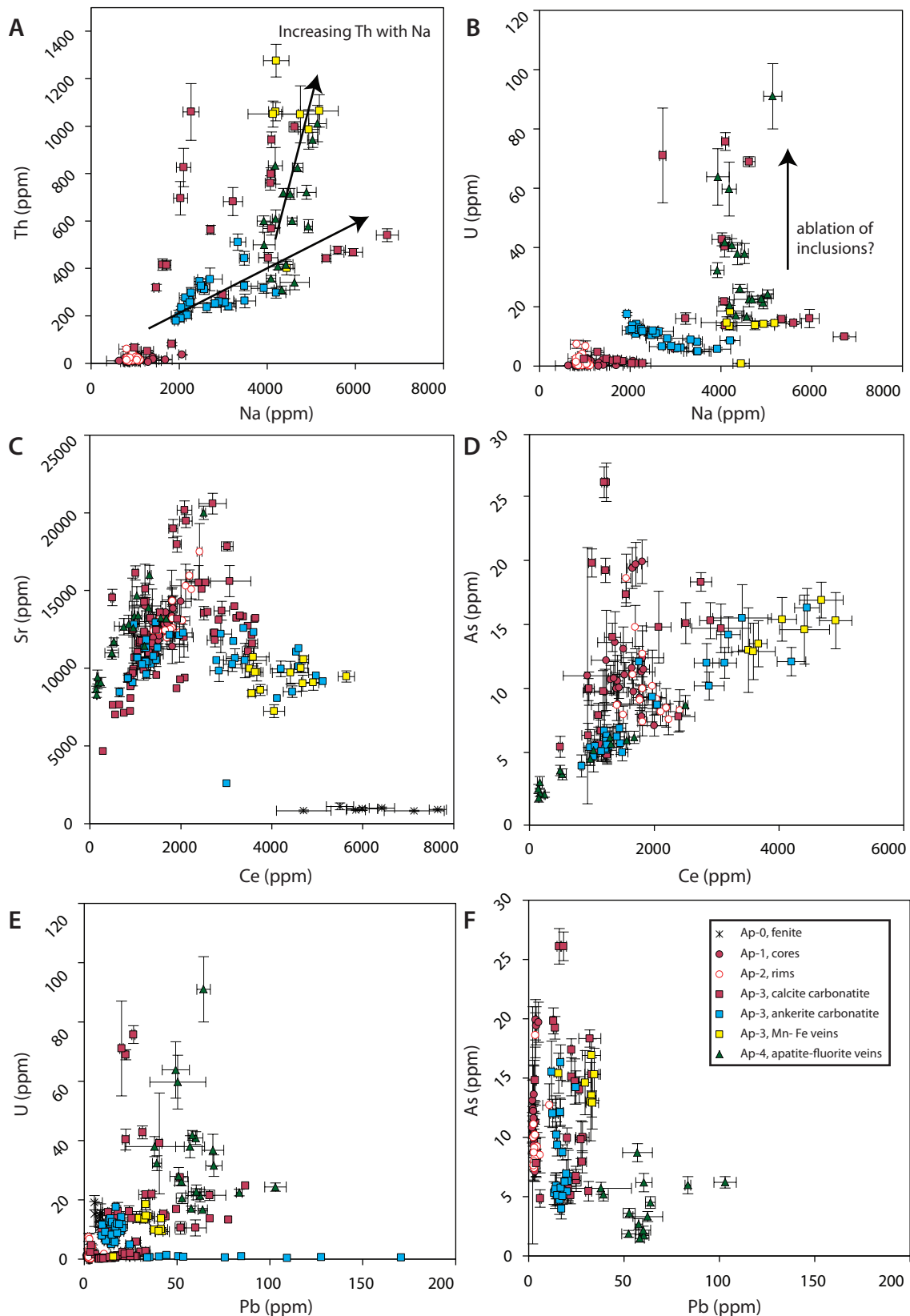


Figure 5.9: Variation in REE and trace element concentrations in Songwe apatite from LA ICP-MS data. Individual carbonatite types are depicted by the colour of the symbols used, while the shape of the symbol indicates the different types of apatite. Error bars represent 2 standard errors derived for each integration.

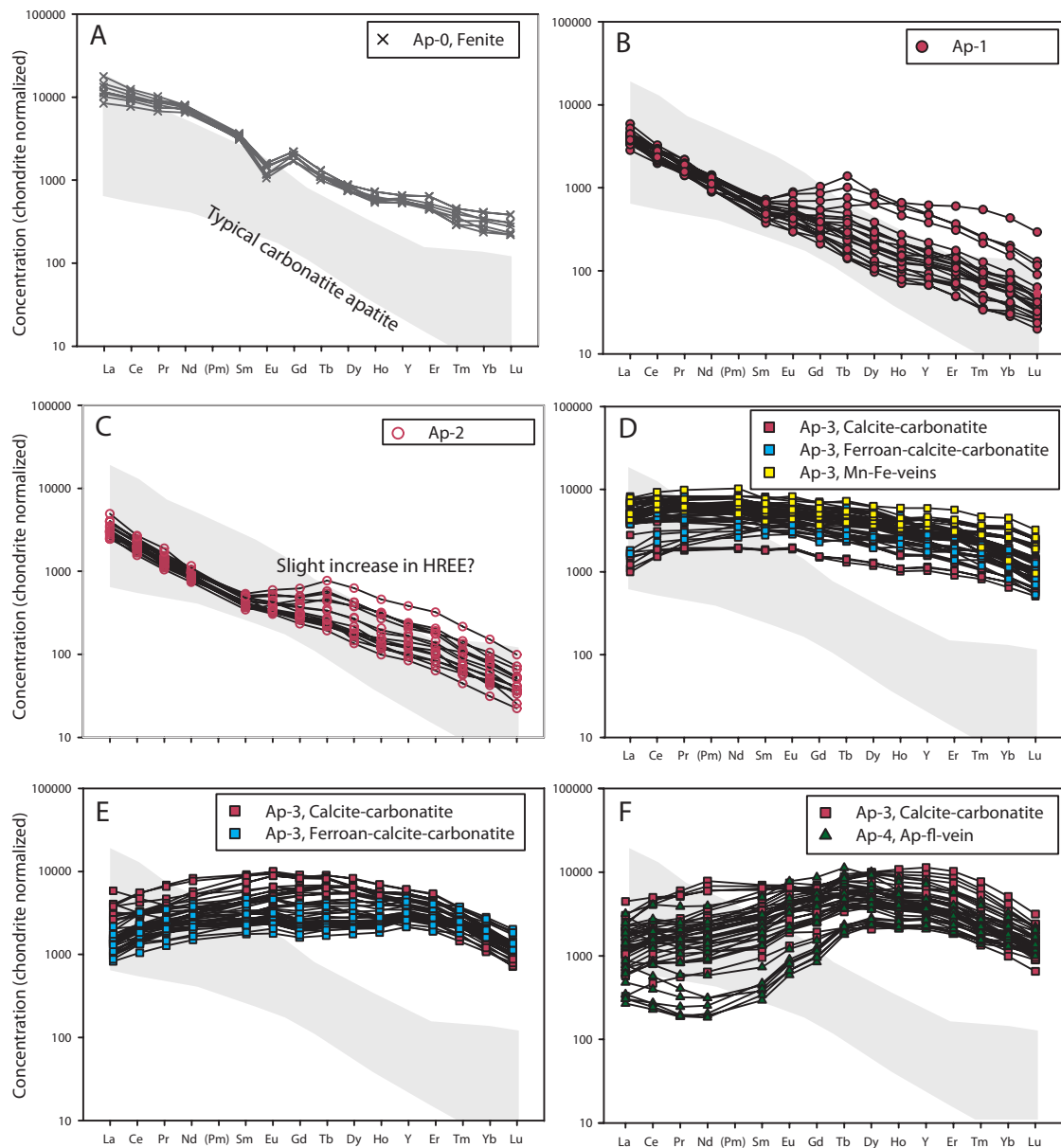


Figure 5.10: Distribution of the REE + Y in apatite samples from fenite, calcite carbonatite, Fe-rich carbonatite, Mn-Fe-veins and apatite-fluorite veins. The plots show the most common REE distributions in the apatite from Songwe: (A) early Ap-0, (B) Ap-1 and (C) Ap-2 with LREE-rich distributions, but with a minor increase in the magnitude of the HREE distribution in Ap-2; (D) flat, MREE-rich distribution found in Ap-3 from some calcite-carbonatite, Fe-rich carbonatite and Mn-Fe veins; (E) MREE-rich distribution from Ap-3 analyses from calcite-carbonatite and Fe-rich carbonatite; (F) LREE-poor and M/HREE-rich Ap-4 from some calcite carbonatite and from Apatite-fluorite veins. The REE distributions are normalised using the values of McDonough and Sun (1995). Background shaded values represent the range of REE distributions in apatite from other carbonatite complexes, re-plotted after Hornig-Kjarsgaard (1998).

Rock type Apatite type Symbol	Fenite Ap-0 X			Calcite carbonatite (C1)									Calcite carbonatite (C2)											
	T0134	Avg (12)	2sd	Ap-1 ● T0206	Avg (15)	2sd	Ap-1 ● T0218	Avg (24)	2sd	Ap-2 ○ T0206	Avg (3)	2sd	Ap-2 ○ T0218	T0218	Avg (26)	2SD	Ap-3 ■ T0327	T0327	Avg (24)	2sd	Ap-3 ■ T0322	T0322	Avg (23)	2sd
Na ₂ O	0.15	0.14	0.01	0.96	0.45	0.18	0.23	0.18	0.03	0.11	0.15	0.08	0.77	0.19	0.24	0.09	0.65	0.63	0.58	0.02	0.56	0.47	0.48	0.02
SiO ₂	0.90	0.81	0.06		0.07	0.07	0.06	0.05	0.02		0.01	0.03		0.60	0.05	0.06	0.01	0.01	0.02	0.01		0.01	0.02	0.02
P ₂ O ₅	41.68	42.40	0.20	41.25	42.94	0.55	42.78	43.33	0.14	43.63	43.78	0.17	42.37	42.17	43.07	0.21	40.62	40.56	40.54	0.09	41.30	40.97	40.82	0.22
CaO	53.53	54.12	0.24	50.02	52.86	0.95	52.93	53.92	0.18	54.26	54.14	0.25	51.52	53.14	53.32	0.30	53.43	52.58	53.07	0.11	53.54	53.70	53.53	0.25
MnO																		0.01	0.02	0.01			0.01	0.01
FeO	0.10	0.12	0.02		0.03	0.05		0.00	0.01		0.08	0.08			0.00	0.01		0.01	0.03	0.03		0.04	0.06	0.02
SrO	0.61	0.73	0.06	2.19	2.03	0.24	2.05	2.12	0.05	2.35	2.38	0.12	2.76	2.34	2.42	0.08	1.64	1.69	1.68	0.04	1.57	1.42	1.41	0.06
Y ₂ O ₃	0.10	0.12	0.02	1.60	0.62	0.38							0.77		0.15	0.16	0.41	0.54	0.43	0.02	1.07	0.85	0.88	0.03
La ₂ O ₃	0.36	0.27	0.04		0.03	0.04		0.02	0.02						0.06	0.04	0.12	0.12	0.13	0.01	0.05	0.01	0.06	0.02
Ce ₂ O ₃	0.93	0.73	0.09	0.40	0.16	0.08		0.09	0.05		0.10	0.20			0.45	0.34	0.42	0.42	0.02	0.19	0.15	0.22	0.04	
Pr ₂ O ₃															0.09	0.06	0.09	0.01		0.02	0.03	0.05	0.01	
Nd ₂ O ₃																	0.36	0.37	0.37	0.02	0.23	0.22	0.22	0.02
SO ₃	0.32	0.37	0.03		0.03	0.03	0.12	0.02	0.02				0.25		0.05	0.04	0.23	0.25	0.18	0.02	0.04	0.01	0.03	0.02
F	5.60	5.24	0.22	6.17	6.01	0.48	5.82	5.76	0.17	5.78	5.86	0.09	5.85	5.25	6.08	0.26	4.76	5.06	4.91	0.08	4.60	5.00	4.85	0.11
Sub-total	103.41	104.73	0.32	102.58	105.20	1.01	104.00	105.48	0.38	106.13	106.50	0.37	104.29	104.31	105.65	0.33	103.05	102.52	102.67	0.15	103.57	103.00	102.95	0.47
O=F ₂ , Cl ₂	1.98	2.18	0.08	2.60	2.53	0.20	2.45	2.43	0.07	2.43	2.47	0.04	2.46	2.21	2.56	0.11	2.00	2.13	2.07	0.03	1.94	2.02	2.04	0.05
Total	101.42	102.56	0.26	99.99	102.67	0.92	101.55	103.06	0.34	103.70	104.04	0.35	101.83	102.10	103.10	0.27	101.05	100.39	100.61	0.14	101.63	100.98	100.90	0.44

Rock type Apatite type Symbol	Calcite carbonatite (C2)				Ap-3				Ap-3				Fe-rich carbonatite (C3)				Ap-3						
	T0324	T0324	Avg (18)	2SD	Ap-3 ■ T0262	T0262	Avg (13)	2SD	Ap-3 ■ T0225	T0225	Avg (33)	2SD	Ap-3 ■ T0206	T0206	Avg (23)	2SD	Ap-3 ■ T0250	T0250	Avg (2)	2SD	Ap-3 ■ T0167	T0167	2SD
Na ₂ O	0.46	0.47	0.45	0.03	0.23	0.22	0.28	0.03	0.42	0.46	0.54	0.07	1.06	1.23	0.52	0.12	0.74	0.78	0.76	0.04	0.35	0.34	0.03
SiO ₂			0.01	0.00							0.01	0.01	0.04		0.02	0.01							
P ₂ O ₅	40.55	39.79	40.38	0.27	40.29	43.01	42.40	0.56	42.23	42.03	41.95	0.21	42.03	41.09	42.78	0.27	42.44	42.39	42.42	0.05	41.13	40.72	0.23
CaO	54.02	54.12	54.08	0.23	52.13	53.91	52.96	0.58	52.72	52.37	51.94	0.41	49.62	49.17	52.65	0.61	52.01	52.37	52.19	0.36	53.42	53.72	0.24
MnO	0.19	0.06	0.05	0.04																			0.03
FeO	0.13	0.28	0.13	0.05	1.39	0.14	0.16	0.21		0.13	0.06	0.06			0.08	0.04							0.03
SrO	1.40	1.24	1.31	0.06	1.60	1.75	1.85	0.12	2.54	3.30	2.74	0.19	2.50	2.66	2.02	0.20	1.32	1.50	1.41	0.18	2.07	1.79	0.06
Y ₂ O ₃	0.99	0.84	0.82	0.06	0.15		0.23	0.09		0.39	0.46	0.10	2.67	3.62	0.97	0.39	1.19	1.35	1.27	0.15			
La ₂ O ₃	0.03	0.04	0.04	0.01							0.05	0.03			0.01	0.02							
Ce ₂ O ₃	0.06	0.10	0.11	0.02			0.11	0.07			0.33	0.12			0.10	0.06	0.21	0.22	0.22	0.01			0.07
Pr ₂ O ₃	0.08	0.01	0.03	0.01																			
Nd ₂ O ₃	0.11	0.13	0.14	0.02																			
SO ₃	0.04	0.04	0.05	0.01		0.12	0.08	0.05		0.22	0.14	0.04		0.15	0.06	0.04							0.03
F	4.74	5.00	5.05	0.11	5.81	5.68	5.78	0.22	5.04	6.01	5.87	0.18	6.33	5.92	5.66	0.21	5.64	5.60	2.81	0.41	2.52	2.69	0.06
Sub-total	103.06	102.33	102.82	0.45	101.60	104.84	103.85	1.03	102.96	104.91	104.08	1.42	104.24	103.83	104.88	0.40	103.56	104.22	103.89	0.66	99.62	99.06	0.45
O=F ₂ , Cl ₂	2.00	2.10	2.12	0.04	2.45	2.39	2.43	0.09	2.12	2.53	2.47	0.08	2.67	2.49	2.38	0.09	2.37	2.36	2.37	0.02	1.11	1.05	0.02
Total	101.06	100.23	100.70	0.44	99.15	102.45	101.42	1.02	100.83	102.38	101.61	1.35	101.58	101.34	102.50	0.36	101.18	101.86	101.52	0.68	98.50	98.01	0.45

Table 5.5: Representative and average EPMA analyses of apatite from Songwe (part 1). Symbols indicate how these samples are represented graphically.

Rock type	Fe -rich carbonatite (C3)				Ap-FI-veins (C4)				Ap-4			Ap-4			Mn-Fe veins				Ap-3			
Apatite type	Ap-3				Ap-4				Ap-4			Ap-4			Ap-3				Ap-3			
Apatite type	■				▲				▲			▲			■				■			
	U4904	U4904	Avg (24)	2SD	T0134	T0134	Avg (76)	2SD	T0178C	Avg (49)	2SD	U4909	U4909	Avg (24)	2SD	U4927	U4927	Avg (37)	2SD	T0227	Avg (34)	2SD
Na ₂ O	0.61	0.61	0.55	0.04	0.49	0.53	0.54	0.04	0.84	0.69	0.07	0.78	1.20	0.68	0.09	0.73	0.67	0.61	0.08	0.69	0.64	0.07
SiO ₂			0.02	0.04			0.02	0.02		0.01	0.01	0.32		0.04	0.03			0.01	0.01		0.01	0.01
P ₂ O ₅	42.07	42.19	42.40	0.16	41.18	40.38	40.75	0.17	41.29	40.97	0.27	41.20	41.29	42.15	0.31	42.35	42.39	41.74	0.17	42.42	41.83	0.22
CaO	52.01	51.94	52.17	0.23	54.11	53.97	53.16	0.29	53.17	52.02	0.44	51.64	49.70	52.33	0.47	51.76	51.97	51.97	0.40	51.97	52.70	0.31
MnO							0.01	0.01													0.01	0.01
FeO		0.15	0.10	0.03		0.26	0.08	0.02	0.12	0.06	0.06	0.22		0.07	0.05			0.07	0.06		0.03	0.03
SrO	2.55	1.84	2.06	0.11	2.02	1.74	2.27	0.15	1.25	2.27	0.22	2.12	3.05	2.12	0.25	1.38	1.40	1.64	0.12	1.62	1.93	0.08
Y ₂ O ₃	0.32		0.44	0.07					0.38	0.32	0.21	0.58	1.07	0.68	0.19	0.66	0.55	0.44	0.12	0.85	0.27	0.15
La ₂ O ₃			0.03	0.03			0.00	0.01		0.07	0.05			0.01	0.03			0.10	0.05		0.06	0.04
Ce ₂ O ₃	0.40	0.50	0.39	0.07			0.05	0.04		0.16	0.08		0.37	0.12	0.08	1.23	1.24	0.80	0.16	0.66	0.48	0.10
Pr ₂ O ₃										0.19	0.09											
Nd ₂ O ₃										0.12	0.04							0.02	0.02		0.04	0.03
SO ₃	0.12	0.15	0.06	0.03			0.09	0.02	0.25	0.12	0.04	0.20	0.55	0.19	0.06							
F	4.86	4.66	5.29	0.16	3.14	2.90	3.14	0.13	5.41	5.64	0.31	7.52	5.59	6.00	0.33	4.98	4.52	5.89	0.28	4.79	3.58	0.50
Cl							0.00	0.00						0.00	0.01							
Sub-total	102.94	102.05	103.50	0.30	100.66	100.11	100.13	0.40	102.71	100.27	0.67	104.59	102.83	104.40	0.59	103.09	102.74	103.29	0.49	103.09	101.59	0.73
O=F ₂ , Cl ₂	2.05	1.96	2.23	0.07	1.21	1.34	1.32	0.05	2.28	1.44	0.17	3.17	2.35	2.53	0.14	2.10	1.90	2.48	0.12	2.10	1.51	0.20
Total	100.90	100.08	101.28	0.27	99.46	98.77	98.81	0.37	100.43	98.83	0.53	101.42	100.47	101.87	0.52	100.99	100.83	100.81	0.41	100.99	100.08	0.54

Table 5.6: Representative and average EPMA analyses of apatite from Songwe (part 2). Symbols indicate how these samples are represented graphically.

Apatite type Symbol Sample	Ap-0 ×		Ap-1 ●		Ap-2 ○		Ap-3 ■		Ap-3 ■		Ap-3 ■		Ap-3 ■		Ap-3 ■		Ap-3 ■			
	T0134 n = 8	2SD	T0218 n = 23	2SD	T0218 n = 15	2SD	T0324 n = 11	2SD	T0206 n = 2	2SD	T0202 n = 7	2SD	T0322 n = 15	2SD	T0234 n = 5	2SD	T0232 n = 2	2SD	T0225 n = 6	2SD
Na			1085	136	945	56			2926	2188	5006	1001			3691	484				
Mg			30	10	21	2			176	188	14	2			91	89				
Mn			270	16	278	36			174	53	97	22			136	57				
Fe			121	36	135	65			511	639	528	363			1997	996				
As			12	1	10	2	<i>n.a.</i>	<i>n.a.</i>	5	1	19	4	<i>n.a.</i>	<i>n.a.</i>	14	3	<i>n.a.</i>	<i>n.a.</i>	<i>n.a.</i>	<i>n.a.</i>
Sr	935	67	12580	480	13617	848	8553	1188	13025	3050	14154	918	10696	893	13258	1450	11340	500	19170	920
Y	921	55	290	100	382	95	6611	935	6865	6490	11956	3376	7321	832	6066	592	10025	70	5443	1189
Zr	2	1	1	0	1	0	6	2	131	260	158	101	1	0	250	183	<i>n.a.</i>	<i>n.a.</i>	<i>n.a.</i>	<i>n.a.</i>
Cd	<i>n.a.</i>	<i>n.a.</i>	0.21	0.09	0.27	0.17	<i>n.a.</i>	<i>n.a.</i>	<i>n.a.</i>	<i>n.a.</i>	0.02	0.08	<i>n.a.</i>	<i>n.a.</i>	0.24	0.32	<i>n.a.</i>	<i>n.a.</i>	<i>n.a.</i>	<i>n.a.</i>
Ba	28	32	39	10	36	10	97	54	79	11	120	78	95	15	88	25	160	80	170	9
La	2921	486	949	64	1134	123	217	57	419	554	374	56	446	107	634	264	969	49	852	255
Ce	6154	652	1546	107	1863	149	815	192	868	752	1209	152	1336	200	2466	706	3525	90	2276	388
Pr	789	72	159	9	184	15	146	32	103	48	195	28	240	31	447	118	658	27	382	34
Nd	3430	176	531	34	615	38	841	181	479	75	1204	225	1374	169	2718	741	3840	300	2298	322
Sm	501	25	81	7	95	7	371	73	229	104	646	104	613	80	894	168	1411	52	948	278
Eu	77	8	28	4	33	4	176	32	146	79	331	49	276	35	353	55	573	32	419	129
Gd	394	27	82	17	106	17	741	132	559	353	1187	188	1060	134	1007	129	1757	70	1365	420
Tb	42	3	14	5	19	5	163	25	125	95	261	49	205	25	176	17	342	3	245	69
Dy	201	11	71	23	100	26	1208	179	978	925	1995	426	1420	164	1117	106	2136	32	1335	355
Ho	34	3	12	4	16	4	238	34	237	237	431	109	267	31	222	20	398	5	238	56
Er	82	9	25	9	32	8	571	78	641	618	1095	318	632	71	538	58	897	25	478	95
Tm	9	1	3	1	3	1	58	7	72	66	121	36	67	7	62	7	94	3	50	7
Yb	52	7	14	6	16	4	265	29	323	284	527	143	288	30	309	38	425	21	220	22
Lu	7	1	1	1	2	0	25	3	40	35	50	13	27	3	32	4	48	1	23	2
Pb	8	1	3	0	4	1	42	16	19	25	19	4	10	1	28	4	32	3	50	10
Th	96	11	16	4	23	8	358	39	263	364	633	177	265	32	619	183	771	23	3031	916
U	14.2	1.9	1.0	0.4	2.0	1.2	14.9	3.7	22.1	41.2	38.8	23.5	0.2	0.1	19.5	11.6	2.6	0.2	19.7	8.7

Table 5.7: Average LA ICP-MS data for apatite from Songwe fenite and calcite-carbonatite samples. Cells are empty where the blank concentrations were too high for the data to be meaningful; *n.a.*, not analysed. Symbols are representative of how these samples are plotted graphically.

Apatite type Symbol Sample	Ap-3 ■ T0327 n = 16		Ap-3 ■ T0262 n = 6		Ap-3 ■ U4904 n = 8		Ap-3 ■ T0167 n = 23		Ap-3 ■ T0317 n = 11		Ap-3 ■ T0227 & U4927 n = 13		Ap-4 ▲ U4909 n = 14		Ap-4 ▲ T0134 n = 3		Ap-4 ▲ T0178C n = 4	
	2SD		2SD		2SD		2SD		2SD		2SD		2SD		2SD		2SD	
Na			1870	252	3356	364	2405	195			4547	313	4485	175	4417	738		
Mg			82	67	169	127	25	14			46	11	125	57	89	35		
Mn			224	113	511	78	143	17			380	44	214	24	211	53		
Fe			998	531	666	271	185	231			617	273	1858	539	1307	480		
As	<i>n.a.</i>	<i>n.a.</i>	7	2	13	1	6	1	<i>n.a.</i>	<i>n.a.</i>	15	1	4	1	<i>n.a.</i>	<i>n.a.</i>	<i>n.a.</i>	<i>n.a.</i>
Sr	13068	739	10535	799	10504	863	10764	489	9903	1678	9410	525	12247	1784	12157	1180	11383	2338
Y	4175	291	2115	343	3305	239	4997	395	4848	557	6520	552	5129	761	5467	1263	8138	4365
Zr	57	12	54	8	8	3	195	26	65	26	45	20	1273	220	<i>n.a.</i>	<i>n.a.</i>	<i>n.a.</i>	<i>n.a.</i>
Cd	<i>n.a.</i>	<i>n.a.</i>	0.37	0.16	0.17	0.22	0.15	0.11	<i>n.a.</i>	<i>n.a.</i>	0.40	0.39	0.18	0.11	<i>n.a.</i>	<i>n.a.</i>	<i>n.a.</i>	<i>n.a.</i>
Ba	76	15	144	40	87	7	69	7	161	41	116	13	101	14	191	47	85	16
La	1045	78	319	55	1019	228	331	34	1440	209	1310	134	283	116	288	83	432	176
Ce	3031	249	1074	83	3232	593	1239	135	3987	502	4211	372	874	390	692	220	892	376
Pr	479	43	193	21	431	68	215	22	628	75	618	59	124	56	96	46	109	49
Nd	2531	239	1170	279	1921	226	1179	119	3016	392	3052	338	628	281	515	291	502	242
Sm	758	69	412	128	552	47	417	43	919	125	764	81	275	113	222	150	222	116
Eu	269	22	164	50	195	12	165	17	327	42	312	31	166	65	126	76	138	75
Gd	874	76	465	148	623	53	484	52	1074	143	928	95	689	249	525	273	706	405
Tb	144	12	71	19	101	7	93	9	184	24	173	18	179	55	128	52	222	125
Dy	907	70	403	85	611	46	645	63	1171	138	1072	92	1148	282	966	320	1624	902
Ho	162	12	73	13	130	10	147	14	208	24	213	23	195	38	199	60	305	164
Er	406	28	187	27	279	19	444	38	473	52	583	68	425	61	487	115	661	332
Tm	53	3	24	2	39	3	62	5	49	5	80	8	48	6	62	16	75	36
Yb	282	18	127	12	194	14	320	22	208	22	476	67	266	29	339	74	371	149
Lu	32	2	14	1	24	2	34	2	20	2	55	7	31	3	38	7	41	14
Pb	19	1	25	2	16	3	16	1	75	27	35	4	61	9	55	10	67	11
Th	462	42	622	236	289	29	273	38	372	79	1311	234	581	103	781	300	905	168
U	1.0	0.1	1.5	0.5	6.2	0.8	11.2	1.0	0.7	0.2	11.7	2.4	27.4	4.7	71.5	19.6	30.5	4.8

Table 5.8: Average LA ICP-MS data for apatite from Songwe Fe-rich carbonatite, Mn-Fe veins and apatite-fluorite vein samples. Cells are empty where the blank concentrations were too high for the data to be meaningful; n.a., not analysed. Symbols are representative of how these samples are plotted graphically.

negative slope, chondrite-normalised distribution, with a low concentration of the HREE, and a small negative Eu-anomaly (Fig. 5.10).

Ap-1, Ap-2, (C1—Early igneous carbonatite)

Ap-1 and Ap-2 have chemical similarities. Their REE contents are positively correlated with Na₂O (Figure 5.7A–B). This trend is closest between the HREE Y₂O₃ and Na₂O in all samples, but is more scattered between Ce₂O₃ and Na₂O. Ap-1, in calcite carbonatite, typically has the lowest TREO¹³, Na₂O, U and Th concentrations and moderate SrO concentration relative to the other apatite types (Figures 5.7 and 5.9). Ap-2 has higher SrO and Ce₂O₃, slightly higher SiO₂ and slightly lower Na₂O concentrations relative to Ap-1. Ap-1 has a REE distribution similar to Ap-0, but with a lower LREE concentration and no Eu anomaly (Fig. 5.10). Ap-2 has the same LREE distribution as Ap-1, but commonly shows a bulge in distribution around Dy, indicating a slight enrichment in the HREE.

Ap-3 (C2, C3 —Main Songwe apatite)

Ap-3 from calcite carbonatite (C2) and Fe-rich carbonatite (C3) has higher Na₂O and REE concentrations than Ap-1 and 2; the SrO concentration varies more widely than in Ap-1 and Ap-2 (Fig. 5.7). The positive correlation between Na₂O and the REE, observed in Ap-1 and Ap-2, is also present in Ap-3 (Fig. 5.8A). This trend is strongest between Na and the HREE, especially in samples from calcite carbonatite. Ap-3 samples have higher concentrations of radioactive elements than Ap-1 and Ap-2, with a high-Th trend and a lower-Th, higher-U trend (Figure 5.9A–B). Increasing concentration of the radioactive elements is correlated with increasing HREE concentration, although there is considerable variation between samples. Variation within Ap-3 from different carbonatite types is also observed. SrO concentrations in apatite from the Mn-Fe-veins have a significantly different trend to the apatite analyses from other carbonatite types, with both Ce₂O₃ and Y₂O₃ negatively correlating with SrO.

The REE distribution of Ap-3 is mid and heavy REE enriched relative to other apatite analyses from carbonatites (Fig. 5.10). These distributions are all smooth, with no anomalies. They can be sub-divided into three groups: (1) HREE-rich, with no MREE bulge; (2) MREE-bulge, centered on Gd-Tb; and (3) LREE-poor, with a strong Dy enrichment (Figure 5.10; B, C and D respectively). Analyses from calcite-carbonatite (C2) include all three of these REE distributions, but analyses from Fe-rich carbonatite (C3) and Mn-Fe-veins are restricted to the more LREE-rich groups, 1 and 2.

¹³Total Rare Earth Oxide

Ap-4 (C4 — apatite-fluorite veins)

Apatite analyses from the apatite-fluorite veins have very similar chemistry to Ap-3 from calcite carbonatite and from Fe-rich carbonatite. Na₂O, SrO and REE concentrations are typically among the highest of all the apatite analysed (Fig. 5.8). In all samples the Na₂O and Y₂O₃ contents of Ap-4 are positively related, while Ce₂O₃ and Na₂O show a weak relationship. Ap-4 samples have among the highest U contents of all the apatite types analysed. The REE distribution of Ap-4 is LREE poor and HREE enriched, with a maximum at Dy (Fig. 5.10 F).

Xenotime from C4 (apatite-fluorite veins)

EPMA analyses of xenotime from C4 apatite-fluorite veins are divided into xenotime associated with apatite and xenotime associated with rutile, zircon and Fe-oxides (e.g. Fig 5.6; Tables 5.10 and 5.9). The EPMA results show that the chemistry of these xenotime types is similar. The only elements which show differences are the radioactive elements UO₂ and ThO₂ (e.g. Figures 5.11 A–C). These elements appear to be slightly more concentrated in the xenotime associated with apatite, compared to the xenotime associated with rutile–zircon–Fe-oxides. This trend is clearer for ThO₂ than for UO₂, as UO₂ concentrations show a large degree of scatter. ThO₂ and SiO₂, in the xenotime associated with apatite, are weakly correlated. SiO₂ also has a weak positive correlation with CaO in both xenotime types. There is little difference between the REE distribution of the xenotime types. Both are enriched in HREE, peaking at Y. No Y or Eu anomalies are present (Fig. 5.11D).

5.3.3 Fluorite from C4 apatite-fluorite veins

Extensive fluorite mineralisation is found in association with Ap-4 in the apatite-fluorite veins. Fluorite is anhedral and appears to crystallise after the formation of apatite. It occurs as stringers or as discreet patches, and is often associated with bright-orange luminescent calcite (Fig. 5.12). It contains many simple liquid–vapour fluid inclusions which will be discussed in chapter 6.

Fluorite was analysed from one sample of the C4 apatite-fluorite veins (U4909). Fourteen analyses were taken from fluid inclusion-poor areas of the fluorite (Table 5.11). The concentrations of most trace elements, including the REE, are low compared to those in apatite. TREE¹⁴ concentration in all analyses is less than 1000 ppm, of which most (>500 ppm) is Y. The high Y concentration appears as a positive Y anomaly on chondrite-normalised REE diagrams (Fig. 5.13). The fluorite is depleted in the L/MREE, with the lowest chondrite-normalised distributions

¹⁴total REE

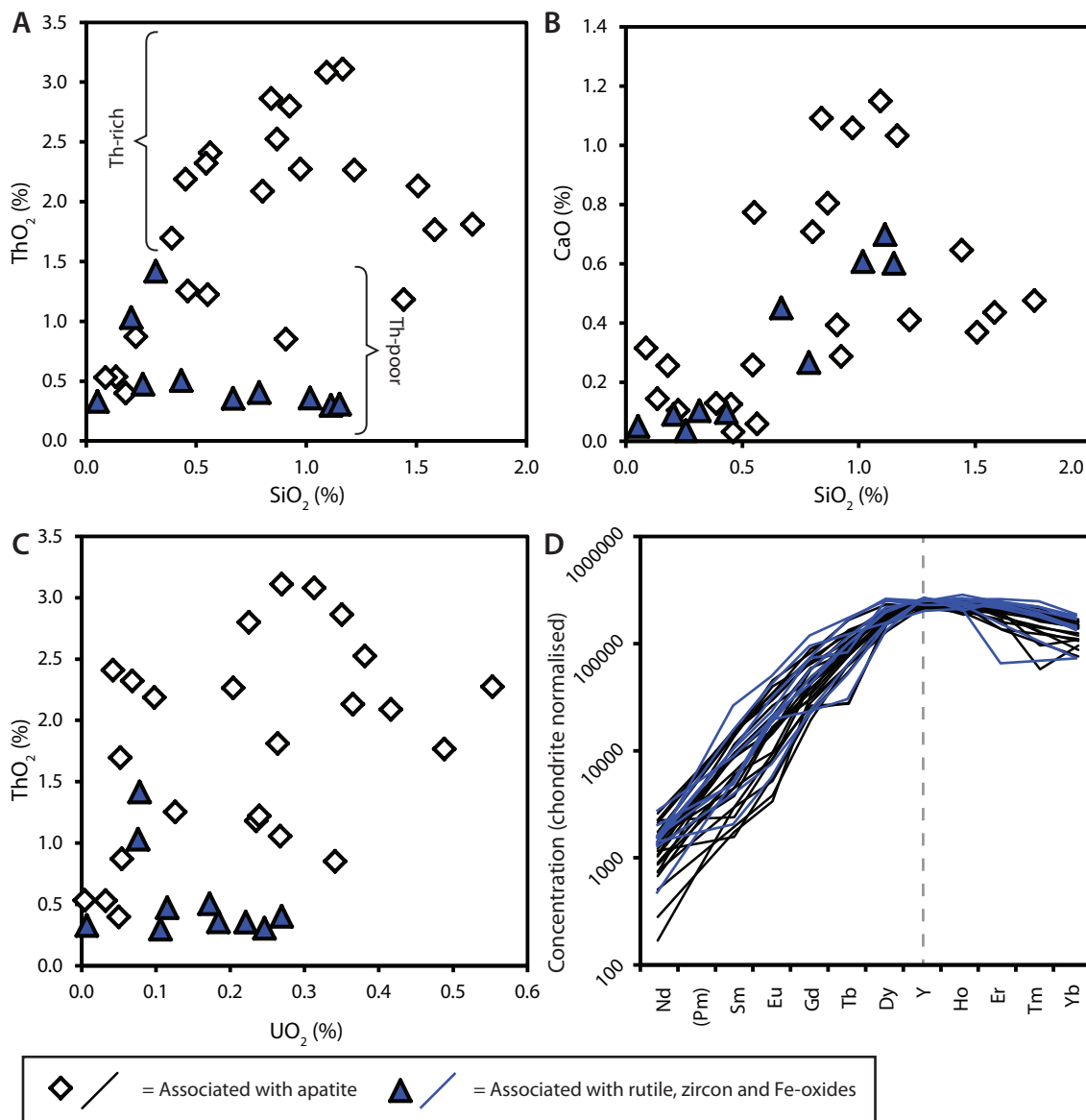
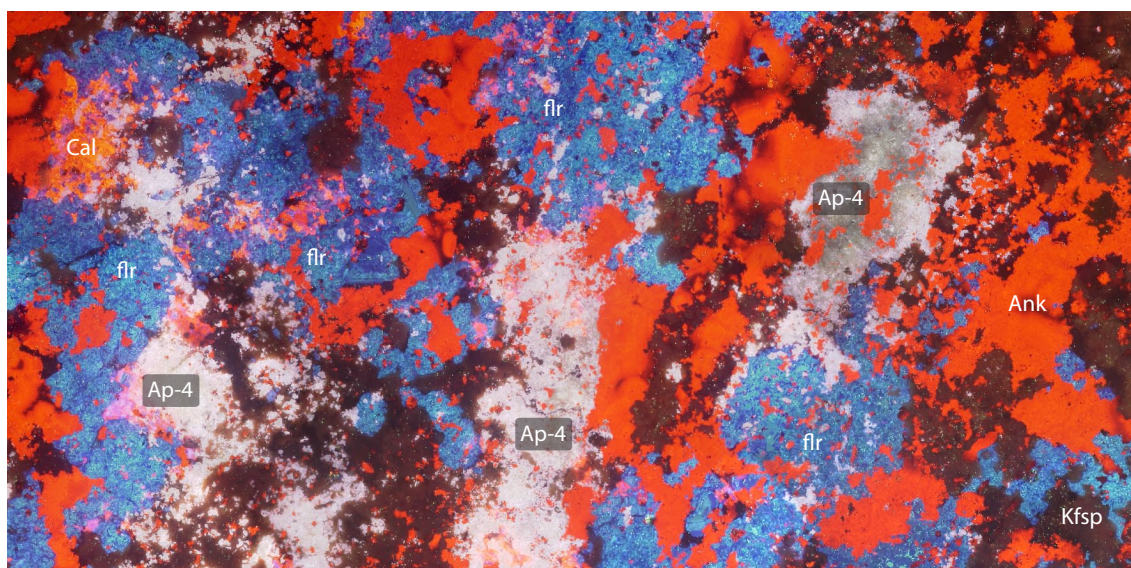


Figure 5.11: Binary plots of minor elements in xenotime (A–C), and the REE distribution (D). Analyses are split into xenotime associated with apatite and xenotime associated with rutile, zircon and Fe-oxides. Higher concentrations of radioactive elements are present in xenotime associated with apatite.

No.	Xenotime associated with rutile, zircon and Fe-oxide schlieren									
	36	37	38	39	40	41	42	43	44	45
SiO ₂	0.32	0.21	0.79	1.11	1.02	1.15	0.67	0.43	0.05	0.26
P ₂ O ₅	35.11	35.16	27.81	32.21	32.77	32.68	31.92	34.74	35.06	35.40
CaO	0.10	0.09	0.27	0.70	0.61	0.60	0.45	0.10	0.05	0.04
FeO	0.11	0.07	14.79	0.12	0.07	0.10	3.90	0.60	0.11	0.11
Y ₂ O ₃	49.83	50.58	38.40	51.11	49.58	49.52	43.56	47.05	47.50	47.59
Nd ₂ O ₃	0.11	0.03	0.08	0.08	0.08	0.07	0.07	0.08	0.14	0.07
Sm ₂ O ₃	0.08	0.09	0.26	0.04	0.09	0.07	0.44	0.17	0.15	0.17
Eu ₂ O ₃	0.12	0.13	0.26	0.04	0.12	0.05	0.31	0.15	0.12	0.20
Gd ₂ O ₃	1.04	0.92	2.10	0.52	0.52	0.49	2.61	1.61	1.24	1.62
Tb ₂ O ₃	0.39	0.39	0.00	0.12	0.25	0.21	0.00	0.33	0.45	0.66
Dy ₂ O ₃	5.47	5.31	4.22	3.55	4.16	4.00	6.76	6.76	5.86	7.02
Ho ₂ O ₃	1.42	1.39	1.26	1.21	1.46	1.28	1.37	1.70	1.54	1.58
Er ₂ O ₃	3.71	3.86	1.15	4.24	4.31	4.30	2.68	4.21	4.55	4.03
Tm ₂ O ₃	0.48	0.52	0.00	0.59	0.55	0.59	0.00	0.49	0.67	0.52
Yb ₂ O ₃	2.39	2.46	1.29	3.16	2.93	2.99	1.29	2.54	3.26	2.32
Lu ₂ O ₃	0.55	0.48	0.44	0.48	0.45	0.52	0.42	0.60	0.63	0.53
ThO ₂	1.42	1.03	0.40	0.30	0.36	0.31	0.36	0.51	0.33	0.48
UO ₂	0.08	0.08	0.27	0.11	0.18	0.25	0.22	0.17	0.01	0.12
PbO	0.36	0.40	0.30	0.42	0.37	0.37	0.34	0.37	0.36	0.37
Total	103.09	103.17	94.09	100.09	99.89	99.55	97.38	102.61	102.07	103.06
Si	0.04	0.03	0.11	0.15	0.14	0.15	0.09	0.06	0.01	0.03
P	3.86	3.86	3.44	3.67	3.73	3.72	3.74	3.86	3.91	3.90
Ca	0.01	0.01	0.04	0.10	0.09	0.09	0.07	0.01	0.01	0.01
Fe	0.01	0.01	1.81	0.01	0.01	0.01	0.45	0.07	0.01	0.01
Y	3.44	3.49	2.99	3.66	3.54	3.54	3.21	3.29	3.33	3.30
Nd	0.005	0.001	0.004	0.004	0.004	0.003	0.003	0.004	0.007	0.003
Sm	0.004	0.004	0.013	0.002	0.004	0.003	0.021	0.008	0.007	0.008
Eu	0.005	0.006	0.013	0.002	0.006	0.002	0.015	0.007	0.006	0.009
Gd	0.04	0.04	0.10	0.02	0.02	0.02	0.12	0.07	0.05	0.07
Tb	0.017	0.017	0.000	0.005	0.011	0.009	0.000	0.014	0.020	0.028
Dy	0.23	0.22	0.20	0.15	0.18	0.17	0.30	0.29	0.25	0.29
Ho	0.06	0.06	0.06	0.05	0.06	0.05	0.06	0.07	0.06	0.07
Er	0.15	0.16	0.05	0.18	0.18	0.18	0.12	0.17	0.19	0.16
Tm	0.02	0.02	0.00	0.02	0.02	0.02	0.00	0.02	0.03	0.02
Yb	0.09	0.10	0.06	0.13	0.12	0.12	0.05	0.10	0.13	0.09
Lu	0.02	0.02	0.02	0.02	0.02	0.02	0.02	0.02	0.03	0.02
Th	0.045	0.032	0.014	0.010	0.012	0.010	0.012	0.016	0.011	0.015
U	0.002	0.002	0.009	0.003	0.006	0.007	0.007	0.005	0.000	0.003
Pb	0.012	0.013	0.011	0.014	0.013	0.013	0.012	0.012	0.012	0.012
O	7.80	7.79	8.78	8.08	8.07	8.08	8.33	7.89	7.92	7.82
P site	3.90	3.89	3.56	3.82	3.86	3.88	3.84	3.92	3.92	3.94
Y site	4.18	4.20	5.39	4.39	4.30	4.29	4.47	4.18	4.15	4.12

Table 5.9: Composition of xenotime associated with zircon, Fe-oxides and rutile in the apatite-fluorite veins (C4). Results are expressed first in wt. %, and then converted to atoms per formula unit, on the basis of 16 atoms of oxygen. Total Fe is expressed as FeO.



CL (U4909)

5 mm

Figure 5.12: CL image of fluorite (flr) in association with bright-orange calcite, crystallising after apatite-4 (Ap-4) and ankerite (ank) from a sample of C4 apatite-fluorite veins (U4909).

No.	Xenotime overgrowing on apatite																							
	18	19	20	21	22	23	24	25	26	27	28	29	30	31	32	33	34	35	46	47	48	49	50	51
SiO ₂	1.58	0.91	0.92	0.45	1.51	3.56	1.44	0.87	1.17	0.97	1.09	0.84	0.80	0.56	0.18	0.55	1.75	0.14	1.22	0.23	0.46	0.55	0.39	0.09
P ₂ O ₅	31.57	31.81	32.85	34.33	29.77	28.16	32.53	31.87	31.21	31.77	30.82	32.22	31.50	34.44	34.50	34.37	32.47	35.29	30.56	35.28	34.64	30.31	34.53	35.24
CaO	0.44	0.39	0.29	0.13	0.37	1.47	0.65	0.81	1.03	1.06	1.15	1.09	0.71	0.06	0.26	0.26	0.48	0.14	0.41	0.11	0.03	0.77	0.13	0.32
FeO	0.80	4.21	0.39	0.44	7.21	0.07	1.74	0.16	0.04	0.04	0.13	0.07	0.09	0.05	0.06	0.11	0.59	0.09	5.58	0.16	0.09	6.96	0.14	0.55
Y ₂ O ₃	46.25	45.70	46.89	49.22	42.72	43.29	44.72	48.54	46.25	46.21	46.49	47.73	47.24	50.68	49.46	49.75	45.67	48.63	44.92	51.36	49.33	42.63	50.21	49.75
Nd ₂ O ₃	0.07	0.08	0.06	0.01	0.04	0.09	0.09	0.09	0.12	0.06	0.06	0.07	0.04	0.03	0.05	0.07	0.11	0.08	0.05	0.12	0.02	0.14	0.04	0.02
Sm ₂ O ₃	0.16	0.11	0.03	0.05	0.10	0.24	0.25	0.15	0.27	0.16	0.23	0.16	0.20	0.00	0.08	0.07	0.26	0.08	0.10	0.04	0.03	0.26	0.05	0.02
Eu ₂ O ₃	0.14	0.09	0.04	0.06	0.06	0.30	0.23	0.10	0.20	0.10	0.26	0.12	0.17	0.03	0.11	0.11	0.19	0.05	0.11	0.06	0.02	0.22	0.03	0.06
Gd ₂ O ₃	1.36	0.88	0.57	0.60	1.04	1.89	1.68	1.00	1.54	1.31	1.48	1.12	1.07	0.44	0.80	0.70	1.55	0.96	0.70	0.65	0.77	2.06	0.53	0.73
Tb ₂ O ₃	0.35	0.00	0.12	0.11	0.00	0.69	0.00	0.32	0.56	0.50	0.44	0.39	0.45	0.27	0.40	0.32	0.37	0.41	0.00	0.27	0.34	0.00	0.23	0.03
Dy ₂ O ₃	6.19	4.94	4.33	4.64	4.30	6.61	5.98	4.94	5.21	5.82	5.26	5.09	5.44	4.27	5.28	4.66	6.22	5.88	3.67	4.87	5.03	5.33	4.32	5.29
Ho ₂ O ₃	1.44	1.49	1.16	1.36	1.22	1.48	1.24	1.32	1.27	1.59	1.44	1.42	1.60	1.29	1.50	1.42	1.54	1.47	1.29	1.33	1.60	1.41	1.26	1.48
Er ₂ O ₃	3.56	3.20	3.84	3.94	2.48	3.38	3.06	3.95	3.53	4.04	3.67	3.87	4.06	3.89	4.17	3.96	3.38	4.25	2.90	3.81	4.09	2.47	3.88	4.31
Tm ₂ O ₃	0.27	0.00	0.52	0.45	0.00	0.37	0.16	0.52	0.48	0.54	0.51	0.56	0.53	0.50	0.54	0.46	0.36	0.55	0.00	0.49	0.60	0.00	0.51	0.46
Yb ₂ O ₃	2.00	2.18	2.92	2.63	2.03	1.60	1.76	3.09	2.78	2.70	2.73	2.90	2.96	2.62	2.96	2.57	1.95	2.68	2.28	2.55	2.67	1.39	2.52	2.57
Lu ₂ O ₃	0.69	0.62	0.57	0.53	0.61	0.60	0.64	0.70	0.62	0.67	0.64	0.62	0.66	0.60	0.67	0.53	0.57	0.69	0.40	0.41	0.50	0.43	0.50	0.50
ThO ₂	1.77	0.85	2.80	2.19	2.13	1.06	1.18	2.53	3.11	2.27	3.08	2.86	2.09	2.41	0.40	2.32	1.81	0.54	2.27	0.87	1.26	1.22	1.70	0.53
UO ₂	0.49	0.34	0.23	0.10	0.37	0.27	0.24	0.38	0.27	0.55	0.31	0.35	0.42	0.04	0.05	0.07	0.26	0.00	0.20	0.05	0.13	0.24	0.05	0.03
PbO	0.39	0.45	0.38	0.38	0.35	0.33	0.37	0.37	0.36	0.38	0.36	0.34	0.35	0.44	0.37	0.38	0.32	0.37	0.35	0.38	0.34	0.35	0.42	0.34
Total	99.50	98.25	98.88	101.62	96.29	95.44	97.93	101.69	99.99	100.74	100.13	101.82	100.36	102.61	101.83	102.67	99.85	102.31	96.99	103.01	101.95	96.74	101.43	102.30
Si	0.22	0.12	0.13	0.06	0.21	0.51	0.20	0.12	0.16	0.13	0.15	0.11	0.11	0.07	0.02	0.07	0.24	0.02	0.17	0.03	0.06	0.08	0.05	0.01
P	3.66	3.69	3.78	3.83	3.55	3.41	3.75	3.65	3.64	3.68	3.61	3.68	3.67	3.81	3.85	3.81	3.71	3.90	3.61	3.86	3.85	3.62	3.84	3.88
Ca	0.06	0.06	0.04	0.02	0.06	0.23	0.09	0.12	0.15	0.16	0.17	0.16	0.10	0.01	0.04	0.04	0.07	0.02	0.06	0.01	0.00	0.12	0.02	0.04
Fa	0.09	0.48	0.04	0.05	0.85	0.01	0.20	0.02	0.00	0.00	0.01	0.01	0.01	0.01	0.01	0.01	0.07	0.01	0.65	0.02	0.01	0.82	0.01	0.06
Y	3.37	3.33	3.39	3.45	3.21	3.29	3.24	3.50	3.39	3.36	3.43	3.43	3.46	3.52	3.47	3.47	3.28	3.38	3.33	3.53	3.45	3.20	3.51	3.45
Nd	0.003	0.004	0.003	0.000	0.002	0.005	0.004	0.004	0.006	0.003	0.003	0.003	0.002	0.001	0.002	0.003	0.005	0.004	0.002	0.005	0.001	0.007	0.002	0.001
Sm	0.008	0.005	0.001	0.002	0.005	0.012	0.012	0.007	0.013	0.007	0.011	0.007	0.009	0.000	0.003	0.003	0.012	0.003	0.005	0.002	0.001	0.012	0.002	0.001
Eu	0.006	0.004	0.002	0.003	0.003	0.014	0.010	0.005	0.009	0.005	0.012	0.006	0.008	0.001	0.005	0.005	0.009	0.002	0.005	0.002	0.001	0.011	0.002	0.003
Gd	0.06	0.04	0.03	0.03	0.05	0.09	0.08	0.04	0.07	0.06	0.07	0.05	0.05	0.02	0.04	0.03	0.07	0.04	0.03	0.03	0.03	0.10	0.02	0.03
Tb	0.016	0.000	0.005	0.005	0.000	0.032	0.000	0.014	0.025	0.023	0.020	0.017	0.020	0.012	0.017	0.014	0.016	0.018	0.000	0.011	0.015	0.000	0.010	0.001
Dy	0.27	0.22	0.19	0.20	0.20	0.30	0.26	0.22	0.23	0.26	0.23	0.22	0.24	0.18	0.22	0.20	0.27	0.25	0.16	0.20	0.21	0.24	0.18	0.22
Ho	0.06	0.06	0.05	0.06	0.05	0.07	0.05	0.06	0.06	0.07	0.06	0.06	0.07	0.05	0.06	0.06	0.07	0.06	0.06	0.05	0.07	0.06	0.05	0.06
Er	0.15	0.14	0.16	0.16	0.11	0.15	0.13	0.17	0.15	0.17	0.16	0.16	0.18	0.16	0.17	0.16	0.14	0.17	0.13	0.15	0.17	0.11	0.16	0.18
Tm	0.01	0.00	0.02	0.02	0.00	0.02	0.01	0.02	0.02	0.02	0.02	0.02	0.02	0.02	0.02	0.02	0.01	0.02	0.00	0.02	0.02	0.00	0.02	0.02
Yb	0.08	0.09	0.12	0.11	0.09	0.07	0.07	0.13	0.12	0.11	0.12	0.12	0.12	0.10	0.12	0.10	0.08	0.11	0.10	0.10	0.11	0.06	0.10	0.10
Lu	0.03	0.03	0.02	0.02	0.03	0.03	0.03	0.03	0.03	0.03	0.03	0.03	0.03	0.02	0.03	0.02	0.02	0.03	0.02	0.02	0.02	0.02	0.02	0.02
Th	0.059	0.028	0.092	0.070	0.073	0.037	0.039	0.083	0.104	0.075	0.103	0.094	0.070	0.076	0.013	0.074	0.059	0.017	0.077	0.027	0.040	0.042	0.054	0.017
U	0.015	0.010	0.007	0.003	0.011	0.008	0.007	0.011	0.008	0.017	0.010	0.011	0.013	0.001	0.001	0.002	0.008	0.000	0.006	0.002	0.004	0.008	0.002	0.001
Pb	0.013	0.015	0.013	0.013	0.012	0.012	0.013	0.013	0.012	0.013	0.013	0.012	0.012	0.015	0.012	0.012	0.011	0.012	0.012	0.012	0.011	0.013	0.014	0.011
O	8.22	8.24	8.17	7.92	8.47	8.59	8.18	8.14	8.28	8.22	8.32	8.11	8.27	7.85	7.92	7.87	8.10	7.85	8.37	7.76	7.89	8.48	7.90	7.82
P site	3.87	3.82	3.91	3.89	3.77	3.92	3.94	3.77	3.80	3.81	3.76	3.79	3.78	3.88	3.87	3.88	3.94	3.92	3.78	3.89	3.91	3.70	3.89	3.89
Y site	4.32	4.52	4.20	4.20	4.74	4.37	4.24	4.44	4.40	4.39	4.47	4.41	4.42	4.20	4.23	4.22	4.20	4.15	4.64	4.20	4.17	4.82	4.19	4.21

Table 5.10: Composition of xenotime associated with apatite in the apatite-fluorite veins (C4). Results are expressed first in wt. %, and then converted to atoms per formula unit, on the basis of 16 atoms of oxygen. Total Fe is expressed as FeO.

centred between Pr–Sm. All analyses of fluorite show that it is HREE-enriched, with the highest chondrite-normalised values (excluding Y) being for the REE Ho–Lu. With the exception of the Y anomaly, the REE pattern is similar to that of Ap-4, except an order of magnitude lower (Fig 5.10 F) Few correlations between the different trace-elements are present in the data. Sr and Y concentrations are high in the fluorite, relative to other analysed trace elements (Table 5.11).

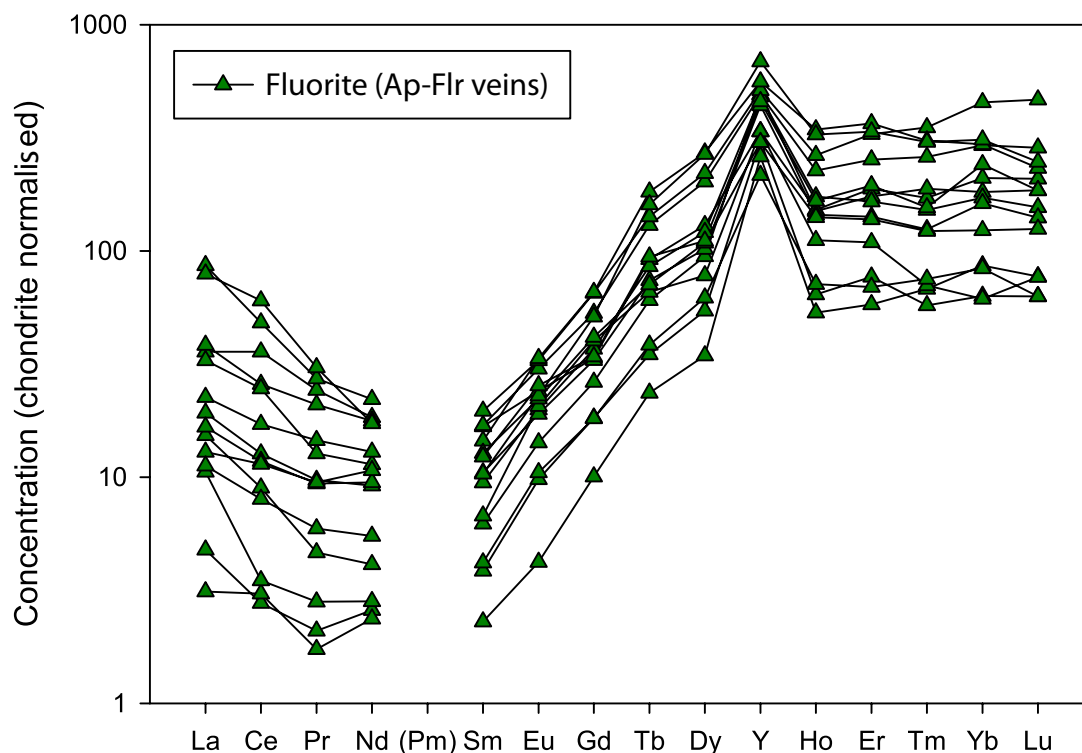


Figure 5.13: Chondrite-normalised REE distribution of fluorite from C4 calcite carbonatite. Chondrite values from McDonough and Sun (1995)

5.3.4 Interpretation

Apatite luminescence colours

In general, there is little change between the luminescence colour of the different apatite types. Most of the apatite luminesces violet, with some more white-violet, and others more greenish-violet. The subtle variations in the luminescence colour are interpreted to be due to changing REE concentrations and possibly also to changes in Mn contents. Violet luminescence is commonly caused by Ce^{3+} activation (Marshall, 1988; Mitchell, 2014). However, analyses of the CL spectrum from three Ap-3 samples and an Ap-4 sample show that the luminescence is most intense in the 550–650 nm, and 450–500 nm ranges (Fig. 5.14). Peaks of similar relative intensity and wavelength are associated with Dy activation (Marshall, 1988; Mitchell, 2014), with contributions from Tb and Sm. These peaks are marked on Figure 5.14. In the analysed spectra, no contribution from Ce or Mn is

Sample Spot	U4909 F1	U4909 F2	U4909 F3	U4909 F4	U4909 F5	U4909 F6	U4909 F7	U4909 F9	U4909 F10	U4909 F14	U4909 F15	U4909 F16	U4909 F17	U4909 F18	U4909 F19	U4909 F20
Na	52	151	193	68	134	237	62.6	172	74	41	39	108	123	67	98	80
Mg	8	9.3	8.2	38.4	8.7	8.9	176	36	7.31	7.4	660	8	32	28	169	62
Al	5.6	19	11.1	11.4	23.2	39.1	277	8.9	9.9	8.9	5.8	12.3	45	118	149	30
K	2.5	7.2	9.8	3.2	5.7	10.2	23	2.9	2.2	3.5	6	4.9	9.8	16.6	20.3	4.4
Mn	2.9	1.67	1.43	0.87	1.63	3.5	1.09	3.1	0.79	0.36	1.9	22	22.3	12.9	120	27
Fe	31	3.7	11	3.8	3.5	9.1	35	9.3	1.28	5.3	9.8	19	45	80	101	61
Co	1.7	0.064	0.48	0.122	0.19	0.25	0.53	0.059	0.28	0.038	0.7	0.14	0.058	0.8	0.77	1.3
Rb	-	0.118	0.091	0.006	0.065	0.1	0.141	0.126	0.153	0.093	0.017	0.27	0.32	0.28	0.36	0.154
Sr	1370	1350	1820	1830	1130	1160	1430	940	1860	1050	900	1080	800	880	1160	1110
Y	411	531	774	772	756	692	483	582	807	530	340	860	880	476	1080	720
Zr	0.64	0.68	0.84	0.97	1.99	4.6	0.68	0.67	0.91	3	0.38	1.95	5.3	9.6	5.5	8.9
Ba	1.4	28.3	4.28	8.6	10.8	13.8	2.67	2.78	7.4	1.29	2.58	7.5	3.36	1.69	2.13	7.9
La	3.63	8.5	4.56	9.1	3.95	7.8	1.13	5.74	20.5	0.74	2.5	102	5.35	3.06	2.66	18.8
Ce	5.5	22	7.78	15.8	7.22	15.1	1.7	9.4	29.6	1.87	2.14	148	10.5	7	4.9	37
Pr	0.431	2.25	0.9	1.94	0.87	1.18	0.194	0.99	2.53	0.161	0.261	12.7	1.35	0.88	0.55	2.84
Nd	1.88	8.4	4.19	8.1	4.33	5.2	1.18	5.97	10.1	1.08	1.29	58	5.9	4.9	2.51	7.9
Sm	0.34	2.48	0.92	2.51	1.4	1.55	0.57	3.25	2.9	1	0.62	11.4	2.14	1.89	1.53	1.82
Eu	0.237	1.35	0.8	1.7	1.12	1.07	0.551	3	1.85	1.16	0.59	5.6	1.89	1.25	1.29	1.43
Gd	2	6.7	5.24	10.6	7.35	6.55	3.64	20.4	13	8	3.62	21.1	13.1	8.3	10.2	6.8
Tb	0.85	3.32	2.19	4.7	3.09	2.68	1.26	10.1	5.13	2.38	1.39	6	6.6	2.57	5.8	3.41
Dy	8.5	32	23.3	49.9	29.8	25.1	13.4	85	54.3	19.2	15.3	50	67	26.8	66	27.3
Ho	2.92	8.31	8.2	12.4	9.5	7.9	3.51	23.5	14.5	6.1	3.9	14.3	18.8	7.7	17.9	9.1
Er	9.3	30.2	27.9	40.6	26.5	22.7	12.3	58	52.6	17.5	11.1	45	58.7	22.1	54	31.2
Tm	1.68	4.24	4.66	6.44	3.75	3.08	1.42	8	8.69	1.74	1.86	5.4	7.6	3.03	7.5	3.85
Yb	13.9	33.9	29.4	47.3	27.7	26.2	10.2	54.9	73.1	9.9	13.5	40	47.7	19.9	50	38.9
Lu	1.9	5.14	4.57	7.04	3.84	3.46	1.55	6.3	11.5	1.89	1.55	6.5	5.73	3.08	6.1	4.56
Pb	0.04	0.61	0.101	0.073	0.099	0.115	0.223	0.451	0.06	0.077	0.158	0.441	1.36	0.46	4.65	3.55
Th	0.35	53.9	1.55	2.78	4.58	3.69	2.93	13.6	3.98	2.6	1.1	32.5	4.6	2.61	3.06	13
U	0.079	0.266	0.083	0.0248	0.162	0.13	0.078	0.056	0.0233	0.176	0.064	0.363	0.35	0.217	0.24	0.32

Table 5.11: Composition of fluorite from C4 apatite-fluorite veins. All results in ppm. Concentrations marked with a hyphen (-) are below detection.

observed. It is suggested that CL could be used as a cost-effective technique for rapidly evaluating whether apatite from carbonatite may be HREE-enriched.

Variation in CL colour and intensity is also matched by variations in BSE, with darker CL colours relating to darker patches under BSE (Figure 5.3 A–D). In Ap-3, areas with less intense luminescence also correspond to areas of darker BSE intensity and reduced REE concentration. In these areas it is likely that the reduced REE concentration is the cause of the diminished luminescence intensity.

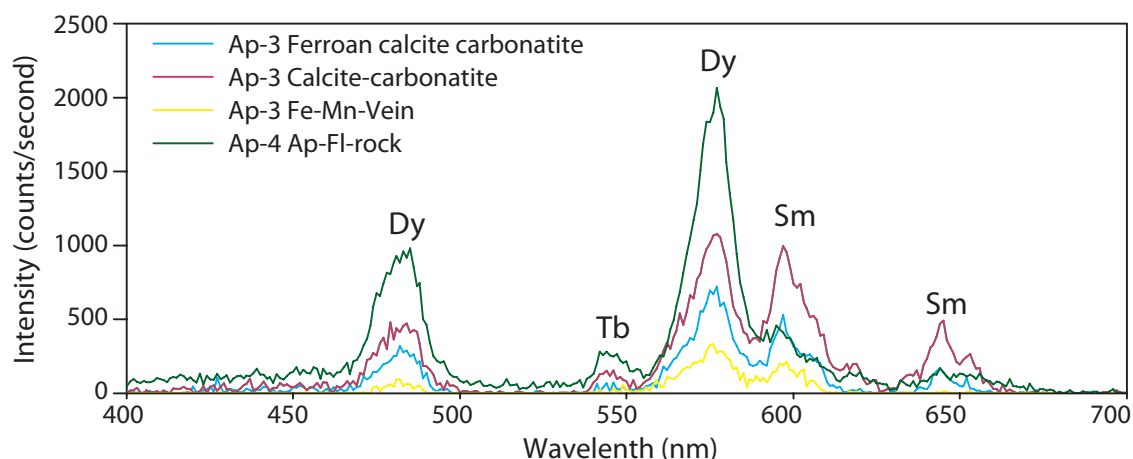


Figure 5.14: Cathodoluminescence spectra from apatite representative of the different rock types at Songwe. Activation peaks caused by REE are labelled after Marshall (1988).

Paragenesis of apatite at Songwe Hill

The paragenesis of the Songwe Hill carbonatites is presented in Figures 5.15 and 5.16. In many cases, cross-cutting relationships between different carbonatite generations, especially during the emplacement of C2 calcite-carbonatite, are ambiguous. Many pulses of hydrothermal fluids may have overprinted the carbonatite and previous hydrothermal stages. The paragenetic sequence is, therefore, presented as a guide, rather than a robust, unequivocal, interpretation. The most important observation, however, is that apatite predominantly crystallises before the formation of the LREE-fluorcarbonate -bearing mineral assemblage.

Fenitisation is generally considered to be an early, multi-stage process in carbonatite emplacement (Le Bas, 2008). The fenite-derived Ap-0 has a distinct negative Eu anomaly, and LREE enriched REE distribution with a straight slope to lower values for the HREE. Fenite-derived apatite from Chilwa Island and Kangankunde with similar chemistry has also been described by Dowman (2014). The observed pattern is, therefore, interpreted to be a distinct fenite signature, postulated to be caused by carbonatite-derived fluid mixing with country rock and groundwater (Dowman, 2014).

In a carbonatite melt, apatite is commonly an early liquidus phase occurring

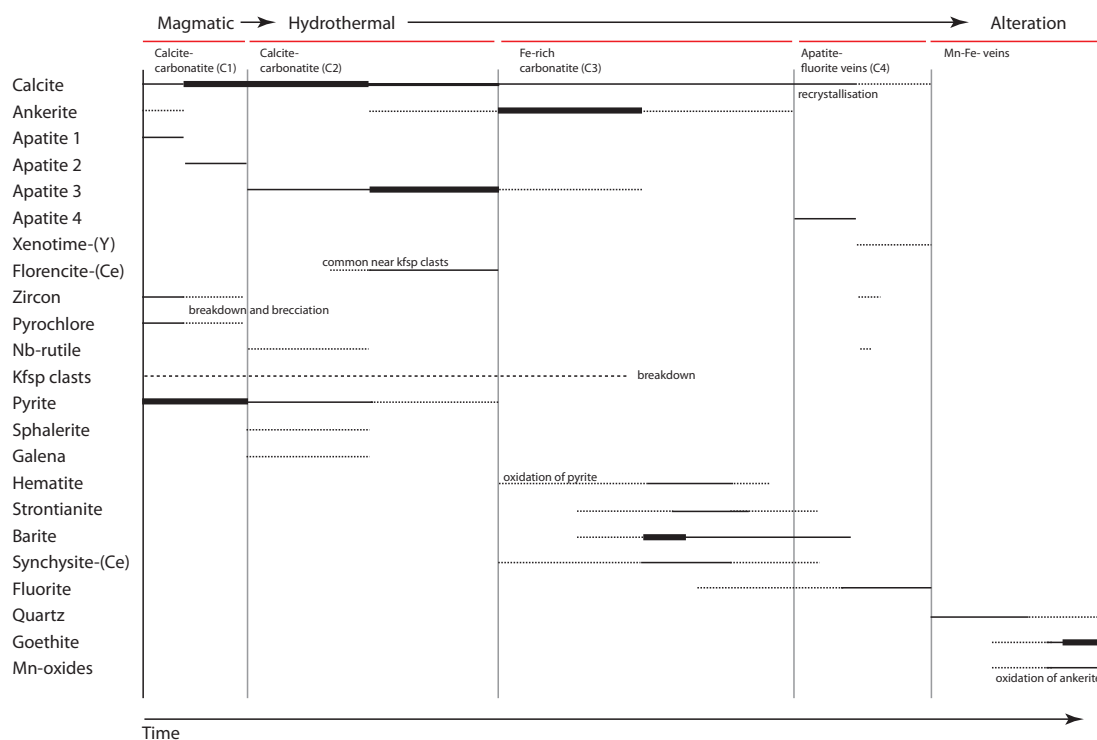


Figure 5.15: Paragenetic diagram of the different carbonatite stages and apatite types at Songwe.

as LREE-rich ovoid grains in bands (e.g. Fig. 5.17), reflecting crystallisation from a turbulent LREE-rich melt (Le Bas, 1989; Hornig-Kjarsgaard, 1998; Bühn et al., 2001). Apatite from such occurrences is LREE enriched, as demonstrated by the ‘typical’ apatite analyses in Figure 5.10. Where apatite crystallises in a less turbulent carbonatite magma, its high specific gravity relative to that of a carbonatite fluid can lead to the formation of apatite-rich cumulates, possibly including phoscorites (Krasnova et al., 2004). Zoning is known to occur on early ovoid apatite. Costanzo et al. (2006) interpreted zoning in apatite from Jacupiranga, Brazil, as evidence for a stratified magma chamber which is fluid-rich at the top, and fluid-poor at the base.

On the basis of comparison with apatite from other carbonatites (e.g. Kapustin, 1980; Hogarth, 1989), Ap-1 from Songwe is interpreted as an early, magmatic phase. Common features between Ap-1 and published occurrences include rounding, flow-banding, LREE-rich REE distribution, low Mn and high Sr concentrations (cf. Figures 5.3 and 5.17). Other minerals occurring eu-subhedrally in this early magmatic stage include pyrochlore, zircon and pyrite, which also occur in the flow-bands with apatite (Fig. 5.15). Rounding and remnant flow-banding is attributed to turbulent movement and sorting during magma emplacement (Le Bas, 1989). This phase is represented schematically in Figure 5.16-1, but is not actually found at Songwe due to the presence of alteration and the ubiquity of Ap-2 with Ap-1.

Evidence for a change in crystallisation conditions is present in the overgrowth

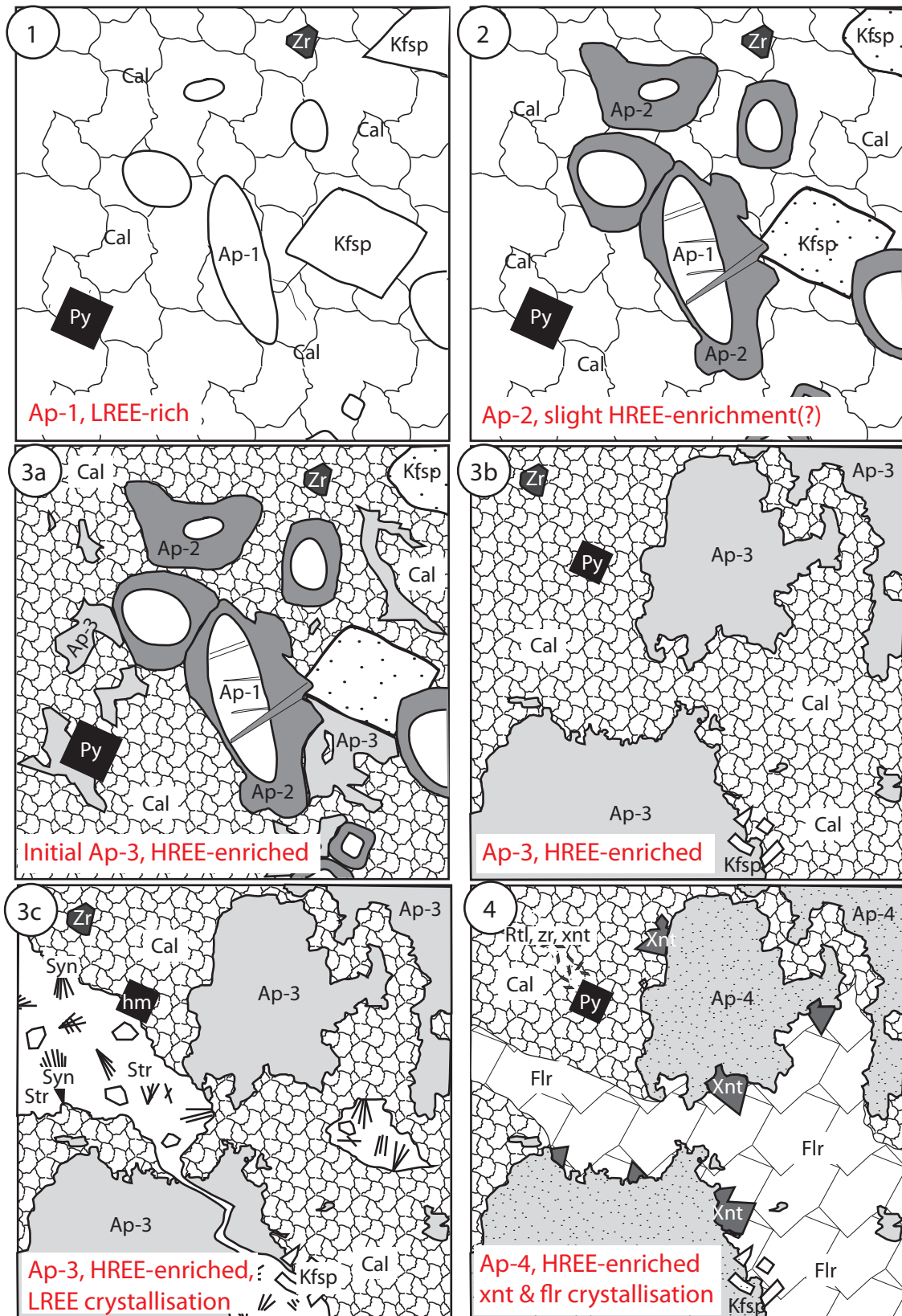


Figure 5.16: Schematic representation of different apatite generations at Songwe. 1) Hypothetical early magmatic carbonatite with primary igneous carbonatite textures and LREE enriched apatite Ap-1. 2) Calcite-carbonatite partially altered by fluids, growth of Ap-2. 3a) Calcite-carbonatite altered by HREE-bearing fluids, formation of Ap-3. 3b) Hydrothermal calcite carbonatite with no remnant magmatic crystals and extensive Ap-3 crystallisation. 3c) Formation of LREE-assemblage of synchysite (syn), barite (bar) and strontianite (str). 4) Hydrothermal calcite carbonatite with fluorite (flr), xenotime (xnt) and Ap-4 formation.

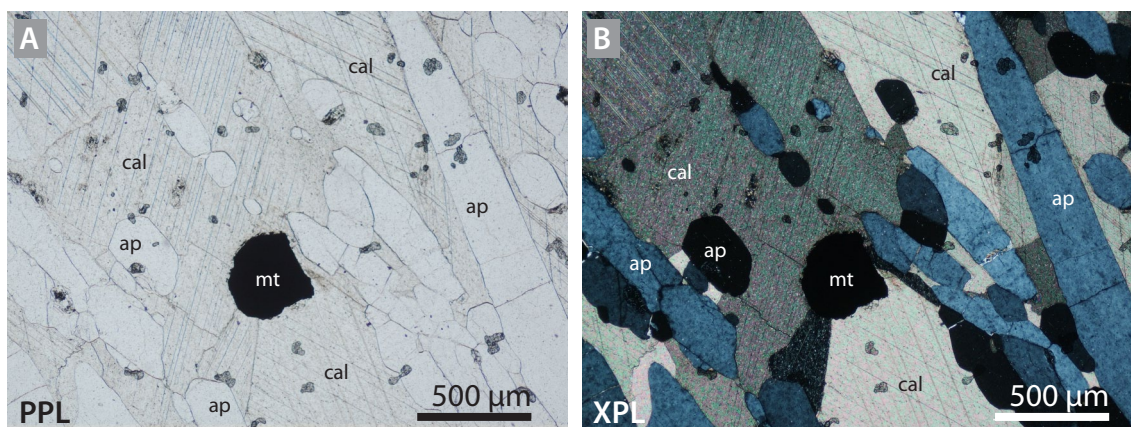


Figure 5.17: PPL^a (A) and XPL^b (B) images showing an example of early, primary ovoid apatite from Jacupiranga. Sample = Jaq-12; abbreviations: cal, calcite; mt, magnetite; ap, apatite.

^aplane-polarised light

^bcross-polarised light

of Ap-1 by Ap-2, the latter being more HREE enriched than Ap-1. Post-ablation checking of the spots using a SEM indicated that these are not due to contamination from another phase. It is therefore likely that the Ap-2 rims represent a shift towards a more HREE-enriched crystallisation environment. Similar overgrowths or continued crystallisation is not observed in zircon or pyrochlore, and these are considered to be a product of early formation only (Fig. 5.16-2).

Morphologically, Ap-2 is similar to apatite rims from Jacupiranga, Brazil (Costanzo et al., 2006). However, there are some important chemical differences between apatite from Songwe and Jacupiranga: Ap-2 has no Ce anomaly, higher REE and Sr concentrations and a weak shift to the HREE. Furthermore, the paucity of fluid inclusions in Ap-1 and Ap-2 makes it difficult to judge whether the stratified magma chamber model can be applied at Songwe.

Carbonatites commonly show evidence of multiple stages of fluid reworking, with apatite known to crystallise until the relatively late stages of carbonatite emplacement (Kapustin, 1980; Hogarth, 1989). Late-stage apatite is much more variable in habit than apatite from an early liquidus stage, forming overgrowths, schlieren, patches and microveinlets (Kapustin, 1980). Relatively few analyses of late-stage apatite are present in the literature. Examples include the carbonatites at Tundulu and Kangankunde, Malawi (see section 5.4), and Juquiá, Brazil (Ngwenya, 1994; Walter et al., 1995; Wall and Mariano, 1996). In these cases, apatite forms a eu-subhedral overgrowth on earlier apatite grains. It has higher total REE contents than the early apatite and may be preferentially enriched in the HREE. The overgrowths at Kangankunde are also associated with growths of xenotime-(Y) (Wall and Mariano, 1996). Ting et al. (1994) describes fine-grained late apatite forming veinlets at the Sukulu carbonatite, Uganda. REE, SrO and Na enrichment is reported, in common with other examples from the literature,

but no detail is provided with respect to whether the late-stage apatite is LREE- or HREE-enriched.

Ap-3 occurs paragenetically after Ap-1 and Ap-2, as illustrated by the juxtaposition between ovoid and anhedral apatite (Ap-1/2 and Ap-3, respectively; Figures 5.3 B, D–F, and 5.16-3a). Ap-3 and Ap-4 have a similar habit to the late-stage apatite described by Kapustin (1980) and Ting et al. (1994) and are therefore interpreted as such. This is supported by the cross-cutting occurrence of Ap-3-rich veins through C2 calcite-carbonatite. The habit and complexity, with respect both to chemistry and texture, of Ap-3 are interpreted as being caused by a late-stage carbo-hydrothermal fluid or fluids. This is reinforced by the incorporation of feldspar xenoliths of earlier fenite, and rarely, clasts of C1 sövitic carbonatite into C2 and C3 carbonatite, which contain abundant Ap-3. Commonly, fenite clasts show evidence of reaction with the fluid, such as feldspar breakdown and replacement by calcite and the formation of replacement minerals such as florencite.

The lack of ovoid apatite in most samples with abundant Ap-3 may be due to two processes:

1. formation of Ap-3 completely replaced and recrystallised Ap-1 and Ap-2
2. crystallisation of Ap-1 and Ap-2 was suppressed in these rocks during the melt stage.

The presence of ovoid/pseudo-ovoid areas (e.g. Fig. 5.4), with lower REE concentrations within Ap-3 bands, suggests that in some Ap-3 -bearing samples Ap-1/2 may be partially replaced and recrystallised. This interpretation is also supported by the juxtaposition between Ap-1, -2 and -3 in sample T0206 (Fig. 5.3). If Ap-1/2 are not present in Ap-3 then a mechanism is required to explain the low degree of apatite crystallisation during early magmatic carbonatite stages. No such mechanism is known, although experimental studies on apatite crystallisation in carbonatite are few. Therefore Ap-3 is equivocally interpreted as having formed through replacement and recrystallisation of Ap-1 and Ap-2.

As Ap-3 is found in all carbonatite types it is likely that the formation of Ap-3 represents a distinct late-magmatic or hydrothermal event, cross-cutting calcite-carbonatite (C2) and Fe-rich carbonatite (C3) emplacement but preceding fluor-carbonate mineralisation. This is supported by the cross-cutting relationships between bands of Ap-3 within C2 and C3 carbonatite. Ap-3 is, therefore, interpreted as forming after widespread calcite (in C2) and most ankerite (C3) formation, but prior to LREE mineralisation (Figures 5.15 and 5.16-3b).

LREE mineralisation in carbonatites can occur as a primary magmatic assemblage, forming REE-fluorcarbonates or burbankite (Jones and Wyllie, 1983; Wyllie et al., 1996; Zaitsev et al., 2002). However, it is most commonly found as a late-stage hydrothermal assemblage (Mariano, 1989). Such hydrothermal

assemblages are typically polycrystalline, with the REE hosted in a mixture of fluorcarbonates, and/or monazite, with associated strontianite, barite and calcite. Commonly, the REE-bearing assemblage forms in hexagonal pseudomorphs, most likely after burbankite (Wall and Mariano, 1996; Zaitsev et al., 2002; Wall et al., 2004; Moore et al., 2014). In other cases, crystallisation of REE-bearing hydrothermal mineral assemblages occurs along fractures, in small cavities or is widespread, and pseudomorphs are not reported (Andrade et al., 1999b; Doroshkevich et al., 2009).

REE-fluorcarbonate mineralisation at Songwe forms paragenetically after Ap-3 mineralisation, as show by cross-cutting assemblages of calcite and synchysite-(Ce) (e.g. Figures 5.4 C, 5.15 and 5.16-3c). REE-fluorcarbonate assemblages are associated with strontianite and barite, and locally with fluorite, calcite, K-feldspar, pyrochlore and titanite (see chapter 4, and Swinden and Hall, 2012; Brady et al., in prep). In places, possible hexagonal pseudomorphs could be after burbankite, but the majority of the mineralisation occurs as small cavity fillings, or, where mineralisation is more widespread, as stringers (Swinden and Hall, 2012; Brady et al., in prep), occurring after ankerite crystallisation.

In the apatite-fluorite veins, apatite crystallises before extensive fluorite mineralisation (Fig. 5.5), and LREE crystallisation is not found. As late-fluorite mineralisation is common in many carbonatites (e.g. Palmer and Williams-Jones, 1996; Williams-Jones and Palmer, 2002), the formation of these veins at Songwe is interpreted as late.

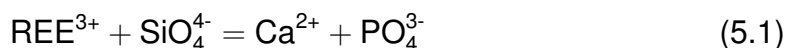
It is evident that xenotime formed after the apatite, and it appears to be synchronous with recrystallised calcite, which is commonly found in association with the fluorite (Fig. 5.16-4). Two xenotime associations are found, one typically with K-feldspar associated with Fe-oxide, rutile and microcrystals of zircon, and the other as an overgrowth on apatite. The xenotime associations are interpreted as being synchronous on the basis of their similar chemistry. The subtle differences in the concentrations of radioactive elements in the different xenotime types may be due to their incorporation into zircon or rutile, where they are better structurally accommodated, than in xenotime. After fluorite mineralisation in these rocks, late-stage quartz crystallisation occurs, followed by alteration of the carbonatite by meteoric fluids.

As previously discussed (chapters 3 and 4) the Mn-Fe-veins are likely to be caused by post-emplacement hydrothermal alteration. Therefore, Ap-3 in these samples is most likely to be surviving crystals from crystallisation in Fe-rich carbonatite, rather than crystallisation from the Fe-Mn-veins themselves. This is reflected in the similar chemistry of Ap-3 from Mn-Fe-veins with that of Fe-rich carbonatite. The negative correlation between Ce and Sr in the apatite (Fig. 5.9 C) suggests that Sr could be preferentially removed from the apatite and replaced

by Ce through post-emplacement hydrothermal alteration.

Apatite substitutions at Songwe Hill

The REE can substitute into the Ca site in apatite, either into the 9-coordinated Ca1 site or the 7-coordinated Ca2 site (Pan and Fleet, 2002). To balance the charge in the mineral, this is part of a coupled substitution with a monovalent or tetravalent cation (e.g. Na⁺ or SiO₄⁴⁻ respectively). Examples of substitution mechanisms are:

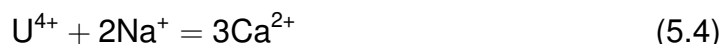


In the apatite samples from carbonatite (Ap-1–4), SiO₂ is typically below detection on the microprobe, and Si blank concentrations were relatively high in the results from LA ICP-MS. Consequently it is difficult to determine if Si is contributing to a coupled substitution. However, the Na concentration in Ap-1–Ap-4 correlates strongly (Fig. 5.8), and stoichiometrically, with the REE, which suggests that Na is the element with which the REE are forming a coupled substitution in these samples. It should be noted, however, that the Na concentration is higher than expected in some samples of Ap-4, this is due to the ablation of saline fluid inclusions.

U and Th are positively correlated with Na in the apatite. This indicates that Th⁴⁺ is most likely substituting for Ca²⁺, as part of a coupled substitution with Na⁺ (Luo et al., 2009, 2011):



Uranium can exist in both the 6+ and 4+ oxidation state, but based on XANES¹⁵ analysis, is generally considered to substitute as U⁴⁺ (Luo et al., 2009). Therefore, to balance charge, the substitution mechanism is similar to that of Th:



Some analyses of U and Th do not show a correlation with Na (Fig. 5.9). In these cases it is possible that ablation included small grains of thorite, or another U-Th-rich mineral hosted in inclusions in the apatite. This is also indicated by the relatively large errors on these analyses, caused by non-flat count-peaks during integration. Such sudden spikes in concentration of a element are typically indicative of ablation of another phase.

¹⁵X-ray absorption near edge structure

Sr is a commonly substituting cation in apatite, especially in carbonatites and alkaline rocks (Chakhmouradian et al., 2002; Liferovich and Mitchell, 2006). As both Ca and Sr exist in the 2+ valence state, Sr substitutes for Ca into the Ca2 site (Pan and Fleet, 2002):



While a Sr-rich end-member of the apatite group has recently been documented (stronadelphite, $\text{Sr}_5(\text{PO}_4)_3\text{F}$; Pekov et al., 2010), most substitution of Sr into apatite is accompanied by the LREE as part of a belovite-type ($\text{NaREE}\text{Sr}_3(\text{PO}_4)_3\text{F}$) substitution (Pasero et al., 2010). The weak positive correlation between Sr and Ce, in most analysed apatite (Fig. 5.7) indicates that a belovite-type substitution is likely to be taking place in the Songwe apatite. A negative correlation exists between Sr and Ce in the Ap-3 from the Mn-Fe-veins. This may be due to preferential removal of Sr during percolation of meteoric fluids during the alteration of the veins.

In analyses of apatite from Ap-3, As and the REE are positively correlated (e.g. Fig. 5.9 D). The correlation between As and all of the REE La–Lu, indicates that the As contents are genuine, and not an analytical artefact of a doubly-charged ion, or an ionised oxide. Arsenate can directly substitute into the PO_4^{3-} site, as demonstrated by the complete solid-solution between pyromorphite ($\text{Pb}_5(\text{PO}_4)_3\text{Cl}$) and mimetite ($\text{Pb}_5(\text{AsO}_4)_3\text{Cl}$) (Pan and Fleet, 2002), where:



Svabite ($\text{Ca}_5(\text{AsO}_4)_3\text{F}$) is the arsenate analogue of fluorapatite (Pasero et al., 2010) and is known to partially substitute for apatite (e.g. Perseil et al., 2000; Gianfagna et al., 2015). As there is no correlation between Pb and As in the apatite analyses, it is likely that a small amount of svabite substitution is taking place.

Incorporation of arsenate into the phosphate site does not involve a coupled substitution and therefore does not readily explain the correlation between As and the REE. Although the increase in As with increasing REE concentration is small, a possible cause could be structural. Incorporation of the REE into fluorapatite is split between the two Ca sites (Ca1 and Ca2), with the LREE showing a preference for the Ca2 site (Fleet and Pan, 1995, 1997b; Pan and Fleet, 2002). This splitting of the REE between different sites is thought to be due to minimisation of the volume change in the unit cell (Fleet and Pan, 1995, 1997b; Pan and Fleet, 2002). However, some volume change during incorporation of large concentrations of the REE is highly likely, and it is suggested that this could cause an increase in the size of the PO_4 site. As arsenate is larger than phosphate, a change in the volume of the unit cell could more readily facilitate incorporation

of arsenate into the phosphate site. This hypothesis has not been tested in this study.

Controls on the REE distribution of apatite

Distribution of the REE into apatite is a balance of intrinsic (crystal-chemical) and extrinsic controls. The intrinsic role of the apatite structure in accommodating the REE is complex. Some authors argue that the degree of structural control on REE partitioning into apatite is minimal, and reflects extrinsic features such as the whole-rock REE abundance and distribution (Roeder et al., 1987; Fleet and Pan, 1997b). This is supported by the generally high partition coefficients for the REE into apatite (Fig. 5.18), and the large range in natural apatite composition (e.g. Fleischer and Altschuler, 1986).

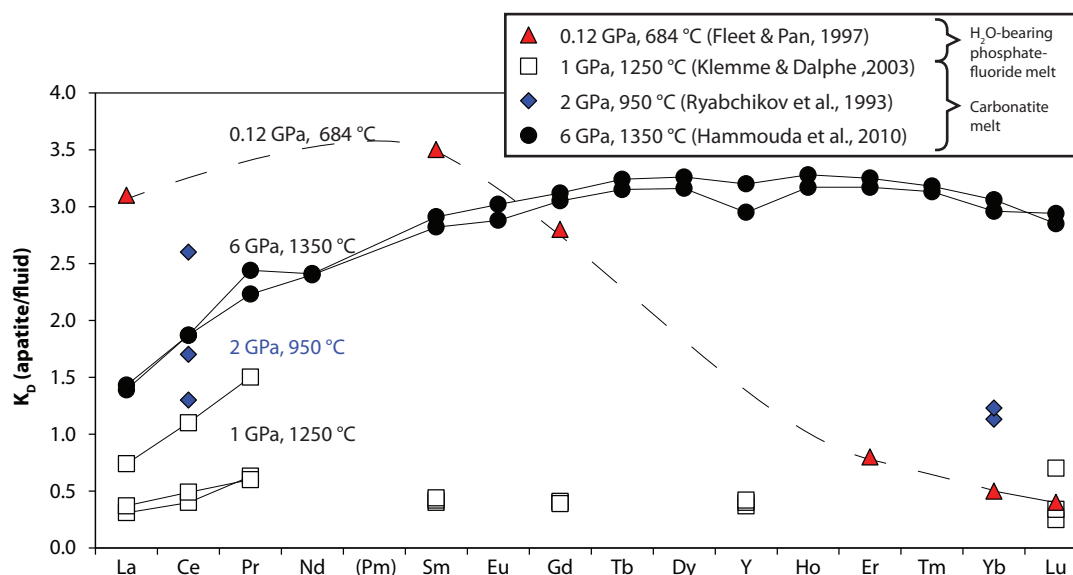


Figure 5.18: Compilation of experimentally-derived partition coefficients for the REE into apatite in carbonatite melts at different pressures, and an H₂O-bearing phosphate–fluorite melt at low pressure. Dashed line inferred to guide the eye between data points. Data sources: Ryabchikov et al. (1993); Fleet and Pan (1997a); Klemme and Dalpé (2003); Hammouda et al. (2010).

Intrinsic controls on REE distribution have been observed in laboratory experiments where apatite has been synthesised in the presence of a single REE. The partition coefficient of the REE into apatite decreases from the LREE to HREE. However, similar experiments show that, in the presence of multiple REE, the MREE are preferentially incorporated into apatite, with the LREE (Nd–La) preferentially accommodated in the Ca₂ site, and the HREE (Sm–Lu) preferentially accommodated in the Ca₁ site (Pan and Fleet, 2002). This indicates that there is a complex inter-play between the different REE substitution into apatite. The major controls on this complex distribution are predicted to be equalisation of bond valence between the Ca sites and F (in fluorapatite), and a minimisation of the

change in unit cell volume in the apatite (Pan and Fleet, 2002). Therefore, substitution of other elements into the apatite structure (e.g. Sr) can compete for space in the Ca2 site, forcing the REE into the Ca1 site.

Extrinsic controls on REE distribution include the pressure, temperature and composition of the melt from which the apatite is crystallising. Variation in apatite-melt K_D values in carbonatite melts varies depending on the pressure of the system, with K_D values decreasing with decreasing pressure (Hammouda et al., 2010, Fig. 5.18). At high pressure, these partition coefficients are MREE enriched, while at lower pressure the paucity of data makes it difficult to infer a coherent distribution shape (Fig. 5.18). Composition can also have an effect on the variation in partition coefficients. For example, apatite/melt partition coefficients in silicate rocks increase with increased silica and melt polymerisation (Watson and Green, 1981; Prowatke and Klemme, 2006). Little experimental work has been carried out on partition coefficients between a hydrothermal fluid and apatite. The most relevant experiment is for an H₂O-bearing, fluorite–phosphate melt at 684 °C (Fleet and Pan, 1997a). K_D values between apatite and fluid in this system are high for the LREE, peaking at Sm, but are much lower for the HREE (Fig. 5.18).

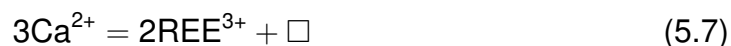
Attempts to derive partition coefficients from natural carbonatite samples through analysis of apatite and bulk-rock composition give contrasting results. The results of Böhn et al. (2001), who analysed apatites from intrusive carbonatites in Namibia, gave K_D values which had the highest values for the LREE, while the analyses of Brassinnes et al. (2005), who studied carbonatites from Vuorijarvi, Russia, peak at Sm. The results of these studies cannot be reconciled and nor do they match experimentally-derived partition coefficients.

Controls on the REE distribution of apatite at Songwe

Relating the wide range of K_D values for carbonatite apatite to the composition of apatite from Songwe is difficult. The closest approximation for the crystallisation environment is likely to be the H₂O-bearing phosphate-fluoride melt. This experiment indicates that apatite–fluid partition coefficients for the LREE and MREE are likely to be highly enriched. This could explain the MREE enriched patterns at Songwe (e.g. Fig. 5.10 D–E), but does not readily explain the HREE enriched distributions (Fig. 5.10 F). Further experimental studies of the partitioning of apatite at low pressure and temperature are required to improve the understanding of the relationship between the REE and apatite under these conditions.

REE distribution of late-stage fluorite

The REE substitute for Ca in the fluorite structure through the following mechanisms (Möller et al., 1998):



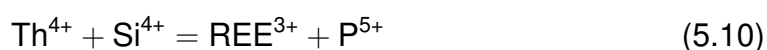
Where \square represents a structural vacancy. The LA ICP-MS data indicate that there is no correlation between Na and the REE in the fluorite data generated in this study. This indicates that the substitution of the REE is charge balanced by either addition of F or a vacancy in the fluorite structure. With the current dataset, neither of these options can be excluded.

The fluorite structure, like that of apatite, readily accommodates the REE and it is frequently used to trace the REE distribution of fluorite-forming fluids (e.g. Gagnon et al., 2003; Schwinn and Markl, 2005; Xu et al., 2012). Almost all analyses of fluorite from carbonatite display a positive Y anomaly (Bühn et al., 2003; Xu et al., 2012). For example, analyses of fluorite REE distributions at Okorusu, Namibia, show that La/Yb (i.e. degree of HREE enrichment) and Y/Ho ratios (magnitude of Y anomaly) decrease in paragenetically later fluorite (Bühn et al., 2003, Fig. 5.19). The composition and REE distributions of fluorite from different carbonatites, however, are varied. Sr concentrations vary from 1 ppm to 1 wt. % and Y concentrations are between 1–1000 ppm (Fig. 5.19 A). LREE enriched distributions are common (e.g. fluorite from Daluxiang, Maoniuping, Bayan Obo and Okorusu), as are roof-shaped MREE enriched distributions (e.g. Lizhuang, Maoniuping). HREE enriched distributions, characterised by their low La/Yb ratios, of the magnitude seen at Songwe, however, have not been observed in fluorite from other carbonatites (Fig. 5.19).

U and Th in xenotime

It is clear that the xenotime overgrowths on apatite, in the C4 apatite-fluorite veins at Songwe, crystallised after the apatite and, on the basis of having a similar chemistry, the xenotime in association with zircon, rutile and Fe-oxides is assumed to have formed at the same time. The only substantial difference in the chemistry of these two xenotime types is in their U and Th compositions.

Th strongly partitions into monazite, if present, and U and Th both partition into xenotime (Förster, 2006). This occurs via the following coupled substitutions with Si^{4+} :



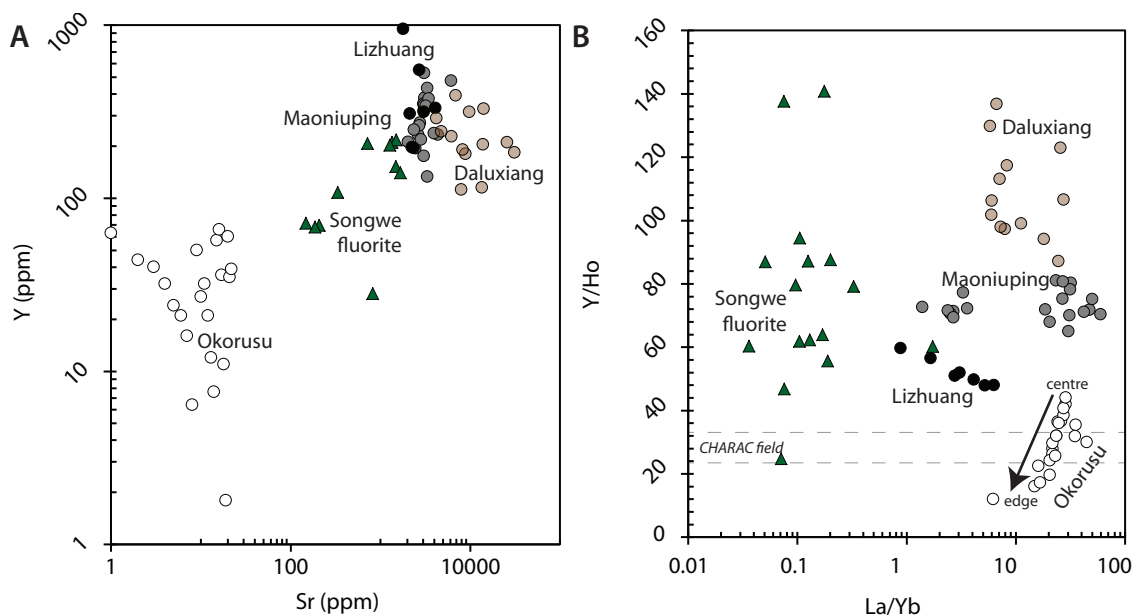


Figure 5.19: Composition of Songwe fluorite compared to other carbonatite fluorites. Data sources: Okorusu, Bühn et al., 2003; Maoniuping, Daluxiang, Lizhuang, Xu et al., 2012. CHARAC^a field after Bau, 1996.

^aCharge and Radius controlled

Substitution occurs through solid-solution with the minerals thorite/huttonite (tetragonal and monoclinic polymorphs of ThSiO_4) and coffinite for Th and U, respectively (Förster, 2006). The weak correlation between ThO_2 and SiO_2 in xenotime associated with apatite is therefore most likely due to a solid-solution with thorite/huttonite. Correlation between Ca and Si is difficult to account for. Cheralite ($\text{CaTh}(\text{PO}_4)_2$) can substitute for monazite, but has not been observed substituting for xenotime.

5.4 HREE-bearing minerals associated with carbonatite (2): comparison with apatite from Kangankunde and Tundulu

For comparison with the HREE-rich, late-stage (C3–C4) apatite from Songwe, samples were sourced from carbonatites where late-stage apatite has previously been described. Such occurrences include: Juquiá, Brazil (Walter et al., 1995); Sukulu, Uganda (Ting et al., 1994); Tundulu, Malawi (Ngwenya, 1994); and Kangankunde, Malawi (Wall and Mariano, 1996). Samples of these occurrences were available from Kangankunde and Tundulu (Table 5.12).

Sample number	Location	Collected by:	Rock type	Other minerals	Reference
Kangankunde					
BM-1962-(131) (G1175)	1/2 mile SW of Southern Knoll	MS Garson	Quartz druse rock	Qtz, Fe-carb, Nb-rtl, xnt	Garson and Smith (1965); Wall and Mariano (1996); Wall (2000)
Tundulu					
NHAC	Eastern flank of Nathace Hill	S Broom-Fendley	Silicified apatite carbonatite	Qtz, Fe-carb, cal, pyro, REE-fc, rtl	N/A
T142	Nathace Hill	JD Appleton	Silicified apatite carbonatite	As above	Styles (1988)
T160	Nathace Hill	JD Appleton	Silicified apatite carbonatite	As above	Styles (1988)

Table 5.12: Late-apatite-bearing samples analysed from Kangankunde and Tundulu. Mineral abbreviations: Qtz, Quartz; Fe-carb, rhombohedral carbonate broken down to a mixture of carbonate and Fe-oxides; cal, calcite; pyro, pyrochlore; REE-fc, REE-fluorcarbonate; rtl/Nb-rtl, (niobian)-rutile; xnt, xenotime-(Y).

5.4.1 Kangankunde

One sample from Kangankunde (BM-1962-(131)) was acquired from the NHM¹⁶, London. This sample was collected by MS Garson, and is referenced as sample number G1175 in Garson and Smith (1965). The rock type is described as a quartz-druse rock (apatite-rich), found in an elongated outcrop 1/2 mile SW of the top of the Southern Knoll of Kangankunde hill, outside the main carbonatite intrusion. Garson and Smith (1965) give a basic petrographic description, identifying major apatite and quartz, and minor rhombohedral carbonate and rare florencite. Wall and Mariano (1996) describes the apatite in greater detail, identifying turbid cores and clear euhedral overgrowths with oscillatory zoning (e.g. Figure 5.20). BSE imagery and some EPMA data are provided, showing that the turbid cores are not zoned, and contain 1–2 wt. % SrO, while the rims are more REE-rich, with varying degrees of enrichment in the MREE. On the edge of many overgrowths is an unidentified REE-rich, P₂O₅-bearing phase. Xenotime is also found as an overgrowth on niobian-rutile.

Additional petrography carried out in this study using CL and BSE at CSM supports the findings of Wall and Mariano (1996). BSE imagery shows that the turbid cores luminesce variably blue–green, while the euhedral clear rims luminesce orange–brown (Fig. 5.20 A). The oscillatory zoning in the rims is visible

¹⁶Natural History Museum

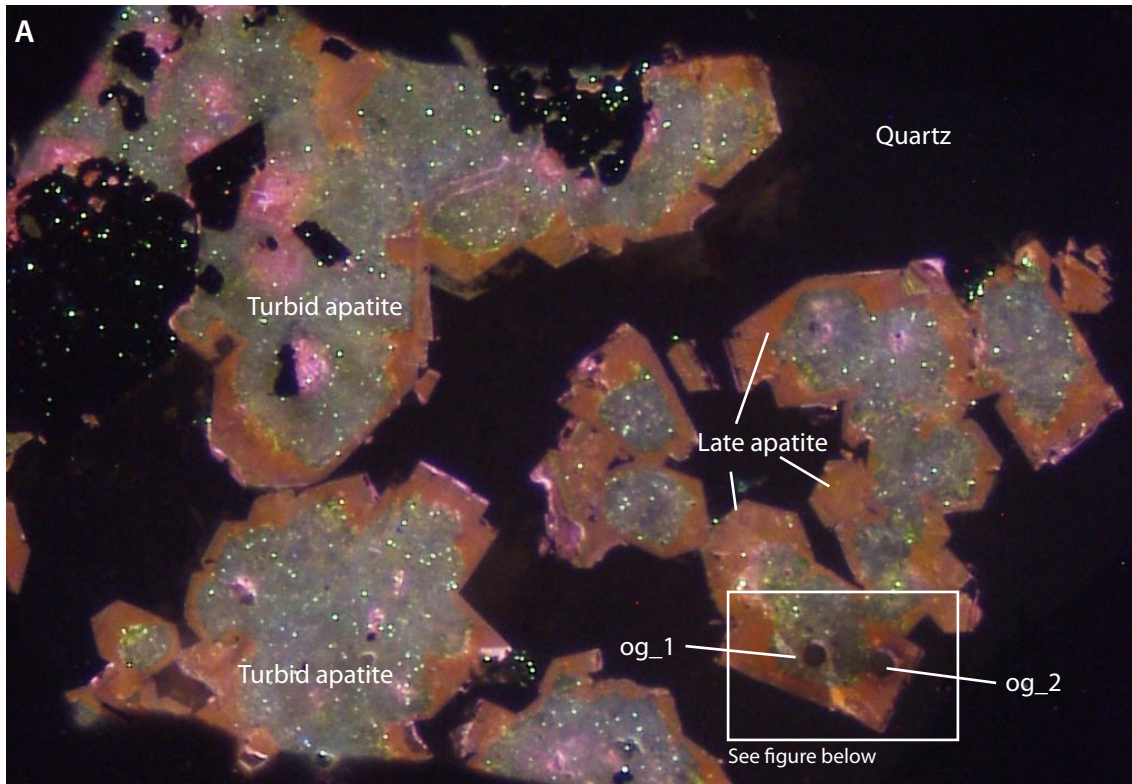
under BSE (Fig. 5.20 B) but is not resolvable using CL at the magnification and conditions used.

5.4.2 Tundulu

It is evident from the whole-rock data (chapter 4; Styles and Appleton *unpublished*), that apatite from Tundulu has similar characteristics to the apatite from Songwe. Whole-rock data from both carbonatites shows a positive correlation between Y and P_2O_5 , with samples from Tundulu having slightly higher P_2O_5 concentrations for an equivalent concentration of Y to Songwe. The samples with the highest Y and P_2O_5 concentration are of silicified apatite-carbonatite from Nathace Hill.

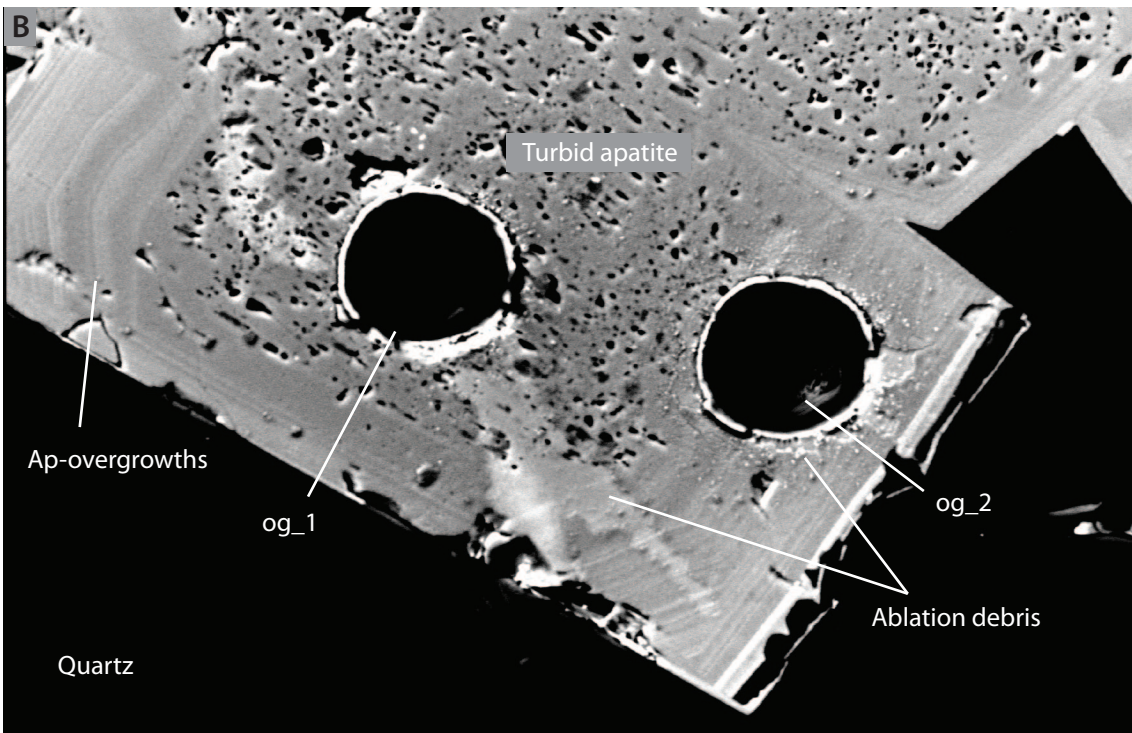
Three samples of silicified apatite-carbonatite (nomenclature after Ngwenya, 1994, equivalent to apatite-rock/apatite-sölvite of Garson, 1962) were acquired from Nathace Hill, Tundulu, Malawi. Garson (1962) provides a description of these rocks which is very similar to the quartz-druse rock from Kangankunde. Apatite is abundant, with turbid cores and clear, euhedral rims, and the matrix is formed of quartz. Accessory minerals include hematite, barite, anatase, pseudomorphic Fe-carbonate rhombs and bastnäsite. Styles (1988) and Ngwenya (1994) describe the apatite from these rocks in greater detail. Styles (1988), in addition to optical petrography, carried out EPMA analyses on cores and rims from samples T142 and T160 (used in this study). It was observed that the size of the rims varies between different samples, with T160 having larger rims than T142. Fine oscillatory zoning was identified in the euhedral apatite rims. Core and rim EPMA analyses showed a negative correlation between Na and P, interpreted as part of a coupled substitution of CO_3 for P_2O_5 . The presence of some CO_2 in the samples was confirmed by an infra-red spectrometry analysis, which suggested that the apatites were fluorapatites, with some CO_3^{2-} and OH^- substitution. Ngwenya (1991, 1994) carried out additional EPMA analyses, including a wider range of REE and a traverse from core to rim. He showed that the zoning of the REE in the rim is due to varying REE concentration, and that Na, Ce and Y are higher in the rim than the core of the apatite. A four-fold increase in Y concentration, relative to Ce, was observed in the rims. Both Ngwenya (1994) and Styles (1988) suggest that the formation of the apatite rims, and associated late quartz and REE-fluorcarbonates, is due to crystallisation from, or alteration by, hydrothermal fluids.

Samples T142 and T160 were generously loaned by JD Appleton and MT Styles (BGS), and an additional sample (NHAC) was acquired from Nathace Hill during fieldwork in Malawi (Table 5.12). Additional CL petrography, BSE imagery and some EDS maps were obtained from the samples. The presence of turbid cores and euhedral, oscillatory-zoned overgrowths was confirmed. Turbid



CL

1 mm



BSE

50 μm

Figure 5.20: CL (A) and BSE (B) images of turbid apatite cores and clear rims in Kangankunde sample BM 1962 73 (131). (cf. imagery in Wall and Mariano, 1996). Speckled blue–green apatite represents turbid cores and orange–brown apatite represents the clear euhedral overgrowths. Fine oscillatory zoning is evident in the apatite overgrowth under BSE (B). Ablation pit labels refer to labels in appendix D.2.

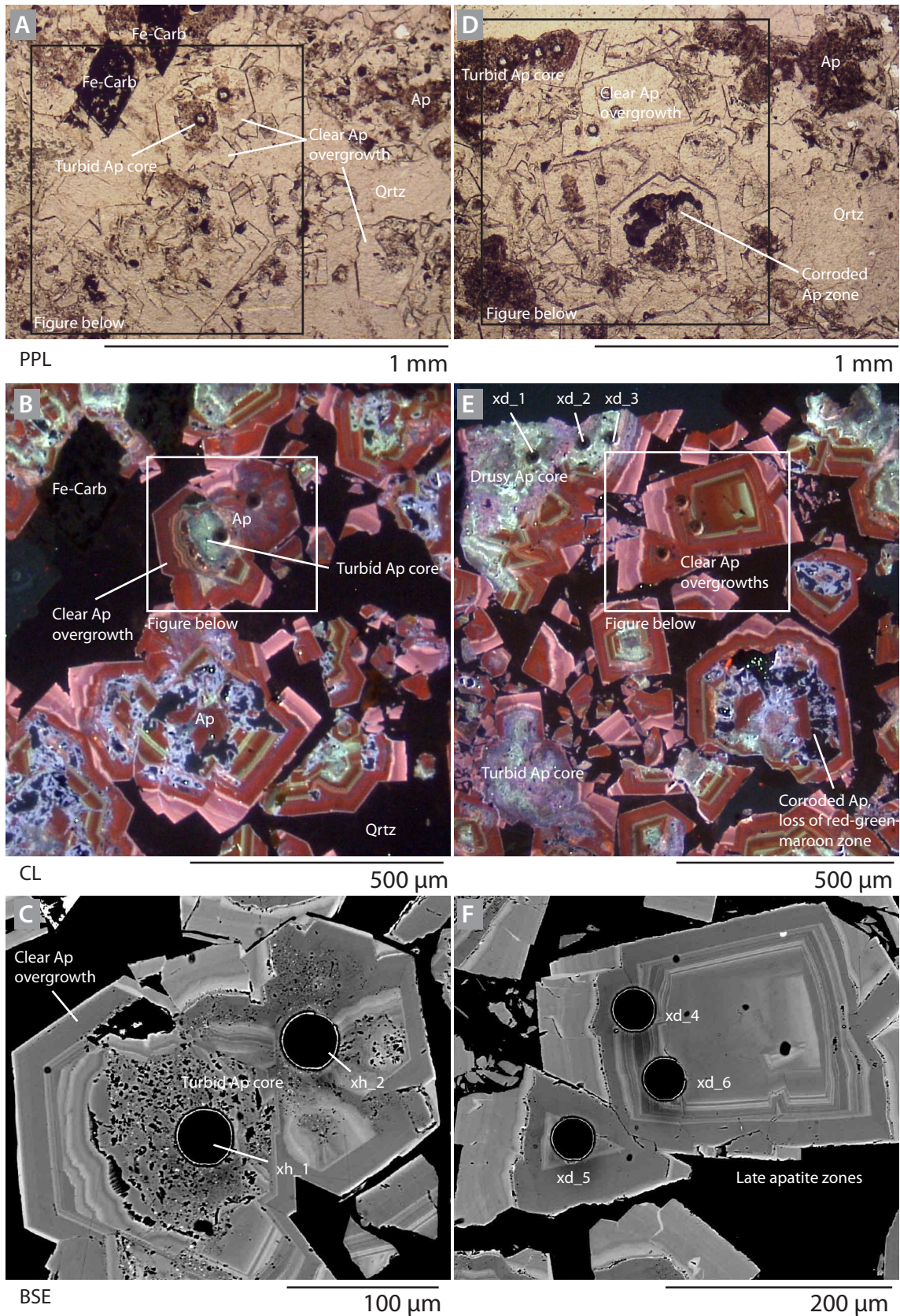


Figure 5.21: PPL (A, D), CL (B, E) and BSE (C, F) images of apatite from Nathace Hill sample T160. Images A–C focus on an area with a turbid, corroded apatite cores, displaying purple, blue and green luminescence and multiple overgrowths. Images D–F show and area with multiple large overgrowths, with maroon, green, red and mauve CL luminescence.

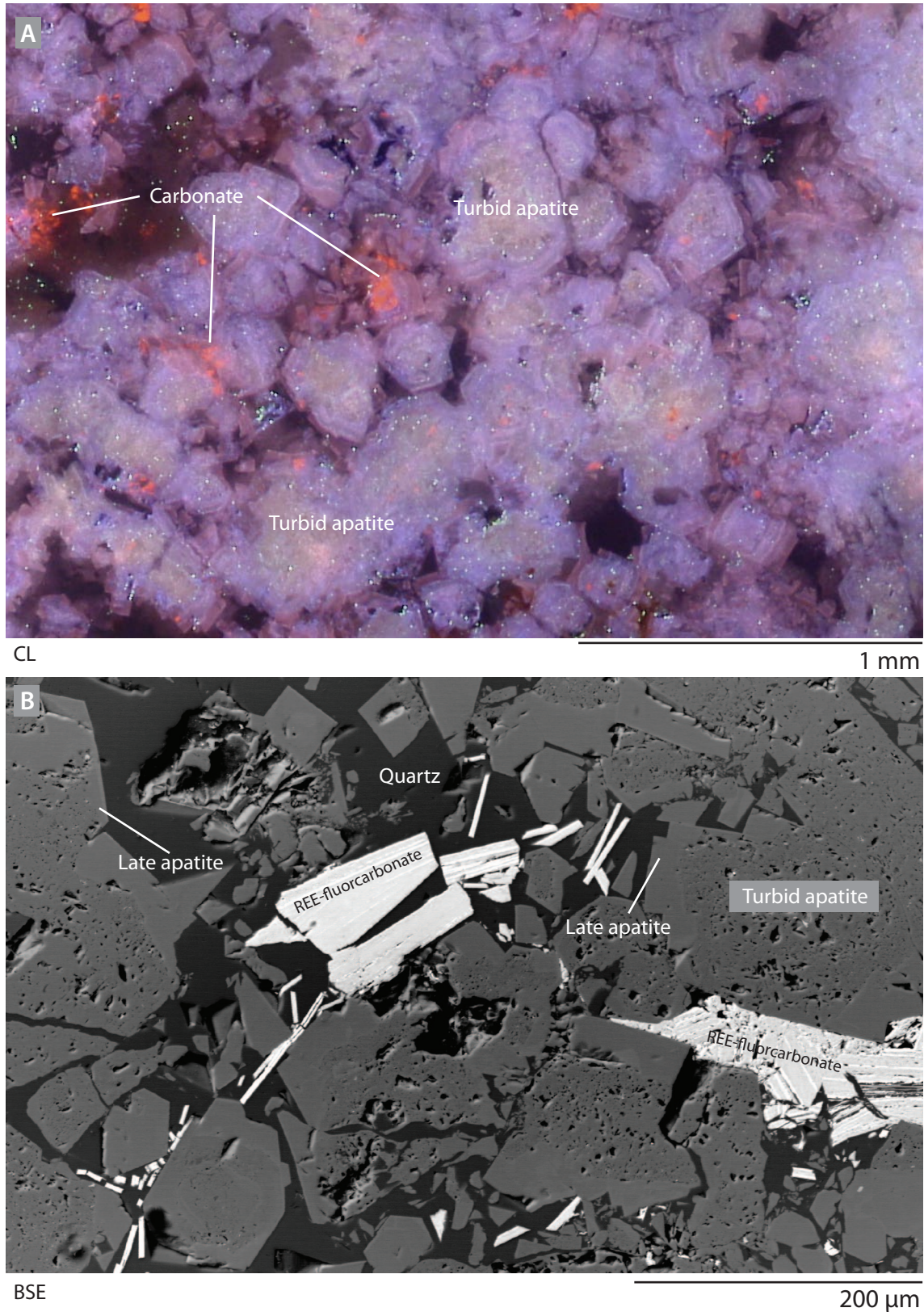


Figure 5.22: CL (A) and BSE (B) images of silicified apatite carbonatite from Nathace Hill, Tundulu. Note the abundance of apatite (A) and the early, anhedral, spongy apatite core (B) with a euhedral, inclusion-free late apatite overgrowth. Also of note in (B) is the euhedral REE-fluorcarbonate crystallising after apatite, and the anhedral quartz groundmass.

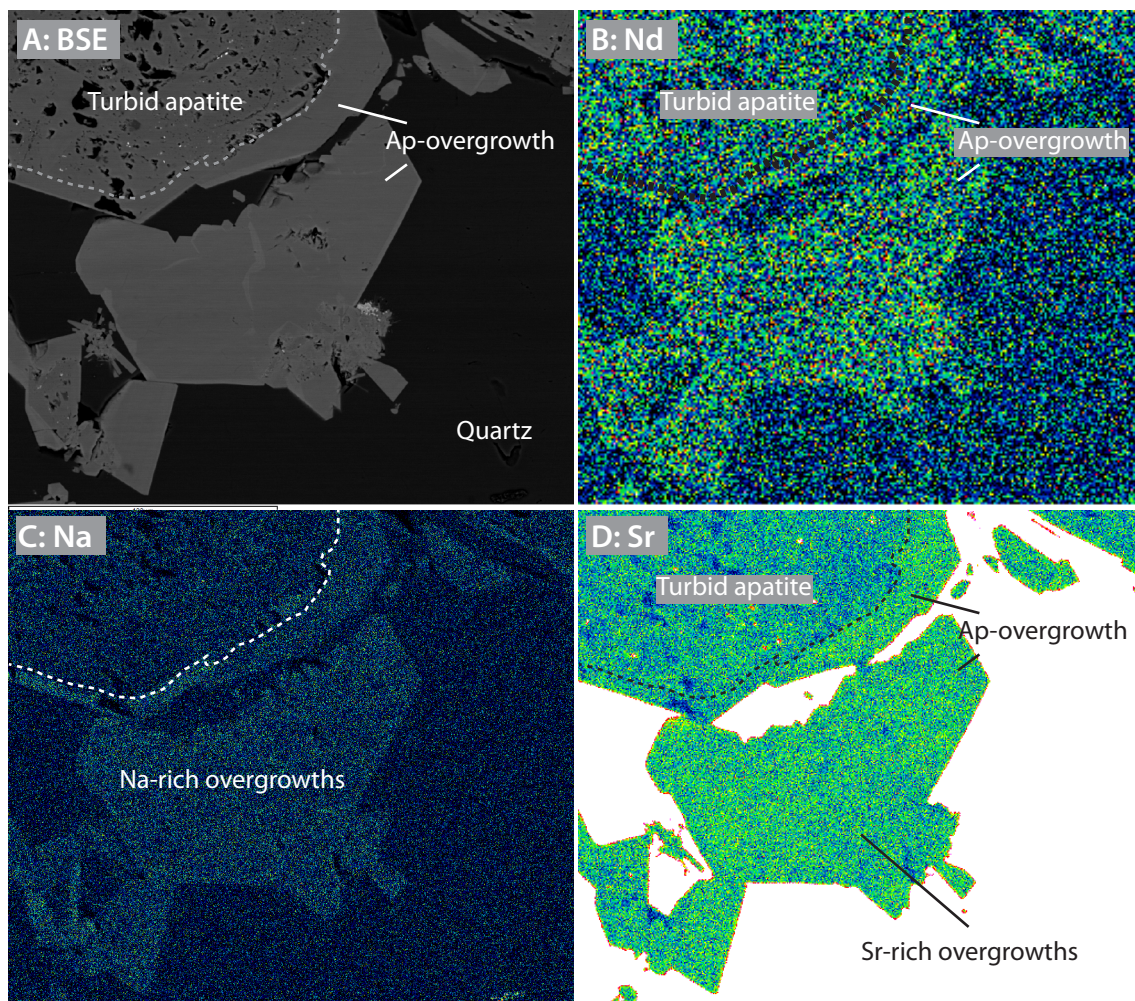


Figure 5.23: EDS maps of early turbid apatite and late apatite overgrowths, with a BSE image for reference (A). Note the increased concentration of Na (C) and Sr (D) in the late overgrowths. No difference in Nd concentration (as a proxy for the LREE) is observable using this technique.

cores luminesce blue–green under CL, similar to cores from Kangankunde, but the luminescence in cores from Tundulu is much more vibrant. Zoning in the overgrowths is observable in both CL and in BSE (Figures 5.21 and 5.22). CL revealed that zoning in the euhedral overgrowths was more complex than previously described (Styles, 1988; Ngwenya, 1994), and is comprised of maroon, green, red and mauve zones. The maroon–green–red zones are most prominently displayed in sample T160, where they form both as overgrowths and as rare euhedral crystals without a turbid core (Figure 5.21 D–F). Zones of corroded turbid apatite are also present in sample T160, where it appears that blue–green and maroon–green–red luminescent apatite has been dissolved and replaced by quartz/pore-space. These features are much less abundant in sample T142 and are not observed in sample NHAC (Fig. 5.22). Common, however, to all the apatite from these samples is a final mauve zone, which typically displays little zoning (e.g. Fig. 5.22B). EDS maps of this euhedral, clear, mauve-luminescent apatite zone, from sample NHAC, confirm that the late apatite at Tundulu is Na-rich, and has a higher Sr concentration than the turbid apatite core. No resolvable differences in REE concentration between the cores and the rims were found by this technique, nor any detail on additional zoning within the rim.

5.4.3 Laser ablation analyses

Cores and rims of apatite from all the investigated samples from Kangankunde and Tundulu were analysed using LA ICP-MS for the REE and 16 other trace elements (Section 5.2.3). Eleven apatite grains were analysed from Kangankunde, comprising 10 core and 11 rim data points. In the three Tundulu samples, 36 grains were analysed, comprising 57 core and 47 rim analyses. Data from sample NHAC utilised EPMA points collected at the BGS as an internal standard for Ca, while data from samples T142 and T160 utilised median values for core and rim data from Styles (pers comm.) and data from Kangankunde utilised median Ca values for cores and rims from Wall and Mariano (1996).

The results of the LA ICP-MS analyses are presented in appendix D.2 and Figures 5.24 and 5.25. In general, rim analyses from Kangankunde and Tundulu both have higher concentrations of Na, REE, Th and Sr than the counterpart cores (Figures 5.24 and 5.25). Data from rim analyses are split according to their colour under CL. Maroon–green–red luminescent zones in samples from Tundulu have a distinctly different chemistry to the more common, later mauve zones. The maroon zones have significantly higher Na contents but these are not correlated with other analysed elements, except Sr, which shows a weak positive correlation with Na (Fig. 5.25B). Some element-element discrimination diagrams (e.g. Ce/Na, Y/Na, Sr/Na) appear to show a continuum of values between the maroon and mauve luminescent apatite types. However, based on reassessment

of the ablation pits, it is apparent that the continuum is due to ablation pits overlapping separate zones.

While the relationship between trace elements is similar for core and rim data from Tundulu and Kangankunde, there are considerable differences in the actual REE and Sr concentrations present. The Sr concentration in Kangankunde rims is substantially higher than in Tundulu (10000–25000 ppm, compared to 8000–12000 ppm). Cores and rims from Kangankunde have much lower Y concentrations, while Ce is relatively similar in cores and rims from both localities. Additionally, maroon luminescent apatite from Tundulu has particularly prominent HREE enrichment in some samples, relative to the LREE (Fig. 5.24F). Mn and Fe correlate in samples from Kangankunde and Tundulu, indicating contamination by trace amounts of goethite in the analyses (goethite has been identified in apatite cores from Tundulu, Styles, 1988; and is present in cores from Kangankunde). It is, therefore, not possible to assess the variation in the Mn contents of apatite from these data.

Chondrite-normalised REE distributions from Kangankunde and Tundulu reflect the differences in Y and Ce concentrations between the two localities (Figures 5.26 and 5.27). Distributions from Kangankunde cores show a prominent Sm–Eu-centred peak, with smoothly decreasing LREE and HREE concentrations. A consistent negative Y anomaly is present in all the analyses. Turbid cores from Tundulu have generally higher REE concentrations than those from Kangankunde (note the difference in scale between Figures 5.26A and 5.26B–F). The distribution patterns of the REE in the cores from Tundulu, however, are variable:

1. Relatively flat, LREE-rich, HREE-poor, with a small Y anomaly (Fig. 5.26C).
2. Relatively flat, LREE-rich, but with a distinct enrichment in the MREE/HREE, starting at Gd and peaking at approximately Y. Most analyses have a minor negative Y anomaly, and some have a small positive Eu anomaly (Fig. 5.26D).
3. A convex-up curved distribution, peaking at the MREE, around Gd and a minor Y anomaly. Most analyses from sample NHAC have this distribution (Figures 5.26B, E).
4. LREE-poor with a prominent HREE-rich bulge peaking around Y. This distribution pattern displays both positive and negative Y anomalies.

Few of the distributions are smooth, while some (e.g. Figures 5.26B–D) show a marked change between Gd and Tb.

Chondrite-normalised REE patterns for Kangankunde rims have smooth distributions, similar to the cores, but with a much higher concentration of the LREE. The positive Y anomaly observed in the cores is also present in the rims. Mauve

luminescent rims from Tundulu are broadly LREE–MREE enriched, peaking at Sm–Eu, with steep, negative-sloping, HREE patterns. A prominent negative Y anomaly is present. Maroon-luminescent, Na-rich rims have a variable REE distribution. Some have a relatively flat shape, while four analyses display a prominent HREE-enrichment, similar to that seen in the turbid apatite cores (Fig. 5.26F), but an order of magnitude more HREE enriched. These distributions correspond to the samples with high HREE+Y concentrations, and low LREE concentrations in Figure 5.24. Sample NHAC shows distribution patterns with features of both distribution patterns described above, suggesting that some maroon zones are present in sample NHAC.

5.4.4 Interpretation and comparison with previously published data

Luminescence colour

Changing luminescence colour in all the apatite types is interpreted as due to changing REE concentrations, and possible changes in Mn concentration. No CL spectra were obtained from the Tundulu and Kangankunde samples, and therefore interpretation of the luminescence is limited to a subjective comparison of colours with reference samples (e.g. Marshall, 1988; Mitchell, 2014).

Blue–green cores from Kangankunde may be representative of mixed violet Ce^{3+} , yellow Mn^{2+} and red–orange Sm^{3+} activation (interpretation based on spectral peaks from Marshall, 1988 and Mitchell, 2014). The orange–brown luminescence in the euhedral, clear zones from Kangankunde apatite is representative of the order-of-magnitude increase in Sm concentration relative to the turbid cores, which greatly increases the proportion of red–orange luminescence, relative to yellow Mn and violet Ce luminescence. Wall and Mariano (1996) interpreted the variation in zoning in the euhedral apatite rims to be due to variation in the REE concentration. Such variation in REE concentration would most likely lead to fine changes in luminescence, which is not observed (Fig. 5.20 A). The oscillatory zoning is therefore interpreted here as due to fine scale variations in Sr concentration, which is much more enriched in the rims of Kangankunde apatite than the REE. The turbid, blue-green luminescent cores from Tundulu are interpreted as being caused by mixed violet Ce^{3+} activation and yellow Dy^{3+} and Tb^{3+} activation, with possible contribution from Mn^{2+} . Variation in green and blue luminescent areas may represent variation between MREE and HREE -rich distributions, as reflected in the chondrite-normalised diagrams (Fig. 5.26). Maroon-green-red rims are difficult to interpret. Sm contents are low and, therefore, it is unlikely that this element is causing the red luminescence. It is possible that the low REE concentration in these rims means that Mn^{2+} activation has a stronger influence

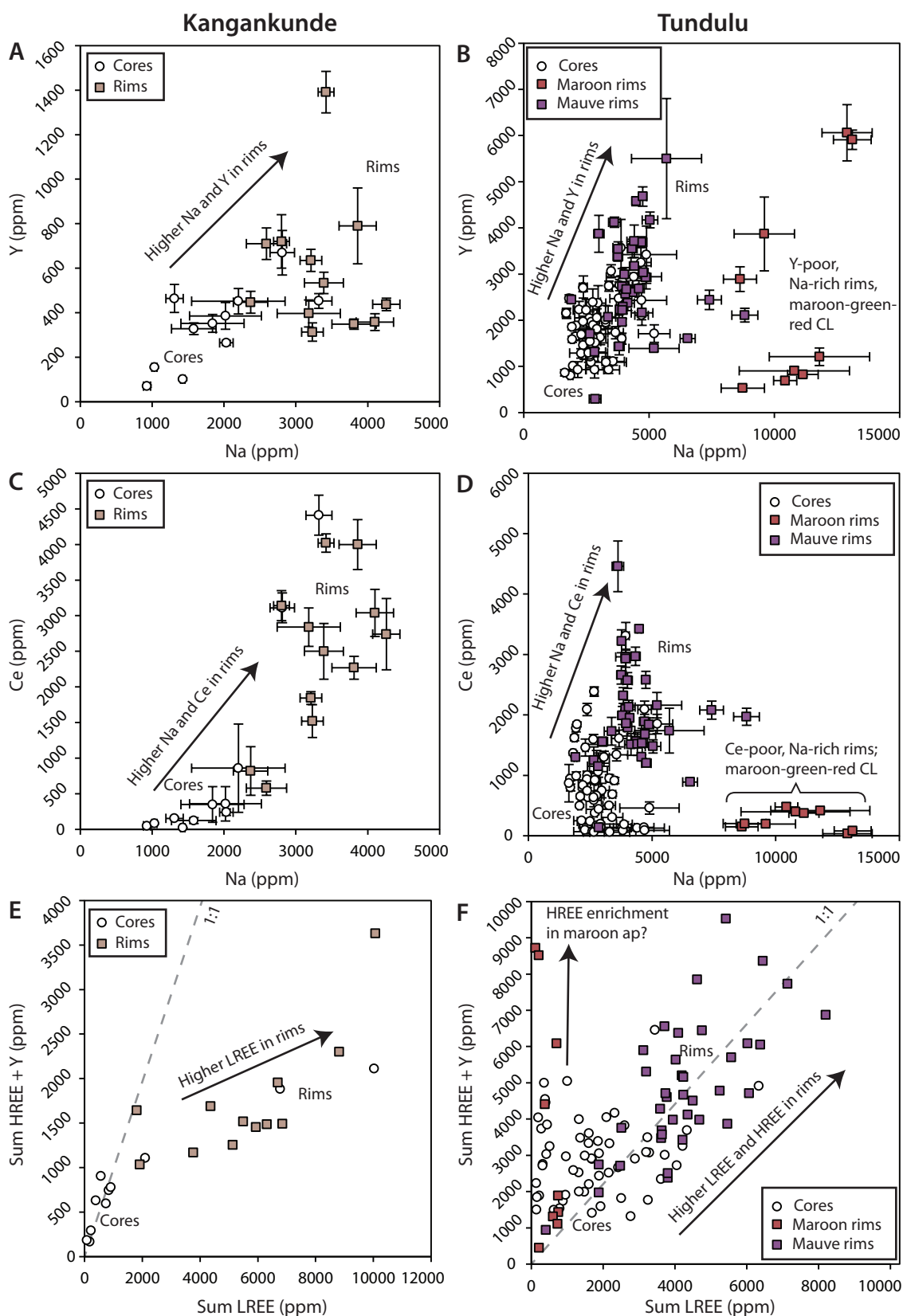


Figure 5.24: Binary plots of REE and Na data from the cores and rims of apatites from Kangankunde (A, C, E) and Tundulu (B, D, F). The colour of the symbols representing the rim data are representative of the CL luminescence colour. Orange–brown luminescent rims, from Kangankunde, and purple–mauve rims, from Tundulu, have associated enrichments in Na, Y and Ce. Maroon rims from Tundulu have high Na concentration, but little attendant REE enrichment.

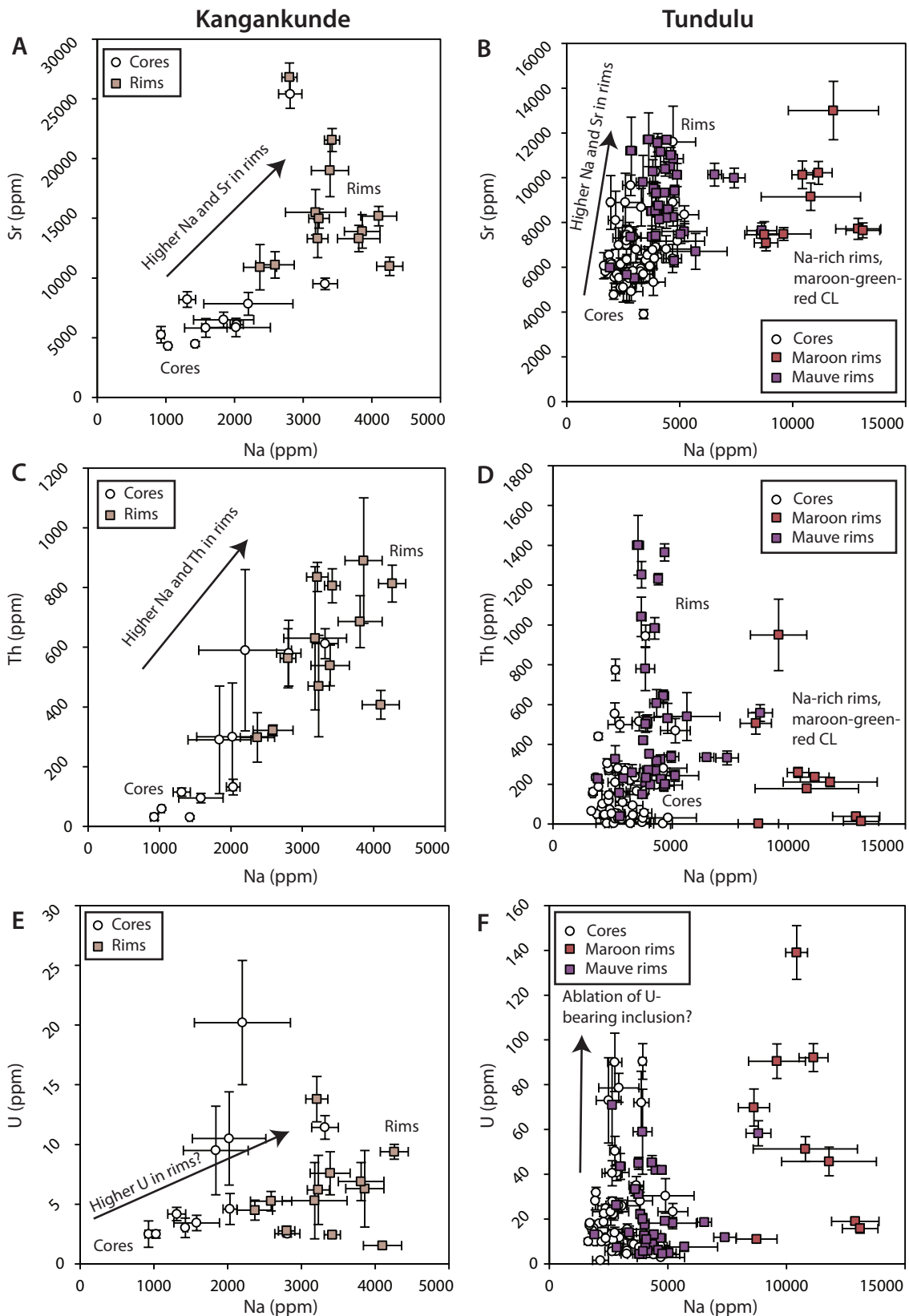


Figure 5.25: Binary plots of Sr, U, Th and Na data from the cores and rims of apatite from Kangankunde (A, C, E) and Tundulu (B, D, F). The colour of the symbols representing the rim data are representative of the CL luminescence colour. Orange–brown luminescent rims, from Kangankunde, and purple–mauve rims, from Tundulu, have associated enrichments in Na, Sr and Th. Maroon rims from Tundulu have high Na concentration and, in some samples, increased Sr concentration.

Turbid core chondrite normalised diagrams

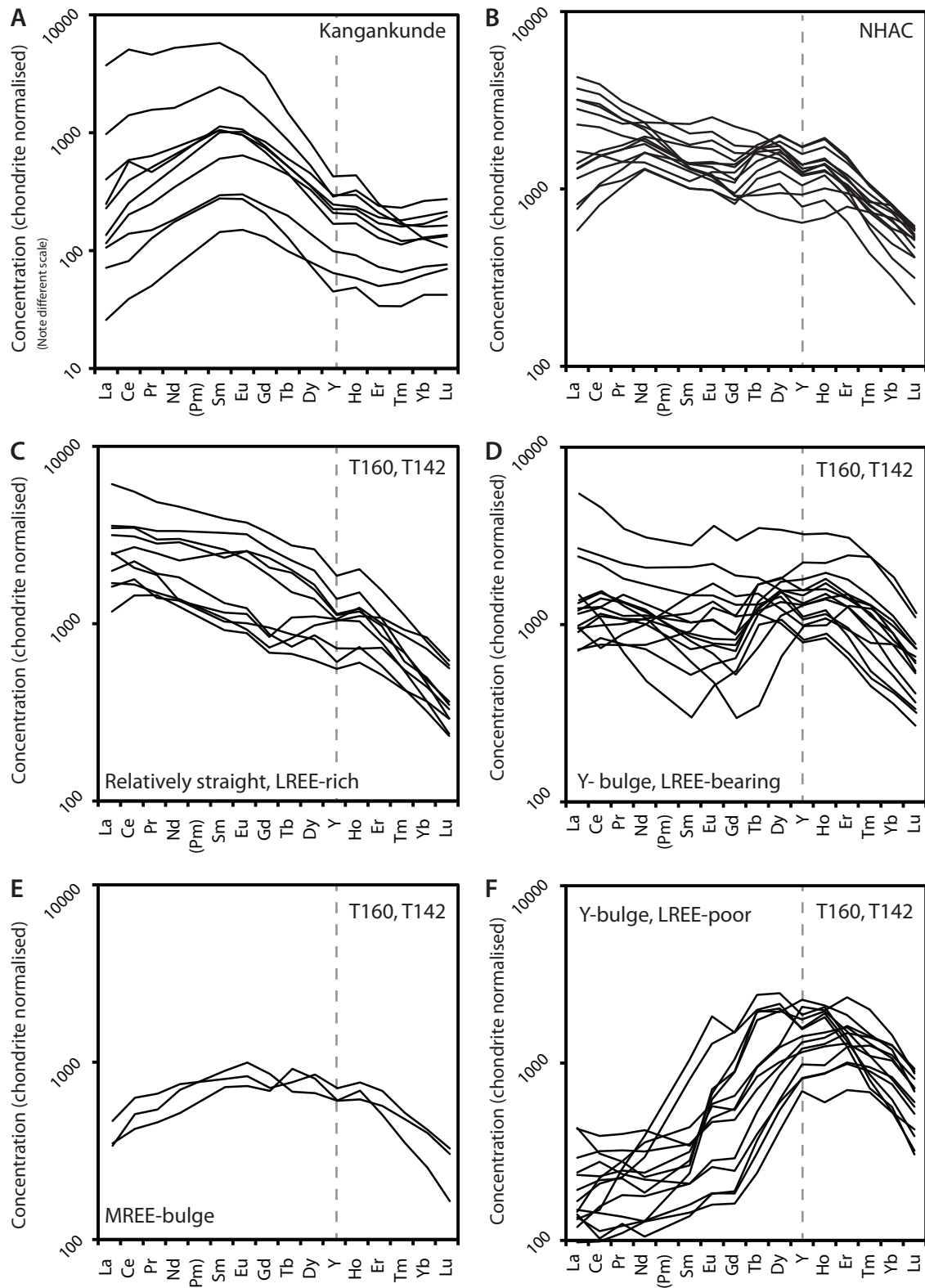


Figure 5.26: Chondrite-normalised REE distributions for turbid cores from (A) Kangankunde and (B–F) Tundulu. Distributions from samples T142 and T160 are split into groups according to the shape of the distribution to aid visualisation. Yttrium is highlighted with a grey dashed line for clarity. Chondrite values from McDonough and Sun (1995).

Euhedral rims, chondrite normalised diagrams

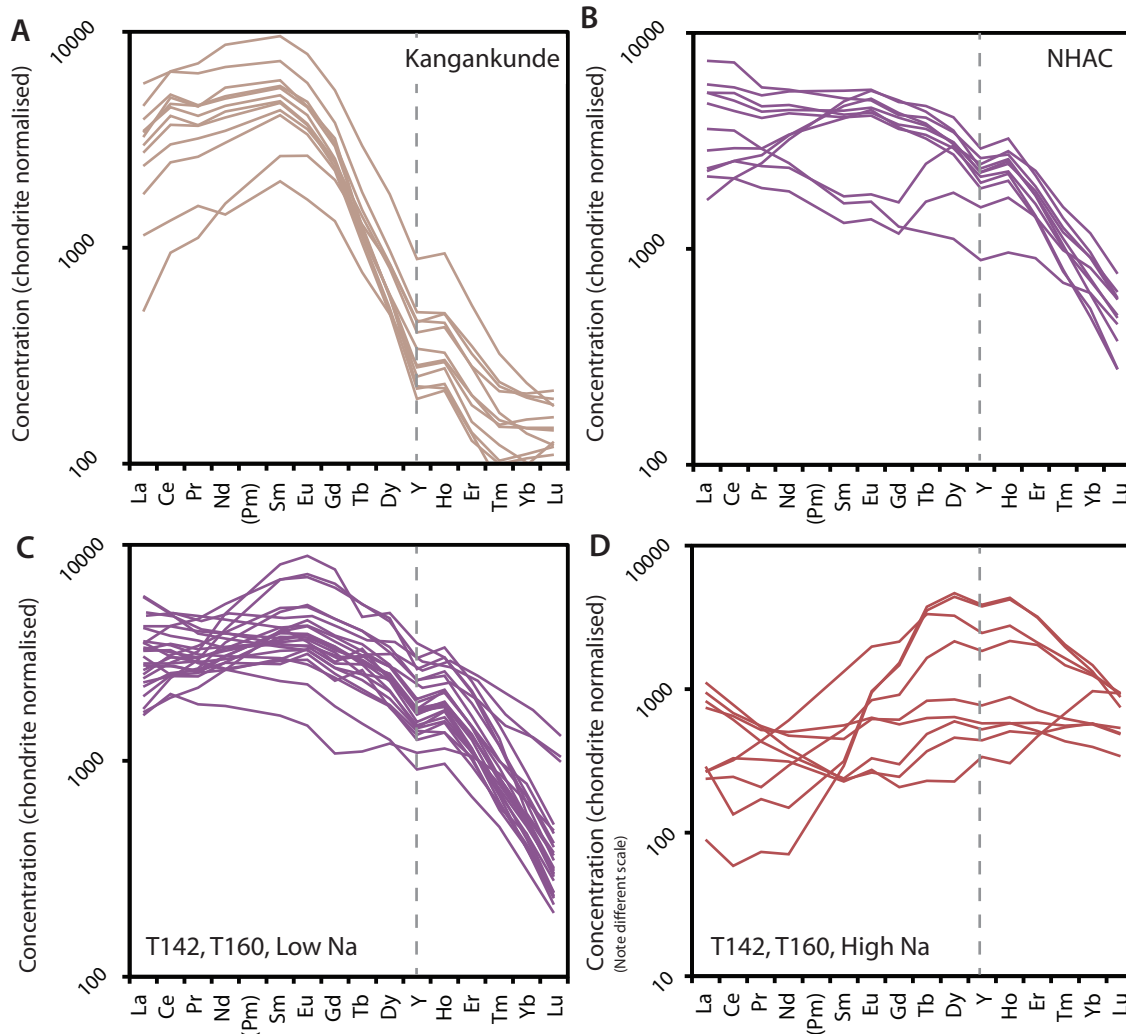


Figure 5.27: Chondrite-normalised REE distributions for euhedral apatite rims from Kangankunde (A), and Tundulu (B–D). Rim data from Tundulu is separated into data from NHAC (B) and data from T142 and T160 with purple–mauve luminescence (C) and maroon–green–red zones luminescence (D), corresponding to high and low Na concentration, respectively. Line colours represent the apatite luminescence under CL. Yttrium is highlighted with a grey dashed line for clarity. Chondrite values from McDonough and Sun (1995).

over the luminescence colour, and that increases in the REE concentration occur in the green luminescent bands. Mauve luminescent rims from Tundulu are interpreted to be caused by mixed violet Ce^{3+} , red-orange Sm^{3+} and possibly yellow Dy^{3+}/Tb^{3+} activation.

Paragenetic interpretation of apatite at Kangankunde

Both the quartz-druse rock from Kangankunde and the silicified apatite-carbonatite from Tundulu form late in the carbonatite petrogenesis on the basis of field relationships (Garson, 1962; Garson and Smith, 1965). The paragenesis of Kangankunde and Tundulu has been interpreted previously (Ngwenya, 1994; Wall and Mariano, 1996). Wall and Mariano (1996) interpreted the turbid cores at Kangankunde as forming early, followed by apatite overgrowths, co-crystallising xenotime and altered Fe-bearing carbonate, followed by a REE-rich phosphate phase and quartz mineralisation. The additional petrography carried out in this study supports this interpretation.

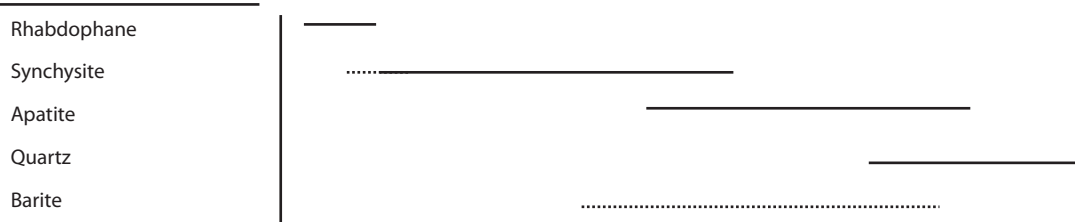
The co-crystallisation of xenotime and late apatite at Kangankunde can help to elucidate why Kangankunde apatite rims are LREE-rich but rims of a very similar habit at Tundulu are not. EPMA analyses of the xenotime showed that it is HREE enriched, with chondrite-normalised distributions peaking at Tb. This was interpreted by Wall and Mariano (1996) as a function of crystal-chemical control of the distribution of a MREE-distributed fluid into apatite and xenotime. The new LA ICP-MS data support this interpretation, and it is suggested that the late, euhedral apatite preferentially incorporated the LREE–MREE, while xenotime crystallisation incorporated the HREE. Such an interpretation is supported by the concentration of the REE in the apatite, which is much more LREE enriched than equivalent apatite from Tundulu (Fig. 5.24 E).

Paragenetic interpretation of apatite at Tundulu

Ngwenya (1991, 1994) suggested that rhabdophane (not identified in this study) and synchysite, both LREE enriched minerals, formed early in the paragenesis of silicified apatite carbonatite at Tundulu. This was followed by apatite and barite, and, finally, by quartz (Fig. 5.28 A). This is *not* supported by the new petrographic data and a revised interpretation is suggested in Figure 5.28 B. In the new model, turbid apatite is interpreted as forming early, followed by maroon and mauve luminescent apatite rims. This is clearly supported by the new CL images of zoning in the apatite (e.g. Figures 5.21 B and E). Some breakdown and dissolution of the preceding apatite stage is interpreted to have occurred during the formation of the subsequent apatite generation, as indicated by the corroded apatite zones, turbid, resorbed cores and the lack of maroon-luminescent apatite in sample NHAC.

Pyrochlore and rutile are interpreted as forming at the same time, or soon after the maroon or mauve luminescent apatite stages. All apatite stages and pyrochlore are slightly fragmented and brecciated, suggesting a minor brecciation event after crystallisation of these minerals (e.g. Figures 5.21 D and 5.22 B). Rhombohedral Fe-bearing carbonate and euhedral LREE-fluorcarbonates are not fragmented, indicating that these formed after fragmentation of the apatite and pyrochlore. Mineralisation terminated with the crystallisation of anhedral calcite and quartz. Barite was not observed in the samples studied. The most important observation here is that all apatite stages were formed *before* crystallisation of LREE-fluorcarbonates.

A: (redrawn after Ngwenya, 1994)



B: (this study)

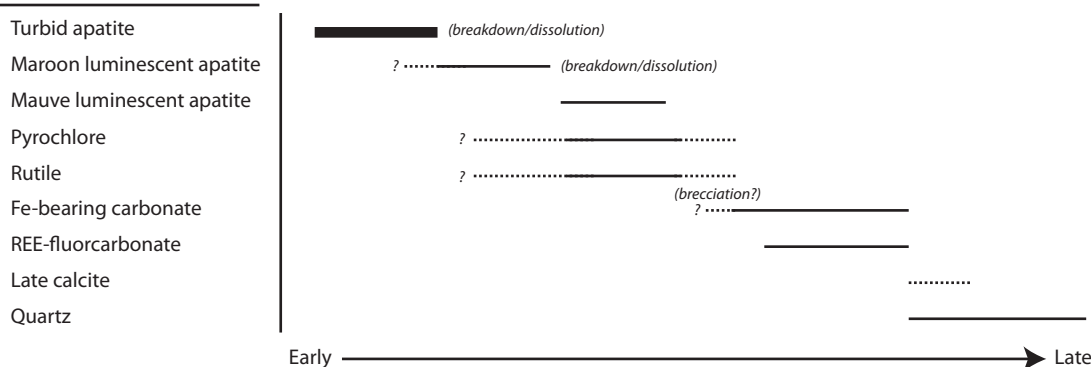


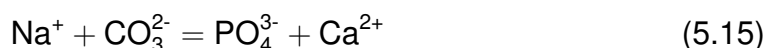
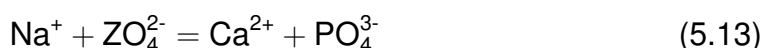
Figure 5.28: Interpretations of the paragenetic sequence at Tundulu: (A) after Ngwenya (1991, 1994), (B) this study.

Apatite substitutions

As is the case for the REE in Ap-3 and Ap-4 from Songwe, it is very likely that Na^+ is responsible for charge balancing the REE in both the cores and the rims of apatite from Kangankunde and Tundulu. Blank concentrations for Si from LA ICP-MS data were too high to evaluate the Si concentrations, but published EPMA data shows that the Si concentrations in both the cores and rims are low, and that the Si concentration in the rim is lower than in the core, despite the increased REE concentration (Ngwenya, 1991; Wall and Mariano, 1996). Indeed, in many of the rim analyses from both Kangankunde and Tundulu, Si is below the LOD on the EPMA. Na and REE concentrations from the new LA ICP-MS data have a strong positive correlation, suggesting a belovite-type substitution

(nomenclature after Pasero et al., 2010).

High Na concentration in the maroon rims of Tundulu apatite does not correlate with any of the other analysed elements with the possible exception of Sr, yet incorporation of Sr into the apatite structure must be charge balanced. Possible charge balancing mechanisms for incorporation of Na into apatite include:



Where M^{3+} represents a trivalent cation, \square represents a vacancy and ZO_4^{2-} represents a divalent anion. Trivalent substitutions for elements other than the REE (e.g. Bi^{3+} and Cr^{3+}) are known from synthetic apatites, but are unlikely to occur in sufficiently high concentrations in natural apatite (Pan and Fleet, 2002). Divalent anion substitution is possible (Equation 5.13), and SO_4^{2-} is a common substitute in apatite. Unfortunately, no analyses for SO_4^{2-} have been carried out and thus it is difficult to determine if SO_4^{2-} is substituting with Na^+ . The formation of a vacancy during substitution is a possibility, and a negative correlation between F and Na would be expected if this were taking place. Although no such correlation is observable in the data from Styles (1988) or Ngwenya (1991), the X site (fluorine site) in all these analyses is under-full. This means that vacancies are possible in these apatite analyses, although accurate analyses of F from apatite are notoriously difficult (Stormer et al., 1993) and the under-full X site is most likely related to analytical difficulty. Coupled substitution of CO_3^{2-} is interpreted as the most likely cause of Na enrichment (e.g. Equation 5.15). The presence of CO_3 was suggested by infra-red spectrometry on an acid-treated, hand-picked, bulk-apatite sample from Tundulu (Styles, 1988). Although this bulk sample would have incorporated all apatite types, it provides the best evidence that CO_3 is present in at least one of the apatite stages at Tundulu. Therefore, it is concluded that the Na-rich, maroon-luminescent apatite stage is most likely CO_3 -rich, although SO_4^{2-} may also play a role.

Apatite REE distribution and the tetrad effect

All REE distributions of apatite from Kangankunde and Tundulu display an Y anomaly. With the exception of LREE-poor apatite from some Tundulu core analyses, these are all negative Y anomalies. Given that fractionation between Y and Ho is unlikely to be crystal-chemical controlled it is likely that the negative Y anomaly is due to retention of Y in the solution due to the greater stability of

YF²⁺ complexes (Bau and Dulski, 1995; Loges et al., 2013). This implies that F is present in the precipitating fluid. This suggestion is supported by the composition of the apatite (fluorapatite) (Wall and Mariano, 1996; Ngwenya, 1994) and the presence of REE-fluorcarbonates crystallising after apatite. Another implication is that the REE-fluorcarbonates would have a positive Y anomaly, to balance the negative anomalies observed in the apatite. Unfortunately, the published EPMA analyses do not include analyses of Y and the HREE.

5.5 Discussion

5.5.1 Comparison between apatite from Songwe, Tundulu and Kangankunde

Texturally, apatite from Songwe is quite different from that found at Tundulu and Kankankunde. The core–rim overgrowths, which are readily identifiable at Kangankunde and Tundulu, are only poorly displayed in Ap-3 from Songwe, and the closest equivalent is only readily observable in X-ray count maps (Fig. 5.4). Mineral associations, too, are different between late apatite from Songwe and the other studied carbonatites. At Kangankunde and Tundulu, quartz is associated with the late apatite overgrowths, but at Songwe quartz is not commonly found with Ap-3, and only forms very late after Ap-4. Extensive calcite is associated with the apatite at Songwe, but very little calcite, or other carbonate, formation is found in association with the late-stage apatite at Kangankunde or Tundulu. Both apatite from Songwe and Tundulu, however, precede REE-fluorcarbonate mineralisation. No REE-fluorcarbonate mineralisation is observable in the quartz-druse rocks from Kankankunde (Wall and Mariano, 1996).

Geochemically, late-stage apatite from Songwe (Ap-3 and Ap-4), Tundulu and Kangankunde have many similarities. Selected Ap-3 and Ap-4 analyses from Songwe, and core and rim analyses from Kangankunde and Tundulu, are shown in Figure 5.29. It should be noted that the high-Na, maroon-luminescent rims from Tundulu have been excluded from these plots. The REE in each intrusion positively correlates with Na (Fig. 5.29 A–B). Sr concentrations are highest in apatite rims from Kangankunde, and lowest in the cores from both Kangankunde and Tundulu. Sr and Ce have a weak positive correlation (Fig. 5.29 C–D) and this, combined with the stronger correlation between the REE and Na, suggests a belovite-type substitution is occurring in all the apatite types.

Apatite from Songwe is much more HREE enriched than samples from Kangankunde and Tundulu, as indicated both by the chondrite-normalised REE distributions (Figures 5.10, 5.26 and 5.27), and the total concentration of the LREE and HREE+Y (Fig. 5.29 E). Typically, the total concentration of the HREE+Y

in apatite from Songwe is greater than the total LREE concentration, while apatite rims from Kangankunde show LREE-rich distributions and those from Tundulu have roughly equal proportions of both the LREE and the HREE.

Uranium concentrations in all the late-stage apatite types are low. The concentration, however, is typically up to 1000 ppm, and in some of the Songwe Ap-3, it is much higher, up to 5000 ppm.

Xenotime is a rare phase in carbonatites and has only been identified at Kangankunde, Malawi, (Wall and Mariano, 1996) and Lofdal, Namibia, (Wall et al., 2008). The weathered equivalent, churchite, has been identified at Mt Weld, Australia (Lottermoser, 1987, 1990). Of these examples, only xenotime from Kangankunde has formed in a late-stage environment similar to that at Songwe, as xenotime from Lofdal is considered to have formed magmatically while churchite is a weathering product. Xenotime is observed both in association with Ap-4 at Songwe and in the quartz-druse rocks at Kangankunde. Wall and Mariano (1996) analysed the xenotime using EPMA, permitting comparison with the new xenotime EPMA data from Songwe. Interestingly, the xenotime from Kangankunde is more MREE enriched, peaking at Tb, while xenotime from Songwe is more typical, with the REE distribution centred on Y. Wall and Mariano (1996) interpreted this as a function of the partition coefficients of apatite and xenotime co-crystallising from an MREE-rich fluid. Texturally, the xenotime overgrowths on apatite at Songwe appear to have formed after the apatite, and therefore co-crystallisation is unlikely. Xenotime at Songwe is interpreted to have formed from re-crystallisation of apatite, and, therefore, its REE distribution is likely to be representative of the some of the REE expelled from the apatite structure. The ThO₂ concentration of xenotime from Kangankunde varies between 0.82 and 1.27 wt. %, which is lower than that found in both xenotime types at Songwe. Xenotime analyses from Songwe, Kangankunde and Lofdal do not display an Eu-anomaly, in contrast to xenotime from granitic rocks (e.g. Förster, 1998).

5.5.2 Comparison with apatite from other localities

There are numerous published lists of apatite chemistry from different rock types, and one of the most comprehensive is that of Fleischer and Altschuler (1986). Additionally, Hogarth (1989) compiled data to compare apatite from carbonatite with apatite from granitoid, skarn and phosphorite. Data from these compilations, however, are mostly from EPMA analyses, and concentrations of some elements may be close to the detection limit using this technique. It was, therefore, decided that it was best to compile a list of relatively recently published analyses (post 1989) of apatite, that used techniques with lower detection limits than the EPMA. However, there are very little data from mafic/ultramafic rocks, Kiruna-type deposits, phosphorites and volcanic rocks, and so the data compilation is

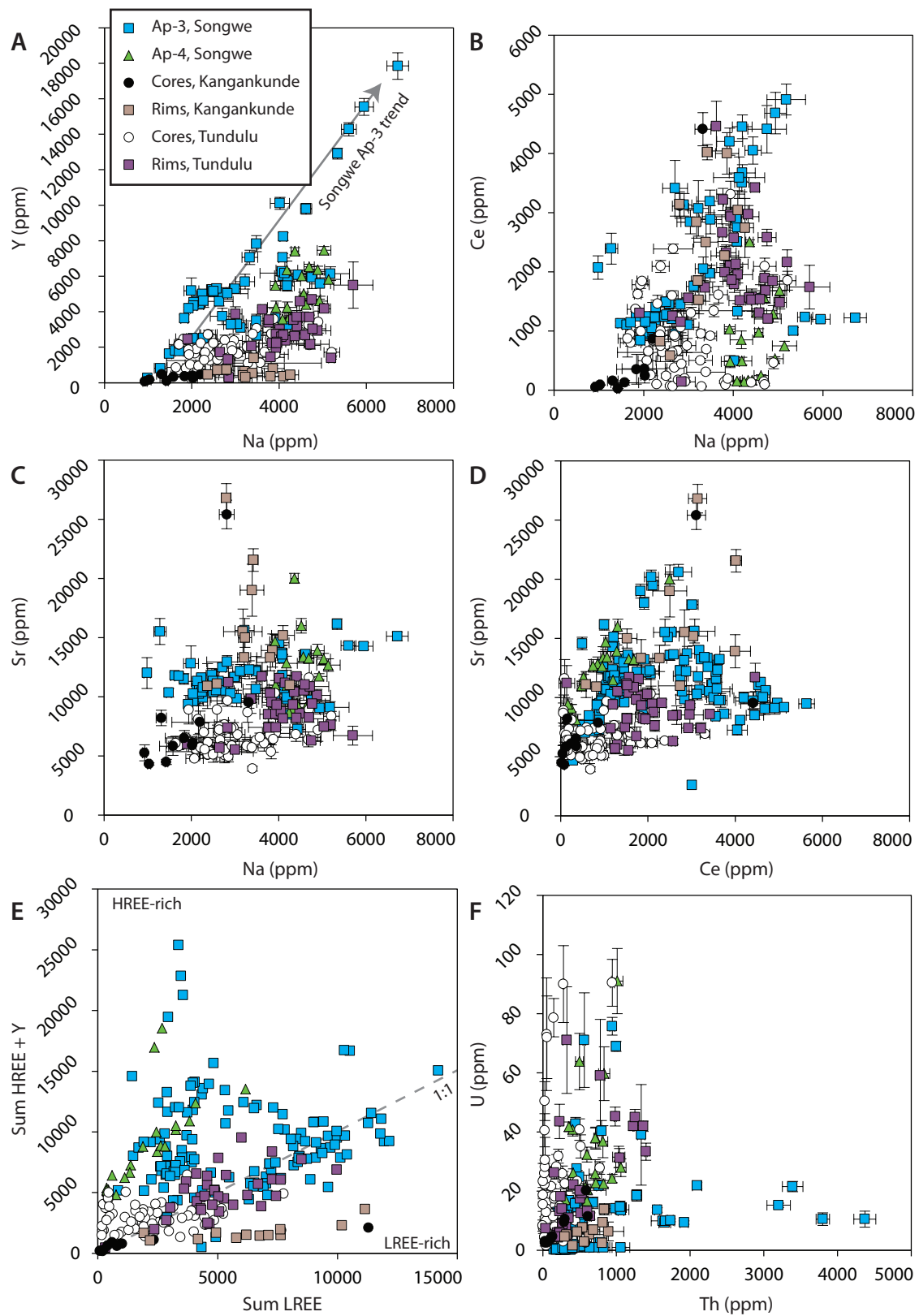


Figure 5.29: Comparison of data from late-stage apatite from Songwe (Ap-3 and Ap-4), Kangankunde and Tundulu. Rim analyses from Tundulu do not include areas of maroon luminescence.

restricted to granitoid and carbonatite occurrences. The data sources of the published analyses and the location of the carbonatites and granitoids are listed in Table 5.13.

Location	Reference
Carbonatites	
Oka	Hornig-Kjarsgaard (1998) Chen and Simonetti (2013)
Kaiserstuhl	Hornig-Kjarsgaard (1998)
Alno	Hornig-Kjarsgaard (1998)
Sokli	Hornig-Kjarsgaard (1998)
Sillijarvi	Hornig-Kjarsgaard (1998)
Jacupiranga	Hornig-Kjarsgaard (1998)
Phalaborwa	Hornig-Kjarsgaard (1998) Dawson and Hinton (2003)
Fen	Hornig-Kjarsgaard (1998)
Miaoya	Xu et al. (2010)
Vuriyarvi	Brassinnes et al. (2005)
Juquia	Walter et al. (1995)
Kovdor	Kempe and Götze (2002)
Ermakovka	Kempe and Götze (2002)
Ondurakorume	Bühn et al. (2001)
Kalkfeld	Bühn et al. (2001)
Otjisuzu	Bühn et al. (2001)
Homa Bay	Bühn et al. (2001)
North Ruri	Bühn et al. (2001)
Okorusu	Bühn et al. (2001)
Granites:	
Ehrenfriederdorf	Kempe and Götze (2002)
Mt. Takakuma	Nagasawa (1970)
English River Subprovince	Pan and Breaks (1997)
Lachlan fold belt	Sha and Chappell (1999)
Central Kazakhstan	Cao et al. (2012)
Himilaya	Chu et al. (2009)
Nanling Mountains	Hsieh et al. (2008)
West Tatra Mts	Szopa et al. (2013)
Luzong	Tang et al. (2012)
Zijinshan	Lingdi and Yangchuan (1989)
Geşinieç	Pietranik et al. (2011)

Table 5.13: Compiled sources of REE data from apatite.

Hogarth (1989) and Belousova et al. (2002) have devised classification diagrams for determining rock classification from apatite chemistry. These diagrams have been amalgamated here, and expanded using published analyses, for comparison with the Songwe, Tundulu and Kangankunde apatite data (Fig. 5.30). Where additional published data plot outside the published fields, these have

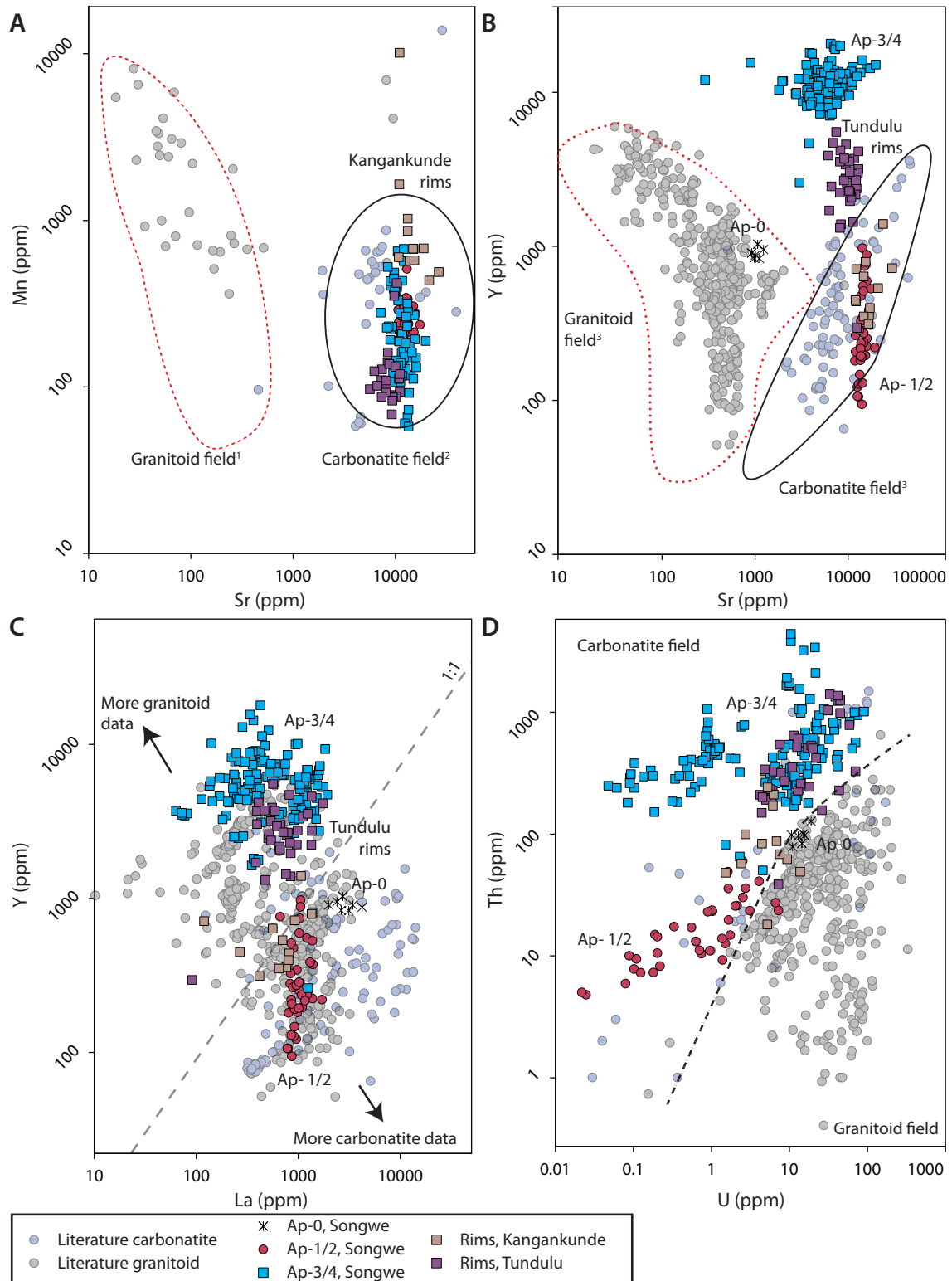


Figure 5.30: Songwe, Kangankunde and Tundulu apatite compositions compared with published carbonatite and granitoid analyses (for data sources see Table 5.29) and modified fields after Belousova et al. (2002) and Hogarth (1989). Fields marked with superscript 1 are unmodified from Belousova et al. (2002), those marked with superscript 2 are combined fields of Belousova et al. (2002) and Hogarth (1989), while those marked with a 3 are re-drawn to better represent the spread of data when incorporating additional published data. The fields in C and D are arbitrarily defined, where the compositions of the different apatite types can be separated. There is overlap between the two fields of Y/La ratios.

been modified and expanded to accommodate the larger data range. The Mn-Sr apatite classification diagram of Hogarth (1989) remains robust for carbonatite analyses. However, for granitoid rocks, when combined with a similar plot from Belousova et al. (2002) and additional LA ICP-MS analyses, the field of Hogarth (1989) needs to be extended to lower Sr concentrations. This may be because the analyses used to construct the original diagram were largely from EPMA, whereas the more recent LA-ICP-MS results have lower detection limits.

The Y-Sr diagram of Belousova et al. (2002) is reasonably robust for granitoid analyses. A comparison of 440 published granitoid analyses shows reasonable overlap with published fields for granitoids (Fig 5.30 B). The carbonatite field, however, was based on 61 analyses from 4 carbonatites and comparison to 90 analyses from 20 carbonatites from the literature shows a large disparity between the two groups. All the published analyses have higher Sr concentration than the analyses from the 4 carbonatites of Belousova et al. (2002), and also significantly higher Y concentrations.

Two new classification diagrams have been plotted using the collected literature data for REE and U-Th concentration (Figure 5.30 C, D). It was necessary to use Y and La to represent HREE and LREE on Fig 5.30C as published REE data are commonly incomplete. There are few data available for U and Th in carbonatite apatite and so this group should be treated with caution. However, it is observed that granitoids typically have lower La and Th and higher Y and U concentrations than the carbonatite analyses.

All the apatite data from Songwe, Kangankunde and Tundulu plot in the carbonatite Mn-Sr field (Fig 5.30 A) re-affirming their carbonatitic origin. The fenite apatite compositions from Songwe, with just 1000 ppm Sr, is most likely an exception to this but Mn analyses have poor accuracy and are not plotted.

When compared with the modified Y-Sr plot (Fig. 5.30 B) groups of Songwe, Tundulu and Kangankunde apatite plot outside the established carbonatite field. Ap-0 from fenite has more granitoid-like chemistry and Ap-3 and Ap-4 clearly have higher Y concentrations (representing HREE) than any previously published carbonatite analyses (Figure 5.30 B). This pattern is also clearly shown by Figure 5.30 C, on which Ap-3 and Ap-4 extend the range of carbonatite apatite-hosted heavy REE (Y) into the granitoid field; Ap-3 from Songwe has higher La and Y concentrations than most granitoid analyses. With increasing REE contents, Songwe apatite is also enriched in Th and U, up to 5000 ppm, towards the higher concentrations seen in carbonatite-derived apatite (Figure 15 D). The intermediate granitoid-carbonatite compositions of the fenite Ap-0 at Songwe are consistent with the formation of the metasomatic fenite by mixing of carbonatite and country rock granitic components. The small amounts of radioactive U and Th that follow the HREE could have implications for the environmental impact of

HREE-extraction (see Weng et al., 2013; Wall, 2014) although the contents are similar to granitoid-derived apatite.

5.5.3 What can the changing apatite composition tell us about the nature of late-stage fluids in carbonatites?

Just as fluorite can be used to investigate the REE distributions of the crystallising fluid, so too can apatite. By combining the paragenetic information and the composition of apatite from Songwe it is possible to make some inferences about the nature of late-stage fluids in carbonatites, and the behaviour of the REE in these fluids.

The composition of Ap-1 is typical of primary magmatic apatite with a LREE-enriched distribution. This reflects the typical LREE-enriched composition of carbonatites. It is evident from the petrographic relationship of Ap-3 with the other carbonatite types and fluid phases at Songwe that Ap-3 crystallised after the formation of the magmatic carbonatites (C1–C3), but before widespread LREE-fluorcarbonate mineralisation or fluorite mineralisation. It is, therefore, inferred that it crystallised as an early precipitating phase from an expelled hydrothermal fluid. Fluid exsolution during carbonatite evolution is a process which is predicted to occur in many carbonatites, and is likely to be responsible for REE, fluorite and barite mineralisation (Le Bas, 1989; Rankin, 2005). Fluids are exsolved as the melt ascends, decompresses and cools (Rankin, 2005). The exsolved fluids are poorly understood but, from the limited studies where they have been characterised, are generally considered to be composed of Na-K-chloride-carbonate/bicarbonate brines (Rankin, 2005). The only study where the chemistry of these fluids has been characterised showed that they are rich in the REE (up to 40,000 ppm total REE) as well as Ba, Sr, Na and K (Bühn and Rankin, 1999).

Some information on the nature of the hydrothermal fluid can be inferred from the composition of the apatite at Songwe. Given that only fluorapatite crystallised, the fluid *must* have contained F, and it is highly likely that it also carried P and Ca, although the incorporation of these elements through reaction with the magmatic carbonatite cannot be ruled out. Apatite is also commonly associated with calcite, implying a high CO₂ activity in the fluid. Given the high concentration of the REE in the apatite, it is evident that this fluid phase was capable of transporting the REE. The high HREE concentration in the apatite suggests that either the HREE were preferentially partitioned into the hydrothermal phase or that HREE precipitated out of solution earlier than the LREE. The correlation of U and Th with the HREE indicates that the behaviour of the actinides follows that of the HREE.

It is assumed here that the crystallisation of the LREE-fluorcarbonate–strontianite–barite assemblage and the crystallisation of apatite are related. Such an assumption is logical as it requires only one, evolving, fluid rather than the generation of multiple different exsolved fluids from the carbonatite at different stages. Given this assumption, the mineralogy of the LREE-fluorcarbonate–strontianite–barite assemblage implies that the anions SO_4^{2-} , CO_3^{2-} , HCO_3^- and F^- are likely to have been present in the carbonatite-derived fluid. If the interpreted relationship between the two mineral assemblages is real, then the cross-cutting relationships indicate that apatite would have precipitated out of solution very early during the fluid evolution.

Early precipitation of phosphate is logical as REE phosphates, such as monazite and xenotime, have a relatively low solubility in hydrothermal fluids, especially at elevated temperatures (Poitrasson et al., 2004; Cetiner et al., 2005; Gysi et al., 2015). The solubility of apatite in a hydrothermal fluid is less well constrained, but experiments in silicate melts show that apatite is more soluble than monazite and solubility increases with increasing NaCl concentration (Ayers and Watson, 1991; Wolf and London, 1995; Piccoli and Candela, 2002). The low solubility of apatite is also indicated in alteration assemblages of monazite, apatite and bastnäsite from Bayan Obo (Smith et al., 1999). Given the lower solubility of monazite and xenotime than apatite, it is not known why apatite formed, rather than monazite, especially given the abundance of LREE in the system. One such possibility is that in alkali, Cl⁻- or F⁻-bearing fluids, the solubility of monazite can be greater than that of apatite, and in these situations, apatite has a great capacity to incorporate high concentrations (up to 23 wt. %) of the REE (Krenn et al., 2012). Another possibility is that the abundance of Ca may have played a role, as apatite can readily be synthesised through reaction of P-bearing fluids with carbonates (Kasioptas et al., 2008, 2011). Where apatite was already present in the carbonatite (as Ap-1), the fluids may have reacted with the magmatic apatite, forming HREE-enriched Ap-2 overgrowths.

Continued evolution and cooling of the exsolved fluid leads to the precipitation of the LREE fluorcarbonates, strontianite and barite, implying that F^- , SO_4^{2-} and $\text{CO}_3^{2-}/\text{HCO}_3^-$ remained stable in solution after the formation of apatite.

The comparable parageneses at Tundulu and, to a lesser extent, Kangankunde implies that a similar process occurred at these localities. Apatite at each locality is interpreted to have formed from a hydrothermal fluid, and in each occurrence apatite forms early, followed by later fluorcarbonate crystallisation. The anions inferred to be present in the fluids are therefore the same as at Songwe. The chemistry of the apatite is slightly different between each deposit, and it is difficult to reconcile the presence of an Y anomaly in the Kangankunde and Tundulu apatite with the lack of an anomaly in the Songwe apatite. It is suggested that

the role of F^- may be greater in the transport of the REE at Kangankunde and Tundulu.

Further discussion on the role of different complexes in transporting and fractionating the REE is provided in Chapter 6.

5.5.4 Reconciling apatite REE distributions with whole-rock distributions

Whole-rock distributions at Songwe are LREE enriched, sloping linearly towards lower HREE concentrations, but with a negative Y anomaly (Chapter 4). The bulk of the whole-rock LREE can be assumed to be hosted by LREE-fluorcarbonates but the high concentration of HREE in Ap-3 and Ap-4 means that these phases are the dominant control on the HREE distribution. For most of the HREE this is the case, but apatite from Songwe does not have a negative Y anomaly, whereas the whole-rock distribution does.

The only feasible phase, other than apatite, which could host sufficiently high Y concentrations would be the LREE fluorcarbonates. EPMA analyses of the REE-fluorcarbonates have been carried out (Brady, *unpublished data*), and Y_2O_3 concentrations can reach over 3 %. The elements analysed, however, do not include the HREEs Ho–Lu and it is therefore difficult to judge whether the chondrite-normalised distributions show an Y anomaly. Given the small size of the synchysite-(Ce) crystals, further investigation of the trace-element composition by LA ICP-MS was not feasible. However, as the likelihood of another phase containing sufficiently high Y to have a significant effect on the REE distribution is low, synchysite is assumed to host the anomalously low Y concentration to reconcile the whole-rock data with the trace-element data.

The analyses of fluorite in the apatite-fluorite veins display a prominently positive Y anomaly. Such an anomaly from the Okorusu carbonatite was interpreted by Bühn (2008) to be representative of the composition of expelled carbonatite fluid. It is possible that such a process is taking place at Songwe and that fluorite in the apatite-fluorite veins is representative of the fluids expelled from the carbonatite.

5.6 Summary and conclusions

Textural and geochemical data for different generations of apatite from Songwe Hill have been presented. The apatite generations are divided into 5 types, each with increasingly more HREE enriched REE distributions:

0. Apatite from fenite— anhedral, fragmented, LREE-rich, minor Eu-anomaly, Sr and Mn poor relative to carbonatite apatite

1. Cores of ovoid ('lozenge-shaped') grains in C1 calcite-carbonatite— LREE-rich, low U and Th.
2. Rims of ovoid ('lozenge-shaped') grains in C1 calcite-carbonatite— similar to Ap-1, but potentially higher HREE
3. Anhedral apatite, sometimes forming stringers in C2 and C3 carbonatite— high Na concentration, HREE enriched, relatively high Th.
4. Anhedral apatite, in apatite-fluorite veins— similar to Ap-3, but spongy, and with xenotime overgrowths.

'Lozenge-shaped' and LREE enriched Ap-1 is interpreted to form in an early magmatic stage of the carbonatite, on the basis of comparison with apatite from other carbonatites. Ap-2–4 are interpreted as forming during various stages of sub-solidus alteration but, importantly, are interpreted to have formed prior to the widespread crystallisation of the REE-fluorcarbonates.

Ap-2–4 show various degrees of HREE-enrichment, relative to typical carbonatite-apatite, with some analyses containing over 2 wt. % HREE+Y. HREE-enrichment culminates with the crystallisation of xenotime. With increased HREE concentration, however, the concentration of the 'penalty' element Th also increases, reaching up to 3 wt. % in xenotime related to Ap-4. The incorporation of Na, Sr and the REE into the apatite structure is interpreted to be a belovite-type substitution.

The first analyses of As in carbonatitic apatite are also presented in this chapter, with As reaching up to 30 ppm in apatite from Songwe. The As concentration correlates with increasing REE concentrations. This may be explained by expansion of the PO₄ site during REE substitution, enabling the larger AsO₄ ion to substitute. Further experimental work is required to test this.

Trace element concentrations of fluorite associated with Ap-4 are also presented in this chapter. The fluorite is HREE enriched with a similar distribution to that of the Ap-4. It has, however, a prominent positive Y anomaly. Comparison with carbonatite-derived fluorite from other deposits indicates that such an anomaly is common, although the fluorite from Songwe is the most HREE-rich carbonatite-associated fluorite analysed to date.

Ap-3 is interpreted to have crystallised early from an exsolved hydrothermal fluid. This is assumed to be a single, continuously-evolving fluid which also led to the formation of LREE-fluorcarbonates, rather than the first of a series of different fluids. HREE-enrichment is interpreted to have been caused by either preferential incorporation of the HREE in the exsolved fluid phase, or preferential precipitation of the HREE from a fluid. The mineralogy of these hydrothermal stages implies that ligands available to transport the REE included SO₄²⁻, CO₃²⁻, HCO₃⁻, F⁻ and PO₄³⁻. The mechanisms of HREE enrichment are discussed in Chapter 6.

For comparison with the late-stage apatite at Songwe, apatite described as 'late-stage' from the Kangankunde and Tundulu carbonatite, Malawi, has also been investigated. Apatite from these localities shows a clear textural distinction between early and late crystallisation. Early apatite comprises turbid cores, with lower Sr, REE, Na, U and Th. Late apatite comprises clear euhedral rims, with increased REE, Sr, U, Th, and Na. Similarly to Songwe, this is interpreted as a belovite-type substitution.

The petrographic sequence at Tundulu has been revised. Previous interpretations envisaged that the REE-fluorcarbonates crystallised before the apatite rims (Ngwenya, 1994). This study shows that the synchysite crystallised *after* the apatite rims, in a manner similar to the formation of REE-fluorcarbonates at Songwe. A more detailed study of the apatite rims at Tundulu, using CL has also revealed the presence of an Na-rich zone, which luminesces maroon-red. As the high Na concentration in this zone does not correlate with any other analysed element, it is interpreted to be due to substitution of CO_3^{2+} into the apatite structure, as has been suggested by Styles (1988) using infra-red spectroscopy.

Comparison of Ap-3, and rim analyses from Kangankunde and Tundulu, to a compilation of published apatite analyses shows that the apatite from Songwe contains the highest Y concentration (and therefore the HREE) of apatite from any previously analysed carbonatite. Classification diagrams have been devised using the published data, and the apatite from Songwe extends the range of HREE content in carbonatitic apatite through the granitoid field, opening up carbonatites as potential sources of the sought-after mid and heavy REE. Apatite from Tundulu is also HREE enriched, relative to typical carbonatite apatite, but not to the same degree as the apatite from Songwe. This suggests that, although HREE-rich apatite is not common, it is likely to occur in other carbonatites that have been subject to pervasive sub-solidus alteration, especially where early apatite formation may have been suppressed.

Chapter 6

Fluid process and mobility of the REE in carbonatites

In the previous chapter it was established that apatite types Ap-3 and Ap-4 from Songwe are HREE-enriched relative to typical apatite from carbonatite (e.g. Hornig-Kjarsgaard, 1998). This chapter attempts to elucidate why HREE mineralisation took place in an otherwise LREE-enriched rock type. New fluid inclusion data from apatite and fluorite are presented to constrain the temperature and composition of the mineralising fluids. These data are then combined with the mineral composition data presented in the preceding chapters to constrain the controls on the transportation, fractionation and deposition of the REE. Using these constraints, a mineralisation model is suggested for Songwe.

6.1 Methodology

6.1.1 Sample selection

Wafers for fluid inclusion analysis were prepared from eight Songwe samples to represent apatite from C2–C4 carbonatite. Additionally, for comparison, a fluid inclusion wafer was prepared from a sample of quartz-druse rock rich in apatite from Kangankunde (BM 1962 73 (131); Wall and Mariano, 1996). Of these samples, however, observable and analysable inclusions were only found in two wafers (T0167, T0178). Within these, observable inclusions were in Ap-3, Ap-4 and fluorite. These samples, while few in number, crystallised over a wide paragenetic range. Therefore, they provide a useful insight to the constraint of fluid temperature and chemistry during apatite mineralisation.

6.1.2 Wafer preparation

Fluid inclusion wafers were doubly polished between 100–200 μm thick. The wafers were mounted in epoxy resin on a large-format (3×2 inches) glass slide to reduce the risk of detachment of the wafer from the slide during polishing. These slides were then used for petrographic analysis using a petrographic microscope with a $\times 50$ objective lens, at CSM¹.

Areas of interest for microthermometry were drilled out using a dentist's drill affixed to a microscope with a motor-driven rotating stage. The area of interest was aligned to the centre of the stage using the microscope and the drill adjusted to the desired width of the plug (chip for microthermometry). With the stage rotating, winding down the focus at approximately 10–15 μm intervals freed small (100–500 μm diameter) plugs, suitable for microthermometry. When all the areas of interest had been drilled from a section, the glass-mounted fluid inclusion wafer was immersed in acetone, softening the epoxy resin and allowing the plugs to be removed from the slide. If this was carefully timed, the plugs can be removed whilst keeping the rest of the wafer affixed to the slide, allowing further petrographic use. Any residual epoxy resin on the slide was removed using an acetone-soaked paper towel.

6.1.3 Microthermometry

Microthermometric measurements were carried out at the BGS², UK, and at McGill University, Canada. At the BGS, data were collected using a Linkam THM600 stage, attached to a Leitz Ortholux II petrographic microscope. Instrument calibration was done using synthetic fluid inclusion standards at -56.6, 0 and 374 °C. Estimated analytical error is ± 0.2 °C for low (<50 °C) and ± 2 °C for higher (>75 °C) temperatures. Analyses at McGill were carried out using a Linkam TS1500 stage attached to an Olympus model BX 60 optical microscope. Instrument calibration was done on both instruments using (different) synthetic fluid inclusion standards at -56.6, 0 and 374 °C. Estimated analytical error is ± 0.2 °C for low (<50 °C) and ± 2 °C for higher (>75 °C) temperatures.

Stretching and leaking is common during microthermometric measurements of fluid inclusions in fluorite. This can cause the vapour bubble to expand, potentially giving artificially high homogenisation temperatures. To avoid this issue, fluid inclusions were first heated, contrary to the typical method of analysis (e.g. Shepherd et al., 1985). This ensured that the vapour bubble was homogenised prior to any leaking, and prior to stretching upon freezing. Any damage to the inclusion, such a leakage, would not affect the freezing and melting point of the

¹Camborne School of Mines

²British Geological Survey

fluid as the salinity would remain the same, despite any fluid loss. Stretching and leakage during freezing is not considered to be an issue in apatite-hosted inclusions, and low-temperature phase-changes were therefore analysed prior to heating, as is the normal procedure for FI³ analysis (Shepherd et al., 1985).

6.2 Results

6.2.1 Petrography

Ap-3 (C3)

Inclusions in Ap-3 occur as rare, irregular clusters that often appear disrupted and opened (Fig. 6.1 A–C). They are interpreted as primary inclusions on the basis of their occurrence in randomly distributed clusters away from grain boundaries (Fig. 6.1 C). Assemblages from Ap-3 comprise single vapour-phase (V) inclusions, mixed 2-phase aqueous LV⁴ and three-phase carbonic LLV⁵ with 5–40 % vapour bubble volume (estimated using techniques after Shepherd et al., 1985; Fig. 6.1 B–C). Trapped solids are also present in a small number of inclusions: these are rusty brown under PPL and isotropic under XPL indicating that they are probably Fe-oxides.

Ap-4 (C4)

Small inclusions in Ap-4 are abundant but most occur in areas of turbid apatite and are therefore partially obscured and not amenable to study (Fig. 6.1 D). In the rare areas where the inclusions are discernible, they are interpreted as primary on the basis of their elongate habits, parallel to grain boundaries (Fig. 6.1 D–E). Many inclusions, however, appear to have leaked and few LV inclusions remain. There are no inclusions with more than two phases and few had a readily visible vapour bubble (Fig. 6.1 D–E).

Fluorite, (C4)

Data from inclusions in fluorite provide information on conditions following apatite crystallisation. Fluorite contains abundant LV inclusions that are interpreted as primary on the basis of uniform vapour volumes (15–20 %), negative mineral shapes and a random distribution within the host mineral grain (Fig. 6.1 F–G). A small number of the inclusions also contained a trapped, highly birefringent, mineral, interpreted as a carbonate phase (Fig. 6.1 F).

³fluid inclusion

⁴liquid-vapour

⁵liquid-vapour-CO₂

Other minerals

Both barite and quartz also form after apatite mineralisation and contain fluid inclusions. Barite hosts small LV inclusions which are interpreted as secondary because of their occurrence in regular straight lines, parallel to cleavage planes. Many also appear to have leaked. Inclusions in quartz are all LV, with some containing unidentified trapped solids (Fig. 6.1 H). These include a highly birefringent phase, likely to be carbonate, and a radiating lamellar highly-birefringent mineral (nahcolite?). As inclusions in both quartz and barite occur late in the paragenesis, significantly after formation of REE-bearing phases, these were not studied.

6.2.2 Microthermometry

Microthermometric measurements on inclusions in Ap-3, Ap-4 and fluorite are presented in Tables 6.1, 6.2 and 6.3, respectively.

Ap-3 (C3)

Microthermometric data were collected from 38 inclusions. These comprise a mixture of three-phase LLV and two-phase LV inclusions. In the LLV inclusions, the carbonic phase melts at $-56.75\text{ }^{\circ}\text{C}$ (median) indicating that the inclusions are relatively pure CO_2 . Clathrate melting occurs between $1.8\text{--}6.9\text{ }^{\circ}\text{C}$ (median $4.9\text{ }^{\circ}\text{C}$), CO_2 homogenisation to liquid (LH) occurs between $13.4\text{--}29.9\text{ }^{\circ}\text{C}$ (median $27.65\text{ }^{\circ}\text{C}$). Homogenisation to a single liquid phase occurred between $200\text{--}350\text{ }^{\circ}\text{C}$ (median $290\text{ }^{\circ}\text{C}$) if a single outlier LV inclusion is excluded (Fig. 6.2).

Ap-4 (C4)

Due to the turbid nature of the apatite and the small size of the inclusions there are few data available from inclusions in Ap-4. No ice melting was observable. Homogenisation temperatures, by disappearance of the vapour phase, ranged between $160\text{--}230\text{ }^{\circ}\text{C}$ if a single outlier is excluded (Fig. 6.2).

Fluorite (C4)

Microthermometric data were acquired from 44 inclusions. Homogenisation temperatures to a single liquid phase ranged between $120\text{--}170\text{ }^{\circ}\text{C}$ (median $151\text{ }^{\circ}\text{C}$; Fig. 6.2) and final ice melting temperatures between -8.6 to $-0.3\text{ }^{\circ}\text{C}$. Heating of the sample was aborted after $170\text{ }^{\circ}\text{C}$ to reduce the impact of leakage from the inclusions; consequently one data point does not have a homogenisation temperature. Decrepitation also occurred in some samples, this took place after homogenisation, but meant that no melting temperatures could be acquired. Although the data

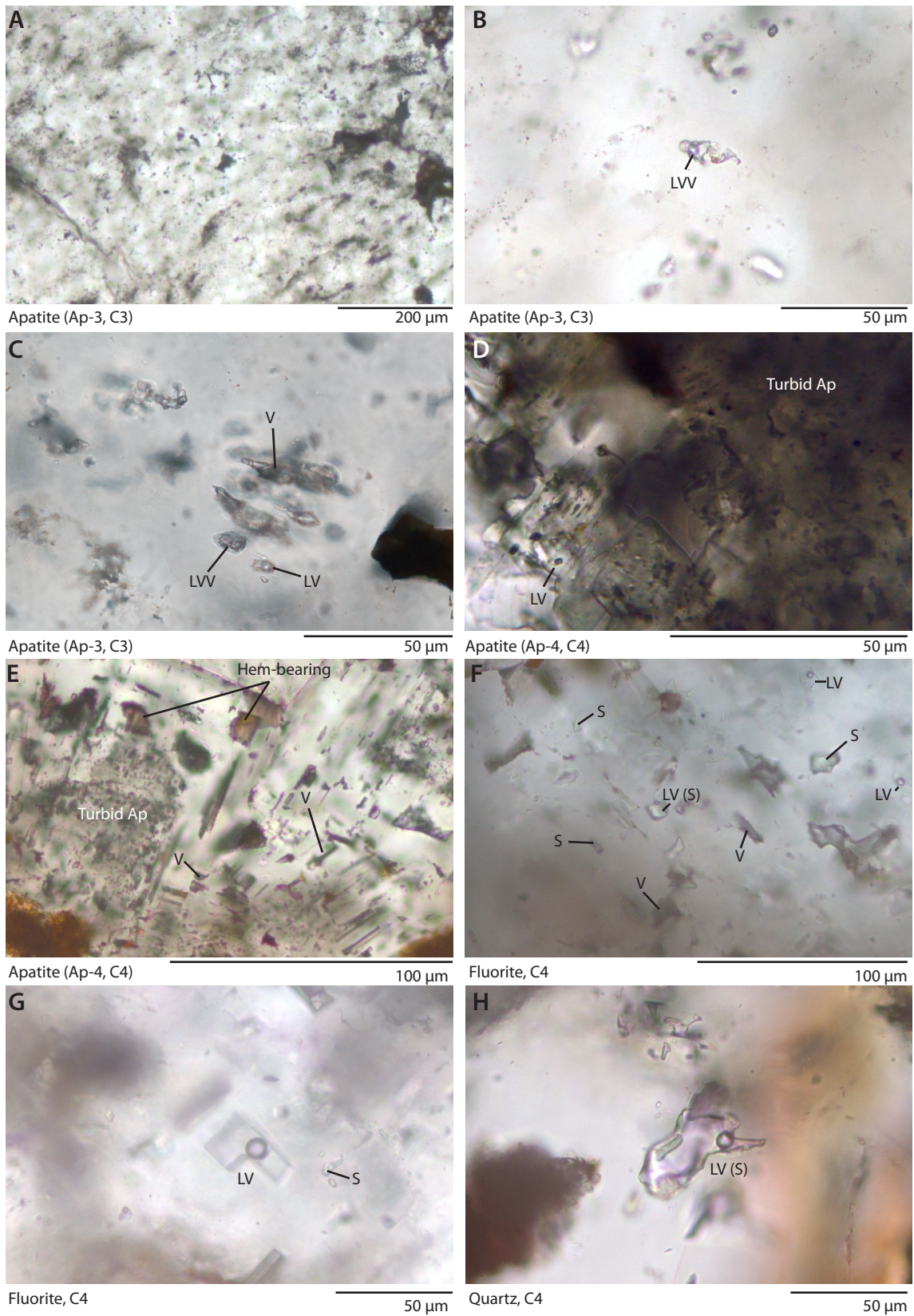


Figure 6.1: Images of fluid inclusions in apatite (Ap-3 and Ap-4), fluorite and quartz from C3 and C4 carbonatites. Abbreviations: L, liquid; V, vapour; S, solid; Hem, hematite.

Type	Size (μm)	Vol (%)	T _H CO ₂ (°C)	Melt type	T _M CO ₂ (°C)	T _M Clath (°C)	T _H (°C)	T _M H ₂ O (°C)	Wt. % NaCl eq.
PLLV	11	25	28.5	LH	-56.9	5.1			8.86
PLLV	8	40	29.9	LH	-56.9	5.7			8.16
PLLV	7.5	40	29.6	LH	-57	4.6			8.93
PLLV	8	35	25.2	LH	-57.2	3.2	265		10.77
PLLV	8	35	27.7	LH		5.5			8.72
PLLV	8	25	26.8	LH	-57.1	4.4			9.68
PLLV	10	20	26.8	LH	-56.9	4.9			9.33
PLLV	6	30	13.8	LH		5.6			9.52
PLLV	5	40	27.7	LH	-56.9	5.1			9.02
PLLV	5	30	27.7	LH					
PLLV	5	30	27.5	LH					
PLLV	7	15	27.6	LH					
LV	5						119	-0.9	
PLLV	7	15	23.8	LH	-50.8	3.6	291.5		10.81
PLLV	8	15	13.4	LH	-56.3				
PLLV	8	20	28.2	LH	-56.1	5.2			8.85
LV	8							-11.4	
LV	7							-7.1	
LV	7.5						291.7	-5.9	
LV	4						335.7		
PLLV	5				-56.3				
PLLV	11	20	28.9	LH	-56.6	3.6	350		9.64
LLV	10	20	28.6	LH		3.2	296.5		9.91
LV	7	20					248		
LLV(S?)	10	20			-56.2	1.8	312.2		
LLV	12	30				6.9	286.5		
LV	4					6			
LLV	12	20	22.5	LH	-56.6	4	350		10.74
LV	4	40					352.7	-7.9	
LV	6	30					289.7	-3.3	
LV	7	5					256.1		
LV	8	10					350		
LV	8	20					288.9	-7.7	
LV(S?)	5						321		
LV	5						283.9		
LV	5						275.3		
LV	6						244.5		

Table 6.1: Fluid inclusion data from Ap-3. Abbreviations: PLLV, primary 3-phase (2 liquids and vapour) inclusion; LV, liquid-vapour inclusion of indeterminate origin; S?, possible solid in inclusion; Vol %, volume of vapour bubble(s); T_H CO₂, homogenisation temperature of CO₂ bubble; LH, homogenisation of CO₂ bubble to liquid; T_M CO₂, melting temperature of CO₂; T_M Clath, melting temperature of clathrate; T_H, homogenisation temperature of the inclusion; T_M H₂O, melting point of water ice; Wt. % NaCl eq. concentration of NaCl in the inclusion calculated using clathrate melting temperatures after Diamond (1992). Where no data are present, no phase changes were observed due to the changes being too small to be observable or absent in the inclusions.

Type	Size (μm)	Vol %	T_H
PLV	5	5	122
PLV	9	5	166.4
PLV	4	5	190
PLV	8	5	160.5
PLV	6	5	196.6
PLV	5	5	186
PLV	7	5	210
PLV	6	5	215
PLV	5	5	186.2
PLV	9	5	228
PLV	9	5	200
PLV	8	5	215
PLV	7	5	122
PLV	7	5	228
PLV	5	5	122

Table 6.2: Fluid inclusion data from Ap-4. Abbreviations: PLLV, primary 3-phase (2 liquids and vapour) inclusion; Vol %, volume of vapour bubble(s); T_H , homogenisation temperature of the inclusion; T_{fm} ice, ice first melting temperature; T_m ice, ice final melting temperature. NB— T_{fm} and T_m were not observable in the inclusions.

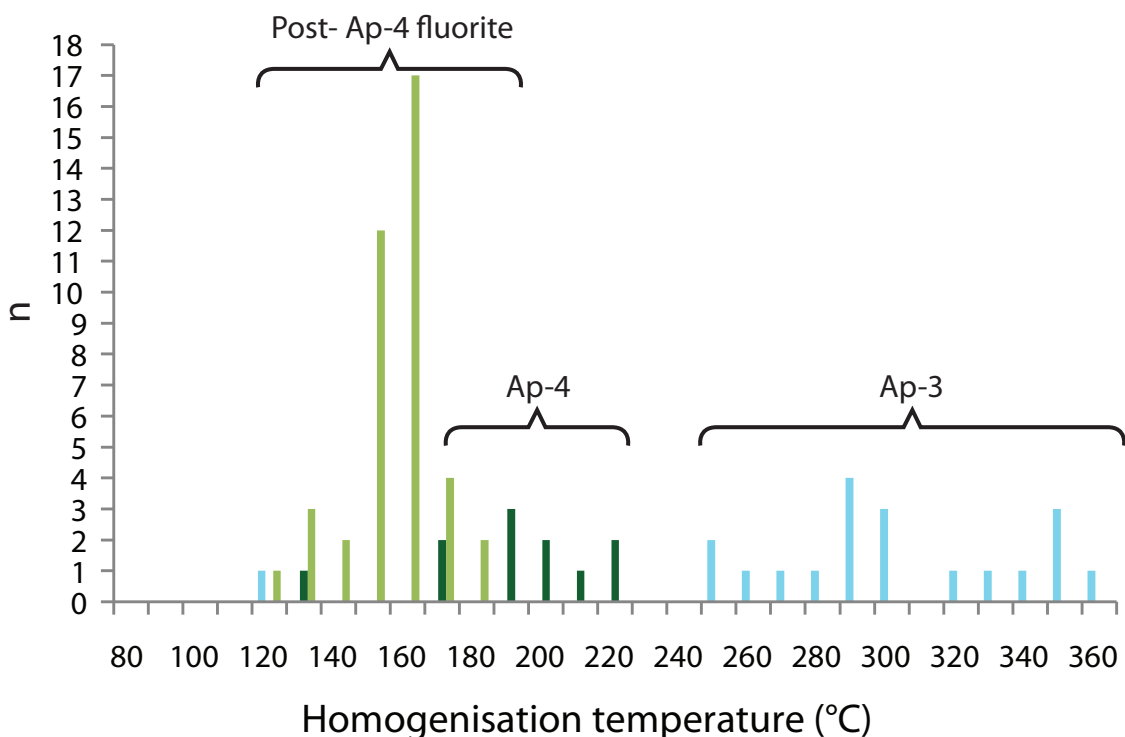


Figure 6.2: Histogram of homogenisation temperatures of fluid inclusions in apatite (Ap-3 and Ap-4) and fluorite in C3 and C4 carbonatite at Songwe.

Type	Size (μm)	Vol %	T_H ($^{\circ}\text{C}$)	T_{fm} ($^{\circ}\text{C}$)	T_m ($^{\circ}\text{C}$)	NaCl (wt. %)	Comments
PLV	17	5–10	145	-17	-4.6	7.31	
PLV	23	5–10	135		-1.2	2.07	Leaked after freezing
PLV	14	5–10	125		-1.2	2.07	Leaked before freezing
PLV	21	5–10	149				Decrepitated
PLV	12	5–10	130				Decrepitated
PLV	10	10–15	148				Decrepitated
PLV	25	20–25	141		-2	3.39	Melted quickly
PLV	18	10–15	151	-7	-2	3.39	Melted quickly
PLV	15	10–15	147		-2.1	3.55	
PLV	15	10–15	163				Decrepitated
PLV	15	5–10	149				Decrepitated
PLV	17	10–15	142				Decrepitated
PLV	27	5–10	155	-18	-6.1	9.34	
PLV	13	5–10		-16.2	-5	7.86	
PLV	15	5–10	124				Decrepitated
PLV	20	10–15	153				Decrepitated
PLV	22	15–20	152	-3.1	-1.8	3.06	Melted quickly
PLV	29	5–10	156	-19	-5.7	8.81	
PLV	16	10–15	161	-22	-8.4	12.16	Froze at -55°C
PLV	18	5–10	151		-1.1	1.91	
PLV	28	10–15	149		-6.8	10.24	
PLV	24	10–20	157		-3.4	5.56	
PLV	26	10–20	154				Leaked after freezing
PLV	29	10–20	155				Leaked after freezing
PLV	19	10–15	171		-8.6	12.39	
PLV	14	15–20	172		-7.6	11.22	
PLV	23	5–10	119		-0.3	0.53	
PLV	14	10–20	152		-1.2	2.07	
PLV	22	10–15	152				Decrepitated
PLV	16	40–50	157				Decrepitated
PLV	13	10–20	148		-3.1	5.11	
PLV	27	15–20	145		-1.3	2.24	
PLV	21	15–20	164		-1.8	3.06	
PLV	28	15–20	154		-1.2	2.07	
PLV	20	5–10	166.7		-1.4	2.41	
PLV	17	5–10	150.9		-2.5	4.18	
PLV	14	5–10	147.4		-3.2	5.26	
PLV	26	5–10	152.1		-0.5	0.88	
PLV	29	5–10	151.6		-2.8	4.65	
PLV	23	5–10	156.2		-1.9	3.23	
PLV	26	5–10	147.8				
PLV	12	5–10	137		-2.8	4.65	

Table 6.3: Fluid inclusion microthermometric data from C4 fluorite. Abbreviations: PLV, primary liquid-vapour inclusion; Vol %, volume of vapour phase; T_H , homogenisation temperature of the inclusion; T_{fm} ice, ice first melting temperature; T_m ice, ice final melting temperature. Wt. % NaCl calculated after Bodnar (1993). Empty cells indicate data that were not observed, typically due to reasons explained in the comments column.

are limited, the final ice melting temperature and homogenisation temperatures display a weak negative correlation (Fig. 6.3; $R^2 = 0.27$).

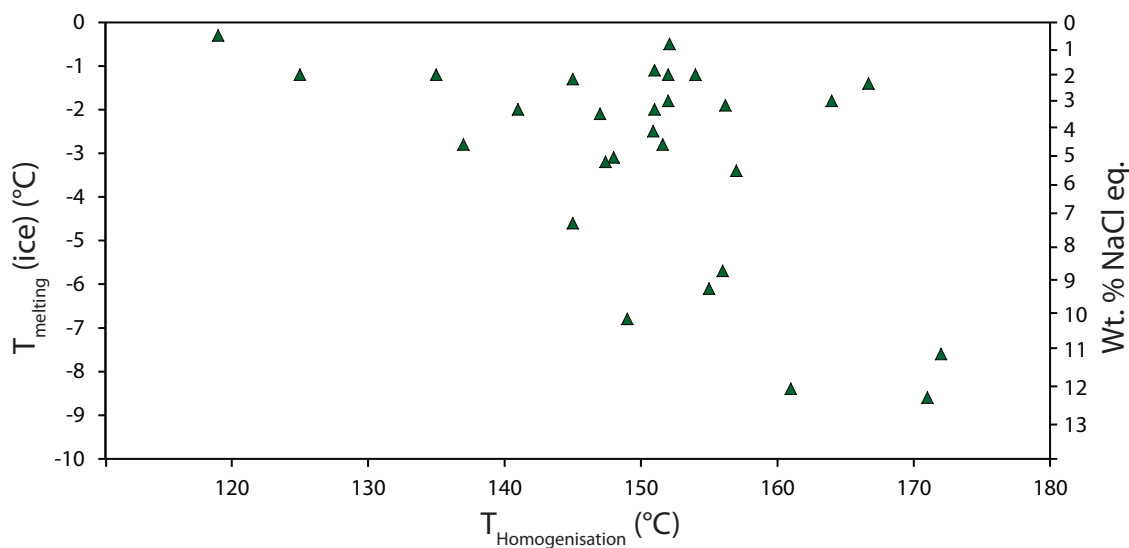


Figure 6.3: Plot of Homogenisation temperature and ice melting temperature for fluorite. Wt % NaCl equivalent calculation after Bodnar (1993).

6.3 Interpretation

6.3.1 Salinity

Two methods are applicable for salinity calculations from the inclusions assemblages, depending on the composition of the fluid inclusions. The salinity of LV inclusions was calculated using ice melting temperatures, while in LLV, clathrate melting temperatures were used.

NaCl–H₂O system

It is important, when calculating the salinity of fluid inclusions, that the composition of the salt in the inclusion is known. Common salts in hydrothermal fluids include NaCl, KCl and CaCl₂ (Bodnar, 2003). The composition of the salt in the LV fluid inclusions is assumed to be NaCl. This is because the limited first melting temperature data (T_{FM}) range between -22 and -3.1 °C, most of which are higher than the decomposition temperature of hydrohalite (NaCl·2H₂O; -21.2 °C). Ideally, to be certain of the NaCl-rich composition, all observed T_{FM} would be -21.2 °C, however, T_{FM} observations are notoriously inaccurate, and are often greater than the actual T_{FM} temperature. Therefore the range of data, which are less than, or within error of, the hydrohalite decomposition temperature are considered indicative of a relatively pure NaCl composition.

As the composition of the inclusions is assumed to be close to pure NaCl, the salinity of the inclusions can be calculated empirically using the ice melting temperature (T_M). This was done using the equation of Bodnar (1993), and the corresponding range in salinities is between 0.5–12.5 wt. % NaCl equivalent. The lowest salinities broadly correlate to inclusions with the lowest homogenisation temperature.

CO₂–NaCl–H₂O system

The salinity of three-phase LLV inclusions with CO₂ were calculated on the basis of clathrate melting and CO₂ homogenisation temperatures (Diamond, 1992). Salinity data is limited as it could only be calculated for inclusions where both phases changes were observed. The calculated values for the salinity of these inclusions varies between 8 to 11 wt. % NaCl equivalent.

6.3.2 Temperature

Homogenisation temperatures represent minimum temperatures of fluid inclusions, with the true trapping temperature plotting along lines of constant fluid density and increasing pressure. Few pressure constraints are available, although the CAP⁶ intrusions are generally assumed to have been intruded at high crustal levels (Eby et al., 1995). This inference is based on the presence of brecciation in several of the intrusions, including Songwe; as well as down-faulted blocks of contemporaneous volcanics, ring dykes and cauldron subsidence, all of which are indicative of shallow, brittle behaviour. Eby et al. (1995) estimated that the intrusions were emplaced at a depth of approximately 3 km, which is equivalent to 90 MPa lithostatic, or 30 MPa hydrostatic pressure. Such low pressures have little effect on the difference between homogenisation temperatures and the true fluid temperature (Bodnar, 2003). Therefore, homogenisation temperatures are considered as broadly representative of the true temperature of the fluid during crystallisation.

6.3.3 Changes in composition and temperature with paragenesis

The shortage of data makes a full interpretation of fluid evolution of the carbonatite difficult. However, some general observations can be made:

1. CO₂ is only present in inclusions in Ap-3, and a large proportion of the inclusions in this apatite type are vapour rich.

⁶Chilwa Alkaline Province

2. The proportion of single-phase vapour inclusions decreases later in the paragenesis
3. The homogenisation temperature of the inclusions decreases at later stages in the paragenesis.
4. Salinity and homogenisation temperature show a weak negative correlation, indicating that mixing with a low salinity, cool fluid could be occurring.

These observations are represented schematically in Figure 6.4, with the location of the mineral in the overall paragenesis indicated. The composition of the inclusions indicates that during Ap-3 formation both chloride and carbonate/bicarbonate may have been present in a fluid, on the basis of the presence of CO₂ and the saline nature of these inclusions. In inclusions in Ap-4 and fluorite, however, only chloride can be inferred because of the lack of a CO₂ bubble. While the homogenisation temperatures represent the minimum temperatures of a fluid, the relative temperature difference between the fluids is likely to be representative of the true temperature difference as a large change in pressure between the different fluid stages is unlikely. Therefore, the decrease in homogenisation temperature in the three paragenetic stages investigated is likely to represent a true drop in temperature between each stage. The homogenisation temperature of the inclusions in fluorite, because of its crystallisation after the final apatite stages, provides an absolute minimum temperature for HREE mineralisation of approximately 160 °C.

The weak correlation between T_M and T_H , in the fluorite-hosted inclusions, implies that the decreasing temperature of the fluid may be related to the decreasing salinity of a fluid. A possible cause for this is mixing between a low-salinity water, such as ground water, and a higher-salinity hotter fluid, such as one derived from a carbonatite. Such a mechanism has been proposed for the formation of fluorite deposits at other carbonatites such as Amba Dongar, India (Simonetti and Bell, 1995; Palmer and Williams-Jones, 1996). Others, however, contest this model and argue for the formation of fluorite through the reaction of fluorite-bearing fluids with calcareous wall-rocks (Bühn et al., 2002, 2003).

6.4 Discussion

The fluid inclusion data presented in this chapter, combined with the paragenetic and mineral-chemistry data presented in the preceding chapters, allow some inferences to be made about the composition and controls on HREE-bearing fluids and HREE-mineralisation in carbonatites, and these are discussed below.

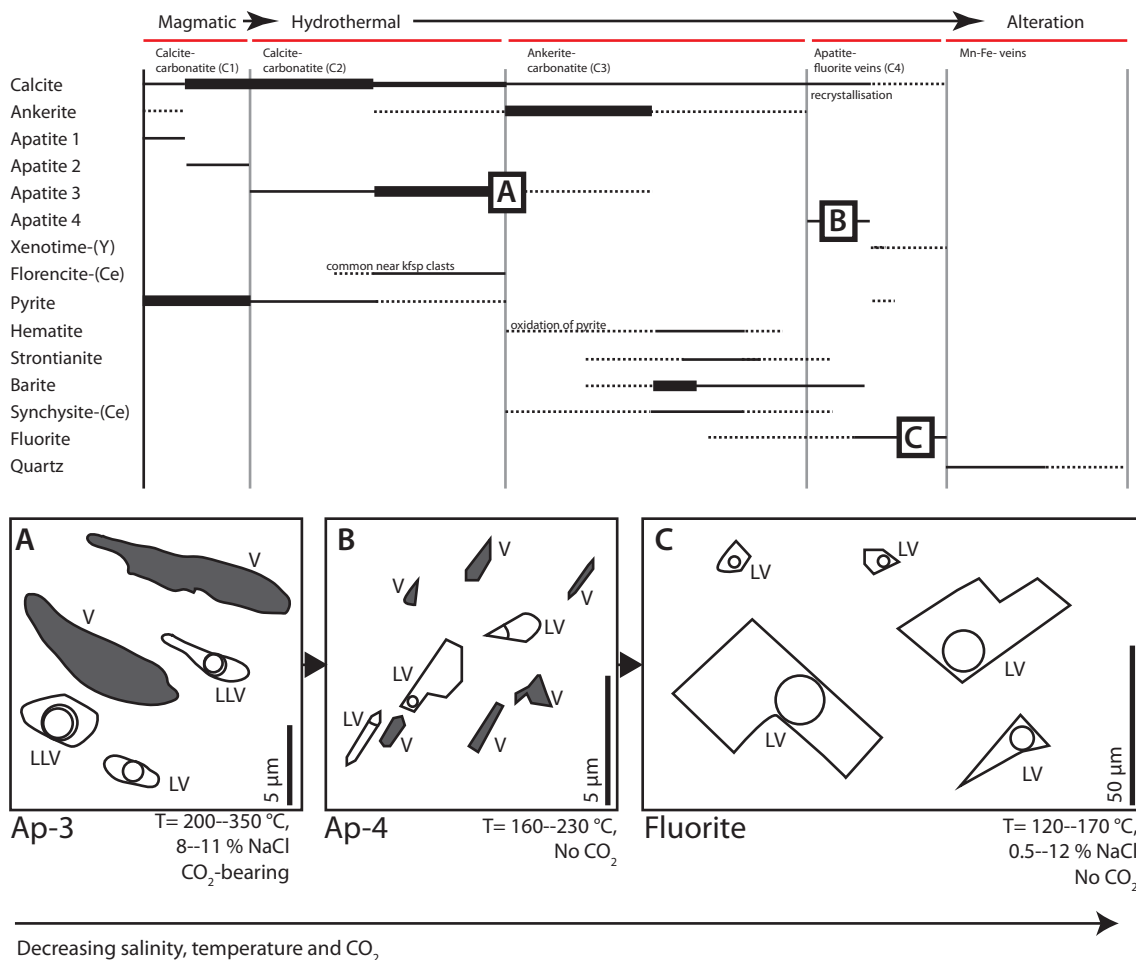


Figure 6.4: Schematic diagram of changing fluid inclusion compositions and temperatures with the paragenetic positions of the minerals analysed marked on a simplified paragenetic diagram.

6.4.1 Composition of HREE-bearing fluids

Any model would have to include the following observations at Songwe:

1. Ap-3 forms paragenetically early, relative to other late-stage minerals, and is commonly associated with carbonate.
2. Ap-4 crystallises late, and is associated with calcite and fluorite.
3. Xenotime-(Y) crystallises after Ap-4 formation, and is also associated with calcite and fluorite.
4. Whole-rock analyses all show a subtle negative Y anomaly.
5. All Songwe apatite shows no Y anomaly.
6. Fluorite displays a prominent, positive Y-anomaly, with a similar REE distribution to Ap-4.
7. A mineral assemblage of synchysite-(Ce), barite, strontianite and calcite crystallised after Ap-3.
8. The above minerals are assumed to form from a continually evolving, carbonatite-derived, hydrothermal fluid on the basis of cross-cutting relationships.
9. The composition of the expelled fluid is inferred to contain F^- , CO_3^{2-}/HCO_3^- , Cl^- and SO_4^{2-} as potential REE-transporting ligands.
10. Fluid inclusions support the inference of a CO_2 -bearing fluid in Ap-3, but evidence of CO_2 activity is absent in fluids trapped in Ap-4 and fluorite.
11. Fluids are saline, with NaCl equivalents reaching up to 12 wt. %. Salinity decreases with decreasing temperature.
12. The homogenisation temperature of inclusions later in the paragenesis is lower than those from earlier stages.

6.4.2 HREE enrichment of apatite

Given these criteria, three possible controls on the fractionation of the HREE in a hydrothermal fluid are considered:

1. fractionation via early crystallisation of synchysite
2. preferential transport of the LREE or HREE due to ligand chemistry
3. crystal-chemical control on REE substitution into apatite

Fractionation via early crystallisation of synchysite

The most simplistic option, inferred from the HREE-enriched apatite rims at Tundulu, is that REE-fluorcarbonates crystallised before apatite (Ngwenya, 1994). This mechanism would remove LREE from the fluid by the precipitation of LREE-fluorcarbonates, leaving a residually HREE-enriched fluid from which HREE-enriched apatite crystallises. However, this process could not have operated at Songwe because the synchysite-(Ce) crystallised *after* apatite. Indeed, the new paragenetic interpretation at Tundulu (Chapter 5) also precludes this process being applicable there.

Preferential transport of the LREE or HREE due to ligand chemistry

The relative importance of the other two controls considered for REE fractionation depends on which ligands are available to complex the REE. Although there is no direct evidence, the available mineralogical and fluid inclusion data suggest that carbonate/bicarbonate (from the presence of CO₂ in inclusions) or fluoride (from the extensive fluorite mineralisation) complexes are highly likely candidates. Many depositional models for the REE in alkaline systems consider chloride and sulphate complexes as important ligands for the transport of the REE (Sheard et al., 2012; Williams-Jones et al., 2012; Migdisov and Williams-Jones, 2014; Xie et al., 2014). Although these ligands cannot be entirely discounted at Songwe, the available fluid inclusion and mineralogical data do not indicate that either is a major component of the fluid.

If the fluid is fluoride- (or chloride-) rich, then the REE could be fractionated according to the preferential stability of LREE-fluoride and -chloride complexes, over their HREE equivalents, at the measured temperature range of the hydrothermal system (160–400 °C) (Chapter 2; Migdisov et al., 2009; Williams-Jones et al., 2012). As previously discussed (Chapter 5), the low solubility of phosphate would lead to rapid precipitation of apatite and in turn leading to the destabilisation of HREE complexes (Migdisov and Williams-Jones, 2014). LREE-complexes with F⁻ or Cl⁻ would remain in solution as these are relatively more stable. Causes of precipitation of the LREE later in the paragenesis could include simple cooling, mixing with groundwater, or further reaction with the host carbonatites.

Complexes of YF₂⁺ are more stable than the equivalent complexes with Dy or Ho (Bau, 1996; Loges et al., 2013), leading to fractionation between Y and Ho in F-complexed REE-bearing fluids. However, apatite at Songwe shows no Y/Ho fractionation suggesting that the role of REE-fluoride complexes is limited. Furthermore, chloride complexation is most efficient under acidic conditions and Cl⁻-complexes become less important in higher pH fluids (Williams-Jones et al., 2012; Migdisov and Williams-Jones, 2014). While the pH of the REE-bearing

fluids is not known, a low pH fluid is unlikely to exist in a carbonatite due to the large amount of carbonate to buffer. Additionally, the low salinity of the fluid inclusions suggests that chloride activity is low.

Crystal-chemical control on REE substitution into apatite

An alternative control on the REE fractionation might involve complexing of the REE by carbonate, bicarbonate, sulphate or phosphate ligands. Complexation by phosphate is unlikely due to the low solubility of REE-phosphate minerals. Understanding of the stability of carbonate, bicarbonate and sulphate complexes is limited to extrapolations of low-temperature experiments (Haas et al., 1995), and a small number of high-temperature experiments (e.g., S; Migdisov et al., 2006; Migdisov and Williams-Jones, 2008). These studies indicate that the LREE and HREE complexes with these anions have similar stabilities in solution. If these anions are complexing the REE then the similar stability of the LREE and HREE complexes means that the stability of the ligands is not likely to fractionate the REE. Therefore, another mechanism for the HREE-enrichment in apatite must be operating.

Such a mechanism could involve a crystal-chemical control, dictated by the preferential substitution of REE of a certain radii, into the apatite structure. As previously discussed (Chapter 5, section 5.3.4), the partition coefficients of the REE into apatite, in a hydrothermal environment, are poorly constrained. This renders it difficult to equivocally assess this potential control on fractionation. For instance, it has been suggested that the apatite structure has no control on the substitution of different REE and that its composition is representative of the REE distribution of the fluid from which it precipitated (Roeder et al., 1987). However, experiments at high temperature and pressure indicate that apatite preferentially incorporates the MREE (Watson and Green, 1981; Ayers and Watson, 1993; Fleet and Pan, 1997a; Klemme and Dalpé, 2003; Hammouda et al., 2010). If this behaviour extends to lower temperatures, then crystallisation of apatite could selectively remove the MREE from a fluid, structurally excluding the LREE. However, experimental data on the partitioning of the REE into apatite under low temperature hydrothermal conditions, considered to be prevailing at Songwe, are lacking. The only study for which experimental conditions are close is a study of a phosphate-fluoride fluid at 684 °C and 0.12 GPa (Pan, 1997). This study showed that the LREE and, to a lesser extent, the MREE were preferentially incorporated into apatite, while the partition coefficients for the HREE were less than 1. If this experiment is representative of the late, carbonatite-derived, hydrothermal fluids at Songwe, then apatite would preferentially incorporate the LREE. This is not the case and, therefore, a crystal-chemical control is not considered to be the main cause of fractionation of the REE into apatite at Songwe.

Preferential transport of the LREE or HREE due to carbonate complexation?

Fractionation of the REE by transport in fluoride and chloride complexes has been ruled out, as has fractionation via a crystal-chemical control. However, CO₂ concentrations are high in fluids from carbonatites, and carbonate complexation of the REE could be a major carrier of the REE, especially given the 'hard' nature of carbonate complexes (e.g. Fig. 2.8). Our current understanding of REE-carbonate complexes, however, is such that it is difficult to assess their importance in the transport and fractionation of the REE at Songwe. It is postulated that REE-carbonate complexes could have different stabilities between the LREE and the HREE, in a manner akin to the stability of fluoride and chloride REE complexes (e.g. Williams-Jones et al., 2012). This would be in contrast to the theoretical projections of the stability of REE-carbonate complexes (Haas et al., 1995). However, given that recent experimental work on the stability of REE-fluoride and -chloride complexes contrasts to the theoretical stabilities, these theoretical extrapolations of low temperature experiments for carbonate complexes may, too, not be as robust as previously considered. Therefore, preferential transport of the HREE in carbonate complexes is suggested to be the cause of fractionation at Songwe, but experimental work is required to confirm that this is possible. Experiments, however, to test if this is the case are underway (Williams-Jones, *pers comm*).

The presence of mixed LV, LLV and V fluid inclusions in Ap-3 could be due to fluid unmixing and degassing of a hydrothermal fluid. This could provide a rapid crystallisation mechanism as degassing would rapidly remove CO₂ from a fluid, destabilising HREE-carbonate complexes. Alternatively, the destabilisation could be limited by the concentration of phosphate in a fluid, which acts as a crystallisation mechanism. The hypothetically lower stability of a HREE-carbonate complex would cause the HREE to co-crystallise with P into apatite. If P was not limited, then eventually all the REE would precipitate, probably as monazite. However, the potentially limiting P concentration means that only the HREE substitute, and the LREE are retained in solution.

Further hydrothermal alteration

The presence of extensive fluorite mineralisation associated with Ap-4, late in the paragenesis, indicates that some remobilisation of the REE and recrystallisation of apatite took place. Fluid inclusions from fluorite show that this occurred at about 160 °C, comparable with mineralisation from many other carbonatite-related fluorite deposits (Palmer and Williams-Jones, 1996; Williams-Jones and Palmer, 2002; Bühn et al., 2002). Fluorite in association with Ap-4 displays a strong Y/Ho anomaly, suggesting that there may be an increased role for fluo-

ride complexation during late-stage remobilisation of the REE. It is this fluorite crystallisation which is anticipated to account for the negative Y anomaly in the whole-rock analyses.

The solubility of REE-phosphates is retrograde (i.e. it increases with decreasing temperature; Poitrasson et al., 2004; Cetiner et al., 2005; Gysi et al., 2015). The solubility of apatite at low temperature is not known, but it is assumed to behave in a similar manner. As late Ap-4 is depleted in the LREE, relative to Ap-3, and slightly enriched in the HREE (Fig. 5.10), it is proposed that fluorine and/or chlorine, from the fluorite-mineralising fluid, attacked the REE-bearing apatite, preferentially removing the LREE and Y. The limited stability of the HREE in this fluid led to its retention in the apatite, or rapid re-precipitation as xenotime on the grain edges (Fig. 5.6 D–E). The LREE were then transported out of the system.

6.5 Conclusions

In this chapter, new fluid inclusion data have been presented to constrain the temperature and composition of the mineralising fluids. Due to difficulties in finding and analysing inclusions in most of the selected samples, data are limited to inclusions from Ap-3, Ap-4 and post-apatite fluorite.

Fluid inclusions span a range of homogenisation temperatures between 360–120 °C. Minerals from earlier paragenetic stages have higher homogenisation temperatures, ranging between: 250–360, for Ap-3; 160–220, for Ap-4; and, 120–180, for fluorite. Compositionally, inclusions in Ap-3 are mixed vapour-only, liquid-vapour and liquid-vapour-carbonic inclusions; while those in Ap-4 and fluorite are just liquid-vapour inclusions. Salinities calculated range between 0–12 wt. % NaCl eq. and these show a weak negative correlation with homogenisation temperature, possibly indicating mixing with groundwater.

The fluid inclusion data, combined with the mineralogical data from the previous chapter, are used to suggest some possible controls on the REE fractionation in Songwe apatite. These are:

1. preferential transport of the LREE or HREE due to ligand chemistry
2. crystal-chemical control on REE substitution into apatite

Fractionation via early crystallisation of synchysite was suggested for the formation of HREE-bearing apatite at Tundulu (Ngwenya, 1994), but does not occur at Songwe due to the formation of synchysite after apatite. It is also suggested that this mechanism is not taking place at Tundulu on the basis of the new paragenetic data presented in Chapter 5.

Preferential transport of the LREE would occur if Cl⁻ or F⁻ are the dominant REE-complexing ligands in solution. Fluoride is excluded as a likely ligand due

to the lack of a Y anomaly in the HREE-enriched apatite. Chloride is also considered as an unlikely ligand to transport the REE, despite being favoured in REE deposits related to alkaline rocks (e.g. Williams-Jones et al., 2012; Migdisov and Williams-Jones, 2014), because of the low salinity of the fluid inclusions in apatite. Furthermore, Cl⁻ is only a major transporting ligand in acidic solutions; these are difficult to infer in a carbonatite due to the large amount of carbonate to buffer.

Transport by carbonate complexes is favoured due to the abundance of carbonate in carbonatites, and the presence of CO₂-bearing fluid inclusions in Ap-3. As carbonate complexes do not readily fractionate the REE, it is proposed that this is due to a crystal-chemical control (i.e. the partition coefficient of the REE in apatite) during crystallisation or due to preferential mobility of LREE-carbonate complexes over HREE-carbonate complexes. Neither of these two proposed mechanisms are currently reconcilable with our current understanding of the partitioning of REE into apatite at low temperature conditions, or our understanding of the transport of REE-carbonate complexes. Further research into these two areas is suggested to better understand the controls on REE fractionation in hydrothermal fluids.

Alteration and recrystallisation of apatite is inferred for the formation of Ap-4. The presence of extensive fluorite mineralisation is testament to the role of F in these late stage fluids, as well as the presence of a large Y-anomaly. These led to removal of the REE from apatite and recrystallisation of the HREE in xenotime on the apatite grain edge. It is suggested that the late-stage fluorite could be the crystallisation product of the expelled fluid which could be the cause of the negative Y anomaly in the Songwe whole-rock analyses.

Chapter 7

Mobility of the REE in carbonatites — stable isotope tracers

In this chapter the results of O and C isotope analyses in carbonates are presented, together with results from determining a new protocol for O isotope analyses in apatite. These results are interpreted, in combination with fluid inclusion data and modelling, to trace the mineralising fluid source and to further constrain the temperature of HREE mineralisation at Songwe. The chapter begins with a brief review of some of the general principals of stable isotope analyses in carbonatites. Subsequently, the experimental rationale is outlined, and sample selection justified on the basis of six hypotheses. Three of the hypotheses relate to the development of the new method of measuring oxygen isotopes in apatite. These are:

1. Is it possible to develop an isoscape for $\delta^{18}\text{O}_{\text{PO}_4}$ in carbonatites?
2. Is $\delta^{18}\text{O}_{\text{PO}_4}$ in apatite susceptible to diffusion and isotopic re-setting when interacting with a hydrothermal fluid?
3. Can the preparation technique be carried out on a bulk powder, or do apatite grains need to be picked before analysis?

The other three hypotheses presented relate to the interpretation of the isotope results from analyses from Songwe. These are:

1. Do the variations in isotope ratios relate to Rayleigh Fractionation, fluid alteration or sediment assimilation?
2. Can the fluid inclusion data be linked to the isotope data to reconstruct the conditions of the mineralising fluid?
3. Can carbonate and apatite data be reconciled into a general model of fluid evolution?

This chapter includes a large degree of method development for analysis of $\delta^{18}\text{O}$. The methodology section is an adaptation of a version written by Tim Heaton (*pers comm*, 2014).

7.1 Review of controls on stable isotope compositions

Stable isotopes in magmatic rocks can be used to derive crystallisation temperatures or to constrain the isotopic composition of the crystallising fluid and thus interpret a source from known isotopic reservoirs.

7.1.1 General principals of temperature control on stable isotope ratios

Temperatures can be estimated for mineral pairs in equilibrium. For any given mineral–mineral or mineral–fluid pair, the isotopic difference can be expressed as a fractionation factor:

$$\alpha_{A-B} = \frac{\delta^{18}\text{O}_A}{\delta^{18}\text{O}_B} \quad (7.1)$$

Values for α are typically close to 1, and vary in the third decimal place, such that the following equation is a close approximate:

$$\alpha = 1.00n, 1000\ln\alpha = n \quad (7.2)$$

$1000\ln\alpha$ is a smooth, often linear, function of $1/T^2$ which gives rise to the expression:

$$1000\ln\alpha_{\text{MinA}-\text{MinB}} = x(10^6/T^2) + y \quad (7.3)$$

Where x and y are constants which can be derived either empirically, theoretically or experimentally. Leaving the unknowns as $\delta^{18}\text{O}_{\text{MinA}}$, $\delta^{18}\text{O}_{\text{MinB}}$ and T (Kelvin). The isotopic ratios of minerals can be measured, and thus equation 7.3 can be solved for T .

For many mineral pairs (e.g. calcite–magnetite) x and y have been determined experimentally. Thus, multiple mineral pairs have been used by (for example) Haynes et al. (2003) and Demény et al. (2004b) to calculate crystallisation temperatures for different minerals in carbonatites.

Knowledge of the fractionation factors between minerals of interest is key to interpreting the isotopic composition of the ore-depositing fluid. In this chapter the two main ‘mineral’ pairs of interest are apatite–calcite and apatite–water.

Apatite-calcite fractionation

No published experimental fractionation factors exist between calcite and fluorapatite. Empirical fractionation factors have been derived for low temperature systems in hydroxylapatite, such as phosphorite beds (Shemesh et al., 1988) and mammalian teeth (Daniel Bryant et al., 1996). These have been derived for palaeotemperature calculations of water, and are not applicable for higher temperature magmatic or hydrothermal systems due to the errors involved in extrapolation of the data. Experimental high-temperature fractionation factors have been derived for hydroxylapatite–calcite between 350–800 °C (Fortier and Lüttge, 1995). The fractionation factors have a relatively low error between 500 and 800 °C, but below 500 °C, the authors recommend that the figures are used with caution (Fig. 7.1A). The derived equation is:

$$1000\ln\alpha_{ap-cc} = -0.68 - (1.60 \pm 0.26) \times 10^6 T^{-2} \quad (7.4)$$

Theoretical fractionation factors have been derived for both fluorapatite and hydroxylapatite by Zheng (1996). Since these are theoretical, they cover the largest temperature range of any of the published fractionation factors, between 0 and 1200 °C (Fig. 7.1A). The derived equation for fluorapatite–calcite is:

$$1000\ln\alpha_{ap-cc} = 0.21 \times \frac{10^6}{T^2} + 1.97 \times \frac{10^3}{T} - 0.81 \quad (7.5)$$

Since this equation is based on no experimental data it is difficult to judge the quality or the effect of the assumptions used to derive it. Furthermore, comparison of the theoretically-derived fractionation factors for hydroxylapatite with experimentally derived factors from Fortier and Lüttge (1995) indicates a rather significant offset of approximately 2 ‰ between the two sets (Fig. 7.1A).

The fractionation factors from Fortier and Lüttge (1995) are preferred in this chapter because they are experimentally derived. It is important to note, however, that they are derived for hydroxylapatite, not fluorapatite. Fractionation between the OH and PO₄ site needs to be taken into consideration. Theoretically, the small size and high ionic potential of F means that fluorapatite may be more likely to incorporate the heavier isotope (Hoefs, 2008). This has not been measured experimentally, but has been calculated by Zheng (1996) as an offset of approximately +0.7 ‰ at 25 °C (Fig. 7.1A). At temperatures relevant to this work, the offset is negligible. A comprehensive review of why this offset is towards lighter isotopes is beyond the scope of this introduction and the difference has not been factored into equation 7.4.

Apatite-water fractionation

Fractionation factors between fluorapatite and H₂O are less well constrained than between apatite and calcite. Empirical fractionation factors were originally calibrated between 10 and 37 °C using modern fish teeth (Kolodny et al., 1983) (Fig. 7.1B). Experimentally derived fractionation factors have been calculated between 50 and 135 °C and at 510 °C (Lécuyer et al., 1999; Shemesh et al., 1988) (Fig. 7.1B). Theoretical fractionation factors have been derived by Zheng (1996), and these span the widest range in temperature. These factors, similarly to the difference between theoretical and experimental factors between apatite and calcite, are offset between 1 and 5 ‰ lower than experimental fractionation factors (Zheng, 1996). Since no experimental fractionation factors are available over the temperature range of interest, the fractionation factor from Zheng (1996) is used for calculations of fractionation between apatite and water. The equation is shown below:

$$1000\ln\alpha_{ap-H_2O} = 3.81 \times \frac{10^6}{T^2} - 6.63 \times \frac{10^3}{T} + 2.08 \quad (7.6)$$

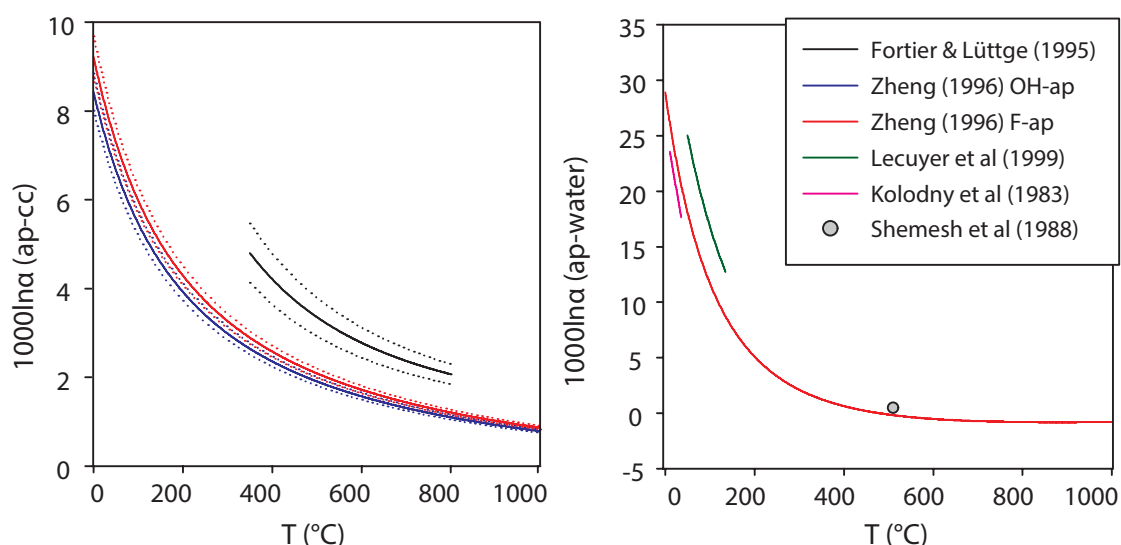


Figure 7.1: Compilation of published fractionation factors for (A) apatite–calcite and (B) apatite–water. Dotted lines indicate uncertainties associated with solid lines of the same colour.

7.1.2 Isotopic composition of crystallising fluid

If the temperature of the system is known, or can be estimated, then the oxygen isotope composition of a mineral can be used to calculate the isotopic composition of the crystallising fluid. For example, if an apatite-bearing rock crystallised from a water-bearing fluid, and the isotopic composition of the apatite and the

temperature are known, then equation 7.6 can be solved for the isotopic composition of water. There are numerous controls on the isotopic composition of a crystallising fluid, these include:

1. Source composition
2. Fractionation during magmatic evolution
3. Post-magmatic alteration

In $\delta^{13}\text{C}$ and $\delta^{18}\text{O}$ space in carbonatites these controls are summarised in Figure 7.2. These data are most commonly obtained from bulk-rock analyses, where whole-rock powder is reacted with acid, dissolving carbonate and releasing CO_2 . Indeed, while there are published analyses of oxygen from other minerals (e.g. Haynes et al., 2003; Demény et al., 2004a; Tichomirowa et al., 2006; Doroshkevich et al., 2008), and from other isotope systems, e.g., sulphur (Deines, 1989; Farrell et al., 2010; Gomide et al., 2013); chlorine (Eggenkamp and Koster van Groos, 1997); clumped isotopes (Dennis and Schrag, 2010); noble gasses (Mourão et al., 2012); and transition metals (Johnson et al., 2010; Ling et al., 2013), the majority of stable isotope studies from carbonatites focus on $\delta^{13}\text{C}$ and $\delta^{18}\text{O}$ in carbonates and, thus, this isotope system is one of the most well understood.

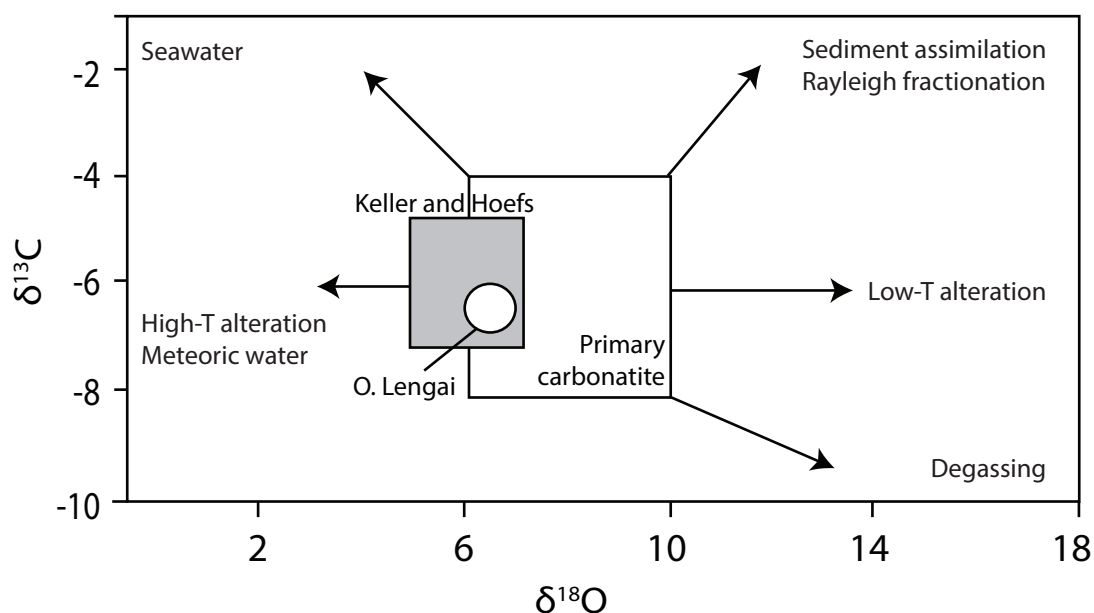


Figure 7.2: Schematic diagram of the controls on carbonatite isotopic composition after Demény et al. (2004a); Deines (1989). Primary carbonatite fields are after Taylor et al. (1967) and Keller and Hoefs (1995)

Source composition

The isotopic composition of a magmatic, mantle-derived carbonatite is well constrained within a PIC¹ box. This is generally considered to be between -3.1 and -7.7 $\delta^{13}\text{C}$ and +5.3 to +8.4 $\delta^{18}\text{O}$ (‰, VPDB² and VSMOW³ respectively; Taylor et al., 1967). This range is supported by estimates derived from meteorites, mantle xenoliths and basalts in conjunction with isotope fractionation factors expected for minerals at upper-mantle temperatures. Models predict that at 1000 °C the fractionation between mantle minerals and calcite amounts to about 2 ‰. Thus, mantle $\delta^{18}\text{O}$ values of between 5 and 6 ‰ convert into calcite values of between 7 and 8 ‰ (Deines, 1989). Unaltered magmatic carbonatite, from almost every analysed carbonatite, falls into the bounds of the PIC box (Santos and Clayton, 1995; Horstmann and Verwoerd, 1997; Demény et al., 2004a; Ray and Ramesh, 2006), including carbonatite intruded into oceanic crust (Demény et al., 1998, 2004b). There are, however, advocates who suggest altering the PIC field. Analyses of fresh natrocarbonatite from Oldionyo Lengai has led Keller and Hoefs (1995) to propose a more restricted range for primary carbonate, between -6.3 and -7.1 $\delta^{13}\text{C}$ and +5.8 to +6.7 $\delta^{18}\text{O}$ but variations in the PIC could also attributed to heterogeneity in the mantle (Deines and Gold, 1973; Zaitsev and Bell, 1995) and the mantle isotope ratios from Oldionyo Lengai may not representative of other locations. Conversely, while the PIC is considered to incorporate primary variations (Keller and Hoefs, 1995), Ray and Ramesh (1999b, 2006) advocate enlarging it to further accommodate larger 'primary variations' within carbonatite caused by primary crystallisation processes. Herein, the values used for PIC are -3.1 and -7.7 $\delta^{13}\text{C}$ and +5.3 to +8.4 $\delta^{18}\text{O}$ as these are most widely used in the literature, and are employed in review papers (e.g. Jones et al., 2013).

O and C fractionation during carbonatite evolution

Extensive data from carbonatites reported in the literature shows a general trend of increasing $\delta^{13}\text{C}$ and $\delta^{18}\text{O}$ values, extending from the primary igneous carbonatite box. The consistent slope between different intrusions led Deines (1989) to propose that it is linked to a process which is integral to carbonatite formation. A likely candidate for this process is Rayleigh Fractionation, where products are incrementally removed from a well-mixed reservoir. For this to occur, the following assumptions are made:

- there are isotopic differences between the products and the reservoir;
- no exchange occurs between the products, post-formation;

¹Primary Igneous Carbonatite'

²Vienna Pee Dee Belemnite

³Vienna standard mean ocean water

- the reservoir is of a limited size, such that removal of products has a measurable effect.

Such a process could take place during separation of a silicate and carbonatite phase from a carbonated-silicate magma, during fractionation of minerals from a magmatic carbonatite fluid (e.g. calcite, apatite, magnetite) or during development of a fluid phase (Pineau et al., 1973; Deines, 1989; Ray and Ramesh, 2000).

Substantial fractionation during separation of a carbonatite and a silicate magma, if such a process exists, was suggested as a possible cause of isotopic fractionation by Deines (1989). Santos and Clayton (1995) and Ray and Ramesh (2006), however, suggest that this processes is unlikely to cause significant change because the isotopic fractionation between a carbonatite and a silicate melt is very small (0.4 ‰, Matthey et al., 1990).

During fractional crystallisation, calcite is likely to be the dominant product due to its high modal abundance. However, because calcite is so abundant, the isotopic fractionation between calcite and a carbonate melt is probably very close to unity and consequently, removal of calcite from a pure carbonate melt is unlikely to cause major isotopic variation (Deines, 1989; Ray and Ramesh, 2006). The role of other minerals may be important for modifying the oxygen isotope composition of a carbonatite magma. Using the apatite-water fractionation factor of Shemesh et al. (1988), Ray and Ramesh (2000) suggest that crystallisation of apatite at magmatic temperatures may deplete the $\delta^{18}\text{O}$ of the residual fluid by approximately 1 ‰.

Crystallisation of calcite in equilibrium with H_2O and CO_2 could cause significant fractionation (Deines, 1989; Ray and Ramesh, 2000, 2006). Fractionation of calcite in the $\text{CO}_2\text{-H}_2\text{O-CaCO}_3$ system has been modelled and shows increasing $\delta^{13}\text{C}$ and $\delta^{18}\text{O}$ where CO_2 or H_2O are the dominant isotopic source components (Ray and Ramesh, 2000).

Other factors influencing the isotopic composition of a carbonatite during its evolution include incorporation of sediment and/or re-equilibration with lower-temperature magmatic fluids. Sediments tend to increase $\delta^{13}\text{C}$ and $\delta^{18}\text{O}$ as sedimentary carbonates are mainly marine, with $\delta^{13}\text{C}$ of about 0 ‰ and high $\delta^{18}\text{O}$ because they contain minerals which have equilibrated with water at low temperatures. Groundwater tends to contain bicarbonate with low $\delta^{13}\text{C}$ values, (-16 to -10 ‰), but prolonged interaction with carbonate sediments would tend to increase values towards 0 ‰. Incorporation of, or interaction of fluid with, sediments has been proposed for the high $\delta^{18}\text{O}$ of carbonatite from St Honoré and for higher $\delta^{13}\text{C}$ and $\delta^{18}\text{O}$ values at Fuerteventura (Deines, 1989; Demény et al., 1998). Because of the low viscosity and short residence time of carbonatite in

the crust, carbonatites are unlikely to directly assimilate much sedimentary material. Demény et al. (1998) suggests assimilation of sedimentary carbonate into a carbonated silicate melt, prior to separation of silicate and carbonatite fluids, as a means of increasing the $\delta^{13}\text{C}$ and $\delta^{18}\text{O}$ of a carbonatite. Deines (1989), however, suggests that a more hydrothermal system causes interaction between sedimentary carbonates and carbonatites. In this example, fluids from groundwater are required to reduce $\delta^{13}\text{C}$. Fluid first interacts with carbonate sediments and incorporates light carbon. The fluxing of this fluid, or interaction of this fluid with the carbonatite, causes the $\delta^{13}\text{C}$ values in the carbonatite to drop.

Post-magmatic (secondary) alteration

Secondary alteration involves changing the isotopic composition of the minerals through hydrothermal processes, defined as interactions between rocks and fluids during, or after, the carbonatite is emplaced into the crust. The nature and effect of the interaction between carbonatite and a fluid is dictated by the fluid composition, temperature and chemistry. Pressure has a negligible effect (Hoefs, 2008). Fluid temperature is the dominant factor in the isotopic composition of a hydrothermal fluid. As shown in Figure 7.1B, the degree of fractionation between apatite and H_2O greatly increases as temperature drops.

The isotopic composition of a fluid is a function of both its initial isotope ratio, and the concentration of dissolved species, such as CO_2 and salts. Fluids which may influence carbonatites include seawater, meteoric water or deuteritic (magma-derived) water. The effects of these different fluids are summarised in Figure 7.2.

Seawater rarely influences carbonatites because are generally emplaced in stable continental locations, away from the sea both in modern and palaeo-locations (Woolley and Kjarsgaard, 2008b). Indeed, even for carbonatites located in an oceanic setting, Demény et al. (1998) calculated that a very substantial amount of seawater would be required to obtain significant carbon and oxygen isotope shifts. Therefore, seawater is not considered further in this section.

Meteoric water generally has a negative $\delta^{18}\text{O}$ value (Hoefs, 2008). The carbon content of meteoric water is negligible (except for, perhaps, where it has interacted with a carbonate sediment previously – see Section 7.1.2). Exchange with meteoric water below approximately 200 °C results in increased $\delta^{18}\text{O}$ in the carbonatite, whereas exchange at temperatures higher than this results in ^{18}O depletion in the carbonatite (Deines, 1989; and see discussion section 7.7.8).

Deuteritic water is assumed to have the same initial $\delta^{18}\text{O}$ as PIC. Exchange between deuteritic water with $\delta^{18}\text{O}$ of approximately 8 ‰ can raise the $\delta^{18}\text{O}$ of a carbonatite with which it interacts. This autometasomatic process can raise the $\delta^{18}\text{O}$ up to 25 ‰, if the temperature of the water is around 100 °C, and correspondingly lower $\delta^{18}\text{O}$ at higher temperatures (Deines, 1989; Santos and Clayton,

1995; Ray and Ramesh, 1999b).

Dissolved species can affect the interaction between carbonatite and hydrothermal fluids. Of most importance to carbonatite systems is oxygen isotope fractionation between dissolved CO_2 and H_2O . Degassing is the removal of dissolved CO_2 from a fluid, and is caused by depressurisation during carbonatite emplacement. This can lead to ^{18}O enrichment if ^{18}O -depleted water escapes preferentially, or if the $\text{CO}_2:\text{H}_2\text{O}$ ratio in the remaining fluid is reduced (Deines, 1989; Zheng, 1990). Addition of salts to water can also affect isotope fractionation. Much of the experimental work investigating these processes has been carried out at low temperature with NaCl and KCl to observe the effects of $\text{H}_2\text{O}-\text{CO}_2$ fractionation (e.g. Lécuyer et al., 2009). NaCl is considered to have minimal effect on fractionation factors, but for other dissolved ions an increase in molarity will result in fractionation between pure water and a solution (Hoefs, 2008).

Hydrothermal processes can be split into interactions where a mineral (e.g. calcite) has precipitated from the hydrothermal fluid, either directly, or by dissolution–re-precipitation; or a diffusion process, where the isotopic ratio of a mineral is reset in the solid-state. Of these processes, direct (or dissolution–reprecipitation) crystallisation from a hydrothermal fluid is a much more effective process at changing isotopic ratios in a mineral than diffusion in the solid-state (Hoefs, 2008). Whether a carbonatite has formed from a hydrothermal fluid is usually easy to determine petrographically. Dissolution–re-precipitation can be observed on a small scale as smaller grains grow on larger grains, or large areas of the carbonatite can develop as a banded, fine-grained rock. Small-scale alterations can be seen by textural changes in thin-section, especial when aided by CL⁴. Isotopic alteration by diffusion is much more difficult to determine and is best estimated by knowing the temperature at which a rock has been altered. The susceptibility of a mineral to diffusion is represented by its diffusion coefficient D , which varies both with temperature and between different minerals. This can be defined by the Arrhenius equation:

$$D = D_0 e^{(-E_a/RT)} \quad (7.7)$$

Where D_0 is a temperature independent factor, E_a is the activation energy, R is the gas constant and T is the temperature (K). There have been several attempts to define the diffusion coefficients of minerals. Plots of D against temperature give a good indication of the rate of isotopic exchange at different temperatures and the point at which a mineral is no longer susceptible to diffusion (closure temperature). A summary plot of D against T for minerals of importance in carbonatite is shown in Figure 7.3. This plot demonstrates that apatite is highly

⁴cathodoluminescence

susceptible to diffusion at higher temperatures, but this susceptibility drops off rapidly as the system cools, and closes at around 550 °C (Cole and Chakraborty, 2001). Calcite, however, is more susceptible to diffusion at lower temperatures, and does not close until 400 °C. Grain boundaries can act as pathways of rapid exchange, and the fast grain boundary model can be used to consider the effect of diffusion between non-adjacent grains (Eiler et al., 1992, 1993). Using this model, the closure temperatures become a strong function of the modal abundances of the constituent minerals and the differences between the diffusion coefficients. The model has been applied to the Oka carbonatite, Canada, to calculate the extent of isotopic resetting of the minerals in the complex (Haynes et al., 2003). They found that biotite is significantly altered by diffusion, and predict that the same may be true for apatite.

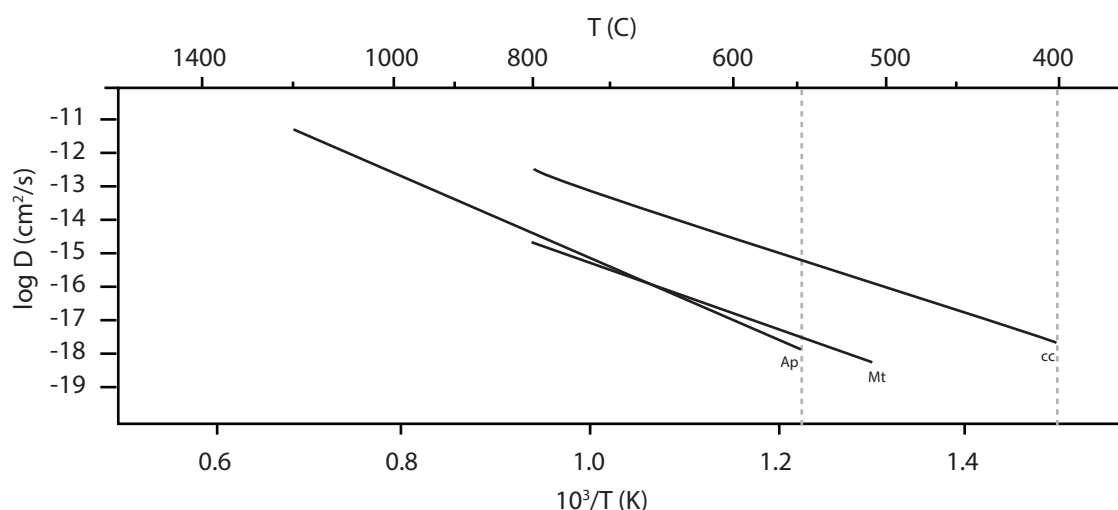


Figure 7.3: Arrhenius plot of diffusion coefficients versus reciprocal temperatures for minerals of importance in carbonatites. Ap = apatite, Mt = magnetite, cc = calcite. Modified after Cole and Chakraborty, 2001; Hoefs, 2008.

7.2 Experiment rationale

The primary objective of the isotope analyses presented in this chapter is to understand the isotopic composition of fluid which led to HREE mineralisation at Songwe. It has already been established in other chapters that the paragenesis of Songwe strongly suggests the exsolution of fluid led to different paragenetic stages (Chapters 3, 4 and 5). Furthermore, it has also been shown that apatite formed in multiple different stages of the paragenesis, with two stages (Ap-3 and Ap-4) forming the major HREE-bearing mineral at Songwe (Chapter 5). The use of C and O isotopes to understand carbonatite evolution has already been reviewed (see previous section). In the remainder of this chapter, O and C isotopes are used in both calcite and apatite to track the isotopic composition of fluids at

Songwe, with particular emphasis on the HREE-mineralising fluids.

In this section, the advantages and disadvantages of measuring O and C in carbonate and apatite are discussed. As analysis of oxygen isotopes in apatite is a relatively new technique, and has largely been developed for this work, previous work on apatite is also reviewed.

7.2.1 Advantages and disadvantages of bulk-carbonate analyses in carbonatite

When attempting to understand the petrogenetic history of a carbonatite intrusion, the advantages of analysing carbonates are numerous: the analytical technique is relatively straightforward, simultaneous analysis of O and C isotopes can be obtained, there is voluminous literature providing data comparison and the causes of isotopic shifts are relatively well understood. There are, nevertheless, issues with the technique. These disadvantages include:

1. It is a bulk-technique, so multiple generations of the same carbonate in a rock sample are averaged, leading to loss of detail on different stages in a samples, if present.
2. Careful paragenetic interpretation is required if the technique is being used to obtain information about mineralisation of another phase in the rock (e.g. REE, pyrochlore, strontianite).
3. There is a high susceptibility to isotopic resetting/diffusion.
4. The possibility of re-equilibration of carbonate with post-emplacement fluids has to be considered.

The first two issues can be resolved through careful petrography and analysis of individual carbonate grains by micro-drilling. Different carbonates (e.g. calcite and dolomite) can be extracted by acids at different temperatures. CL can be used to assist differentiation of carbonate generations, and recrystallisation from hydrothermal fluid can be identified. However, microdrilling, or an alternative spatially-resolved isotope technique, is only applicable when carbonate is crystallising contemporaneously with a phase of interest. For example, it is of little use in looking at the isotopic conditions during synchysite crystallisation (and thus REE mobility) if the calcite is not crystallising at an equivalent stage in the paragenesis. The ambiguity of the relationship between calcite and apatite is one of the key issues with analysis of carbonate at Songwe.

The susceptibility of carbonate to isotopic resetting through diffusion and re-equilibration is difficult to avoid. Diffusion effects can occur in rocks where no petrographic evidence of fluids is present, effectively rendering minerals with a

low closure temperature as ineffective for geothermometry (Haynes et al., 2003). In these cases, the isotopic ratios can inform us about fluid conditions, but, where more than one fluid event has altered the rock, the isotopic ratio in the carbonate is susceptible to record the 'last' conditions it encountered before its closure temperature. Thus, if multiple fluid events have occurred in a carbonatite, the stable isotope ratios of the carbonate record the last fluid effects in the system.

7.2.2 Apatite stable isotope analyses

Apatite stable isotope ratios can be analysed for *both* carbon and oxygen, despite the lack of a carbonate group in the apatite structure. The exact substitution method is debated, but the general consensus is that CO_3^{2-} can substitute into both the phosphate site, and the A-site (fluorine site) in apatite (Pan and Fleet, 2002; Yi et al., 2013). Thus, oxygen isotopes can be measured from three sites in apatite:

1. Structural CO_3
2. OH site in hydroxyl-apatite
3. PO_4 site

Of these sites, the PO_4 site is normally used for oxygen isotope analysis as it is considered the least susceptible to isotopic exchange, after its formation (O'Neil et al., 1994; Vennemann et al., 2002; Kohn and Cerling, 2002). The means of isolating the PO_4 from other varieties of oxygen hosted in apatite depends on the experimental technique used for analysis. Multiple techniques are possible for analysis of $\delta^{18}\text{O}$ in apatite, and these are listed in Table 7.1. Techniques such as direct laser fluorination, laser ablation and the ion-probe directly analyse apatite grains and do not separate the oxygen isotope ratios from different sites in the apatite. If other O sites in the apatite are more susceptible to diagenesis, then samples analysed by these techniques will be isotopically biased (Kohn and Cerling, 2002). Isolation of the PO_4 site is typically obtained chemically, through reaction of the phosphate with Bi or Ag to form $x\text{PO}_4$, where Ag_3PO_4 is most commonly used owing to issues of water absorption with Bi. Ag_3PO_4 can then be analysed for its isotope ratios by dissociation of the oxygen through either fluorination, laser heating with graphite, TC/EA⁵, TIMS⁶ or high temperature reduction with graphite (Holmden et al., 1997; Vennemann et al., 2002; Lécuyer et al., 2007; LaPorte et al., 2009).

⁵thermal conversion elemental analyser

⁶thermal ionisation mass-spectrometry

Method:	Ag ₃ PO ₄ preparation?	References
TIMS	Y	Holmden et al. (1997)
Fluorination	Y	Crowson et al. (1991); Lécuyer et al. (1996); Vennemann et al. (2002)
Bromination	Y	Stuart-Williams and Schwarcz (1995)
High-T reaction with graphite	Y	ONeil et al. (1994)
High-T C-reduction	Y	Lécuyer et al. (2007); LaPorte et al. (2009); Chenery et al. (2012)
Laser ablation	N	Cerling and Sharp (1996)
Laser fluorination	N	Jones et al. (1999)
Ion probe	N	Eiler et al. (1997)

Table 7.1: Summary of different methods applied for deriving O-isotope values from the PO₄ site in apatite

7.2.3 Previous work

Analyses of apatite from teeth is commonly used both for modern ecological studies (e.g. Kohn and Cerling, 2002) and for palaeotemperature analyses (e.g. Dinosaur body temperatures, Barrick and Showers, 1994; fish, Kolodny et al., 1983; Lécuyer et al., 2003; phosphorites, Shemesh et al., 1983, 1988; and mammalian teeth, Grimes et al., 2008). Some studies have utilised both the PO₄ site and structurally-bound CO₃ to obtain a palaeo-thermometer independent of seawater ¹⁸O/¹⁶O ratios (Lécuyer et al., 2010). There have been, however, few studies of oxygen isotopes in phosphates apart from these examples, and ‘hard-rock’ studies are limited to granites (Farquhar et al., 1993), meteorites (Greenwood et al., 2003), pyromorphite deposits (Burmam et al., 2013) and limited studies in carbonatites. Previous analyses of apatite δ¹⁸O from carbonatite are limited to one analysis from Oka (Conway and Taylor, 1969), two analyses from Jacupiranga (Santos and Clayton, 1995), and 18 analyses from the Tiksheozero and Siilinjärvi complexes (Tichomirowa et al., 2006). All of these analyses measured the oxygen isotope ratios of the whole apatite, rather than isolating the PO₄ site, from primary magmatic samples. The results of these studies range between 4.2–5.7 ‰ (Fig. 7.4).

Carbon isotopes in apatite have also been used to investigate the carbon isotope composition of the mantle (Nadeau et al., 1999). The validity of using structurally bound CO₃ in apatite from high-temperature igneous and metamorphic rocks, however, has been questioned on the basis of the possibility of fractionation of C isotope values between different sites in apatite, or in inclusions of

graphite (Peck and Tumpane, 2007).

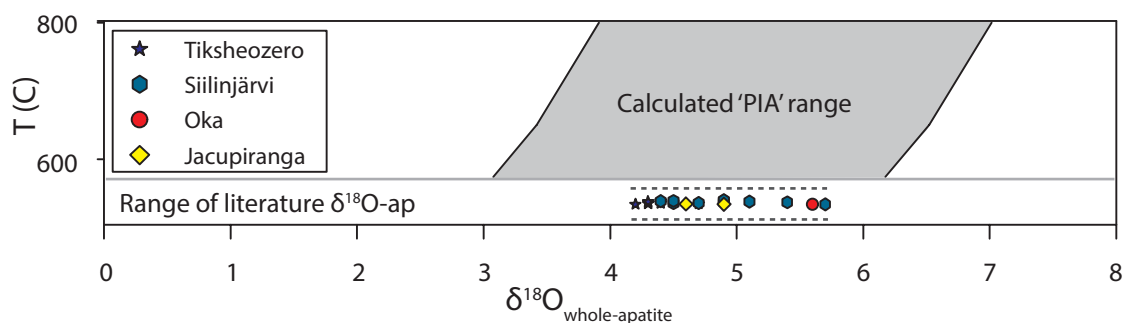


Figure 7.4: Compilation of previous analyses of apatite from Oka (Conway and Taylor, 1969), Jacupiranga (Santos and Clayton, 1995), Tiksheozero, and Siilinjärvi (Tichomirowa et al., 2006), plotted against an estimated PIA^a range using the PIC range (+5.3 to +8.4 ‰) and the fractionation factor from Fortier and Lüttge (1995) for the temperatures 550–800 °C (see section 7.7.2 for details).

^aprimary igneous apatite

7.3 Sample selection and hypotheses

Samples were selected both from worldwide carbonatites and from different stages of the paragenesis at Songwe. Samples from worldwide carbonatites were used to test the validity of measuring $\delta^{18}\text{O}_{\text{PO}_4}$ while samples from Songwe were used to attempt to fingerprint changing fluid conditions in the carbonatite.

7.3.1 Worldwide carbonatites

As analysing $\delta^{18}\text{O}_{\text{PO}_4}$ from carbonatites is a novel technique, 5 samples from other carbonatites were selected to widen the scope of the study and to provide data for comparison with Songwe. The carbonatites selected were from Oka and St Honoré, Canada; Jacupiranga, Brazil; Fen, Norway and Kaiserstuhl, Germany. These carbonatites have been well studied, and a summary of literature about each sample is included in Table 7.2. The hypotheses these samples were selected to test include:

1. Is it possible to develop an isoscape for $\delta^{18}\text{O}_{\text{PO}_4}$ in carbonatites?
2. Is $\delta^{18}\text{O}_{\text{PO}_4}$ in apatite susceptible to diffusion and isotopic re-setting when interacting with a hydrothermal fluid?
3. Can the preparation technique be carried out on a bulk powder, or do apatite grains need to be picked before analysis?

To develop an isoscape for $\delta^{18}\text{O}_{\text{PO}_4}$, samples from Oka, Jacupiranga, Fen, and Kaiserstuhl were selected as the previously published isotope data for these carbonatites falls into, or very close to, the PIC box (Fig. 7.5). Furthermore, Oka and Jacupiranga both have previously published oxygen isotope ratios from apatite which were obtained from the whole mineral, not the PO_4 site. Isotope ratios from the apatite in these samples can be compared to the calcite data (considered as PIC) to check if a range for PIA is within a reasonable range calculated from apatite–calcite fractionation factors (Fortier and Lüttge, 1995).

To interpret if $\delta^{18}\text{O}_{\text{PO}_4}$ of apatite in a sample is susceptible to diffusion when interacting with a hydrothermal fluid, a sample from the St Honoré carbonatite, Canada, was also analysed. Oxygen isotope data from St Honoré spans a wide range in $\delta^{18}\text{O}_{\text{cc}}$ (Fig. 7.5), interpreted as a result of interaction of different fluid stages (Deines, 1989). Imagery of a thin-section of the StH-2 sample under CL clearly shows two generations of calcite (cal-1 and cal-2), with cal-2 growing between cleavage planes in biotite, and incurring into magnetite grains (Fig. 7.6). Apatite grains, however, appear relatively unaffected (see section 7.7).

From the worldwide carbonatite samples, powders were prepared from bulk-rock powder and from powdered apatite grains which had been hand picked (see section 7.4.2). This is to test if the preparation technique can be used for bulk powders, where apatite is considered as the only source of PO_4 in a sample, to shorten preparation time.

7.3.2 Songwe carbonatites

A list of the samples from Songwe is shown in table 7.3. Samples were selected to test:

1. Do the variations in isotope ratios relate to Rayleigh Fractionation, fluid alteration or sediment assimilation?
2. Can the fluid inclusion data be tied with the isotope data to determine the conditions of the mineralising fluid?
3. Can carbonate and apatite data be reconciled into a general model of fluid evolution?

To test these questions, samples were selected from throughout the paragenesis (Fig 7.7). Early, ovoid, magmatic samples (Ap 1 and 2) were selected from T0218 and T0206. HREE-enriched Ap-3 -bearing samples from carbonatite were selected from T0202, T0232, T0225, T0250 and T0262. LREE-enriched, Fe-rich carbonatite is represented by T0167 and areas with extensive supergene alteration, termed Mn-Fe veins, are represented by T0227. HREE-enriched Ap-4 from outside the main intrusion at Chenga was selected from T0178.

Sample #	Carbonatite	Location	Mineralogy	Previous work
Jaq-12	Jacupiranga	Brazil	Cc, Ap	1, 2, 3, 4
OKA-1	Oka	Canada	Cc, Ap, Mt, Bt, Pyro	5, 6, 7
Fen 202/76	Fen	Norway	Cc, Ap, Mt, Bt	8, 9,
K-Stuhl	Kaiserstuhl	Germany	Cc, Ap, Mt, Bt	10, 11, 12
STH-2	St Honoré	Canada	Cc, Ap, Mt, Bt, Pyro	7, 13

Table 7.2: Sample details from worldwide carbonatites. References: (1) Melcher (1966), (2) Santos and Clayton (1995), (3) Costanzo et al. (2006), (4) Morbidelli et al. (1995), (5) Davidson and Gold (1986), (6) Deines (1970), (7) Deines (1989), (8) Barth and Ramberg (1966), (9) Andersen (1987a), (10) Wimmenauer (1966), (11) Hubberten et al. (1988), (12) Keller (1981), (13) Vallée and Dubuc (1970).

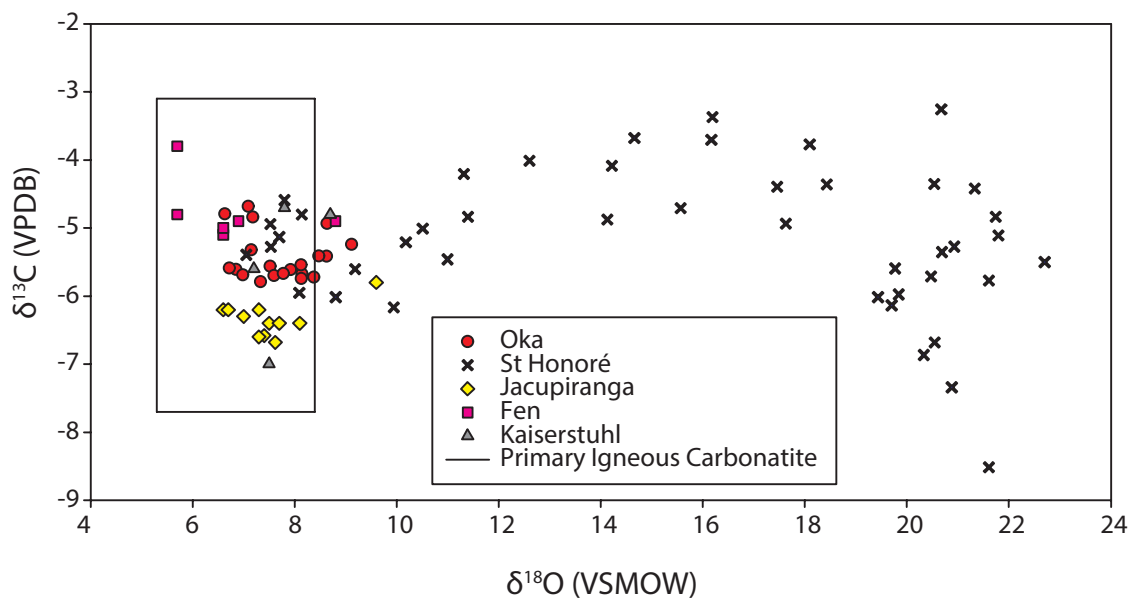


Figure 7.5: Compilation of previous analyses of calcite-carbonatite from Oka (Deines, 1970, 1989; Haynes et al., 2003), St Honoré (Deines, 1989), Jacupiranga (Morikiyo et al., 1990; Santos and Clayton, 1995; Haynes et al., 2003), Fen (Andersen, 1987a), and Kaiserstuhl (Hubberten et al., 1988). Included for reference is the PIC field after Taylor et al. (1967).

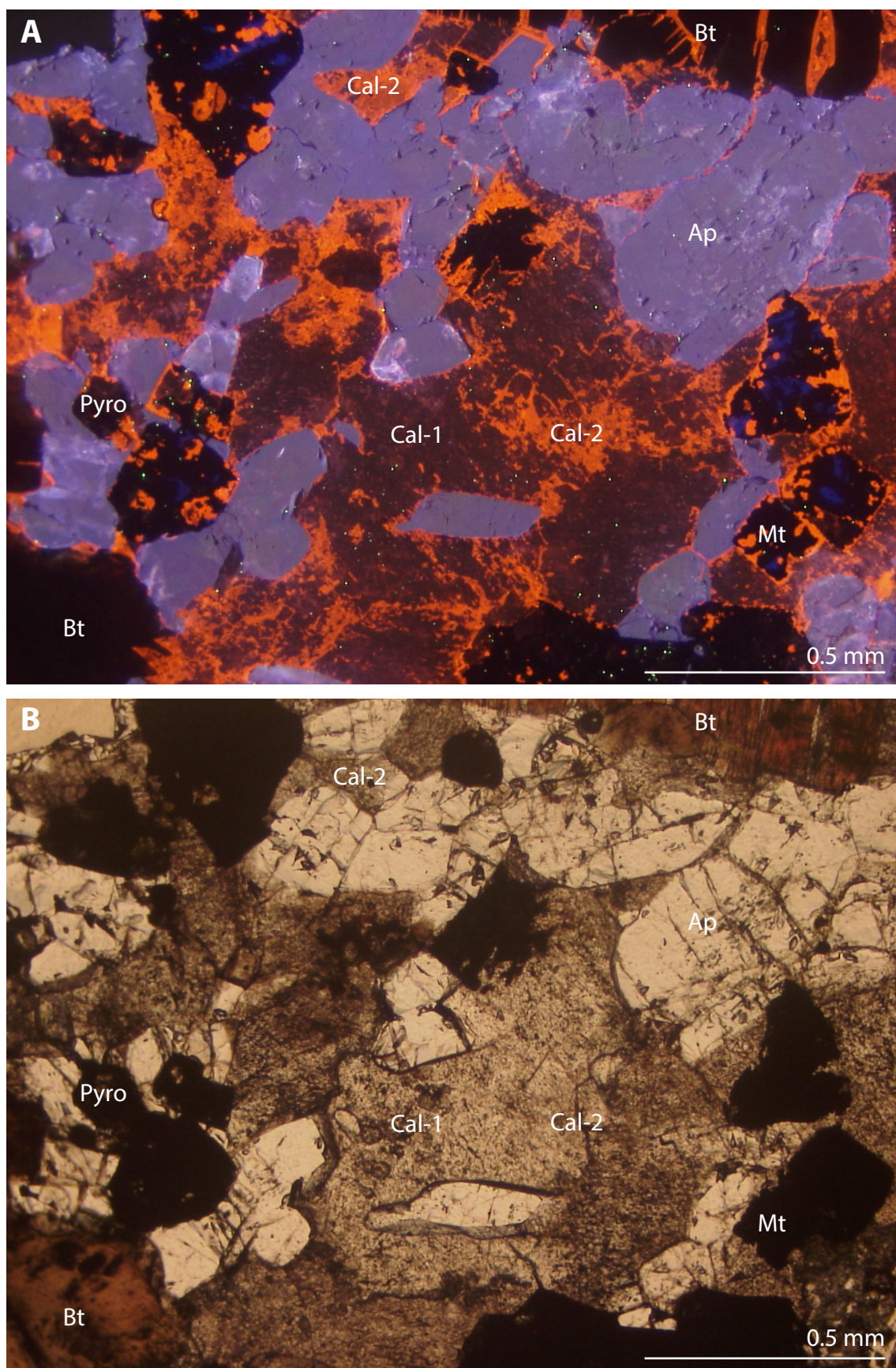


Figure 7.6: CL (A) and PPL (B) images of recrystallisation of calcite in the St Honoré carbonatite. Remnant rhombohedra of cal-1 are overprinted by later cal-2. Cal-2 also is overprinting magnetite (mt), pyrochlore (pyro) and biotite (bt) while apatite (ap) appears unaffected.

The mineralogy of the samples is summarised in Table 7.3. Common to many of the samples is a mixture of ankerite and calcite: for carbonate isotope analyses this is not an issue, and the separation of these carbonates for isotope data is described in the methodology (section 7.4.2). Nevertheless, multiple generations of calcite are apparent in CL images of the samples. This presents an issue for interpreting bulk-carbonate data as the bulk $\delta^{18}\text{O}$ and $\delta^{13}\text{C}$ will represent a mixed signal if there are any difference between the isotopic composition of each generation of calcite formation. This issue is not present when interpreting $\delta^{18}\text{O}_{\text{PO}_4}$, *except* in sample T0206, where two generations of apatite (Ap-1/2 and Ap-3) are present.

Samples with fluid inclusion data were selected to try and tie together homogenisation temperatures, as a proxy for crystallisation temperatures, with isotope data. These data can then be used to try and obtain information on the isotopic composition of the mineralising fluid, and to determine if it is of deuteritic or meteoric origin.

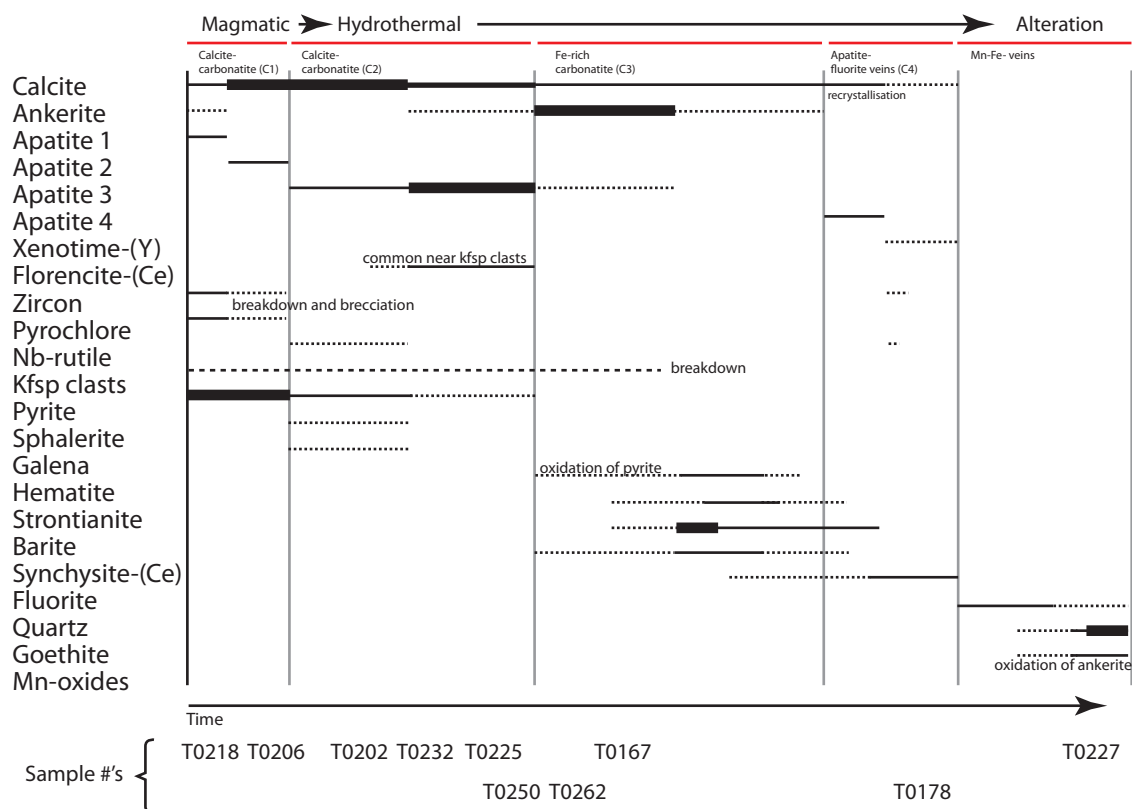


Figure 7.7: Paragenetic diagram of the Songwe Hill carbonatite, with approximate position of the samples selected for isotope analysis.

7.4 Methodology

Stable isotope analyses were carried out at the NIGL⁷ of the BGS⁹ in collaboration with Tim Heaton. The preparation of crushing, grinding and picking was carried out at CSM¹⁰, while all other preparation and analyses were carried out at NIGL. The method for preparing silver phosphate from bulk-apatite powders was developed by Tim Heaton as part of an NIGL grant to Frances Wall (IP-1387-111), conceived and written by Sam Broom-Fendley, and the following methodology is a modification of a version written by Heaton (*pers comm*).

7.4.1 Carbonates

Carbonate gasses were prepared offline. The bulk carbonatite powders for each sample were reacted with phosphoric acid at 16 °C for one hour to ensure calcite-only dissolution. The resultant gas was then passed over a cold finger, to remove H₂O, before running on a dual-inlet, Optima mass-spectrometer.

7.4.2 Apatite

Apatite samples were prepared as either a crushed carbonatite sample or as a crushed apatite-separate sample. Carbonatite samples were crushed and ground to a fine powder using a tungsten carbide TEMA mill, and then prepared as a silver phosphate. For apatite-separates, the carbonatite samples were crushed and sieved into different size fractions. The carbonate was removed from these fractions by dissolution in 20 % acetic acid at 50 °C for 72 hours. This is a relatively common technique in archaeological science, used to remove carbonate from phosphate samples, without altering the $\delta^{18}\text{O}_{\text{PO}_4}$ of the apatite (Koch et al., 1997; Garvie-Lok et al., 2004). Samples were then sieved again, before hand-picking of apatite from the largest size fractions (Fig. 7.8). These were then prepared as a silver phosphate for analysis.

Silver phosphate preparation

Two different methods of preparation for silver phosphate were used. Initially, the ‘tooth method’ was used for samples with a high PO₄ concentration. Subsequently, a ‘bulk-powder’ method was developed for samples with a lower bulk PO₄ concentration. These two techniques are outlined below.

⁷NERC⁸ Isotope Geosciences Laboratory

⁹British Geological Survey

¹⁰Camborne School of Mines

Sample #	Rock type	Ap type	Mineralogy
T0218	CC	1,2	Ap, Zr, Cal, (ank), goethite, ksp
T0206	CC	1,2,(3)	Ap, Zr, Cal, Ksp, Py
T0202	CC	3	Ksp, Ap, Zr, Cal, Goethite
T0232	CC	3	Ap, Cal, Ank, Fl, MnO
T0225	CC	3	Ap, Flr, Ank, Cal, Ksp, Py, Zr
T0250	CC	3	Cal, Goethite, Ap, Ank
T0262	CC	3	Ap, Cal, Ksp, Pyro, Py, Zr
T0178	Ap-Fl-V	4	Ap, Flr, Cal, Ksp, Xnt, Syn
T0167	AC	3	Ap, Flr, Ank, Str, Syn
T0227	Mn-Fe-V	3	Ap, Goethite

Table 7.3: Sample details and mineralogy of carbonatite samples from Songwe. CC= calcite carbonatite, AC= Fe-rich carbonatite, Ap-Fl-V= apatite-fluorite veins, Mn-Fe-V= Mn-Fe veins.



Figure 7.8: Example of glassy, hand-picked apatite from sample Jac-12

Tooth method preparation

The tooth method largely follows that developed for the preparation of silver phosphate from tooth enamel phosphate (Chenery et al., 2012), but was found to be impractical for samples with low phosphate concentration.

Bulk method preparation

To determine the amount of sample powder needed for analysis an approximate assessment of the phosphate content was made by adding 4 ml of 3M HCl to 100 mg of sample powder in a 50 ml centrifuge tube, shaking for half an hour, diluting the solution to 30 mL, removing undissolved powder by centrifugation and filtering, and then testing the solution by colorimetry (DR 800 colorimeter with PhosVer 3 reagent; HACH company). If practical, sufficient sample was then used to provide about 30 mg silver phosphate .

The method for preparing silver phosphate utilises procedures from McLaughlin et al. (2004). 2M HNO₃ was added to the sample in increments of 2 mL, with the total amount of acid being just sufficient to ensure that the pH is below 2 after all the reactive carbonate had been dissolved. This was shaken and stirred for half an hour, and then diluted by adding an amount of DIW¹¹ 20 times the volume of HNO₃ added. The solution was separated by centrifugation and filtering, and mixed overnight with cation resin in nitrate form (1 ml resin for every 10 ml of solution). Again, the solution was separated and filtered, and the resin was washed once. The pH was raised to c. 2.5 with drops of 5M KOH, and 5 ml 1M MgCl₂.6H₂O was mixed in, followed by a further 1 ml 5M KOH. This led to the formation of a gelatinous brucite flocculent, which was left to settle for one hour, centrifuged and decanted off discarding the supernatant solution (Fig. 7.9A). 2 ml 10 % acetic acid and 1 ml 0.5 M potassium acetate were added to the gel, followed by increments of 2 M HNO₃ vigorously shaking until the gel dissolved. The pH was then adjusted to 5.5 by addition of KOH or HNO₃ before adding 400 mg cerium nitrate dissolved in 2–3 ml DIW. This was stirred, pH checked to ensure it was between 5.0 to 5.5, and left overnight. The cerium precipitate was centrifuged and supernatant discarded (Fig. 7.9B). 20 ml of 0.5 M potassium acetate was added, shaken vigorously to re-suspend and wash the precipitate, centrifuge-discard again, and repeated twice more (i.e. a total of 3 potassium acetate washes). The cerium precipitate was dissolved with vigorous shaking in 2 ml 1M nitric acid, to which 18 ml DIW and 4 ml of cation resin were added and mixed overnight. The solution was separated and filtered (washing the resin once) into a clean 100 ml glass beaker placed in a dust-free environment (Fig. 7.9C). 7.5 ml of ammoniacal silver nitrate solution was added, mixed, and place in a hotplate

¹¹deionised water

jacket at 70 °C. As ammonia volatilises off and pH lowers towards neutral yellow-green crystals of silver phosphate form on the surface and bottom of the solution (Fig. 7.9D). If needed, the volume was occasionally topped up to at least 20 ml, and left covered and unheated overnight (Fig. 7.9E). Precipitation is regarded as complete when the pH has stopped dropping at between c. 6.8 to 7.2, which might take 6–12 hours on the hotplate. The silver phosphate is recovered on 0.2 μm polycarbonate membranes, washed several times with DIW, dried at 70°C, weighed, lightly ground and homogenised in an agate mortar, and transferred to a 1.5 ml glass vial (Fig. 7.9F). The sample is finally examined for impurities under a microscope.

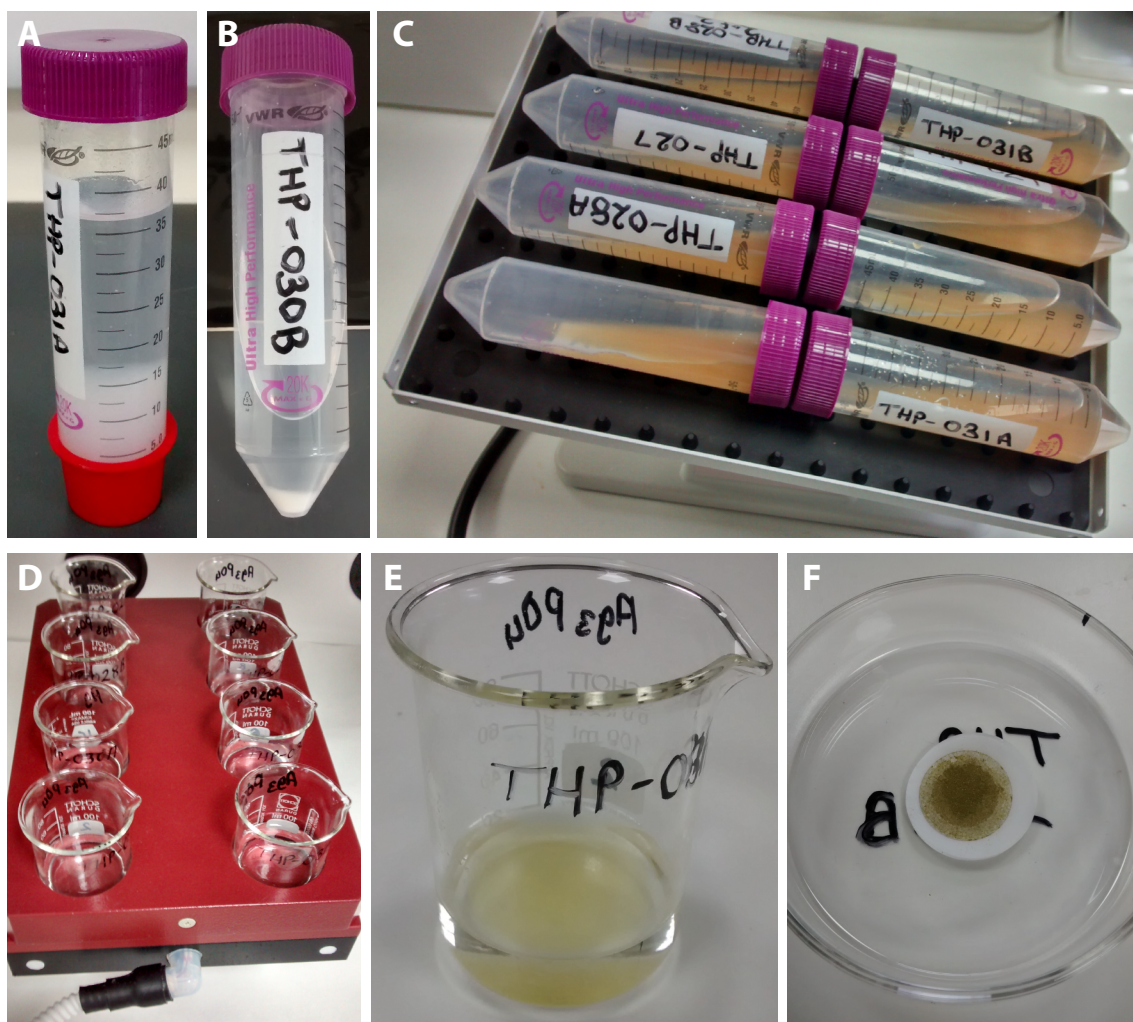


Figure 7.9: Stages of preparation of AgPO_4 . (A) Brucite flocculate settling after the addition of magnesium chloride. (B) Cerium phosphate settling after centrifuging. (C) Ce removal with cation resin. (D) Heating Ag solution to drive off ammonia. (E) Precipitation of silver phosphate. (F) Final silver phosphate residue after filtering.

$^{18}\text{O}/^{16}\text{O}$ analysis of silver phosphate

Up to 99 silver phosphate samples and standards were weighed to between 380 to 420 micrograms in silver capsules and placed in a Zero Blank Autosampler (Costech Analytical Technologies, Valencia, USA) atop a TC/EA (ThermoFinnigan, Bremen, Germany). The carbon monoxide produced by thermal decomposition of the phosphate in the graphite crucible of the TC/EA at 1400 °C is passed under continuous helium flow to a Delta+XL mass spectrometer (ThermoFinnigan, Bremen, Germany) where the $^{18}\text{O}/^{16}\text{O}$ ratio is calculated by comparing the abundance ratios of mass 30 ($^{12}\text{C}^{18}\text{O}^{16}\text{O}$) and mass 28 ($^{12}\text{C}^{16}\text{O}^{16}\text{O}$), to those of a reference gas and an internally run silver phosphate laboratory standard. $\delta^{18}\text{O}$ values versus VSMOW are based on calibrating the laboratory standard against a silver phosphate reference material. In the absence of an agreed international reference material we utilised silver phosphate standard 'B2207' (supplied by Elemental Microanalysis Ltd, Okehampton, England) which has been measured in an inter-laboratory comparison study to have a certified $\delta^{18}\text{O}$ value of 21.7 ‰ versus SMOW. All samples were run in triplicate, with a typical precision of $\sigma \leq 0.3$ ‰.

7.5 Results

7.5.1 Worldwide carbonatites

Results for carbonate and apatite $\delta^{18}\text{O}$ and $\delta^{13}\text{C}$ are shown in Table 7.4. Carbonate $\delta^{18}\text{O}$ and $\delta^{13}\text{C}$ values from Jacupiranga, Kaiserstuhl, Oka and Fen are between -4.49 and -6.57 ‰ $\delta^{13}\text{C}$ and between +7.6 to +8.15 ‰ $\delta^{18}\text{O}$ —within the PIC field (-3.1 to -7.7 ‰ $\delta^{13}\text{C}$ and +5.3 to +8.4 ‰ $\delta^{18}\text{O}$). These results are in line with the previous literature analyses of calcite-carbonatite from these carbonatites (Fig. 7.5). Correspondingly, $\delta^{18}\text{O}_{\text{PO}_4}$ from apatite analyses of these samples range between 4.1 to 5.4 ‰ $\delta^{18}\text{O}_{\text{PO}_4}$, with multiple analyses of the sample from Jacupiranga within 0.11 ‰ of 5.4 ‰.

Carbonate $\delta^{13}\text{C}$ from St Honoré is -5.5 ‰, and falls in the PIC field, but $\delta^{18}\text{O}$ is significantly higher, at +16.4 ‰. Apatite $\delta^{18}\text{O}_{\text{PO}_4}$ values, in contrast to the carbonate $\delta^{18}\text{O}$ values, are much lower, at 4.6 ‰ and replica samples are within 0.04 ‰.

Variations between preparation techniques

Apatite-separates were not picked from Kaiserstuhl as the grains were too small to be able to obtain a sufficient amount for analysis. Results from the two preparation methods (bulk powder and picked apatite separates) for $\delta^{18}\text{O}_{\text{PO}_4}$ broadly

Sample	Carbonate		Est %PO ₄	Apatite							
	$\delta^{13}\text{C}$	$\delta^{18}\text{O}$		$\delta^{18}\text{O}_{\text{PO}_4}$	$\pm (1\sigma)$	Replication	$\pm (1\sigma)$	$\delta^{18}\text{O}_{\text{PO}_4}$ (T)	$\pm (1\sigma)$	$\delta^{18}\text{O}_{\text{PO}_4}$ (S)	$\pm (1\sigma)$
T0178	-0.1	26.66	27	-0.7	0.12			-0.8	0.71		
T0232	-4.02	19.77	2					2.9	0.30		
T0250	-3.95	19.72									
T0167			12	1.1	0.24			1.8	0.38		
T0202	-3.65	10.01	0.3	1.9	0.43						
T0206	-3.42	7.8	1	2.2	0.02	0.25	0.11				
T0218	-4.33	14.01	0.2	2.5	0.08						
T0225	-4.62	12.66	5	1.7	0.04	0.17	0.48				
T0262	-2.47	19.64	18	1.5	0.01	0.05	0.07				
T0227			26	3.0	0.06			3.2	0.36		
FEN 202/76	-4.79	7.67	3	4.1	0.40					4.7	0.10
JAQ-12	-6.34	7.95	29	5.4	0.33	0.11	0.06			5.2	0.09
K-STUHL	-6.57	8.15	2	5.0	0.24						
OKA-1	-4.49	7.71	3	5.3	0.10					5.3	0.11
STH-2	-5.5	16.41	10	4.6	0.12	0.04	0.41			4.4	0.08

Table 7.4: Stable isotope results for carbonates and apatite from Songwe and other carbonatites. Oxygen isotope ratios are relative to VSMOW, carbon isotope ratios relative to VPDB. Where analyses are reported with a replication value, these data are for repeat silver phosphate preparations on the same sample. Here, the reported $\delta^{18}\text{O}_{\text{PO}_4}$ value is an average, and the replication errors indicate the range from at least 2 separate preparations. Analytical error is indicated by \pm , these are 1σ of at least 2 replica analyses of the same sample preparation. Results from the tooth method are indicated with (T), and results from apatite separates are indicated with (S).

7.6 Results

overlap. Indeed, the $\delta^{18}\text{O}_{\text{PO}_4}$ values from Oka are exactly the same for the two methods (Fig. 7.10). However, there is a difference of 0.6 ‰ between the two preparation techniques from Fen, within the bounds of 1σ analytical uncertainty (± 0.3 ‰) and well within 2σ .

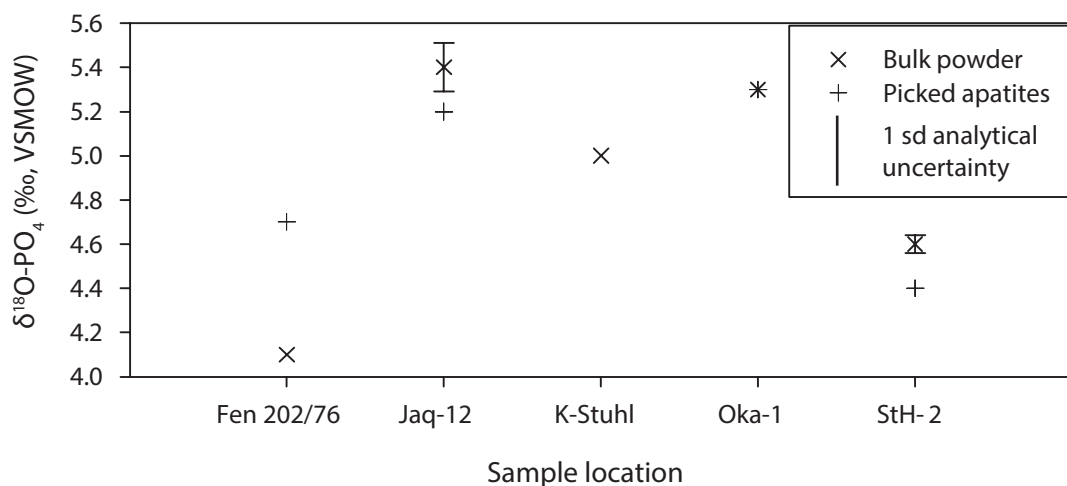


Figure 7.10: Comparison of $\delta^{18}\text{O}$ results from analysis as a bulk powder and from picked apatite analysis. Error bars represent the range of repeat analyses using the same technique. Analytical error (1σ) is represented graphically in the legend.

7.6.1 Songwe samples

The results of carbonate and apatite stable isotope analyses are shown in Table 7.4 and Figures 7.11 and 7.12.

Carbonate

Due to the lack of an adequate quantity of calcite, the samples from ankerite carbonatite and Mn-Fe-veins (T0167 and T0227) were not analysed for carbonate isotopes. Results from the calcite carbonatite and Ap-Fir vein samples are shown in Figure 7.11. The results show a correlation ($R^2 = 0.4286$) between $\delta^{18}\text{O}$ and $\delta^{13}\text{C}$, away from the PIC box, towards higher $\delta^{18}\text{O}$ and slightly higher $\delta^{13}\text{C}$ values. The apatite-fluorite vein sample (T0178) has the highest $\delta^{18}\text{O}$ and $\delta^{13}\text{C}$ levels, up to 26.7 ‰ $\delta^{18}\text{O}$ and -0.1 ‰ $\delta^{13}\text{C}$. While magmatic carbonate has the lowest $\delta^{18}\text{O}$ value, at 7.8 ‰, within the top right-hand corner of the PIC box.

Apatite

Apatite isotope results from Songwe are plotted in Figure 7.12. This plot incorporates results from the standard method for samples with low concentrations of

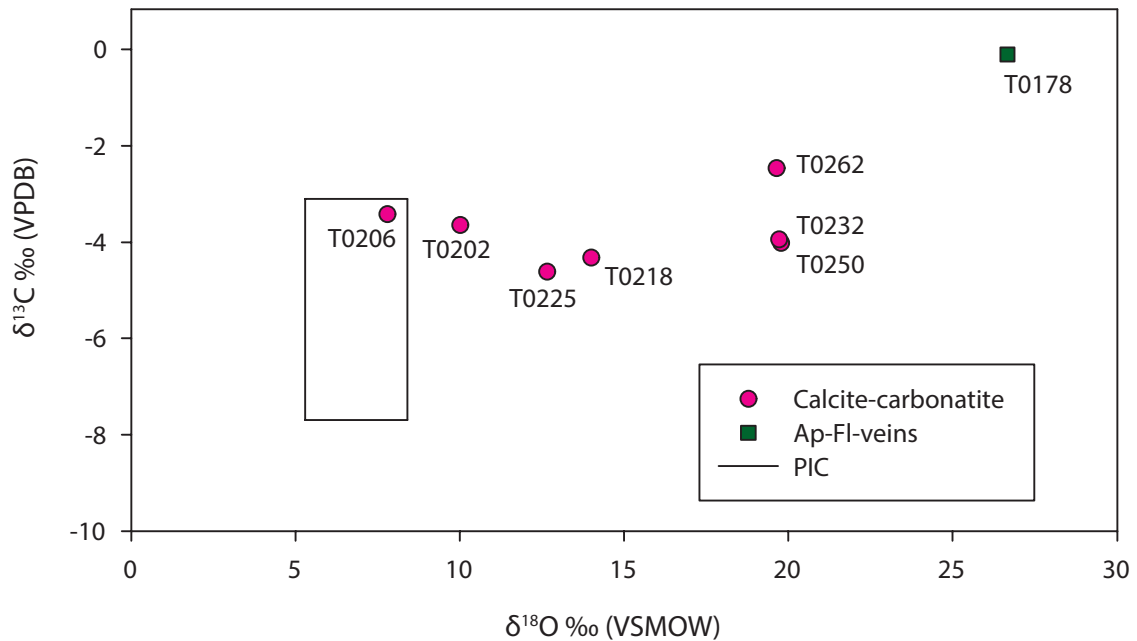


Figure 7.11: $\delta^{18}\text{O}$ and $\delta^{13}\text{C}$ results for bulk carbonates from Songwe, plotted against the PIC field (Jones et al., 2013).

PO_4 and results using the ‘tooth’ method, for higher PO_4 concentrations. The ‘tooth’ technique was used for T0178, T0227, T0167 and T0232. Generally the two techniques are in good agreement with each other. For T0178 and T0227 the difference between the results for the two methods is 0.1 and 0.2 ‰, respectively. The results from each technique for T0167, where the difference is 0.7 ‰, are outside analytical uncertainty and represent a real difference between the two techniques, which cannot be readily explained. For the result from T0232 there is no other data-point for the bulk-powder technique with which to make a comparison.

Arranged in approximate paragenetic order, the $\delta^{18}\text{O}_{\text{PO}_4}$ values decrease with increased evolution of the carbonatite system (exceptions are detailed below). Initial $\delta^{18}\text{O}_{\text{PO}_4}$ values for Ap-1,2 from T0218 and T0216 are among the higher isotope ratios, between 2.5–2 ‰, but still notably lower than the predicted PIA values. Values for Ap-3 from calcite carbonatites span a range between 2–1 ‰. While Apatite-fluorite veins from Chenga (T0178) have the lowest values, at -0.7 ‰.

There are two exceptions to the trend of decreasing $\delta^{18}\text{O}_{\text{PO}_4}$ with carbonatite evolution. These exceptions are T0232 and T0227. The result for T0232, measured by the ‘tooth’ method as 2.9 ‰, is higher than any of the other Ap-3, or the ovoid Ap-1,2 which are considered as primary. It is also significantly higher than expected for its position in the paragenetic sequence. The $\delta^{18}\text{O}_{\text{PO}_4}$ value for T0227 is also significantly higher than expected isotope ratio at the point in the paragenesis, and indeed is the highest $\delta^{18}\text{O}_{\text{PO}_4}$ for all of the Songwe results, at approximately 3 ‰.

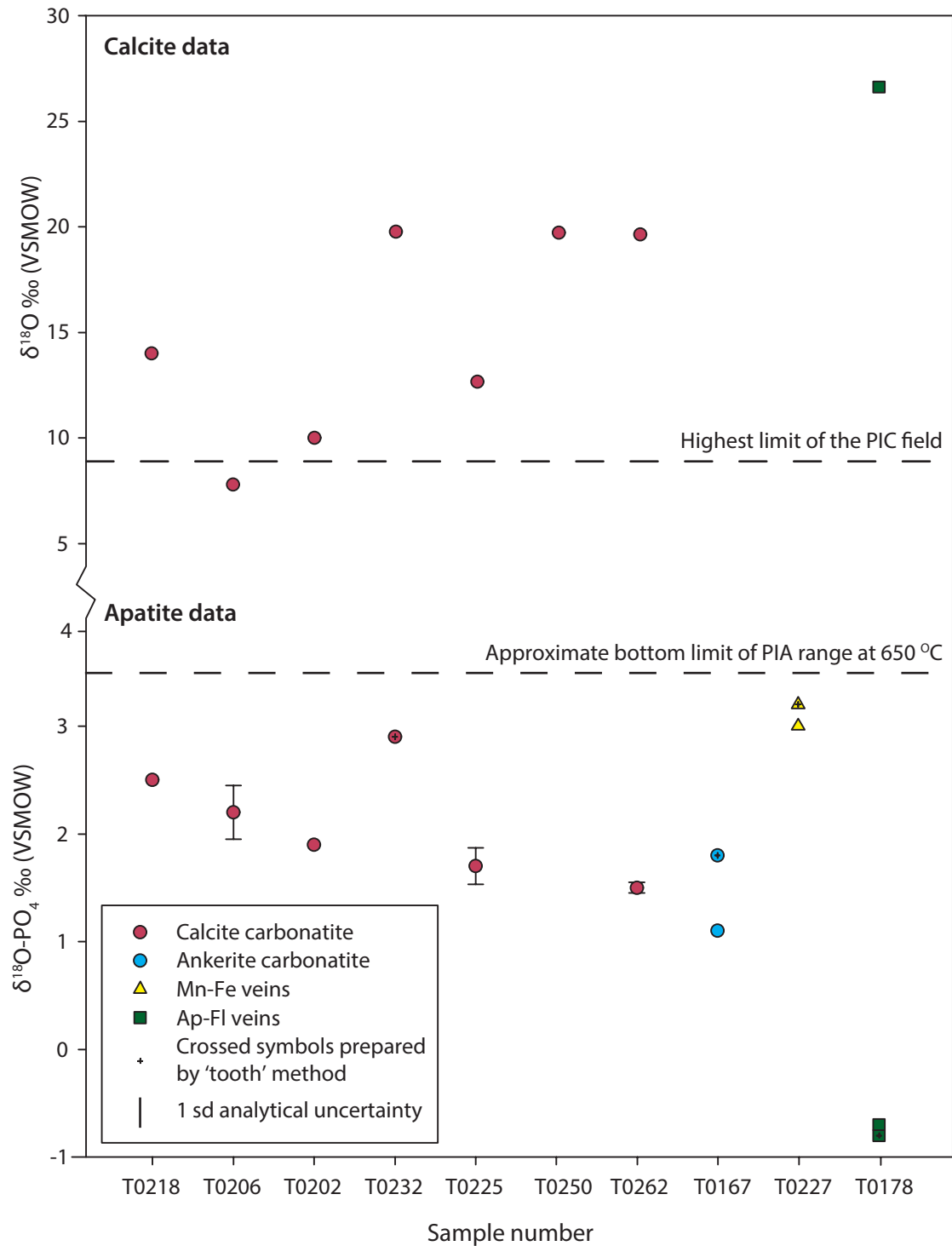


Figure 7.12: Songwe $\delta^{18}\text{O}$ results from calcite (above) and $\delta^{18}\text{O}$ results from apatite (below), arranged in approximate paragenetic order. Error bars on apatite results represent replica values. Crossed symbols represent apatite results analysed by the 'tooth' method. Also included is the approximate bottom limit of the PIA and upper limit of the PIC field (Jones et al., 2013).

7.7 Discussion

The discussion is broadly split into two parts: firstly, looking at the techniques used for preparation and analysis of apatite for O-isotopes, using data from world-wide carbonatites to ratify a PIA field; secondly, discussing the implications of the Songwe isotope results for HREE mobility.

7.7.1 Comparison of apatite preparation techniques

For some of the samples, data for $\delta^{18}\text{O}_{\text{PO}_4}$ was acquired using both the bulk-powder technique and the 'tooth' method. These are discussed below.

Analysis of apatite as a bulk powder

Results for $\delta^{18}\text{O}_{\text{PO}_4}$ from both picked apatite separates and bulk powder (Fig. 7.8) show that the two techniques give similar results, with the exception of the result from Fen (Fig. 7.10). While the results are within 2σ analytical error, possible other causes of variation include:

1. Phosphate is present in phases other than apatite in the rock
2. A sampling bias is present when picking individual grains
3. Apatite is isotopically heterogeneous, and the picked sample is not representative
4. The isotopic composition of the apatite is altered during dissolution of the carbonate in acetic acid
5. Arsenic is present in appreciable concentrations in the bulk powder, which can exchange with water during preparation

The only significant phosphate phase present in many calcite-carbonatites is apatite, with other phosphate phases present in insignificant amounts (Kapustin, 1980; Hogarth, 1989). The only other phosphate phases which may occur are monazite and crandallite group minerals. These phases have not been documented in calcite carbonatite from Fen (Barth and Ramberg, 1966), and are not found in sample 202/76.

Isotopic heterogeneity of the apatite is a possibility, and chemically zoned apatite has been documented from numerous calcite carbonatites (Campbell and Henderson, 1997; Dawson and Hinton, 2003; Costanzo et al., 2006). In all of these cases, however, apatite zoning is apparent in all of the grains in a sample. It seems unlikely that a sampling bias would result from picking a proportion of these grains compared to taking a bulk-powder average of all the apatite in the

sample. Nevertheless, it is difficult to completely exclude this potential source of bias without using an ion-probe to check to see if the grains are heterogeneous.

Alteration of the isotopic composition through exchange with acetic acid is unlikely. The grains showed no sign of alteration when being picked, and the PO_4 site in apatite is not particularly susceptible to isotopic exchange through diffusion.

If arsenic is present in appreciable concentrations in the bulk sample, then it can present problems. This is because arsenate oxygen is very exchangeable, and, unlike phosphate, might exchange with the water used during sample preparation. Furthermore, if arsenate was present in the bulk-sample, it would precipitate out with the silver phosphate and would be difficult to check for before analysis (Burmann et al., 2013). Typically, however, bulk-rock concentrations of arsenic in carbonatites are very low. It is not routinely analysed for and reviews of average carbonatite composition do not list it as a trace element (Woolley, 1989; Le Bas, 1999), nor are arsenic-bearing minerals commonly known from carbonatites (Kapustin, 1980). Indeed, the most likely As-bearing mineral in carbonatites is apatite, where it can substitute for P. Analyses of As from carbonatite-apatite are uncommon (Chapter 5), but As data from apatite from Songwe, as an example of As concentration in carbonate-apatite, is typically less than 20 ppm. Thus, when compared to the concentration of phosphorus in an apatite sample (4 orders of magnitude greater) the As concentration is negligible.

Despite the anomalous results from Fen, the data from the other carbonatites suggests that preparation of silver phosphate from a bulk-rock powder could be a much faster way to obtain $\delta^{18}\text{O}_{\text{PO}_4}$ results than through slower techniques such as picking, especially when apatite grains are small such as in the case of Kaiserstuhl. Furthermore, bulk-powder $\delta^{18}\text{O}_{\text{PO}_4}$ analysis may, potentially, be a cheaper technique than more costly techniques such as ion-probe.

Use of the ‘tooth’ method for analysis

A number of repeat tests on the tooth method were carried out during development, which gave somewhat variable results. In particular, it sometimes gave impure silver phosphate with erroneously high $\delta^{18}\text{O}_{\text{PO}_4}$ values (Heaton, *pers comm*). The low number of data points from Songwe samples obtained by the tooth method makes evaluation of the quality of the data difficult, especially given that only three samples have comparison bulk-powder values. Where comparison can be made, two out of the three tooth method samples do indeed have higher $\delta^{18}\text{O}_{\text{PO}_4}$ values (Fig. 7.12). Thus confidence in the tooth method results is lower than that of the bulk-powder method (Heaton, *pers comm*).

7.7.2 Primary igneous apatite

The processes which can affect stable isotope data from carbonates in carbonatites are reasonably well understood (see section 7.1). When interpreting stable isotope data, results are typically interpreted relative to the PIC field, and deviations from the PIC are attributed to various processes depending on their isotopic values and comparison with other known data and published studies (Fig. 7.2). For isotope data from apatite, no PIC field exists. Thus, it is important to constrain a field for the equivalent PIA¹² field to use when interpreting $\delta^{18}\text{O}_{\text{PO}_4}$ results.

A calculated primary igneous apatite field

A field for PIA can be estimated using known fractionation factors for hydroxylapatite (Fortier and Lüttge, 1995). Using equation 7.4, the isotopic composition of apatite can be calculated by using the range of $\delta^{18}\text{O}$ for PIC carbonates (+5.3–+8.4 ‰) and making the assumption that the temperature of formation was between 600–700 °C. This temperature range is selected as it is the range established for the carbonatite solidus in a range of synthetic systems (Wyllie, 1966; Jago and Gittins, 1991). Experimental and petrographic data suggest that PIA is likely to crystallise early in the petrogenesis of a carbonatite (Wyllie, 1966; Le Bas, 1989). Thus, using these data at the higher temperature of 700 °C, the expected range for PIA is between 3.6 and 6.7 ‰ (Fig. 7.4). Although, as Figure 7.4 shows, the ranges do not change significantly down to 550 °C, due to insignificant changes in the fractionation factor over this temperature range (Fortier and Lüttge, 1995). At higher temperatures (800+ °C), the difference between PIC and PIA becomes negligible.

Validation of the primary igneous apatite field using textural information

The analyses of apatite from samples which are ‘classically’ and texturally considered as primary carbonatites can be used to validate the PIA field. These analyses from Oka, Jacupiranga, Tikshezero and Siilinjärvi fall into the PIA range (e.g. Figure 7.4, Conway and Taylor, 1969; Santos and Clayton, 1995; Tichomirowa et al., 2006), as do the new $\delta^{18}\text{O}_{\text{PO}_4}$ analyses from Oka, Jacupiranga, Kaiserstuhl and Fen. Apatite from these samples all form ovoid grains at carbonate grain boundaries and/or as flow-banded clusters. These textures are considered to have formed early in the carbonatite petrogenesis (Kapustin, 1980; Le Bas, 1989; Hogarth, 1989). This gives strong support that the calculated PIA field could be a reasonable basis for interpretation of apatite oxygen isotope data, in the same way that the PIC field is used for carbonates.

¹²primary igneous apatite

Validation of the primary igneous apatite field using temperature calculation

Using equation 7.4, the validity of the PIA field can be checked by using $\delta^{18}\text{O}_{\text{cc}}$ and $\delta^{18}\text{O}_{\text{PO}_4}$ to calculate the crystallisation temperature. In theory, the temperature for PIA and PIC, in equilibrium, should be between 600–700 °C, based on the solidus temperatures (Wyllie, 1966; Jago and Gittins, 1991). The calculated temperatures, including the errors propagated from equation 7.4, span a range from 341–608 °C, excluding data from St Honoré which will be discussed in section 7.7.4 (Fig. 7.13). The data are toward the lower end of the predicted temperature range, but it should be noted that the calcite-apatite fractionation is not the optimum system to use as there is not a very large fractionation between the two minerals, especially at higher temperatures (Haynes et al., 2003; Fortier and Lüttge, 1995). Furthermore, unless the system crystallises very rapidly, the minerals will be susceptible to diffusion until the closure temperature is passed. While apatite is closed to diffusion from 550 °C, calcite continues to be open until 400 °C (Cole and Chakraborty, 2001, Figure 7.3).

While the temperatures are lower than what might be predicted for magmatic crystallisation temperatures, they are roughly equivalent to the diffusion closure temperatures. This precludes the use of apatite-calcite as a geo-thermometer for igneous systems, but means that the PIA field is likely to be valid, and post-primary processes can be monitored by measuring $\delta^{18}\text{O}_{\text{PO}_4}$ relative to the PIA range, as long as consideration is given to the effects of any diffusion from crystallisation down to 550 °C.

7.7.3 Comparison of $\delta^{18}\text{O}_{\text{PO}_4}$ and $\delta^{18}\text{O}_{\text{whole-apatite}}$ data

This study has focussed on analyses of the PO_4 site in apatite, rather than isotope analyses of O from all the sites in apatite. Thus analysis of the PO_4 site excludes an isotopic contribution of O from any other sites in the mineral. These can include structurally bound OH in the Z-site as well as any carbonate in the structure — both of which are more susceptible to isotopic exchange with other fluids after the mineral has formed (Vennemann et al., 2002).

As a first-order check of the quality of the PO_4 data, the results for Oka and Jacupiranga can be compared to analyses of oxygen isotopes acquired from all oxygen sites in an apatite ($\delta^{18}\text{O}_{\text{whole-apatite}}$) by different techniques in previous studies (Conway and Taylor, 1969; Santos and Clayton, 1995). Given that both samples from these localities contain magmatic apatite, it can be assumed that the temperature of crystallisation for apatite in each sample is quite high (Haynes et al., 2003). Thus, any fractionation between PO_4 , OH and, if present, CO_3 can be assumed to be minimal and, as such, the isotopic composition of the PO_4 site and the bulk O-isotope values for the apatite should be approximately the same.

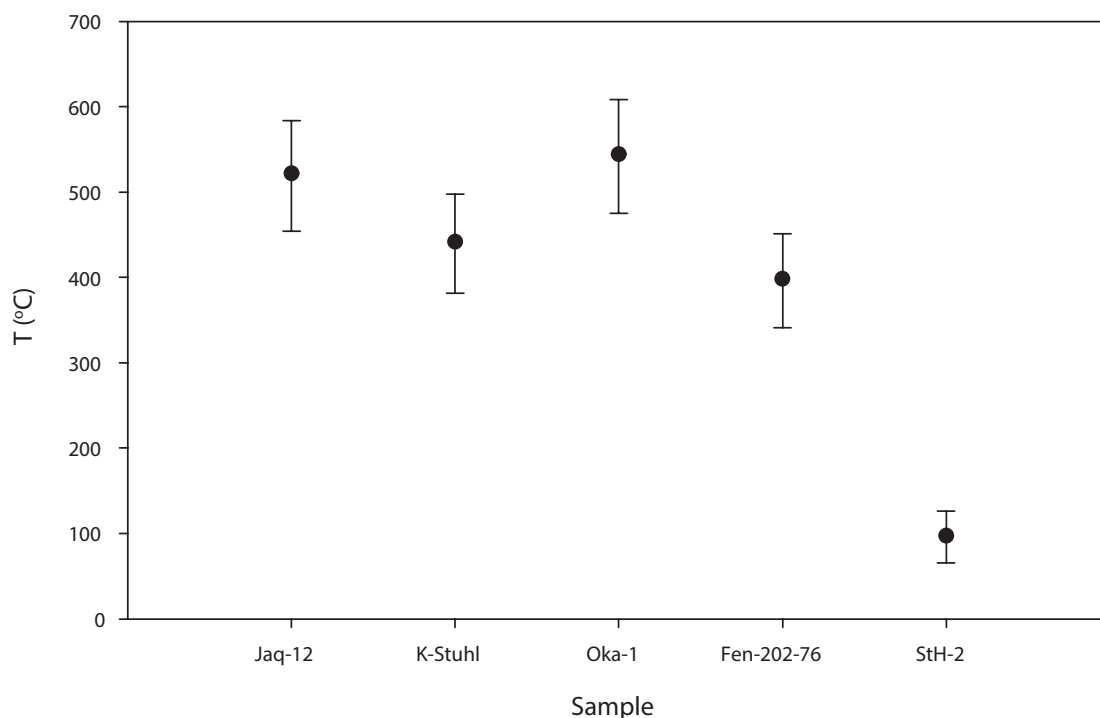


Figure 7.13: Calculated equilibrium temperatures between calcite and apatite using the fractionation factor of Fortier and Lüttge (1995). Error bars indicate the range in temperature from using the maximum and minimum values from equation 7.4.

Although the analysed apatite grains are from different samples to those analysed by Santos and Clayton (1995) and Conway and Taylor (1969), the samples are of the same rock type. Comparison of the data from Oka shows two different results within error (5.3 and 5.6 ‰, $\delta^{18}\text{O}_{\text{PO}_4}$ and $\delta^{18}\text{O}_{\text{whole-apatite}}$ respectively). Data from Jacupiranga are outside the range of analytical error, although the values are similar (5.4 and 4.6–4.9 ‰, $\delta^{18}\text{O}_{\text{PO}_4}$ and $\delta^{18}\text{O}_{\text{whole-apatite}}$ respectively). Given that no error bars for the apatite isotope results are provided in Santos and Clayton (1995), it is likely that these data are also within error of the $\delta^{18}\text{O}_{\text{PO}_4}$ results.

While only a first-order check, these data show that the PO_4 results are broadly consistent with the previous published data. To expand this study in the future, a useful check would be to compare whole-apatite data to PO_4 data from low-temperature apatite, especially hydroxylapatite, to evaluate the strength of any fractionation.

7.7.4 Isotopic diffusion in apatite

The high closure temperature of the PO_4 site in apatite to isotopic diffusion (see section 7.2.1) means that it is not susceptible to alteration from low-temperature fluids, especially during dissolution-reprecipitation of calcite. A good example of where the apatite has preserved its isotopic composition is at the St Honoré car-

bonatite. Here, CL images show that the carbonatite has experienced at least two carbonate crystallisation stages, with an early, probably euhedral, calcite stage (cal-1) overprinted by a later anhedral stage, or stages (cal-2) (Fig. 7.6). The CL image shows that cal-2 has interacted with magnetite, pyrochlore and biotite which are the other primary minerals that crystallised with cal-1. Apatite, however, shows little textural evidence of interaction with cal-2. Oxygen isotope ratios from bulk analyses of the carbonates reach high values, up to 23 ‰ in the literature (Deines, 1989), and 16.41 ‰ in sample StH-2 analysed in this study (Fig. 7.5, Table 7.4). These high oxygen isotope ratios are interpreted as due to interaction with low-temperature fluids, late in the carbonatite emplacement, although a specific temperature is not known (Deines, 1989). The result from this study show that the $\delta^{18}\text{O}_{\text{PO}_4}$ value from St Honoré falls into the PIA field, despite the fact that $\delta^{18}\text{O}$ from carbonates does not. This is interpreted as evidence that apatite, once past its closure temperature, provides a good record of the isotopic conditions at crystallisation. Thus, any apatite which crystallised below 550 °C will preserve the isotopic conditions of the crystallising fluid, rather than any subsequent altering fluid.

7.7.5 Using isotopes to track the evolution of Songwe — carbonate

In the following sections, the isotope results from Songwe will be discussed, starting with results from the carbonates and followed by those from apatite. These results will then be combined into an isotopic model for the mineralising fluid at Songwe.

As shown in Figure 7.11, $\delta^{18}\text{O}$ and $\delta^{13}\text{C}$ from Songwe show a broadly positive correlation from T0206, in the PIC field, towards T0178, samples which are, respectively, early and late in the paragenesis of Songwe (Fig. 7.7). This is a common trend in carbonatites, and has been observed in carbonatites at Barro do Itapirapūa (Andrade et al., 1999b), Tamazeght (Marks et al., 2009), Ondurakorum, Kalkfeld, Decker Willem, Spitskop (Horstmann and Verwoerd, 1997), Amba Dongar (Ray and Ramesh, 2006), and Catalão (Santos and Clayton, 1995). Interestingly, the trend is also observed in the HREE carbonatites at Lofdal, Namibia (Do Cabo, 2014). As discussed in section 7.1.2 (Fig. 7.2), these isotopic shifts could be caused by:

1. Sediment assimilation; or
2. Rayleigh Fractionation; or
3. Low temperature alteration.

Sediment assimilation

Sediment assimilation causes increased $\delta^{13}\text{C}$ due to incorporation of heavier carbon, from carbonate-bearing sediments, into water which interacts with the carbonatite. This process is an unlikely candidate for increased $\delta^{13}\text{C}$ in samples from Songwe as the country rock in this part of Malawi is a mixture of granulite and gneiss, with only very minor calc-silicate bands (up to a few cm) found in the rock nearby (Garson, 1965). None of these calc-silicate bands are found in immediate proximity to the carbonatite, or to the sample with the highest $\delta^{13}\text{C}$ values (T0178). Thus, the average carbon concentration in the country rock is low, and to cause large isotopic shifts through assimilation, the $\delta^{13}\text{C}$ ratio of the incorporated carbon will have to be very high. While no data exist in Malawi for carbon isotopes in the marble bands, values from the continuation of the Mozambique Belt, in Mozambique, have ratios between -3.5 and -2.0 ‰ (Melezhik et al., 2008). As the $\delta^{13}\text{C}$ values for T0178 are higher than this, it seems highly unlikely that sediment assimilation of country rock caused the increased carbon isotope ratios.

Rayleigh Fractionation

A more likely cause of the increased $\delta^{18}\text{O}$ and $\delta^{13}\text{C}$ is a combination of Rayleigh fractionation and/or alteration by low temperature fluids. Models for both of these processes have been developed (Ray and Ramesh, 2000 and Santos and Clayton, 1995; Ray and Ramesh, 1999a, respectively). Rayleigh fractionation of calcite from a fluid containing both CO_2 and H_2O leads to increased $\delta^{18}\text{O}$ and $\delta^{13}\text{C}$, but values for $\delta^{13}\text{C}$ and $\delta^{18}\text{O}$ for this process do not usually reach higher than -2 ‰ and 12 ‰ respectively (Ray and Ramesh, 2000). Thus, to reach the high $\delta^{18}\text{O}$ values seen in the Songwe carbonatites, Rayleigh fractionation is, alone, an unlikely candidate. Furthermore, the general trend of Rayleigh fractionation in carbonatites is that of a positive correlation with a gradient of approximately 0.4 on a graph of $\delta^{18}\text{O}$ against $\delta^{13}\text{C}$. This is a far higher gradient than observed in the Songwe stable isotope data (Fig. 7.11).

Low-temperature alteration

Low temperature fluid alteration is capable of much larger changes in $\delta^{18}\text{O}$ than Rayleigh fractionation and has been suggested as the cause of high $\delta^{18}\text{O}$ in many carbonatites.

The role of low-temperature alteration can be evaluated using models. Changes in C and O isotope ratios during low-temperature fluid-rock interaction between calcite, H_2O , and CO_2 can be defined as a function of two mass-balance equations (Santos and Clayton, 1995; Ray and Ramesh, 1999a):

$$\delta^{13}C_{rock}^{final} = \frac{(F_C/R_C)(\delta^{13}C_{fluid}^{initial} + \Delta_{rock-fluid}^C) + \delta^{13}C_{rock}^{initial}}{1 + (F_C/R_C)} \quad (7.8)$$

and:

$$\delta^{18}O_{rock}^{final} = \frac{(\frac{2r+2}{3r})(F_C/R_C)(\delta^{18}O_{fluid}^{initial} + \Delta_{rock-fluid}^O) + \delta^{18}O_{rock}^{initial}}{1 + (\frac{2r+1}{3r})(F_C/R_C)} \quad (7.9)$$

Where:

- F_C = Moles of carbon in the fluid
 R_C = Moles of carbon in the rock
 $\Delta_{rock-fluid}^C$ = Difference in carbon isotopes between the rock and the fluid
 r = Molar ratio of CO₂ to H₂O in the fluid

and:

$$\Delta_{rock-fluid}^O = 10^3 \ln \alpha^{18}O_{cc-CO_2} + 10^3 \ln(1 + 2r) - 10^3 \ln(2r + \alpha^{18}O_{H_2O-CO_2}) \quad (7.10)$$

Where $\alpha^{18}O_{cc-CO_2}$ and $\alpha^{18}O_{H_2O-CO_2}$ are fractionation factors between calcite–CO₂ and H₂O–CO₂ respectively, at a given temperature. Here, calcite is used to represent an assumed bulk carbonatite rock. Fractionation factors for calcite–CO₂ are taken from Chacko et al. (1991), while H₂O–CO₂ is taken from Richet et al. (1977).

These equations can be used to model the final isotopic composition of carbonate under certain fluid conditions in a *closed* system. They can only be used as a guide for interpretation as there are 6 unknowns in the equation, these are: (1) initial $\delta^{18}O$ and (2) $\delta^{13}C$ of the rock, and (3, 4) the fluid, (5) temperature of the system, and (6) the CO₂/H₂O ratio of the fluid. Some of these unknowns can be reasonably assumed. The initial $\delta^{18}O$ and $\delta^{13}C$ can be assumed to be from within the PIC field, while the fluid composition, if it is magmatically derived, would have the same initial composition as the rock, but if it were meteoric, would have lower $\delta^{18}O$ values. Other assumptions cannot easily be made but the effects of different temperatures and CO₂/H₂O ratios can be incorporated onto different graphs and evaluated (see below).

Two models are presented in Figure 7.14. These models represent interaction of a PIC with a deuteritic fluid and a meteoric fluid. Deep crustal fluids (e.g. metamorphic fluids) were discounted on the basis that the metamorphic country rock around Songwe is predominantly dry, with few hydrous mineral phases, and the likely shallow depth of intrusion at Songwe. The initial isotope values for the PIC

($\delta^{13}\text{C}_{\text{rock}}^{\text{initial}}$, $\delta^{18}\text{O}_{\text{rock}}^{\text{initial}}$) were chosen as +6 ‰ $\delta^{18}\text{O}$, -4 ‰ $\delta^{13}\text{C}$ because these values lay within the centre of the PIC field, and close to the values of T0206 — texturally the most primary Songwe sample analysed. The isotope ratio for the interacting fluids ($\delta^{13}\text{C}_{\text{fluid}}^{\text{initial}}$, $\delta^{18}\text{O}_{\text{fluid}}^{\text{initial}}$) were selected as broadly representative of a deuteritic fluid and a meteoric fluid. For the deuteritic fluid, the assumed isotopic composition was the same PIC values. The selected isotopic composition for meteoric fluid had a $\delta^{18}\text{O}$ value of -5 ‰ which was selected as a meteoric value broadly representative of a latitude of around -45° (Bowen and Wilkinson, 2002; Bowen, 2010) which was the approximate position of Malawi at 130 Ma (Fig. 7.15). A $\text{CO}_2/\text{H}_2\text{O}$ ratio (r) of 0.001 (low CO_2 , high H_2O) was selected following Santos and Clayton (1995). This ratio represents a fluid with a low CO_2 activity. It should be noted that a higher ratio, and thus a higher CO_2 activity in the fluid, causes steeper changes in $\delta^{13}\text{C}$ and smaller changes in $\delta^{18}\text{O}$, leading to major increases in $\delta^{13}\text{C}$ not observed in the data. For reference, these effects are sketched onto Figure 7.14. The isotopic ratios are modelled between 900 and 100 °C. The isotope ratios at temperatures below 100 °C have not been modelled, as this is well below the experimental temperature range for which CO_2 –calcite fractionation factors were measured (Chacko et al., 1991). Three different fluid/rock ratios (F_C/R_C) have been included in Figure 7.14: 0.1, 1 and 5, representing minor, moderate and complete alteration, respectively.

The models indicate that when the temperature of deuteritic water starts to drop below 400 °C, the oxygen isotope values of the rock start to increase from the PIC field. For low degrees of alteration (i.e. low F/R ratios), this is accompanied by negligible $\delta^{13}\text{C}$ change, while at higher degrees of alteration modest changes (up to approximately -2 ‰) in $\delta^{13}\text{C}$ occur (Fig. 7.14A). For alteration from meteoric fluid, at temperatures above 200 °C, $\delta^{18}\text{O}$ trends away from the PIC field, towards more negative values for all degrees of alteration. At lower temperatures $\delta^{18}\text{O}$ increases, to values higher than the PIC field, accompanied by little $\delta^{13}\text{C}$ change at low degrees of alteration, but higher $\delta^{13}\text{C}$ with complete alteration (Fig. 7.14B).

Meteoric or deuteritic alteration?

Based on the above models of Santos and Clayton (1995) and Ray and Ramesh (1999a), it is clear that low temperature alteration, from either deuteritic or meteoric water, can cause large increases in $\delta^{18}\text{O}$ (Fig. 7.14). Deuteritic alteration at high temperatures causes minimal changes to the isotopic ratios of the final carbonate while meteoric water at high temperature can shift $\delta^{18}\text{O}$ to lower (lighter-O) values. This alteration can help explain why samples which would otherwise be considered as primary magmatic samples (e.g. StH-1 and T0218) have higher $\delta^{18}\text{O}$ values. These higher values correspond to evidence for alteration in the sample, such as multiple calcite generations and exsolution of Fe-oxides from carbonates

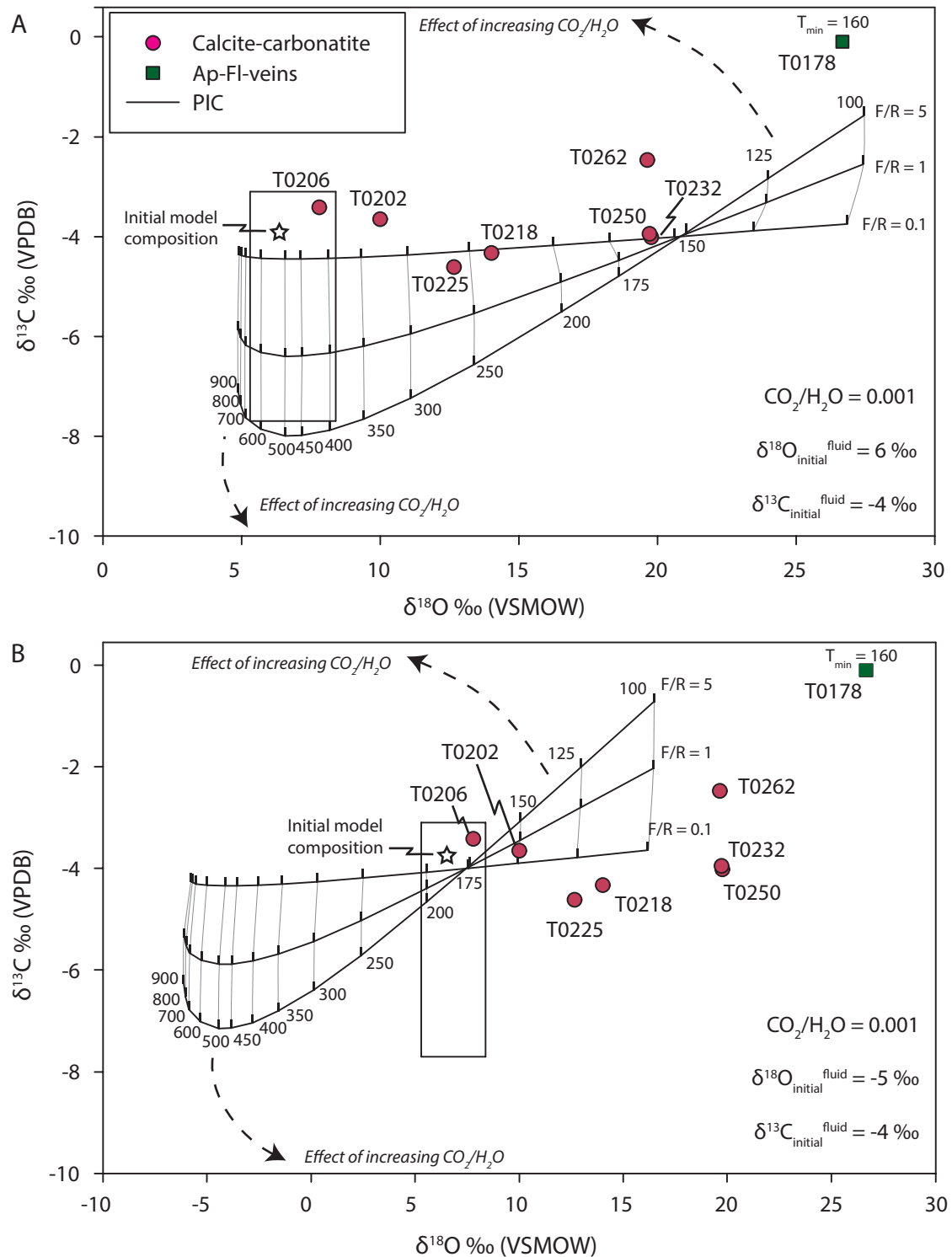


Figure 7.14: Songwe stable isotope values compared with models for fluid-rock interaction between PIC and deuteritic water (A) and meteoric water (B) after Santos and Clayton (1995); Ray and Ramesh (1999a). Models are shown for fluid/rock ratios of 0.1, 1 and 5 (effectively ∞). Temperatures are shown in $^{\circ}\text{C}$. The lowest 'cut-off' temperature of 160°C from fluid inclusion homogenisation temperature in fluorite is indicated for sample T0178. $\text{CO}_2/\text{H}_2\text{O}$ ratios are constant, at 0.001; increases in the ratio would result in lower magnitude $\delta^{18}\text{O}$ changes and steeper $\delta^{13}\text{C}$ curves, indicated by the dashed curved arrows.

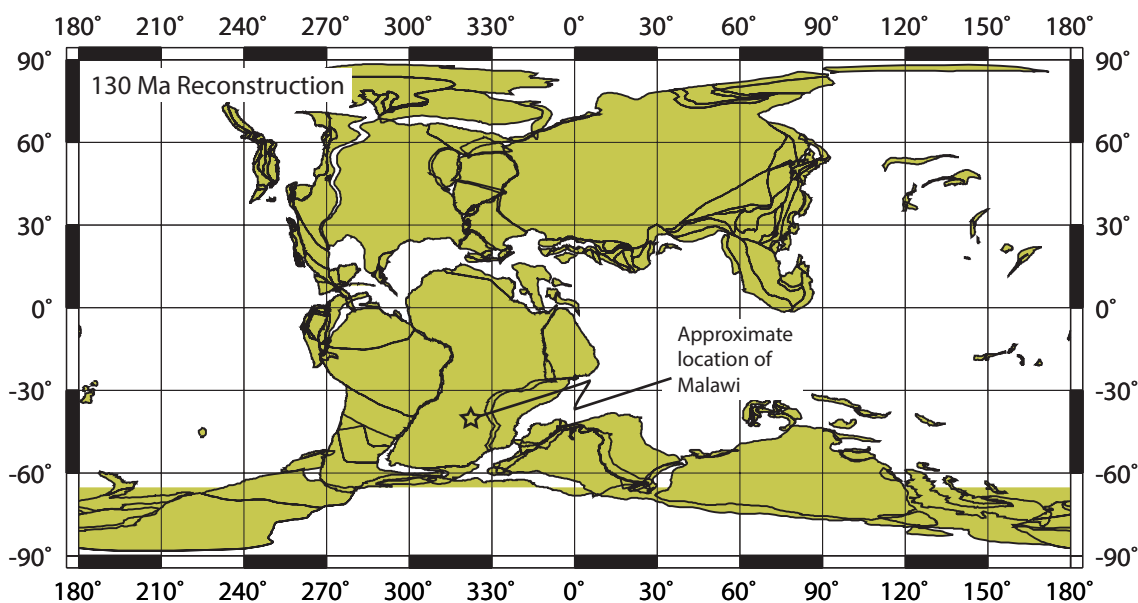


Figure 7.15: Palaeomap reconstruction of the world at 130 Ma with the approximate position of Malawi indicated. The latitude is approximately between -30° and -60° , compared to a modern latitude of 14° . Map reconstruction adapted from Ocean Drilling Stratigraphic Network (ODSN) Paleomap project (<http://www.odsn.de/odsn/services/paleomap/paleomap.html>).

(Fig. 7.16B). It is important to note, however, that these closed-system models represent only the extreme of what can occur in carbonatites (i.e. 100 % meteoric water or 100 % deuteritic water). Furthermore, they do not represent open-system processes, although these can be qualitatively assessed from interpretation of the model output (see section 7.7.8 and Figure 7.17).

It is evident from the models in Figure 7.14, that low-temperature alteration also increases $\delta^{13}\text{C}$ towards lower temperatures. This is a function of increasing carbon-isotope fractionation between the carbon in the fluid (assumed to be a dissolved species) and the precipitating carbonate mineral. At lower temperatures, and at higher C concentration in the fluid, the effect of this fractionation is much greater and thus the carbon isotope value of the final product is much greater than that of the initial model composition (-4‰ for both meteoric and deuteritic water).

Carbonate stable isotope data from Songwe broadly plots along the line of alteration from a deuteritic fluid at decreasing temperature (Fig. 7.14A). The magnitude of change in oxygen isotopes is broadly similar to that observed in the range of data from Songwe. The increasing carbon isotope values, however, cannot be explained by deuteritic alteration alone. The $\delta^{13}\text{C}$ increase could be due to earlier Rayleigh fractionation, but this would require invoking an early $\delta^{13}\text{C}$ increase and a later $\delta^{18}\text{O}$ increase (i.e. up and right on Figure 7.11, rather than right and up). This is not seen in the data. A more plausible scenario is that of an initial deuteritic fluid, with C and O isotope ratios in equilibrium with the carbonatite, which

gradually mixes with meteoric water as the temperature drops, shifting towards higher $\delta^{18}\text{O}$ values. This scenario of open-system mixing effectively combines the models of Figure 7.14A and B, and would explain the larger increase in $\delta^{18}\text{O}$ and the slight increase in $\delta^{13}\text{C}$ in T0178.

Post-emplacement alteration

The question remains, however, whether the alteration was caused by groundwater circulating in the carbonatite after emplacement, or is it caused by fluids, meteoric or deuteric, circulating in a hydrothermal system during crystallisation and cooling of the intrusion? Carbonates are very susceptible to recrystallisation, even at temperatures below 200 °C (Malone et al., 1996). Deines (1989) considered the effect of post-emplacement water as negligible as there is no correlation between $\delta^{18}\text{O}$ values in altered carbonatite with latitude. While this is true, it is possible that dissolution-reprecipitation, caused by groundwater, records an integrated climate signal, in the same manner as that of speleotherm growth. Thus, it would not be expected that altered carbonate would correlate with the current latitudinal and climatic variations in $\delta^{18}\text{O}$, but rather a bulk sample would integrate all of the variations in $\delta^{18}\text{O}$ over the last 140 Ma (e.g. a range of 0 to 6 ‰, Zachos et al., 2001; Littler et al., 2014). Field and petrographic evidence at Songwe indicates that dissolution-reprecipitation is widespread. Evidence for this includes features such as karstic weathering, including cavities in drill core and caves up to many metres wide, and ‘tiger-stripe’ weathering in carbonates caused by exsolution of Fe-oxides from the carbonate structure (Fig. 7.16). In addition, Wall (2014, *pers comm*) has measured oxygen isotopes from carbonate grains, in the nearby Kangankunde carbonatite, which are increasingly darker in colour. This increase in darkness is a function of alteration, as seen in the field at Songwe, and corresponds to increasing $\delta^{18}\text{O}$.

7.7.6 Using isotopes to track the evolution of Songwe — apatite $\delta^{18}\text{O}_{\text{PO}_4}$ analyses

One of the main advantages of analysing the O isotope ratio in apatite is that apatite is much less susceptible to dissolution-reprecipitation than calcite, and it is not susceptible to diffusion below temperatures of around 550 °C (Cole and Chakraborty, 2001). Furthermore, since the apatite is the HREE-bearing mineral, $\delta^{18}\text{O}_{\text{PO}_4}$ provides a means of directly tracing the fluid conditions at the time of HREE enrichment. It is, thus, an ideal mineral to measure the $\delta^{18}\text{O}$ of the hydrothermal fluid during crystallisation.

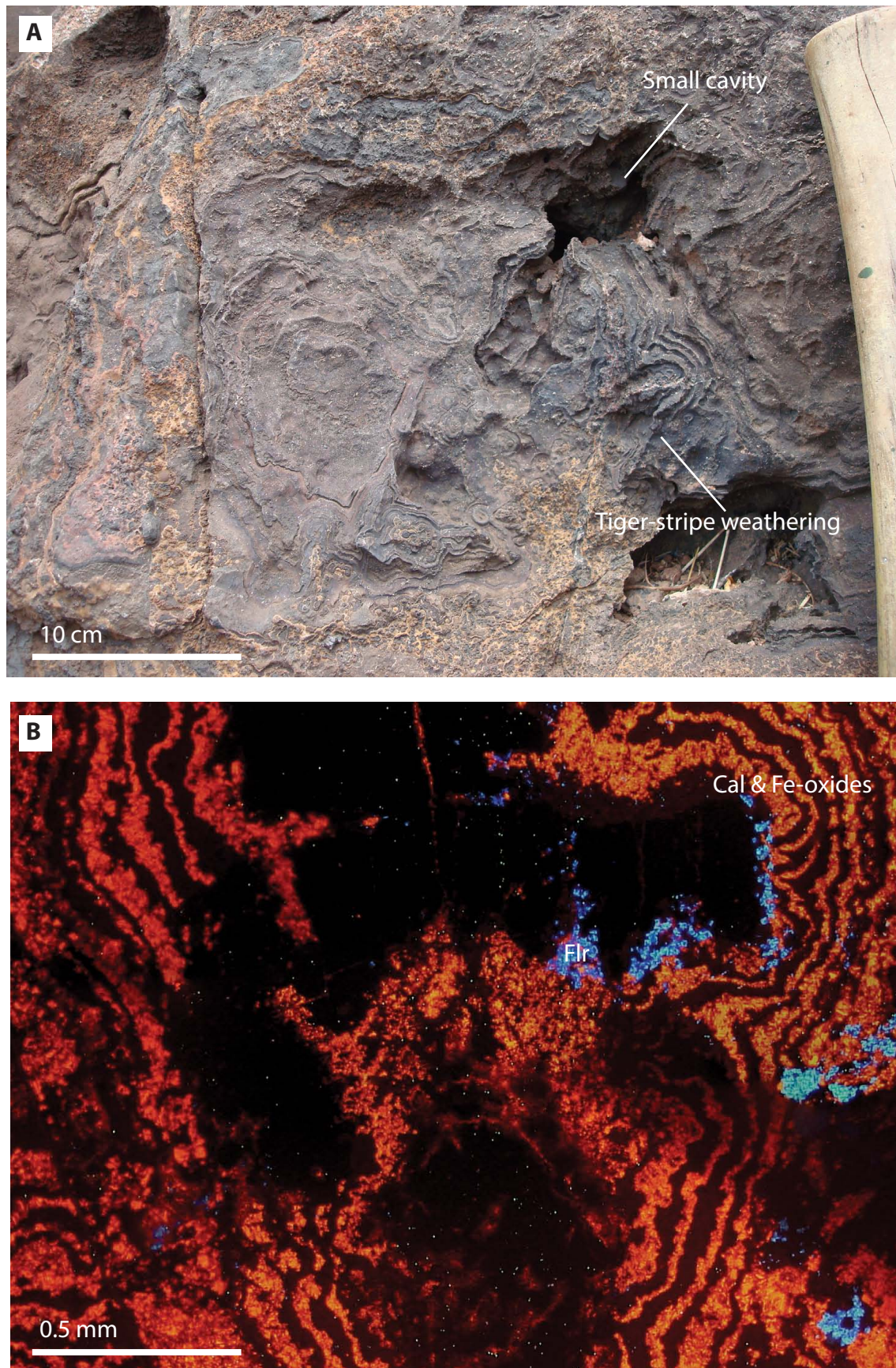


Figure 7.16: Examples of 'tiger-stripe' weathering and dissolution cavities in (A) outcrop and (B) under CL. Abbreviations: Cal = calcite, Flr = fluorite. Carbonatite photo credit: Frances Wall.

Justification of ordering $\delta^{18}\text{O}_{\text{PO}_4}$ data by paragenesis

The results for $\delta^{18}\text{O}_{\text{PO}_4}$ in Figure 7.12 are plotted in paragenetic order and this is also schematically represented in Figure 7.18. This is perhaps a subjective order in which to present the data, and samples T0202–T0262 could be rearranged depending on re-interpretation of the other minerals in the sample. Nevertheless, samples T0218, T0167 and T0178 are paragenetically well constrained as they all contain apatite which clearly belongs to a particular type: T0218 contains Ap-1/2 from early magmatic calcite-carbonatite; T0167, contains Ap-3 from Fe-rich carbonatite; and in T0178 the apatite is Ap-4, from Chenga Hill, outside the Songwe carbonatite (with each of these stages represented in Figure 7.18 as 2, 3b and 4, respectively). Sample T0206 is also predominantly Ap-1/2, similar to T0218, but the sample also contains a small percentage of Ap-3 (as shown in Figure 7.8 3a). Samples T0202–T0262 are all Ap-3 -bearing samples from calcite carbonatite. Thus, the samples in Figure 7.12 are in the order of Ap-1, 2, 3, 4.

Changing $\delta^{18}\text{O}_{\text{PO}_4}$ with paragenesis

Samples which have crystallised later at Songwe show decreasing $\delta^{18}\text{O}_{\text{PO}_4}$ (Fig. 7.12). This is in contrast to the increasing $\delta^{18}\text{O}$ from the carbonate data where later samples have higher $\delta^{18}\text{O}$ values (Fig. 7.12). It is, additionally, lower than the PIA values calculated in section 7.7.2. Very few mechanisms can be envisaged to reduce the oxygen isotope ratio of a mineral crystallising in a carbonatite. It is rarely documented, and has only been observed in rocks at the Igaliko dyke swarm (syn. Igaliku), Gardar Province, Greenland (Pearce and Leng, 1996), in rørdberg (calcite or calcite–dolomite carbonite with hematite alteration) from Fen, Norway (Andersen, 1984), and in the Arshan carbonatite, Transbaikalia, Russia (Doroshkevich et al., 2008). At these locations, the lowering of $\delta^{18}\text{O}$ has been ascribed to the role of fluorine and meteoric water, respectively. Each is briefly reviewed below:

Fluorine: at Igaliko, the low $\delta^{18}\text{O}$ values, relative to PIC, were interpreted as primary values by Pearce and Leng (1996) and Pearce et al. (1997), and fractionation of calcite led to increased $\delta^{18}\text{O}$ and $\delta^{13}\text{C}$. Fluorine is proposed as a means of suppressing $\delta^{18}\text{O}$ to lower values on the basis of a high F concentration in the lowest $\delta^{18}\text{O}$ samples, although little additional evidence is provided to support the theory (Pearce and Leng, 1996; Pearce et al., 1997). Other reviews of stable isotope data from the Gardar Province focus on the interpretation of stable isotope data with respect to the link between the carbonatites and alkaline rocks of the region; they do not consider the decrease in $\delta^{18}\text{O}$ at Igaliko in great detail, but suggest that alteration could

could be a viable way of changing $\delta^{18}\text{O}$ values in the samples (Coulson et al., 2003; Taubald et al., 2004; Halama et al., 2005).

Meteoric water: at the Fen carbonatite, Norway, post-magmatic hydrothermal oxidation by meteoric water is proposed as the mechanism for lowering the $\delta^{18}\text{O}$ of ferrocarnatite, forming rødbeg (haematite-carbonatite; Andersen, 1984). Here $\delta^{18}\text{O}$ is lowered by 2 ‰ in the rødbeg, relative to the ferrocarnatite, at an estimated temperature of 250–300 °C. This reduction is calculated to have been caused by a fluid with a maximum $\delta^{18}\text{O}$ of approximately 0.84 ‰, a composition only considered to be reconcilable with meteoric water. At the Arshan Carbonatite, calcite, bastnäsité-(Ce), allanite-(Ce) and phlogopite were analysed for O and $\pm\text{C}$ isotopes (Doroshkevich et al., 2008). Bastnäsité-(Ce) was considered a magmatic mineral, as its carbon and oxygen isotope ratios plot within the PIC field. Calcite is texturally recrystallised, and this is reflected in its $\delta^{18}\text{O}$ values, which lay between -4 ‰ and -7.2 ‰. Isotope data from altered bastnäsité-(Ce) (altered to parisite-(Ce) and allanite-(Ce)), allanite-(Ce) and phlogopite form a continuum between the PIC field and the calcite data. Doroshkevich et al. (2008) estimate that the composition of the altering fluid would have been between -10 to -15 ‰ and, from fluid inclusion data, at a temperature of 345–397 °C.

Implications for Songwe

Although fluorine is a major element in fluorapatite, suggesting that fluorine is present in the system in major quantities, it is possible that the relationship between decreasing $\delta^{18}\text{O}$ and F could just be a coincidence. It has not been considered in other reviews of stable isotope processes in carbonatites (e.g. Santos and Clayton, 1995; Horstmann and Verwoerd, 1997; Demény et al., 2004a; Ray and Ramesh, 2006) and is thus not considered further here. The simplest interpretation is that meteoric water caused the lowering of $\delta^{18}\text{O}$ in the apatite. As apatite is not susceptible to low temperature dissolution-reprecipitation processes, it is not likely that this change in isotope composition was caused by post-emplacement meteoric fluid at ambient temperature. To aid in the interpretation of the apatite isotope data, the models derived for isotope variations in carbonates can be used as a guide (Fig. 7.14). These models indicate that to shift the isotope values to lower temperatures, it is necessary for the apatite to be in equilibrium with meteoric water ($\delta^{18}\text{O}$ in the models of -5 ‰) at temperatures above 200 °C. Clearly, meteoric water with a lower $\delta^{18}\text{O}$ value will reduce the $\delta^{18}\text{O}$ of the apatite at lower temperatures. However, as a 'first-order' interpretation, these data give a good indication that the simplest cause of the mineralisation is a high-temperature (greater than 200 °C) meteoric fluid.

Figure 7.12 shows that during the paragenetic sequence shown, the $\delta^{18}\text{O}_{\text{PO}_4}$ values decrease. If the composition of the fluid remains the same during this sequence then the only explanation, using the models from Figure 7.14B as a basis for interpretation, would be increasing temperature. Clearly this is not realistic as temperature is highly unlikely to increase during carbonatite evolution. A more likely interpretation is that the decreasing $\delta^{18}\text{O}_{\text{PO}_4}$ is due to an increasing proportion of meteoric water in the fluid towards the late stages of crystallisation, in a similar manner to the interpretation of the carbonate data. This requires *open-system* evolution of carbonatites, incorporating more meteoric water as they cool.

7.7.7 Compositional estimates for mineralising water

It is possible to calculate the isotopic composition of water which led to crystallisation of HREE-enriched apatite by combining the fluid inclusion and isotope data (see section 7.1.1 for review and chapter 6 for fluid inclusion data).

Sufficiently reliable homogenisation temperatures in apatite were only obtained from samples from Fe-rich carbonatite (T0167) and from apatite-fluorite veins from Chenga (T0178). The isotopic composition of water in equilibrium with apatite at these temperatures is calculated using the equilibrium fractionation equations for apatite-water from Zheng (1996). The isotopic values for T0167 and T0178, at 200 and 160 °C, are -4 ‰ and -7.8 ‰ respectively indicating that later in the paragenetic sequence the role of meteoric water is increased.

Where no fluid inclusion data are available, the temperature of crystallisation can be reasonably assumed. For samples T0206 and T0218, the apatite habit is indicative of PIA, thus, assuming the apatite has been affected by isotopic resetting, then the minimum temperature of resetting is 550 °C (Cole and Chakraborty, 2001). The equilibrium fractionation at these temperatures would result in an isotopic composition of water of 2.6 ‰ and 2.9 ‰ respectively. This is clearly lower than the value for PIA, and is probably due to the influence of Ap-2 in these samples which overprints Ap-1, which is considered as a primary magmatic apatite.

7.7.8 Reconciling calcite $\delta^{18}\text{O}$ and apatite $\delta^{18}\text{O}_{\text{PO}_4}$ data

The diverging trends of $\delta^{18}\text{O}_{\text{PO}_4}$ in apatite (which decreases with progressing paragenesis) and $\delta^{18}\text{O}$ in calcite (which increases with paragenesis) reported from this work are unusual as it has not been previously reported (Fig. 7.12). This trend cannot be accounted for simply through equilibrium fractionation between the two minerals at different temperatures. This is because, even if temperatures close to the freezing point of water are responsible for fractionation (a scenario which is most unlikely), the fractionation factor between apatite and calcite is still below 10 ‰. Fractionation at temperatures higher than this result in a smaller fractiona-

tion factor (Fig. 7.1). Thus, offsets in $\delta^{18}\text{O}$ of approximately 25 ‰ between calcite and apatite in observed in T0178 cannot be produced by equilibrium fractionation and, thus, are not in equilibrium. The disequilibrium between the two phases is further supported by the ambiguous textural relationship between apatite and calcite, where calcite appears to form both before, during, and after apatite crystallisation (e.g. Fig. 7.7).

A meteoric mixing model, in an open-system, has already been discussed for both the data from the apatite and the calcite. Both models envisage a cooling hydrothermal system, which progressively incorporates more meteoric water. In the case of the apatite, the isotopic compositional change requires both cooling of a fluid from a high temperature and further incorporation of meteoric water, while for calcite, the model requires the same, but at cooler temperatures. Given the limited available data, it is difficult to quantitatively reconcile these divergent trends. However, it is possible to show, conceptually, that a cooling fluid, incorporating an increasing proportion of meteoric water can first, at high temperatures, shift the isotopic composition of the products to the lighter (lower $\delta^{18}\text{O}$) isotope values, before, at lower temperature, trending towards higher $\delta^{18}\text{O}$ (Fig. 7.17). Clearly, the model presented in Figure 7.17 is based on many assumptions and should only be used as a rough guide. The most critical assumption, for which few constraining factors are available, is the rate at which meteoric water and deuteritic water mix, and the relationship of this with temperature. In the model presented in Figure 7.17, a linear relationship between temperature and concentration of meteoric water has been selected for simplicity. This relationship is shown below:

$$\%_{\text{Meteoric-water}} = -0.2T + 100 \quad (7.11)$$

While it is logical to assume that over time, and thus with decreasing temperature, the percentage of meteoric water in a carbonatite system will increase, there is no special justification for a linear relationship between these two factors. Perhaps more likely, given the high degree of brecciation at Songwe-Hill, is that of a sudden influx of meteoric water, and a rapid decrease in temperature — akin to a depressurisation event. This is, however, conceptually difficult to model as it requires a judgement of when (at what temperature) to place the influx of meteoric water. Thus, a simple linear relationship has been retained until this can be better constrained. Other assumptions in the model include treating the composition of the fluid (r) and the fluid/rock ratio (F_c/R_c) as constant. Of course, if meteoric water was mixing with magmatic water, the concentration of CO_2 in the water would decrease, and the degree of alteration would progressively increase. Both of these variables were kept constant in the conceptual model to show only the effects of temperature and isotopic composition.

Despite the assumptions made in the models, they clearly show a common

trend when mixing meteoric and deuteritic water. This trend suggests that open-system mixing between meteoric and deuteritic water may cause the observed divergent isotope data in the different minerals.

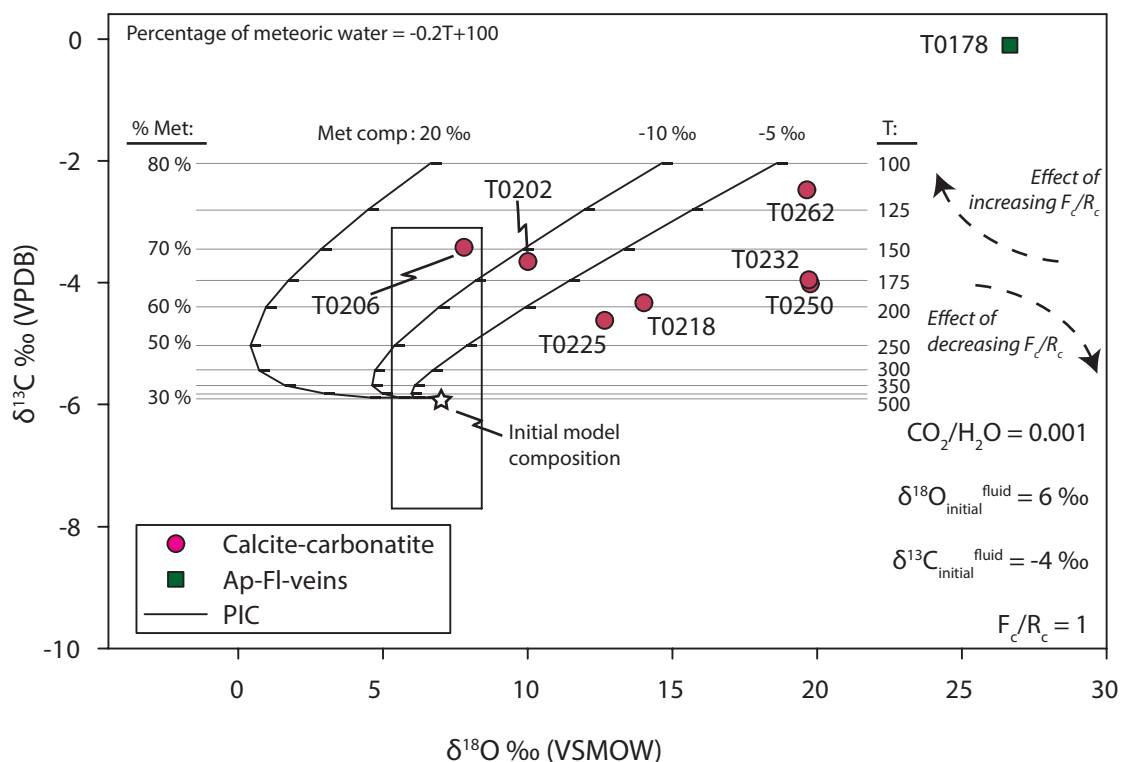


Figure 7.17: Conceptual model of mixing between meteoric water and deuteritic water to show that a deuteritic fluid, progressively mixing with meteoric water as it cools, can first decrease in $\delta^{18}\text{O}$, before increasing. The model is based on fluid-alteration models after Santos and Clayton (1995) and Ray and Ramesh (1999b), but incorporates a linear relationship between the temperature of the fluid, and the composition of the fluid, such that $\%_{\text{MeteoricFluid}} = -0.2T + 100$.

7.7.9 A model for the mineralising fluid

Using the new isotope data, a model for the transport and deposition of the HREE can be proposed (Figures 7.18 and 7.19).

Using the data for PIA from the other worldwide carbonatites, a value for PIA at Songwe can be estimated. This is likely to be somewhere between 4–6 ‰ for O, and would be in equilibrium with calcite. Apatite in this stage is LREE-enriched, typical of magmatic apatite (Fig. 7.18 - 1).

It is difficult to determine the isotopic composition of the fluid which Ap-2 formed under as all of the isotope data for Ap-2 is a mix of Ap-1 and Ap-2. If Ap-1 is between 4–6 ‰, then Ap-2 must have $\delta^{18}\text{O}_{\text{PO}_4}$ values greater than 2.5 to balance the proportion of Ap-1 with higher $\delta^{18}\text{O}_{\text{PO}_4}$ in these samples. This is, however, speculation. It is possible that Ap-1 may not preserve the isotopic conditions from magmatic temperatures (above 550 °C) because of isotopic diffusion

from the fluids which caused crystallisation of Ap-2. Thus all apatite from these samples could have the same isotopic value. This cannot be resolved with the current dataset and would require data from a spatially-resolved stable isotope technique, either microdrilling or ion-probe. Nevertheless, the data for combined Ap-1 and Ap-2 are clearly lower than might be expected from PIA, and this is interpreted as an indication of the first effects of an influx of meteoric water (Fig. 7.18 - 2).

Apatite types Ap-1 and Ap-2 are only found in clasts of calcite-carbonatite, which indicates that brecciation took place after the formation of these apatite types. Brecciation could have been caused by depressurisation of CO₂ from a dissolved fluid, or overpressure of a fluid trapped in the carbonatite. Either way, after the brecciation, hydrothermal calcite carbonatite containing Ap-3 is widespread. In a few relict samples, it can be found in association with Ap-1 and 2, (e.g. Fig. 7.18 - 3a), but typically it forms large anhedral masses (e.g. Fig. 7.18 - 3b). After brecciation it would be much easier for meteoric fluids to interact with the carbonatite, and it is likely that a convection cell was established relatively soon after brecciation occurred (Fig. 7.19). In this system, it is envisaged that the HREE-bearing fluid is a predominantly deuteritic fluid, with an initial O isotope ratio of approximately 5–10 ‰. This fluid transports the REE, preferentially carrying the LREE, away from the carbonatite. As the convection cell becomes increasingly diluted with meteoric water, the salinity, temperature and O-isotope ratio of the fluid decreases. Apatite crystallises early, at a relatively high temperature, retaining the low $\delta^{18}\text{O}$ values of the fluid it crystallised from. The progressive drop in salinity, or falling temperature, then causes the other REE to crystallise (Fig. 7.18 - 3c). In areas where the Ca concentration is low, such as outside the main carbonatite, there is insufficient Ca to form apatite, and thus xenotime forms instead (Fig. 7.18 - 4).

As the system cools, dissolution-reprecipitation of calcite continues, causing the O-isotope ratios in the calcite to increase to values up to 27 ‰. At these lower temperatures, however, diffusion from the fluid does not affect the isotopic composition of the already-crystallised apatite, and the high-T low $\delta^{18}\text{O}$ values are preserved.

7.8 Conclusions

A new method for analysing oxygen isotopes in apatite has been presented. This method has been used, in combination with conventional O and C isotope analyses of carbonates, to measure the isotopic ratios of apatite and carbonate from several different carbonatites.

The new method of analysing O isotopes in apatite is a bulk-rock technique

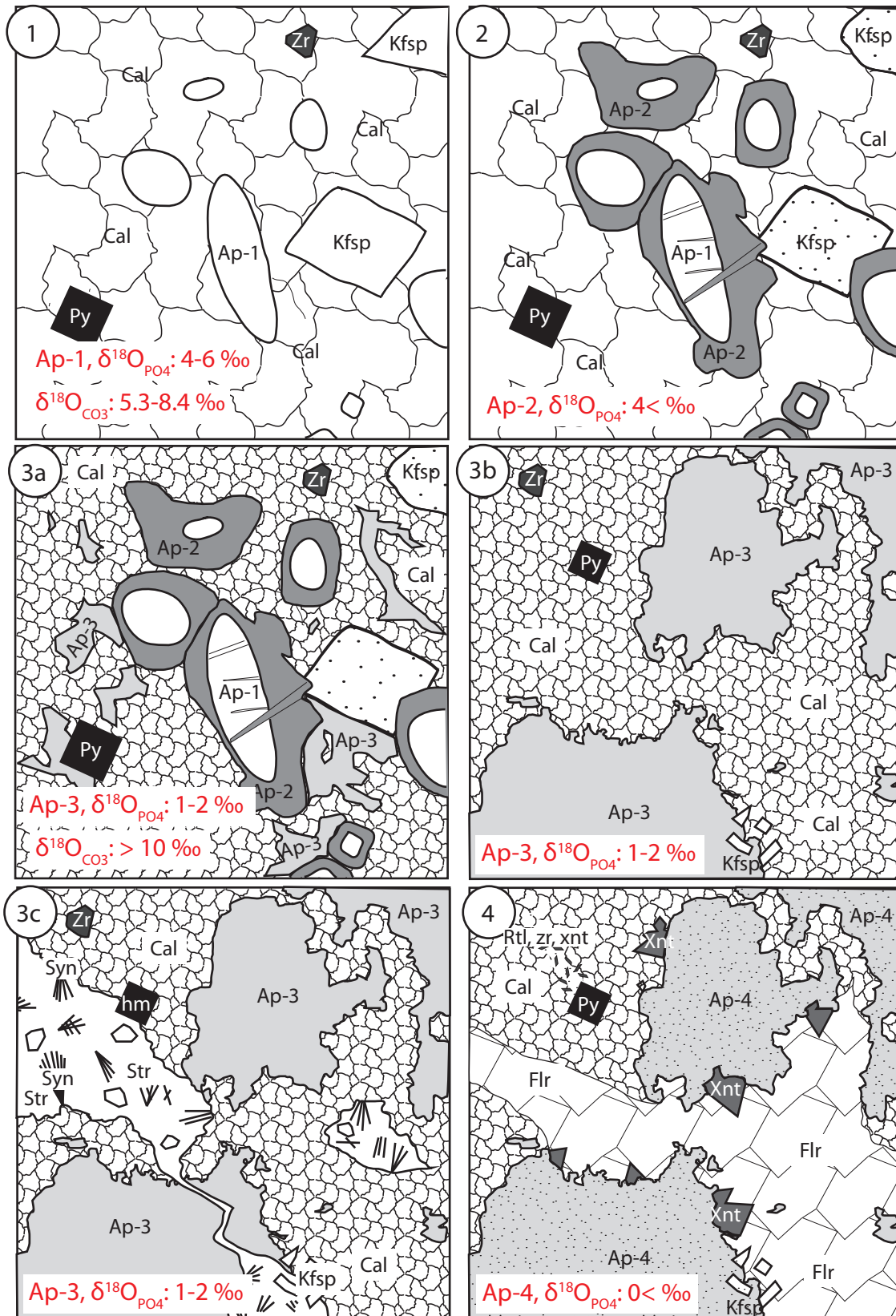


Figure 7.18: Schematic representation of each apatite type and the isotopic conditions of formation: (1) hypothetical early magmatic carbonatite, texturally and isotopically PIC; (2) calcite-carbonatite partially altered by fluids. Growth of Ap-2 and rounding of feldspars; (3a) calcite-carbonatite altered by HREE-bearing fluids. Growth of Ap-3, breakdown of zircon, carbonate recrystallisation, isotope ratios affected by hydrothermal fluids; (3b) hydrothermal calcite carbonatite with no remnant magmatic crystals. Extensive Ap-3 formation; (3c) evolution of REE-bearing fluid and formation of LREE-assemblage; (4) hydrothermal calcite-carbonatite with fluorite, xenotime and Ap-4 formation. The number on each sketch corresponds to a hypothetical location in Figure 7.19.

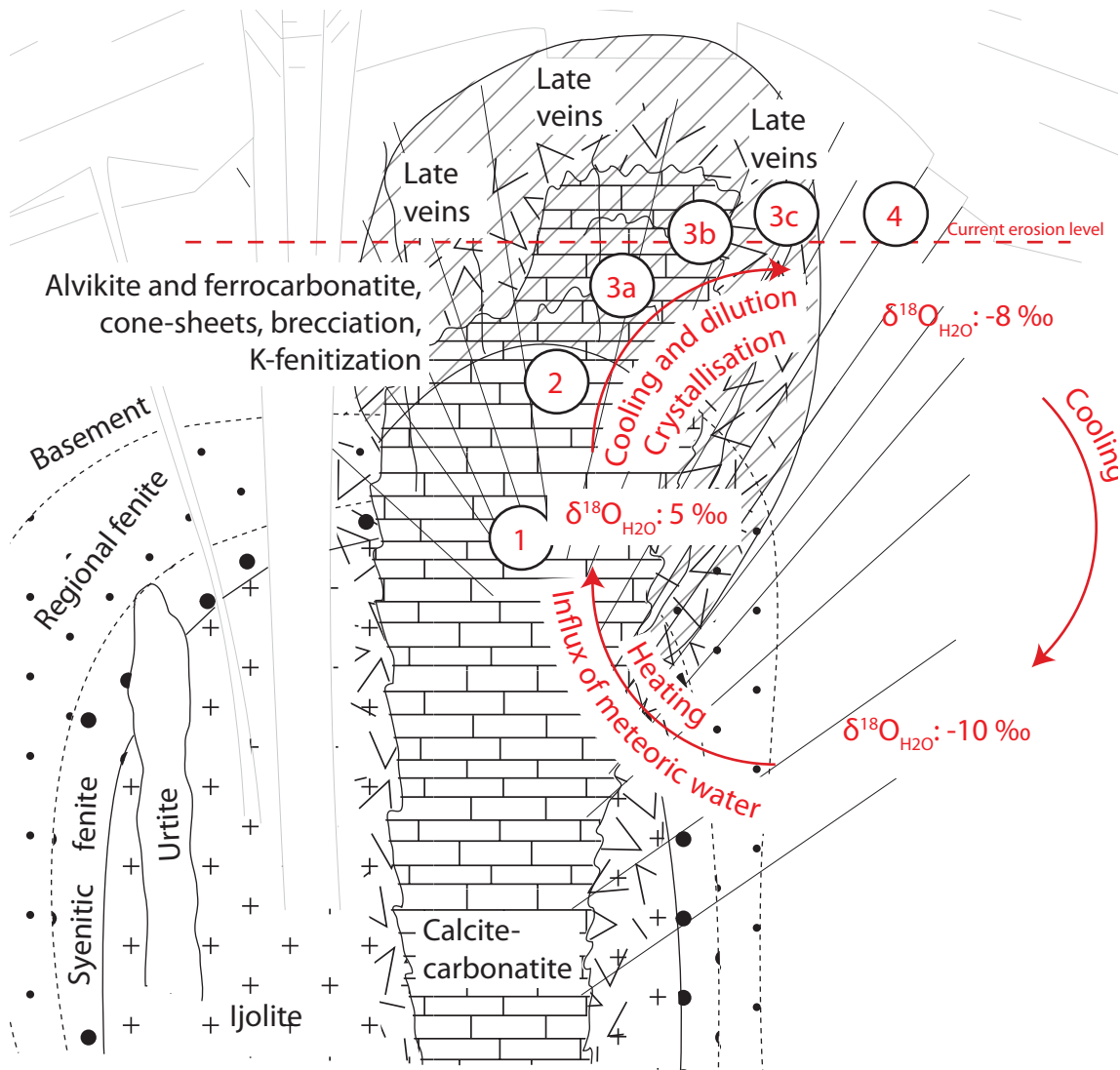


Figure 7.19: A schematic model for fluid transport around a carbonatite based on the carbonatite model after Le Bas (1987). The evolution of the carbonatite leads to excess deuteritic water (1). Deuteritic water, with an initial O isotope ratio of approximately 5–10 ‰ carries the HREE (2). This water interacts with surrounding meteoric water, with a lower salinity, temperature and O isotope ratio. As the solutions mix, the HREE-bearing deuteritic fluid is diluted, the isotopic ratio of the water decreases and the temperature drops. As the mixing takes place, The decreasing temperature, salinity or both cause the HREE to precipitate out of solution and substitute into crystallising apatite (3a, 3b). The cycle continues, and as the fluid cools it re-circulates into the carbonatite, causing further dissolution and re-precipitation of calcite (4). This causes the calcite isotope ratios to increase as per the low-T alteration models of Santos and Clayton (1995) and Ray and Ramesh (1999b). Apatite, however, is not affected by this dissolution-reprecipitation and records the isotopic conditions under which the HREE were originally formed. Numbers also refer to sketches in Figure 7.18.

where only the oxygen from the more stable PO_4 site is analysed. The phosphate is extracted through a series of wet chemical steps, and is prepared as AgPO_3 . Oxygen is liberated through thermal decomposition, and the isotope ratios are measured in a continuous flow mass spectrometer. To check the data validity of this new bulk-powder technique, 5 carbonatite samples were prepared as hand-picked apatite separates and prepared in the same way as the bulk powder samples. The results showed no significant difference, each falling within 2 standard deviations of each other.

When interpreting O isotope data from carbonatites it is common to evaluate the data relative to a PIC¹³ range. Since no data exists for apatite from PIC, a range for PIA¹⁴ has been calculated and tested by analysing 4 apatite samples from carbonatites which are considered primary in the literature. The preliminary range determined for PIA is 3.6 – 6.7 ‰. Further analyses are ongoing to ratify this value.

Ten samples from the Songwe Hill carbonatite were isotopically analysed, with 9 apatite analyses and 8 carbonate analyses carried out in total. Results from the C and O isotope analyses of carbonates show a general trend, from early to late in the paragenetic sequence, towards higher $\delta^{18}\text{O}$ values, with a slight increase in $\delta^{13}\text{C}$. Oxygen isotope ratios from apatite show a contrary trend, with values decreasing from a PIA field towards more negative values. The large increases in $\delta^{18}\text{O}$ in the carbonate results are interpreted as the result of low temperature fluid interaction, derived from either a meteoric or deuteritic source. Although modelling shows that both fluid sources are possible, it is most likely that the changes in calcite stable isotope ratios are caused by a contribution from each reservoir. The decreases in $\delta^{18}\text{O}_{\text{PO}_4}$ in the apatite are interpreted as being due to a preserved record of higher temperature interaction with meteoric water. This interaction has been preserved due to the high closure temperature of diffusion in apatite, as well as a greatly reduced susceptibility to dissolution-reprecipitation. The diverging trends are conceptually reconciled with a simple mixing model between deuteritic and meteoric water.

Based on the isotope data, a model is proposed where a convection cell develops from a carbonatite, interacting with the surrounding meteoric water in the country rock. Such a model has been proposed before, but the new isotopic data from apatite shows that meteoric water reaches high temperatures (possibly up to 300 °C). It is proposed that the REE are transported in the fluids of this convection cell and are precipitated either as salinity drops through further mixing with meteoric water, as temperature decreases, or a combination of both.

¹³Primary Igneous Carbonatite'

¹⁴primary igneous apatite

Chapter 8

New U-Pb ages of Songwe and Mauze

In the following chapter new U-Pb zircon ages for Songwe Hill and Mauze are presented. These data were acquired to understand the following:

1. What is the age of the Songwe carbonatite?
2. What is the temporal relationship between Songwe and Mauze?
3. Could Mauze provide a heat source for REE mineralisation at Songwe?
4. How does the Songwe carbonatite relate to other carbonatites and alkaline intrusions in the CAP¹?

8.1 Introduction

The age of the CAP is currently constrained by K-Ar ages acquired in the 1960s and by some subsequent K-Ar and titanite FT² ages (Eby et al., 1995). These data have relatively high uncertainties and are mostly confined to intrusions in the north of the CAP. Given that neither Songwe or Mauze have previously been dated, and relatively large zircons have been found in both, it was decided that new age data would be acquired from each intrusion. These data can be used to understand the temporal relationship between Songwe and Mauze, and with the other intrusions of the province.

Defining the temporal relationship between Songwe and Mauze is important for elucidating the genetic relationship between carbonatite and associated silicate rocks, and for understanding the processes of HREE mineralisation at Songwe. In the preceding chapters, a hydrothermal model has been favoured

¹Chilwa Alkaline Province

²fission-track

to explain the REE mineralisation, and the preponderance of hydrothermal apatite compared to ovoid magmatic apatite. However, the question remains: what is the driver of this hydrothermal mineralisation, and why is it extensively found at Songwe and not in other intrusions of the CAP? The new age data are used to test the hypothesis that Mauze could provide a source of heat for hydrothermal mineralisation at Songwe. Songwe is distinct in the CAP for having a large nepheline-syenite intrusion in close proximity while the other carbonatites in the CAP have only small, or no, associated silicate intrusions. If Mauze and Songwe were intruded at approximately the same time, then it is likely, given the size of the Mauze intrusion, that Mauze provided a greater source of heat than the relatively small (and cool) intrusion at Songwe.

8.2 Methodology

In-situ laser-ablation U-Pb dating of zircon was carried out over three separate sessions at NIGL³ (BGS⁵), in collaboration with Matt Horstwood. The following methodology is an adaptation of a version written by Matt Horstwood from Thomas et al. (2010).

Ablation was conducted using a New Wave Research UP193SS (193nm), Nd:YAG laser ablation system and a large volume cell designed to contain 6 standard-sized polished thin sections. Zircons were ablated in-situ and were imaged using cold-CL⁶ and BSE⁷ imagery (using both the Jeol JSM-5400LV SEM⁸, and the Jeol JX1 8200 EPMA⁹) at CSM¹⁰ (see section 4.2.3 for methods used). Ablated sample material was transported from the laser cell into a Nu Instruments 'HR Nu Plasma' MC-ICP-MS¹¹ using a continuous flow of 500 ml/min of He gas. Operational parameters of the laser are detailed in Table 8.1.

Data were collected using static mode acquiring ²⁰⁷Pb, ²⁰⁶Pb and ²⁰⁴Pb and Hg in IC¹² detectors. Instrumental parameters are detailed in Table 8.1. The MC-ICP-MS was tuned at the start of each analytical session whilst aspirating a 500 ppt solution of TI-²³⁵U introduced via a Nu Instruments DSN-100 de-solvating nebuliser using an ESI PFA-50 nebuliser. IC-Faraday gains were determined for each of the three ICs using a weaker 100 ppt TI-²³⁵U solution, jumping the ²⁰⁵Tl peak through each IC and comparing the equivalent Faraday signal. IC gains

³NERC⁴ Isotope Geosciences Laboratory

⁵British Geological Survey

⁶cathodoluminescence

⁷back-scattered electron

⁸scanning electron microscope

⁹electron probe micro-analyser

¹⁰Camborne School of Mines

¹¹multi-collector inductively coupled plasma mass spectrometer

¹²ion-counter

were of the order of 73, 87 and 89 % for IC0, IC1 and IC2 respectively. Repeat measurement of the gains showed that these values were reproducible to within $\ll 0.5$ % (2 standard deviations) over an approximate 8 hour operating period.

Data were acquired using the Nu Instruments time resolved analysis software. An instrument zero and on-peak zero were measured at the start of each run, each for a total of 30 seconds. After completion of the baselines, the laser was fired and sample data were acquired for approximately 40 seconds per ablation for a run of 10-15 ablations. During the course of each acquisition the TI- ^{235}U solution was co-aspirated to allow for the measurement and correction of instrument induced mass bias and plasma induced elemental fractionation. ^{202}Hg was measured simultaneously, and used to correct for the isobaric interference of ^{204}Hg on the ^{204}Pb peak, (assuming $^{204}\text{Hg}/^{202}\text{Hg} = 0.229887$).

Sampling initially employed a 20 μm static spot, but the Pb concentration was too low at these volumes. Subsequent laser sampling employed a 35 μm static spot with a fluence of approximately 2.2 $\text{J}\cdot\text{cm}^{-2}$. Typical ablation pit depths for fluence of this magnitude are of the order of 16 μm as measured previously using an SEM.

The internationally recognised 91500 zircon (Wiedenbeck et al., 1995) was used as a matrix matched reference material and analysed at regular intervals throughout each session. GJ-1 (Jackson et al., 2004) and Mud Tank (Black and Gulson, 1978; Jackson et al., 2004) zircons were variously used as appropriate secondary reference materials in order to validate the data for each day. Data were normalised according to the deviation of the average daily $^{207}\text{Pb}/^{206}\text{Pb}$ and $^{206}\text{Pb}/^{238}\text{U}$ values obtained for 91500. In the case of the latter, this is to correct for elemental fractionation in the plasma (during dynamic ablation) and/or within-run (during static ablation), whilst the former corrects for any drift or offset from the gain value recorded previously for the ion-counters. Uncertainties for each ratio are propagated relative to the respective reproducibility of the standard, to take into account the errors associated with the normalisation process and additionally to allow for variations in reproducibility according to count rate of the less abundant ^{207}Pb peak.

All data were processed using an NIGL in-house spreadsheet calculation routine. Data recording $\ll 0.01$ mV ^{207}Pb have been rejected and those reporting $> 300\text{cps}$ ^{204}Pb in the sample after correction for the isobaric interference of ^{204}Hg have been assessed with respect to the contribution of common-Pb and rejected where required. Systematic variance and decay constant errors are propagated into all quoted ages, except where stated. Variance was assessed on repeat analyses of the zircon check-standards GJ1 and Mud-Tank (Fig. 8.1). Additional external error to the population was calculated using Isoplot (Ludwig, 2009), and the largest errors in variance (Mud Tank) were applied to the unknown data.

Table 8.1: Metadata for laser-ablation MC-ICP-MS U-Pb dating.

Laboratory & Sample Preparation	
Laboratory name	NIGL, BGS
Sample type/mineral	Carbonatite-hosted and nepheline-syenite -hosted zircons
Sample preparation	In-situ 100 µm polished thick sections
Imaging	Cold-CL, BSE
Laser ablation system	
Make, Model & type	ESI/New Wave Research UP193SS (193 nm), Nd:YAG laser
Ablation cell & volume	In-house built large-format cell, volume ca. 9 cm ³
Laser wavelength (nm)	196 nm
Pulse width (ns)	<3 ns
Fluence	3.6 J.cm ⁻² (01/15) 2.2 J.cm ⁻² (04/15)
Repetition rate	10 Hz
Ablation duration	40 s
Ablation pit depth / ablation rate	Not measured
Spot size	35 µm
Sampling mode / pattern	Static spot ablation
Carrier gas	100 % He in the cell, Ar make-up gas combined using a Y-piece 50 % along the sample transport line to the torch
Cell carrier gas flow	0.4 l/min
ICP-MS Instrument	
Make, Model & type	Nu Instruments 'HR Nu Plasma' MC-ICP-MS
Sample introduction	Ablation aerosol combined with co-aspiration of desolvated Tl- ²³⁵ U tracer
RF power	1500 W
Make-up gas flow	Sourced from Nu Instruments DSN-100 desolvating nebuliser. Nebuliser pressure is 24 psi (estimated at 0.7 l/min) Ar
Detection system	Mixed Faraday-multiple ion counting array
Masses measured	202–207, 235, 238
Integration time per peak/dwell times	200 ms for each isotope

Total integration time per output datapoint	200 ms
Sensitivity as useful yield	0.4 % U
IC Dead time	6, 9 & 7 ns IC0, IC1 & IC2 resp.

Data Processing

Gas blank	30 second on-peak zero subtracted
Calibration strategy	91500 used as primary reference material, GJ1 and Mud Tank used as secondaries/validation
Reference Material info	91500 (Wiedenbeck et al., 1995) Mudtank (Black and Gulson, 1978; Jackson et al., 2004) GJ1 $^{206}\text{Pb}/^{238}\text{U}$ 0.09781 \pm 0.06 %, $^{207}\text{Pb}/^{206}\text{Pb}$ 0.060114 \pm 0.03 % (in-house chemical-abrasion TIMS ¹³)
Data processing package used / Correction for LIEF	Nu Instruments Nu Plasma TRA software and in-house spreadsheet for data normalisation, uncertainty propagation and age calculation
Mass discrimination	TI-U tracer solution used for initial mass bias correction with $^{207}\text{Pb}/^{206}\text{Pb}$ and $^{206}\text{Pb}/^{238}\text{U}$ additionally normalised to reference material
Common-Pb correction, composition and uncertainty	No common-Pb correction applied to the data.
Uncertainty level & propagation	Ages are quoted at 2σ absolute, propagation is by quadratic addition. Reproducibility and age uncertainty of reference material and common-Pb composition uncertainty are propagated where appropriate
Quality control / Validation	Mud tank (22/1/15) — Wtd ave $^{206}\text{Pb}/^{238}\text{U}$ age = 739.1 \pm 4.8 (2σ , MSWD = 1.6) Mud tank (28/04/15) — Wtd ave $^{206}\text{Pb}/^{238}\text{U}$ age = 723 \pm 3.9 (2σ , MSWD = 2.5) Mud tank (29/04/15) — Wtd ave $^{206}\text{Pb}/^{238}\text{U}$ age = 733.6 \pm 4.7 (2σ , MSWD = 2.9) GJ-1 (22/1/15) — Wtd ave $^{206}\text{Pb}/^{238}\text{U}$ age = 598.0 \pm 2.3 (2σ , MSWD = 1.12) GJ-1 (28/04/15) — Wtd ave $^{206}\text{Pb}/^{238}\text{U}$ age = 601.6 \pm 2.1 (2σ , MSWD = 1.2)

¹³thermal ionisation mass-spectrometry

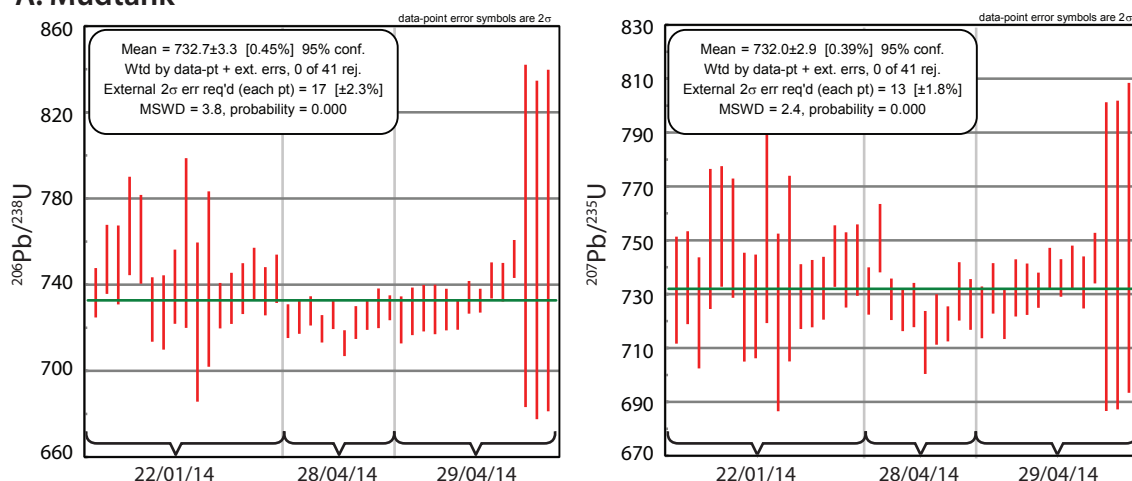
GJ-1 (29/04/15) — Wtd ave $^{206}\text{Pb}/^{238}\text{U}$ age = 604.6 ± 3.0 (2σ , MSWD = 0.62)

Systematic uncertainty for propagation is 2.3 % (2σ).

Other information

Sample line of 3 m from ablation cell to torch and a 30 second wait time between ablations. Cell washout time was ca.0.8 seconds to 1 % of peak signal

A: Mudtank



B: GJ1

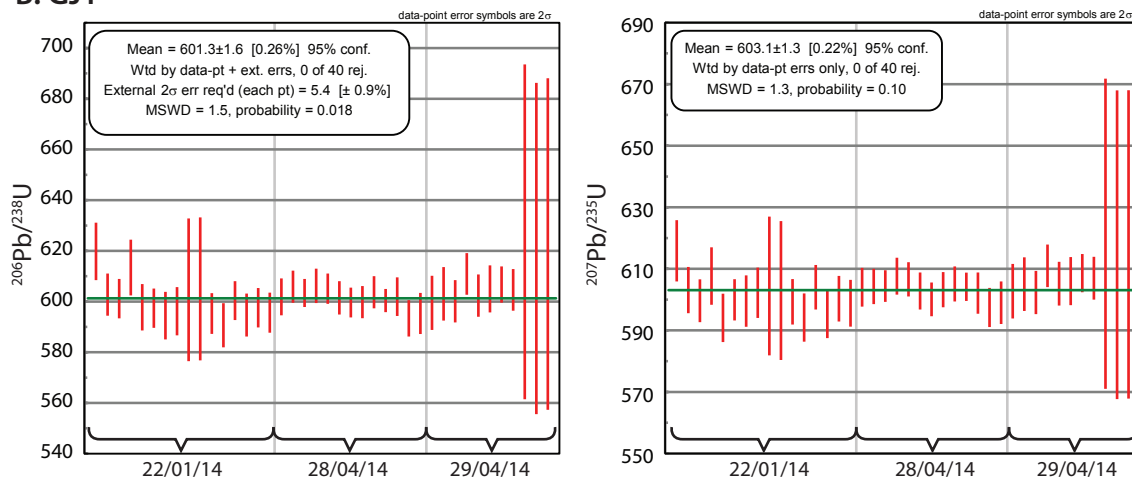


Figure 8.1: Systematic variance in the Mud Tank (A) and GJ1 (B) zircons, measured in January and April 2014.

8.3 Results

Zircon U-Pb ages were acquired from carbonatite, nepheline syenite and trachyte samples (Table. 8.2). These samples were selected to span the major intrusion events, including the emplacement of Mauze, C1 and C2 carbonatite at Songwe, and trachyte at Mantrap (appendix A).

Rock type	Sample #	# of sections	# of zircons analysed
Nepheline syenite	U4913	4	16
	U4914	1	4
Calcite carbonatite (C1)	T0206	2	26
	T0218	2	13
Alvikite carbonatite (C2)	T0225	1	5
Trachyte	T0138	1	8*

*All trachyte zircon analyses had U concentration below detection

Table 8.2: Sample selection for zircon U-Pb dating and number of analysed zircons from each sample.

8.3.1 Zircon petrography

Mauze zircons

Zircons from nepheline-syenite samples exhibited three different habits: (1) subhedral, partially eroded grains; (2) anhedral grains following fractures; and (3) corroded anhedral grains:

1. Subhedral, partially eroded grains are associated with euhedral titanite, biotite, K-feldspar, apatite and nepheline. The grains are characteristically large (up to 0.5 mm), exhibit well developed growth zoning, are often rich in inclusions, are commonly fractured and are occasionally overgrown by a Ca–Ti–Zr-rich phase (Fig. 8.2A–C). Possible sector zoning is present in some grains, and there is evidence of growth discontinuities and some recrystallisation of fractures during growth.

This zircon type is interpreted as having formed magmatically, and the different zones are representative of different Zr and other trace-element saturation in the evolving magma (Corfu et al., 2003). The grains are interpreted as being out of equilibrium with the final mineral assemblage, as indicated by the fracturing, chemical dissolution and the Ca–Ti–Zr-bearing overgrowths. Transport distance is interpreted to be low because the disaggregated zircon fragments remain proximal to other parts of the grain. The Ca–Ti–Zr-bearing overgrowths are interpreted as calzirtite ($\text{Ca}_2\text{Zr}_5\text{Ti}_2\text{O}_{16}$). Other Ca–Ti–Zr-bearing minerals, such as zirconolite ($\text{CaZrTi}_2\text{O}_7$) and zirkelite ($(\text{Ti,Ca,Zr})\text{O}_{2-x}$), were excluded due to the significantly high Zr:Ti peak ratio during qualitative EDS¹⁴ analyses. No quantitative analysis of the Ca–Ti–Zr overgrowths was undertaken and thus calzirtite is interpreted as the most likely mineral.

2. Subhedral–anhedral zircon grains are found following fractures, commonly

¹⁴electron dispersive spectroscopy

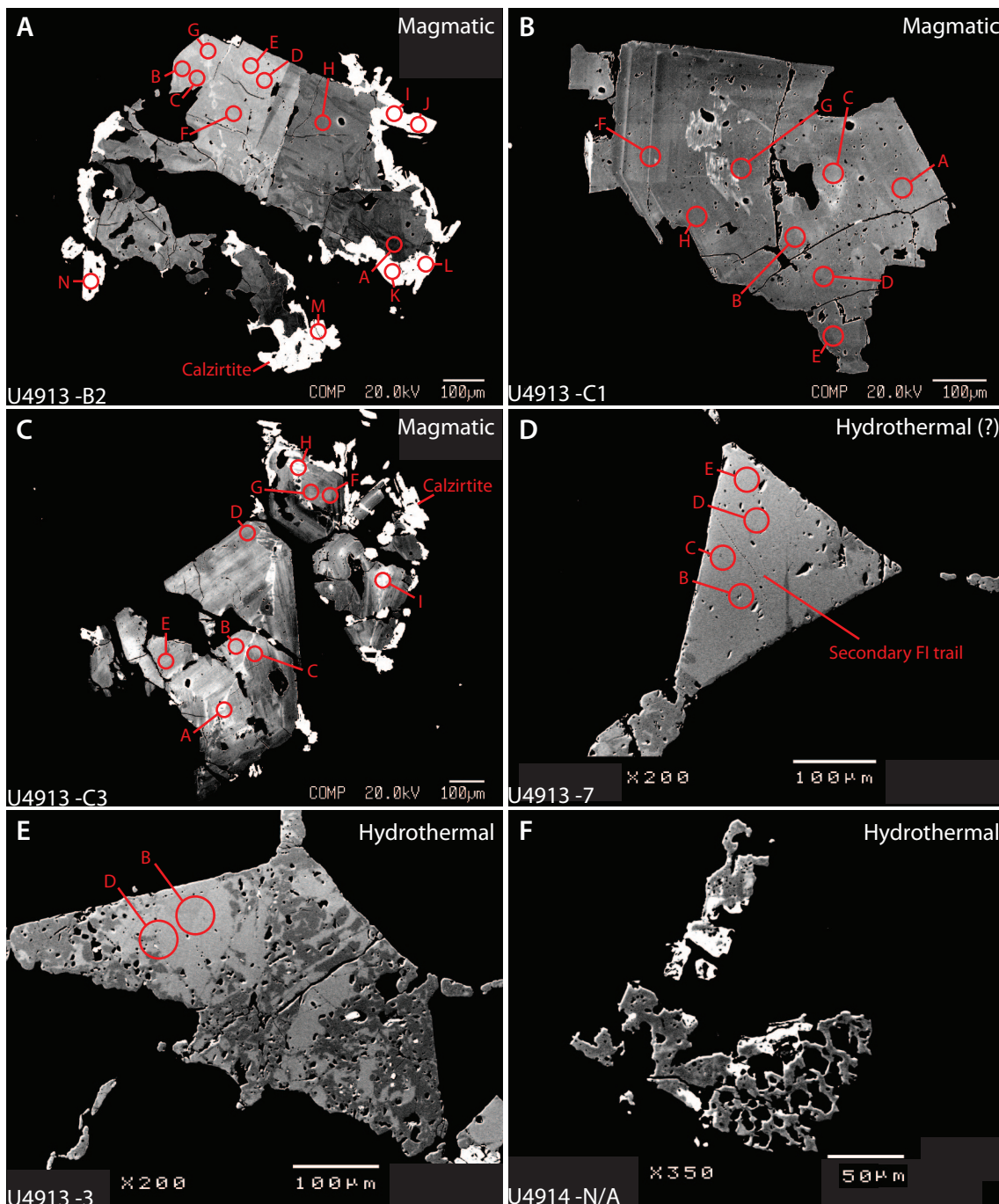


Figure 8.2: BSE images of different zircon habits found in samples from Mauze. A–C: eroded and fragmented, originally euhedral, magmatic zircons, with (A) complex zoning and (B–C) oscillatory zoning, and (A, C) calzirtite overgrowth (bright BSE). D–F: hydrothermally formed zircons, ranging from simple (D) through to complexly zoned (E–F), with varying degrees of breakdown. Circles are an approximate representation of ablation pits, and labels correspond to results in Table 8.3.

occurring in broken-down and resorbed K-feldspar megacrysts (Figs. 8.2D–E, 8.3). K-feldspar associated with these fractures luminesce blue, rather than red (Fig. 8.3B). No other phase is directly associated with this zircon type. It is typically texturally complex, with bright green CL luminescence and varied BSE intensity occurring in a speckled pattern. Small fractures are common. The grains are commonly inclusion-rich, hosting trapped mineral inclusions, vapour-rich primary inclusions and small secondary fluid inclusions. Areas of dark CL and bright BSE in these grains appear relatively unaltered (e.g. Fig. 8.2D) and are fluid inclusion poor.

Anhedral zircon grains are interpreted as having formed during transition between late-stage magma emplacement and hydrothermal fluid influx. They cross-cut all other phases in the rock and thus must have formed late. During this emplacement, Fe^{3+} CL activation in feldspars was altered to blue Ti^{4+} activation, indicating either removal of Fe, or addition of Ti, or both. The zircons, however, cannot be truly hydrothermal as hydrothermal zircons display textures similar to those found forming in magmatic conditions (Schaltegger, 2007). Rather, the areas with dark CL, bright BSE, few fluid inclusions and a subhedral habit are interpreted as forming from a late melt, while the speckled and spongy inclusion-rich zircons which display bright luminescence are interpreted to have formed from fluid-induced alteration. The principal basis for such an assumption is the abundance of inclusions in these zircons, including inclusions of Th-rich phases, and the anhedral habit. Abundant inclusions and a spongy texture are both considered reasonable evidence for inferring a hydrothermal fluid (Corfu et al., 2003; Schaltegger, 2007). Such inclusions and spongy texture are interpreted by Putnis (2009) and Soman et al. (2010) to be caused by a process of dissolution of metastable impurity-rich zircon and re-precipitation of relatively pure zircon. The associated volume change and release of structurally-bound impurities (e.g. Th, Y), results in pore-space and inclusions of Th- and Y-rich minerals. The development of pore-space allows this reaction interface to move inward through the zircon grain (Putnis, 2009; Soman et al., 2010). Superficially, the example given from Zomba (Malawi) by Putnis (2009) and Soman et al. (2010) display very similar textures to the anhedral zircon grains from Mauze. Furthermore, hydrothermal transport of zirconium and recrystallisation/reprecipitation of zircon are known to occur in alkaline igneous rocks. It is, therefore, likely that similar processes occurred at Mauze (e.g. Salvi et al., 2000; Soman et al., 2010; Kynicky et al., 2011; McCreath et al., 2012).

3. Corroded grains of anhedral zircon are found predominantly in the pegmatitic sample U4914. The zircons occur in small vugs and are not clearly

associated with any other minerals. Similarly to hydrothermal zircons, they are anhedral, texturally complex and display speckled zoning, fractures and inclusions. There is strong evidence for dissolution and all of the grains are corroded with well developed cavities (e.g. Fig. 8.2F).

These grains are interpreted as an extension of the hydrothermal zircons found at Mauze, having undergone more extreme alteration and dissolution.

These three zircon types are interpreted as a continuum, having undergone varying amounts of dissolution and breakdown. It is likely that as the intrusion evolved, it became more fluid rich. Given that the solubility of Zr increases with increasing alkaline content in the fluid (Ayers et al., 2012; Wilke et al., 2012), the stability of zircon may have decreased as the pluton evolved and fluid concentration increased.

Songwe Zircons

Zircons were found in C1, C2 and C3 carbonatite types at Songwe. Of these, only zircons from C1 and C2 were analysed, as the zircons found in the later stages of the carbonatite showed textures that were increasingly out of equilibrium, including dissolution and resorption.

By far the most abundant zircons were found in C1 carbonatite. Zircons are found in equilibrium assemblages with calcite, pyrite, pyrochlore and rounded apatite, or in partially fragmented C1 assemblages with brecciated feldspar. Zircons from C1 carbonatite are eu-subhedral, range from small (approximately 50 μm) to relatively large (up to 0.5 mm) grains (Fig. 8.4), and can exhibit well developed zoning. Zoning textures vary, with some grains exhibiting very few zones (e.g. Fig. 8.4A), while larger grains can display many stages of concentric zoning, interrupted by textural discontinuities where previous zones are resorbed. Some grains have a particularly bright core under BSE, which could be an inherited zircon (e.g. Fig. 8.4B, D, F). As the zircons from C1 carbonatite become larger, they are more commonly found as fragmented grains, with some of the grain missing. In many, the residual shape of the zircon is apparent (e.g. Fig. 8.4B–D), indicating that the transport distance of the zircon is low.

The zircons from C1 carbonatite are interpreted as a magmatic phase, forming early in the carbonatite evolution. The zoning indicates a protracted crystallisation history, and, given that the larger zircons exhibit greater amounts of zoning, it can be inferred that these record a greater amount of crystallisation than the smaller grains. The brighter cores present in some of the zircons are difficult to interpret. It is possible that they are from an earlier magmatic stage, or that they represent inherited cores of older zircons incorporated during carbonatite emplacement. Given that the bright cores show little compositional variation, it is probable, how-

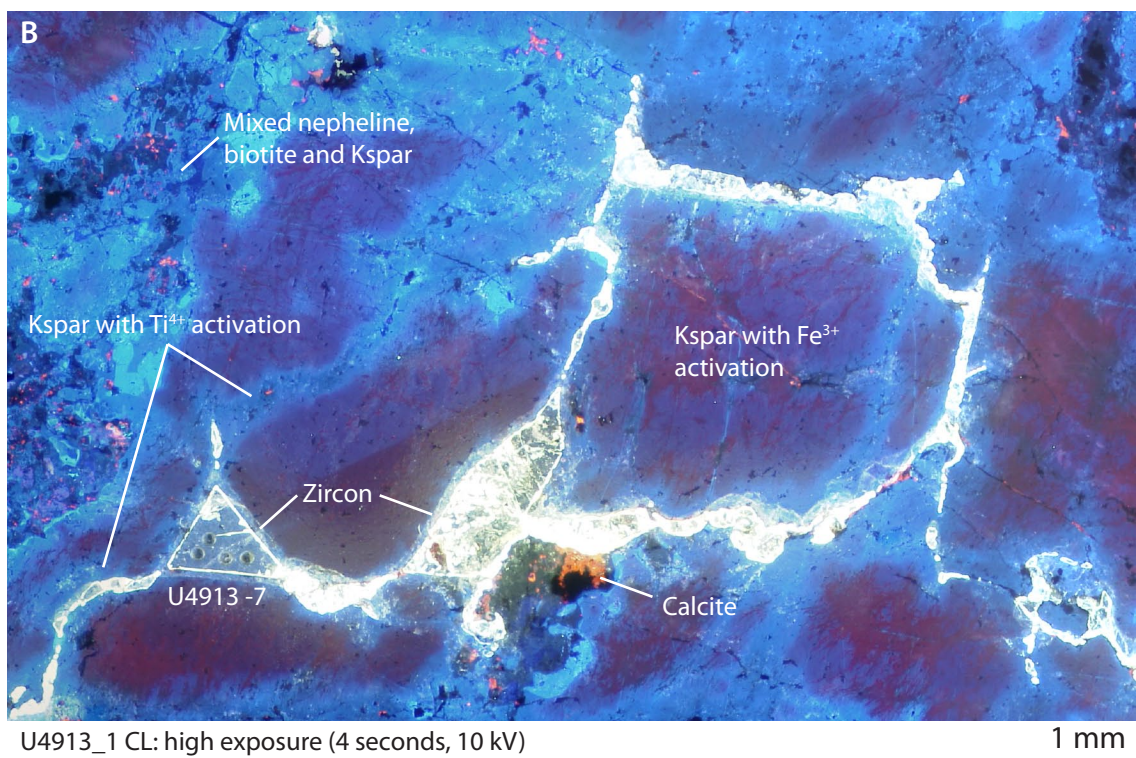
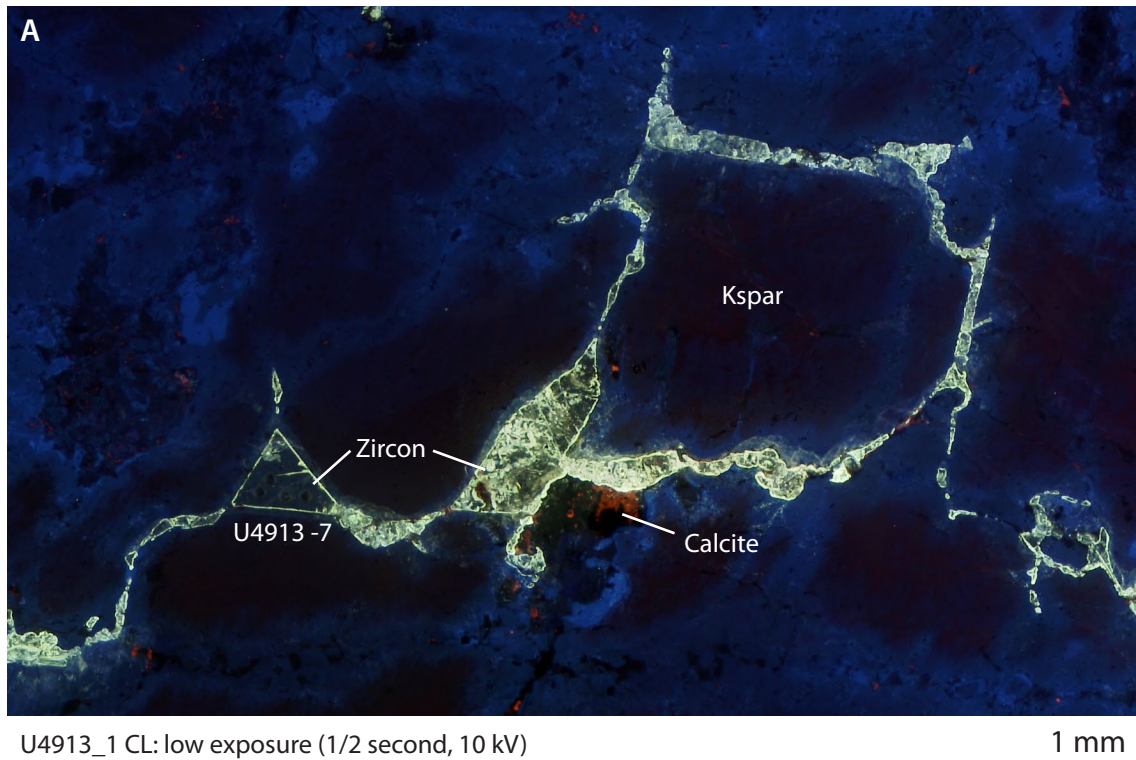


Figure 8.3: Low (A) and high (B) exposure cold-CL images of hydrothermal zircon in samples from Mauze. Zircon forms sub-anhedral grains following fractures in K-feldspar (Kspar). High-exposure images reveal the alteration to the anhedral K-feldspar phenocrysts, with red Fe^{3+} luminescence replaced/overprinted by blue Ti^{4+} activation along fractures associated with the zircon mineralisation. Zircon grain number corresponds to analysis number in Table 8.3 and Figure. 8.2.

ever, that they represent an early stage of emplacement, rather than an inherited grain. It is interesting that the larger zircons are more fragmented. This could indicate that upon a certain saturation of zirconium, various volatiles have also become saturated and are a cause of brecciation and fragmentation in the carbonatite.

Zircons from C2 and C3 are small, subhedral and appear out of equilibrium with the host rock. The edges are embayed and the cores can appear pitted and corroded. No clear zoning is apparent. They are interpreted as residual zircons from earlier magmatic stages, similar to the broken-down pyrochlore grains described in Chapter 4. They are not considered representative of the host carbonatite, rather they could be grains from earlier crystallisation products that have been carried in the ascent of the C2, and subsequent, magmas.

Trachyte Zircons

Zircons observed in samples from Mantrap (appendix A) are large (up to 0.5 mm) and often eu-subhedral. They display clear concentric zoning, but their edges are often resorbed. Xenotime overgrowths are common and appear to replace areas where zircon has been removed.

These zircons are interpreted as to have formed magmatically during trachyte evolution. However, subsequent alteration has resulted in dissolution and removal of zircon and replacement with secondary xenotime. It is possible that this was the product of alteration by a fenite fluid, related to the emplacement of Mauze (or Songwe), but the incorporated carbonatite and (nepheline?)-syenite clasts in the trachyte matrix suggests that the trachyte was emplaced last in the sequence. It is also possible that zircon breakdown and xenotime precipitation was caused by the same fluid which led to xenotime mineralisation at Mantrap.

8.3.2 U-Pb dates

U-Pb dates were successfully acquired from Mauze and Songwe samples. Unfortunately zircons from Mantrap contained insufficient U to be dated with the analytical set-up used and there was insufficient time to re-calibrate the laser-ablation system and re-tune the MC-ICP-MS to carry out another analysis. Dates from samples from Songwe and Mauze are listed in Table 8.3. These results are dominated by samples U4913 (nepheline syenite), T0206 and, to a lesser extent, T0218 (C1 carbonatite). This is because few analyses from C2 carbonatite, or from the other nepheline syenite sample (U4914), gave good results. Much of the data had high common Pb ratios, low ^{207}Pb signals, low U concentration or a combination of all three, and these were rejected.

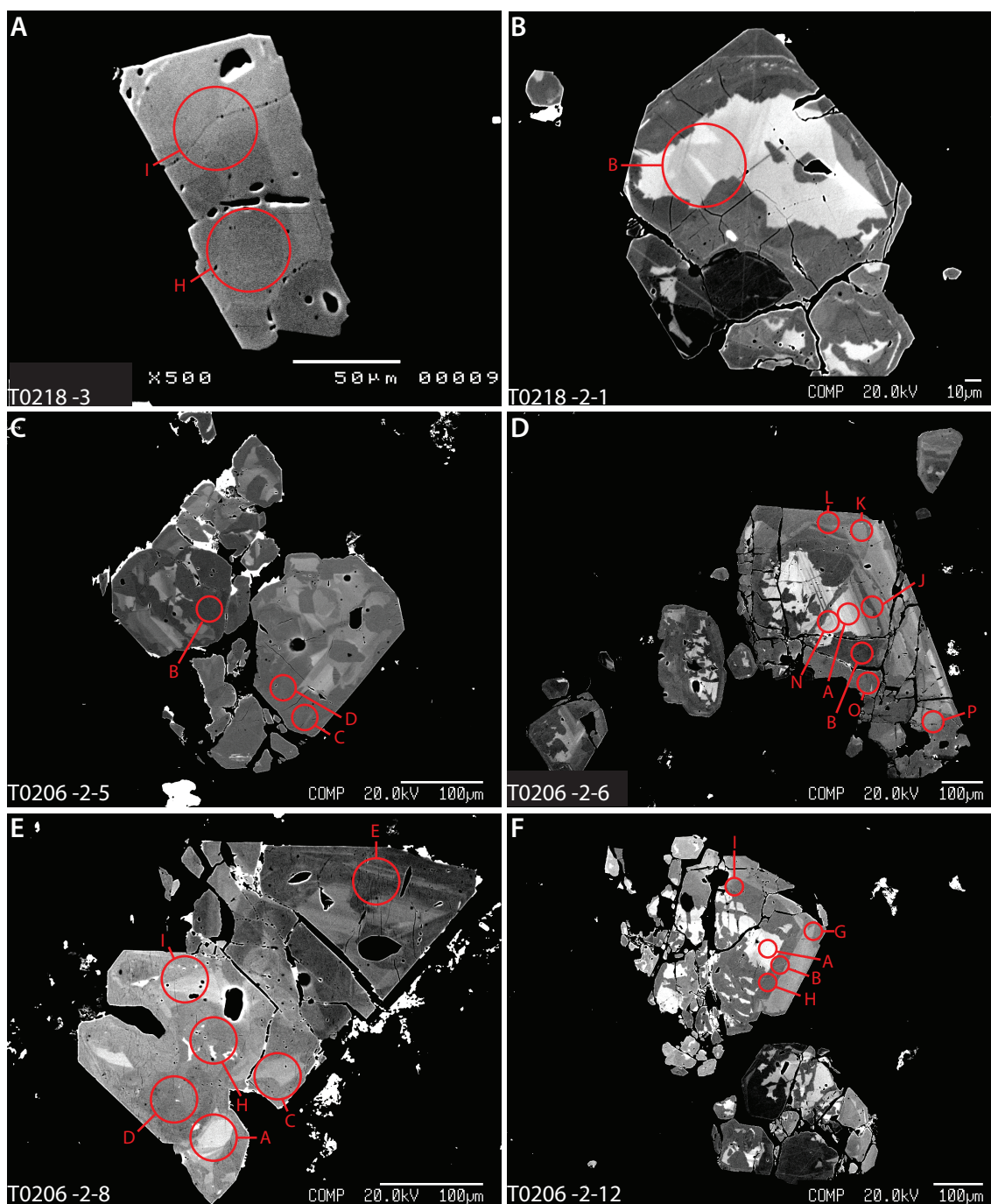


Figure 8.4: High-contrast BSE images of zircon habits found in carbonatite from Songwe. All grains are from C1 carbonatite. Habits range from subhedral (A–B) to fragmented euhedral grains (B–F). Zoning varies from minor (A–B), through to complex (C, F) and oscillatory (D–E) zoning. Zircons T0218 -2-1, T0206 -2-6 and -2-12 have distinctly brighter cores, which are possibly inherited. Of these, only T0218 -2-1B gives a date which could be interpreted as earlier (see Fig. 8.8). Circles are an approximate representation of ablation pits, and labels correspond to results in Table 8.3.

Of the data passing the threshold of acceptability, many of the data are still discordant. The degree of discordance is calculated as a function of the $^{206}\text{Pb}/^{238}\text{U}$ and $^{207}\text{Pb}/^{235}\text{U}$ ratios, such that:

$$\frac{^{206}\text{Pb}}{^{238}\text{U}} / \frac{^{207}\text{Pb}}{^{235}\text{U}} \times 100 \quad (8.1)$$

Concordance ranges from 24 % through to 108 %. Of the 52 zircons analysed from carbonatite, 12 (23 %) are within a concordance range of 95–105 %. More of the data from the nepheline syenite samples are concordant, with 27 out of 54 (50 %) data-points falling within the range of 95–105 %. Calculated dates (using terminology of Schoene et al., 2013) are not corrected for common Pb. $^{206}\text{Pb}/^{238}\text{U}$ dates range between 116–468 Ma, while $^{207}\text{Pb}/^{235}\text{U}$ dates range between 123–965 Ma. This range in dates is due to the discordance in the data, and therefore least-square regression ages of multiple zircon dates are required to interpret the age (section 8.4.1). Absolute error (2σ) for $^{207}\text{Pb}/^{206}\text{Pb}$ dates is greater than most calculated dates, and these data are not interpreted.

8.4 Discussion

8.4.1 Age interpretation

U-Pb dates are plotted in Figures 8.5, 8.6, 8.7 and 8.8. Data are plotted as Tera-Wasserberg plots, with Wetherill plots (scaled between 100–200 Ma) where discordant data points span a large range of geological time. Data point ellipses are coloured depending on the date the data were acquired. This is to help determine if differences in data are true differences, or if they are caused by analytical artefacts. All plotted data incorporate systematic error, and this is always plotted as 2σ .

Mauze age interpretation

Paragenetically, zircons analysed from Mauze can be split into three types (section 8.3.1). However, only types 1 (partially eroded magmatic) and 2 (late-stage hydrothermal) are discussed here because no good analyses were acquired from type 3. It is clear that type-2, late-stage hydrothermal, zircons must have crystallised *after* the partially eroded magmatic zircons.

Analyses of zircons from Mauze were carried out on 22/01/14 and 29/04/14. Analyses on the 22/01/14 included *only* hydrothermal zircons, while those analysed on 29/04/14 included *only* broken-down magmatic zircons. No data from different zircon types were collected from the same analytical run.

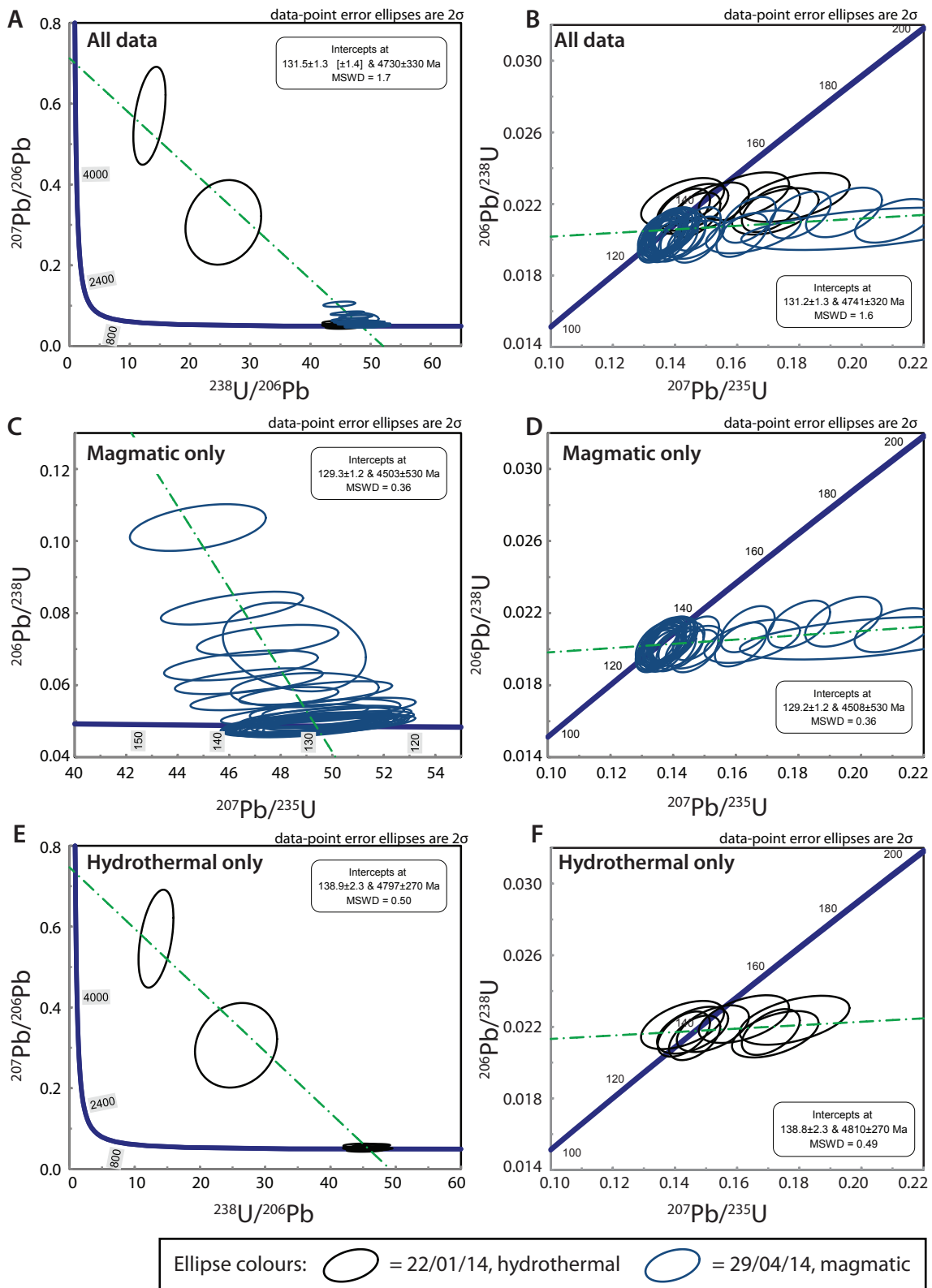


Figure 8.5: Tera-Wasserburg (A, C, E) and equivalent Wetherill (B, D, F) plots (scaled between 100–200 Ma) of Mauze-hosted zircons. Plots A and B display projected age with all analyses included. Plots C and D denote dates analysed on 29/04/14, derived from partially broken-down magmatic zircons (see Fig. 8.2A–C). Plots E and F denote dates analysed on 22/01/14, derived from hydrothermal zircons (see Fig. 8.2D–F). Data-point ellipses are 2σ and incorporate systematic error. Green lines denote calculated ages. Note the difference in calculated age between data in plots C and E.

Identifier	Comments	$f^{206}\text{C}$	^{206}Pb (mV)	U (ppm ¹)	Data for Tera-Wasserburg plot ²								Data for Wetherill plot ²				Dates ²				conc ³ (%)	
					$\frac{^{206}\text{Pb}}{^{204}\text{Pb}}$	1σ	$\frac{^{207}\text{Pb}}{^{206}\text{Pb}}$	1σ	$\frac{^{207}\text{Pb}}{^{235}\text{U}}$	1σ	$\frac{^{206}\text{Pb}}{^{238}\text{U}}$	1σ	Rho	$\frac{^{207}\text{Pb}}{^{206}\text{Pb}}$	2σ	$\frac{^{206}\text{Pb}}{^{238}\text{U}}$	2σ	$\frac{^{207}\text{Pb}}{^{235}\text{U}}$	2σ			
					(%)	(%)	(%)	(%)	(%)	(%)	(%)	(%)	(%)	(abs)	(abs)	(abs)	(abs)					
22nd January 2014, NERC Isotope Geosciences Laboratory, British Geological Survey																						
T0206 -1-3A		54	0.1	90	32	72	47.7	2.7	0.05235	7.51	0.15140	2.86	0.02099	2.68	0.94	301	171.20	134	7.09	143	7.61	94
T0206 -1-3B		20	0.2	308	74	65	44.7	2.5	0.11903	8.02	0.36702	3.92	0.02237	2.53	0.65	1942	143.38	143	7.14	317	21.13	45
T0206 -1-3D		10	0.3	492	172	93	48.5	2.5	0.04941	7.34	0.14036	2.14	0.02061	2.46	1.15	167	171.48	132	6.41	133	5.34	99
T0206 -1-4A		5	0.4	601	274	113	41.6	2.7	0.17848	9.95	0.59086	7.14	0.02402	2.72	0.38	2639	165.22	153	8.22	471	52.50	32
T0206 -1-6A		7	0.9	1494	240	85	48.2	2.8	0.09392	9.12	0.26855	5.95	0.02075	2.75	0.46	1506	172.26	132	7.21	242	25.26	55
T0206 -1-8A		12	0.3	503	137	153	46.7	2.4	0.06168	8.29	0.18184	4.37	0.02139	2.39	0.55	663	177.58	136	6.46	170	13.56	80
T0206 -1-8C		-18	0.1	22	-88	376	43.9	3.6	0.09517	15.49	0.29898	14.05	0.02280	3.56	0.25	1531	291.65	145	10.23	266	63.62	55
T0206 -1-9A		5	0.4	719	334	105	48.0	2.4	0.04997	7.33	0.14332	2.06	0.02081	2.41	1.17	194	170.48	133	6.34	136	5.24	98
T0218 -1-3H		-36	0.1	117	-40	84	40.9	3.0	0.12852	11.28	0.43327	9.00	0.02446	3.01	0.33	2078	198.60	156	9.25	365	53.78	43
T0225 -7A		15	0.2	264	103	121	43.2	2.5	0.11157	9.09	0.35562	5.79	0.02313	2.51	0.43	1825	164.82	147	7.30	309	30.38	48
U4913 -2B		76	0.1	130	23	30	46.3	2.4	0.04800	7.44	0.14285	2.40	0.02159	2.39	0.99	99	176.11	138	6.50	136	6.08	102
U4913 -2C		-54	0.1	146	-33	70	46.8	2.4	0.04965	7.41	0.14633	2.30	0.02139	2.38	1.03	178	172.86	136	6.43	139	5.95	98
U4913 -2D		57	0.1	137	30	42	46.3	2.5	0.05791	7.76	0.17227	3.30	0.02158	2.45	0.74	526	170.10	138	6.68	161	9.80	85
U4913 -3B		-39	0.0	77	-45	123	44.7	2.5	0.05790	8.09	0.17846	4.05	0.02237	2.50	0.62	526	177.39	143	7.05	167	12.37	86
U4913 -3D		-1	0.1	71	-1674	4586	25.5	10.1	0.30643	14.43	1.65397	15.94	0.03916	10.06	0.63	3503	223.05	248	48.70	991	184.06	25
U4913 -6B		13	0.1	22	69	177	13.3	8.2	0.05039	8.36	5.92572	9.07	0.07538	8.24	0.91	4434	121.88	468	74.00	1965	146.53	24
U4913 -7B		-58	0.0	39	-30	189	44.6	2.4	0.05246	7.93	0.16218	3.66	0.02243	2.43	0.66	306	180.58	143	6.86	153	10.31	94
U4913 -7C		-80	0.0	55	-22	77	45.7	2.4	0.05044	7.69	0.15220	3.12	0.02190	2.43	0.78	215	178.11	140	6.71	144	8.32	97
U4913 -7D		-35	0.0	37	-52	331	45.8	2.5	0.04846	7.72	0.14568	3.21	0.02181	2.45	0.76	122	181.92	139	6.75	138	8.25	101
U4913 -7E		-93	0.0	39	-19	111	45.2	2.5	0.04677	7.99	0.14244	3.83	0.02210	2.49	0.65	37	191.20	141	6.94	135	9.65	104
U4913 -8B		-4	0.2	326	-390	357	46.1	2.4	0.05710	7.38	0.17083	2.23	0.02171	2.41	1.08	495	162.74	138	6.59	160	6.59	86
28th April 2014, NERC Isotope Geosciences Laboratory, British Geological Survey																						
T0206 -2-11		-159	0.1	22	-11	42	47.0	2.4	0.05521	9.91	0.16198	6.99	0.02129	2.44	0.35	421	221.30	136	6.54	152	19.60	89
T0206 -2-12A		-46	0.1	54	-33	43	43.6	2.4	0.10480	7.57	0.33137	2.81	0.02294	2.42	0.86	1711	139.34	146	6.99	291	14.08	50
T0206 -2-12B		-15	0.1	44	-104	136	44.5	2.4	0.10511	7.53	0.32567	2.62	0.02248	2.36	0.90	1716	138.34	143	6.69	286	12.98	50
T0206 -2-13A		10	0.6	240	150	43	43.2	3.3	0.10977	13.91	0.35027	12.21	0.02315	3.28	0.27	1796	253.30	148	9.55	305	62.35	48
T0206 -2-13B		16	0.3	81	76	57	38.2	3.5	0.26476	12.85	0.95402	11.06	0.02615	3.53	0.32	3275	202.04	166	11.59	680	104.13	24
T0206 -2-14		15	0.1	38	110	176	45.4	2.7	0.07198	11.29	0.21869	8.91	0.02205	2.67	0.30	985	229.88	141	7.43	201	31.95	70
T0206 -2-19A		-35	0.1	34	-53	94	48.4	2.4	0.04722	7.67	0.13436	3.03	0.02065	2.40	0.79	60	182.73	132	6.25	128	7.27	103
T0206 -2-19B		-100	0.0	17	-18	71	47.0	2.5	0.04890	8.09	0.14351	4.05	0.02130	2.50	0.62	143	189.85	136	6.73	136	10.26	100
T0206 -2-19C		3	0.1	40	538	624	47.7	2.4	0.05184	7.56	0.14990	2.76	0.02098	2.42	0.88	278	172.98	134	6.42	142	7.28	94
T0206 -2-19D		-14	0.2	75	-133	136	48.4	2.4	0.04900	7.39	0.13943	2.22	0.02065	2.39	1.08	148	173.20	132	6.22	133	5.50	99
T0206 -2-19G		-9	0.2	81	-210	141	48.3	2.4	0.04740	7.48	0.13525	2.53	0.02071	2.40	0.95	69	178.04	132	6.27	129	6.10	103
T0206 -2-8D	Young	-82	0.1	32	-20	57	51.7	2.4	0.08514	8.11	0.22686	4.01	0.01933	2.37	0.59	1319	157.20	123	5.79	208	14.93	59
T0206 -2-8E	Very short ablation, Young	-65	0.1	65	-24	69	49.3	2.9	0.09814	8.08	0.27409	4.30	0.02026	2.91	0.68	1589	151.07	129	7.44	246	18.60	53
T0206 -2-9		-7	0.6	244	-257	80	47.7	2.4	0.04852	7.34	0.14014	2.02	0.02096	2.36	1.17	125	172.80	134	6.24	133	5.03	100
T0206 -2-1		5	0.1	48	339	465	47.4	2.4	0.09730	7.71	0.28271	3.12	0.02108	2.37	0.76	1573	144.37	134	6.31	253	13.86	53
T0206 -2-1		7	0.5	198	209	53	43.1	2.9	0.11037	10.95	0.35268	8.55	0.02319	2.93	0.34	1805	199.04	148	8.55	307	44.29	48
T0206 -2-4		2	0.3	114	678	653	45.0	2.6	0.13793	10.29	0.42199	7.59	0.02220	2.65	0.35	2201	178.73	142	7.40	357	44.73	40
T0206 -2-5B		-37	0.1	35	-36	41	37.7	2.7	0.20328	7.82	0.74337	3.62	0.02653	2.69	0.74	2853	127.40	169	8.96	564	30.89	30
T0206 -2-5C	Short ablation	12	0.1	51	149	367	46.1	2.3	0.04708	7.74	0.14084	3.16	0.02171	2.34	0.74	53	184.62	138	6.42	134	7.90	103
T0206 -2-5D		-37	0.1	26	-49	154	47.1	2.4	0.05590	8.13	0.16361	4.06	0.02124	2.38	0.59	449	180.71	135	6.38	154	11.53	88
T0206 -2-6A		-2	0.4	182	-1070	348	46.8	2.3	0.06006	8.25	0.17706	4.25	0.02139	2.32	0.55	606	178.39	136	6.27	166	12.91	82
T0206 -2-6B	Young	-12	0.1	33	-155	442	55.2	2.7	0.05229	7.92	0.13048	3.82	0.01810	2.68	0.70	298	180.67	116	6.15	125	8.91	93
T0206 -2-6F		-1	0.1	58	-1342	1337	47.3	2.3	0.05531	7.53	0.16128	2.60	0.02116	2.34	0.90	425	167.88	135	6.24	152	7.30	89
T0206 -2-6G		4	1.0	390	411	89	44.4	2.8	0.10627	11.91	0.32993	9.71	0.02253	2.78	0.29	1736	218.45	144	7.88	290	47.77	50

Continued on next page . . .

Continued from previous page ...

Identifier	Comments	²⁰⁶ C	²⁰⁶ Pb (mV)	U (ppm1)	²⁰⁶ Pb ₂₀₄ Pb	1σ (%)	²³⁸ U ₂₀₆ Pb	1σ (%)	²⁰⁷ Pb ₂₀₆ Pb	1σ (%)	²⁰⁷ Pb ₂₃₅ U	1σ (%)	²⁰⁶ Pb ₂₃₈ U	1σ %	Rho	²⁰⁷ Pb ₂₀₆ Pb	2σ (abs)	²⁰⁶ Pb ₂₃₈ U	2σ (abs)	²⁰⁷ Pb ₂₃₅ U	2σ (abs)	conc4 (%)
T0206 -2-6I		-19	0.1	49	-98	115	48.2	2.4	0.04712	7.45	0.13469	2.38	0.02074	2.36	0.99	55	177.62	132	6.18	128	5.73	103
29th April 2014, NERC Isotope Geosciences Laboratory, British Geological Survey																						
T0206 -2-12G		-7	0.2	35	-215	181	45.3	6.0	0.12046	8.48	0.36635	7.28	0.02207	6.03	0.83	1963	151.37	141	16.75	317	38.87	44
T0206 -2-12H		8	0.2	29	162	177	36.1	6.3	0.24877	8.54	0.95069	7.59	0.02773	6.33	0.83	3177	135.26	176	21.99	678	72.50	26
T0206 -2-12I		-30	0.1	15	-50	108	43.1	6.2	0.11953	8.03	0.38211	6.86	0.02320	6.16	0.90	1949	143.57	148	17.97	329	37.83	45
T0206 -2-6J		-179	0.0	7	-10	74	48.1	6.1	0.04498	8.33	0.12896	7.12	0.02080	6.06	0.85	-57	202.96	133	15.90	123	16.39	108
T0206 -2-6K		-18	0.2	40	-82	64	43.8	6.3	0.12389	11.50	0.38975	10.80	0.02283	6.31	0.58	2013	203.93	145	18.12	334	59.71	44
T0206 -2-6K	Short ablation	-58	0.2	37	-26	28	43.4	6.1	0.12032	9.55	0.38179	8.58	0.02302	6.15	0.72	1961	170.40	147	17.82	328	47.05	45
T0206 -2-6L		-7	0.3	65	-242	140	49.2	6.0	0.05409	7.44	0.15165	6.02	0.02034	6.02	1.00	375	167.41	130	15.46	143	15.98	91
T0206 -2-6N		-1	1.8	421	-1308	128	49.0	6.0	0.05032	7.32	0.14158	5.86	0.02042	6.02	1.03	210	169.60	130	15.50	134	14.66	97
T0206 -2-6O		-62	0.1	10	-19	45	32.3	6.2	0.28730	7.92	1.22423	6.73	0.03092	6.16	0.91	3403	123.30	196	23.78	812	72.61	24
T0206 -2-6P		-9	0.3	60	-170	89	46.0	6.1	0.09555	10.35	0.28655	9.40	0.02176	6.06	0.64	1539	194.59	139	16.61	256	41.66	54
T0206 -2-7X1		-19	0.3	118	-95	54	48.5	2.4	0.05596	7.37	0.15893	2.13	0.02061	2.37	1.11	451	163.59	131	6.18	150	5.92	88
T0206 -2-7X2		30	0.1	42	62	73	48.8	2.3	0.04801	7.47	0.13564	2.45	0.02050	2.34	0.96	100	176.82	131	6.05	129	5.92	101
T0206 -2-7X3		-62	0.2	81	-29	23	48.6	2.4	0.05518	7.46	0.15658	2.43	0.02059	2.37	0.98	419	166.54	131	6.17	148	6.66	89
T0206 -2-8H		-19	0.3	57	-92	70	47.7	6.0	0.06497	8.33	0.18787	7.06	0.02098	5.99	0.85	773	175.26	134	15.85	175	22.44	77
T0206 -2-8I	Short ablation	-9	0.5	119	-189	86	50.6	6.1	0.05535	7.86	0.15069	6.59	0.01976	6.09	0.92	426	175.21	126	15.19	143	17.38	88
T0218 -2-1B	Short ablation Core?	-14	0.0	9	-132	540	42.5	2.4	0.04798	7.60	0.15557	2.88	0.02353	2.44	0.85	98	179.74	150	7.23	147	7.86	102
T0218 -2-3		3	0.6	128	560	132	45.5	2.5	0.05314	7.40	0.16104	2.35	0.02199	2.48	1.06	335	167.66	140	6.87	152	6.59	92
U4913 -B-2A		8	0.4	81	197	74	46.1	2.4	0.08143	7.33	0.24338	2.09	0.02169	2.45	1.17	1232	143.83	138	6.70	221	8.27	63
U4913 -B-2B		-1	0.3	80	-1406	538	49.1	2.5	0.04853	7.33	0.13615	2.18	0.02036	2.52	1.16	125	172.59	130	6.49	130	5.30	100
U4913 -B-2C		-14	0.3	71	-126	73	48.7	2.4	0.04933	7.35	0.13974	2.14	0.02055	2.41	1.13	164	171.92	131	6.27	133	5.31	99
U4913 -B-2D		1	0.6	146	1828	517	48.9	2.5	0.04963	7.32	0.14000	2.06	0.02047	2.46	1.20	178	170.59	131	6.37	133	5.13	98
U4913 -B-2E		-10	0.6	130	-177	50	48.7	2.5	0.04938	7.31	0.13964	2.09	0.02052	2.50	1.20	166	170.86	131	6.48	133	5.19	99
U4913 -B-2F		-5	0.3	76	-384	132	48.6	2.5	0.04908	7.35	0.13906	2.20	0.02056	2.50	1.13	152	172.10	131	6.49	132	5.45	99
U4913 -B-2G		-15	0.4	88	-120	37	49.3	2.4	0.05107	7.33	0.14265	2.10	0.02027	2.45	1.17	244	168.90	129	6.27	135	5.31	96
U4913 -B-2H		-1	0.8	195	-1625	400	48.7	2.4	0.04909	7.32	0.13880	2.02	0.02051	2.41	1.20	152	171.50	131	6.25	132	4.99	99
U4913 -C-1A		3	1.9	396	445	50	44.8	2.4	0.10381	7.53	0.31947	2.68	0.02233	2.41	0.90	1693	138.84	142	6.78	281	13.07	51
U4913 -C-1B		-2	0.4	93	-905	405	49.7	2.4	0.05295	7.49	0.14675	2.55	0.02011	2.40	0.94	327	169.95	128	6.10	139	6.59	92
U4913 -C-1C		-2	0.6	142	-929	210	50.3	2.4	0.05355	7.35	0.14682	2.12	0.01989	2.42	1.14	352	166.00	127	6.08	139	5.48	91
U4913 -C-1D		-5	0.6	152	-372	73	50.1	2.4	0.05092	7.33	0.14014	2.09	0.01997	2.45	1.17	237	169.03	127	6.18	133	5.20	96
U4913 -C-1E		-28	0.3	79	-63	30	49.4	2.5	0.05785	7.32	0.16155	2.08	0.02026	2.46	1.18	524	160.59	129	6.30	152	5.87	85
U4913 -C-1F		5	0.3	79	369	261	48.5	2.3	0.07064	10.68	0.20061	8.01	0.02061	2.34	0.29	947	218.58	131	6.08	186	26.81	71
U4913 -C-1G		-3	0.7	165	-553	128	50.3	2.4	0.04915	7.32	0.13475	2.00	0.01989	2.40	1.20	155	171.38	127	6.04	128	4.81	99
U4913 -C-1H		-25	0.3	64	-71	50	48.9	2.4	0.05866	7.99	0.16521	3.78	0.02044	2.40	0.64	554	174.33	130	6.19	155	10.81	84
U4913 -C-2A		-13	0.3	74	-137	78	50.0	2.4	0.04910	7.37	0.13528	2.19	0.01999	2.40	1.10	153	172.70	128	6.07	129	5.27	99
U4913 -C-2B		-9	0.6	148	-213	60	49.8	2.4	0.04958	7.33	0.13720	2.05	0.02008	2.42	1.18	175	170.98	128	6.13	131	5.01	98
U4913 -C-2C		-4	0.7	167	-407	112	49.9	2.4	0.04903	7.32	0.13533	1.95	0.02003	2.37	1.22	149	171.48	128	6.01	129	4.72	99
U4913 -C-2D		-12	0.4	98	-152	69	49.6	2.4	0.04905	7.32	0.13632	2.02	0.02017	2.41	1.19	150	171.60	129	6.15	130	4.92	99
U4913 -C-2E		-19	0.5	116	-94	30	49.3	2.4	0.04904	7.32	0.13710	2.00	0.02028	2.40	1.20	150	171.55	129	6.14	130	4.87	99
U4913 -C-2F		-28	0.4	96	-64	18	49.5	2.4	0.04884	7.33	0.13601	2.06	0.02020	2.41	1.17	140	172.15	129	6.16	129	4.99	100
U4913 -C-2G		-59	0.2	38	-30	34	49.9	2.4	0.05143	7.37	0.14218	2.16	0.02006	2.40	1.11	260	169.20	128	6.08	135	5.45	95
U4913 -C-2H		-8	0.4	87	-214	92	50.3	2.4	0.05014	7.33	0.13750	1.98	0.01990	2.36	1.19	202	170.11	127	5.94	131	4.86	97
U4913 -C-3A		0	5.5	1218	4698	105	46.5	2.6	0.06551	7.42	0.19435	2.57	0.02153	2.63	1.02	791	155.67	137	7.13	180	8.45	76
U4913 -C-3B		0	4.3	963	14748	600	46.8	2.5	0.06113	7.36	0.18016	2.26	0.02138	2.51	1.11	644	158.14	136	6.77	168	6.97	81
U4913 -C-3C		-9	0.4	80	-202	61	47.4	2.5	0.05628	7.34	0.16374	2.16	0.02111	2.48	1.15	463	162.63	135	6.60	154	6.15	87
U4913 -C-3D		-25	0.4	87	-73	34	48.5	2.4	0.05187	7.33	0.14727	2.05	0.02060	2.41	1.17	280	167.83	131	6.26	140	5.34	94
U4913 -C-3E		-20	0.3	72	-93	43	48.7	2.4	0.04967	7.34	0.14058	2.11	0.02053	2.44	1.16	180	171.05	131	6.32	134	5.27	98
U4913 -C-3F		-13	0.3	73	-137	84	48.8	2.5	0.04938	7.37	0.13941	2.26	0.02049	2.47	1.09	166	172.26	131	6.39	133	5.60	99
U4913 -C-3G		-29	0.3	78	-63	33	48.9	2.4	0.04855	7.33	0.13693	2.06	0.02047	2.41	1.17	126	172.65	131	6.22	130	5.03	100

Continued on next page ...

Continued from previous page ...

Identifier	Comments	f^{206c}	^{206}Pb (mV)	U (ppm1)	$\frac{^{206}Pb}{^{204}Pb}$	1σ (%)	$\frac{^{238}U}{^{206}Pb}$		$\frac{^{207}Pb}{^{206}Pb}$		$\frac{^{207}Pb}{^{235}U}$		$\frac{^{206}Pb}{^{238}U}$		Rho	$\frac{^{207}Pb}{^{206}Pb}$		$\frac{^{206}Pb}{^{238}U}$		$\frac{^{207}Pb}{^{235}U}$		conc4 (%)
							1σ (%)	1σ (%)	1σ (%)	1σ (%)	2σ (abs)	2σ (abs)	2σ (abs)	2σ (abs)								
U4913 -C-3H		-11	0.7	153	-173	47	48.7	2.4	0.04852	7.33	0.13742	2.05	0.02055	2.41	1.18	125	172.61	131	6.25	131	5.01	100
U4913 -C-3I		-10	0.6	145	-183	46	49.3	2.4	0.04820	7.33	0.13480	2.04	0.02029	2.41	1.18	109	173.04	129	6.18	128	4.90	101
U4913 -C-4A		-2	1.1	259	-1031	166	49.1	2.4	0.04894	7.31	0.13733	1.96	0.02036	2.38	1.22	145	171.59	130	6.13	131	4.79	99
U4913 -C-4B		2	0.5	102	890	253	47.5	2.4	0.07252	7.46	0.21043	2.43	0.02106	2.37	0.97	1001	151.50	134	6.29	194	8.55	69
U4913 -B-2I	Calzirtite	2	0.6	112	798	190	41.0	2.5	0.15156	7.35	0.50887	2.25	0.02436	2.52	1.12	2364	125.53	155	7.71	418	15.32	37
U4913 -B-2J	Calzirtite	-3	0.6	117	-553	157	39.9	2.5	0.10554	7.32	0.36474	2.12	0.02508	2.51	1.18	1724	134.44	160	7.90	316	11.46	51
U4913 -B-2K	Calzirtite	3	1.0	208	484	78	43.9	2.4	0.08545	7.31	0.26795	2.03	0.02275	2.45	1.21	1326	141.59	145	7.01	241	8.66	60
U4913 -B-2L	Calzirtite	9	0.8	137	134	24	34.0	2.6	0.24623	7.75	0.99819	3.38	0.02942	2.59	0.76	3161	122.98	187	9.52	703	33.76	27
U4913 -B-2M	Calzirtite	4	0.4	84	307	110	38.8	2.6	0.17787	8.76	0.63118	5.31	0.02575	2.61	0.49	2633	145.55	164	8.44	497	40.89	33
U4913 -B-2N	Calzirtite	4	0.8	162	345	71	43.5	2.4	0.11762	7.45	0.37225	2.40	0.02296	2.38	0.99	1920	133.51	146	6.88	321	13.13	46
U4913 -C-2I	Calzirtite	-12	0.5	112	-151	43	50.0	2.4	0.05159	7.35	0.14206	2.14	0.01998	2.45	1.14	267	168.52	128	6.18	135	5.40	95
U4913 -C-2J	Calzirtite	2	0.4	104	848	332	49.0	2.4	0.05416	7.33	0.15225	2.03	0.02040	2.38	1.18	378	164.95	130	6.14	144	5.42	90

91500 as primary reference material

Decay constants of Jaffey et al. (1971) used

Uncertainties quoted with components related to systematic error unless otherwise stated

Total systematic uncertainties: $^{206}Pb/^{238}U = 2.3\%$, $^{207}Pb/^{206}Pb = 7.3\%$, $^{207}Pb/^{235}U = 1.8\%$ (2σ) f^{206c} = fraction of ^{206}Pb derived from common Pb¹ concentration uncertainty c. 1 %² data not corrected for common Pb³ Concordance calculated as $^{206}Pb-^{238}U \text{ age} / ^{207}Pb-^{235}U \text{ age} \times 100$

Table 8.3: Laser-ablation U-Pb dating results

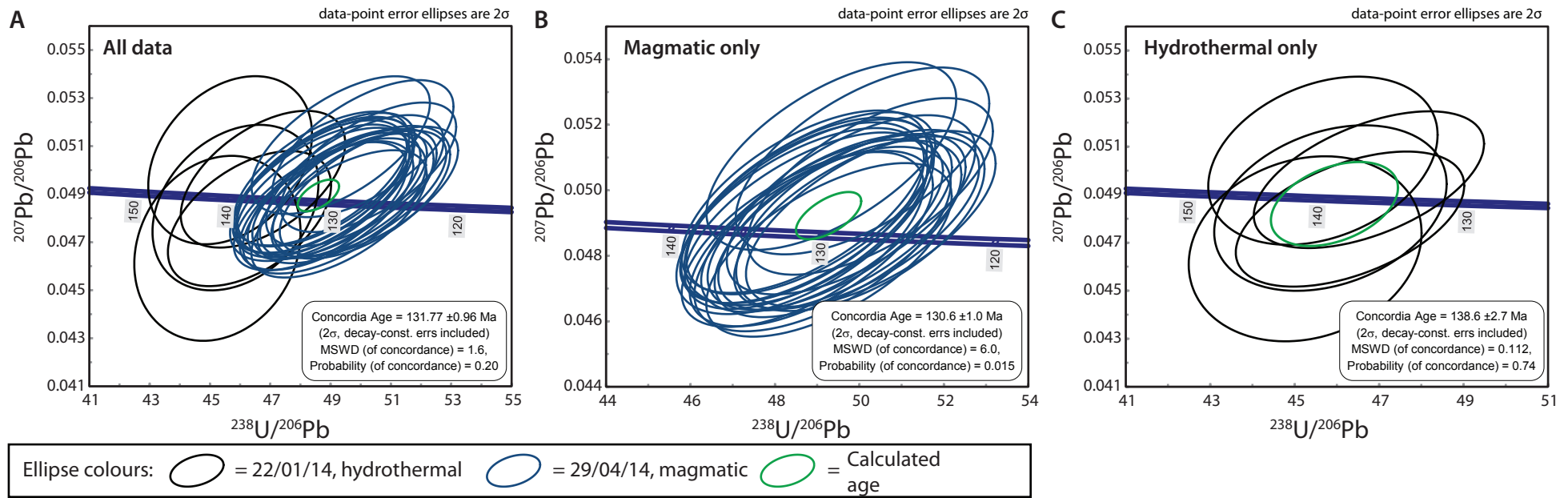


Figure 8.6: Tera-Wasserburg concordia ages of Mauze zircons with discordant data points (data with $\frac{^{206}\text{Pb}}{^{238}\text{U}} / \frac{^{207}\text{Pb}}{^{235}\text{U}} \times 100$ outside of 95–105) excluded. Plot A incorporates all non-discordant dates from Mauze, while plots B and C incorporate data collected on the 29/04/14 and 22/01/14 respectively. Data collected on each representative day is from zircons interpreted as magmatic (B) and hydrothermal (C). Data are equivalent to that plotted in Figure 8.5. Data-point ellipses are 2σ and incorporate systematic error. Green ellipses denote calculated ages. Note the difference in calculated age between data in plots B and C.

Half of the dates collected from Mauze zircons are discordant, and when the data are plotted as Tera-Wasserberg plots, the dates fall along a regression line which intercepts the concordia curve at approximately 4.5 Ga and 130 Ma (Fig. 8.5). If all the data from hydrothermal zircons and partially broken-down magmatic zircons are considered as one population then the regression-line intercepts the concordia curve at 131.5 ± 1.3 Ma, with a MSWD¹⁵ of 1.7 (Fig. 8.5A–B). Rejecting data which are less than 95 % concordant, the data give a calculated concordia age of 131.77 ± 0.96 Ma, with a low probability of concordance (Fig. 8.6A). The projected and concordia ages of the combined-data population are each within error of the other.

Data from hydrothermal zircons (22/01/14) and magmatic zircons (29/04/14) appear to form two populations, although there is overlap between the data-point ellipses of each potential population (Figs. 8.5A–B and 8.6A). If the data from the magmatic zircons and hydrothermal zircons are interpreted as separate populations, the regression age of each is 129.3 ± 1.2 and 138.9 ± 2.3 Ma respectively (Fig. 8.5C–F). Ages calculated from concordant data only are within error of the discordant regression ages: 130.6 ± 1.0 and 138.6 ± 2.7 Ma for magmatic and hydrothermal zircons, respectively (Fig. 8.6B–C). These ages cannot represent distinct events, as the hydrothermal mineralisation at Songwe cannot precede the magmatic. Therefore, the differences between dates from data collected on 22/01/14 and data collected on 29/04/14 are considered to be caused by inaccuracy due to variance in data collected on different days. Such long-term variance in the standard is propagated into the 2σ data ellipses, and data-points from the analyses on separate days overlap (e.g. Fig. 8.5A–B). Therefore, any true difference in the age of the different zircon groups is not considered resolvable using data where the systematic errors do not cancel and, with hindsight, the different zircon types should have been analysed on the same day. The age of the nepheline syenite is therefore considered to be best represented by interpreting all of the analysed zircons as a single population (Fig. 8.5), giving an age of 131.5 ± 1.3 Ma for Mauze.

Calzirtite age interpretation

Calzirtite (and associated minerals such as zirconolite and zirkelite) have not been extensively utilised for U-Pb dating, despite containing relatively abundant U concentrations (Table 8.3 and Platt et al., 1987; Bellatreccia et al., 1999; Bulakh et al., 2006; Wu et al., 2010). The main reasons for calzirtites infrequent use is the relatively sporadic occurrence of these minerals, the difficulty in their identification and their small size. Zirconolite shows promise as a geochronometer in mafic and lunar rocks where Si is undersaturated (e.g. Rasmussen and

¹⁵Mean Square of Weighted Deviates

Fletcher, 2004; Norman and Nemchin, 2014), however, only one published study has investigated in-situ U-Pb dating of calzirtite, using SIMS¹⁶ (Wu et al., 2010). A key issue in dating these minerals is the lack of an internationally recognised standard (Heaman, 2009). Matrix-matching during laser-ablation is therefore not possible (no in-house standards are available at NIGL) and data are therefore of lower precision than dates derived from zircon dating.

Calzirtite grains around partially broken-down magmatic zircons were preliminarily analysed in this study to see if any major age difference was discernible. The analyses are mostly discordant but this may be due to ablation of matrix minerals due to the small size of the calzirtite grains. Indeed, two of the analyses of larger grains plot close to the concordia curve, which suggests that calzirtite could be developed as a promising geochronometer in carbonatite and alkaline rocks (Fig. 8.7). This would be an interesting direction for further study. Least-square regression through the data gives an interpreted age of 132.8 ± 8.1 , with a high MSWD (= 3.2). This age overlaps with the ages for zircons from Mauze and suggests that no major temporal difference is resolvable, using this technique, between different paragenetic stages.

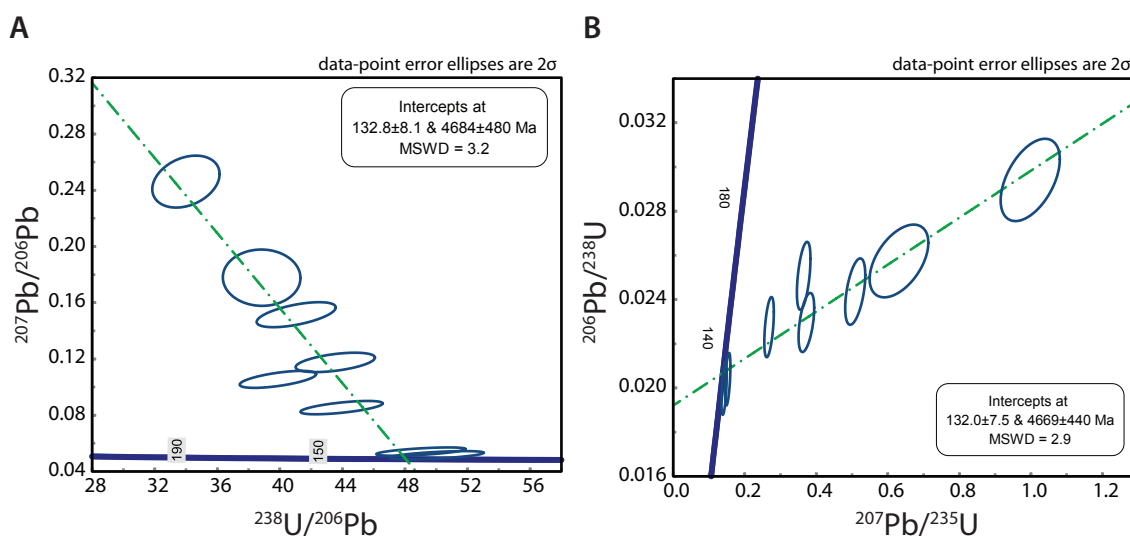


Figure 8.7: Tera-Wasserburg (A) and equivalent Wetherill (B) plots of calzirtite rims around Mauze-hosted zircons (see Fig. 8.2A, C). Data-point ellipses are 2σ and incorporate systematic error. Green lines denote calculated ages.

Songwe age interpretation

Zircons from Songwe were analysed on all three analysis days at NIGL. Over 75 % of the dates from the carbonatite-hosted zircons are discordant and, when plotted as Tera-Wasserberg plots, these data fall along a regression line which intercepts the concordia curve at 133.1 ± 2.0 and 5072 ± 290 Ma (Fig. 8.8A–B). All

¹⁶Secondary Ionisation Mass Spectrometry

zircon analyses are from C1 zircons, with the exception of one data-point (T0225-7A) which is interpreted as an inherited C1 zircon. Highlighted in Figures 8.8A–B are data points which are older (T0218 -1B) or younger (T0206 -6B, -8D and 8E) than the majority of the rest of the data-point ellipses. In the case of T0218 -1B, this data point represents a bright core (Fig. 8.4B) which could represent an inherited age, or remnant zircon from a significantly earlier stage of the intrusion. An inherited age seems unlikely given the contrast between the age of the country-rock granulites and gneisses (571–549 Kröner et al., 2001). Fenite zircons are likely to retain the age of the protolith, rather than the intrusion (Dowman et al., in prep.), and thus are an unlikely source of an inherited age. Therefore, it is likely that this date, given the small difference between this data-point and the regression age, is a strongly resorbed fragment from an earlier stage of the intrusion. The cause of the younger dates is unknown. These dates are from grains which were analysed multiple times in different locations (Fig. 8.4D–E). The majority of other analyses on the same grain plotted along the regression line. It is possible that the younger dates are caused by a small amount of Pb-loss, as such a process would lead to seemingly younger, discordant dates.

Figures 8.8C–D show a least-square regression of the Songwe data, but with the three younger, and one older, data-points removed. The interpreted age for these data is 133.4 ± 1.3 Ma, within error of the age which incorporates all of the data-points.

Using concordant dates only, a concordia age can be calculated for Songwe (Fig. 8.8E–F). If all of the data are used, including the older datapoint (T0218 -1B) described above, then the concordia age is 133.8 ± 2.5 Ma. Excluding the older data-point, the age is 132.7 ± 1.7 Ma. It is important to note that these concordia ages have a low probability of concordance and that all the different age interpretations of the dates are within error. Therefore, the age which incorporates all of the data points is taken as the most robust interpretation of the age of Songwe (133.1 ± 2.0).

8.4.2 Implications of new age data for REE mineralisation

In the preceding chapters, a hydrothermal model has been favoured to explain the REE mineralisation at Songwe, and the preponderance of HREE-enriched apatite over typical ovoid apatite from carbonatites. However, the driver of this hydrothermal mineralisation is unknown nor is the reason for its extensive development only at Songwe.

It is possible that hydrothermal mineralisation is driven by the release of heat through the crystallisation of minerals in the carbonatite. Quantifying the cooling history of a carbonatite is complex, but this model can be empirically evaluated through comparison with larger carbonatites in the CAP. These carbonatites,

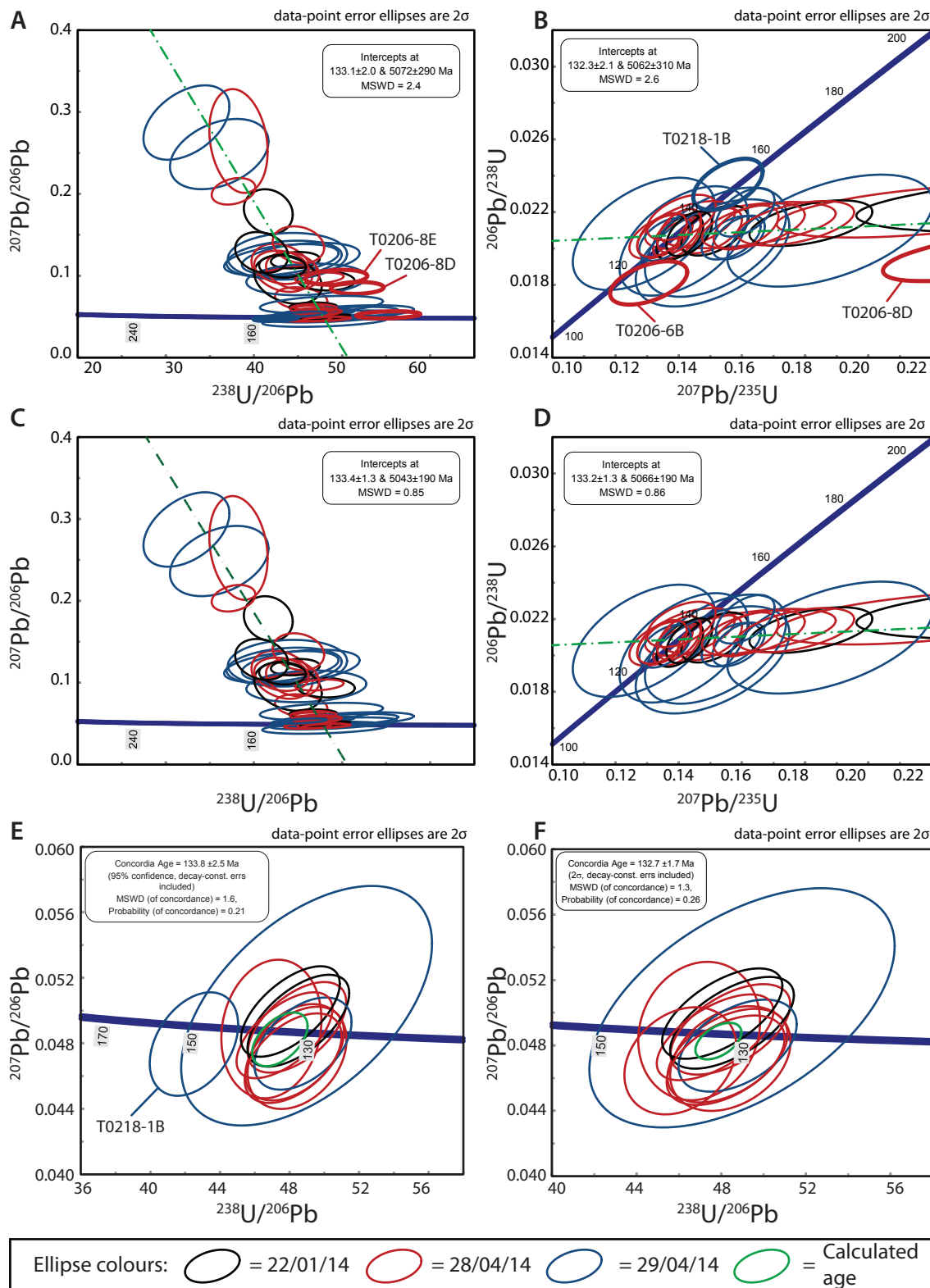


Figure 8.8: Tera-Wasserburg (A, C, E–F) and equivalent Wetherill (B, D) plots (scaled between 100–200 Ma) of Songwe-hosted zircons. Plots A and B denote projected age with all analyses included. Plots C and D denote age with one older (inherited?) and three younger analyses excluded (T0218-1B, T0206-8D, -8E and -6B; see text). Plots E and F denote concordia ages with discordant data excluded (data with $\frac{^{206}\text{Pb}}{^{238}\text{U}} / \frac{^{207}\text{Pb}}{^{235}\text{U}} \times 100$ outside of 95–105%), including (E) and excluding (F) potentially older sample T0218-1B respectively (See Fig. 8.4 B). Data-point ellipses are 2σ and incorporate systematic error. Green lines/ellipses denote calculated ages. Note the low probabilities of concordance in plots E and F, and the overlap between the ages (within error) in all plots.

such as Chilwa Island, Kangankunde and Tundulu, do not demonstrate the similar apatite habit as found at Songwe. Some HREE-enrichment is observed in apatite from Tundulu, but these apatite retain clearly magmatic cores and do not display the fully hydrothermal textures observed in apatite from Songwe.

In comparison to other carbonatite–silicate paired intrusions in the CAP, Mauze is considerably larger than the silicate counterparts of any of the other carbonatite intrusions. Given that the age data for Songwe and Mauze are within error, it is possible that Mauze was still hot when Songwe was intruded. Hydrothermal activity, with temperatures calculated by Ti in zircon thermometry of approximately 500–600 °C, was estimated to continue at Zomba (although larger than Mauze) for up to 3 Ma (Soman et al., 2010). Furthermore, for the same intrusion, Eby et al. (1995), calculated from K-Ar amphibole and FT zircon ages, that the cooling rate of Zomba was approximately 23 °C per million years. As such, it is suggested that Mauze may provide the ‘heat-engine’ required to cause extensive hydrothermal mineralisation. This could explain why extensive apatite remobilisation is not observed in other CAP complexes: in these complexes there isn’t enough heat to lead to remobilisation.

In addition, it has been assumed, so far, that the source of the REE (and P) in the model for hydrothermal mineralisation at Songwe is from the carbonatite. However, given that Mauze was crystallising at approximately the same time as Songwe, then it is possible that Mauze is the source of the HREE-bearing fluid(s). Support is lent to this suggestion by the MREE-depleted nature of the late-stage pegmatoidal vein samples from Mauze (Fig. 4.16) and by the low P content of these rocks.

It is possible that acidic, REE-complexing, fluids were exsolved during the late stages of Mauze’s evolution. These could have then transported the REE away from Mauze where they would have come into contact with Songwe, reacting with the carbonate to form apatite. The relatively low concentration of the REE in the fluids precluded the formation of REE phosphates and the MREE substituted into the apatite structure. Any LREE present in the fluid stayed in solution to form LREE minerals. Given the current data-set, this possibility cannot be excluded, and given that the two intrusive bodies (carbonatite and nepheline syenite) would have similar isotope signatures, it is difficult to propose a method to differentiate the source of the fluids.

8.4.3 Songwe and Mauze ages in the context of the CAP

It is well established that the CAP formed in the late Jurassic–early Cretaceous (Dixey et al., 1955; Garson, 1965; Eby et al., 1995), and is temporally distinct from the Pan-African metamorphic basement (571–549 Ma; Kröner et al., 2001) and metamorphosed nepheline-bearing gniesses (e.g. Ashwal et al., 2007). The

relationship with the Karroo dolerite intrusions (Stormberg Series) is less well understood. These intrusions are generally considered to be late Jurassic because of their cross-cutting relationships with late-Triassic to early-Jurassic sediments and intrusions of the CAP (Macdonald et al., 1983). While no petrological connection is apparent, the events leading to the intrusion of the Stormberg series may be linked to up-doming and metasomatism in the mantle. This, in turn, may be linked to the formation of the intrusions of the CAP (Woolley, 1987). A temporal connection between LIPs¹⁷ and carbonatites has been suggested for other alkaline provinces (Ernst and Bell, 2010).

For comparison with other age data, the ages of Songwe and Mauze are taken from least-square regressions, which incorporate all of the zircon dates from each intrusion, as 133.1 ± 2.0 and 131.5 ± 1.3 Ma, respectively. These data clearly confirm that Songwe and Mauze are part of the CAP. The new age data are the first U-Pb zircon dates of carbonatite from the CAP, and some of the first age data from the southern and eastern intrusions of the CAP.

The ages of the intrusions from the rest of the CAP are compiled in Table 8.4 and summarised in Figure 8.9. Many of these ages are old K-Ar analyses, with little detail on the methodology, decay-constants used or the level of uncertainty represented in the reported error. Relatively recently-published ages were acquired from K-Ar dating and FT analyses of titanite (Eby et al., 1995). For this technique, titanite has a closure temperature of 240–300 °C (Reiners et al., 2005) and may not be directly comparable with K-Ar or U-Pb zircon dates. Eby et al. (1995) estimated that, based on a shallow intrusion depth, the largest intrusions would cool to below 275 °C within 1 Ma of intrusion and, therefore, may be comparable with other data. Eby et al. (1995) also published cooling ages using FT dating in apatite and zircon (closure temperature: 90–120 °C and 330–350 °C, respectively; Reiners et al., 2005). In addition, newer Pb-Pb and U-Pb dates for zircon from Zomba are available (Högdahl and Jonsson, 1999, 2002; Soman et al., 2010).

Comparison of the new U-Pb ages from Songwe and Mauze and previously published data indicates that the new ages fall approximately within the early/middle temporal stages of the CAP (Fig. 8.9). Detailed interpretation is difficult to make because of the age uncertainty in the legacy data and problems with comparing ages from different dating techniques (Schoene et al., 2013). The new age data roughly overlap with the other dated carbonatites in the province; the ages of Chilwa Island and Tundulu are within error, while Kangankunde is slightly younger. Some published ages from Chambe, Chikala, Mpyupyu and Zomba are younger than Songwe based on K-Ar dating. Although the 10 different published analyses for the age of Zomba span a range of 138–108 Ma, the most recent Pb-Pb and

¹⁷large igneous provinces

U-Pb zircon ages are most likely to be the most reliable data.

Woolley and Jones (1987) and Woolley (1987) have argued, on the basis of geochemical relationships, that essentially three rock types are present in the CAP, potentially derived from three separate parental magmas:

1. Trachytic, evolving to the syenite–quartz-syenite–granite series: Zomba, Malosa, Mpyupyu, Mulanje, Michese(?), Gorongosa. Zomba and Malosa are separated on the basis of different mafic mineral compositions (Woolley and Jones, 1992).
2. Phonolitic, evolving to the syenite–nepheline-syenite series: Chikala, Chanoë, Mongolowe, Chinduze, Junguni, Mauze, Chiperone, Milange.
3. Nephelinitic and carbonatitic, evolving to the carbonatite–nephelinite–nepheline-syenite series: Chilwa Island, Tundulu, Nkalonje(?).

Eby et al. (1995) suggested that these petrogenetic groups are temporally related, with group 3 intruding first, followed by groups 2 and 1. The group to which each intrusion is assigned is included on Table 8.4. Based on the geochemical analyses of Mauze (see Chapter 4), and one published analysis (Dixey et al., 1955), it is assigned, tentatively, to group 2 (Woolley and Jones, 1987). Despite being associated with nepheline-syenite from Mauze, Songwe is tentatively assigned to the nephelinitic and carbonatitic group (3) to facilitate comparison with Tundulu and Chilwa Island. The ages of each intrusion are arranged by the proposed parental magma source in Figure 8.9B. Given the uncertainty in the legacy data, especially FT data, it is difficult to see the basis for such a trend proposed by Eby et al. (1995). It is possible that group 1, the syenite–quartz-syenite–granite series, is younger than the other intrusions as most of these ages are around 115 Ma. Such a grouping seems more valid when data acquired pre-1995 are excluded. Groups 2 and 3, however, appear contemporaneous, especially given the addition of within-error ages for Songwe and Mauze. A younging of the CAP towards the south of the province, also suggested by Eby et al. (1995), is not observed in the new data.

Potential for further work in the CAP

Overall, the new U-Pb data raise more questions about the CAP than they answer. Part of the issue with comparing the new age data with legacy data is the problems of inaccuracy between different dating techniques — notwithstanding the large uncertainty from some of the literature data. It is simply not possible to test hypotheses about the temporal relations of intrusions of the CAP where

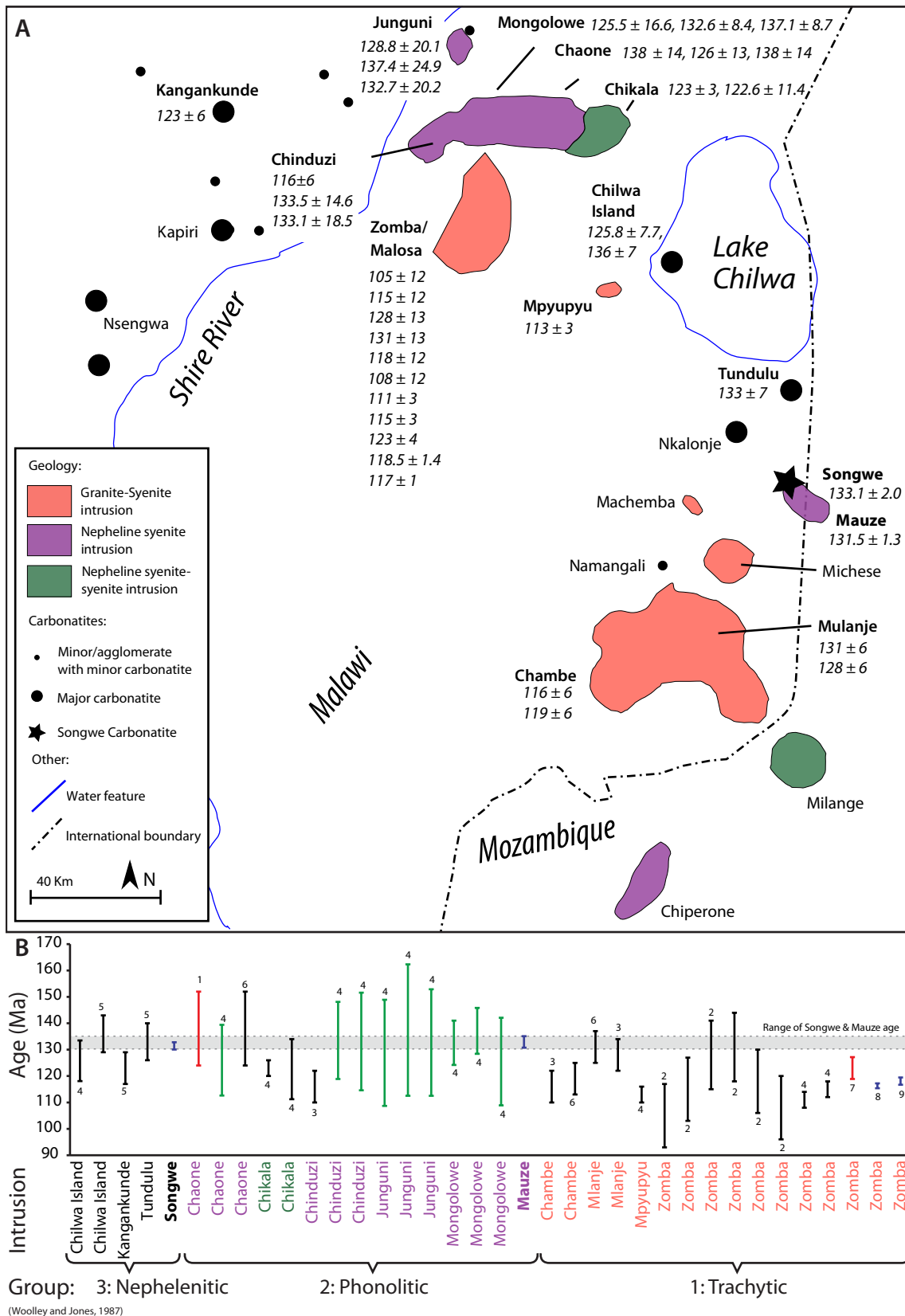


Figure 8.9: New Songwe and Mauze U-Pb zircon ages compared with published age data (see Table 8.4). Data are presented as a map (A), redrawn from Woolley (2001), with minor dykes and fault data removed. Dates in (B) are arranged by paragenetic groups, after Woolley and Jones (1987); Woolley (1987) and Eby et al. (1995). Data bars are coloured by technique: Black = K-Ar dating, red = Pb-Pb, green = FT titanite ages, blue = new U-Pb zircon ages. Numbers adjacent to the data bars indicate the data source, from Table 8.4.

Intrusion	Ref	Sample	Technique	Mineral	Age	Group
Chaone	1		Pb-Pb	Zrc*	138 ± 14	2
Zomba	2		K-Ar	Hbl	105 ± 12	1
Zomba	2		K-Ar	Hbl	115 ± 12	1
Zomba	2		K-Ar	Hbl	128 ± 13	1
Zomba	2		K-Ar	Hbl	131 ± 13	1
Zomba	2		K-Ar	Hbl	118 ± 12	1
Zomba	2		K-Ar	Hbl	108 ± 12	1
Mlanje	3		K-Ar	Bt	128 ± 6	1
Chinduzi	3		K-Ar	Bt	116 ± 6	2
Chambe	3		K-Ar	Bt	116 ± 6	1
Mpyupyu	4	P26 (3)	K-Ar	Amph	113 ± 3	1
Zomba	4	P18 (17)	K-Ar	Amph	111 ± 3	1
Zomba	4	P18 (19)	K-Ar	Amph	115 ± 3	1
Chaone	4	P21 (20)	FT	Tit	126 ± 13.4	2
Chikala	4	P22 (9)	K-Ar	Amph	123 ± 3	2
Chikala	4	P22 (9)	FT	Tit	122.6 ± 11.4	2
Chinduzi	4	P20 (23)	FT	Tit	133.5 ± 14.6	2
Chinduzi	4	P20 (4)	FT	Tit	133.1 ± 18.5	2
Junguni	4	P25 (17)	FT	Tit	128.8 ± 20.1	2
Junguni	4	P25 (4)	FT	Tit	137.4 ± 24.9	2
Junguni	4	P25 (9)	FT	Tit	132.7 ± 20.2	2
Mongolowe	4	P21 (10)	FT	Tit	125.5 ± 16.6	2
Mongolowe	4	P21 (48)	FT	Tit	132.6 ± 8.4	2
Mongolowe	4	P21 (49)	FT	Tit	137.1 ± 8.7	2
Chilwa Island	4	P28 (3)	FT	Tit	125.8 ± 7.7	3
Chilwa Island	5		K-Ar	Bt	136 ± 7	3
Kangankunde	5		K-Ar	Phl	123 ± 6	3?
Tundulu	5		K-Ar	Bt	133 ± 7	3
Mlanje	6		K-Ar	Bt + Hbl	131 ± 6	1
Chaone	6		K-Ar	Bt	138 ± 14	2
Chambe	6		K-Ar	Bt	119 ± 6	1
Zomba**	7		Pb-Pb	Zrc	123 ± 4	1
Zomba**	8		U-Pb	Zrc	117 ± 1	1
Zomba**	9		U-Pb	Zrc	119.3 ± 2.1	1

*Detrital zircon of unknown origin

**Pegmatite

Table 8.4: Published intrusion ages, reported error (degree of confidence unknown) and analysed mineral from the intrusions of the CAP. Also included is the grouping of each intrusion using the scheme of Woolley and Jones (1987). Abbreviations: FT = fission-track, Zrc = zircon, Hbl = hornblende, Bt = biotite, Amph = amphibole, Tit = titanite. References: 1, Bloomfield (1961); 2, Bloomfield (1965a); 3, Cahen and Snelling (1966); 4, Eby et al. (1995); 5, Snelling (1966); 6, Snelling (1967); 7, Högdahl and Jonsson (1999); 8, Högdahl and Jonsson (2002); 9, Soman et al. (2010)

so many of the data-points are within error. Advances in high-precision U-Pb geochronology mean that there is significant potential to obtain a detailed intrusion history of the CAP and to test the hypotheses of Woolley and Jones (1987); Woolley (1987) and Eby et al. (1995). Standardising the technique, analysed mineral, and laboratory will mean that error between the ages of each intrusion could be reduced such that different stages of the paragenesis of an intrusion could be elucidated. Many of the rocks have minerals that are datable, and zircon has been identified at Junguni (Woolley and Platt, 1988), Zomba (Woolley and Jones, 1992), Chikala, Chaone, Mongolowe, and Chinduzi (Woolley and Platt, 1986). Additionally, catapleiite has been described from Chinduzi (Woolley and Platt, 1986), and zirconolite has been reported from Chikala (Platt et al., 1987). A proposal to utilise the abundance of these minerals to comprehensively date the intrusions of the CAP is currently in preparation.

8.5 Summary and conclusions

The results of U-Pb zircon dating at Songwe and Mauze have been described. An attempt to determine an age for Mantrap was made, but this was not possible because of a lack of instrument time and low U concentrations in the zircons.

Prior to dating, the zircons were analysed using cold-CL and BSE imagery. Zircons from the selected samples exhibit a range of textures. Those from Mauze are subdivided into three groups, interpreted as a continuum from magmatic through to late-stage hydrothermal grains. Zircons from Songwe were preferentially selected from C1 carbonatite. Zircons from later carbonatite stages are present, but these are typically reabsorbed, small and broken-down and are, therefore, unsuitable for dating.

The zircons were analysed in-situ using laser-ablation MC-ICP-MS. A total of 72 zircons from six samples were dated, although not all of these zircons gave good quality data. In addition, eight analyses of a calzirtite overgrowth on zircons from Mauze were performed.

Individual zircon dates from Songwe and Mauze exhibit a range of concordant and discordant values, and consequently zircon populations were evaluated in order to obtain an interpreted age for each intrusion. Zircons from each intrusion were treated as separate populations. The interpreted ages for Songwe and Mauze are:

Mauze: 131.5 ± 1.3 Ma

Songwe: 133.1 ± 2.0 Ma

Variation between the different zircon textures observed from Mauze could

not be resolved with the technique utilised, and the calzirtite age interpretation is within error of the zircon ages from the same samples.

The interpreted ages, which are within error of each other, have two main implications:

1. Mauze, as a large igneous body intruded at the same time, could provide a 'heat-engine' for hydrothermal mineralisation at Songwe. This might explain why there is extensive hydrothermal apatite at Songwe, but not at other, larger, carbonatites in the CAP. Given the MREE-depleted nature of rocks from Mauze, it could also potentially provide the MREE-mineralising fluid which caused the MREE/HREE-enriched apatite at Songwe.
2. The ages of Songwe and Mauze do not fit with the suggestion of Eby et al. (1995) that the intrusions of the CAP young towards the south. It is suggested that further U-Pb dating should be carried out to elucidate the temporal relationship between the different intrusions of the CAP.

Chapter 9

Summary, conclusions and further work

The HREE are critical for high-tech applications such as wind turbines and electric vehicles. Carbonatites are some of the largest and highest grade sources of the REE and, accordingly, are frequently targeted by exploration companies. However, most carbonatites are typically HREE-poor. In this thesis the principal objectives have been to find whether HREE mineralisation can occur in carbonatites and how this can take place. To this end, the Songwe Hill carbonatite in the CAP¹, south-east Malawi, has been used as a case study of a REE-rich carbonatite under active exploration, in collaboration with Mkango Resources Ltd. (Chapters 3 and 4). In addition to investigating potential HREE-mineralisation, new whole-rock, petrographic and mineralogical data are also presented on this intrusion, for which there are few previous data.

Songwe Hill abuts the north-west flank of Mauze Mountain, a large (3.5×6 km) nepheline syenite intrusion straddling the Malawi–Mozambique border. The carbonatite has been shown to comprise three different generations (C1–C3) of sövitic calcite carbonatite, alvikitic calcite-carbonatite and a Fe-rich carbonatite stage. These are followed by apatite-fluorite veins (C4), which are volumetrically minor but important due to their HREE-rich nature, and also by late-stages of supergene alteration leading to Mn-Fe- veins. Brecciation is extensive at Songwe and is manifested as clasts of both C1 carbonatite and fenite in a matrix of C2 or C3 carbonatite. Field relations, including extensive brittle deformation, indicate a shallow level of intrusion (<5 km), common to other intrusions in the CAP.

Whole-rock analyses, from drillcore provided by Mkango Resources Ltd., reveal that, common to most carbonatites, the Fe-rich, later stages of the intrusion are the most LREE-rich (Chapter 4). Petrographic analyses of the carbonatites show that the LREE are predominantly hosted in LREE-fluorcarbonates (synchysite-(Ce)). These are associated with crystallisation of strontianite, barite

¹Chilwa Alkaline Province

and some late calcite. The concentration of Y, as a proxy for the HREE, is positively correlated with P_2O_5 in all the carbonatite types. As apatite is the only major phosphate mineral found at Songwe, it is proposed that apatite hosts the majority of the HREE mineralisation. All whole rock analyses display a minor negative Y anomaly, interpreted as evidence for the exsolution of a hydrothermal, HREE-bearing, fluid.

In-situ, major and trace-element analyses of apatite at Songwe show that it is a major host of the HREE, but it is compositionally and texturally heterogeneous (Chapter 5). Five different apatite generations have been identified:

0. Apatite from fentite, which is anhedral, fragmented, LREE-rich with a minor Eu-anomaly and has low Sr and Mn contents relative to carbonatite apatite
1. Cores of ovoid ('lozenge-shaped') grains in C1 calcite-carbonatite, which are LREE-rich, low U and Th.
2. Rims of ovoid ('lozenge-shaped') grains in C1 calcite-carbonatite, which are similar to Ap-1, but with low tenors of HREE enrichment
3. Anhedral apatite, sometimes forming stringers in C2 and C3 carbonatite, this apatite has a high Na concentration, is HREE enriched and has relatively high Th.
4. Anhedral apatite, in apatite-fluorite veins, this apatite type is similar to Ap-3, but is spongy, and can display xenotime overgrowths.

The different apatite habits are used to infer crystallisation conditions. Ap-1 is interpreted as being formed in a magmatic environment on the basis of comparison with apatite from other localities (e.g. Le Bas, 1989; Hogarth, 1989). Ap-2 is interpreted as representing a transition to a late-stage crystallisation environment, and Ap-3 is interpreted to be an early crystallisation product of a (carbo?)-hydrothermal fluid. This is based on the habit of Ap-3, which forms stringers cross-cutting earlier carbonate and incorporates fragments of earlier magmatic minerals such as zircon and pyrochlore. LREE-fluorcarbonates, strontianite and barite crystallise after Ap-3, as indicated by the truncation of apatite stringers. Very late stage crystallisation products include fluorite and xenotime which forms overgrowths on Ap-4 in C4 apatite-fluorite veins. Major and trace element analyses of the fluorite and xenotime grains show that both are HREE-enriched, with fluorite displaying a prominent positive Y anomaly. These late-stage phases are interpreted as being the crystallisation products of an expelled Y-rich hydrothermal fluid which led to the negative Y anomaly in the whole-rock analyses.

The REE contents of Songwe apatite are compared to new trace element analyses of late-stage apatite from the Tundulu and Kangankunde carbonatites,

Malawi. Ap-3 and Ap-4 from Songwe are shown to have the highest Y concentrations compared to apatite from any other analysed carbonatite-derived apatite from the published literature. The Y (and therefore the HREE) concentration of Songwe apatite extends to concentrations found in granitoid rocks, opening up carbonatite-derived apatite as a potential co-product of LREE-extraction from carbonatites. This could supplement the shortfall in HREE production in the short to medium term, although further work is required to develop an efficient, low-energy and cost-effective mineral processing technique. Increased HREE concentrations in apatite are correlated with increased U and Th contents. This presents potential environment problems for the transport and processing of such HREE-enriched apatite (Weng et al., 2013; Wall, 2014).

The paragenesis of the Songwe Hill carbonatite is presented and, although it is complex and not equivocal, the formation of LREE-fluorcarbonates is shown to occur *after* the crystallisation of HREE-enriched apatite. Extensive fluorite mineralisation is interpreted to have formed late. An attempt is made to determine the composition and temperature of apatite-precipitating fluids through fluid inclusion analyses of apatite and fluorite (Chapter 6). Difficulties with the size of the inclusions and problems due to decrepitation mean that robust data from apatite are lacking. However, homogenisation temperatures from fluorite, which crystallised after apatite mineralisation, give an unambiguous constraint on the lower temperature bounds for apatite crystallisation of 160 °C. Homogenisation temperatures from inclusions within Ap-3 and Ap-4 range between 250–360 and 160–220, respectively, providing a constraint on the crystallisation temperature of the apatite. Compositionally inclusions from apatite are mixed, comprising liquid, liquid-vapour, liquid-liquid-vapour and vapour-rich inclusions. Commonly present are a CO₂-bubble and a low-salinity brine, with an equivalent NaCl concentration of 0–12 wt. %. These inclusions, as well as the composition of minerals from the late hydrothermal assemblages, indicate that a wide range of REE transporting anions are available to complex the REE, including CO₃²⁻, HCO₃⁻, F⁻, Cl⁻, and SO₄²⁻.

The paragenesis of apatite-rich carbonatite at Tundulu is also reassessed, following a previous interpretation by Ngwenya (1994). Contrary to this previous interpretation, synchysite-(Ce) is considered to have formed after apatite, in a manner similar to that at Songwe. The similar compositions of the apatite types from Songwe and Tundulu, and the similar orders of crystallisation, indicate that a common process may cause the crystallisation at each complex.

Apatite formation during the early stages of hydrothermal activity in carbonatites is suggested to be due to the low solubility of phosphate in a hydrothermal fluid. The cause of fractionation of the REE, however, cannot be equivocally determined. Two mechanisms are suggested:

1. preferential transport of the LREE or HREE due to ligand chemistry

2. crystal-chemical control on REE substitution into apatite

Fractionation via early crystallisation of synchysite was suggested for the formation of HREE-bearing apatite at Tundulu (Ngwenya, 1994), but does not occur at Songwe due to the formation of synchysite after apatite. It is also suggested that this mechanism is not taking place at Tundulu on the basis of the new paragenetic interpretation.

Complexation of the REE by F^- or Cl^- could lead to REE fractionation as the stability of LREE complexes with these anions are greater than the equivalent HREE complexes. However, fluoride is excluded as a likely transport ligand due to the lack of a Y anomaly in the HREE-enriched apatite. Chloride is also considered as an unlikely ligand to transport the REE, despite being favoured in REE deposits related to alkaline rocks (e.g. Williams-Jones et al., 2012; Migdisov and Williams-Jones, 2014), because of the low salinity of the fluid inclusions in apatite. Furthermore, Cl^- is only a major transporting ligand in acidic solutions; these are difficult to infer in a carbonatite due to the large amount of carbonate to act as a buffer.

Transport of the REE by carbonate complexes is the favoured mechanism at Songwe due to the abundance of carbonate in carbonatites, and the presence of CO_2 -bearing fluid inclusions in Ap-3. As carbonate complexes do not readily fractionate the REE, it is proposed that fractionation of the HREE into apatite is due to a crystal-chemical control (i.e. the partition coefficient of the REE in apatite) during crystallisation. However, there are few studies of the partition coefficients for the REE at the conditions considered to be prevalent during apatite crystallisation. The closest experimentally-determined analogue is considered to be a phosphate-fluorite liquid, at 0.12 GPa and 684 °C (Pan, 1997). However, the partition coefficients for the REE under these conditions are highest for the LREE and MREE which cannot be reconciled with the MREE and HREE-enriched distribution observed in Ap-3.

An alternative suggestion is that, as is the case for F^- and Cl^- , LREE-carbonate complexes are more stable than HREE-carbonate complexes. This hypothesis contrasts with our current understanding of the stability of REE-carbonate complexes from extrapolations of stability at ambient temperature (Haas et al., 1995). However, where experimentally-determined stability constants have been compared with the extrapolated equivalents (e.g. F and Cl; Williams-Jones et al., 2012) the theoretically determined stabilities have been incorrect.

In order to determine the source of the mineralising fluid, a stable isotope study has been presented (Chapter 7). This study combines conventional C and O analyses in carbonates with a novel method developed for the determination of O isotopes in apatite. Results from Songwe are interpreted relative to a PIC² field,

²'Primary Igneous Carbonatite'

which is well established for carbonate analyses from carbonatites. No such field exists for the O isotope composition of apatite and, therefore, analyses from well-studied magmatic carbonatites have been used to determine a similar field for PIA³. This is preliminarily between 3.6–6.7 ‰, and further analyses are underway to ratify this value.

The data for $\delta^{18}\text{O}$ in carbonate and $\delta^{18}\text{O}_{\text{PO}_4}$ (in apatite) are difficult to reconcile. Results from carbonate trend towards more positive $\delta^{18}\text{O}$ values in samples from later in the paragenetic sequence, while $\delta^{18}\text{O}_{\text{PO}_4}$ from apatite in the same samples trends towards more negative values. To reconcile these results, a conceptual model is presented where a hot, deuteric, hydrothermal fluid is mixing with a reservoir of more negative, cool meteoric water. It is suggested that this mixing is a driver for crystallisation of apatite and REE minerals at Songwe (Fig. 7.19).

U-Pb zircon dates are presented for Mauze and Songwe, and the ages of both are within error, at 131.5 ± 1.3 and 133.1 ± 2.0 Ma, respectively (Chapter 8). Given that these intrusions formed at approximately the same time, Mauze is proposed as a 'heat-engine' to drive the hydrothermal mineralisation at Songwe. New, whole-rock, geochemical data are also presented for samples from Mauze. These rocks are MREE-depleted, P_2O_5 -poor and field relations show that they formed relatively late in the crystallisation sequence at Mauze. It is suggested that fluid derived from Mauze could be the source of MREE and HREE mineralisation at Songwe. However, as hydrothermal fluids sourced from carbonatite and nepheline syenite would be of a similar isotopic composition it is difficult to equivocally determine the fluid source.

Compared to other intrusions associated with carbonatites in the CAP (e.g. Woolley and Jones, 1987), Mauze is demonstrated to be significantly less mafic, and more akin to nepheline-syenite intrusions not associated with carbonatites. The paucity of data, however, make it difficult to establish reliable conclusions and, given the potential importance of Mauze as heat and/or fluid source, further field and laboratory investigations are required to substantiate its origins.

It is proposed that the most REE-enriched and also the few HREE-enriched carbonatites are those of a shallow depth of intrusion, where mixing between meteoric and magmatic waters can take place. This is a common feature of the most REE-rich carbonatites of the CAP. To enrich the REE, substantial evolution of a primary carbonatite is required, and this could occur via fractionation of REE-poor phases or through immiscible separation of a carbonate and a silicate fluid. A balance is required where precipitation of REE-poor silicate phases from a carbonatite liquid can lead to carbonatite evolution without the crystallisation and settling of REE-rich phosphates, removing REE from the melt. At Songwe, magmatic apatite crystallisation (and therefore fractionation) is considered to be

³primary igneous apatite

minor, as supported by the very low abundance of typical primary ovoid apatite which is common in most intrusive, REE-poor, carbonatites.

To target HREE-bearing carbonatites, it is best to aim for those with abundant, late-stage, overprinting from a hydrothermal fluid. 'Classic' intrusions with coarse grained calcite, apatite and magnetite are commonly not HREE-rich. CL⁴ is recommended as an effective tool to petrographically determine if late-stage apatite is present, and the CL colour can provide a quick, qualitative determination of the approximate REE distribution. In any exploration campaign at a carbonatite-hosted REE deposit, it is important to establish if the HREE correlate with P₂O₅ as this would strongly indicate that the HREE are being taken up in apatite. This could present a potential HREE-rich co-product of LREE-extraction.

All these are incremental and, like many others, this body of work raises more new questions than it answers. Some of these, and suggestions for ways to answer them, are listed below:

- What is the role of alkaline silicate rocks in the generation of (H)REE-related mineralisation in carbonatites?
 - This could potentially be answered through a more thorough and detailed study of the Mauze intrusion, with additional whole-rock data, mapping and geochemistry. Distinguishing magmatic and hydrothermal textures would be key, and the recognition of similar mineral assemblages between Songwe and Mauze could indicate a single source for HREE-bearing apatite.
- How common are whole-rock Y/Ho anomalies in carbonatites, and do these reflect the expulsion of a fluid phase during carbonatite evolution, or do they reflect a more deep seated signature of mantle metasomatism?
 - Initially, it is suggested that a large-scale literature review is undertaken to evaluate how widespread a whole-rock Y/Ho anomaly is in carbonatites. Further work could explore, if the anomaly is caused by expulsion of a fluid with a positive Y/Ho anomaly, what mineral this anomaly is manifested in. For example, fluorite has been suggested as an example of a carbonatite-derived mineral with a positive Y/Ho anomaly (Bühn, 2008). In this thesis it was suggested that the REE-fluorocarbonate minerals could also be a reservoir. This could be tested by using a high spatial resolution trace-element technique, such as SIMS⁵, which could obtain data for all of the REE allowing complete REE distributions.

⁴cathodoluminescence

⁵Secondary Ionisation Mass Spectrometry

- What is the composition of REE-transporting fluids in carbonatite, and what is the role of carbon-bearing species in transporting and depositing the REE?
 - Further research into REE complexes with carbonate ligands is strongly suggested to aid our understanding of the transport and fractionation of the REE in carbonatite-derived fluids. Furthermore, experimental determinations of the partition coefficients for the REE in apatite at low temperatures and pressures would greatly aid the interpretation of trace-element contents in apatite to reconstruct hydrothermal fluid chemistry.

To better constrain how the REE are transported and fractionated in carbonatite-derived hydrothermal fluids, the composition of such fluids needs to be determined. This could occur either through laser-ablation of individual fluid inclusions, or through crush-leach analyses of bulk-inclusion assemblages. Neither, however, is appropriate for determining the composition of fluids at Songwe due to the small size and disrupted nature of the inclusions. Analyses of inclusions at other complexes is recommended to further advance our understanding of REE transport in fluids, and is an area the author is going to work on as part of a post-doctoral study.

Bibliography

JICA⁶ AND MMAJ⁷ 1987. Report on the cooperative mineral exploration in the Chilwa Alkaline area Republic of Malawi, phase I. Technical report, Japan International Cooperation Agency & Metal Mining Agency Of Japan.

JICA AND MMAJ 1988. Report on the cooperative mineral exploration in the Chilwa Alkaline Area Republic of Malawi, phase II. Technical report, Japan International Cooperation Agency & Metal Mining Agency Of Japan.

JICA AND MMAJ 1989a. Report on the cooperative mineral exploration in the Chilwa Alkaline Area Republic of Malawi, consolidated report. Technical report, Japan International Cooperation Agency & Metal Mining Agency Of Japan.

JICA AND MMAJ 1989b. Report on the cooperative mineral exploration in the Chilwa Alkaline Area Republic of Malawi, phase III. Technical report, Japan International Cooperation Agency & Metal Mining Agency Of Japan.

ALLEN, D. E. AND SEYFRIED JR, W. 2005. REE controls in ultramafic hosted MOR hydrothermal systems: an experimental study at elevated temperature and pressure. *Geochimica et Cosmochimica Acta* 69:675–683.

ALONSO, E., SHERMAN, A. M., WALLINGTON, T. J., EVERSON, M. P., FIELD, F. R., ROTH, R., AND KIRCHAIN, R. E. 2012. Evaluating rare earth element availability: A case with revolutionary demand from clean technologies. *Environmental science & technology* 46:3406–3414.

ANDERSEN, J. C., ROLLINSON, G. K., SNOOK, B., HERRINGTON, R., AND FAIRHURST, R. J. 2009. Use of QEMSCAN for the characterization of Ni-rich and Ni-poor goethite in laterite ores. *Minerals Engineering* 22:1119–1129.

ANDERSEN, T. 1984. Secondary processes in carbonatites: petrology of 'Rødberg' (hematite-calcite-dolomite carbonatite) in the Fen central complex, Telemark (South Norway). *Lithos* 17:227–245.

ANDERSEN, T. 1986a. Compositional variation of some rare earth minerals from the Fen complex (Telemark, SE Norway): implications for the mobility of rare earths in a carbonatite system. *Mineralogical Magazine* 50:9.

ANDERSEN, T. 1986b. Magmatic fluids in the Fen carbonatite complex, SE Norway. *Contributions to Mineralogy and Petrology* 93:491–503.

⁶Japan International Co-operation Agency

⁷Metal Mining Agency of Japan

- ANDERSEN, T. 1987a. Mantle and crustal components in a carbonatite complex, and the evolution of carbonatite magma: REE and isotopic evidence from the Fen complex, southeast Norway. *Chemical Geology: Isotope Geoscience section* 65:147–166.
- ANDERSEN, T. 1987b. A model for the evolution of hematite carbonatite, based on whole-rock major and trace element data from the Fen complex, southeast Norway. *Applied geochemistry* 2:163–180.
- ANDERSON, A. J., JAYANETTI, S., MAYANOVIC, R. A., BASSETT, W. A., AND CHOU, I. 2002. X-ray spectroscopic investigations of fluids in the hydrothermal diamond anvil cell: the hydration structure of aqueous La^{3+} up to 300 °C and 1600 bars. *American Mineralogist* 87:262–278.
- ANDRADE, F., MÖLLER, P., AND HÖHNDORF, A. 1999a. The effect of hydrothermal alteration on the Sr and Nd isotopic signatures of the Barra do Itapirapuã carbonatite, southern Brazil. *The Journal of geology* 107:177–191.
- ANDRADE, F., MÖLLER, P., LÜDERS, V., DULSKI, P., AND GILG, H. 1999b. Hydrothermal rare earth elements mineralization in the Barra do Itapirapuã carbonatite, southern Brazil: behaviour of selected trace elements and stable isotopes (C, O). *Chemical geology* 155:91–113.
- ANDREOLI, M., SMITH, C., WATKEYS, M., MOORE, J., ASHWAL, L., AND HART, R. 1994. The geology of the Steenkampskraal monazite deposit, South africa; implications for REE-Th-Cu mineralization in charnockite-granulite terranes. *Economic Geology* 89:994–1016.
- ANOVITZ, L. M. AND ESSENE, E. 1987. Phase equilibria in the system CaCO_3 - MgCO_3 - FeCO_3 . *Journal of Petrology* 28:389–415.
- ASHWAL, L., ARMSTRONG, R., ROBERTS, R., SCHMITZ, M., CORFU, F., HETHERINGTON, C., BURKE, K., AND GERBER, M. 2007. Geochronology of zircon megacrysts from nepheline-bearing gneisses as constraints on tectonic setting: implications for resetting of the U-Pb and Lu-Hf isotopic systems. *Contributions to Mineralogy and Petrology* 153:389–403.
- AYERS, J. C. AND WATSON, E. B. 1991. Solubility of apatite, monazite, zircon, and rutile in supercritical aqueous fluids with implications for subduction zone geochemistry. *Philosophical Transactions of the Royal Society of London. Series A: Physical and Engineering Sciences* 335:365–375.
- AYERS, J. C. AND WATSON, E. B. 1993. Rutile solubility and mobility in supercritical aqueous fluids. *Contributions to Mineralogy and Petrology* 114:321–330.
- AYERS, J. C., ZHANG, L., LUO, Y., AND PETERS, T. 2012. Zircon solubility in alkaline aqueous fluids at upper crustal conditions. *Geochimica et Cosmochimica Acta* 96:18–28.
- BAILEY, D. AND KEARNS, S. 2012. New forms of abundant carbonatite–silicate volcanism: recognition criteria and further target locations. *Mineralogical Magazine* 76:271–284.

- BANKS, D., YARDLEY, B., CAMPBELL, A., AND JARVIS, K. 1994. REE composition of an aqueous magmatic fluid: a fluid inclusion study from the Capitan Pluton, New Mexico, USA. *Chemical Geology* 113:259–272.
- BARKER, D. 1989. Field relations of carbonatites. In K. Bell (ed.), *Carbonatites: genesis and evolution*. Unwin Hyman, London.
- BARRICK, R. E. AND SHOWERS, W. J. 1994. Thermophysiology of *Tyrannosaurus rex*: evidence from oxygen isotopes. *Science* 265:222–224.
- BARTH, T. AND RAMBERG, I. 1966. The Fen circular complex, p. 257. In O. Tuttle and J. Gittins (eds.), *Carbonatites*. Interscience, New York.
- BAU, M. 1991. Rare-earth element mobility during hydrothermal and metamorphic fluid-rock interaction and the significance of the oxidation state of europium. *Chemical Geology* 93:219–230.
- BAU, M. 1996. Controls on the fractionation of isovalent trace elements in magmatic and aqueous systems: evidence from Y/Ho, Zr/Hf, and lanthanide tetrad effect. *Contributions to Mineralogy and Petrology* 123:323–333.
- BAU, M. AND DULSKI, P. 1995. Comparative study of yttrium and rare-earth element behaviours in fluorine-rich hydrothermal fluids. *Contributions to Mineralogy and Petrology* 119:213–223.
- BAU, M. AND DULSKI, P. 1999. Comparing yttrium and rare earths in hydrothermal fluids from the Mid-Atlantic Ridge: implications for Y and REE behaviour during near-vent mixing and for the Y/Ho ratio of Proterozoic seawater. *Chemical Geology* 155:77–90.
- BAU, M., KOSCHINSKY, A., DULSKI, P., AND HEIN, J. R. 1996. Comparison of the partitioning behaviours of yttrium, rare earth elements, and titanium between hydrogenetic marine ferromanganese crusts and seawater. *Geochimica et Cosmochimica Acta* 60:1709–1725.
- BAU, M., ROMER, R. L., LÜDERS, V., AND DULSKI, P. 2003. Tracing element sources of hydrothermal mineral deposits: REE and Y distribution and Sr-Nd-Pb isotopes in fluorite from MVT deposits in the Pennine Orefield, England. *Mineralium Deposita* 38:992–1008.
- BAUER, D., DIAMOND, D., LI, J., SANDALOW, D., TELLEEN, P., AND WANNER, B. 2011. US department of energy critical metals strategy. Electronic Resource.
- BELL, K. AND BLENKINSOP, J. 1989. Neodymium and strontium isotope geochemistry of carbonatites. In *Carbonatites: genesis and evolution*. Unwin Hyman, London.
- BELL, K., KJARSGAARD, B., AND SIMONETTI, A. 1998. Carbonatites—into the twenty-first century. *Journal of Petrology* 39:1839–1845.
- BELL, K. AND SIMONETTI, A. 2010. Source of parental melts to carbonatites—critical isotopic constraints. *Mineralogy and Petrology* 98:77–89.
- BELL, K. AND TILTON, G. 2001. Nd, Pb and Sr isotopic compositions of East African carbonatites: evidence for mantle mixing and plume inhomogeneity. *Journal of Petrology* 42:1927–1945.

- BELLATRECCIA, F., VENTURA, G. D., CAPRILLI, E., WILLIAMS, C., AND PARODI, G. 1999. Crystal-chemistry of zirconolite and calzirtite from Jacupiranga, São Paulo (Brazil). *Mineralogical Magazine* 63:649–649.
- BELOUSOVA, E., GRIFFIN, W., O'REILLY, S. Y., AND FISHER, N. 2002. Apatite as an indicator mineral for mineral exploration: trace-element compositions and their relationship to host rock type. *Journal of Geochemical Exploration* 76:45–69.
- BLACK, L. AND GULSON, B. 1978. The age of the Mud Tank carbonatite, Strangways Range, Northern Territory. *BMR Journal of Australian Geology and Geophysics* 3:227–232.
- BLOOMFIELD, K. 1961. The age of the Chilwa Alkaline Province (unread reference in Bloomfield 1965a).
- BLOOMFIELD, K. 1965a. The geology of the Zomba area. *Bulletin of the Geological Survey of Malawi* 16.
- BLOOMFIELD, K. 1965b. Intracrustal ring-complexes of Southern Malawi. *Memoirs of the Geological Survey of Malawi* 4.
- BLOOMFIELD, K. 1968. The pre-Karoo geology of Malawi. *Memoirs of the Geological Survey of Malawi* 4.
- BODNAR, R. 1993. Revised equation and table for determining the freezing point depression of H₂O–NaCl solutions. *Geochimica et Cosmochimica Acta* 57:683–684.
- BODNAR, R. J. 2003. Introduction to aqueous-electrolyte fluid inclusions. *Fluid Inclusions: Analysis and Interpretation* 32:81–100.
- BOWEN, G. J. 2010. Isoscapes: spatial patterns in isotopic biogeochemistry. *Annual Review of Earth and Planetary Sciences* 38:161–187.
- BOWEN, G. J. AND WILKINSON, B. 2002. Spatial distribution of $\delta^{18}\text{O}$ in meteoric precipitation. *Geology* 30:315–318.
- BRASSINNES, S., BALAGANSKAYA, E., AND DEMAIFFE, D. 2005. Magmatic evolution of the differentiated ultramafic, alkaline and carbonatite intrusion of Vuoriyarvi (Kola Peninsula, Russia). a LA-ICP-MS study of apatite. *Lithos* 85:76–92.
- BROOKINS, D. 1989. Aqueous geochemistry of rare earth elements. *Reviews in Mineralogy and Geochemistry* 21:201–225.
- BUCHERT, M., SCHÜLER, D., AND BLEHER, D. 2009. Critical metals for future sustainable technologies and their recycling potential. Technical report, Öko-Institut e.V.
- BUCKLEY, H. AND WOOLLEY, A. 1990. Carbonates of the magnesite–siderite series from four carbonatite complexes. *Mineralogical Magazine* 54:413–418.
- BÜHN, B. 2008. The role of the volatile phase for REE and Y fractionation in low-silica carbonate magmas: implications from natural carbonatites, Namibia. *Mineralogy and Petrology* 92:453–470.

- BÜHN, B. AND RANKIN, A. 1999. Composition of natural, volatile-rich Na–Ca–REE–Sr carbonatitic fluids trapped in fluid inclusions. *Geochimica et Cosmochimica Acta* 63:3781–3797.
- BÜHN, B., RANKIN, A., SCHNEIDER, J., AND DULSKI, P. 2002. The nature of orthomagmatic, carbonatitic fluids precipitating REE, Sr-rich fluorite: fluid-inclusion evidence from the Okorusu fluorite deposit, Namibia. *Chemical Geology* 186:75–98.
- BÜHN, B., RANKIN, A. H., RADTKE, M., HALLER, M., AND KNOECHEL, A. 1999. Burbankite, a (Sr, REE, Na, Ca)-carbonate in fluid inclusions from carbonatite-derived fluids: Identification and characterization using laser raman spectroscopy, SEM-EDX, and synchrotron micro-XRF analysis. *American Mineralogist* 84:1117–1125.
- BÜHN, B., SCHNEIDER, J., DULSKI, P., AND RANKIN, A. 2003. Fluid–rock interaction during progressive migration of carbonatitic fluids, derived from small-scale trace element and Sr, Pb isotope distribution in hydrothermal fluorite. *Geochimica et Cosmochimica Acta* 67:4577–4595.
- BÜHN, B., WALL, F., AND LE BAS, M. 2001. Rare-earth element systematics of carbonatitic fluorapatites, and their significance for carbonatite magma evolution. *Contributions to Mineralogy and Petrology* 141:572–591.
- BULAKH, A. G., NESTEROV, A. R., AND WILLIAMS, C. T. 2006. Zirconolite, $\text{CaZrTi}_2\text{O}_7$, re-examined from its type locality at Afrikanda, Kola Peninsula, Russia and some Synroc implications. *Neues Jahrbuch für Mineralogie-Abhandlungen: Journal of Mineralogy and Geochemistry* 182:109–121.
- BURKE, K., ASHWAL, L., AND WEBB, S. 2003. New way to map old sutures using deformed alkaline rocks and carbonatites. *Geology* 31:391.
- BURMANN, F., KEIM, M. F., OELMANN, Y., TEIBER, H., MARKS, M. A., AND MARKL, G. 2013. The source of phosphate in the oxidation zone of ore deposits: Evidence from oxygen isotope compositions of pyromorphite. *Geochimica et Cosmochimica Acta* 123:427–439.
- BYRNE, R. H. AND KIM, K.-H. 1993. Rare earth precipitation and coprecipitation behavior: The limiting role of PO_4^{3-} on dissolved rare earth concentrations in seawater. *Geochimica et Cosmochimica Acta* 57:519–526.
- BYRNE, R. H., LEE, J. H., AND BINGLER, L. S. 1991. Rare earth element complexation by PO_4^{3-} ions in aqueous solution. *Geochimica et Cosmochimica Acta* 55:2729–2735.
- CAHEN, L. AND SNELLING, N. 1966. The geochronology of equatorial Africa. North-Holland Publishing Company.
- CAMPBELL, A. R., BANKS, D. A., PHILLIPS, R. S., AND YARDLEY, B. W. 1995. Geochemistry of Th-U-REE mineralizing magmatic fluids, Capitan Mountains, New Mexico. *Economic Geology* 90:1271–1287.
- CAMPBELL, L. S. AND HENDERSON, P. 1997. Apatite paragenesis in the Bayan Obo REE-Nb-Fe ore deposit, Inner Mongolia, China. *Lithos* 42:89–103.

- CAO, M., LI, G., QIN, K., SEITMURATOVA, E. Y., AND LIU, Y. 2012. Major and trace element characteristics of apatites in granitoids from Central Kazakhstan: implications for petrogenesis and mineralization. *Resource Geology* 62:63–83.
- CASTOR, S. 2008. The Mountain Pass rare-earth carbonatite and associated ultrapotassic rocks, California. *The Canadian Mineralogist* 46:779–806.
- CERLING, T. E. AND SHARP, Z. D. 1996. Stable carbon and oxygen isotope analysis of fossil tooth enamel using laser ablation. *Palaeogeography, Palaeoclimatology, Palaeoecology* 126:173–186.
- CETINER, Z. S., WOOD, S. A., AND GAMMONS, C. H. 2005. The aqueous geochemistry of the rare earth elements. part XIV. the solubility of rare earth element phosphates from 23 to 150 C. *Chemical Geology* 217:147–169.
- CHACKO, T., MAYEDA, T. K., CLAYTON, R. N., AND GOLDSMITH, J. R. 1991. Oxygen and carbon isotope fractionations between CO₂ and calcite. *Geochimica et Cosmochimica Acta* 55:2867–2882.
- CHAKHMOURADIAN, A. AND WALL, F. 2012. Rare earth elements: Minerals, mines, magnets (and more). *Elements* 8:333–340.
- CHAKHMOURADIAN, A. R., REGUIR, E. P., AND MITCHELL, R. H. 2002. Strontium-apatite: new occurrences, and the extent of Sr-for-Ca substitution in apatite-group minerals. *The Canadian Mineralogist* 40:121–136.
- CHAKHMOURADIAN, A. R. AND ZAITSEV, A. N. 2012. Rare earth mineralization in igneous rocks: sources and processes. *Elements* 8:347–353.
- CHEN, W. AND SIMONETTI, A. 2013. In-situ determination of major and trace elements in calcite and apatite, and U–Pb ages of apatite from the Oka carbonatite complex: Insights into a complex crystallization history. *Chemical Geology* 353:151–172.
- CHENERY, C. A., PASHLEY, V., LAMB, A. L., SLOANE, H. J., AND EVANS, J. A. 2012. The oxygen isotope relationship between the phosphate and structural carbonate fractions of human bioapatite. *Rapid Communications in Mass Spectrometry* 26:309–319.
- CHU, M.-F., WANG, K.-L., GRIFFIN, W. L., CHUNG, S.-L., OREILLY, S. Y., PEARSON, N. J., AND IIZUKA, Y. 2009. Apatite composition: tracing petrogenetic processes in Transhimalayan granitoids. *Journal of Petrology* 50:1829–1855.
- COLE, C. S., JAMES, R. H., CONNELLY, D. P., AND HATHORNE, E. C. 2014. Rare earth elements as indicators of hydrothermal processes within the East Scotia subduction zone system. *Geochimica et Cosmochimica Acta* .
- COLE, D. R. AND CHAKRABORTY, S. 2001. Rates and mechanisms of isotopic exchange. *Reviews in Mineralogy and Geochemistry* 43:83–223.
- CONWAY, C. M. AND TAYLOR, H. P. 1969. O¹⁸/O¹⁶ and C¹³/C¹² ratios of coexisting minerals in the Oka and Magnet Cove carbonatite bodies. *The Journal of Geology* 77:618–626.

- COOPER, A. AND REID, D. 2000. The association of potassic trachytes and carbonatites at the Dicker Willem Complex, southwest Namibia: coexisting, immiscible, but not cogenetic magmas. *Contributions to Mineralogy and Petrology* 139:570–583.
- CORFU, F., HANCHAR, J. M., HOSKIN, P. W., AND KINNY, P. 2003. Atlas of zircon textures. *Reviews in mineralogy and geochemistry* 53:469–500.
- COSTANZO, A., MOORE, K. R., WALL, F., AND FEELY, M. 2006. Fluid inclusions in apatite from Jacupiranga calcite carbonatites: evidence for a fluid-stratified carbonatite magma chamber. *Lithos* 91:208–228.
- COULSON, I., GOODENOUGH, K., PEARCE, N., AND LENG, M. 2003. Carbonatites and lamprophyres of the Gardar province—a ‘window to the sub-Gardar mantle? *Mineralogical Magazine* 67:855–872.
- COULSON, I. M. 1997. Post-magmatic alteration in eudialyte from the North Qôroq centre, South Greenland. *Mineralogical Magazine* 61:99–109.
- CRADDOCK, P. R., BACH, W., SEEWALD, J. S., ROUXEL, O. J., REEVES, E., AND TIVEY, M. K. 2010. Rare earth element abundances in hydrothermal fluids from the Manus Basin, Papua New Guinea: indicators of sub-seafloor hydrothermal processes in back-arc basins. *Geochimica et Cosmochimica Acta* 74:5494–5513.
- CROLL, R., SWINDEN, S., HALL, M., BROWN, C., BEER, G., SCHEEPERS, J., REDELLINGHUYS, T., WILD, G., AND TRUSLER, G. 2014. Mkango Resources Limited., Songwe REE project, Malawi: NI 43-101 pre-feasibility report. Technical report, MSA Group (Pty) Ltd.
- CROWSON, R. A., SHOWERS, W. J., WRIGHT, E. K., AND HOERING, T. C. 1991. Preparation of phosphate samples for oxygen isotope analysis. *Analytical Chemistry* 63:2397–2400.
- DANIEL BRYANT, J., KOCH, P. L., FROELICH, P. N., SHOWERS, W. J., AND GENNA, B. J. 1996. Oxygen isotope partitioning between phosphate and carbonate in mammalian apatite. *Geochimica et Cosmochimica Acta* 60:5145–5148.
- DAVIDSON, A. AND GOLD, D. P. 1986. Carbonatites, diatremes and ultra-alkaline rocks in the Oka area, Quebec. Geological Association of Canada.
- DAWSON, J. 1962. Sodium carbonate lavas from Oldoinyo Lengai, Tanganyika. *Nature* 195:1075–1076.
- DAWSON, J. AND HINTON, R. 2003. Trace-element content and partitioning in calcite, dolomite and apatite in carbonatite, Phalaborwa, South Africa. *Mineralogical Magazine* 67:921–930.
- DEINES, P. 1970. The carbon and oxygen isotopic composition of carbonates from the Oka carbonatite complex, Quebec, Canada. *Geochimica et Cosmochimica Acta* 34:1199–1225.
- DEINES, P. 1989. Stable isotope variations in carbonatite. *In* Carbonatites: genesis and evolution. Unwin Hyman, London.

- DEINES, P. AND GOLD, D. 1973. The isotopic composition of carbonatite and kimberlite carbonates and their bearing on the isotopic composition of deep-seated carbon. *Geochimica et Cosmochimica Acta* 37:1709–1733.
- DEMÉNY, A., AHIJADO, A., CASILLAS, R., AND VENNEMANN, T. 1998. Crustal contamination and fluid/rock interaction in the carbonatites of Fuerteventura (Canary islands, Spain): a C, O, H isotope study. *Lithos* 44:101–115.
- DEMÉNY, A., SITNIKOVA, M., AND KARCHEVSKY, P. 2004a. Stable C and O isotope compositions of carbonatite complexes of the Kola Alkaline Province: phoscorite-carbonatite relationships and source compositions, p. 407. In F. Wall and A. Zaitsev (eds.), Phoscorites and carbonatites from mantle to mine: the key example of the Kola Alkaline Province, volume 10 of *Mineralogical Society Series*.
- DEMÉNY, A., VENNEMANN, T., AHIJADO, A., AND CASILLAS, R. 2004b. Oxygen isotope thermometry in carbonatites, Fuerteventura, Canary Islands, Spain. *Mineralogy and Petrology* 80:155–172.
- DENNIS, K. J. AND SCHRAG, D. P. 2010. Clumped isotope thermometry of carbonatites as an indicator of diagenetic alteration. *Geochimica et Cosmochimica Acta* 74:4110–4122.
- DIAMOND, L. W. 1992. Stability of CO₂ clathrate hydrate + CO₂ liquid + CO₂ vapour + aqueous KCl-NaCl solutions: Experimental determination and application to salinity estimates of fluid inclusions. *Geochimica et Cosmochimica Acta* 56:273–280.
- DIXEY, F., BISSET, C., AND SMITH, W. 1955. The Chilwa Series of Southern Nyasaland: A group of alkaline and other intrusive and extrusive rocks and associated limestones. *Bulletin of the Geological Survey of Malawi* 5.
- DO CABO, V. 2014. Geological, geochemical and mineralogical characteristics of the HREE-rich carbonatites at Lofdal, Namibia. PhD thesis, University of Exeter.
- DONOVAN, J., HANCHAR, J., PICOLLI, P., SCHRIER, M., BOATNER, L., AND JAROSEWICH, E. 2003. A re-examination of the rare-earth-element orthophosphate standards in use for electron-microprobe analysis. *The Canadian Mineralogist* 41:221–232.
- DOROSHKEVICH, A. G., RIPP, G. S., VILADKAR, S. G., AND VLADYKIN, N. V. 2008. The Arshan REE carbonatites, southwestern Transbaikalia, Russia: mineralogy, paragenesis and evolution. *The Canadian Mineralogist* 46:807–823.
- DOROSHKEVICH, A. G., VILADKAR, S. G., RIPP, G. S., AND BURTSEVA, M. V. 2009. Hydrothermal REE mineralization in the Amba Dongar carbonatite complex, Gujarat, India. *The Canadian Mineralogist* 47:1105–1116.
- DOSTAL, J., KONTAK, D., HANLEY, J., AND OWEN, V. 2011. Geological investigation of rare earth element and uranium deposits of the Bokan mountain complex, Prince of Wales Island, southeastern Alaska. *US Geological Survey Mineral Resources External Research Program Report GO9PA00039 (122 pp.)*

- DOSTAL, J., KONTAK, D. J., AND KARL, S. M. 2014. The early Jurassic Bokan Mountain peralkaline granitic complex (southeastern Alaska): Geochemistry, petrogenesis and rare-metal mineralization. *Lithos* 202:395–412.
- DOUVILLE, E., BIENVENU, P., CHARLOU, J. L., DONVAL, J. P., FOUQUET, Y., APPRIOU, P., AND GAMO, T. 1999. Yttrium and rare earth elements in fluids from various deep-sea hydrothermal systems. *Geochimica et Cosmochimica Acta* 63:627–643.
- DOUVILLE, E., CHARLOU, J., OELKERS, E., BIENVENU, P., JOVE COLON, C., DONVAL, J., FOUQUET, Y., PRIEUR, D., AND APPRIOU, P. 2002. The rainbow vent fluids (36 14 N, MAR): the influence of ultramafic rocks and phase separation on trace metal content in Mid-Atlantic Ridge hydrothermal fluids. *Chemical Geology* 184:37–48.
- DOWMAN, E. 2014. Mineralisation and fluid processes in the alteration zone around the Chilwa Island and Kangankunde carbonatite complexes, Malawi. PhD thesis, Kingston University.
- DURAIWAMI, R. A. AND SHAIKH, T. N. 2014. Fluid-rock interaction in the Kangankunde Carbonatite Complex, Malawi: SEM based evidence for late stage pervasive hydrothermal mineralisation. *Central European Journal of Geosciences* 6:476–491.
- EBY, G., RODEN-TICE, M., KRUEGER, H., EWING, W., FAXON, E., AND WOOLLEY, A. 1995. Geochronology and cooling history of the northern part of the Chilwa Alkaline Province, Malawi. *Journal of African Earth Sciences* 20:275–288.
- EBY, G. N. 1975. Abundance and distribution of the rare-earth elements and yttrium in the rocks and minerals of the Oka carbonatite complex, Quebec. *Geochimica et cosmochimica acta* 39:597–620.
- EGGENKAMP, H. AND KOSTER VAN GROOS, A. 1997. Chlorine stable isotopes in carbonatites: evidence for isotopic heterogeneity in the mantle. *Chemical geology* 140:137–143.
- EILER, J. M., BAUMGARTNER, L. P., AND VALLEY, J. W. 1992. Intercrystalline stable isotope diffusion: a fast grain boundary model. *Contributions to Mineralogy and Petrology* 112:543–557.
- EILER, J. M., GRAHAM, C., AND VALLEY, J. W. 1997. SIMS analysis of oxygen isotopes: matrix effects in complex minerals and glasses. *Chemical Geology* 138:221–244.
- EILER, J. M., VALLEY, J. W., AND BAUMGARTNER, L. P. 1993. A new look at stable isotope thermometry. *Geochimica et Cosmochimica Acta* 57:2571–2583.
- EMSBO, P., MCLAUGHLIN, P. I., BREIT, G. N., DU BRAY, E. A., AND KOENIG, A. E. 2015. Rare earth elements in sedimentary phosphate deposits: Solution to the global REE crisis? *Gondwana Research* 27:776–785.
- ERNST, R. E. AND BELL, K. 2010. Large igneous provinces (LIPs) and carbonatites. *Mineralogy and Petrology* 98:55–76.

- EUROPEAN COMMISSION 2014. Report on critical raw materials for the EU, report of the ad hoc working group on defining critical raw materials. Technical report, European Commission.
- FAN, H.-R., XIE, Y.-H., WANG, K.-Y., TAO, K.-J., AND WILDE, S. A. 2004. REE daughter minerals trapped in fluid inclusions in the giant Bayan Obo REE-Nb-Fe deposit, Inner Mongolia, China. *International Geology Review* 46:638–645.
- FARQUHAR, J., CHACKO, T., AND FROST, B. R. 1993. Strategies for high-temperature oxygen isotope thermometry: a worked example from the Laramie Anorthosite Complex, Wyoming, USA. *Earth and Planetary Science Letters* 117:407–422.
- FARRELL, S., BELL, K., AND CLARK, I. 2010. Sulphur isotopes in carbonatites and associated silicate rocks from the Superior Province, Canada. *Mineralogy and Petrology* 98:209–226.
- FIRSCHING, F. H. AND BRUNE, S. N. 1991. Solubility products of the trivalent rare-earth phosphates. *Journal of chemical and engineering data* 36:93–95.
- FLEET, M. E. AND PAN, Y. 1995. Site preference of rare earth elements in fluorapatite. *American Mineralogist* 80:329–335.
- FLEET, M. E. AND PAN, Y. 1997a. Rare earth elements in apatite: Uptake from H₂O-bearing phosphate-fluoride melts and the role of volatile components. *Geochimica et Cosmochimica Acta* 61:4745–4760.
- FLEET, M. E. AND PAN, Y. 1997b. Site preference of rare earth elements in fluorapatite: Binary (LREE + HREE)-substituted crystals. *American Mineralogist* 82:870–877.
- FLEISCHER, M. AND ALTSCHULER, Z. 1986. The lanthanides and yttrium in minerals of the apatite group — an analysis of the available data. *Neues Jahrbuch fuer Mineralogie, Monatshefte* .
- FÖRSTER, H.-J. 1998. The chemical composition of REE-Y-Th-U-rich accessory minerals in peraluminous granites of the Erzgebirge-Fichtelgebirge region, Germany; part II, xenotime. *American Mineralogist* 83:1302–1315.
- FÖRSTER, H.-J. 2006. Composition and origin of intermediate solid solutions in the system thorite–xenotime–zircon–coffinite. *Lithos* 88:35–55.
- FORTIER, S. M. AND LÜTTGE, A. 1995. An experimental calibration of the temperature dependence of oxygen isotope fractionation between apatite and calcite at high temperatures (350–800 C). *Chemical geology* 125:281–290.
- GAGNON, J. E., SAMSON, I. M., FRYER, B. J., AND WILLIAMS-JONES, A. E. 2003. Compositional heterogeneity in fluorite and the genesis of fluorite deposits: insights from LA-ICP-MS analysis. *The Canadian Mineralogist* 41:365–382.
- GAMMONS, C., WOOD, S., AND WILLIAMS-JONES, A. 1996. The aqueous geochemistry of the rare earth elements and yttrium: VI. stability of neodymium chloride complexes from 25 to 300 C. *Geochimica et Cosmochimica Acta* 60:4615–4630.

- GAMMONS, C. H., WOOD, S. A., AND LI, Y. 2002. Complexation of the rare earth elements with aqueous chloride at 200 C and 300 C and saturated water vapor pressure. *Geochemical Society Special Publications* 7:191–207.
- GARSON, M. 1962. The Tundulu carbonatite ring-complex in southern Nyasaland. *Memoirs of the Geological Survey of Malawi* 2.
- GARSON, M. 1965. Carbonatites in southern Malawi. *Bulletin of the Geological Survey of Malawi* 15.
- GARSON, M. AND SMITH, W. 1958. Chilwa Island. *Memoirs of the Geological Survey of Malawi* 1.
- GARSON, M. AND SMITH, W. 1965. Carbonatite and agglomeratic vents in the western Shire Valley. *Memoirs of the Geological Survey of Malawi* 3.
- GARSON, M. AND WALSHAW, R. 1969. The geology of the Mlanje area. *Bulletin of the Geological Survey of Malawi* 21.
- GARVIE-LOK, S. J., VARNEY, T. L., AND KATZENBERG, M. A. 2004. Preparation of bone carbonate for stable isotope analysis: the effects of treatment time and acid concentration. *Journal of Archaeological Science* 31:763–776.
- GEOSTATS accessed 2015. Certified rare earth reference material - GRE-04.
- GIANFAGNA, A., MAZZIOTTI-TAGLIANI, S., CROCE, A., ALLEGRINA, M., AND RINAUDO, C. 2015. As-rich apatite from Mt. Calvario: Characterization by micro-Raman spectroscopy. *The Canadian Mineralogist*.
- GIERÉ, R. 1996. Formation of rare earth minerals in hydrothermal systems, pp. 105–150. In A. Jones, F. Wall, and C. Williams (eds.), Rare Earth Minerals. Chemistry, origin and ore deposits, volume 6 of *Mineralogical Society Series*.
- GILBERT, C. AND WILLIAMS-JONES, A. 2008. Vapour transport of rare earth elements (REE) in volcanic gas: Evidence from encrustations at Oldoinyo Lengai. *Journal of Volcanology and Geothermal Research* 176:519–528.
- GITTINS, J. 1989. The origin and evolution of carbonatite magmas, pp. 580–600. In K. Bell (ed.), Carbonatites: genesis and evolution. Unwin Hyman, London.
- GITTINS, J., BECKETT, M. F., AND JAGO, B. C. 1990. Composition of the fluid phase accompanying carbonatite magma; a critical examination. *American Mineralogist* 75:1106–1109.
- GITTINS, J. AND HARMER, R. 1997. What is ferrocarnatite? a revised classification. *Journal of African Earth Sciences* 25:159–168.
- GOMIDE, C. S., BROD, J. A., JUNQUEIRA-BROD, T. C., BUHN, B. M., SANTOS, R. V., BARBOSA, E. S. R., CORDEIRO, P. F. O., PALMIERI, M., GRASSO, C. B., AND TORRES, M. G. 2013. Sulfur isotopes from Brazilian alkaline carbonatite complexes. *Chemical Geology* 341:38–49.
- GREENWOOD, J. P., BLAKE, R. E., AND COATH, C. D. 2003. Ion microprobe measurements of $^{18}\text{O}/^{16}\text{O}$ ratios of phosphate minerals in the martian meteorites ALH84001 and Los Angeles. *Geochimica et Cosmochimica Acta* 67:2289–2298.

- GRIMES, S. T., COLLINSON, M. E., HOOKER, J. J., AND MATTEY, D. P. 2008. Is small beautiful? a review of the advantages and limitations of using small mammal teeth and the direct laser fluorination analysis technique in the isotope reconstruction of past continental climate change. *Palaeogeography, Palaeoclimatology, Palaeoecology* 266:39–50.
- GÜLTEKIN, A. H., ÖRGÜN, Y., AND SUNER, F. 2003. Geology, mineralogy and fluid inclusion data of the Kizilcaören fluorite–barite–REE deposit, Eskisehir, Turkey. *Journal of Asian Earth Sciences* 21:365–376.
- GYSI, A. P. AND WILLIAMS-JONES, A. E. 2013. Hydrothermal mobilization of pegmatite-hosted REE and Zr at Strange Lake, Canada: A reaction path model. *Geochimica et Cosmochimica Acta* 122:324–352.
- GYSI, A. P. AND WILLIAMS-JONES, A. E. 2014. The thermodynamic properties of bastnäsite-(Ce) and parisite-(Ce). *Chemical Geology* .
- GYSI, A. P., WILLIAMS-JONES, A. E., AND HARLOV, D. 2015. The solubility of xenotime-(Y) and other HREE phosphates (DyPo₄, ErPo₄ and YbPo₄) in aqueous solutions from 100 to 250 C and p_{sat} . *Chemical Geology* .
- HAAS, J. R., SHOCK, E. L., AND SASSANI, D. C. 1995. Rare earth elements in hydrothermal systems: estimates of standard partial molal thermodynamic properties of aqueous complexes of the rare earth elements at high pressures and temperatures. *Geochimica et Cosmochimica Acta* 59:4329–4350.
- HALAMA, R., VENNEMANN, T., SIEBEL, W., AND MARKL, G. 2005. The Grønnedal-ika carbonatite–syenite complex, South Greenland: carbonatite formation by liquid immiscibility. *Journal of Petrology* 46:191–217.
- HAMMOUDA, T., CHANTEL, J., AND DEVIDAL, J.-L. 2010. Apatite solubility in carbonatitic liquids and trace element partitioning between apatite and carbonatite at high pressure. *Geochimica et Cosmochimica Acta* 74:7220–7235.
- HARMER, R. AND GITTINS, J. 1997. The origin of dolomitic carbonatites: field and experimental constraints. *Journal of African Earth Sciences* 25:5–28.
- HARMER, R. AND GITTINS, J. 1998. The case for primary, mantle-derived carbonatite magma. *Journal of Petrology* 39:1895–1903.
- HATCH, G. 2011. Critical rare earths. global supply and demand projections and the leading contenders for new sources of supply. Technical report, Technology Metals Research.
- HATCH, G. 2012. Dynamics in the global market for rare earths. *Elements* 8:341–346.
- HAYNES, E. A., MOECHER, D. P., AND SPICUZZA, M. J. 2003. Oxygen isotope composition of carbonates, silicates, and oxides in selected carbonatites: constraints on crystallization temperatures of carbonatite magmas. *Chemical Geology* 193:43–57.
- HEAMAN, L. M. 2009. The application of U–Pb geochronology to mafic, ultramafic and alkaline rocks: an evaluation of three mineral standards. *Chemical Geology* 261:43–52.

- HEINRICH, E. W. AND MOORE, D. 1970. Metasomatic potash feldspar rocks associated with igneous alkalic complexes. *The Canadian Mineralogist* 10:571–584.
- HENDERSON, P. 1996. The rare earth elements: introduction and review, pp. 1–19. In W. F. W. C. Jones, A.P. (ed.), Rare earth minerals: Chemistry, origin and ore deposits, volume 6 of *Mineralogical Society Series*, chapter 1. Chapman & Hall.
- HENDERSON, P., GLUYAS, J., GUNN, A., WALL, F., AND WOOLLEY, A. 2011. Rare earth elements briefing note. Technical report, The Geological Society of London.
- HIATT, E. AND PUFAHL, P. 2014. Cathodoluminescence petrography of carbonate rocks: a review of application for understanding diagenesis, reservoir quality, and pore system evolution, p. 75. In I. Coulson (ed.), Cathodoluminescence and its application to geoscience, volume 45 of *Short course Series*. Mineralogical Association of Canada.
- HOATSON, D., JAIRETH, S., AND MIEZITIS, Y. 2011. The major rare-earth-element deposits of Australia: geological setting, exploration, and resources. Technical report, Geoscience Australia.
- HOEFS, J. 2008. Stable isotope geochemistry. Springer.
- HOGARTH, D. 1989. Pyrochlore, apatite and amphibole: distinctive minerals in carbonatite, pp. 105–148. In K. Bell (ed.), Carbonatites: genesis and evolution. Unwin Hyman, London.
- HÖGDAHL, K. AND JONSSON, E. 1999. Age and mineral assemblages of apatitic pegmatites in the Chilwa Alkaline Province, Malawi, SE Africa. *Journal of Conference Abstracts* 4:767.
- HÖGDAHL, K. AND JONSSON, E. 2002. CL characteristics versus Th, U, Hf contents in alkaline pegmatite-hosted zircon. In J. SS (ed.), The 25th nordic geological winter meeting January 6th–9th 2002. Reykjavik, Iceland, Abstract Volume.
- HOLMDEN, C., PAPANASTASSIOU, D., AND WASSERBURG, G. 1997. Negative thermal ion mass spectrometry of oxygen in phosphates. *Geochimica et cosmochimica acta* 61:2253–2263.
- HOLTSTAM, D. AND ANDERSSON, U. B. 2007. The REE minerals of the Bastnäs-type deposits, south-central Sweden. *The Canadian Mineralogist* 45:1073–1114.
- HOLTSTAM, D., ANDERSSON, U. B., BROMAN, C., AND MANSFELD, J. 2014. Origin of REE mineralization in the Bastnäs-type Fe-REE-(Cu-Mo-Bi-Au) deposits, Bergslagen, Sweden. *Mineralium Deposita* pp. 1–34.
- HORNIG-KJARSGAARD, I. 1998. Rare earth elements in sövitic carbonatites and their mineral phases. *Journal of Petrology* 39:2105–2121.
- HORSTMANN, U. E. AND VERWOERD, W. J. 1997. Carbon and oxygen isotope variations in southern African carbonatites. *Journal of African Earth Sciences* 25:115–136.

- HOU, Z., TIAN, S., XIE, Y., YANG, Z., YUAN, Z., YIN, S., YI, L., FEI, H., ZOU, T., BAI, G., ET AL. 2009. The Himalayan Mianning–Dechang REE belt associated with carbonatite–alkaline complexes, eastern Indo-Asian collision zone, SW China. *Ore Geology Reviews* 36:65–89.
- HSIEH, P.-S., CHEN, C.-H., YANG, H.-J., AND LEE, C.-Y. 2008. Petrogenesis of the Nanling Mountains granites from South China: constraints from systematic apatite geochemistry and whole-rock geochemical and Sr–Nd isotope compositions. *Journal of Asian Earth Sciences* 33:428–451.
- HUBBERTEN, H.-W., KATZ-LEHNERT, K., AND KELLER, J. 1988. Carbon and oxygen isotope investigations in carbonatites and related rocks from the Kaiserstuhl, Germany. *Chemical geology* 70:257–274.
- HUMPHRIES, M. 2013. Rare earth elements: The global supply chain. Technical report, Congressional Research Service.
- IHLEN, P. M., SCHIELLERUP, H., GAUTNEB, H., AND SKÅR, Ø. 2014. Characterization of apatite resources in Norway and their REE potentiala review. *Ore Geology Reviews* 58:126–147.
- JACKSON, S. E., PEARSON, N. J., GRIFFIN, W. L., AND BELOUSOVA, E. A. 2004. The application of laser ablation-inductively coupled plasma-mass spectrometry to in situ U–Pb zircon geochronology. *Chemical Geology* 211:47–69.
- JAFFEY, A., FLYNN, K., GLENDENIN, L., BENTLEY, W. T., AND ESSLING, A. 1971. Precision measurement of half-lives and specific activities of U 235 and U 238. *Physical Review C* 4:1889.
- JAGO, B. C. AND GITTINS, J. 1991. The role of fluorine in carbonatite magma evolution. *Nature* 349:56–58.
- JAROSEWICH, E. AND BOATNER, L. 1991. Rare-earth element reference samples for electron microprobe analysis. *Geostandards Newsletter* 15:397–399.
- JIANG, N., SUN, S., CHU, X., MIZUTA, T., AND ISHIYAMA, D. 2003. Mobilization and enrichment of high-field strength elements during late- and post-magmatic processes in the Shuiquangou syenitic complex, Northern China. *Chemical Geology* 200:117–128.
- JOHANNESSON, K. H., STETZENBACH, K. J., HODGE, V. F., AND BERRY LYONS, W. 1996. Rare earth element complexation behavior in circumneutral pH groundwaters: assessing the role of carbonate and phosphate ions. *Earth and Planetary Science Letters* 139:305–319.
- JOHNSON, C. M., BELL, K., BEARD, B. L., AND SHULTIS, A. I. 2010. Iron isotope compositions of carbonatites record melt generation, crystallization, and late-stage volatile-transport processes. *Mineralogy and Petrology* 98:91–110.
- JONES, A. 1989. Upper-mantle enrichment by kimberlitic or carbonatitic magmatism. In K. Bell (ed.), *Carbonatites, Genesis and Evolution*. Unwin Hyman.
- JONES, A. AND EKAMBARAM, V. 1985. New INAA analysis of a mantle-derived titanate mineral of the crichtonite series, with particular reference to the rare earth elements. *American Mineralogist* 70:414–418.

- JONES, A. M., IACUMIN, P., AND YOUNG, E. D. 1999. High-resolution $\delta^{18}\text{O}$ analysis of tooth enamel phosphate by isotope ratio monitoring gas chromatography mass spectrometry and ultraviolet laser fluorination. *Chemical Geology* 153:241–248.
- JONES, A. P., GENGE, M., AND CARMODY, L. 2013. Carbonate melts and carbonatites. *Reviews in Mineralogy and Geochemistry* 75:289–322.
- JONES, A. P. AND WYLLIE, P. J. 1983. Low-temperature glass quenched from a synthetic, rare earth carbonatite; implications for the origin of the Mountain Pass Deposit, California. *Economic Geology* 78:1721–1723.
- KAPUSTIN, I. 1980. Mineralogy of carbonatites. Amerind Publishing Co.
- KASIOPTAS, A., GEISLER, T., PERDIKOURI, C., TREPMMANN, C., GUSSONE, N., AND PUTNIS, A. 2011. Polycrystalline apatite synthesized by hydrothermal replacement of calcium carbonates. *Geochimica et Cosmochimica Acta* 75:3486–3500.
- KASIOPTAS, A., PERDIKOURI, C., PUTNIS, C., AND PUTNIS, A. 2008. Pseudomorphic replacement of single calcium carbonate crystals by polycrystalline apatite. *Mineralogical Magazine* 72:77–80.
- KATO, Y., FUJINAGA, K., NAKAMURA, K., TAKAYA, Y., KITAMURA, K., OHTA, J., TODA, R., NAKASHIMA, T., AND IWAMORI, H. 2011. Deep-sea mud in the Pacific Ocean as a potential resource for rare-earth elements. *Nature Geoscience* 4:535–539.
- KELLER, J. 1981. Carbonatitic volcanism in the Kaiserstuhl alkaline complex: evidence for highly fluid carbonatitic melts at the Earth's surface. *Journal of Volcanology and Geothermal Research* 9:423–431.
- KELLER, J. AND HOEFS, J. 1995. Stable isotope characteristics of recent natrocarbonatites from Oldoinyo Lengai, pp. 113–123. In K. Bell and J. Keller (eds.), *Carbonatite Volcanism*. Springer.
- KEMPE, U. AND GÖTZE, J. 2002. Cathodoluminescence (CL) behaviour and crystal chemistry of apatite from rare-metal deposits. *Mineralogical Magazine* 66:151–172.
- KEMPE, U., MÖCKEL, R., GRAUPNER, T., KYNICKY, J., AND DOMBON, E. 2014. The genesis of Zr–Nb–REE mineralisation at Khalzan Buregte (Western Mongolia) reconsidered. *Ore Geology Reviews* .
- KEPPLER, H. 1993. Influence of fluorine on the enrichment of high field strength trace elements in granitic rocks. *Contributions to Mineralogy and Petrology* 114:479–488.
- KLEMME, S. AND DALPÉ, C. 2003. Trace-element partitioning between apatite and carbonatite melt. *American Mineralogist* 88:639–646.
- KLINKHAMMER, G., ELDERFIELD, H., EDMOND, J., AND MITRA, A. 1994. Geochemical implications of rare earth element patterns in hydrothermal fluids from mid-ocean ridges. *Geochimica et Cosmochimica Acta* 58:5105–5113.

- KLUNGNESS, G. D. AND BYRNE, R. H. 2000. Comparative hydrolysis behavior of the rare earths and yttrium: the influence of temperature and ionic strength. *Polyhedron* 19:99–107.
- KOCH, P. L., TUROSS, N., AND FOGEL, M. L. 1997. The effects of sample treatment and diagenesis on the isotopic integrity of carbonate in biogenic hydroxylapatite. *Journal of Archaeological Science* 24:417–429.
- KOHN, M. J. AND CERLING, T. E. 2002. Stable isotope compositions of biological apatite. *Reviews in mineralogy and geochemistry* 48:455–488.
- KOLODNY, Y., LUZ, B., AND NAVON, O. 1983. Oxygen isotope variations in phosphate of biogenic apatites, I. fish bone apatite—rechecking the rules of the game. *Earth and Planetary Science Letters* 64:398–404.
- KRASNOVA, N., PETROV, T., BALAGANASKAYA, E., GARCIA, G., MOUTTE, J., ZAITSEV, A., WALL, F., WALL, F., AND ZAITSEV, A. 2004. Introduction to phoscorites: occurrence, composition, nomenclature and petrogenesis. In F. Wall and A. Zaitsev (eds.), *Phoscorites and carbonatites from mantle to mine: the key example of the Kola alkaline province*, number 10 in Mineralogical Society Series.
- KRAVCHENKO, S. AND POKROVSKY, B. 1995. The Tomtor alkaline ultrabasic massif and related REE-Nb deposits, Northern Siberia. *Economic Geology* 90:676–689.
- KRENN, E., HARLOV, D. E., FINGER, F., AND WUNDER, B. 2012. LREE-redistribution among fluorapatite, monazite, and allanite at high pressures and temperatures. *American Mineralogist* 97:1881–1890.
- KRÖNER, A., WILLNER, A., HEGNER, E., JAECKEL, P., AND NEMCHIN, A. 2001. Single zircon ages, PT evolution and Nd isotopic systematics of high-grade gneisses in southern Malawi and their bearing on the evolution of the Mozambique belt in southeastern Africa. *Precambrian Research* 109:257–291.
- KYNICKY, J., CHAKHMOURADIAN, A. R., XU, C., KRMICEK, L., AND GALIOVA, M. 2011. Distribution and evolution of zirconium mineralization in peralkaline granites and associated pegmatites of the Khan Bogd complex, southern Mongolia. *The Canadian Mineralogist* 49:947–965.
- KYNICKY, J., SMITH, M. P., AND XU, C. 2012. Diversity of rare earth deposits: the key example of China. *Elements* 8:361–367.
- LAPORTE, D., HOLMDEN, C., PATTERSON, W., PROKOPIUK, T., AND EGLINGTON, B. 2009. Oxygen isotope analysis of phosphate: improved precision using TC/EA CF-IRMS. *Journal of mass spectrometry* 44:879–890.
- LE BAS, M. 1981. Carbonatite magmas. *Mineralogical Magazine* 44:133–140.
- LE BAS, M. 1987. Ultra-alkaline magmatism with or without rifting. *Tectonophysics* 143:75–84.
- LE BAS, M. 1989. Diversification of carbonatite. In K. Bell (ed.), *Carbonatites: genesis and evolution*. Unwin Hyman, London.

- LE BAS, M. 1999. Sovite and alvikite; two chemically distinct calciocarbonatites C1 and C2. *South African Journal of Geology* 102:109–121.
- LE BAS, M. 2008. Fenites associated with carbonatites. *The Canadian Mineralogist* 46:915–932.
- LE BAS, M. AND HANDLEY, C. 1979. Variation in apatite composition in ijolitic and carbonatitic igneous rocks.
- LE BAS, M. J. 1977. Carbonatite-nephelinite volcanism: an African case history. John Wiley & Sons.
- LE MAITRE, R. 2002. Igneous rocks: a classification and glossary of terms: recommendations of the International Union of Geological Sciences, Subcommittee on the Systematics of Igneous Rocks. Cambridge Univ Pr.
- LÉCUYER, C., BALTER, V., MARTINEAU, F., FOUREL, F., BERNARD, A., AMIOT, R., GARDIEN, V., OTERO, O., LEGENDRE, S., PANCZER, G., ET AL. 2010. Oxygen isotope fractionation between apatite-bound carbonate and water determined from controlled experiments with synthetic apatites precipitated at 10–37 C. *Geochimica et Cosmochimica Acta* 74:2072–2081.
- LÉCUYER, C., FOUREL, F., MARTINEAU, F., AMIOT, R., BERNARD, A., DAUX, V., ESCARGUEL, G., AND MORRISON, J. 2007. High-precision determination of $^{18}\text{O}/^{16}\text{O}$ ratios of silver phosphate by EA-pyrolysis-IRMS continuous flow technique. *Journal of Mass Spectrometry* 42:36–41.
- LÉCUYER, C., GARDIEN, V., RIGAUDIER, T., FOUREL, F., MARTINEAU, F., AND CROS, A. 2009. Oxygen isotope fractionation and equilibration kinetics between CO_2 and H_2O as a function of salinity of aqueous solutions. *Chemical Geology* 264:122–126.
- LÉCUYER, C., GRANDJEAN, P., AND EMIG, C. 1996. Determination of oxygen isotope fractionation between water and phosphate from living lingulids: potential application to palaeoenvironmental studies. *Palaeogeography, Palaeoclimatology, Palaeoecology* 126:101–108.
- LÉCUYER, C., GRANDJEAN, P., AND SHEPPARD, S. M. 1999. Oxygen isotope exchange between dissolved phosphate and water at temperatures ≤ 135 C: inorganic versus biological fractionations. *Geochimica et Cosmochimica Acta* 63:855–862.
- LÉCUYER, C., PICARD, S., GARCIA, J.-P., SHEPPARD, S. M., GRANDJEAN, P., AND DROMART, G. 2003. Thermal evolution of Tethyan surface waters during the Middle-Late Jurassic: Evidence from $\delta^{18}\text{O}$ values of marine fish teeth. *Paleoceanography* 18.
- LEE, W.-J. AND WYLLIE, P. J. 1997. Liquid immiscibility between nephelinite and carbonatite from 1.0 to 2.5 GPa compared with mantle melt compositions. *Contributions to Mineralogy and Petrology* 127:1–16.
- LEE, W.-J. AND WYLLIE, P. J. 1998. Processes of crustal carbonatite formation by liquid immiscibility and differentiation, elucidated by model systems. *Journal of Petrology* 39:2005–2013.

- LEWIS, A., KOMNINO, A., YARDLEY, B., AND PALMER, M. 1998. Rare earth element speciation in geothermal fluids from Yellowstone National Park, Wyoming, USA. *Geochimica et Cosmochimica Acta* 62:657–663.
- LEWIS, A. J., PALMER, M. R., STURCHIO, N. C., AND KEMP, A. J. 1997. The rare earth element geochemistry of acid-sulphate and acid-sulphate-chloride geothermal systems from Yellowstone National Park, Wyoming, USA. *Geochimica et Cosmochimica Acta* 61:695–706.
- LIFEROVICH, R. AND MITCHELL, R. 2006. Apatite-group minerals from nepheline syenite, Pilansberg alkaline complex, South Africa. *Mineralogical Magazine* 70:463–484.
- LING, M.-X., LIU, Y.-L., WILLIAMS, I. S., TENG, F.-Z., YANG, X.-Y., DING, X., WEI, G.-J., XIE, L.-H., DENG, W.-F., AND SUN, W.-D. 2013. Formation of the world's largest REE deposit through protracted fluxing of carbonatite by subduction-derived fluids. *Scientific reports* 3:1776.
- LINGDI, Z. AND YANGCHUAN, W. 1989. REE geochemical characteristics of apatite, sphene and zircon from alkaline rocks. *Chinese Journal of Geochemistry* 8:245–253.
- LITTLER, K., RHL, U., WESTERHOLD, T., AND ZACHOS, J. C. 2014. A high-resolution benthic stable-isotope record for the south atlantic: Implications for orbital-scale changes in late paleocene/early eocene climate and carbon cycling. *Earth and Planetary Science Letters* 401:18 – 30.
- LIU, C.-Q. AND ZHANG, H. 2005. The lanthanide tetrad effect in apatite from the Altay No. 3 pegmatite, Xingjiang, China: an intrinsic feature of the pegmatite magma. *Chemical geology* 214:61–77.
- LIU, X. AND BYRNE, R. H. 1997. Rare earth and yttrium phosphate solubilities in aqueous solution. *Geochimica et Cosmochimica Acta* 61:1625–1633.
- LIU, X. AND BYRNE, R. H. 1998. Comprehensive investigation of yttrium and rare earth element complexation by carbonate ions using ICP–mass spectrometry. *Journal of solution chemistry* 27:803–815.
- LOGES, A., MIGDISOV, A. A., WAGNER, T., WILLIAMS-JONES, A. E., AND MARKL, G. 2013. An experimental study of the aqueous solubility and speciation of Y (III) fluoride at temperatures up to 250 C. *Geochimica et Cosmochimica Acta* 123:403–415.
- LONG, K., VAN GOSEN, B., FOLEY, N., AND CORDIER, D. 2010. The principal rare earth elements deposits of the United States— a summary of domestic deposits and a global perspective. Technical report, Geological Survey Scientific Investigations Report 20105220.
- LOTTERMOSER, B. 1990. Rare-earth element mineralisation within the Mt Weld carbonatite laterite, Western Australia. *Lithos* 24:151–167.
- LOTTERMOSER, B. 1992. Rare earth elements and hydrothermal ore formation processes. *Ore Geology Reviews* 7:25–41.

- LOTTERMOSER, B. G. 1987. Churchite from the Mt Weld carbonatite laterite, Western Australia. *Mineralogical Magazine* 51:468–469.
- LUDWIG, K. 2009. Isoplot v. 4 for Excel 2007. *Berkeley Geochronological Centre, Berkeley, California*.
- LUO, Y., HUGHES, J. M., RAKOVAN, J., AND PAN, Y. 2009. Site preference of U and Th in Cl, F, and Sr apatites. *American Mineralogist* 94:345–351.
- LUO, Y., RAKOVAN, J., TANG, Y., LUPULESCU, M., HUGHES, J. M., AND PAN, Y. 2011. Crystal chemistry of Th in fluorapatite. *American Mineralogist* 96:23–33.
- LUO, Y.-R. AND BYRNE, R. H. 2000. The ionic strength dependence of rare earth and yttrium fluoride complexation at 25 C. *Journal of solution chemistry* 29:1089–1099.
- LUO, Y.-R. AND BYRNE, R. H. 2001. Yttrium and rare earth element complexation by chloride ions at 25 C. *Journal of solution chemistry* 30:837–845.
- LUO, Y.-R. AND BYRNE, R. H. 2004. Carbonate complexation of yttrium and the rare earth elements in natural waters. *Geochimica et Cosmochimica Acta* 68:691–699.
- LUSTY, P. AND WALTERS, A. 2011. Rare earth elements. *British Geological Survey*.
- MACDONALD, R., BAGIŃSKI, B., DZIERŻANOWSKI, P., AND JOKUBAUSKAS, P. 2013. Apatite-supergroup minerals in UK palaeogene granites: composition and relationship to host-rock composition. *European Journal of Mineralogy* 25:461–471.
- MACDONALD, R., CROSSLEY, R., AND WATERHOUSE, K. 1983. Karoo basalts of southern Malawi and their regional petrogenetic significance. *Mineralogical Magazine* 47:281–289.
- MALONE, M. J., BAKER, P. A., AND BURNS, S. J. 1996. Recrystallization of dolomite: An experimental study from 50 to 200 C. *Geochimica et Cosmochimica Acta* 60:2189 – 2207.
- MANGLER, M. F., MARKS, M. A., ZAITZEV, A. N., EBY, G. N., AND MARKL, G. 2014. Halogens (F, Cl and Br) at Oldoinyo Lengai volcano (Tanzania): Effects of magmatic differentiation, silicate–natrocarbonatite melt separation and surface alteration of natrocarbonatite. *Chemical Geology* 365:43–53.
- MARIANO, A. N. 1989. Nature of economic mineralization in carbonatites and related rocks, pp. 149–176. *In* K. Bell (ed.), *Carbonatites: genesis and evolution*. Unwin Hyman, London.
- MARIANO, A. N. AND MARIANO, A. 2012. Rare earth mining and exploration in North America. *Elements* 8:369–376.
- MARIANO, A. N. AND MARIANO, A. 2014. Cathodoluminescence as a tool in mineral exploration, p. 97. *In* I. Coulson (ed.), *Cathodoluminescence and its application to geoscience*, volume 45 of *Short course Series*. Mineralogical Association of Canada.

- MARKS, M. A., NEUKIRCHEN, F., VENNEMANN, T., AND MARKL, G. 2009. Textural, chemical, and isotopic effects of late-magmatic carbonatitic fluids in the carbonatite–syenite Tamazeght complex, High Atlas Mountains, Morocco. *Mineralogy and Petrology* 97:23–42.
- MARSHALL, D. 1988. Cathodoluminescence of geological materials. Unwin Hyman.
- MASAU, M., ČERNÝ, P., AND CHAPMAN, R. 2000. Dysprosian xenotime-(Y) from the Annie Claim# 3 granitic pegmatite, southeastern Manitoba, Canada: evidence of the tetrad effect? *The Canadian Mineralogist* 38:899–905.
- MATTEY, D. P., TAYLOR, W., GREEN, D., AND PILLINGER, C. 1990. Carbon isotopic fractionation between CO₂ vapour, silicate and carbonate melts: an experimental study to 30 kbar. *Contributions to Mineralogy and Petrology* 104:492–505.
- MAYANOVIC, R. A., ANDERSON, A. J., BASSETT, W. A., CHOU, I., ET AL. 2007. On the formation and structure of rare-earth element complexes in aqueous solutions under hydrothermal conditions with new data on gadolinium aqua and chloro complexes. *Chemical geology* 239:266–283.
- MAYANOVIC, R. A., ANDERSON, A. J., BASSETT, W. A., CHOU, I., ET AL. 2009a. The structure and stability of aqueous rare-earth elements in hydrothermal fluids: new results on neodymium (III) aqua and chloroaqua complexes in aqueous solutions to 500 C and 520 MPa. *Chemical Geology* 259:30–38.
- MAYANOVIC, R. A., ANDERSON, A. J., BASSETT, W. A., AND CHOU, I.-M. 2009b. Steric hindrance and the enhanced stability of light rare-earth elements in hydrothermal fluids. *American Mineralogist* 94:1487–1490.
- MAYANOVIC, R. A., JAYANETTI, S., ANDERSON, A. J., BASSETT, W. A., AND CHOU, I.-M. 2002. The structure of Yb³⁺ aquo ion and chloro complexes in aqueous solutions at up to 500 C and 270 MPa. *The Journal of Physical Chemistry A* 106:6591–6599.
- MCCREATH, J., FINCH, A., SIMONSEN, S., DONALDSON, C., AND ARMOUR-BROWN, A. 2012. Independent ages of magmatic and hydrothermal activity in alkaline igneous rocks: The Motzfeldt Centre, Gardar Province, South Greenland. *Contributions to Mineralogy and Petrology* 163:967–982.
- MCDONOUGH, W. AND SUN, S. 1995. The composition of the Earth. *Chemical Geology* 120:223–253.
- MCLAUGHLIN, K., SILVA, S., KENDALL, C., STUART-WILLIAMS, H., AND PAYTAN, A. 2004. A precise method for the analysis of δ¹⁸O of dissolved inorganic phosphate in seawater. *Limnology and Oceanography: Methods* 2:202–212.
- MCLENNAN, S. M. 1994. Rare earth element geochemistry and the “tetrad” effect. *Geochimica et Cosmochimica Acta* 58:2025–2033.
- MCWHA, M. AND SMEE, B. 2011. AMIS0185.

- MEEN, J. K., EGGLE, D. H., AND AYERS, J. 1989. Experimental evidence for very low solubility of rare-earth elements in CO₂-rich fluids at mantle conditions. *Nature* 340:301–303.
- MELCHER, G. C. 1966. The carbonatites of Jacupiranga, Sao Paulo, Brazil, pp. 1361–1382. In O. Tuttle and J. Gittins (eds.), Carbonatites, volume 169. Interscience Publishers.
- MELEZHIK, V., BINGEN, B., FALICK, A., GOROKHOV, I., KUZNETSOV, A., SANDSTAD, J., SOLLI, A., BJERKGÅRD, T., HENDERSON, I., BOYD, R., ET AL. 2008. Isotope chemostratigraphy of marbles in northeastern Mozambique: apparent depositional ages and tectonostratigraphic implications. *Precambrian Research* 162:540–558.
- METAL-PAGES 2014.
- MICHARD, A. 1989. Rare earth element systematics in hydrothermal fluids. *Geochimica et Cosmochimica Acta* 53:745–750.
- MICHARD, A. AND ALBARÈDE, F. 1986. The REE content of some hydrothermal fluids. *Chemical Geology* 55:51–60.
- MICHARD, A., ALBAREDE, F., MICHARD, G., MINSTER, J., AND CHARLOU, J. 1983. Rare-earth elements and uranium in high-temperature solutions from East Pacific Rise hydrothermal vent field (13 N). *Nature* 303:795–797.
- MICHARD, A., BEAUCAIRE, C., AND MICHARD, G. 1987. Uranium and rare earth elements in CO₂-rich waters from Vals-les-Bains (France). *Geochimica et Cosmochimica Acta* 51:901–909.
- MICHARD, G., ALBAREDE, F., MICHARD, A., MINSTER, J.-F., CHARLOU, J.-L., AND TAN, N. 1984. Chemistry of solutions from the 13 N East Pacific Rise hydrothermal site. *Earth and Planetary Science Letters* 67:297–307.
- MIGDISOV, A. A., REUKOV, V., AND WILLIAMS-JONES, A. 2006. A spectrophotometric study of neodymium (III) complexation in sulfate solutions at elevated temperatures. *Geochimica et Cosmochimica Acta* 70:983–992.
- MIGDISOV, A. A. AND WILLIAMS-JONES, A. 2002. A spectrophotometric study of neodymium (III) complexation in chloride solutions. *Geochimica et Cosmochimica Acta* 66:4311–4323.
- MIGDISOV, A. A. AND WILLIAMS-JONES, A. 2006. A spectrophotometric study of erbium (III) speciation in chloride solutions at elevated temperatures. *Chemical geology* 234:17–27.
- MIGDISOV, A. A. AND WILLIAMS-JONES, A. 2007. An experimental study of the solubility and speciation of neodymium (III) fluoride in F-bearing aqueous solutions. *Geochimica et Cosmochimica Acta* 71:3056–3069.
- MIGDISOV, A. A. AND WILLIAMS-JONES, A. 2008. A spectrophotometric study of Nd (III), Sm (III) and Er (III) complexation in sulfate-bearing solutions at elevated temperatures. *Geochimica et Cosmochimica Acta* 72:5291–5303.

- MIGDISOV, A. A. AND WILLIAMS-JONES, A. 2014. Hydrothermal transport and deposition of the rare earth elements by fluorine-bearing aqueous liquids. *Mineralium Deposita* pp. 1–11.
- MIGDISOV, A. A., WILLIAMS-JONES, A., NORMAND, C., AND WOOD, S. 2008. A spectrophotometric study of samarium (III) speciation in chloride solutions at elevated temperatures. *Geochimica et Cosmochimica Acta* 72:1611–1625.
- MIGDISOV, A. A., WILLIAMS-JONES, A., AND WAGNER, T. 2009. An experimental study of the solubility and speciation of the rare earth elements (III) in fluoride- and chloride-bearing aqueous solutions at temperatures up to 300 C. *Geochimica et Cosmochimica Acta* 73:7087–7109.
- MILLERO, F. J. 1992. Stability constants for the formation of rare earth-inorganic complexes as a function of ionic strength. *Geochimica et Cosmochimica Acta* 56:3123–3132.
- MITCHELL, R. 2005. Carbonatites and carbonatites and carbonatites. *The Canadian Mineralogist* 43:2049–2068.
- MITCHELL, R. 2014. Cathodoluminescence of apatite, p. 143. In I. Coulson (ed.), Cathodoluminescence and its application to geoscience, volume 45 of *Short course Series*. Mineralogical Association of Canada.
- MITCHELL, R. H. 1996. Classification of undersaturated and related alkaline rocks. *Undersaturated alkaline rocks: mineralogy, petrogenesis, and economic potential, Mineralogical Association of Canada Short Course* 24:1–22.
- MITCHELL, R. H. 1997. Preliminary studies of the solubility and stability of perovskite group compounds in the synthetic carbonatite system calcite-portlandite. *Journal of African Earth Sciences* 25:147–158.
- MITCHELL, R. H. AND KJARSGAARD, B. A. 2004. Solubility of niobium in the system $\text{CaCO}_3\text{--CaF}_2\text{--NaNbO}_3$ at 0.1 GPa pressure: implications for the crystallization of pyrochlore from carbonatite magma. *Contributions to Mineralogy and Petrology* 148:281–287.
- MITCHELL, R. H. AND LIFEROVICH, R. P. 2006. Subsolidus deuteric/hydrothermal alteration of eudialyte in lujavrite from the Pilansberg alkaline complex, South Africa. *Lithos* 91:352–372.
- MÖLLER, P. 2002. The distribution of rare earth elements and yttrium in water-rock interactions: field observations and experiments, pp. 97–123. In *Water-Rock Interaction*. Springer.
- MÖLLER, P., BAU, M., DULSKI, P., AND LÜDERS, V. 1998. REE and Y fractionation in fluorite and their bearing on fluorite formation. In *Proceedings of the Ninth Quadrennial IAGOD Symposium*. Schweizerbart, Stuttgart, pp. 575–592.
- MÖLLER, P., DULSKI, P., AND MORTEANI, G. 2003. Partitioning of rare earth elements, yttrium, and some major elements among source rocks, liquid and vapor of Larderello-Travale Geothermal Field, Tuscany (Central Italy). *Geochimica et cosmochimica acta* 67:171–183.

- MÖLLER, P., DULSKI, P., SALAMEH, E., AND GEYER, S. 2006. Characterization of the sources of thermal spring-and well water in Jordan by rare earth element and yttrium distribution and stable isotopes of H₂O. *Acta hydrochimica et hydrobiologica* 34:101–116.
- MÖLLER, P., DULSKI, P., SAVASCIN, Y., AND CONRAD, M. 2004. Rare earth elements, yttrium and Pb isotope ratios in thermal spring and well waters of West Anatolia, Turkey: a hydrochemical study of their origin. *Chemical geology* 206:97–118.
- MÖLLER, P., WOITH, H., DULSKI, P., LÜDERS, V., ERZINGER, J., KÄMPF, H., PEKDEGER, A., HANSEN, B., LODEMANN, M., AND BANKS, D. 2005. Main and trace elements in KTB-VB fluid: composition and hints to its origin. *Geofluids* 5:28–41.
- MONECKE, T., DULSKI, P., AND KEMPE, U. 2007. Origin of convex tetrads in rare earth element patterns of hydrothermally altered siliceous igneous rocks from the Zinnwald Sn–W deposit, Germany. *Geochimica et cosmochimica acta* 71:335–353.
- MONECKE, T., KEMPE, U., MONECKE, J., SALA, M., AND WOLF, D. 2002. Tetrad effect in rare earth element distribution patterns: a method of quantification with application to rock and mineral samples from granite-related rare metal deposits. *Geochimica et Cosmochimica Acta* 66:1185–1196.
- MONECKE, T., KEMPE, U., TRINKLER, M., THOMAS, R., DULSKI, P., AND WAGNER, T. 2011. Unusual rare earth element fractionation in a tin-bearing magmatic-hydrothermal system. *Geology* 39:295–298.
- MOORE, M., CHAKHMOURADIAN, A. R., MARIANO, A. N., AND SIDHU, R. 2014. Evolution of rare-earth mineralization in the Bear Lodge carbonatite, Wyoming: Mineralogical and isotopic evidence. *Ore Geology Reviews* .
- MORBIDELLI, L., GOMES, C., BECCALUVA, L., BROTZU, P., CONTE, A., RUBERTI, E., AND TRAVERSA, G. 1995. Mineralogical, petrological and geochemical aspects of alkaline and alkaline-carbonatite associations from Brazil. *Earth-Science Reviews* 39:135–168.
- MORIKIYO, T., HIRANO, H., AND MATSUHISA, Y. 1990. Carbon and oxygen isotopic composition of the carbonates from the Jacupiranga and Catalão I carbonatite complexes, Brazil.
- MORTEANI, G. AND PREINFALK, C. 1996. REE distribution and REE carriers in laterites formed on the alkaline complexes of Araxá and Catalão (Brazil). In A. Jones, F. Wall, and W. C. Terry (eds.), *Rare Earth minerals, Chemistry Origin and ore-deposits*. Chapman and Hall.
- MOURÃO, C., MOREIRA, M., MATA, J., RAQUIN, A., AND MADEIRA, J. 2012. Primary and secondary processes constraining the noble gas isotopic signatures of carbonatites and silicate rocks from Brava Island: evidence for a lower mantle origin of the Cape Verde plume. *Contributions to Mineralogy and Petrology* 163:995–1009.

- NADEAU, S. L., EPSTEIN, S., AND STOLPER, E. 1999. Hydrogen and carbon abundances and isotopic ratios in apatite from alkaline intrusive complexes, with a focus on carbonatites. *Geochimica et cosmochimica acta* 63:1837–1851.
- NAGASAWA, H. 1970. Rare earth concentrations in zircons and apatites and their host dacites and granites. *Earth and Planetary Science Letters* 9:359–364.
- NGWENYA, B. 1991. Magmatic and post-magmatic geochemistry of phosphorus and rare earth elements in carbonatites. PhD thesis, Reading University.
- NGWENYA, B. 1994. Hydrothermal rare earth mineralisation in carbonatites of the Tundulu complex, Malawi: Processes at the fluid/rock interface. *Geochimica et cosmochimica acta* 58:2061–2072.
- NORMAN, M. D. AND NEMCHIN, A. A. 2014. A 4.2 billion year old impact basin on the moon: U–Pb dating of zirconolite and apatite in lunar melt rock 67955. *Earth and Planetary Science Letters* 388:387–398.
- ONEIL, J. R., ROE, L. J., REINHARD, E., AND BLAKE, R. 1994. A rapid and precise method of oxygen isotope analysis of biogenic phosphate. *Israel Journal of Earth Sciences* 43:203–12.
- PACK, A., RUSSELL, S. S., SHELLEY, J. M. G., AND VAN ZUILEN, M. 2007. Geo- and cosmochemistry of the twin elements yttrium and holmium. *Geochimica et Cosmochimica Acta* 71:4592–4608.
- PALMER, D. AND WILLIAMS-JONES, A. 1996. Genesis of the carbonatite-hosted fluorite deposit at Amba Dongar, India; evidence from fluid inclusions, stability isotopes, and whole rock-mineral geochemistry. *Economic Geology* 91:934–950.
- PAN, Y. 1997. Controls on the fractionation of isovalent trace elements in magmatic and aqueous systems: evidence from Y/Ho, Zr/Hf, and lanthanide tetrad effect—a discussion of the article by M. Bau (1996). *Contributions to mineralogy and petrology* 128:405–408.
- PAN, Y. AND BREAKS, F. W. 1997. Rare-earth elements in fluorapatite, Separation Lake area, Ontario; evidence for S-type granite-rare-element pegmatite linkage. *The Canadian Mineralogist* 35:659–671.
- PAN, Y. AND FLEET, M. E. 2002. Compositions of the apatite-group minerals: substitution mechanisms and controlling factors. *Reviews in Mineralogy and Geochemistry* 48:13–49.
- PASERO, M., KAMPF, A. R., FERRARIS, C., PEKOV, I. V., RAKOVAN, J., AND WHITE, T. J. 2010. Nomenclature of the apatite supergroup minerals. *European Journal of Mineralogy* 22:163–179.
- PATON, C., HELLSTROM, J., PAUL, B., WOODHEAD, J., AND HERGT, J. 2011. Iolite: Freeware for the visualisation and processing of mass spectrometric data. *Journal of Analytical Atomic Spectrometry* 26:2508–2518.
- PEARCE, N. AND LENG, M. 1996. The origin of carbonatites and related rocks from the Igaliko Dyke Swarm, Gardar Province, South Greenland: field, geochemical and CO-Sr-Nd isotope evidence. *Lithos* 39:21–40.

- PEARCE, N., LENG, M., EMELEUS, C., AND BEDFORD, C. 1997. The origins of carbonatites and related rocks from the Gronnedal-Ika nepheline syenite complex, South Greenland; CO-Sr isotope evidence. *Mineralogical Magazine* 61:515–529.
- PEARSON, R. G. 1963. Hard and soft acids and bases. *Journal of the American Chemical Society* 85:3533–3539.
- PECK, W. H. AND TUMPANE, K. P. 2007. Low carbon isotope ratios in apatite: An unreliable biomarker in igneous and metamorphic rocks. *Chemical Geology* 245:305–314.
- PEKOV, I. V., BRITVIN, S. N., ZUBKOVA, N. V., PUSHCHAROVSKY, D. Y., PASERO, M., AND MERLINO, S. 2010. Stronadelphite, $\text{Sr}_5(\text{PO}_4)_3\text{F}$, a new apatite-group mineral. *European Journal of Mineralogy* 22:869–874.
- PERSEIL, E.-A., BLANC, P., AND OHNENSTETTER, D. 2000. As-bearing fluorapatite in manganeseiferous deposits from St. Marcel–Praborna, Val d'Aosta, Italy. *The Canadian Mineralogist* 38:101–117.
- PETRELLA, L., WILLIAMS-JONES, A. E., GOUTIER, J., AND WALSH, J. 2014. The nature and origin of the rare earth element mineralization in the Misery Syenitic Intrusion, Northern Quebec, Canada. *Economic Geology* 109:1643–1666.
- PICCOLI, P. M. AND CANDELA, P. A. 2002. Apatite in igneous systems. *Reviews in Mineralogy and Geochemistry* 48:255–292.
- PIETRANIK, A., STOREY, C., DHUIME, B., TYSZKA, R., AND WHITEHOUSE, M. 2011. Decoding whole rock, plagioclase, zircon and apatite isotopic and geochemical signatures from variably contaminated dioritic magmas. *Lithos* 127:455–467.
- PINEAU, F., JAVOY, M., AND ALLEGRE, C. J. 1973. Etude systématique des isotopes de l'oxygène, du carbone et du strontium dans les carbonatites. *Geochimica et Cosmochimica Acta* 37:2363–2377.
- PLATT, R., WALL, F., WILLIAMS, C., AND WOOLLEY, A. 1987. Zirconolite, chevkinite and other rare earth minerals from nepheline syenites and peralkaline granites and syenites of the Chilwa Alkaline Province, Malawi. *Mineralogical Magazine* 51:253–263.
- POITRASSON, F., OELKERS, E., SCHOTT, J., AND MONTEL, J.-M. 2004. Experimental determination of synthetic NdPO_4 monazite end-member solubility in water from 21 C to 300 C: implications for rare earth element mobility in crustal fluids. *Geochimica et Cosmochimica Acta* 68:2207–2221.
- POTTS, P. J., TINDLE, A. G., AND WEBB, P. 1992. Geochemical reference material compositions: rocks, minerals, sediments, soils, carbonates, refractories & ores used in research & industry. Taylor & Francis.
- POURTIER, E., DEVIDAL, J.-L., AND GIBERT, F. 2010. Solubility measurements of synthetic neodymium monazite as a function of temperature at 2kbars, and aqueous neodymium speciation in equilibrium with monazite. *Geochimica et Cosmochimica Acta* 74:1872–1891.

- PROWATKE, S. AND KLEMME, S. 2006. Trace element partitioning between apatite and silicate melts. *Geochimica et Cosmochimica Acta* 70:4513–4527.
- PUTNIS, A. 2009. Mineral replacement reactions. *Reviews in mineralogy and geochemistry* 70:87–124.
- PYLE, J., SPEAR, F., AND WARK, D. 2002. Electron microprobe analysis of REE in apatite, monazite and xenotime: protocols and pitfalls. *Reviews in mineralogy and geochemistry* 48:337–362.
- RAGNARSDOTTIR, K. V., OELKERS, E. H., SHERMAN, D. M., AND COLLINS, C. R. 1998. Aqueous speciation of yttrium at temperatures from 25 to 340 °C at P_{sat} : an in situ EXAFS study. *Chemical geology* 151:29–39.
- RAI, D., FELMY, A. R., AND YUI, M. 2003. Thermodynamic model for the solubility of $NdPO_4$ in the aqueous $Na^+ - H^+ - H_2PO_4^- - HPO_4^{2-} - OH^- - Cl^- - H_2O$ system. *Journal of Radioanalytical and Nuclear Chemistry* 256:37–43.
- RANKIN, A. 2005. Carbonatite-associated rare metal deposits: composition and evolution of ore-forming fluids—the fluid inclusion evidence. *Geological Association of Canada, Short Course Notes* 17:299–314.
- RASMUSSEN, B. AND FLETCHER, I. R. 2004. Zirconolite: A new U-Pb chronometer for mafic igneous rocks. *Geology* 32:785–788.
- RAY, J. AND RAMESH, R. 1999a. A fluid-rock interaction model for carbon and oxygen isotope variations in altered carbonatites. *Journal of the Geological Society of India* 64:299–306.
- RAY, J. S. AND RAMESH, R. 1999b. Evolution of carbonatite complexes of the Deccan flood basalt province: stable carbon and oxygen isotopic constraints. *Journal of Geophysical Research: Solid Earth (1978–2012)* 104:29471–29483.
- RAY, J. S. AND RAMESH, R. 2000. Rayleigh fractionation of stable isotopes from a multicomponent source. *Geochimica et Cosmochimica Acta* 64:299–306.
- RAY, J. S. AND RAMESH, R. 2006. Stable carbon and oxygen isotopic compositions of Indian carbonatites. *International Geology Review* 48:17–45.
- REED, S. J. B. 2005. Electron microprobe analysis and scanning electron microscopy in geology. Cambridge University Press Cambridge.
- REINERS, P. W., EHLERS, T. A., AND ZEITLER, P. K. 2005. Past, present, and future of thermochronology. *Reviews in Mineralogy and Geochemistry* 58:1–18.
- RICHET, P., BOTTINGA, Y., AND JANNOY, M. 1977. A review of hydrogen, carbon, nitrogen, oxygen, sulphur, and chlorine stable isotope enrichment among gaseous molecules. *Annual Review of Earth and Planetary Sciences* 5:65–110.
- ROEDER, P. L., MACARTHUR, D., MA, X.-P., PALMER, G. R., AND MARIANO, A. N. 1987. Cathodoluminescence and microprobe study of rare-earth elements in apatite. *American Mineralogist* 72:801–811.
- ROLLINSON, G. K., ANDERSEN, J. C., STICKLAND, R. J., BONI, M., AND FAIRHURST, R. 2011. Characterisation of non-sulphide zinc deposits using QEMSCAN. *Minerals Engineering* 24:778–787.

- RUBERTI, E., CASTORINA, F., CENSI, P., COMIN-CHIARAMONTI, P., GOMES, C., ANTONINI, P., AND ANDRADE, F. 2002. The geochemistry of the Barra do Itapirapuã carbonatite (Ponta Grossa Arch, Brazil): a multiple stockwork. *Journal of South American Earth Sciences* 15:215–228.
- RUBERTI, E., ENRICH, G. E., GOMES, C. B., AND COMIN-CHIARAMONTI, P. 2008. Hydrothermal REE fluorocarbonate mineralization at Barra do Itapirapua, a multiple stockwork carbonatite, Southern Brazil. *The Canadian Mineralogist* 46:901–914.
- RUDNICK, R. AND GAO, S. 2003. Composition of the continental crust. In Vol. 3 Treatise on Geochemistry. Elsevier-Pergamon, Oxford.
- RYABCHIKOV, I., ORLOVA, G., SENIN, V., AND TRUBKIN, N. 1993. Partitioning of rare earth elements between phosphate-rich carbonatite melts and mantle peridotites. *Mineralogy and Petrology* 49:1–12.
- SALVI, S., FONTAN, F., MONCHOUX, P., WILLIAMS-JONES, A., AND MOINE, B. 2000. Hydrothermal mobilization of high field strength elements in alkaline igneous systems: evidence from the Tamazeght Complex (Morocco). *Economic Geology* 95:559–576.
- SALVI, S. AND WILLIAMS-JONES, A. E. 1990. The role of hydrothermal processes in the granite-hosted Zr, Y, REE deposit at Strange Lake, Quebec/Labrador: evidence from fluid inclusions. *Geochimica et Cosmochimica Acta* 54:2403–2418.
- SALVI, S. AND WILLIAMS-JONES, A. E. 1992. Reduced orthomagmatic COHN-NaCl fluids in the Strange Lake rare-metal granitic complex, Quebec/Labrador, Canada. *European journal of mineralogy* 4:1155–1174.
- SALVI, S. AND WILLIAMS-JONES, A. E. 1996. The role of hydrothermal processes in concentrating high-field strength elements in the Strange Lake peralkaline complex, northeastern Canada. *Geochimica et Cosmochimica Acta* 60:1917–1932.
- SALVI, S. AND WILLIAMS-JONES, A. E. 1997. Fischer-Tropsch synthesis of hydrocarbons during sub-solidus alteration of the Strange Lake peralkaline granite, Quebec/Labrador, Canada. *Geochimica et Cosmochimica Acta* 61:83–99.
- SALVI, S. AND WILLIAMS-JONES, A. E. 2006. Alteration, HFSE mineralisation and hydrocarbon formation in peralkaline igneous systems: Insights from the Strange Lake pluton, Canada. *Lithos* 91:19–34.
- SAMSON, I. M., LIU, W., AND WILLIAMS-JONES, A. E. 1995a. The nature of orthomagmatic hydrothermal fluids in the Oka carbonatite, Quebec, Canada: Evidence from fluid inclusions. *Geochimica et cosmochimica acta* 59:1963–1977.
- SAMSON, I. M., WILLIAMS-JONES, A., AND LIU, W. 1995b. The chemistry of hydrothermal fluids in carbonatites: Evidence from leachate and SEM-decrepitate analysis of fluid inclusions from Oka, Quebec, Canada. *Geochimica et cosmochimica acta* 59:1979–1989.

- SAMSON, I. M., WOOD, S. A., AND FINUCANE, K. 2004. Fluid inclusion characteristics and genesis of the fluorite-parisite mineralization in the Snowbird deposit, Montana. *Economic Geology* 99:1727–1744.
- SANEMATSU, K., KON, Y., IMAI, A., WATANABE, K., AND WATANABE, Y. 2013. Geochemical and mineralogical characteristics of ion-adsorption type REE mineralization in Phuket, Thailand. *Mineralium Deposita* 48:437–451.
- SANTOS, R. V. AND CLAYTON, R. N. 1995. Variations of oxygen and carbon isotopes in carbonatites: a study of Brazilian alkaline complexes. *Geochimica et Cosmochimica Acta* 59:1339–1352.
- SCHALTEGGER, U. 2007. Hydrothermal zircon. *Elements* 3:51–79.
- SCHIJF, J. AND BYRNE, R. H. 1999. Determination of stability constants for the mono- and difluoro-complexes of Y and the REE, using a cation-exchange resin and ICP-MS. *Polyhedron* 18:2839–2844.
- SCHIJF, J. AND BYRNE, R. H. 2004. Determination of $\text{SO}_4 \beta_1$ for yttrium and the rare earth elements at $I = 0.66 \text{ m}$ and $t = 25 \text{ C}$ — implications for YREE solution speciation in sulfate-rich waters. *Geochimica et cosmochimica acta* 68:2825–2837.
- SCHMIDT, C., RICKERS, K., BILDERBACK, D. H., AND HUANG, R. 2007. In situ synchrotron-radiation XRF study of REE phosphate dissolution in aqueous fluids to 800 C. *Lithos* 95:87–102.
- SCHMIDT, K., GARBE-SCHÖNBERG, D., BAU, M., AND KOSCHINSKY, A. 2010. Rare earth element distribution in $> 400 \text{ C}$ hot hydrothermal fluids from 5 S, MAR: The role of anhydrite in controlling highly variable distribution patterns. *Geochimica et Cosmochimica Acta* 74:4058–4077.
- SCHOENE, B., CONDON, D. J., MORGAN, L., AND MCLEAN, N. 2013. Precision and accuracy in geochronology. *Elements* 9:19–24.
- SCHWINN, G. AND MARKL, G. 2005. REE systematics in hydrothermal fluorite. *Chemical Geology* 216:225–248.
- SEREDIN, V. V. AND DAI, S. 2012. Coal deposits as potential alternative sources for lanthanides and yttrium. *International Journal of Coal Geology* 94:67–93.
- SHA, L.-K. AND CHAPPELL, B. W. 1999. Apatite chemical composition, determined by electron microprobe and laser-ablation inductively coupled plasma mass spectrometry, as a probe into granite petrogenesis. *Geochimica et Cosmochimica Acta* 63:3861–3881.
- SHANNON, R. 1976. Revised effective ionic radii and systematic studies of interatomic distances in halides and chalcogenides. *Acta Crystallographica Section A: Crystal Physics, Diffraction, Theoretical and General Crystallography* 32:751–767.
- SHEARD, E., WILLIAMS-JONES, A., HEILIGMANN, M., PEDERSON, C., AND TRUEMAN, D. 2012. Controls on the concentration of zirconium, niobium, and the rare earth elements in the Thor Lake rare metal deposit, Northwest Territories, Canada. *Economic Geology* 107:81–104.

- SHEMESH, A., KOLODNY, Y., AND LUZ, B. 1983. Oxygen isotope variations in phosphate of biogenic apatites, II. phosphorite rocks. *Earth and Planetary Science Letters* 64:405–416.
- SHEMESH, A., KOLODNY, Y., AND LUZ, B. 1988. Isotope geochemistry of oxygen and carbon in phosphate and carbonate of phosphorite francolite. *Geochimica et Cosmochimica Acta* 52:2565–2572.
- SHEPHERD, T. J., RANKIN, A. H., AND ALDERTON, D. 1985. A practical guide to fluid inclusion studies, volume 239. Blackie Glasgow.
- SIMANDL, G. 2014. Geology and market-dependent significance of rare earth element resources. *Mineralium Deposita* pp. 1–16.
- SIMONETTI, A. AND BELL, K. 1994. Isotopic and geochemical investigation of the Chilwa Island carbonatite complex, Malawi: evidence for a depleted mantle source region, liquid immiscibility, and open-system behaviour. *Journal of Petrology* 35:1597–1621.
- SIMONETTI, A. AND BELL, K. 1995. Nd, Pb, and Sr isotope systematics of fluorite at the Amba Dongar carbonatite complex, India; evidence for hydrothermal and crustal fluid mixing. *Economic Geology* 90:2018–2027.
- SMITH, M., CAMPBELL, L., AND KYNICKY, J. 2014. A review of the genesis of the world class Bayan Obo Fe–REE–Nb deposits, Inner Mongolia, China: Multistage processes and outstanding questions. *Ore Geology Reviews* .
- SMITH, M., HENDERSON, P., AND PEISHAN, Z. 1999. Reaction relationships in the bayan obo Fe-REE-Nb deposit Inner Mongolia, China: implications for the relative stability of rare-earth element phosphates and fluorocarbonates. *Contributions to mineralogy and petrology* 134:294–310.
- SMITH, M., STOREY, C., JEFFRIES, T., AND RYAN, C. 2009. In situ U–Pb and trace element analysis of accessory minerals in the Kiruna district, Norrbotten, Sweden: new constraints on the timing and origin of mineralization. *Journal of Petrology* 50:2063–2094.
- SMITH, M. P. AND HENDERSON, P. 2000. Preliminary fluid inclusion constraints on fluid evolution in the Bayan Obo Fe-REE-Nb deposit, Inner Mongolia, China. *Economic Geology* 95:1371–1388.
- SNELLING, N. 1966. Age determination unit. *Report of the Overseas Geological Survey* p. 53.
- SNELLING, N. 1967. Age determination unit. *Report of the Overseas Geological Survey* p. 146.
- SOMAN, A., GEISLER, T., TOMASCHEK, F., GRANGE, M., AND BERNDT, J. 2010. Alteration of crystalline zircon solid solutions: a case study on zircon from an alkaline pegmatite from Zomba–Malosa, Malawi. *Contributions to Mineralogy and Petrology* 160:909–930.
- STOPPA, F. AND LIU, Y. 1995. Chemical composition and petrogenetic implications of apatites from some ultra-alkaline Italian rocks. *European Journal of Mineralogy* 7:391–402.

- STORMER, J., PIERSON, M. L., AND TACKER, R. C. 1993. Variation of F and Cl X-ray intensity due to anisotropic diffusion in apatite. *American Mineralogist* 78:641–648.
- STUART-WILLIAMS, H. L. Q. AND SCHWARCZ, H. P. 1995. Oxygen isotopic analysis of silver orthophosphate using a reaction with bromine. *Geochimica et Cosmochimica Acta* 59:3837–3841.
- STYLES, M. 1988. A preliminary report on the mineralogy of the Tundulu and Songwe carbonatite complexes, Malawi. Technical report, British Geological Surver Mineralogy and Petrology report: WG/88/6R.
- SUTHERLAND, D. 1965. Potash-trachytes and ultra-potassic rocks associated with the carbonatite complex of the Toror Hills, Uganda. *Mineralogical Magazine* 35:363–378.
- SUTHERLAND, D. 1967. A note on the occurrence of potassium-rich trachytes in the Kaiserstuhl carbonatite complex, West Germany. *Mineralogical Magazine* 36:334–341.
- SVERJENSKY, D. A. 1984. Europium redox equilibria in aqueous solution. *Earth and Planetary Science Letters* 67:70–78.
- SWINDEN, S. AND HALL, M. 2012. NI 43-101 technical report and mineral resource estimate for the Songwe Hill rare earth element (REE) project, Phalombe District, Republic of Malawi. Technical report, MSA Group (Pty) Ltd.
- SZOPA, K., GAWĘDA, A., MÜLLER, A., AND SIKORSKA, M. 2013. The petrogenesis of granitoid rocks unusually rich in apatite in the Western Tatra Mts. (S-Poland, Western Carpathians). *Mineralogy and Petrology* 107:609–627.
- TANG, M., WANG, X.-L., XU, X.-S., ZHU, C., CHENG, T., AND YU, Y. 2012. Neoproterozoic subducted materials in the generation of Mesozoic Luzong volcanic rocks: evidence from apatite geochemistry and Hf–Nd isotopic decoupling. *Gondwana Research* 21:266–280.
- TANIS, E. A., SIMON, A., TSCHAUNER, O., CHOW, P., XIAO, Y., SHEN, G., HANCHAR, J. M., AND FRANK, M. 2012. Solubility of xenotime in a 2 M HCl aqueous fluid from 1.2 to 2.6 GPa and 300 to 500 C. *American Mineralogist* 97:1708–1713.
- TAUBALD, H., MORTEANI, G., AND SATIR, M. 2004. Geochemical and isotopic (Sr, C, O) data from the alkaline complex of Grønnedal-Íka (South Greenland): evidence for unmixing and crustal contamination. *International Journal of Earth Sciences* 93:348–360.
- TAYLOR, G. AND MARTEL, L. 2003. Lunar prospecting. *Advances in Space Research* 31:2403–2412.
- TAYLOR, H. P., FRECHEN, J., AND DEGENS, E. T. 1967. Oxygen and carbon isotope studies of carbonatites from the Laacher See district, West Germany and the Alnö district, Sweden. *Geochimica et Cosmochimica Acta* 31:407–430.

- TAYLOR, R. AND POLLARD, P. 1996. Rare earth element mineralization in peralkaline systems: the T-zone REE-Y-Be deposit, Thor Lake, Northwest Territories, Canada, pp. 167–192. *In* A. Jones, F. Wall, and C. Williams (eds.), *Rare Earth Minerals: Chemistry, Origin and Ore deposits*, volume 7. CHAPMAN & HALL.
- TEAGUE, A. J., HANLEY, J., SEWARD, T. M., AND REUTTEN, F. 2011. Trace-element distribution between coexisting aqueous fumarole condensates and natrocarbonatite lavas at Oldoinyo Lengai volcano, Tanzania. *Geological Society of America Special Papers* 478:159–172.
- TECHNOLOGY METALS RESEARCH 2015. Tmr advanced rare-earth projects index.
- THOMAS, R., JACOBS, J., HORSTWOOD, M., UEDA, K., BINGEN, B., AND MATOLA, R. 2010. The Mecubúri and Alto Benfica groups, NE Mozambique: Aids to unravelling ca. 1 and 0.5 Ga events in the east African orogen. *Precambrian Research* 178:72–90.
- THOMPSON, R., SMITH, P., GIBSON, S., MATTEY, D., AND DICKIN, A. 2002. Ankerite carbonatite from Swartbooisdrif, Namibia: the first evidence for magmatic ferrocarbonatite. *Contributions to Mineralogy and Petrology* 143:377–396.
- TICHOMIROWA, M., GROSCHE, G., GÖTZE, J., BELYATSKY, B., SAVVA, E., KELLER, J., AND TODT, W. 2006. The mineral isotope composition of two Precambrian carbonatite complexes from the Kola Alkaline Province—alteration versus primary magmatic signatures. *Lithos* 91:229–249.
- TING, W., BURKE, E. A., RANKIN, A. H., AND WOOLLEY, A. R. 1994. Characterisation and petrogenetic significance of CO₂, H₂O and CH₄ fluid inclusions in apatite from the Sukulu Carbonatite, Uganda. *European Journal of Mineralogy* 6:787–803.
- TROPPER, P., MANNING, C., AND HARLOV, D. 2013. Experimental determination of CePO₄ and YPO₄ solubilities in H₂O–NaF at 800 C and 1 GPa: implications for rare earth element transport in high-grade metamorphic fluids. *Geofluids* 13:372–380.
- TROPPER, P., MANNING, C. E., AND HARLOV, D. E. 2011. Solubility of CePO₄ monazite and YPO₄ xenotime in H₂O and H₂O–NaCl at 800 C and 1GPa: Implications for REE and Y transport during high-grade metamorphism. *Chemical Geology* 282:58.
- VALLÉE, M. AND DUBUC, F. 1970. St-Honoré carbonatite complex, Quebec. *The Canadian mining and metallurgical bulletin* 63:1384.
- VAN HINSBERG, V. J., MIGDISOV, A. A., AND WILLIAMS-JONES, A. E. 2010. Reading the mineral record of fluid composition from element partitioning. *Geology* 38:847–850.
- VAN MIDDLESWORTH, P. E. AND WOOD, S. A. 1998. The aqueous geochemistry of the rare earth elements and yttrium. part 7. REE, Th and U contents in thermal springs associated with the Idaho batholith. *Applied Geochemistry* 13:861–884.

- VEKSLER, I. V., DORFMAN, A. M., DULSKI, P., KAMENETSKY, V. S., DANYUSHEVSKY, L. V., JEFFRIES, T., AND DINGWELL, D. B. 2012. Partitioning of elements between silicate melt and immiscible fluoride, chloride, carbonate, phosphate and sulfate melts, with implications to the origin of natrocarbonatite. *Geochimica et Cosmochimica Acta* 79:20–40.
- VENNEMANN, T. W., FRICKE, H. C., BLAKE, R. E., O'NEIL, J. R., AND COLMAN, A. 2002. Oxygen isotope analysis of phosphates: a comparison of techniques for analysis of Ag_3PO_4 . *Chemical Geology* 185:321–336.
- WALL, F. 2000. Mineral chemistry and petrogenesis of rare earth-rich carbonatites with particular reference to the Kangankunde carbonatite, Malawi. PhD thesis, Univeristy of London.
- WALL, F. 2014. Rare earth elements. In A. Gunn (ed.), *Critical Metals Handbook*. Wiley Blackwell,.
- WALL, F. AND MARIANO, A. 1996. Rare earth minerals in carbonatites: a discussion centred on the Kangankunde Carbonatite, Malawi, pp. 193–226. In A. Jones, F. Wall, and C. T. Williams (eds.), *Rare Earth Minerals: Chemistry Origin and Ore Deposits*, volume 7.
- WALL, F., NIKU-PAAVOLA, V., STOREY, C., MÜLLER, A., AND JEFFRIES, T. 2008. Xenotime-(Y) from carbonatite dykes at Lofdal, Namibia: unusually low LREE: HREE ratio in carbonatite, and the first dating of xenotime overgrowths on zircon. *The Canadian Mineralogist* 46:861–877.
- WALL, F., ZAITSEV, A., WALL, F., AND ZAITSEV, A. 2004. Rare earth minerals in Kola carbonatites. In F. Wall and A. Zaitsev (eds.), *Phoscorites and carbonatites from mantle to mine: the key example of the Kola alkaline province*, number 10 in *The Mineralogical Society Series*.
- WALTER, A.-V., NAHON, D., FLICOTEAUX, R., GIRARD, J., AND MELFI, A. 1995. Behaviour of major and trace elements and fractionation of REE under tropical weathering of a typical apatite-rich carbonatite from Brazil. *Earth and Planetary Science Letters* 136:591–602.
- WALTERS, A., GOODENOUGH, K., HUGHES, H., ROBERTS, N., GUNN, A., RUSHTON, J., AND LACINSKA, A. 2013. Enrichment of rare earth elements during magmatic and post-magmatic processes: a case study from the Loch Loyal Syenite Complex, northern Scotland. *Contributions to Mineralogy and Petrology* 166:1177–1202.
- WANG, L.-X., MARKS, M. A., WENZEL, T., VON DER HANDT, A., KELLER, J., TEIBER, H., AND MARKL, G. 2014. Apatites from the Kaiserstuhl Volcanic Complex, Germany: new constraints on the relationship between carbonatite and associated silicate rocks. *European Journal of Mineralogy* .
- WATSON, E. AND GREEN, T. 1981. Apatite/liquid partition coefficients for the rare earth elements and strontium. *Earth and Planetary Science Letters* 56:405–421.
- WENG, Z., JOWITT, S., MUDD, G., AND HAQUE, N. 2013. Assessing rare earth element mineral deposit types and links to environmental impacts. *Applied Earth Science (Trans. Inst. Min. Metall. B)* 122:83–96.

- WIEDENBECK, M., ALLE, P., CORFU, F., GRIFFIN, W., MEIER, M., OBERLI, F., QUADT, A. V., RODDICK, J., AND SPIEGEL, W. 1995. Three natural zircon standards for U-Th-Pb, Lu-Hf, trace element and REE analyses. *Geostandards newsletter* 19:1–23.
- WILKE, M., SCHMIDT, C., DUBRAIL, J., APPEL, K., BORCHERT, M., KVASHNINA, K., AND MANNING, C. E. 2012. Zircon solubility and zirconium complexation in $H_2O + Na_2O + SiO_2 \pm Al_2O_3$ fluids at high pressure and temperature. *Earth and Planetary Science Letters* 349:15–25.
- WILLIAMS, C. 1996. Analysis of rare earth minerals. *MINERALOGICAL SOCIETY SERIES* 7:327–348.
- WILLIAMS-JONES, A., MIGDISOV, A., AND SAMSON, I. 2012. Hydrothermal mobilisation of the rare earth elements: A tale of "Ceria" and "Yttria". *Elements* 8:355.
- WILLIAMS-JONES, A. AND PALMER, D. 2002. The evolution of aqueous–carbonic fluids in the Amba Dongar carbonatite, India: implications for fenitisation. *Chemical Geology* 185:283–301.
- WILLIAMS-JONES, A., SAMSON, I., AND OLIVO, G. 2000. The genesis of hydrothermal fluorite-REE deposits in the Gallinas Mountains, New Mexico. *Economic Geology* 95:327–341.
- WILLIAMS-JONES, A. E. AND HEINRICH, C. A. 2005. 100th Anniversary special paper: vapor transport of metals and the formation of magmatic-hydrothermal ore deposits. *Economic Geology* 100:1287–1312.
- WILLIAMS-JONES, A. E. AND WOOD, S. A. 1992. A preliminary petrogenetic grid for REE fluorocarbonates and associated minerals. *Geochimica et Cosmochimica Acta* 56:725–738.
- WIMMENAUER, W. 1966. The eruptive rocks and carbonatites of the Kaiserstuhl, Germany. *Carbonatites*. Wiley, London pp. 183–204.
- WOLF, M. B. AND LONDON, D. 1995. Incongruent dissolution of REE- and Sr-rich apatite in peraluminous granitic liquids: Differential apatite, monazite, and xenotime solubilities during anatexis. *American Mineralogist* 80:765–775.
- WOOD, S. 2003. REE and yttrium in geothermal waters. *Society of Economic Geologists special publications* 10:133–158.
- WOOD, S. A. 1990a. The aqueous geochemistry of the rare-earth elements and yttrium: 1. review of available low-temperature data for inorganic complexes and the inorganic REE speciation of natural waters. *Chemical Geology* 82:159–186.
- WOOD, S. A. 1990b. The aqueous geochemistry of the rare-earth elements and yttrium: 2, theoretical predictions of speciation in hydrothermal solutions to 350 C at saturation water vapor pressure. *Chemical Geology* 88:99–125.
- WOOD, S. A. 2006. Rare earth element systematics of acidic geothermal waters from the Taupo Volcanic Zone, New Zealand. *Journal of Geochemical Exploration* 89:424–427.

- WOOD, S. A., PALMER, D. A., WESOLOWSKI, D. J., AND BÉNÉZETH, P. 2002. The aqueous geochemistry of the rare earth elements and yttrium. part XI. the solubility of Nd(OH)₃ and hydrolysis of Nd³⁺ from 30 to 290 C at saturated water vapor pressure with in-situ pHm measurement. *Water–rock interactions, ore deposits, and environmental geochemistry: a tribute to David Crerar, Special Publication 7*:229–256.
- WOOD, S. A. AND SHANNON, W. M. 2003. Rare-earth elements in geothermal waters from Oregon, Nevada, and California. *Journal of Solid State Chemistry* 171:246–253.
- WOOD, S. A. AND WILLIAMS-JONES, A. E. 1994. The aqueous geochemistry of the rare-earth elements and yttrium 4. monazite solubility and REE mobility in exhalative massive sulfide-depositing environments. *Chemical Geology* 115:47–60.
- WOOLLEY, A. 1969. Some aspects of fenitization with particular reference to Chilwa Island and Kangankunde, Malawi. *Bulletin of the British Museum (Natural History), Mineralogy* 2.
- WOOLLEY, A. 1987. Lithosphere metasomatism and the petrogenesis of the Chilwa Province of alkaline igneous rocks and carbonatites, Malawi. *Journal of African Earth Sciences (1983)* 6:891–898.
- WOOLLEY, A. 1989. The spatial and temporal distribution of carbonatites. In K. Bell (ed.), *Carbonatites: genesis and evolution*. Unwin Hyman, London.
- WOOLLEY, A. 2001. *Alkaline rocks and carbonatites of the World. Part 3: Africa*. The Geological Society.
- WOOLLEY, A. AND BAILEY, D. 2012. The crucial role of lithospheric structure in the generation and release of carbonatites: geological evidence. *Mineralogical Magazine* 76:259–270.
- WOOLLEY, A. AND CHURCH, A. 2005. Extrusive carbonatites: a brief review. *Lithos* 85:1–14.
- WOOLLEY, A. AND GARSON, M. 1970. Petrochemical and tectonic relationship of the Malawi carbonatite-alkaline province and the Lupata-Lebombo volcanics, pp. 237–262. In G. I. Clifford, T.N. (ed.), *African Magmatism and Tectonics*. Edinburgh, Oliver and Boyd.
- WOOLLEY, A. AND JONES, G. 1987. The petrochemistry of the northern part of the Chilwa Alkaline Province, Malawi. *Geological Society, London, Special Publications* 30:335–355.
- WOOLLEY, A. AND JONES, G. 1992. The alkaline/peralkaline syenite-granite complex of Zomba-Malosa, Malawi: mafic mineralogy and genesis. *Journal of African Earth Sciences (and the Middle East)* 14:1–12.
- WOOLLEY, A. AND KEMPE, D. 1989. Carbonatites: nomenclature, average chemical compositions, and element distribution. In K. Bell (ed.), *Carbonatites: genesis and evolution*. Unwin Hyman, London.

- WOOLLEY, A. AND KJARSGAARD, B. 2008a. Carbonatite occurrences of the world: map and database; geological survey of Canada, open file 5796.
- WOOLLEY, A. AND KJARSGAARD, B. 2008b. Paragenetic types of carbonatite as indicated by the diversity and relative abundances of associated silicate rocks: evidence from a global database. *The Canadian Mineralogist* 46:741–752.
- WOOLLEY, A. R. AND PLATT, R. G. 1986. The mineralogy of nepheline syenite complexes from the northern part of the Chilwa Province, Malawi. *Mineralogical Magazine* 50:597.
- WOOLLEY, A. R. AND PLATT, R. G. 1988. The peralkaline nepheline syenites intrusion, Chilwa province. *Mineralogical Magazine* 52:425–33.
- WU, F.-Y., SUN, D.-Y., JAHN, B.-M., AND WILDE, S. 2004. A Jurassic garnet-bearing granitic pluton from NE China showing tetrad REE patterns. *Journal of Asian Earth Sciences* 23:731–744.
- WU, F.-Y., YANG, Y.-H., MITCHELL, R. H., BELLATRECCIA, F., LI, Q.-L., AND ZHAO, Z.-F. 2010. In situ U–Pb and Nd–Hf–(Sr) isotopic investigations of zirconolite and calzirtite. *Chemical Geology* 277:178–195.
- WYLLIE, P. 1966. Experimental studies of carbonatite problems: the origin and differentiation of carbonatite magmas, pp. 311–352. In O. Tuttle and J. Gittins (eds.), *Carbonatites*. John Wiley and Sons, New York.
- WYLLIE, P., JONES, A., AND DENG, J. 1996. Rare earth elements in carbonate-rich melts from mantle to crust.
- XIE, Y., HOU, Z., YIN, S., DOMINY, S. C., XU, J., TIAN, S., AND XU, W. 2009. Continuous carbonatitic melt–fluid evolution of a REE mineralization system: Evidence from inclusions in the Maoniuping REE deposit, Western Sichuan, China. *Ore Geology Reviews* 36:90–105.
- XIE, Y., LI, Y., HOU, Z., COOKE, D. R., DANYUSHEVSKY, L., DOMINY, S. C., AND YIN, S. 2014. A model for carbonatite hosted REE mineralisation—the Mianning–Dechang REE belt, Western Sichuan Province, China. *Ore Geology Reviews*.
- XU, C., CAMPBELL, I. H., ALLEN, C. M., HUANG, Z., QI, L., ZHANG, H., AND ZHANG, G. 2007. Flat rare earth element patterns as an indicator of cumulate processes in the Lesser Qinling carbonatites, China. *Lithos* 95:267–278.
- XU, C., KYNICKY, J., CHAKHMOURADIAN, A. R., CAMPBELL, I. H., AND ALLEN, C. M. 2010. Trace-element modeling of the magmatic evolution of rare-earth-rich carbonatite from the Miaoya deposit, Central China. *Lithos* 118:145–155.
- XU, C., TAYLOR, R. N., LI, W., KYNICKY, J., CHAKHMOURADIAN, A. R., AND SONG, W. 2012. Comparison of fluorite geochemistry from REE deposits in the Panxi region and Bayan Obo, China. *Journal of Asian Earth Sciences* 57:76–89.
- YI, H., BALAN, E., GERVAIS, C., SEGALIN, L., FAYON, F., ROCHE, D., PERSON, A., MORIN, G., GUILLAUMET, M., BLANCHARD, M., ET AL. 2013. A carbonate-fluoride defect model for carbonate-rich fluorapatite. *American Mineralogist* 98:1066–1069.

- ZACHOS, J., PAGANI, M., SLOAN, L., THOMAS, E., AND BILLUPS, K. 2001. Trends, rhythms, and aberrations in global climate 65 Ma to present. *Science* 292:686–693.
- ZAITSEV, A. AND BELL, K. 1995. Sr and Nd isotope data of apatite, calcite and dolomite as indicators of source, and the relationships of phoscorites and carbonatites from the Kovdor massif, Kola Peninsula, Russia. *Contributions to Mineralogy and Petrology* 121:324–335.
- ZAITSEV, A., DEMÉNY, A., SINDERN, S., AND WALL, F. 2002. Burbankite group minerals and their alteration in rare earth carbonatite source of elements and fluids evidence from C–O and Sr–Nd isotopic data. *Lithos* 62:15–33.
- ZAITSEV, A., SITNIKOVA, M., SUBBOTIN, V., FERNÁNDEZ-SUÁREZ, J., AND JEFFRIES, T. 2004. Sallanlatvi complex—a rare example of magnesite and siderite carbonatites. In F. Wall and A. Zaitsev (eds.), *Phoscorites and Carbonatites, from mantle to mine: the key example of the Kola Alkaline Province*. Mineralogical Society.
- ZAITSEV, A. N., WALL, F., AND LE BAS, M. J. 1998. REE–Sr–Ba minerals from the Khibina carbonatites, Kola Peninsula, Russia: their mineralogy, paragenesis and evolution. *Mineralogical Magazine* 62:225–250.
- ZAMBEZI, P., HALE, M., VONCKEN, J., AND TOURET, J. 1997. Bastnäsit-(Ce) at the Nkombwa hill carbonatite complex, Isoka District, Northeast Zambia. *Mineralogy and Petrology* 59:239–250.
- ZHENG, Y.-F. 1990. Carbon-oxygen isotopic covariation in hydrothermal calcite during degassing of CO₂. *Mineralium Deposita* 25:246–250.
- ZHENG, Y.-F. 1996. Oxygen isotope fractionations involving apatites: application to paleotemperature determination. *Chemical geology* 127:177–187.
- ZIEGLER, U. 1992. Preliminary results of geochemistry, Sm–Nd and Rb–Sr studies of post-Karoo carbonatite complexes in Southern Africa. *Schweizerische Mineralogische und Petrographische Mitteilungen* 72:135–142.

Appendix A

A new vent south of Songwe— “Mantrap” Hill

In this chapter, new field descriptions and mapping of an area 0.8×1.2 km, approximately 1.5 km south of Songwe are presented. Due to the lack of a local name for this area, it has been termed “Mantrap” by Mkango geologists. This area was targeted because remote sensing data suggested it could be REE-rich.

Access is relatively easy. ‘Mantrap’ can be reached by vehicle (high wheel base) by taking the dirt road around Mauze anti-clockwise from Songwe, stopping at UTM 36 S coordinates 800597, 8261063 (WGS 84 datum). Mantrap is located approximately 500 m north towards the edge of un-terraced fields and the base of a prominent knoll. It is important to make contact with the local village before proceeding through the fields.

Although it is not previously documented, the hill appears on the original (1960s) geological map as the second of two discrete lozenges of breccia, surrounded by basement, separated by a fault (Garson and Walshaw, 1969). The area was investigated by Mkango following up on a potentially REE-rich target from ASTER¹ satellite data. This was supported by relatively high Y concentrations indicated by portable XRF² analyses of float samples.

The geological descriptions below are based on reconnaissance field mapping carried out over the course of approximately 5 days. Mapping extended from the area around ‘Mantrap Hill’, up to the southern edge of the Mauze nepheline syenite, and onto the hill immediately to the west of ‘Mantrap’ (Fig. A.2). Exposure is poor as much of the hill is covered by terraced fields (Fig. A.1). Where encountered, some of the outcrops were very weathered, and much of the mapping was based on float samples. Where these were found near the top of the hill, it can be assumed with reasonable confidence that the samples were in-situ. Float samples from valleys and the sides of hills were avoided.

¹Advanced Spaceborne Thermal Emission and Reflection Radiometer

²X-ray fluorescence

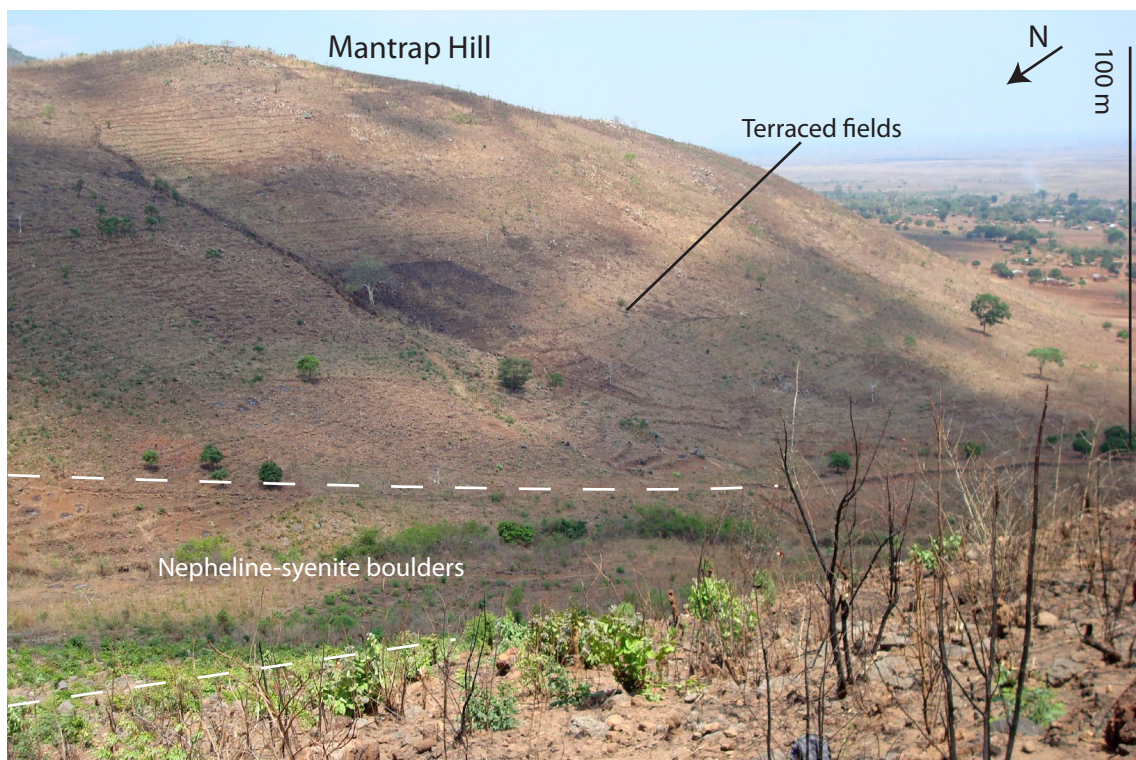


Figure A.1: Mantrap Hill looking from the north. Photo credit: Frances Wall.

355

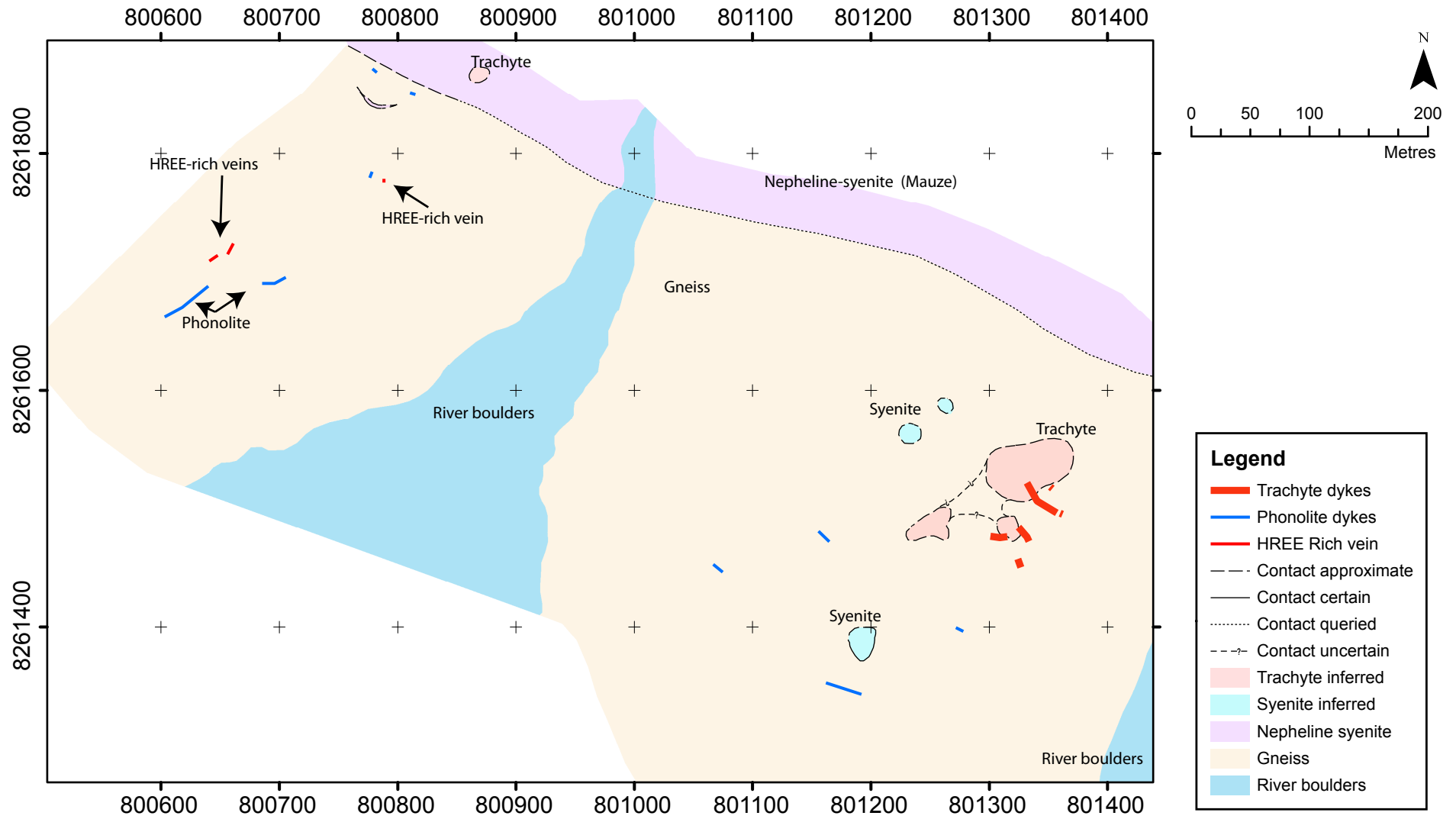


Figure A.2: Sketch map of the vents to the south of Mauze, including "Mantrap" and HREE-rich veins

A.1 Geology

Mantrap is composed of basement gneiss, fenitised to varying degrees, small syenite bodies and phonolite dykes, trachyte with varying amounts of brecciation, and small HREE-rich veins.

A.1.1 Basement

As is common throughout southern Malawi, the basement is composed of granulite and gneiss. Rare calc-silicate bands are observed in thin bands in the banded gneiss around Mantrap, and are most common towards the eastern edge of the mapped area (800650, 8261700; Fig. A.3). Here, the bands are tightly folded, and the calc-silicate minerals distinctly weathered out, with preferential weathering of carbonate and grains of diopside raised on the weathered surface. The bands are typically 5–30 cm thick.

The degree of fenitisation in the basement rocks varies, on the top of 'Mantrap' Hill, fenitisation can be quite strong, with noticeable alteration to K-feldspar. Elsewhere around Mantrap, macroscopic fenitisation is not evident, especially on weathered samples, although some degree of alteration is assumed, based on earlier mapping work (Garson and Walshaw, 1969).

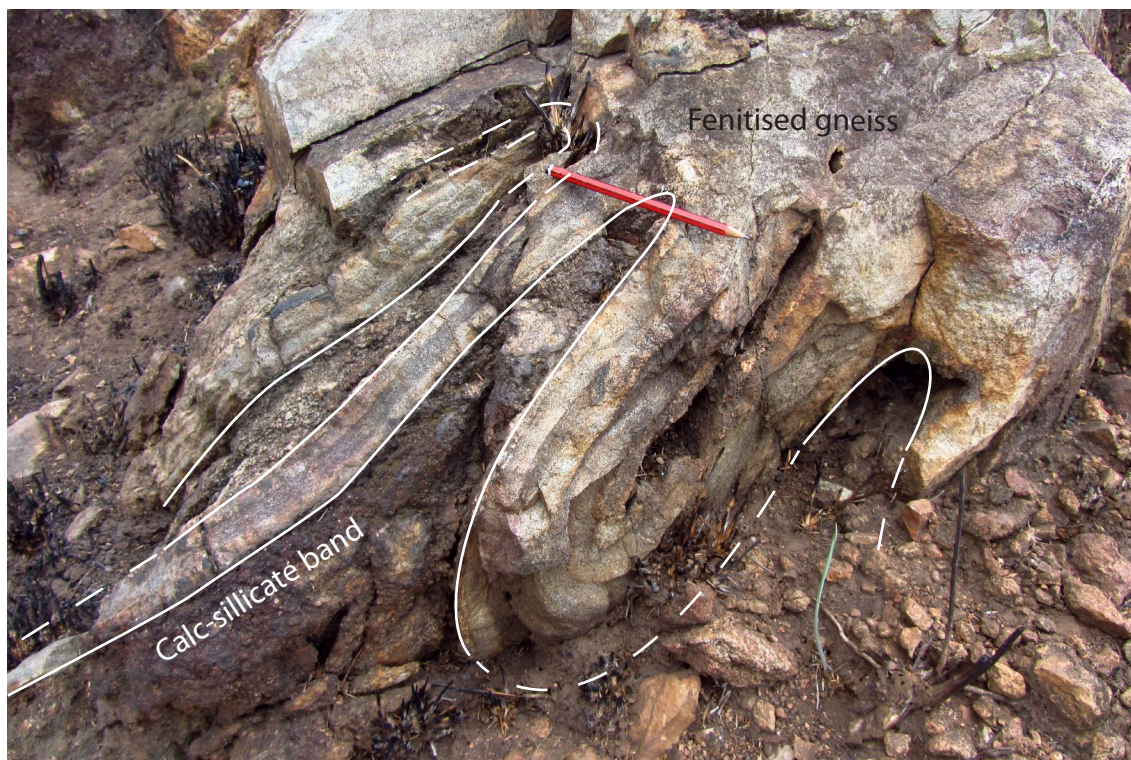


Figure A.3: Example of folded calc-silicate-bearing gneiss.

A.1.2 Syenite

On the north-western and south-western flanks of Mantrap Hill small circular intrusions of coarse-grained–pegmatoidal, equigranular syenite are exposed. Commonly, the contact between the syenite and the gneiss is obscured by cover, but it is well exposed along half of the south-western edge of the intrusion over a distance of about 35 m. The contact is sharp with little evidence of a chilled margin or contact metamorphism. Small veins (approximately 10–20 cm across) can be seen fingering into the gneiss, and the intrusion cross-cuts banding, indicating that the syenite is not part of the basement complex. The syenite is predominantly made up of large perthite crystals, accessory rounded aegirine–augite and a rounded golden-brown mineral tentatively identified as titanite (Fig. A.4).

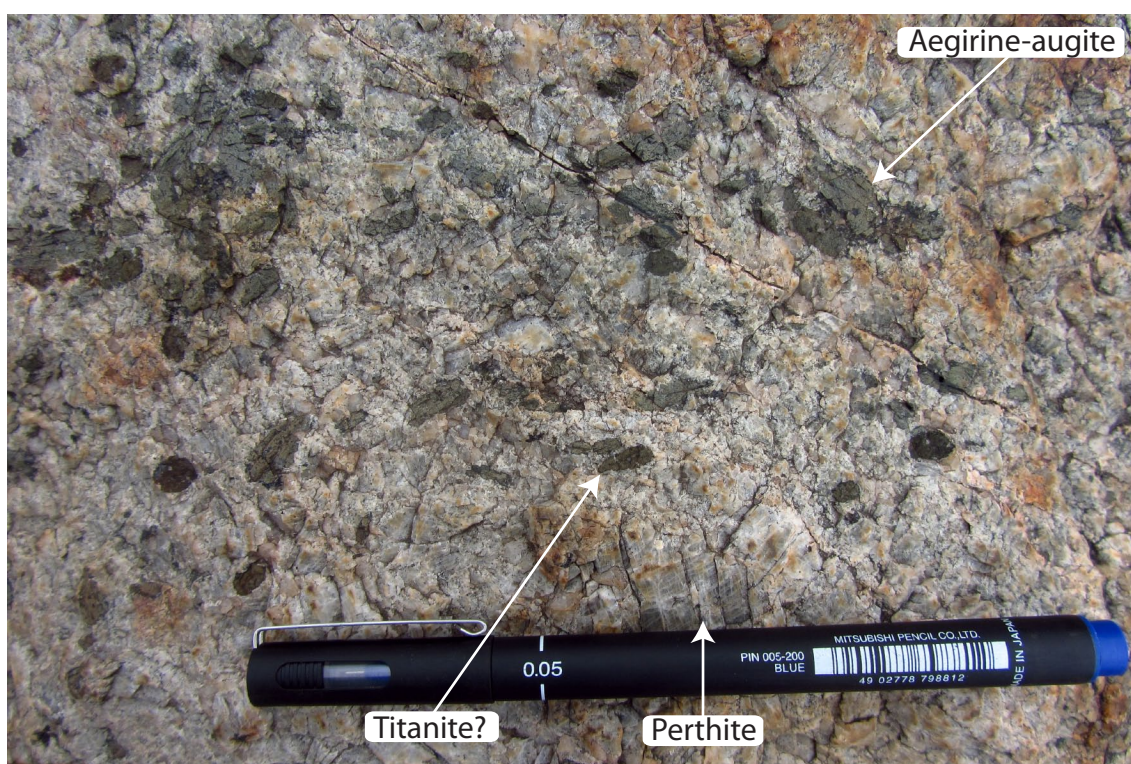


Figure A.4: Typical syenite from the south-west flank of Mantrap Hill.

A.1.3 Phonolite

Phonolite dykes are exposed on the southern side of Mantrap, and on the hill in the west of the mapping area. The dykes are approximately 0.75 m wide. Two of the dykes strike SE–NW, similar to other dykes in this part of the CAP³. However, most of the dykes observed here strike SE–NW, contrary to the strike of other dykes in the region. It is possible that these are ring-dykes related to the intrusion of nepheline syenite on Mauze.

³Chilwa Alkaline Province

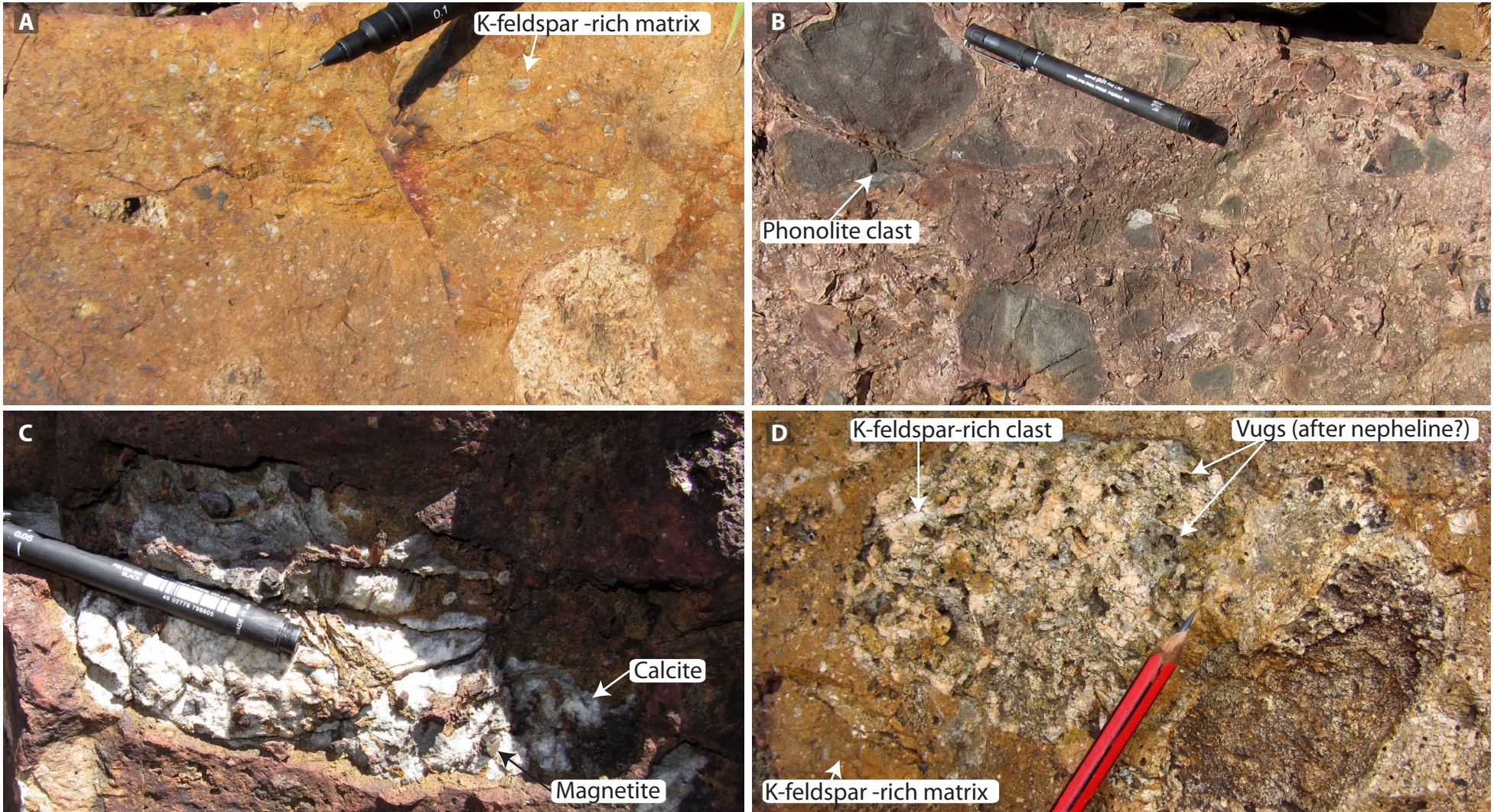


Figure A.5: Examples of trachyte from Mantrap: (A) clast poor, with abundant phenocrysts, (B) with phonolite clasts, (C) with a sövitic carbonatite clast and (D) with an equigranular igneous clast, possibly nepheline syenite. Many of the clasts appear at least partially fenitised.

A.1.4 Trachyte/trachytic breccia

Trachyte is found in three restricted areas at the top of 'Mantrap' hill. Trachyte dykes, approximately a metre wide, radiate from the top of Mantrap Hill, towards the south-east, but cannot be traced further than 50 m. There are no cross-cutting relationships between between the syenite, phonolite and the trachyte.

The trachyte is strongly weathered. Weathered surfaces are yellow–black–dark-red in colour and are commonly irregular (Fig. A.5A). The trachyte contains varying proportions of semi-rounded clasts of different protoliths. The clast-rich areas are supported by a matrix that is conspicuously K-feldspar-phyric. Some of the feldspar appears euhedral, but many grains are fragmented and broken (Fig. A.5A). The matrix is composed of a microcrystalline groundmass. Ferro-magnesian minerals are not evident, but the rocks are strongly weathered to a red-yellow colour, indicating the likely alteration of Fe-bearing minerals to Fe-oxides. Clasts range in size from small, mm-scale, fragments to about 50 cm across. Clearly identifiable clasts include phonolite (Fig. A.5B) and sövitic calcite carbonatite, with euhedral accessory magnetite (Fig. A.5C). Leucocratic, vuggy, equigranular, K-feldspar -rich clasts are also common (Fig. A.5D). This could either be a finer-grained equivalent of the syenite found on the flanks of the hill, or an altered equivalent of the nepheline-syenite from Mauze, where nepheline has weathered out, leaving vugs.

The trachyte dykes are distinctive as they typically contain fewer clasts than the rest of the outcrop; their cross-cutting relationships are ambiguous, and they appear to cross cut breccia-rich areas at the edge of the intrusion, but grade into the centre. It is likely that the dykes and the breccia-rich trachyte are penecontemporaneous.

On the western hill of the mapping area, within the nepheline syenite, a second intrusion of a similar nature can be found. This intrusion is significantly more weathered than the intrusion on Mantrap, and is much smaller, with a diameter of approximately 25 m. This exposure is a similar dark-red–black colour, but is much more clast rich. It is deeply weathered, and surface samples crumble when hammered. Few exposures of matrix are observed.

A.1.5 HREE-rich veins

Thin, HREE-rich veins can be found on the western edge of the mapping area. These were known to be HREE-rich during mapping due to analyses using the portable XRF. The veins are no more than 20 cm across and are found in isolated bands in gneiss, parallel to banding (Fig.A.6A) or within the calc-silicate bands, but not parallel to banding, rather forming anastomosing veins (Fig.A.6B). The veins strike in a NE–SW direction, away from the Mauze nepheline syenite. The

veins are dark-brown–black in colour and are preferentially weathered out against the country-rock gneiss. They are composed of calcite, and some are associated with quartz lenses, to which they could be related (Fig.A.6B; and see chapter 4).

A.2 Portable XRF results

Mantrap was initially targeted as a potential HREE-rich site because HREE float samples were discovered at the base of the hill using a portable XRF. Figure A.7 shows where portable XRF analyses were taken on float and outcrop samples, and the approximate Y concentration from these analyses. The majority of analyses were carried out on higher terrain because this was where exposure is best, and where float samples have a greater probability of representing the outcrop.

On Mantrap hill (in the SE of Figure A.7, and inset), relatively high Y concentrations from float samples on the flank of the hill, were not replicated in outcrop on the peak. Small patches of the trachyte, especially the highly clast-rich trachyte, have above background Y concentration, and four analyses displayed particularly high REE concentrations, but these values are not widespread across the outcrop. Most analyses were between 0–500 ppm Y.

Higher Y concentrations were found in the HREE-rich veins and breccia samples in the west of the mapped area. The Y concentration in these samples varies from 100 to more than 5000 ppm.

A.3 Sampling

19 grab samples of outcrop and float were collected from Mantrap and the surrounding area (appendix C).

A.4 Interpretation and discussion

A.4.1 Order of emplacement

Cross-cutting relationships, and the presence of clasts within the trachytes allow the order of emplacement of the various rocks around Mantrap to be elucidated. This is summarised as:

1. Basement
2. Syenite
3. Mauze and associated phonolite dykes



Figure A.6: HREE rich veins found near Mantrap. Credit for (B): Frances Wall.

362

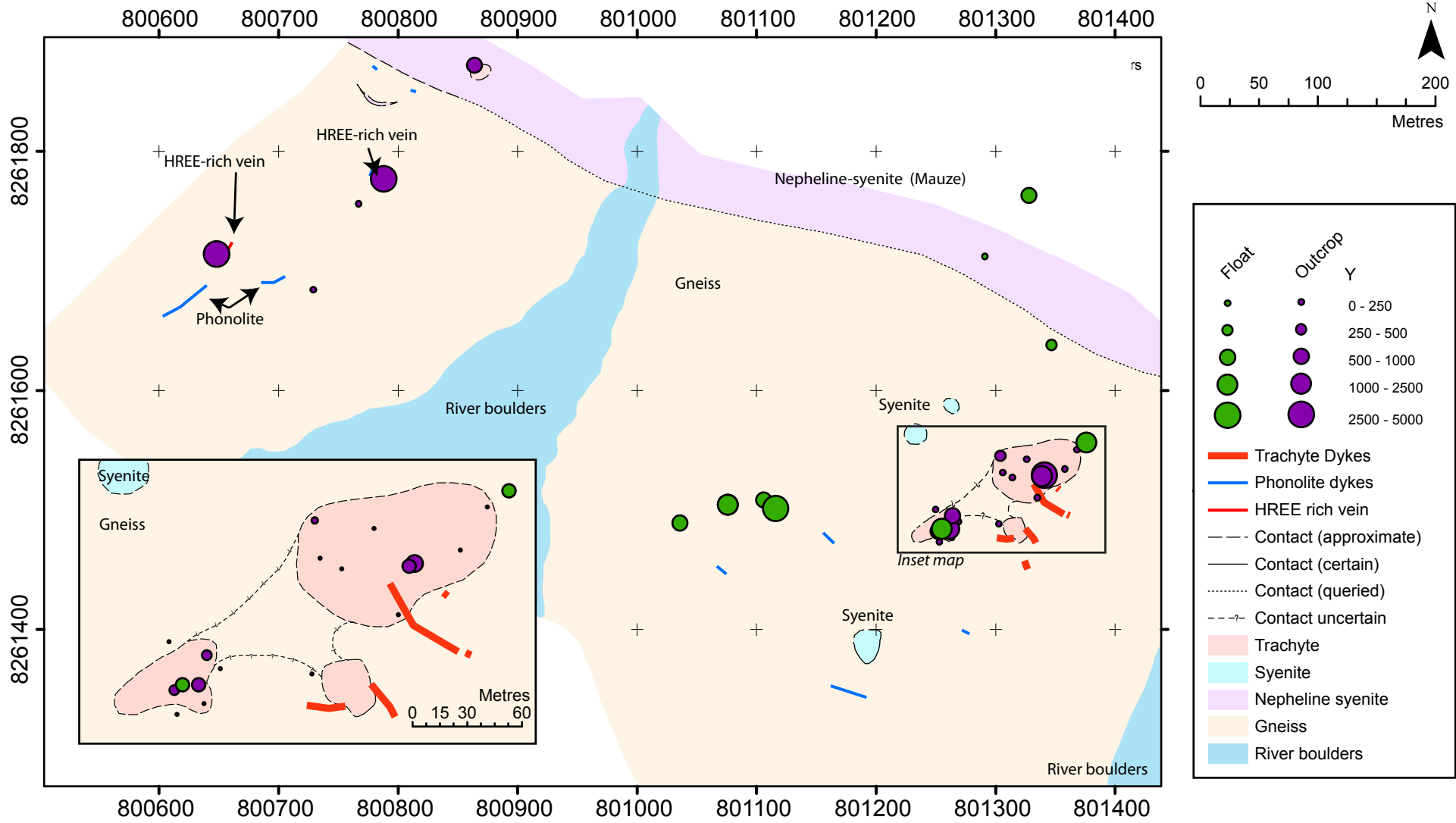


Figure A.7: Geological sketch map of Mantrap and the surrounding area, including spot analyses of Y using a portable XRF.

4. (*Carbonatite — at depth, or derived from Songwe*)
5. Trachyte vents
6. HREE-rich veins

Clearly, the basement precedes all other rock types in the area, although it is likely that emplacement of Mauze has deformed the regional fabric of the gneiss. The small syenite intrusions clearly cross-cut the banding in the gneiss, and thus are interpreted as part of the CAP, and are probably satellite intrusions of Mauze. The temporal relationship of these small intrusions with the other igneous rocks, however, cannot be determined by the field evidence. Based on the cross-cutting relationships of the trachyte vents within the Mauze nepheline-syenite, and the presence of clasts of nepheline-syenite within the trachyte, the intrusion of the nepheline syenite is interpreted to precede that of the trachyte. Phonolite dykes, on the basis of a similar composition, are probably contemporaneous with the intrusion of Mauze, and the strike of the dykes in the south-east of the mapping area is consistent with an interpretation of these rocks as ring-dykes. Carbonatite is inferred to be present at depth from the presence of sövitic carbonatite clasts found within the trachyte. Given that the area around Mantrap is approximately 1.5 km south of Songwe, the two intrusions could be connected at depth. Alternatively the clasts may have been sourced from another, unexposed, satellite carbonatite. The carbonatite clast clearly demonstrates that trachyte forms after formation of C1 carbonatite. The relationship to later-stage carbonatite types is unknown.

Given that the REE mineralisation follows calc-silicate veins in the country-rock gneiss, it is assumed that it was caused through the neutralisation of an REE-bearing, acidic, hydrothermal fluid by carbonate. This fluid could be derived from Songwe or Mauze. REE enrichment within the trachyte *could* be caused by a similar process, but there is currently no clear field evidence to support this. However, the great variability in the REE concentration indicates that HREE-enrichment is not an intrinsic feature of the trachyte (Fig. A.7), and that the REE-enrichment in the trachyte could be caused by the same fluid that produced the HREE-enrichment in some veins. As such, these veins are tentatively considered to have formed after the intrusion of the trachyte.

A.4.2 Trachyte or pseudotrachyte?

True trachytes are defined as volcanic rocks composed essentially of K-feldspar (Le Maitre, 2002). Pseudotrachytes (or terms considered synonymous by Le Bas, 2008), however, have been described from carbonatite complexes (e.g. Garson,

1962; Sutherland, 1965, 1967; Heinrich and Moore, 1970), where fenite transitions to a re-mobilised product which intrudes host rocks as small bodies or dykes (Le Bas, 2008). Such rocks are petrographically similar to trachyte, and composed of small fragments of K-feldspar, recrystallised to structurally-maximum microcline. In some cases, the rock can carry rock clasts, and/or large feldspar fragments which can be mistaken for phenocrysts (Le Bas, 2008). Pseudotrachyte, however, is geochemically distinct from volcanic trachytes. Cooper and Reid (2000) proposed that they form magmatically, generated by the melting of fenite in response to a high heat flux from an emplaced carbonatite. Cross-cutting relationships, at Dicker Willem, Namibia, show that the formation of trachyte was after intrusion of early sövite carbonatite, but followed by late-stage carbonatite emplacement (Cooper and Reid, 2000). Additionally, the presence of trachyte/fenite pellets or globules within the carbonatite means that trachyte formation is interpreted as contemporaneous with the carbonatite emplacement at this intrusion (Cooper and Reid, 2000).

Both mechanisms of trachyte formation (true and pseudotrachyte) could be viable processes for the formation of trachyte at Mantrap. Regionally, sölvbergite (which is a peralkaline microsyenite or peralkaline trachyte; Le Maitre, 2002) dykes are reported (e.g. Garson and Walshaw, 1969), and these formed after carbonatite and alkaline rock mineralisation. The sölvbergite dykes seldom exceed 15 m in width, but can be traced for several kilometres, typically striking in a radial pattern northwards from Mulanje Mountain (to the south of Mauze). They are normally heavily weathered, with a pinkish–buff surface. Where fresh rock is found, the rock consists of dominant K-feldspar, with minor amphibole and pyroxene and interstitial magnetite. The description is similar to that of the trachyte found at Mantrap, but the description of clasts is notable by its absence. The dykes at Mantrap are not traceable for a particularly great distance, and the strike is not aligned north-south. Therefore, these rocks are not considered to be related to the regional sölvsebergite dykes.

The descriptions of pseudotrachytes from Dicker Willem and trachytes from Kaiserstuhl and Toror have many overlaps with the trachyte at Mantrap (Garson, 1962; Sutherland, 1965, 1967; Cooper and Reid, 2000). Trachyte has also been described from Tundulu, having formed from the evolution of feldspathic breccia (Garson, 1962). Not all of the published descriptions of (pseudo)trachyte are directly associated with breccia/feldspathic breccia, but fenitised clasts are commonly found in the (pseudo)trachyte and clasts of sövite were identified in pseudotrachytes at Dicker Willem (Cooper and Reid, 2000), similarly to the trachyte at Mantrap. The temporal relationship between the pseudotrachytes and the spatially associated carbonatites/alkaline rocks is important. Commonly, the pseudotrachytes are emplaced contemporaneously, or prior to the carbonatite.

This is not the case at Mantrap, given the presence of clasts of nepheline syenite and carbonatite in the trachyte which indicate formation after calcite carbonatite emplacement. In the example from Dicker Willem, however, a contemporaneous emplacement is implied on the basis of cross-cutting ferroan-calcite–dolomite carbonatites, which occur after calcite-carbonatite emplacement. While such cross-cutting relationships are not observed at Mantrap, this example demonstrates that pseudotrachyte formation, after intrusion of silicate rocks and calcite-carbonatite, can occur elsewhere.

While it is possible that the trachyte vents at Mantrap are a manifestation of the late regional sölvbergite dykes, it is most likely that the formation is related to the intrusion of Mauze. This is because of the close spatial relationship between the intrusions, and the incorporation of clasts of sövite, syenite and phonolite in the trachyte. Whether the trachyte is an associated true-trachyte intrusion, or a pseudo-trachyte formed from melting of fenite, is uncertain. However, the many parallels between the trachyte at Mantrap and the localities where pseudotrachyte has been described indicate that the Mantrap trachyte is likely to be a pseudotrachyte.

A.4.3 REE mineralisation

REE mineralisation around Mantrap, akin to mineralisation at Songwe, is one of the latest stages identified. As described above, it is cryptically scattered in the trachyte, but clearly follows calc-silicate bands in the country-rock gneiss.

Appendix B

Supplementary analytical methods

B.1 Xenotime EPMA¹ analyses

Analysis of xenotime is subject to a variety of pitfalls which can make setting up an EPMA protocol challenging. Problems include: standard selection, variations in the matrix effects between standards and samples, inter-element interferences, artefacts from the detector and element detection limits (Pyle et al., 2002). These are covered below.

B.1.1 Standard selection

The REE were initially run on Astimex Scientific REE ultra-phosphate standards (REEP₅O₁₄) which are highly susceptible to beam damage. To alleviate this, these standards were run at reduced current and spot size compared to the samples (5 nA and 10 μ m). To circumvent this problem, later runs were calibrated using new REE-phosphate standards, acquired from the Smithsonian institute (Jarosewich and Boatner, 1991; Donovan et al., 2003). However, as some of the Smithsonian standards were damaged/lost during the polishing of the new standard block (Fig. B.1), a mixture of both Smithsonian and Astimex standards was utilised (Table B.1). This is not an ideal scenario, as due to the volatility of the Astimex standards, these standards had to be analysed under different beam conditions to the unknown (Table B.1). The closest conditions to conditions used during unknown analyses, without volatilising the standards, are a defocused beam to 10 μ m and a drastically reduced current to 5 nA.

As many phosphate standards as possible were selected to minimise variation in the ZAF ratio between standards and unknowns, the selection was limited, however, by the availability of standards and for some elements a less than desirable standard was used. Examples are U, Th and Pb, for which pure metals were used.

¹electron probe micro-analyser

Element	Standards	Spot size (μm)	Current (nA)	Voltage (keV)
Nd	Sm_Nd	2	30	20
Sm	Sm_Sm	2	30	20
Eu	Sm_Eu	2	30	20
Gd	Sm_Gd	2	30	20
Tb	Sm_Tb	2	30	20
Dy	Sm_Dy	2	30	20
Ho	Ast_Ho	10	5	20
Er	Sm_Er	2	30	20
Tm	Ast_Tm	10	5	20
Yb	Sm_Yb	2	30	20
Lu	Ast_Lu	10	5	20
Y	Sm_Y	2	30	20
Th	AST-M-Th	2	30	20
U	AST-M-U	2	30	20
Pb	AST-M-Pb	2	30	20
Si	MkII-olivine	2	30	20
Fe	MkII-olivine	2	30	20
Y	Sm_Y	2	30	20
P	AST-Apatite	2	30	20

Table B.1: Standards used, and beam conditions for calibration.

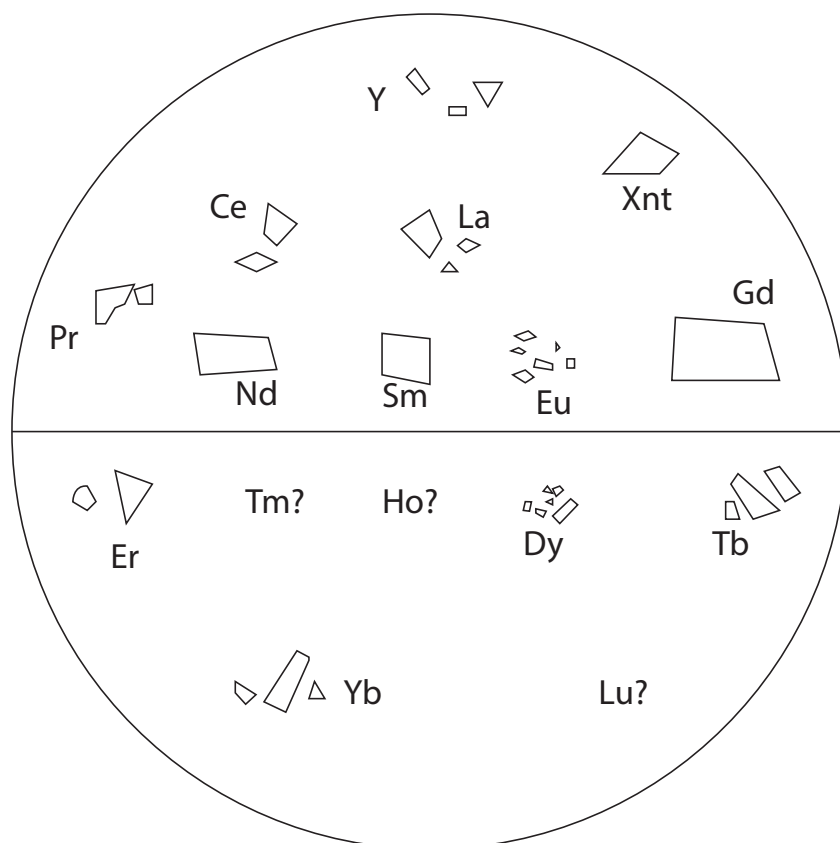


Figure B.1: Mount map of new Smithsonian REE standards

In addition to new calibrations standards, a new check-standard was acquired. Unfortunately, no certified reference standards for xenotime are known (to the best of my knowledge), so a large gem-sized xenotime was acquired from Zagi (*syn: Zegi, Zaga*) Mountain, Pakistan. This was mounted so that it could be routinely re-analysed to help determine the precision of the analyses and to monitor for any drift in the results. The standard is not completely homogenous, but does have large areas of the same BSE² intensity which are assumed to be relatively homogenous (Fig. B.2).

B.1.2 Inter-element interference

Inter-element interferences are a major source of difficulty during EPMA analyses. Background positions were selected using qualitative peak scans on mixed REE glasses, Zagi Mountain xenotime, and on Th, U and Pb metal standards (Table B.2). Where the effects of overlap are significant, a higher resolution detector (e.g. LIF) was used combined with a 30 μm aperture in front of the detector, increasing the spectral resolution of the detector at the sacrifice of a lower peak count. To reduce the analysis time this was only used on elements where the background positions are extremely close to other peaks (Table B.2). Automatic peak seek during analysis was required to be switched off to stop the software mistaking a nearby high intensity peak with the peak of interest. This has the unfortunate side effect of removing the ability to compensate for peak drift on long runs probably caused by stretch in the wire used to position the detector and as such concentrations can decrease through the course of an analytical run.

Where peak overlap was unavoidable empirical corrections were applied, due to time limitations these were only applied to elements where major interferences are known although there are fewer corrections than in published lists (Williams, 1996). This is because many of the overlaps for the HREE are negligible given the low concentrations of the LREE in xenotime (e.g. Ce on Gd). Furthermore, overlaps of Tm on Sm and Ho on Eu are could not be corrected as to measure the overlap the Astimex standards are required and the level of damage cause to the standards during the correction causes spurious results.

Element	Crystal	Peak	Peak position (mm)	BG+	BG-	Overlap
Nd	LifH	L α_1	168.5	2	2	
Sm	LifH	L α_1	153.4	0.6	1.4 ³	Tm ⁴

Continued on next page . . .

²back-scattered electron

³BG is close to Nd L β

⁴Overlap corrections for Tm on Sm and Ho on Eu are no good as to measure the overlap the

Element	Xtal	Peak	Peak	BG+	BG-	Overlap
Eu	LifH	$L\alpha_1$	147.9	1.1	1.9	Dy 0.00478, Ho ⁴
Gd	Lif	$L\alpha_1$	142.7	2.3	1.2	
Tb	Lif	$L\alpha_1$	137.8	0.2	1.8	Er, 0.6986
Dy	Lif	$L\alpha_1$	133.1	2.9 ⁵	2.6	Tm 0.00025
Ho	Lif	$L\beta_1$	114.8	0.45 ⁶	0.4	
Er	Lif	$L\alpha_1$	124.4	3.1 ⁷	1.4	
Tm	Lif	$L\alpha_1$	120.4	0.6	⁸	
Yb	Lif	$L\alpha_1$	116.6	1.4	1.35	
Lu	LifH	$L\beta_1$	99.13	1.87	2.13	
Y	PetH	$L\alpha_1$	210.5	3	2	
Th	Pet	$M\alpha_1$	135	3	3	
U	Pet	$M\beta_1$	125	3	3	
Pb	Pet	$M\beta_1$	167	4	15	
Fe	LifH	$L\alpha_1$	139.5	4	0.5	
Si	Tap	$K\alpha_1$				
P	Pet	$K\alpha_1$	201			
Ca	Pet	$K\alpha_1$	111.5			

Table B.2: Table of analysis conditions for each element analysed. Peak position is in Jeol units. Overlap corrections are empirical correction coefficients.

B.1.3 Detector artefacts

Detector artefacts include problems with changes in the detector energy peak for particular elements and detector gas absorption edge effects where the x-ray continuum changes in a non-linear fashion affecting background placement. These effects have not yet been investigated on the CSM⁹ microprobe.

Astimex standards are required the level of damage cause to the standards during the correction causes spurious results

⁵Bg+ crosses Pb unknown peak (probably not an issue)

⁶Difficult to find BG these are very close to the peak

⁷Bg+ is close to La $L\alpha_1$

⁸No BG- for Tm, cant find acceptable position

⁹Camborne School of Mines

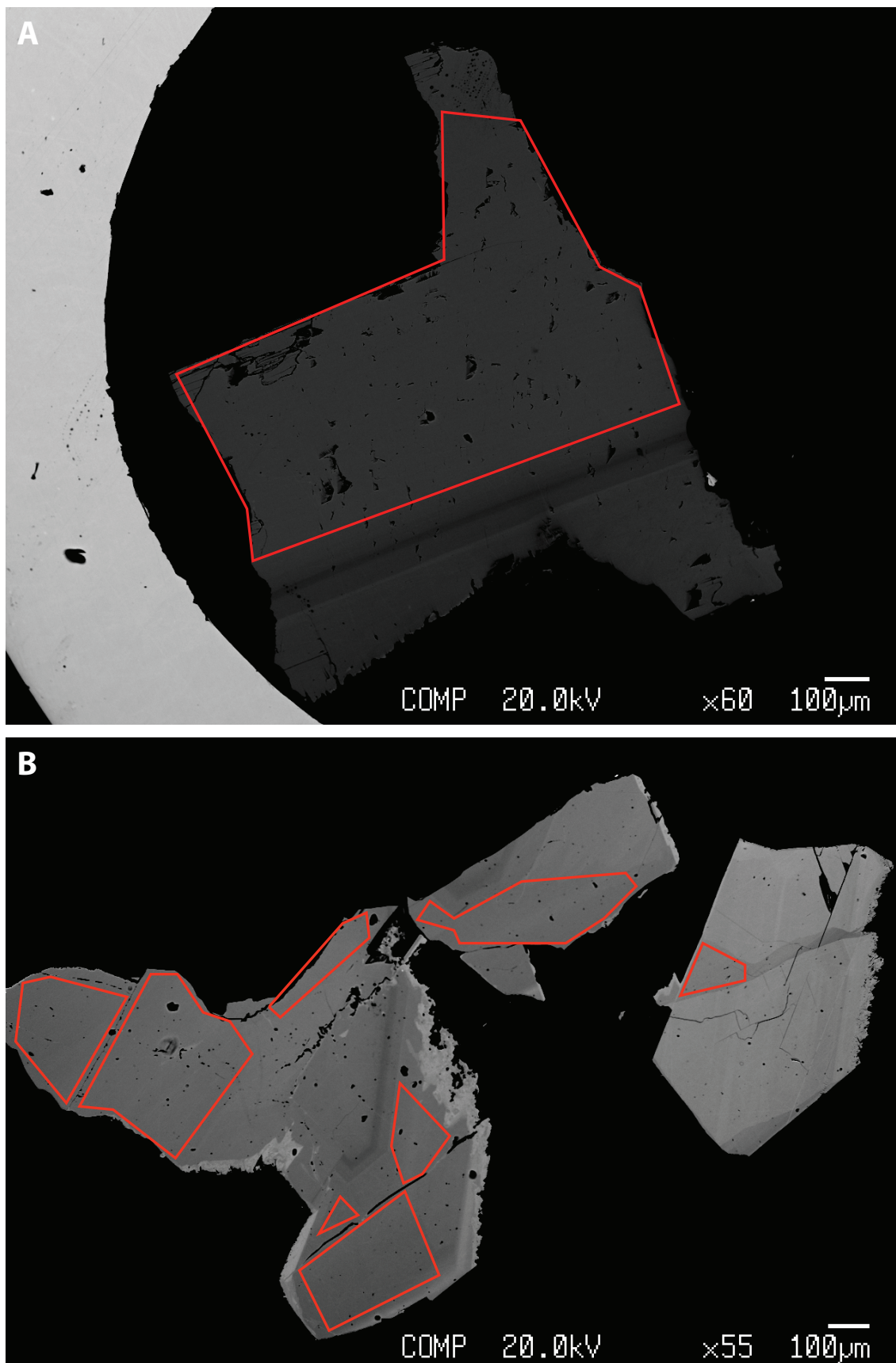
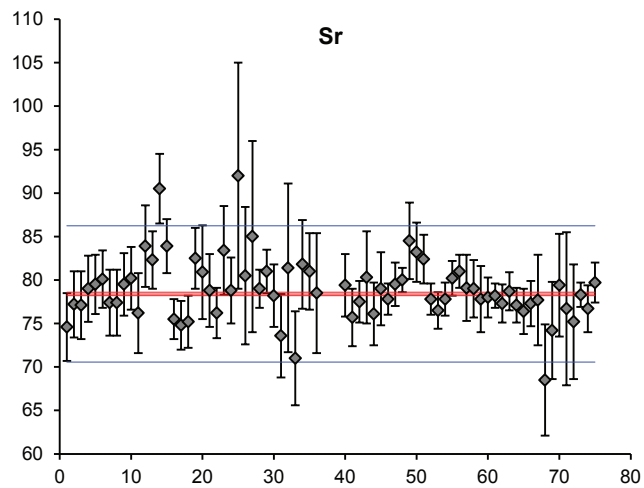
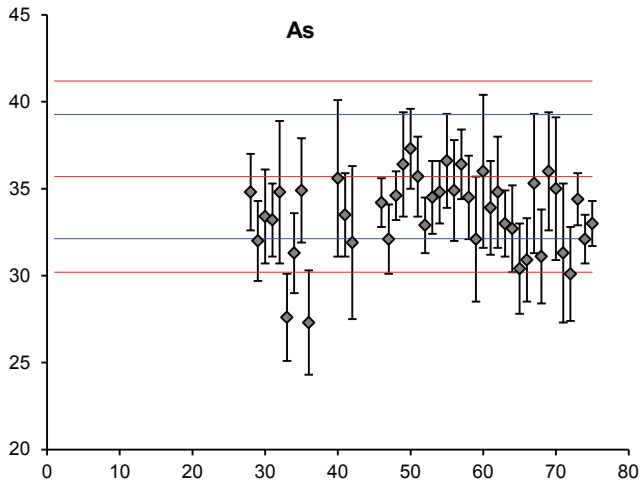
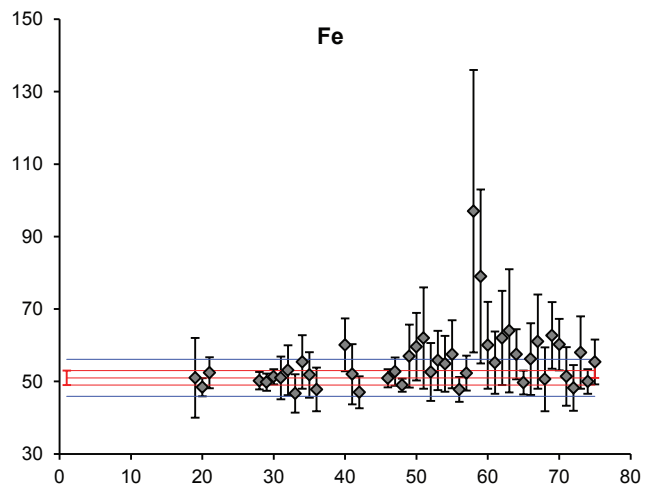
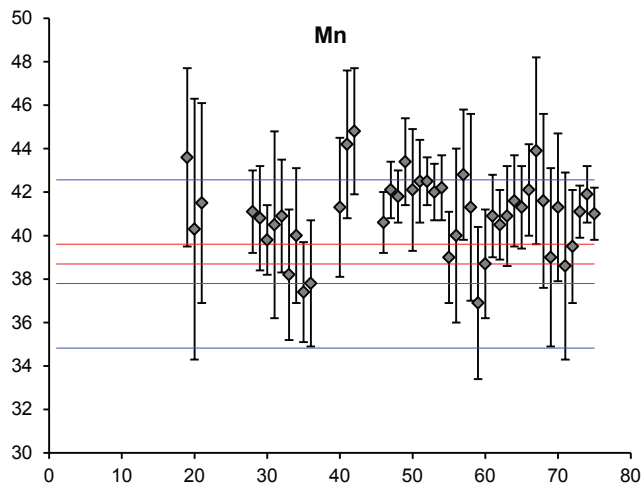
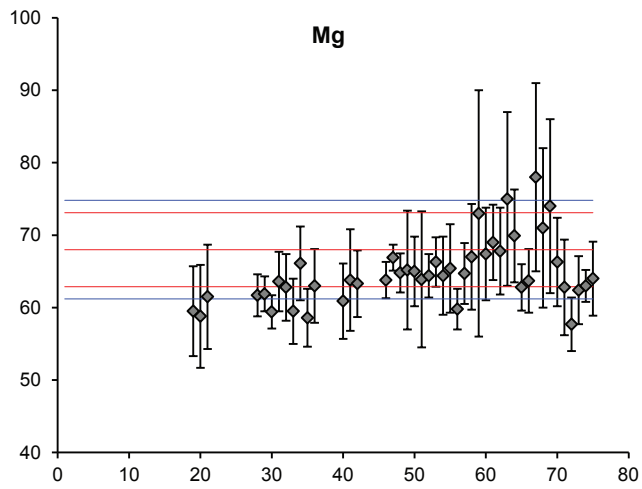
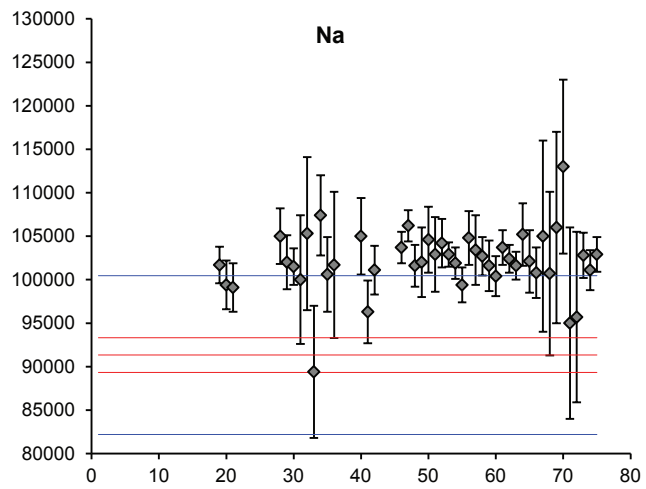


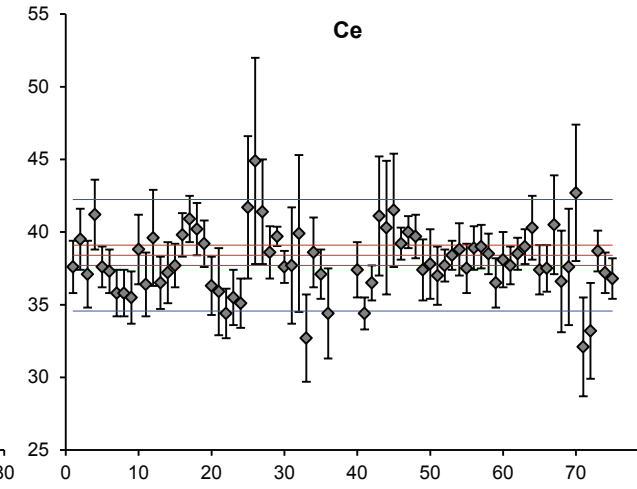
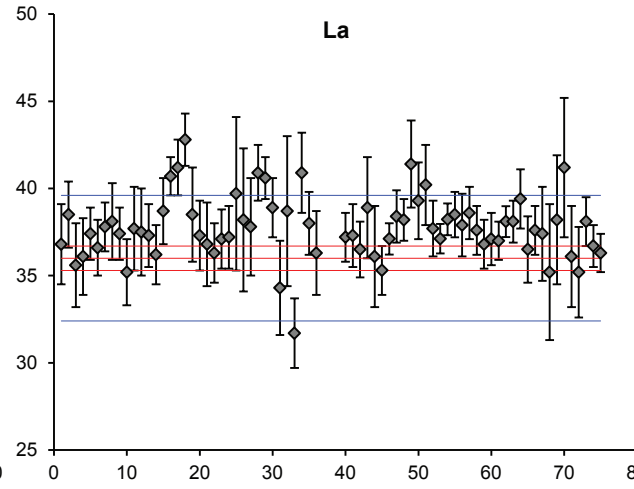
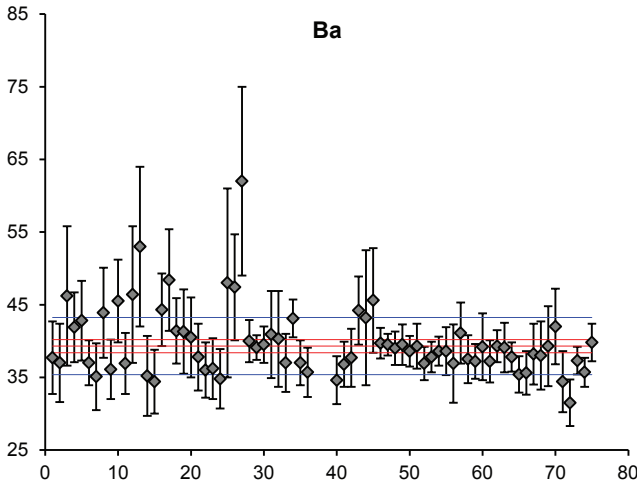
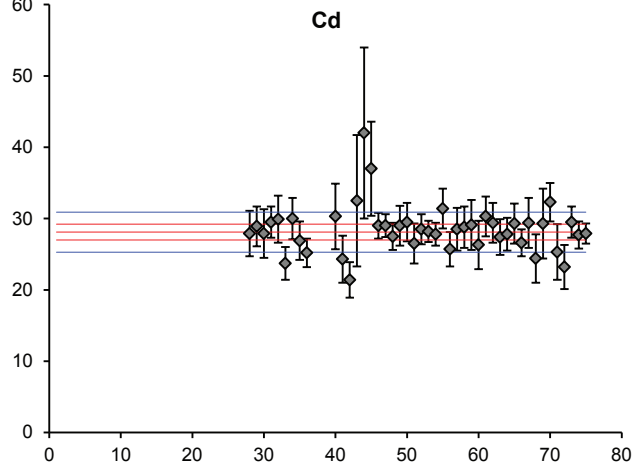
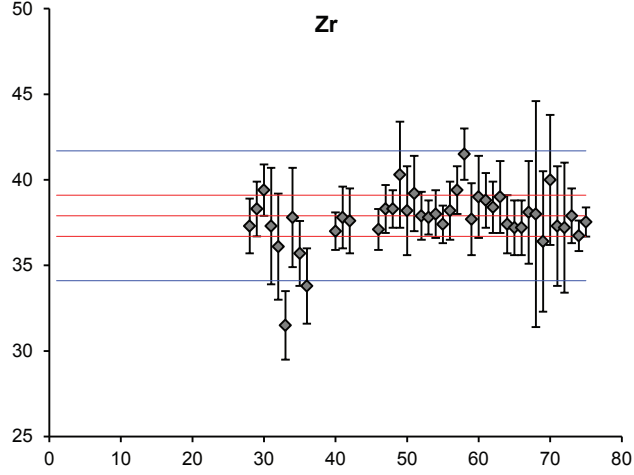
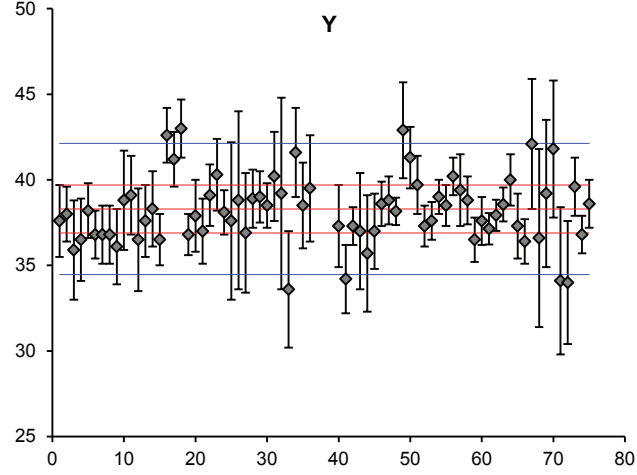
Figure B.2: Areas of approximate equal BSE intensity in the Zagi mountain xenotime check-standard.

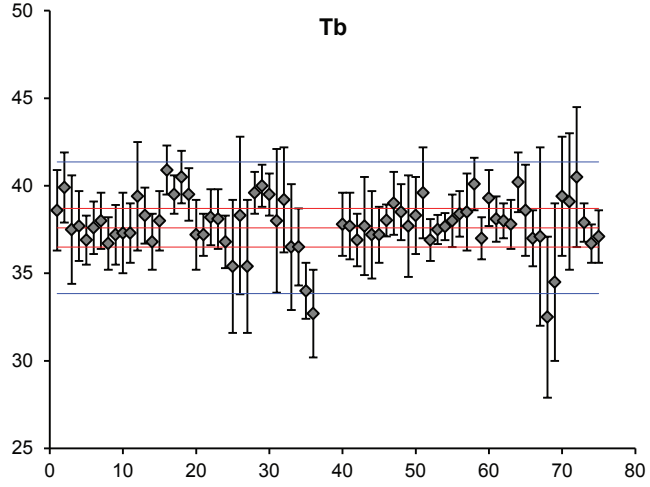
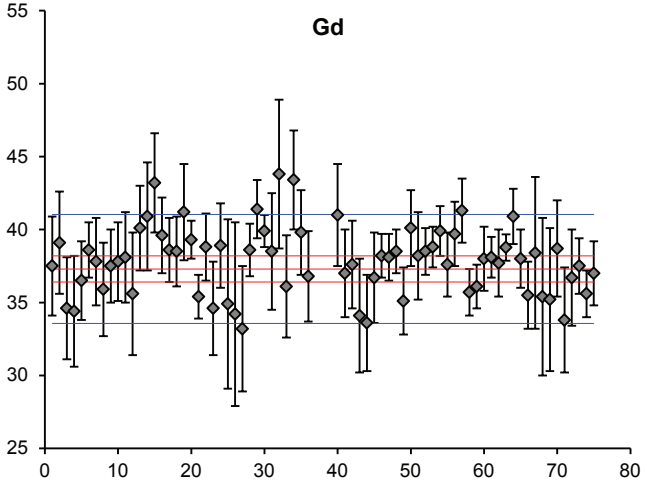
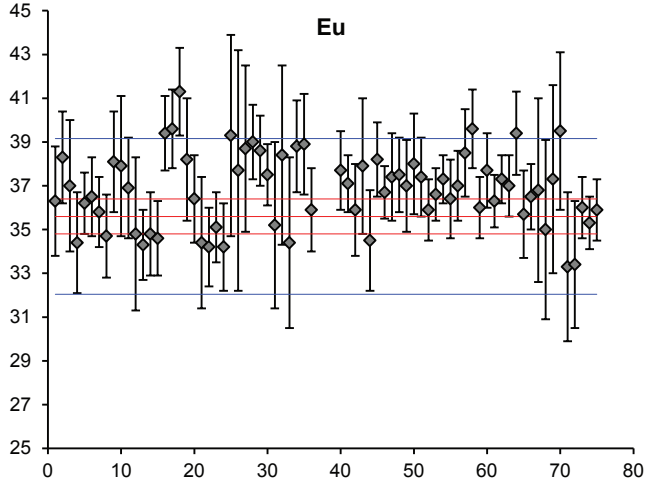
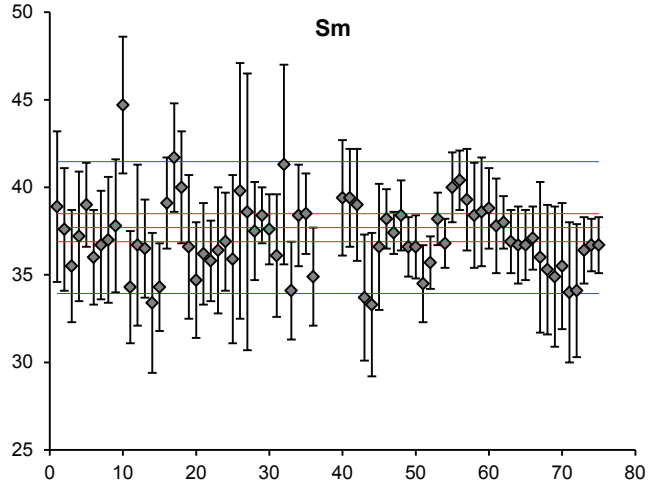
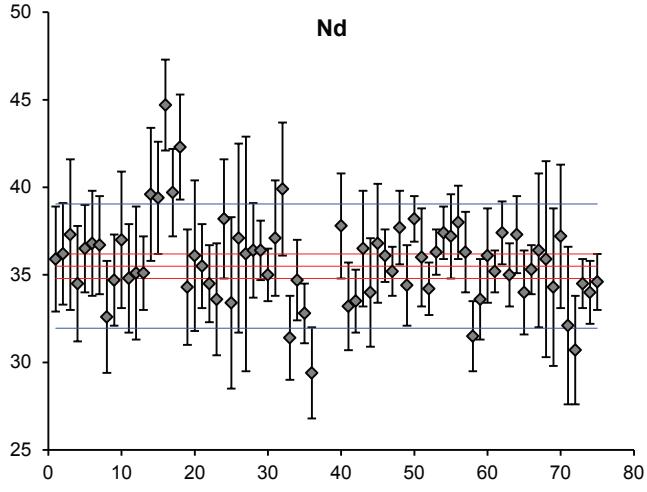
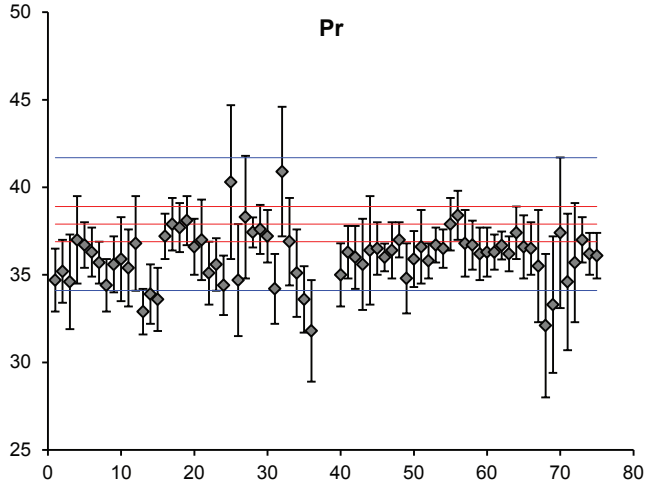
B.2 Laser ablation

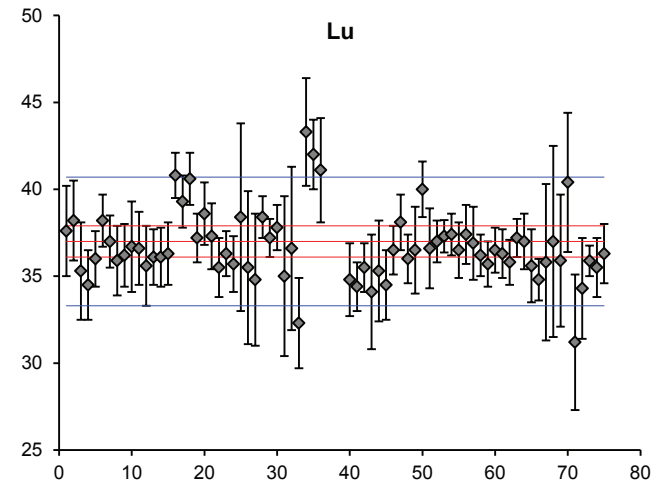
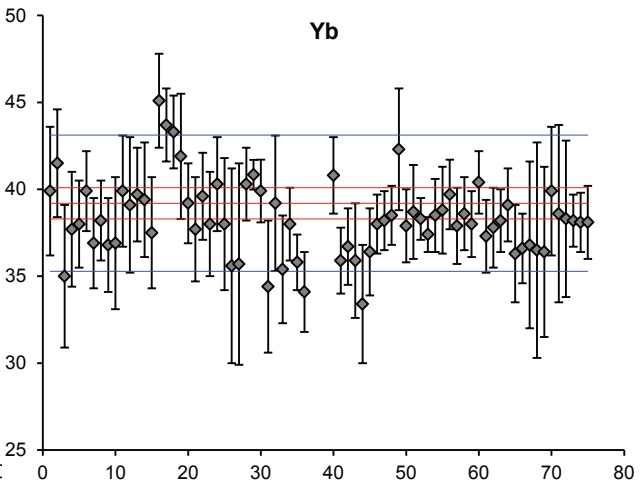
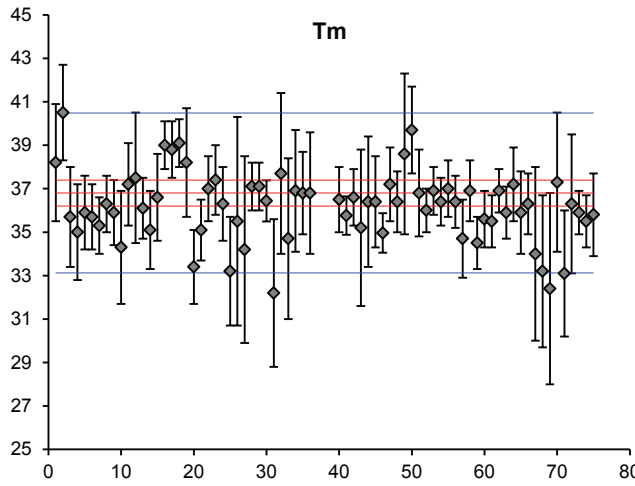
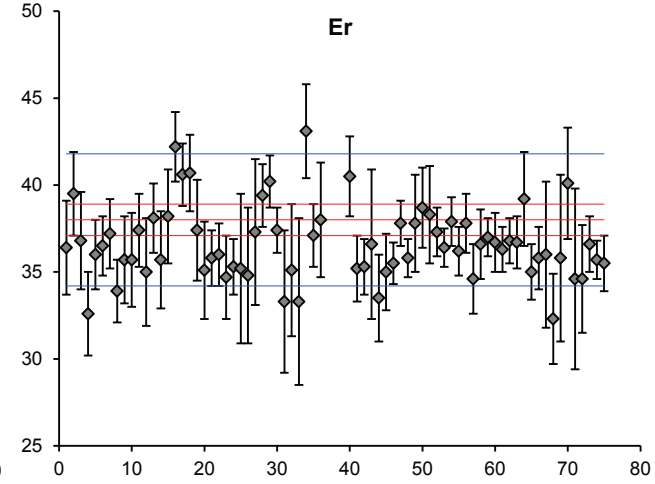
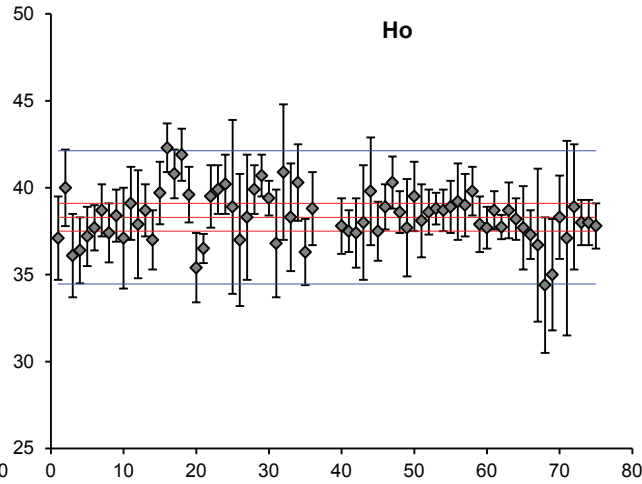
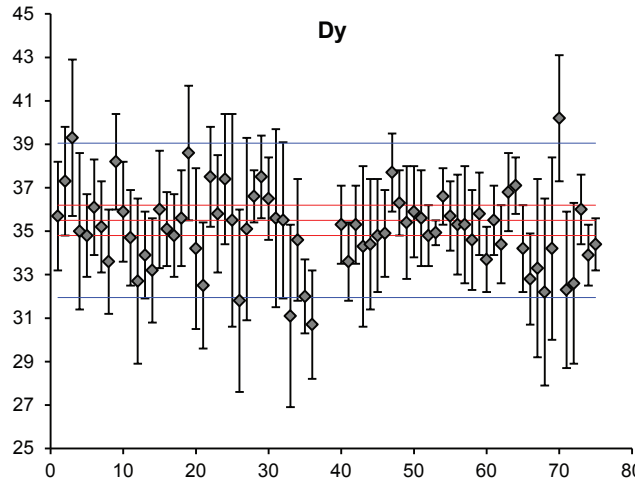
The figures over the next 5 pages are of repeat analyses (x-axis) of SRM¹⁰ 612 by laser ablation, for both results from 2012 and 2013. Both spot and raster analyses are included, but where the accuracy of raster analyses were poor, the data have been deleted and the data from the unknowns were not used. On the graphs, concentration is on the y-axis, and the red lines indicate the published values (centre line) and associated uncertainties to a 95 % confidence (upper and lower red lines). Blue lines indicate values of 5 % above and below the published concentration.

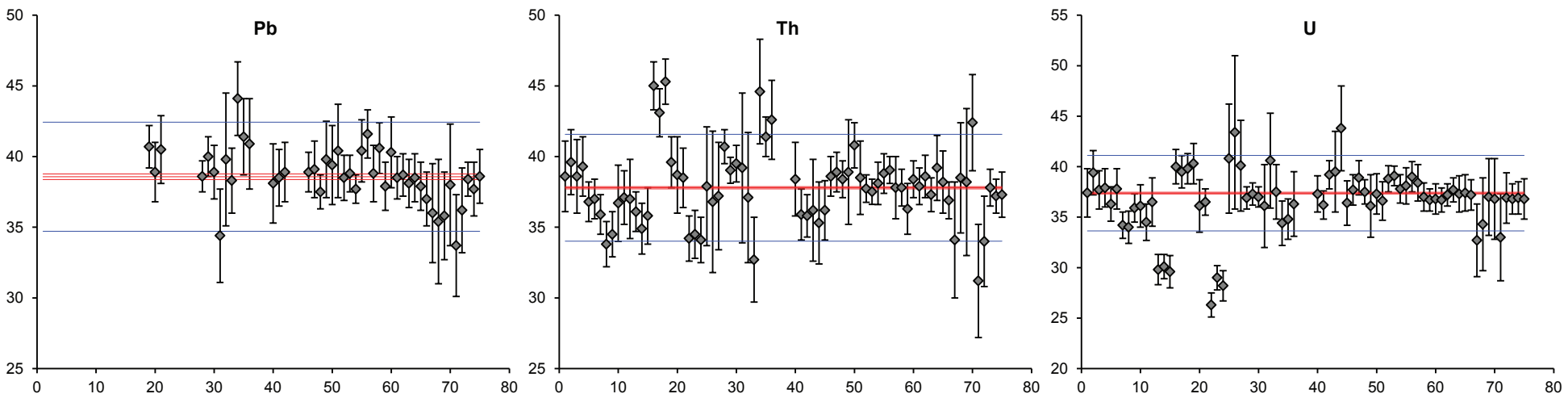
¹⁰Standard Reference Material











Appendix C

Sample list

Hole	Depth (m)	Assay #	Sam #	Lithology	T/S
PX03	89.1	V1299	T0185	Fenite	Y
PX03	79–80	V1290	T0186	Fenitized Phonolite	
PX03	68.5–69	V1279	T0187	Fenite	
PX01	225–226	V3431	T0201	feldspathic breccia	Y
PX27	18–19	X2122	T0202	Fenitized Phonolite	Y
PX27	19–20	X2126	T0203	Fenitized Phonolite	Y
PX27	21–22	X2130	T0204	Calcite Carbonatite	
PX27	22–23	X2131	T0205	Calcite Carbonatite	
PX27	23–24	X2133	T0206	Calcite Carbonatite	Y
PX27	24–25	X2134	T0207	Calcite Carbonatite	
PX27	26–27	X2137	T0208	Carbonatite	Y
PX27	87–87.5	X2215	T0209	Mn/Fe vein	
PX27	88.5–89	X2219	T0210	Carbonatite	Y
PX27	89–90	X2220	T0211	Mn/Fe vein	
PX27	90–91	X2221	T0212	Mn/Fe vein	
PX27	154–155	X2303	T0213	Fenitized Phonolite	
PX30	53–59	X2037	T0214	Fenitized Phonolite	
PX30	53–59	X2037	T0215	Fenitized Phonolite	
PX31	86–87	X2002	T0216	calcite Carbonatite	
PX31	76–77	V1976	T0217	Fenitized Phonolite	
PX31	47–47.1	V1946	T0218	Fenitized Phonolite	Y
PX09	116–119	V1909	T0219	Carbonatite breccia	
PX02	14–14.4	V3559	T0220	Fenite	
PX09	100–100.35	V1892	T0221	Mn/Fe vein	
PX09	20–21	V1801	T0222	Fenitized Phonolite	
PX09	46–47	V1832	T0223	Carbonatite breccia	

Continued on next page...

... Continued from previous page

Hole	Depth (m)	Assay #	Sam #	Lithology	T/S
PX09	49–50	V1839	T0224	Fenite	
PX01	110–110.3	V3263	T0225	Carbonatite	Y
PX09	53–53.5	V1834	T0226	Carbonatite breccia	
PX09	56–58	V1848	T0227	Mn/Fe vein	Y
PX02	61–61.5	V3611	T0228	Mn/Fe vein	
PX02	73–74.3	V3631	T0229	Fenite	
PX11	74–75	V1759	T0230	Fenite	
PX11	47–48	V1722	T0231	Fenitized Phonolite	
PX24	48–49	V1360	T0232	Calcite Carbonatite	Y
PX02	107–108	V3664	T0233	Fenite	
PX11	30–31	V1699	T0234	Calcite Carbonatite	Y
PX11	17–18	V1690	T0235	Fenite	Y
PX23	6–7	V3006	T0236	Calcite Carbonatite	
PX23	8.5–9	V3097	T0237	Calcite Carbonatite	
PX24	20–21	V1332	T0238	Black Carbonatite	
PX24	20–21	V1333	T0239	Black Carbonatite	
PX24	22–23	V1335	T0240	Mn/Fe vein	Y
PX24	23.6–24	V1336	T0241	Mn/Fe vein	Y
PX24	24–25	V1337	T0242	Mn/Fe vein	
PX24	25–26	V1338	T0243	Mn/Fe vein	
PX24	26.6–27	V1340	T0244	Mn/Fe vein	
PX24	31–32	V1343	T0245	Mn/Fe vein	
PX24	32–33	V1411	T0246	Mn/Fe vein	Y
PX24	33–34	V1345	T0247	Mn/Fe vein	
PX05	50.08–50.2	V3732	T0248	Fenite	Y
PX05	0–1	V3676	T0249	Fenite	
PX05	2.3–3	V3677	T0250	Black carbonatite	Y
PX05	3–4	T3675	T0251	no data	
PX05	198–199	V3927	T0252	core loss	
PX05	184–185	V3921	T0253	Fenitized Phonolite	
PX04	211–211.99	V1185	T0254	Fenitized Phonolite	
PX01	16–17	V3121	T0255	Fenite	
PX01	30–31	V3144	T0256	Mn/Fe carbonatic vein	
PX01	45–46	V3166	T0257	Fenitized Phonolite	
PX01	85.15–85.5	V3226	T0258	Mn/Fe vein	
PX04	9–10	V3938	T0258	Fenite	
PX04	119–120	V1080	T0259	Mn/Fe vein	

Continued on next page...

APPENDIX C. SAMPLE LIST

... Continued from previous page

Hole	Depth (m)	Assay #	Sam #	Lithology	T/S
PX12	10–11	V1424	T0262	Fenite	Y
PX12	143–143.5	V1612	T0280	Fenitized Phonolite	
Px18	306–306.5	Y4136	U4921	"Calc-silicate"	Y
Px18	334.4–334.55	Y4173	U4922	"Calc-silicate"	
Px20	347–347.5	Y2828	U4923	Breccia	
Px20	341.3–341.6	Y2821	U4924	Breccia	Y
Px20	342–342.5	Y2825	U4925	Breccia	
Px20	304.5–305	Y2779	U4926	Breccia	Y
Px16	345.5–346	E1122	U4927	"Phonolite"	Y
Px16	344–344.65	E1119	U4928	"Phonolite"	
Px16	363–363.58	E1143	U4929	"Phonolite"	Y

Table C.1: Samples from drillcore

APPENDIX C. SAMPLE LIST

ID	Season	Location	Outcrop	Long	Lat	Hand Specimen names	Notes	Size	T/S?
T0101	10-11 2011	Songwe	o/c	801781	8263438	Carbonatite	grey carbonatite for comparison	4x fist	
T0102	10-11 2011	Songwe	o/c	801726	8263448	Mn rich material	Pink/red fenite w/ microveining	5x >fist	
T0103	10-11 2011	Songwe	o/c	801925	8263567	Fenite	Sample of fenite through grey carbonatite with limonitic weathering.	1x >fist	
T0104	10-11 2011	Songwe	o/c	801925	8263567	Fenite	Standard fenite	1x >fist	
T0105	10-11 2011	Songwe	o/c	px25- px27		Fenite	Heavily altered fenite with limonitic weathering	2x fist	
T0106A	10-11 2011	Songwe	o/c	801904	8263502	Dark carbonatite	Type example of dark ankerite carbonatite with sovite patches	1x >fist, 1x <fist	
T0106B	10-11 2011	Songwe	Float	801904	8263502	veined fenite	Weathered, veined fenite	1x <fist	
T0106C	10-11 2011	Songwe	o/c	801904	8263502	Fenite	Weathered fenite with limonitic coating	1x fist	
T0107	10-11 2011	Songwe	o/c	801924	8263495	Fenite	Partially weathered fenite	3x <fist	
T0108	10-11 2011	Songwe	o/c	801946	8263485	Fenite	Black veins	2x <fist	
T0109	10-11 2011	Songwe	o/c	801745	8263404	Fe rich vein	Weathered yellow, limonitic? Crumbly	1x fist, 2x <fist	
T0110	10-11 2011	Songwe	o/c	801745	8263404	Fe rich vein	Yellow weathered surface, less crumbly	3x <fist	
T0111	10-11 2011	Songwe	o/c	801745	8263404	Fe rich vein	Moderately weathered black Mn/Fe oxide rich rock with white flecks of an unknown mineral and limonitic weathering surface	1x fist	
T0112	10-11 2011	Songwe	o/c	801745	8263404	Fe rich vein	Dark matrix, with white minerals and yellow weathering features	1x fist, 1x <fist	
	10-11 2011	Songwe	o/c	801745	8263404	Fe rich vein	Dark matrix, with white minerals and yellow weathering features	1x >fist	
T0114	10-11 2011	Songwe	Float	801750	8263390	Carbonatite	Nice contact through C-tite and fenite, has fenite, and Mn veins,	fist	
T0115	10-11 2011	Songwe	o/c	801750	8263390	Dark Carbonatite	Sample split through fenite "vein", Mn weathering follows.	1x > fist, 1x fist	
T0116	10-11 2011	Songwe	o/c	801750	8263390	Carbonatite, Breccia, Fenite mix	Weathered, black Mn veins.	1x >fist	
T0117	10-11 2011	Songwe	o/c	801750	8263390	Carbonatite	Weathered carbonatite surface, with black veins of c-tite x cutting.	1x palm slab	
T0118	10-11 2011	Songwe	o/c	801750	8263390	Fenite	Fenite clast found in c-tite, altered by Mn.	1x fist	
T0119	10-11 2011	Songwe	o/c	801750	8263390	carbonatite	weathers white, black c-tite veins	3x <fist	
T0120	10-11 2011	Songwe	o/c	801750	8263390	carbonatite	weathers white, black c-tite veins, fenite vein which bends substantially from the contact.	1x slab	
T0121	10-11 2011	Songwe	o/c	801750	8263386	Breccia	C-tite	3x fist	
T0122	10-11 2011	Songwe	o/c	801747	8263397	C-tite	veined, weathrd c-tite.	4 small broken slabs	
T0123	10-11 2011	Songwe	o/c	801694	8263446	Breccia	Medium, angular fenite clasts in a carbonatite matrix, some clasts are rounded and most are worn at the edges.	1x >fist	
T0131	10-11 2011	Songwe	o/c	Near px3		Dark Carbonatite	Streaked w/ black veins causing dark colouration, sovitic and fenite veins	2x small fists	
T0130	10-11 2011	Songwe	o/c			Dark Carbonatite	Streaked w/ black veins causing dark colouration, probably originally sovitic?	2x fist size	
T0129	10-11 2011	Songwe	o/c	next to px01		Fenite	Mn veined, above PX001	2x > fist, 1x < fist	
T0128	10-11 2011	Songwe	o/c	801859	8263645	Veined fenite	Large peice of veined fenite, veins weather to a coarse black material	1x >fist	
T0127	10-11 2011	Songwe	o/c	801885	8263628	Fenite/ Carbonatite	Breccia w/ fenite and carbonatite clasts	4x fist size, 1x 1/2 fist	
T0126	10-11 2011	Songwe	o/c	801911	8263614	Breccia carbonatite	Classic unveined white c-tite w/ dark bands	1x >fist, 2x <fist	
T0124	10-11 2011	Songwe	o/c			Precipitate	Carbonate precipitate	1x <fist	
T0215	10-11 2011	Songwe	o/c	(next to px09)		Weathered Mn veined Fenite		1x large fist size	
T0132	10-11 2011	Chenga	o/c	801129	8264031	Clast supported breccia	Breccia of Fenitised nepheline syenite, partially fenitised nepheline syenite, Dolerite and partially fenitised gniess. Clast supported, angular clasts ranging from pebbles to boulder size	3x >fist size, 7x <fist size	Y
T0133	10-11 2011	Mantrap	Float	801076	8261504	Breccia	Non-descript, black-dark red breccia, with vugged surface. Feldspathic.	2x <fist	
T0134	10-11 2011	Mantrap	Float	801076	8261504	Breccia	Non-descript, black-dark red breccia, with vugged surface. Feldspathic with purple (fenitised?) core.	1x >fist	Y
T0135	10-11 2011	Mantrap	Float	801333	8261668	Breccia	Light, white core with small red clasts and feldspars, black surface with yellow alteration material	1x >fist	Y
T0136	10-11 2011	Mantrap	Float	801328	8261763	Breccia		1x Fist	Y
T0137	10-11 2011	Mantrap	Float	801376	8261556	Breccia	Close to o/c	2x fist size	
T0138	10-11 2011	Mantrap	o/c	801358	8261534	Breccia	vugged, feldspathic breccia o/c. Light material	1x >fist	Y

Continued on next page...

APPENDIX C. SAMPLE LIST

... Continued from previous page

ID	Season	Location	Outcrop	Long	Lat	Hand Specimen names	Notes	Size	T/S?
T0155	10-11 2011	Mantrap	o/c	801322	8261476	Breccia	Lightly vugged, feldspathic, matrix supported breccia. Clasts are white, very vugged and rounded at the edges	2× >fist	Y
T0156	10-11 2011	Mantrap	o/c	801322	8261476	Breccia	Feldspathic breccia w/ large feldspar phenocrysts, carbonatite clasts and gneiss clasts	2× fist, 2× <fist	
T0157	10-11 2011	Mantrap	o/c	801322	8261476	Breccia	White breccia, weathering purple/red, and yellow	5× fist size	
T0158	10-11 2011	Mantrap	o/c	801322	8261476	Fenitised Gneiss(?)	banded, vugged o/c w/ white & red bands, vugs concentrated in the white bands, black weathering on the white bands.	1× fist size	
T0159	10-11 2011	Mantrap	o/c	801322	8261476	Breccia	Feldspathic Breccia w/ white fractured clasts and gneiss clasts. Some of the clasts are almost completely resorbed while others have distinct edges with the matrix. Weathers yellow and purple	1× fist, 2× <fist	
T0160	10-11 2011	Mantrap	o/c	801322	8261476	Gneiss	Fluid altered gneiss, with gneiss clasts. Clasts have muscovite, plag(?) and quartz with a distinct boundary to the altered material. Altered material has granular texture, is soft and crumbly and has white, tabular minerals on the surface.	1× >fist	
T0167	10-11 2011	Songwe	o/c	801635	8263397	Black Mn/Fe carbonatitic vein	Feldspathic, and white minerals associated,	1× >fist	Y
T0168	10-11 2011	Songwe	Float	n/a	n/a	White ppt on fenite		2× <fist	
T0169	10-11 2011	Songwe	o/c	801566	8263445	Carbonatite	Banded, early stage(?) carbonatite with imbricated fenite(?) clasts indicative of upward flow direction	1× >fist	
T0170	10-11 2011	Songwe	o/c	801660	8263417	Mn Vein	Limonic weathering	1× >fist	
T0171	10-11 2011	Songwe	o/c	801748	8263409	Mn Vein	Wad vein, with some white mineralisation (apatite?) which is a probable carrier for the REEs, Dirty material, which absorbs water very easily. Weathered	1× >fist, 6× <fist	
T0288	10-11 2011	Songwe	o/c	801718	8263424	Mn Vein	Wad vein through carbonatite breccia, white minerals are low; pink minerals in elongate/extruded form are medium. Thin weathering crust is dark on surface. Blue/grey matrix. Reacts w/ acid.	1× >fist, 1× fist	
T0172	10-11 2011	Songwe	o/c	801727	8263446	Mn Vein	Wad vein through carbonatite breccia. Bands of pink minerals concentrated, into strips. (10%).	1× >fist, 1× <fist	
T0173	10-11 2011	Songwe	o/c	801635	8263397	Mn Vein	Wad vein through breccia, pink minerals are concentrated into bands (15%) with minor white minerals (2%) which have small needle structures emanating from a point in a fan like array.	1× <fist, 1× >fist	
T0174	10-11 2011	Songwe	o/c	801642	8263462	Mn Vein	Wad vein through road cut, abundant dirty pink minerals, low white minerals. White minerals are different to previous sample, forming flat masses of small crystals(?) over the surface of the rock. Slightly weathered.	2× fist	
T0175	10-11 2011	Songwe	float	801675	8263506	Mn Vein	Large masses of creamy-white needle-like fanning crystals in wad.	1× >fist	
T0176	10-11 2011	Songwe	o/c	801675	8263506	Mn Vein	Bands of light green/grey minerals in wad	2× fist, 1× <fist	
T0177	10-11 2011	Chenga	o/c	801158	8263789	Breccia	Clast supported breccia with gneiss clasts and brown/grey crystalline matrix	2× >fist	
T0178	10-11 2011	Chenga	o/c	801150	8264006	Breccia	Clast supported breccia with gneiss clasts and brown/grey crystalline matrix, sample has 2× veined material and 1× gneiss clast for reference. Flourite rich matrix	3× >fist	Y
T0264	10-11 2011	Sombani	Float	Hill opposite Songwe	N of Sombani	Breccia	Clast supported breccia w/ red and black pitted weathering surface. Clasts are creamy white, altered plagioclase-rich rock. Pink alteration rim extends 5 mm from matrix	1× <fist	
H0530	10-11 2011	Sombani	Float	Hill opposite Songwe	N of Sombani	Breccia	Clast supported breccia w/ dark red/black weathering surface. "fresh" surface is dirty orange/white w/ black patches. No discernible features or clast boundaries. Thin bands of an unknown white mineral present	1× >fist	
H0531	10-11 2011	Sombani	Float	Hill opposite Songwe	N of Sombani	Breccia	Non-descript pink-grey crystalline mass. Weathers dark w/ black patches. Hammered surface has many small vesicular type pits and trace detritic mineralisation.	1× >fist	
T0265	10-11 2011	Nkaloje	o/c	792675	8274252	Sovite	Coarse grained dark grey carbonatite	3× fist	
T0287	10-11 2011	Nkaloje	o/c	793005	8273920	Sovite	Coarse grained light hite carbonatite with Magnetite phenocrysts	1× >fist	
T0269	10-11 2011	Nkaloje	o/c	792105	8274391	Breccia		1× >fist	

Continued on next page...

APPENDIX C. SAMPLE LIST

... Continued from previous page

ID	Season	Location	Outcrop	Long	Lat	Hand Specimen names	Notes	Size	T/S?
T0304	10-11 2011	Nkalonje	o/c	792197	8273855	Breccia		3 × fist	
T0273	10-11 2011	Nkalonje	o/c	791766	8274302	Breccia		4 × <fist	
T0311	10-11 2011	Mantrap	o/C	801360	8261453	Breccia		2 × fist	
T0277	10-11 2011	Tundulu	O/C	802314	8280379	Carb rich breccia	Dark Fe rich(?) breccia w/ pink fenite clasts. Matrix supported	1 × fist	
T0278	10-11 2011	Tundulu	Float	802279	8280325	Carbonatite	Dark carbonatite with widespread white mineralisation.	1 × fist	
T0279	10-11 2011	Tundulu	o/c	802222	8280304	Banded carbonatite	Flow banded or fluid altered carbonatite with streaks of white and black minerals. Streaks wrap around clasts of calcite carb and fenite	2 × fist	Y
T0280	10-11 2011	Tundulu	o/c	802128	8280159	Carbonatite	Dark carbonatite which weathers knobably and has 2 fenite veins.	1 × fist	
T0281	10-11 2011	Tundulu	Float	802110	8279874	Banded carbonatite	Banded, white and dark carbonatite with pink and black mineralisation	2 × <fist	Y
T0282	10-11 2011	Tundulu	o/c	801976	8279758	Banded carbonatite	Coarse pink and black carb.	1 × fist	Y
T0283	10-11 2011	Tundulu	o/c	n/a		Breccia	Clast supported breccia w/ generally high values in matrix. Choppy, partially fenitised clasts w/ white/grey matrix.	1 × >fist	
T0284	10-11 2011	Tundulu	o/c	801789	82796788	Carbonatite	Banded orange and white carbonatite	1 >fist	
U4902	10-11 2012	Songwe	o/c	n/a	n/a	Fenite	Recrystallised K-spar	1 >fist	
U4903	10-11 2012	Songwe	o/c	n/a	n/a	Fe-carb?	Late stage Fe vein x cutting fenite	a few < fist	
U4913	10-11 2012	Mauze	float						Y
U4914	10-11 2012	Mauze	float						Y
U4904	10-11 2012	Songwe	Trench (px08)						Y
U4909	10-11 2012	Chenga							Y
U4915	10-11 2012	Natache							
U4916	10-11 2012	Natache							
U4905	10-11 2012	Tundulu							
U4908	10-11 2012	Tundulu		802276	8280545				
U4907	10-11 2012	Tundulu							Y
U4906	10-11 2012	Tundulu							Y
U4912	10-11 2012	Nr. Mantrap							Y
U4911	10-11 2012	Mt Mtega							
U4910	10-11 2012	Mantrap							
U4917	10-11 2012	Mantrap							Y
U4919	10-11 2012	Mt. Mtega							Y
U4918	10-11 2012	Manrap							Y
U4920	10-11 2012	Mantrap							
U4916	10-11 2011	Tundulu							Y
F01	10-11 2011	Mauze	float						Y
F02	10-11 2011	Namangali	o/c						Y
F03		Mauze							
F04		Calc-silicate							Y
NHAC	10-11 2012	Tundulu							Y
NHAC 2	10-11 2012	Tundulu							Y
SO-006		Songwe	o/c		Nr. PX-011				Y
T1	10-11 2011	o/c							
T2	10-11 2011	o/c							
T3	10-11 2011	o/c							
T4	10-11 2011	o/c							
T5	10-11 2011	o/c							
T6	10-11 2011	o/c							

Table C.2: List of samples from outcrop

Appendix D

Supplementary analytical data

385

D.1 Whole-rock data

Sample	CC V3115	CC V3116	CC V3434	CC V3435	CC V3436	CC V3441	CC V3442	CC V3444	CC V3445	CC V3446	CC V3447	CC V3448	CC V3450	CC V3452	CC V3454	CC V3455	CC V3457	CC V3458	CC V3461	CC V3462	CC V3463	CC V3464	CC V3466	CC V3467
SiO ₂	0.86	1.07	1.50	0.64	0.86	1.71	3.85	4.06	1.28	0.43	1.28	1.71	1.93	1.28	1.93	1.07	1.50	0.43	2.78	1.28	1.07	3.64	2.14	1.28
TiO ₂	0.15	0.37	0.47	0.35	0.70	0.30	0.17	0.20	0.15	0.13	0.28	0.13	0.25	0.17	0.57	0.13	0.33	0.13	0.23	0.12	0.17	0.38	0.30	0.87
Al ₂ O ₃	0.42	0.55	0.60	0.43	0.36	0.72	1.28	1.42	0.45	0.30	0.51	0.89	1.13	0.70	0.81	0.49	0.74	0.17	0.96	0.51	0.49	1.21	1.27	0.79
FeO _t	3.20	7.47	13.77	13.44	14.22	13.26	11.44	12.56	9.98	13.11	9.49	13.88	11.85	9.97	14.11	7.83	10.68	7.98	14.29	12.49	10.73	14.79	20.30	20.97
MnO	1.55	1.55	2.20	2.45	2.71	2.20	2.07	2.32	2.07	1.55	2.07	2.58	2.32	1.94	2.45	1.94	2.32	2.07	2.32	2.84	2.07	2.32	2.32	2.45
MgO	0.20	0.18	3.02	4.18	4.08	3.42	3.38	3.70	2.82	1.86	2.94	3.83	3.52	2.74	3.18	3.40	3.48	3.32	3.47	4.79	3.33	2.54	2.64	2.70
CaO	48.69	46.03	32.88	31.34	31.20	30.92	30.78	30.36	36.10	35.54	37.36	30.08	33.72	36.52	32.04	38.48	35.12	39.60	31.34	30.08	36.94	31.06	26.72	26.58
Na ₂ O																								
K ₂ O	0.20	0.24	0.42	0.25	0.14	0.41	0.89	1.00	0.46	0.16	0.42	0.52	0.49	0.31	0.42	0.22	0.27	0.11	0.61	0.30	0.28	0.90	0.43	0.27
P ₂ O ₅	1.28	1.70	0.73	2.34	1.95	1.42	2.29	1.01	1.17	8.32	1.86	0.87	2.18	2.57	0.94	1.42	2.73	4.26	1.21	2.80	4.90	1.51	4.26	4.72
SrO	0.96	1.07	1.59	2.22	1.24	3.04	2.80	2.07	2.56	2.47	2.06	2.60	2.22	2.61	1.14	2.28	1.54	2.05	1.95	2.55	1.67	1.54	1.84	1.84
Nb ₂ O ₅	0.03	0.07	0.21	0.20	0.17	0.40	0.23	0.28	0.49	0.34	0.21	0.36	0.13	0.21	0.14	0.29	0.38	0.33	0.44	0.18	0.15	0.57	0.49	0.40
LOI (1000 °C)	39.35	36.52	35.67	35.55	36.25	35.58	33.70	34.29	36.40	29.48	36.13	35.80	35.24	35.23	35.24	38.05	35.94	36.07	35.36	34.59	33.90	28.30	31.45	33.06
Total	96.89	96.83	93.06	93.41	93.88	93.37	92.89	93.27	93.93	93.68	94.61	93.26	94.98	94.23	92.98	95.60	95.02	96.50	94.99	92.54	95.70	88.77	94.17	95.94
ppm																								
Ba																								
Be	2	2	2	2	2	2	5	4	2	2	1	2	6	3	4	2	5	3	4	10	3	2	6	4
Cr	0	0	0	0	0	0	0	0	0	0	0	0	0	0	0	0	0	0	0	0	0	0	0	0
Ga	6	5	14	14	14	11	13	14	15	14	13	14	13	15	13	15	12	14	10	13	12	15	14	14
Hf	0.3	0.9	0.7	0.6	0.6	0.8	0.8	0.5	0.6	0.6	0.5	0.6	0.5	0.7	0.6	0.5	0.7	0.4	0.6	0.5	1	2.2	1.6	3.8
Li	1	1	3	3	3	5	4	2	2	2	2	2	3	3	2	2	5	2	3	4	8	20	3	2
Sc	0	0	0	0	0	0	0	0	0	0	0	0	0	0	0	0	0	0	0	0	0	0	0	0
Sn	4	6	4	4	5	4	3	4	4	3	4	4	4	4	9	4	5	6	4	2	12	5	10	6
Ta	1.1	3.6	1.5	0.8	0.4	1.7	2.1	2.2	0.7	0.6	0.5	2.3	2	0.8	1.1	1.1	0.7	0.4	2.3	0.8	0.7	1.7	1	0.9
Th	197	225.9	172	263.9	171.3	262.9	265.3	220	192.5	163.1	202.8	324	314.5	369.8	219.5	180.4	138.6	193.9	185.5	217.6	163.2	206	181	144.7
U	6	6.6	6.2	13.1	6.5	13.9	9.1	11.4	8.1	6.7	5.9	7.8	10	8.6	3	5.2	8.9	13.7	7.3	8.1	9.6	8.8	5.7	7.9
V	50	91	180	185	261	148	121	149	125	133	145	146	153	120	226	110	144	107	141	118	144	136	190	241
W	2	6	10	11	10	17	8	9	10	9	6	12	7	7	7	7	13	8	16	6	8	21	18	23
Zr	15	47	36	27	28	34	38	26	20	22	15	25	29	25	35	20	35	8	27	20	48	94	84	180
La	949.2	1022	2930.5	3813.6	2892	4818.6	4783.8	3071.4	3363.6	3179.3	3153.8	3955.9	2983.5	2780.4	2581.1	3372.5	3899.8	2687.9	3111.8	5939.4	2914.3	2491.6	2614.2	2393.5
Ce	1876.2	1967.8	6069.8	7338.2	6340.8	7987.4	8225.4	6204.2	6956.5	6918.4	6682	7109.3	6224.3	6020.7	5718.8	6961.3	7964.4	6291.8	6177.7	9961.4	6980.4	5713.2	6037.5	5748.6
Pr	190.97	207.09	670.77	776.32	727.23	781.07	822.38	662.39	771.74	792.99	754.6	740.06	676.78	672.66	662.17	766.31	872.08	722.24	651.28	934.68	801.12	639.28	703.18	643.66
Nd	637.6	682.3	2391.9	2703.8	2601.6	2620.7	2691.5	2420.8	2866.2	2930.1	2744.3	2569.2	2500	2492.9	2462.6	2788.4	2938.5	2598.2	2131.2	2847.7	2835.5	2304.6	2570.9	2384.8
Sm	100.6	112.7	307.2	369.4	332.2	348.1	368.2	335.5	405.3	428.5	385.4	405	391	369.6	363.1	382.4	406.5	409.6	308.2	372.2	416.7	337.2	385	358.2
Eu	34.1	39.7	81.6	101.8	87.5	103.1	105.9	95.4	114.4	125.9	109.4	123.1	114.5	112.7	102.4	105.3	112.5	124.7	89	105.9	115.2	91.8	111.9	102.2
Gd	90.6	103.7	197.3	249.7	205.5	263.2	271.1	238	283.6	332.9	268.5	299.4	293.3	294.2	255.5	250.4	245.3	289.7	201.2	235.6	250	197.2	252.9	225.1
Tb	14.02	15.82	20.05	27.78	20.82	29.56	31.23	26.2	30.3	36.71	29.27	31.93	33.5	36.65	24.32	26.71	33.31	46.54	26.32	34.72	32.95	24.73	35.14	31.34
Dy	72.5	81.1	91	130	99.5	134.6	153.7	118.9	133.1	176.4	138.3	133.7	167.2	184.2	98.9	122.9	155.9	224.5	107	161.9	152.8	107.6	158.3	141.2
Ho	13	13.9	15.3	22.4	17.7	22.9	26.7	20.4	21.6	30.1	23.8	20.3	28.1	31.4	14.3	21.6	27.9	45.5	17.1	31	28.6	19.9	29.9	26
Er	32.9	35.4	37.1	52.6	45.3	53.1	62.3	47.2	48.8	67.9	57.4	42.2	63.8	71.9	32	52.4	64.8	108	37.6	71.1	72.3	48.5	68.7	59.9
Tm	4.75	4.91	5.22	6.63	5.91	6.2	7.36	5.54	5.78	7.7	7	4.5	7.66	8.54	3.85	6.56	8.26	13.69	5.04	8.75	10.18	6.95	8.98	8.16
Yb	30.7	32.4	35.3	37.7	35.1	33.1	39.9	32.1	34.5	40.8	41	26	42.7	48.3	25.6	39	46.8	71.4	30.6	47.1	60.8	44.4	49.6	47.5
Lu	4.25	4.47	4.65	4.64	4.46	4.26	4.69	3.85	4.49	4.78	5.13	3.17	5.31	5.97	3.72	5.02	5.66	8.02	3.93	5.48	7.63	5.72	5.9	5.72
Y	336.9	355	370.4	559.1	470.4	569.4	631.2	509.6	521.5	748.9	574.4	474.3	689.3	791.7	331.7	556.9	693.1	1190.7	408.9	757.7	717.3	484.7	706.5	626.4
Total	97.42	97.40	94.64	95.34	95.54	95.48	95.05	94.91	95.77	95.54	96.38	95.16	96.67	95.89	94.50	97.42	97.08	98.24	96.57	95.07	97.52	90.27	95.80	97.48

¹ Total including REO and traces. Abbreviations: CC, calcite-carbonatite; FCC, ferroan-calcite-carbonatite; MFV, Mn-Fe-veins; AFV, apatite-fluorite-veins

Continued...																								
Sample	CC V3468	CC V3469	CC V3470	CC V3471	CC V3472	CC V3473	CC V3474	CC V3475	CC V3476	CC V3477	CC V3478	CC V3481	CC V3482	CC V3484	CC V3488	CC V3493	CC V3495	CC V3497	CC V3498	CC V3502	CC V3503	CC V3504	CC V3505	CC V3506
SiO ₂	1.28	4.92	1.50	2.78	1.07	0.86	1.28	0.86	1.50	0.64	0.86	1.50	3.21	2.35	0.64	3.21	4.49	4.28	4.49	0.86	2.14	1.07	2.14	1.50
TiO ₂	0.28	0.23	0.12	0.22	0.20	0.30	0.15	0.15	0.15	0.13	0.20	0.18	0.17	0.20	0.12	0.20	0.25	0.28	0.27	0.28	0.35	0.33	0.23	0.23
Al ₂ O ₃	0.62	1.53	0.64	0.94	0.47	0.40	0.57	0.34	0.85	0.45	0.49	0.76	1.02	0.85	0.60	1.32	1.62	1.70	1.70	1.00	0.55	0.70	0.60	
FeO _t	13.03	11.76	11.41	13.51	10.58	11.33	10.91	9.84	11.36	10.51	13.83	11.75	11.95	11.10	10.06	8.80	11.72	8.90	8.12	14.81	14.94	10.82	9.02	8.63
MnO	2.45	2.07	2.45	2.97	2.58	2.45	2.20	2.20	2.32	1.42	1.42	2.20	2.07	1.94	1.42	2.07	1.68	2.20	2.07	2.45	2.07	1.81	1.81	1.55
MgO	3.71	2.45	3.18	4.58	3.76	3.02	3.20	2.62	3.17	1.34	1.26	3.27	2.27	2.22	1.77	2.49	2.30	2.55	2.50	3.10	2.62	2.09	1.92	2.02
CaO	30.22	33.44	35.26	28.82	33.58	34.70	34.00	36.80	30.78	39.88	36.80	31.62	33.16	35.96	38.06	34.42	33.44	35.82	37.08	32.32	32.60	37.92	38.20	39.60
Na ₂ O																								
K ₂ O	0.24	1.24	0.41	0.69	0.19	0.20	0.36	0.14	0.27	0.16	0.12	0.31	0.75	0.63	0.16	0.80	1.05	0.99	1.08	0.18	0.45	0.34	0.52	0.42
P ₂ O ₅	3.80	1.81	0.99	0.96	4.54	4.19	6.37	3.35	4.67	24.38	1.44	2.20	2.13	2.93	6.46	2.84	1.17	1.05	2.43	2.73	6.32	2.70	8.09	2.73
SrO	3.38	2.09	1.90	2.18	3.44	2.60	3.11	2.53	4.75	2.55	1.37	3.48	2.01	1.76	2.92	3.47	2.33	2.39	2.08	2.25	2.06	2.67	2.66	2.43
Nb ₂ O ₅	0.63	0.50	0.25	0.20	0.07	0.05	0.08	0.10	0.06	0.08	0.39	0.22	0.79	0.20	0.13	0.14	0.28	0.05	0.04	0.18	0.30	0.15	0.09	0.10
LOI (1000 °C)	32.89	37.10	35.60	34.20	34.17	34.08	31.65	34.79	31.17	13.70	35.44	34.53	32.21	34.82	29.02	33.94	34.28	35.45	34.44	34.57	28.15	35.42	29.69	35.73
Total	92.56	99.15	93.71	92.05	94.65	94.18	93.88	93.71	91.06	95.25	93.63	92.00	91.74	94.97	91.37	93.69	94.62	95.67	96.31	94.49	92.99	95.86	95.07	95.54
ppm																								
Ba																								
Be	9	23	2	14	3	4	2	2	3	4	3	4	2	3	2	3	7	4	4	3	3	2	1	1
Cr	0	0	0	0	0	0	0	0	0	0	0	0	0	0	0	0	0	0	0	0	0	0	0	0
Ga	12	17	13	8	14	16	14	15	15	16	16	11	20	12	11	8	14	17	16	12	18	17	15	17
Hf	5.2	0.6	0.5	1.1	1.8	2.3	0.5	0.5	0.9	1.4	0.7	0.7	0.4	0.5	0.4	1.2	1.6	1.6	2.5	1	0.7	0.4	0.7	0.4
Li	4	3	2	5	3	4	4	7	8	3	4	7	4	5	8	11	3	5	3	3	5	5	6	6
Sc	0	0	0	0	0	0	0	0	0	0	0	0	0	0	0	0	0	0	0	0	0	0	0	0
Sn	6	7	3	3	3	3	2	0	3	3	4	3	4	6	2	5	3	2	0	3	4	4	3	3
Ta	1	2.5	1	1.5	0.6	0.6	0.6	0.6	0.6	2.1	1.3	1.2	1.6	1.3	1.7	3.3	3.7	4.3	3.9	1	1.4	0.8	0.6	1.1
Th	442.2	298.6	192.5	156.1	322	246	384.8	257.3	405.6	792.8	151.7	423.2	174.5	497.6	187.3	237.5	162.6	283.3	397.6	241.2	166.6	228.7	405.5	345.7
U	19.3	21.6	10.7	7	8.4	8.5	10.7	9.5	11.8	19.4	9.8	12.2	16.9	20.7	16	14.2	9.3	5.7	11.9	7.3	6.9	8.9	23.3	14.9
V	169	135	126	126	156	166	139	85	142	65	93	114	94	122	66	109	128	119	107	149	175	154	129	128
W	25	21	10	8	4	4	5	5	3	10	14	8	20	10	7	7	12	5	5	9	13	8	7	7
Zr	231	32	24	64	86	116	23	21	35	77	32	31	16	27	17	61	91	106	141	48	35	17	25	20
La	6752.5	2728	3622.5	6367.2	3593.7	3131.7	3478.4	6555	9074.7	3139.1	3475.1	6649.5	4146.2	3224.4	6590.1	5735.1	3426.8	3869	3035.9	3318.3	3034.2	3767.3	3610.7	3133.1
Ce	10856	6092.2	7977.8	10683	7530.1	7262.2	7392.4	11207	15103	7455.8	8573.9	11809	9270	7185.1	11461	9853.7	7126.9	8479	7032.6	7245.8	6539.2	8076	8196.1	7399.9
Pr	1030.7	694.78	876.76	968.66	828.61	867.9	840.45	1079.3	1449.6	893.37	1011.5	1157.3	1043.3	802.12	1134.1	966.15	793.89	938.65	791.74	805.48	750.9	893.26	920.65	894.08
Nd	3090.5	2461.8	3043.1	2892.1	2806.3	2951.2	2804.6	3504.5	4555.4	3278.9	3719.9	3863.8	3671.3	2765.6	3714.5	2968.1	2747.7	3278.5	2807.6	2746.5	2568.2	3163.7	3270.3	3235.7
Sm	419.1	368	423.3	349.8	417.4	447.6	453.8	433.8	554.8	658.8	498.6	535.9	457.8	402.9	477.7	395.5	406	490.7	430.5	416.1	378	480.6	495.9	499.3
Eu	121.2	102.4	117.3	94	120.7	123.1	131.9	119.7	153.2	216.8	123.8	147.3	116.2	114.3	133	111.7	114.8	137.7	122.1	119.6	107.2	133.6	146.8	138.9
Gd	289.3	218.8	240.1	201.2	259.8	271.7	306.4	259.8	317.5	505.2	243.3	289.4	223.4	255.8	290.9	245	255.5	309.5	267.4	262	244.7	307.6	333.9	318.8
Tb	41.62	28.87	29.54	24.46	37.18	35.82	45.42	34.25	41.98	77.45	28.37	35.83	25.42	40.24	37.68	33.81	34.41	40.22	37.79	36.85	34.16	40.17	49.14	43
Dy	204.9	138.6	123	103.6	166.4	165.2	217.9	153.7	195.9	382.6	116.7	147.4	112.7	208	170.3	161.5	160.3	185.4	185.9	176.5	170.7	181.7	251.4	201.5
Ho	38.7	25.9	21.1	17.7	30.5	29.8	40.8	29.4	36.9	75.6	18.6	25	21.6	41.9	31.8	33.9	30	33.9	35.7	34.8	35.4	31.8	52.6	37.9
Er	89.1	65.5	47.9	39.7	72.2	65.4	97.1	69.9	93.1	185.5	41.7	56.3	52.5	104.1	76	86.4	66	71.8	87.7	87.2	93	75.6	135.4	91.5
Tm	11.66	8.84	6.23	5.05	9.37	8.57	13.35	9.54	11.95	25.93	5.59	7.56	7.23	13.82	9.88	11.19	8.09	8.67	11.84	11.23	12.39	9.7	18.72	12.53
Yb	68.6	54.7	37.2	29.5	52.3	48.6	82.2	55.4	64	146.9	37.1	44.2	44.1	81.8	56	62	42.3	46.3	69.6	66.9	67.4	58.6	103.4	73.7
Lu	8.42	7.02	4.93	3.7	6.5	6.29	9.64	7.19	7.39	17.21	5	5.62	5.61	9.81	6.77	6.89	4.78	5.63	8.93	8.27	7.9	7.19	11.85	9.07
Y	1020.9	693.4	517.8	414.5	751.5	710.1	1059.7	745.6	1071.8	1986.6	430.5	601.2	552.4	1114.5	761.8	920.7	724.3	825.2	956.5	888.6	1049	817	1429.9	967.3
Total ¹	95.43	100.78	95.73	94.67	96.64	96.10	95.89	96.56	94.92	97.51	95.79	95.01	94.06	96.92	94.29	96.24	96.51	97.89	98.20	96.41	94.77	97.99	97.31	97.56

¹Total including REO and traces. Abbreviations: CC, calcite-carbonatite; FCC, ferroan-calcite-carbonatite; MFV, Mn-Fe-veins; AFV, apatite-fluorite-veins

Continued...

Sample	CC V3508	CC V3509	CC V3511	CC V3512	CC V3513	CC V3514	CC V3515	CC V3525	CC V3526	CC V3532	CC V3534	CC V3535	CC V3537	CC V1220	CC V1221	CC V1222	CC V1225	CC V3681	CC V3682	CC V3683	CC V3684	CC V3685	CC V3686	CC V3687
SiO ₂	1.28	2.14	3.85	4.71	3.21	2.57	2.57	2.57	1.93	2.57	1.50	1.07	3.85	1.07	0.64	1.07	0.00	0.00	0.86	0.00	0.00	2.78	0.00	0.00
TiO ₂	0.32	0.38	0.22	0.15	0.22	0.55	0.45	0.18	0.00	0.23	0.17	0.17	0.18	0.12	0.10	0.20	0.00	0.10	0.17	0.00	0.00	0.33	0.08	0.00
Al ₂ O ₃	0.45	0.62	1.21	1.61	1.11	0.79	0.96	1.15	1.00	1.08	0.55	0.47	1.34	0.79	0.45	0.66	0.13	0.19	0.43	0.25	0.13	0.83	0.19	0.23
FeO _t	7.46	12.61	12.25	6.97	9.93	14.38	15.75	10.37	25.14	8.43	15.19	14.51	6.33	11.72	11.63	16.40	4.91	7.49	10.00	4.93	4.68	11.08	4.22	7.17
MnO	1.16	1.55	1.68	1.42	1.68	1.55	1.42	1.55	4.13	2.07	1.29	1.81	1.29	3.23	3.10	3.36	2.07	1.29	1.55	1.29	1.42	1.81	1.42	1.42
MgO	1.01	1.48	2.14	1.51	1.87	1.92	1.99	1.58	3.53	2.30	1.76	2.06	1.29	2.92	4.10	4.83	2.42	0.28	0.32	0.58	0.45	0.27	0.41	0.51
CaO	43.52	37.36	34.00	38.62	35.96	34.14	33.16	36.52	27.70	37.50	33.58	33.44	40.44	29.80	32.60	26.44	41.56	45.05	43.38	47.15	48.97	41.84	48.13	46.17
Na ₂ O																								
K ₂ O	0.25	0.49	0.82	1.11	0.77	0.53	0.57	0.59	0.42	0.51	0.35	0.29	0.88	0.24	0.19	0.22	0.00	0.10	0.28	0.17	0.14	0.65	0.16	0.10
P ₂ O ₅	1.05	1.90	3.62	3.37	4.10	0.50	1.35	2.45	2.57	2.66	5.27	5.25	5.73	1.95	5.61	3.83	3.92	2.06	1.24	0.53	1.47	1.86	2.06	1.95
SrO	2.00	1.76	2.45	2.59	3.19	1.21	1.50	2.17	1.99	2.43	2.76	2.67	2.20	4.16	2.53	3.10	2.54	1.89	1.37	1.76	0.67	0.31	0.77	0.62
Nb ₂ O ₅	0.08	0.07	0.26	0.08	0.06	0.25	0.21	0.07	0.05	0.11	0.23	0.09	0.06	0.06	0.10	0.42	0.01	0.04	0.07	0.02	0.02	0.11	0.02	0.07
LOI (1000 °C)	38.59	35.15	32.39	33.17	32.60	36.49	34.96	33.54	32.64	34.90	31.55	32.01	31.24	33.06	31.39	28.88	36.39	36.90	35.67	40.22	39.55	33.29	38.53	37.20
Total	97.18	95.51	94.88	95.30	94.71	94.89	94.89	92.74	101.09	94.78	94.19	93.84	94.84	89.12	92.45	89.41	93.95	95.39	95.32	96.89	97.51	95.15	96.00	95.43
ppm																								
Ba																								
Be	1	1	2	3	4	2	2	3	2	3	2	2	2	4	3	6	2	0	2	1	1	2	1	0
Cr	0	0	0	0	0	0	0	0	0	0	0	0	0	0	0	0	0	0	0	50	0	0	0	0
Ga	8	11	15	16	10	18	15	16	18	16	13	13	13	0	0	0	9	10	8	9	11	8	8	8
Hf	0.4	0.5	1	0.7	0.9	0.5	0.5	0.6	0.7	0.8	1	0.8	0.4	0.7	1.1	1.6	0	0	0.2	0.2	0.2	0.2	0.2	0
Li	2	4	5	5	6	3	3	5	8	3	3	4	4	5	4	9	2	3	4	3	3	2	2	2
Sc	0	0	0	0	0	0	0	0	0	0	0	0	0	29	0	23	0	0	0	0	0	0	0	0
Sn	2	10	3	2	4	4	3	0	0	3	3	0	2	0	3	5	0	0	0	0	0	4	0	0
Ta	2.1	2.2	2.6	4.2	1.6	2.3	2	2.1	1.2	2.7	1.3	0.9	2	0.4	0.5	0.9	0	0.5	0.4	0.3	0.2	1.2	0.1	0.4
Th	175.6	725.6	291.7	354.4	559.7	119.1	141.1	592.9	289.2	271.5	267.4	371.4	333	332.2	296.1	301.1	159.1	239.7	268.2	192.5	324.4	530.2	330.8	239.8
U	6.1	30.6	23	16.9	22.3	5	9	25.7	14.2	14.3	20	16.6	5	5.1	5.3	0.8	19.2	17.8	8.6	19.5	37	22.1	25.9	
V	103	149	126	94	111	150	149	102	86	109	105	125	92	98	121	130	0	154	192	121	111	224	93	145
W	6	8	15	7	8	15	13	8	4	7	11	6	5	6	9	17	1	5	6	2	2	9	2	6
Zr	22	22	42	36	37	14	25	22	28	39	50	37	22	38	57	93	17	6	10	8	7	12	8	9
La	1439.7	2233	3148.3	2918.5	3850.8	2535.6	2613	3388.2	3849.7	3389.3	2671.9	3199.1	2765.8	11690	5537.1	9325.4	3616.4	2062.4	2708.5	1946.5	2099.6	2488.6	2005.4	2218.3
Ce	3407.4	5116.8	6978.2	6790.9	7785.4	6192.3	6357	7950.3	9208.1	7546.6	6311.3	7173.3	6344.1	16680	9253	12997	7413.8	3942.7	4818.7	3680.9	3937	4759	3803.9	4195
Pr	378.89	581.22	790.71	787.48	836.67	746	754.46	947.92	1055.9	878.14	747.72	830.52	722.09	1671	1040.6	1251.4	931.04	444.45	507.81	405.82	434.45	515.24	408.67	458.39
Nd	1347.2	2101.7	2805.4	2806.9	2749.5	2805.4	2752	3383.1	3534	3021.3	2669.2	2913.8	2465.5	4996.5	3387.2	3590.5	3334.7	1544.8	1713.1	1400.9	1489.8	1807.5	1412	1580.5
Sm	215.4	332	416.3	434.9	400.9	415.2	420.3	516.4	493.1	441.8	404.9	444.6	367.8	573.7	430.1	369.2	470.7	231.8	237.6	201.6	208	271.7	200.9	216.3
Eu	64.7	99.3	118.3	132.2	116.2	111.6	116.4	146.2	132.1	124.2	114.3	129.5	107.4	143.4	109.6	92.9	124.5	66.8	66	55.9	57.8	77.3	56.7	59.1
Gd	148	238.2	265.4	294.4	272.1	237.6	239.4	326	280.5	268.3	258	295.7	245.3	326.4	252.5	218.1	299.8	182.2	170.9	141.3	144.6	214.5	152.3	162.4
Tb	20.84	39.67	36.33	44.45	39.26	27.82	29.46	45.9	35.59	36.95	35.46	42.83	36.05	39.05	30.95	27.3	39.15	26.47	24.18	19.84	21.2	31.03	23.43	24.85
Dy	102.9	205.1	178.9	216.5	194.6	104.3	123.5	219	157.1	170.9	178.1	221.9	178.6	169.6	148.6	123.9	177.9	151.4	138.7	104.1	126	177.5	143.8	153.1
Ho	19.8	40.8	35.2	41.9	38.7	16.9	22.1	41.3	28.5	32.9	35.9	47.4	34.6	24.4	23.8	19.2	25.3	28.3	25.6	18.5	25	32.4	26.9	28.8
Er	51.1	97.4	88.2	105.5	94.8	37.8	53.2	95.1	68.2	76.8	89	117.9	86.1	50.4	58.8	45.3	52.2	68.9	62.8	44.4	65	75.8	67.1	69
Tm	7.24	13.31	11.52	14.14	13.11	5.08	7.23	12.97	8.55	9.64	10.87	15.24	11.54	6.15	7.87	5.56	5.78	8.97	8.24	5.99	9.1	9.73	8.74	8.95
Yb	48.3	80.9	67.1	81.3	74.5	31.9	44.2	74.7	47.3	52.9	59.3	81.1	64	32.3	44.5	29.8	31.7	49.9	44.9	35	54.2	50	48.1	48.9
Lu	6.3	10.2	7.98	9.84	9.35	4.15	5.6	9.29	5.58	6.32	6.41	9.22	7.64	4.3	5.47	3.8	4.07	6.62	5.97	4.72	7.34	6.52	6.25	6.52
Y	521.6	1052.9	874.7	1116.8	1019.6	396	535.9	955	702.2	823.5	955.6	1296.3	920.7	563.3	599.7	478.6	622.5	708.9	618.3	460.4	627.7	803.2	699.5	706.5
Total ¹	98.11	97.01	96.76	97.16	96.80	96.51	96.55	94.91	103.41	96.78	95.91	95.83	96.54	93.48	94.93	92.80	95.95	96.52	96.65	97.91	98.62	96.53	97.08	96.62

¹Total including REO and traces. Abbreviations: CC, calcite-carbonatite; FCC, ferroan-calcite-carbonatite; MFV, Mn-Fe-veins; AFV, apatite-fluorite-veins

Continued...

Sample	CC V3688	CC V3689	CC V3690	CC V3691	CC V3692	CC V3693	CC V3696	CC V3697	CC V3698	CC V3699	CC V3700	CC V3701	CC V3702	CC V3703	CC V3704	CC V3705	CC V3706	CC V3707	CC V3709	CC V3712	CC V3713	CC V3716	CC V3717	CC V3718
SiO ₂	0.64	0.43	0.43	0.00	0.86	0.00	0.86	1.28	1.07	0.86	0.43	1.71	1.28	2.78	0.86	1.07	1.93	0.43	1.93	0.64	1.07	2.35	2.99	1.28
TiO ₂	0.12	0.12	0.13	0.00	0.00	0.00	0.00	0.15	0.00	0.00	0.00	0.18	0.00	0.40	0.58	0.10	0.25	0.08	0.32	0.22	0.20	0.37	0.43	0.32
Al ₂ O ₃	0.34	0.23	0.15	0.13	0.28	0.19	0.45	0.40	0.38	0.38	0.21	0.59	0.55	0.81	0.36	0.40	0.64	0.23	0.64	0.34	0.40	0.96	1.06	0.85
FeO _t	7.64	9.24	6.59	5.08	3.32	4.00	3.42	5.81	4.39	7.51	5.69	6.63	5.98	17.46	18.86	9.31	12.43	9.83	14.76	11.84	12.75	14.96	17.87	15.43
MnO	1.29	1.94	1.68	1.16	1.16	1.42	1.29	1.81	1.29	1.42	1.29	1.16	1.42	1.29	1.42	1.16	0.90	1.16	0.77	1.29	1.16	1.42	1.42	1.42
MgO	0.32	0.36	0.63	0.76	0.45	0.53	0.32	0.20	0.38	0.25	0.46	0.27	0.70	0.33	0.40	1.18	1.03	0.71	1.18	1.04	0.95	1.06	0.99	0.32
CaO	46.03	42.68	43.10	45.89	47.85	46.59	48.55	45.47	47.71	46.17	47.43	46.59	44.91	37.36	37.36	40.72	38.90	43.66	37.36	40.58	37.64	34.84	34.00	38.76
Na ₂ O																								
K ₂ O	0.18	0.16	0.12	0.12	0.28	0.13	0.31	0.30	0.34	0.33	0.17	0.47	0.43	0.64	0.25	0.37	0.55	0.17	0.54	0.27	0.36	0.64	0.73	0.36
P ₂ O ₅	2.91	2.64	2.31	0.55	0.85	1.28	0.80	1.17	1.51	0.69	1.65	2.73	2.27	2.31	2.91	1.81	1.95	1.54	1.72	7.93	2.45	2.43	3.48	5.39
SrO	0.66	1.47	3.04	2.05	0.92	1.98	2.17	1.32	1.23	0.51	0.93	0.98	2.66	1.23	1.12	1.96	1.74	1.83	1.22	2.01	2.29	1.90	1.45	1.29
Nb ₂ O ₅	0.04	0.01	0.01	0.01	0.02	0.02	0.01	0.02	0.15	0.04	0.03	0.22	0.03	0.20	0.79	0.24	0.41	0.04	0.52	0.53	0.30	0.98	0.15	0.55
LOI (1000 °C)	35.89	34.48	36.51	39.99	39.22	39.39	39.44	37.89	41.77	37.84	38.58	35.69	36.98	30.39	29.96	36.37	34.21	36.88	34.29	30.10	35.26	32.24	27.59	28.00
Total	96.05	93.74	94.70	95.75	95.21	95.54	97.63	95.82	100.22	95.99	96.86	97.35	96.96	95.33	94.74	94.95	95.20	96.30	95.64	96.26	94.95	93.90	92.18	93.95
ppm																								
Ba																								
Be	0	2	1	0	1	1	2	2	1	1	0	2	2	2	2	0	2	1	4	2	1	1	2	3
Cr	0	0	0	0	0	0	0	0	0	0	0	0	0	0	0	0	0	0	0	0	0	0	0	0
Ga	8	14	10	7	8	11	10	10	11	10	10	11	13	13	11	11	12	9	11	11	13	12	10	13
Hf	0.1	0.1	0	0.1	0.1	0.2	0.5	0.4	0.2	0.2	0.2	0.3	0.2	0.3	1.2	0.4	0.5	0.2	1.3	0.8	0.3	2	1.4	1.2
Li	3	4	3	2	1	2	3	3	3	2	3	3	2	3	2	3	2	2	2	2	2	1	2	2
Sc	0	0	0	0	0	0	0	0	0	0	0	0	0	0	0	0	0	0	0	0	0	0	0	0
Sn	0	0	0	0	0	0	0	0	0	0	0	0	0	0	4	8	2	4	0	4	5	3	7	4
Ta	0.4	0.2	0.2	0.2	0.2	0.1	0.5	0.5	0.5	0.3	0.3	0.7	0.2	0.4	0.8	0.4	1	0.2	1.1	1.2	0.6	2.5	2.7	2.1
Th	216.6	351.1	377	152.8	451	144.6	141.4	607.2	264.7	354.6	152	373.1	384.6	280.7	239	237.2	380.4	267.6	130.2	81.5	271.9	126.5	223.6	264.1
U	31.9	18.9	16.2	10.6	28.6	5.9	6.5	24.9	21.7	16.9	10.6	34.3	30.3	29	28	22.2	20.7	14.9	11.6	3.7	12.7	9	5.9	5.8
V	170	147	158	114	111	97	77	173	126	175	146	221	183	465	457	256	280	153	346	383	184	203	286	238
W	3	2	2	1	2	1	1	2	10	4	3	14	3	12	35	12	23	3	19	13	10	29	12	19
Zr	8	0	0	0	5	7	34	22	8	9	11	12	8	12	41	13	22	11	53	26	14	85	84	56
La	2074.9	3028.4	2645.3	1975.1	2162.4	2655.7	2605.6	2698	2371.6	2522.9	2341	2135.3	2281.8	1840.6	1777.4	2268.6	2042.8	2014.8	1821.5	1948.5	1973.5	2057.3	2164	2352.3
Ce	4082.8	5720.6	5022.9	3789.8	4279.9	5260.9	5400.3	5370.2	4892.6	5208.2	4744.9	4441.7	4618.9	3744.1	3643.2	4550.1	4082.2	4180	3795.4	4066.1	4005.2	4058.3	4272.5	4765.8
Pr	447.79	647.42	554.87	411.11	464.99	601.84	621.45	603.75	562.91	587.62	539.82	510.95	537.74	419.27	417.1	513.08	458.74	477.77	429.7	447.86	474.6	451.29	474.55	528.33
Nd	1531.8	2135.4	1863.5	1413.2	1637.4	2065.2	2154.2	2134.3	1977.6	1988.1	1857.7	1776.9	1924.5	1511.2	1465.3	1736.1	1622.2	1693.7	1491.8	1594.7	1648.2	1538	1700.6	1913.8
Sm	219.5	284.9	271	209.6	230	281.8	312.6	298.2	280.5	289.4	261.9	254.4	268.1	205.2	210.7	246.4	243.8	242.6	201.3	223.4	244	210.3	243.9	316.9
Eu	61.6	74.5	74.1	55.8	61.9	70.4	83.5	82.1	78.5	79.2	68.8	67.6	72.2	53.6	61	63.1	66.7	66	51.2	58.9	66	55.8	64.9	89.3
Gd	162.7	192.3	193.8	143.7	169	174.4	214.1	218.7	208.7	213.5	172.5	177.7	189.4	140.8	161	166	174.7	169.1	129.4	152.5	167	139.9	163.5	237.8
Tb	22.92	28.21	28.94	19.24	23.27	21.53	26.74	33.2	29.65	27.1	21.65	25.16	26.54	19.61	23.65	21.83	23.72	21.55	15.67	18.83	22.54	18.07	19.96	30.56
Dy	130.5	171	168.2	94.7	123.9	108.2	130.5	180.4	151.2	135.8	107.1	143.4	142.6	114.6	137.5	117.2	120.1	114.2	79.1	97.8	115.1	87	99.2	156.4
Ho	24.8	33.1	30.3	16.3	20.9	18.9	21.1	30.2	25.7	21.7	18.7	26.2	26.2	21.8	25.7	20.2	20.1	19.8	14.1	16.6	19.7	14.6	16.1	26.1
Er	63.5	82.4	71.2	35.6	46.3	43.2	43.7	68.1	56.9	45.7	42.1	63.2	63	56	63.4	49.2	48.1	45.8	33.3	37.1	45.6	31.5	35.7	55.7
Tm	8.92	10.37	8.7	4.49	5.81	5.21	5.27	8.18	6.99	5.55	5.31	8.16	8.37	7.48	8.26	6.24	6.22	6.01	4.32	4.57	5.68	3.95	4.19	6.13
Yb	50.3	55.7	44.9	23.8	31.4	27.2	26.8	42.9	37.2	31.2	30.3	46.8	48	41.7	46	35.2	34.5	33.7	24.3	23.8	29.6	20.8	20.5	28.1
Lu	6.91	7.17	5.66	3.06	4.28	3.42	3.21	5.63	4.84	4.17	4.16	6.19	6.55	5.72	5.89	4.77	4.67	4.52	3.2	2.93	3.89	2.67	2.55	3.35
Y	627.8	878.5	756.7	375.3	496.4	449.4	477.4	753	606.5	501	433.7	626.8	651	560.6	636.4	496	508.2	488.1	356.7	389.3	466	349.1	374.5	621.1
Total ¹	97.19	95.34	96.10	96.77	96.39	96.93	99.05	97.35	101.56	97.40	98.13	98.60	98.27	96.42	95.82	96.20	96.36	97.45	96.67	97.37	96.07	94.99	93.36	95.29

¹Total including REO and traces. Abbreviations: CC, calcite-carbonatite; FCC, ferroan-calcite-carbonatite; MFV, Mn-Fe-veins; AFV, apatite-fluorite-veins

Continued...

Sample	CC V3719	CC V3721	CC V3722	CC V3728	CC V3729	CC V3730	CC V3733	CC V3736	CC V3737	CC V3738	CC V3739	CC V3744	CC V3745	CC V3746	CC V3748	CC V3825	CC V3826	CC V3827	CC V3828	CC V3829	CC V3848	CC V3849	CC V3850	CC V3851
SiO ₂	0.64	0.00	0.00	1.28	0.00	3.42	2.99	0.64	0.00	0.43	0.43	0.64	3.42	5.35	0.64	2.14	2.99	2.14	4.06	2.57	0.00	0.00	0.00	0.00
TiO ₂	0.43	0.12	0.00	0.28	0.00	0.23	0.37	0.12	0.17	0.18	0.22	0.00	0.32	0.27	0.12	0.25	0.27	0.62	0.33	0.32	0.00	0.00	0.00	0.00
Al ₂ O ₃	0.28	0.26	0.21	0.51	0.19	1.13	1.55	0.53	0.25	0.34	0.30	0.28	1.21	1.81	0.40	1.15	1.32	1.06	1.66	1.13	0.85	0.45	0.38	0.30
FeO _t	16.31	5.48	4.49	13.80	7.51	10.60	19.64	13.50	8.14	11.36	10.69	6.96	9.10	7.35	6.30	8.58	14.95	18.95	13.11	11.40	11.75	9.98	11.22	25.16
MnO	1.29	1.42	1.29	1.55	1.55	1.29	1.03	1.03	1.42	1.29	1.42	1.29	1.55	1.42	1.94	1.55	2.97	3.49	2.84	2.84	1.68	1.42	2.20	5.55
MgO	0.91	0.83	0.56	1.21	0.86	1.48	1.33	0.93	0.41	0.81	2.06	0.15	2.34	1.92	0.85	3.85	3.86	4.01	3.20	2.98	1.44	1.19	1.53	2.97
CaO	35.54	45.47	46.31	38.34	43.93	38.34	32.46	39.04	45.61	38.90	35.68	38.34	37.08	36.52	40.86	24.49	28.54	25.05	30.22	31.62	36.94	39.74	37.78	21.27
Na ₂ O																								
K ₂ O	0.25	0.13	0.11	0.40	0.18	0.98	0.80	0.28	0.14	0.22	0.23	0.19	0.90	1.43	0.19	0.31	0.84	0.61	1.02	0.67	0.39	0.13	0.06	0.16
P ₂ O ₅	3.60	1.03	2.38	1.92	0.78	1.24	5.89	1.01	0.76	2.77	1.26	0.09	0.41	0.16	1.24	0.96	2.54	0.80	1.49	3.05	0.48	0.53	0.60	0.94
SrO	1.47	1.46	1.69	1.06	1.03	1.19	1.07	1.22	0.98	3.68	4.21	0.21	1.40	2.56	5.20	1.73	2.15	1.44	1.99	2.49	1.80	1.91	1.59	0.99
Nb ₂ O ₅	1.30	0.04	0.02	0.28	0.13	0.18	0.24	0.19	0.13	0.29	0.53	0.03	0.19	0.21	0.03	0.20	0.24	0.23	0.21	0.40	0.02	0.00	0.01	0.01
LOI (1000 °C)	35.38	39.76	38.85	34.75	39.80	36.23	27.67	34.47	38.34	34.49	36.31	34.14	37.01	35.85	36.99	33.83	32.77	33.22	32.95	32.93	35.36	37.19	38.43	34.95
Total	97.41	96.01	95.91	95.40	95.97	96.31	95.04	92.95	96.36	94.77	93.34	82.33	94.93	94.84	94.75	79.04	93.47	91.61	93.10	92.41	90.70	92.55	93.78	92.30
ppm																								
Ba																								
Be	0	9	2	0	0	0	4	1	1	1	1	0	1	2	1	2	3	3	4	3	4	3	3	2
Cr	0	0	0	0	0	0	0	0	0	0	0	0	0	0	0	0	0	0	0	0	0	0	0	0
Ga	8	10	11	10	9	12	12	10	12	11	11	10	13	14	8	9	12	11	12	11	15	14	11	10
Hf	3.2	0.1	0.2	0.5	0.2	0.6	1.7	0.8	0.3	1.1	0.9	0.1	0.9	0.7	0.3	2.1	2.2	1.7	2.9	0.8	0.7	0.8	0.6	0.6
Li	2	2	7	2	2	3	2	2	2	3	0	2	0	0	0	11	4	3	3	5	5	3	3	1
Sc	0	0	0	0	0	0	0	0	0	0	0	0	0	0	0	0	0	0	0	0	0	0	0	0
Sn	8	0	0	3	0	3	2	0	2	3	0	2	3	0	2	0	4	4	3	5	2	0	0	0
Ta	1.4	0.2	0.2	1.1	0.4	1.4	3.7	0.8	0.4	0.5	0.2	1.3	1.8	0.9	2	2	3.4	2.6	2.2	1.2	0.3	0.3	0.5	
Th	82.1	132.2	187.9	94.5	67.6	92.8	160.7	107.5	190.6	354	341.1	86.5	150.7	211.3	300	402.5	444.4	366.3	406.7	225.7	343.6	404.3	340.5	214.3
U	8.3	2.7	5.3	9.3	2.7	8.4	8	5.9	7.6	8.4	7.1	3.2	5.8	7	7.1	7.9	11.7	10.1	11.2	10.4	0.9	1.3	0.5	0.8
V	240	136	104	290	154	221	337	170	129	145	201	86	156	106	101	60	109	146	100	95	65	63	74	110
W	26	2	1	14	4	9	15	10	7	9	12	3	9	8	3	11	14	23	14	18	3	1	2	3
Zr	95	6	7	20	9	38	103	37	10	43	29	5	39	29	14	119	135	88	173	42	45	48	29	37
La	2007.3	2620.6	2837.7	2280.1	2320.6	2561.1	1673.3	1919.1	2356.5	2240.8	4555.9	2032.2	3021.6	2406.7	2751.6	4541.1	4344.8	4368.1	4087.5	4253.8	2295.9	2503.2	2774.3	1960
Ce	4038.2	5634.8	5790.3	4630.9	5004.2	4635.8	3334.4	3829.6	4879.7	4721.8	7336	4347.2	5222.2	4648	4897.4	7482.9	7168.2	7346.5	6753.2	7083.1	5403.3	5921	6823.8	4642.3
Pr	453.36	650.39	685.34	515.03	575.17	489.43	383.02	441.05	564.23	549.48	755.06	505.67	565.62	504.74	517.79	724.47	723.91	718.27	675.86	725.02	650.09	742.77	833.63	539.54
Nd	1583.6	2308.1	2421.2	1834.7	1989.4	1630.9	1355.7	1554.1	1938.7	1977.1	2310.7	1780.8	1889.6	1821.2	1730.1	2218.6	2341.1	2319.4	2184.8	2319	2475.6	2790.9	2982.7	1955.3
Sm	230	324.6	341.8	246.9	264.2	220.9	192	223	241.2	307	321.1	227.7	252.8	260.5	252.1	280.8	312.6	298.9	300.3	326.4	478	571.9	583.4	294.8
Eu	62.3	84.7	95.3	63.9	63.4	58.2	52.5	57	58.1	83.1	87.5	56	66.1	73	70.9	75	86.7	75.8	79.7	89.4	142.7	178.2	177.9	78.1
Gd	169.9	210.1	244.9	162.8	150.1	144.8	143.3	144.2	142.5	206.1	229.8	134.5	170.7	190.4	194.3	169.6	202.6	164.7	185.7	204.4	335.9	419.5	424.5	170.4
Tb	23.54	25.53	32.25	20.53	15.92	17.59	21.24	16.82	16.33	25.67	28.84	14.43	20.47	23.41	27.14	21.24	27.37	18.75	23.29	25.62	38.17	47.81	49.64	19.5
Dy	126	117.2	157.3	108.1	70.6	81	125.8	78	82.9	124.6	141.7	61.6	98.1	109	139	96.2	130.6	79.1	107.5	114.7	151.1	183.5	190.2	81.5
Ho	21.9	18	25.7	18.1	11.6	12.8	23.2	13.4	14.8	21.5	23.1	9.6	15.5	17	22	16.1	22.5	12.9	17.8	19.2	23.5	26.9	29.1	14.5
Er	48	38.6	57.4	41.4	28.2	29.7	57.7	31	38.3	54.5	51	23.2	34.8	34.6	48.7	36.1	51.3	27.5	39.8	42.7	49.3	53.3	58.1	36.8
Tm	5.38	4.54	6.81	5.06	3.75	3.89	7.7	4.19	5.54	7.05	6.19	3.36	4.37	4.07	5.92	4.42	6.18	3.28	4.72	5.24	5.33	5.43	6.39	5.22
Yb	25.5	25.1	34.1	26.4	22.8	23.1	41.8	25.2	35.6	40.6	32.1	21.9	24.3	23.4	32.8	25.3	34.1	19.2	27.2	30.4	29.1	29.5	35.4	35.2
Lu	3.13	3.17	4.42	3.55	3.35	3.33	5.49	3.64	5.43	5.43	4.18	3.37	3.35	3.27	4.46	3.18	4.23	2.68	3.7	4.2	3.52	3.69	4.38	4.75
Y	499.1	409.5	627.6	452.3	268.3	303.7	602.8	317.3	357.2	539.4	545.4	231.1	377	369	513.1	391.3	571.5	311.1	435.8	476.4	504.7	576.8	585.3	396.4
Total ¹	98.53	97.48	97.49	96.65	97.24	97.53	96.03	93.99	97.64	96.08	95.30	83.45	96.34	96.10	96.09	80.97	95.40	93.51	94.90	94.28	92.20	94.23	95.62	93.52

¹Total including REO and traces. Abbreviations: CC, calcite-carbonatite; FCC, ferroan-calcite-carbonatite; MFV, Mn-Fe-veins; AFV, apatite-fluorite-veins

391

Continued...

Sample	CC V3858	CC V3859	CC V3860	CC V3863	CC V3892	CC V3893	CC V3897	CC V3898	CC V3900	CC V3901	CC V3902	CC V3903	CC V3005	CC V3008	CC V3028	CC V3045	CC V3052	CC V3055	CC V3056	CC V3057	CC V3064	CC V3065	CC V3067	CC V3069
SiO ₂	0.00	0.00	0.00	0.86	2.14	0.00	1.93	0.00	0.00	0.00	0.00	2.35	1.93	5.13	4.49	1.50	1.07	0.64	0.64	3.42	0.86	1.28	1.07	1.07
TiO ₂	0.15	0.00	0.00	0.00	0.10	0.08	0.20	0.08	0.18	0.12	0.17	0.00	0.18	0.23	0.32	0.00	0.15	0.00	0.00	0.13	0.00	0.10	0.10	0.00
Al ₂ O ₃	0.42	0.45	0.60	1.38	1.68	0.51	1.70	0.53	0.59	0.70	0.72	1.59	0.62	1.89	1.32	0.51	0.42	0.30	0.28	0.21	1.13	0.28	0.40	0.38
FeO _t	13.43	11.22	8.77	12.31	17.30	19.61	19.63	17.38	17.56	9.87	13.75	17.92	4.70	6.37	8.00	4.00	6.66	5.48	4.58	3.98	5.83	5.48	3.83	4.55
MnO	2.84	2.32	1.55	2.58	3.49	3.74	3.23	3.10	3.49	3.10	3.23	2.97	1.16	1.68	1.81	1.55	1.29	1.29	1.16	1.16	1.42	1.42	1.68	1.94
MgO	1.23	1.51	0.98	1.94	5.02	5.26	4.84	4.76	5.64	2.30	3.18	4.26	1.14	1.69	0.20	0.50	0.46	0.23	0.60	0.50	0.71	1.01	0.88	0.81
CaO	36.24	37.22	40.30	34.28	21.13	21.69	19.17	20.57	22.81	34.42	29.52	22.11	44.49	38.62	42.68	45.75	44.77	48.27	48.13	49.67	42.12	45.05	46.17	45.61
Na ₂ O																								
K ₂ O	0.18	0.19	0.23	0.60	1.10	0.25	0.93	0.20	0.33	0.36	0.41	1.13	0.52	1.07	1.05	0.41	0.35	0.24	0.20	0.22	0.90	0.23	0.39	0.31
P ₂ O ₅	0.92	0.85	0.76	1.92	0.05	0.44	1.74	0.46	0.66	1.79	1.74	0.57	1.10	0.80	2.20	1.99	1.49	2.57	1.44	1.21	5.20	0.66	3.39	1.76
SrO	1.60	1.56	1.92	1.18	2.92	3.46	3.58	5.43	4.03	3.35	3.13	3.15	1.02	2.13	0.36	2.24	1.68	0.56	1.73	1.07	3.34	3.53	1.85	1.98
Nb ₂ O ₅	0.00	0.00	0.00	0.01	0.01	0.06	0.18	0.39	0.39	0.17	0.22	0.22	0.01	0.33	0.15	0.02	0.02	0.07	0.02	0.01	0.05	0.01	0.10	0.06
LOI (1000 °C)	36.81	38.20	37.25	32.84	33.33	35.02	31.56	33.53	35.41	34.92	34.08	32.61	38.68	35.41	33.42	37.65	37.00	37.48	39.19	40.17	31.86	39.29	36.63	38.08
Total	93.82	93.53	92.36	89.91	88.27	90.12	88.69	86.42	91.08	91.09	90.16	88.89	95.56	95.36	96.00	96.12	95.64	97.72	97.98	98.84	96.12	97.83	96.70	96.56
ppm																								
Ba																								
Be	3	4	4	7	6	2	11	3	2	2	2	2	2	2	2	1	1	0	0	0	2	0	1	2
Cr	0	0	0	0	0	0	0	0	0	0	0	0	0	54	0	0	0	0	0	0	0	0	0	0
Ga	16	13	13	18	10	4	3	2	0	5	8	8	12	14	14	11	14	9	8	7	14	12	12	11
Hf	0.8	0.7	0.6	0.7	0.3	0.1	1.6	0.4	0.4	0.5	0.6	2	0.3	0.7	1.7	0.3	0.2	0.1	0.1	0	0.2	0.2	0.3	0.3
Li	3	2	2	2	8	8	7	8	6	5	4	6	3	2	1	0	0	0	0	0	1	2	2	2
Sc	0	0	0	0	26	31	32	42	29	22	26	25	0	0	0	0	0	0	0	0	0	0	0	0
Sn	2	0	8	0	0	0	4	8	9	4	10	3	0	3	3	0	0	0	0	0	0	0	0	0
Ta	0.1	0.2	0.3	1.2	3.7	2.1	4.8	2.4	2.3	3.2	2	3.8	0.4	1.6	2.6	0.3	0.1	1.2	0.4	0.3	0.6	0.1	0.4	0.2
Th	323	378.6	477.5	430.1	255.6	267.2	392.6	350	382.2	384	331.8	288.9	465.7	323	410.8	172.5	621.2	402.9	431.8	271.8	557	361.5	109	89.5
U	1	3	2.5	2	2.3	3.1	6.3	4.9	7.6	2.3	3.2	4.5	6.5	7.2	19.7	2.7	6.6	9.4	6	5	15.1	6.8	7.7	3.2
V	92	102	84	105	76	87	89	99	96	57	92	102	64	90	144	0	52	57	0	0	85	58	62	64
W	2	1	2	2	4	15	17	16	9	12	11	2	11	10	2	2	4	2	2	5	0	4	3	3
Zr	43	41	33	38	13	9	79	15	16	23	29	114	17	38	86	15	11	6	0	0	16	9	16	12
La	2742.4	2735.1	2761.5	2661.9	8190.9	10399	11333	15869	9879.9	7542.1	7768.2	8743.2	2295.5	2504.2	2126.2	2436.9	2374.6	1252	1228.3	1299.4	2072.7	2182.1	2305.5	3076.3
Ce	6711.5	6574.8	6318.5	5907	13503	16028	16333	23444	14836	12552	13292	13420	4930.7	5244.2	4422.1	5180.5	5306	2789.6	2724.2	2696.5	4434.8	4785.8	4872.9	6038.2
Pr	811.26	777.12	758.12	676.6	1229.6	1412	1356.4	1950.8	1269.2	1176.8	1299.3	1229.6	536.43	560.62	479.28	564.42	596.9	333.26	320.1	297.82	477.5	528.92	530.2	622.54
Nd	2972.8	2805.5	2774.7	2397.5	3400.1	3840.1	3559	5222.8	3355.6	3606.9	4114.4	3297.3	1896.9	1964.3	1633.4	1935.7	2224.1	1291.7	1213.3	1090.4	1665.8	1841.7	1765.9	2044.8
Sm	548.3	503.4	488.9	432.2	302.7	340	300.8	399.7	295.4	456.4	503.3	304.9	278.2	287.1	244.4	275.8	367.8	220.5	230.1	166.5	252.6	266.6	234.6	261.8
Eu	161.7	150.2	139.2	131.8	68.5	74.2	72.8	88	67.2	128.4	131.8	67.3	76.6	79.5	68.9	76.2	108.1	60.9	67.1	48.7	71.8	73.6	63.1	69.7
Gd	382.4	345.2	320.7	318.4	135.6	145.2	150.3	161.3	136.2	288.9	284.6	131.8	194	192.8	176.3	188.8	264.9	149.8	164.7	121.4	182.9	184.1	156.9	159
Tb	47.02	42.12	37.87	40.41	11.46	13.1	16.61	13.55	13.55	34.44	31.36	12.17	24.87	23.66	24.46	23.39	34.75	21.17	22.11	16.29	27.72	23.89	20.25	19.21
Dy	193.1	168.8	154.6	175.8	38	46.5	74.3	46	47.5	134.1	119	40.3	126.1	108.6	123.5	115.1	162.3	116.1	105.3	82.1	149.3	115.4	106.4	91.6
Ho	31	27.9	26.5	31	5.1	7	13.6	6.1	6.9	21	18.3	5.9	21.2	16.4	21.3	18.9	24.2	20.5	16.8	13.6	25.9	18.2	18.5	15.9
Er	71.1	66.3	64.2	77	9.7	15.1	34.9	12	14.3	44.4	37.6	12.3	51.1	37.2	51.7	44.9	52.7	48.5	39.6	32.5	66.3	42.1	48.4	40.6
Tm	8.61	8.61	8.38	9.97	1.04	1.9	5.01	1.6	1.65	4.93	4.39	1.41	6.29	4.3	6.57	5.2	5.46	5.53	4.91	3.92	7.9	4.95	6.15	4.99
Yb	48.7	50.3	50.6	60.4	5.8	11.4	30.7	10	9.8	29.4	26	7.9	36.6	24.7	39.6	28	27.7	28.7	27.4	23.8	43.4	28.5	37	27.2
Lu	5.78	6.34	6.55	7.6	0.89	1.6	3.97	1.52	1.32	3.66	3.59	1.08	4.28	3.09	4.75	3.19	3.16	3.18	3.24	2.9	5.04	3.32	4.19	3.24
Y	735.1	673.4	648.1	782.2	106.1	170	360	133.1	152.8	463.8	389.5	125.1	552.5	401.1	577.5	448.4	571.5	515.6	420.9	342.8	698.7	452.5	498.7	418.7
Total ¹	95.65	95.31	94.10	91.54	91.47	93.96	92.68	92.02	94.65	94.22	93.47	92.14	96.89	96.74	97.22	97.45	97.11	98.55	98.78	99.59	97.36	99.09	97.95	98.07

¹Total including REO and traces. Abbreviations: CC, calcite-carbonatite; FCC, ferroan-calcite-carbonatite; MFV, Mn-Fe-veins; AFV, apatite-fluorite-veins

Continued...

Sample	CC V3070	FCC V1229	FCC V1238	FCC V1239	FCC V1240	FCC V1241	FCC V1242	FCC V1245	FCC V1246	FCC V1247	FCC V1248	FCC V1249	FCC V1250	FCC V1251	FCC V1252	FCC V1253	FCC V1257	FCC V1258	FCC V1211	FCC V1212	FCC V1213	FCC V1216	FCC V1217	FCC V1226
SiO ₂	0.64	0.86	1.07	0.64	0.64	0.86	0.86	1.28	1.50	0.43	0.00	0.43	0.21	0.64	0.64	4.49	0.64	0.86	1.07	1.07	1.50	1.71	1.28	0.64
TiO ₂	0.00	0.25	0.17	0.17	0.18	0.17	0.23	0.18	0.22	0.18	0.12	0.12	0.00	0.00	0.17	0.12	0.22	0.18	0.22	0.12	0.00	0.00	0.15	0.15
Al ₂ O ₃	0.21	0.51	0.91	0.62	0.55	0.70	0.70	0.85	0.76	0.51	0.85	0.60	0.55	0.55	0.57	1.85	0.60	0.45	0.94	0.81	1.06	1.10	1.10	0.62
FeO _t	3.95	14.69	17.08	14.55	16.27	19.85	12.70	16.27	16.06	13.02	15.58	21.30	14.61	13.47	26.63	13.51	17.15	14.54	18.51	18.13	20.19	12.39	14.81	12.65
MnO	1.94	3.49	3.87	4.00	3.49	3.74	2.71	2.84	3.23	3.74	3.74	4.39	3.23	3.10	2.84	2.58	3.36	3.23	3.49	3.87	4.26	3.74	3.23	3.10
MgO	0.58	1.44	1.59	3.52	3.88	4.41	3.42	4.15	3.95	2.84	3.81	3.40	4.81	3.18	1.81	4.61	4.92	1.64	3.63	1.86	3.02	3.40	4.33	3.35
CaO	46.17	35.54	31.62	30.22	29.94	25.89	31.62	32.04	29.38	31.06	27.56	28.82	31.06	34.98	21.69	27.98	27.00	34.42	26.17	30.22	27.28	29.10	45.89	30.36
Na ₂ O																								
K ₂ O	0.20	0.13	0.14	0.16	0.14	0.18	0.20	0.19	0.39	0.00	0.00	0.10	0.00	0.08	0.00	0.89	0.24	0.16	0.17	0.19	0.34	0.37	0.23	0.10
P ₂ O ₅	0.39	6.07	3.78	4.03	3.30	2.27	2.66	5.06	2.13	3.28	4.63	2.98	3.23	5.98	2.75	3.32	4.33	3.32	3.37	4.58	4.03	2.45	5.36	3.55
SrO	1.95	2.37	2.89	3.09	3.29	1.96	2.47	1.52	2.20	5.69	3.77	1.10	1.66	1.68	1.89	2.40	3.21	3.16	3.37	3.42	3.21	3.80	4.82	4.34
Nb ₂ O ₅	0.01	0.12	0.25	0.10	0.20	0.20	0.15	0.20	0.21	0.19	0.06	0.20	0.17	0.14	0.53	0.28	0.35	0.41	0.30	0.08	0.08	0.12	0.34	0.11
LOI (1000 °C)	40.13	27.38	27.85	29.04	29.50	28.41	33.85	29.92	32.10	29.86	26.88	27.52	32.24	29.61	22.54	30.95	28.95	29.01	26.40	24.30	23.82	30.68	26.46	29.58
Total	96.18	92.85	91.23	90.14	91.39	88.63	91.57	94.52	92.11	90.80	87.01	90.96	91.77	93.42	82.05	92.99	90.99	91.38	87.63	88.65	88.79	88.86	88.00	88.55
ppm																								
Ba																								
Be	0	3	5	5	3	3	3	4	3	3	5	4	3	3	3	5	2	1	6	9	10	6	5	4
Cr	0	0	0	0	0	0	0	0	0	0	0	0	0	0	0	0	0	0	0	0	0	61	0	0
Ga	13	0	0	0	0	0	0	0	0	0	0	0	0	0	0	0	0	0	0	0	0	0	0	0
Hf	0.2	1.9	0.8	1.5	1.9	1.9	4.2	3.1	2.1	2.8	0.9	2.4	1.8	1.7	3.2	5.9	2.3	1.9	1.9	0.7	1	0.8	0.8	1
Li	0	4	9	4	7	4	3	4	3	3	2	4	4	4	6	6	5	3	9	5	7	6	10	6
Sc	0	28	32	24	27	22	0	0	0	29	33	0	22	0	22	0	23	25	39	26	22	27	32	36
Sn	0	5	4	4	4	4	3	4	4	4	4	4	3	3	5	4	4	5	4	3	3	3	5	2
Ta	0	0.2	0.5	0.4	0.5	0.9	0.5	0.4	0.7	0.2	0.5	0.4	0.8	0.7	0.6	1.4	0.9	0.6	1.6	1.3	1.3	1.3	0.9	0.2
Th	91.6	323.1	354.8	467.8	385.6	416.8	246.4	254.4	283.1	381.2	626.9	396.3	375.2	314.7	298.5	259.6	365.9	328.3	451.3	303.4	281.2	331.9	577.5	369.4
U	1.5	4.5	3.4	2.6	6.8	3.9	3.2	2.8	3.2	3.3	5.6	6.5	4.2	4.6	5	7.4	6.6	5.4	13.5	32.6	4	5.1	9.2	3.2
V	0	166	161	149	136	153	104	125	127	127	158	173	118	101	216	122	143	130	138	132	169	115	140	142
W	1	12	17	8	17	15	12	17	18	16	6	19	12	16	25	14	25	25	8	8	8	6	15	6
Zr	7	79	49	64	100	95	264	158	110	159	40	130	117	88	161	292	123	90	74	37	49	37	41	57
La	2836.7	11647	12706	8654.5	9696.5	7047.7	4897.5	4161.4	6817.5	11096	13722	5525.7	8204.1	5309.6	9949.5	4650.9	7982.5	8766.3	17879	8078.4	7504	9950.4	13074	14778
Ce	5699.7	16255	17041	12872	14007	10959	8690.9	7680.3	10652	15912	18510	9582.4	12155	9100.4	13600	8017.8	11605	13156	22225	13148	11789	14056	16628	20281
Pr	595.52	1590.1	1599.9	1340.5	1383.7	1176.7	1024.5	922.07	1128	1588.2	1755.2	1069.2	1266.1	1036.5	1291.9	914.55	1172.1	1371.4	1944.1	1404.2	1231.4	1398.4	1548.8	1908
Nd	2036.2	4767.1	4659.8	4126.5	4087	3644.8	3421.1	3076.5	3521.8	4762.2	5111	3482.4	3876.2	3455.9	3730.6	2998.1	3479.8	4277.3	5336.8	4434.2	3780	4076.5	4202.4	5494.5
Sm	258.5	549.2	502.2	480.6	468.8	437.4	448.4	401.8	433.7	548.5	575.2	415.3	474.8	458.7	387.1	372.5	392.2	532.2	524.4	540	431.8	428.5	463	605.3
Eu	65.7	139.5	122.4	120.3	115.5	105.5	114.9	101.5	111.1	138.5	144.2	99.8	116.7	115.1	91.8	93.5	98	135.9	122.8	133.1	107.3	102	116.6	150.8
Gd	149.4	339.3	277.4	276.1	275.2	240	273.3	238.8	252.9	330.9	342.8	222	267.9	272.6	203	220.9	225.7	316.8	278.8	308.5	249.6	227.9	276.3	349.5
Tb	17.97	44.92	31.75	33.9	33.64	26.86	32.41	29.8	29.53	41.18	42.91	26.07	30.9	33.38	23.31	26.76	26.68	39.22	31.18	36.98	30.26	25.76	34.1	42.62
Dy	81.8	220.3	130.8	156.8	144.6	113.4	145.1	134	125.2	190	185.8	115.8	129.4	147.7	94.4	119.8	123.4	173.5	133.7	164.5	140.6	112.6	156.7	185.2
Ho	13.5	36.3	19.1	24.4	22.2	16.2	21.6	21.5	17.4	31	28	18.6	18.8	22.4	14	19.1	19.4	27	20.2	25.6	21.4	17.4	24.3	28.8
Er	33.6	88.6	42	55.8	51.3	33.9	45.8	49.7	36	69	61.4	42.8	41.3	51.3	30.2	43.8	43.9	62.3	44.5	59.1	49.8	37.2	55.3	65.4
Tm	3.85	11.32	4.88	6.69	5.88	4.01	5.75	6.02	4.05	7.94	6.73	5.48	4.71	6.39	3.95	5.72	5.72	7.38	5.54	7.31	6.27	4.87	6.85	7.65
Yb	22	56.8	24.1	34.4	32.3	21.5	30.5	32.3	20.9	38.4	32	29.7	24.7	34.3	21.5	30.5	29.2	38.5	30	41.6	33.8	28.7	35.5	41.8
Lu	2.58	6.63	3.44	4.24	4.23	2.91	3.98	3.89	2.77	4.68	4.08	3.79	3.1	4.21	2.77	3.66	3.73	4.66	3.92	5.12	4.18	4.01	4.59	5.74
Y	342.4	956.3	463	604	534.3	376.2	520.5	533.6	407	772	689.5	456	439.8	556.8	338.2	450.7	473.4	669.6	486.2	642.9	542.6	417.2	616.1	718.1
Total ¹	97.60	99.18	98.13	96.17	97.84	93.18	96.01	97.88	96.76	99.81	95.09	94.42	96.38	97.29	87.20	97.18	96.76	97.55	96.29	94.97	94.58	95.73	96.50	97.48

¹Total including REO and traces. Abbreviations: CC, calcite-carbonatite; FCC, ferroan-calcite-carbonatite; MFV, Mn-Fe-veins; AFV, apatite-fluorite-veins

Continued...

Sample	FCC V1227	FCC V1208	FCC V1228	FCC V1236	FCC V1237	FCC V1259	FCC V3679	MFV V3740	MFV V3856	FCC V1206	FCC V1207	FCC V1230	FCC V1231	FCC V1232	FCC V1260	FCC V1261	FCC V1262	FCC V1265	FCC V1268	FCC V3677	FCC V3678	FCC V3680	MFV V3146	MFV V3149
SiO ₂	0.86	1.93	1.07	0.86	1.50	1.50	0.00	2.57	0.00	1.50	2.14	1.50	3.42	1.71	2.14	1.93	1.71	1.71	3.64	0.64	0.43	0.43	2.14	2.14
TiO ₂	0.25	0.35	0.28	0.08	0.18	0.00	0.10	0.82	0.00	0.22	0.20	0.13	0.23	0.18	0.20	0.20	0.17	0.27	0.27	0.13	0.15	0.20	0.00	0.00
Al ₂ O ₃	0.42	0.77	0.76	0.36	1.02	0.62	0.30	0.93	0.45	0.96	1.19	0.89	1.91	0.79	0.94	1.06	1.04	0.77	1.38	0.28	0.15	0.36	1.42	0.93
FeO _t	16.43	13.87	18.09	13.12	15.91	8.26	7.90	33.50	35.80	15.53	19.19	12.98	24.49	28.38	22.66	19.40	18.11	15.66	15.67	11.05	6.75	10.48	17.47	32.16
MnO	3.49	3.23	3.49	3.74	3.10	2.84	1.42	1.29	9.17	2.97	3.62	3.62	5.16	6.20	5.29	3.62	4.26	1.94	3.62	1.55	1.16	1.55	5.81	12.14
MgO	2.22	0.51	0.68	0.38	0.36	0.45	0.22	0.40	1.16	0.38	0.45	0.32	0.35	0.33	0.27	0.30	0.25	0.20	0.41	0.28	0.13	0.20	0.33	0.23
CaO	32.04	37.22	30.36	35.40	32.74	40.58	44.77	26.03	18.19	34.00	32.04	35.40	24.35	21.83	24.35	31.06	31.90	39.74	33.86	43.38	47.71	44.07	33.44	20.57
Na ₂ O																								
K ₂ O	0.12	0.34	0.11	0.11	0.23	0.30	0.16	0.66	0.14	0.12	0.19	0.16	0.47	0.10	0.16	0.18	0.18	0.20	0.48	0.14	0.16	0.14	0.39	0.31
P ₂ O ₅	5.06	6.46	3.35	3.28	6.23	1.79	2.96	1.44	0.27	10.93	7.15	5.45	4.97	3.51	2.22	4.58	5.32	2.59	6.00	3.25	0.62	3.23	0.80	0.21
SrO	2.62	1.54	3.26	1.45	3.64	1.47	2.04	1.86	1.02	0.55	0.49	0.71	0.51	0.50	0.36	0.36	0.38	0.29	0.37	0.88	0.66	0.68	0.25	0.25
Nb ₂ O ₅	0.34	0.23	0.38	0.12	0.25	0.13	0.03	0.44	0.00	0.11	0.18	0.05	0.13	0.16	0.19	0.41	0.28	0.33	0.37	0.13	0.05	0.10	0.01	0.00
LOI (1000 °C)	27.27	26.45	26.84	30.04	24.93	34.21	35.25	22.24	24.98	20.19	22.31	26.81	20.40	20.22	22.68	24.42	24.28	30.89	24.66	33.29	38.96	34.24	27.51	27.29
Total	91.11	92.90	88.67	88.94	90.11	92.15	95.14	92.17	91.20	87.45	89.14	88.01	86.40	83.91	81.46	87.52	88.10	94.59	90.73	95.02	96.93	95.69	89.57	96.23
ppm																								
Ba																								
Be	10	3	5	2	4	1	1	2	4	5	7	5	13	12	3	2	17	1	3	2	0	2	6	2
Cr	0	53	0	0	0	0	55	0	0	0	0	0	0	0	0	0	0	0	0	0	0	0	0	0
Ga	0	0	0	0	0	0	8	17	16	0	0	0	0	0	0	0	0	0	0	9	7	10	13	20
Hf	1	1.6	1.5	1.1	6.2	1.3	0.1	1.4	0.4	3.6	1.4	1	1.1	0.9	3	4	7.2	5.9	3.7	0.3	0	0.2	0.3	0.2
Li	5	4	7	8	12	5	3	2	4	11	8	6	4	4	5	21	3	8	1	1	2	8	4	4
Sc	24	0	34	24	39	0	0	0	29	42	30	37	32	33	33	30	32	0	25	0	0	0	0	0
Sn	4	4	5	4	8	2	2	6	0	4	4	2	7	5	4	6	6	5	2	0	3	2	3	3
Ta	0.4	2.4	0.7	0.4	0.3	1.1	0.6	1	0.2	1.7	1	0.4	2.9	0.8	1.9	0.8	1.4	8.6	2.1	1.7	0.7	1	0.6	0.5
Th	303.2	307.6	386.1	340.4	390.2	337	558.4	197.2	315	482.5	348	637.2	592.3	626.9	686	455.8	560.1	180.4	335.3	946.1	311	809.2	461.8	189.3
U	5.9	19.6	7.6	7.4	5.7	3.8	33.1	3.5	1.5	11.4	13.1	11.7	10	10.7	8.4	9	13.9	36.5	9.2	50.7	17.6	41.3	5.8	4.4
V	155	170	204	123	182	63	154	1298	148	165	177	156	245	184	167	154	150	205	156	222	158	213	149	154
W	16	23	28	16	16	7	4	23	1	11	12	6	13	18	14	21	14	17	18	16	7	11	1	0
Zr	52	80	70	59	283	64	10	64	23	168	69	60	64	46	143	211	400	275	187	18	0	12	10	7
La	9349.4	5980.8	12759	9942.9	16588	6616.5	3352.1	1528.4	5495.3	16454	11427	14911	10384	8625.2	10621	11664	12171	2465.1	8561.6	1954.6	1692.9	2458	8326.3	3483.6
Ce	13818	9919.6	17717	15337	21662	11271	5522.3	3127.4	10228	22652	16074	20478	16508	15454	15894	16555	16698	3939.3	12068	3771.5	3232.7	4455.6	14380	7233.4
Pr	1415.6	1112.1	1695.6	1571.4	2032.9	1277.9	557.86	364.47	1038.5	2144.4	1546.2	1974.9	1709.1	1687.7	1606.6	1667.7	1568.3	430.99	1207.8	424.65	366.35	477.22	1351.9	706.74
Nd	4345.2	3610.2	4922.3	4772.7	5765.3	4225.1	1805.3	1318.7	2949.2	6126.9	4501.5	5685.1	5200.1	5302.2	4709.1	5016.3	4549.6	1352.5	3498.7	1527.4	1253.7	1649.9	3730	2205.4
Sm	511.2	465.1	528.8	575.1	615.8	560.2	239.7	205.9	307.5	686.6	482.8	633.2	577.5	602.8	560.6	616.4	504.3	171.9	390.1	267.9	169.5	259.7	422.8	218.7
Eu	128.4	122.2	128.3	146.8	149.5	142.4	67.6	58.2	72.1	169.7	117.3	159	135.7	146.9	141.4	154.6	127.5	47.3	101.9	85.2	46.3	78.9	109.4	47.6
Gd	307.9	296.5	288.4	344.6	344.6	329.2	181.5	150.4	148.8	417.8	274.9	363.6	299.4	331.6	320.5	364.3	310.6	118.7	252	258.9	121.6	240.7	248.8	96.8
Tb	40.98	38.7	33.87	43.04	42.23	37.92	28.76	19.02	14.24	55.03	34.07	45.93	34.75	37.78	36.99	43.21	40.76	16.06	34.46	45.56	16.47	43.41	25.62	9.07
Dy	195.9	194.5	145.8	188.4	184.5	157.4	182.5	89.4	51.5	272.6	162.7	216.7	154.9	158.2	146.9	186.3	188.7	76.8	161	281.1	89.3	280.6	99	31.8
Ho	31.1	33.3	21.5	29.6	28.8	21.8	34.8	13.6	8.2	43.9	26.4	35.9	23.5	22.6	20.4	26.8	29	12.4	24.5	51.2	15.7	53.6	13.9	4.5
Er	70.3	82.2	46.7	65.6	63.7	44.6	90.9	29.5	21.3	103.3	62.9	84.3	53.5	50.9	42.4	59.5	67.4	30.3	54.1	122.5	38.7	130.4	30.5	9.7
Tm	8.34	10.77	5.75	7.66	7.71	5.17	12.43	3.69	3.19	12.62	7.76	10.61	7.25	6.2	5.01	6.97	8.11	3.99	6.93	15.96	5.78	16.94	3.5	1.11
Yb	43.7	59	33.2	39.9	39.9	27.4	71.2	19.5	23	66.7	42.1	55.7	41.6	37.2	28.1	36.9	44.2	24	36.1	83.5	38.2	88.5	22.4	7.3
Lu	5.37	6.96	4.5	4.96	4.97	3.7	10	2.55	3.42	8.09	5.46	6.85	5.49	5.32	3.92	4.59	5.64	3.1	4.68	10.93	5.81	11.5	3.4	1.21
Y	790.6	867.8	506.3	729.5	729	509.4	932.3	318.3	219.9	1120.4	688.1	929.1	581.4	544	473.1	639	735.4	313.8	634.5	1323.5	389.2	1419.2	317	96.5
Total ¹	96.99	96.91	96.03	94.15	98.90	96.37	98.45	94.74	94.51	93.86	93.75	94.00	91.09	88.27	85.90	92.22	92.85	95.95	94.26	97.05	98.40	97.70	93.24	98.13

¹Total including REO and traces. Abbreviations: CC, calcite-carbonatite; FCC, ferroan-calcite-carbonatite; MFV, Mn-Fe-veins; AFV, apatite-fluorite-veins

Continued...

Sample	MFV V3150	MFV V3168	MFV V3169	MFV V3723	MFV V3724	MFV V3725	MFV V3726	MFV V3753	MFV V3852	MFV V3853	MFV V3857	MFV V3861	MFV V3862	MFV V3044	MFV V3046	MFV V3053	MFV V3054	AFV PX016	AFV PX016	AFV PX016	AFV PX016	AFV PX016	AFV PX016	AFV PX016	AFV PX016	
SiO ₂	2.14	3.64	4.71	1.50	2.57	1.07	3.21	4.71	0.00	0.00	0.00	0.00	0.00	3.64	6.20	2.14	1.71	0.64	0.64	0.86	1.28	2.99	38.08	2.99		
TiO ₂	0.00	0.17	0.27	0.30	0.53	0.30	0.27	0.00	0.00	0.00	0.00	0.13	0.00	0.13	0.20	0.00	0.00	bd	0.08	0.17	0.35	0.47	0.63	0.45		
Al ₂ O ₃	1.13	1.32	1.97	0.57	0.96	0.45	1.21	1.74	0.60	1.04	0.66	0.64	0.74	1.19	1.97	1.10	0.45	1.34	0.91	1.08	1.51	2.15	11.68	1.57		
FeO _t	30.41	33.69	14.34	18.17	19.59	13.29	10.52	24.73	25.96	28.86	27.22	33.94	30.82	24.69	29.16	37.13	38.34	11.93	13.34	15.49	16.57	24.06	10.06	22.33		
MnO	10.46	4.91	2.71	1.16	1.42	1.55	1.42	4.78	6.84	7.62	7.49	6.84	7.36	3.74	4.65	6.84	6.71	2.71	2.32	2.45	2.32	3.10	1.16	1.94		
MgO	0.25	0.22	0.23	0.33	0.27	0.22	0.22	0.27	0.75	0.81	0.41	0.66	0.66	0.70	0.48	0.38	0.32	3.83	3.75	4.46	3.93	3.47	1.49	3.03		
CaO	22.67	24.63	36.24	38.06	36.66	41.98	43.24	29.80	28.54	24.49	25.61	20.29	24.07	31.06	25.75	20.01	22.67	34.98	32.74	33.72	28.96	23.37	10.35	26.03		
Na ₂ O																										
K ₂ O	0.31	0.67	0.98	0.41	0.48	0.25	0.87	0.98	0.16	0.18	0.12	0.17	0.19	0.77	1.39	0.47	0.28	0.22	0.24	0.13	0.23	0.61	8.72	0.71		
P ₂ O ₅	0.14	2.29	4.67	2.41	2.93	1.65	3.48	7.75	2.34	1.63	2.29	0.71	2.13	2.02	0.50	0.16	0.71	8.52	10.72	10.11	7.08	1.99	1.95	7.72		
SrO	0.20	0.28	0.27	0.37	0.27	0.20	0.30	0.50	0.47	0.85	0.45	2.25	0.68	0.45	0.31	0.33	0.33	0.70	0.68	0.84	0.94	0.94	0.54	0.61		
Nb ₂ O ₅	0.00	0.01	0.02	0.24	0.34	0.28	0.19	0.02	0.01	0.00	0.00	0.02	0.01	0.07	0.04	0.00	0.01	0.04	0.11	0.21	0.15	0.24	0.14	0.54		
LOI (1000 °C)	22.61	19.49	25.28	30.88	28.39	34.12	31.74	17.97	24.09	23.44	22.45	21.28	22.10	25.72	23.36	20.45	20.85	0.00	0.00	0.00	0.00	0.00	0.00	0.00		
Total	90.33	91.31	91.69	94.39	94.41	95.36	96.66	93.23	89.76	88.92	86.71	86.93	88.77	94.18	94.01	89.01	92.37	64.91	65.54	69.52	63.33	63.39	84.81	67.93		
ppm																										
Ba																										
Be	2	2	3	1	2	1	2	5	3	7	6	6	8	2	7	4	2	0	0	0	0	0	0	0	0	
Cr	0	0	0	0	0	0	0	0	0	51	0	0	0	0	0	71	0	0	0	0	0	0	0	0	0	
Ga	19	14	15	12	13	9	12	11	9	12	16	8	13	12	15	22	13	0	0	0	0	0	15	0		
Hf	0	0.6	1.5	0.6	0.7	0.4	2.2	8.2	2.4	2.2	2.2	0.4	0.6	0.1	0.2	0.6	0.1	6.1	3.6	5.1	5.2	2.3	1.6	3.4		
Li	3	3	12	3	1	2	3	0	1	5	3	4	3	0	1	4	0	0	0	0	0	0	0	0	0	
Sc	0	0	0	0	0	0	0	0	22	37	25	38	26	0	0	0	0	0	0	0	0	0	0	0	0	
Sn	0	3	4	4	5	3	3	0	0	0	0	0	0	0	2	0	2	0	0	0	0	0	0	0	0	
Ta	0.3	2.3	2.5	0.6	2	0.7	4.5	2.7	0.7	0.4	0.3	1.1	0.9	0.7	2	0.1	0.1	0	0	0	0	0	0	0	0	
Th	206.2	454.7	673.4	384.7	310.3	116.3	201.1	189.5	237.2	404.3	401.2	857.9	392.7	297.3	331.8	495.2	241.6	315	484.6	332.5	367.3	296.6	265	331.3		
U	3.9	3.3	4.1	20.3	15	11	15	5.5	2.2	2.5	5.4	4.8	5.7	8.2	9.3	8.5	6.4	11.3	12.1	14.5	11.5	16.8	13.4			
V	126	62	119	274	299	266	216	75	165	172	131	181	154	136	139	148	141	0	0	0	0	0	0	0		
W	0	2	5	12	22	14	12	7	3	2	2	6	6	5	4	2	1	0	0	0	0	0	0	0		
Zr	6	47	92	26	29	14	118	382	145	114	134	24	39	10	10	29	8	266	206	263	296	169	105	212		
La	3471.3	2292.5	2805.2	2055	1928.7	2449.3	2426.7	1697.5	2633.6	6270.6	2685.3	7596.8	3888.5	1207.5	1760.5	2434.1	1202.7	3883.3	3313.1	3415.4	3083.2	1856.1	760.8	2635.9		
Ce	7516.6	5323.4	5807.1	4252	3963.5	5028.8	5030.9	3281.2	5467.4	12260	6266.5	16131	8320.5	2950	4282	6744	3116.2	8173.5	7089.8	7410.8	6767.8	3917.6	1776.1	5796.8		
Pr	772.83	610.48	643.95	482.67	465.25	570.27	582.69	363.71	550.6	1256.5	762.45	1683.5	899.27	349.97	494.26	840.98	387.35	976.83	812.08	860.11	792.1	449.66	221.14	674.52		
Nd	2419.5	2217.5	2362.4	1741.8	1701.7	1969	2054	1278.5	1778.9	3764.6	2657.3	5309.8	2798.1	1288.1	1777.2	3118.7	1428.5	3358.1	3076.3	3214.6	3007.3	1696.8	880.9	2541.4		
Sm	248.4	473.2	581.1	272.4	299.7	256.2	275.2	204.3	239.6	433.5	440.9	591.8	350.6	185.5	216.8	460.2	237.7	461.3	480.8	497.8	459.4	268	167.7	389.9		
Eu	55.7	160	223.8	77.6	85.3	63.6	69.6	56.4	68.9	106.1	130.1	143.7	89.9	48.7	52.3	120.7	62.5	131.3	145.3	148.1	134.4	72.7	52.6	115.5		
Gd	108.6	416.3	667.5	209.9	227.1	154.6	179.7	148.4	166.5	231.6	296.7	292.8	195.2	115.5	114.6	290.7	147.5	315.1	367.1	362.1	316.9	163.5	132.6	284		
Tb	9.89	56.85	98.28	31.72	29.72	18.75	23.53	20.15	25.18	26.18	37.77	29.76	24.13	15.11	12.47	30.88	16.22	42.72	53.11	51.15	42.81	18.77	17.64	39.5		
Dy	32.7	248	454.1	167	148.1	92.6	125.4	110.2	123.1	106.3	164.7	118.2	110.3	75.2	53.8	118	62	229.7	296.8	278.1	226.3	87.5	88.8	215.7		
Ho	4.2	34.7	65.3	28.7	24.8	16.1	22.3	19.4	23.6	19.8	28.7	19.7	22.7	13.3	8	13.8	7.8	40.9	53.4	49.9	39.6	14.9	15.3	38.7		
Er	8	61.4	114.7	66	55.3	39	55.8	50.6	66.3	56.3	72.3	49.7	65	32.5	17.3	21.8	14.8	117.8	157.7	142.8	114.5	42.8	44.4	116.8		
Tm	0.91	5.3	10.01	7.86	6.46	4.91	7.31	7.05	9.94	8.24	9.6	6.72	9.46	3.83	1.9	1.96	1.54	16.53	22.18	19.23	15.61	6.11	6	16.47		
Yb	5.9	24	47	42.4	35	28.8	42.7	41.8	65.3	55.9	60	40.5	60.7	20.8	10.3	10	8.1	96.1	128.2	109.7	89.7	37.2	34.9	95.2		
Lu	1.02	2.89	6.03	5.53	4.47	3.91	5.8	6.04	8.93	7.37	7.95	5.22	7.76	2.48	1.29	1.21	1.08	12.7	16.66	14.14	11.39	5	4.82	12.53		
Y	80.1	744.3	1483.3	709.1	581.4	368.4	543	598.8	714.8	540.4	751.4	508.5	657	343.3	190.3	285.4	175.5	1096.3	1530.6	1409.7	1050.3	389.8	419.5	1055.7		
Total ¹	92.25	93.06	93.76	95.94	95.81	96.86	98.29	94.63	91.59	92.64	88.82	92.73	91.44	95.38	95.37	91.05	93.49	67.75	68.19	72.35	66.04	65.28	85.83	70.12		

¹Total including REO and traces. Abbreviations: CC, calcite-carbonatite; FCC, ferroan-calcite-carbonatite; MFV, Mn-Fe-veins; AFV, apatite-fluorite-veins

Continued...

Sample	AFV PX016	AFV PX016	AFV PX016	AFV PX016	AFV PX016	AFV PX016	AFV PX016	AFV PX016	AFV PX016	AFV PX016	AFV PX016	AFV PX016	AFV PX016	AFV PX016	AFV T0178	AFV T0134
SiO ₂	5.99	0.86	1.28	0.43	0.86	0.43	0.64	0.86	0.86	2.14	0.43	1.71	1.50	1.93	22.68	47.70
TiO ₂	0.45	0.63	0.30	0.43	0.53	0.48	0.72	0.68	0.62	0.53	0.32	0.47	0.08	0.00	0.82	1.63
Al ₂ O ₃	2.32	1.00	1.32	0.94	0.98	0.76	0.81	0.98	1.42	1.30	1.10	2.36	1.81	3.48	4.29	14.19
FeO _t	18.71	24.01	14.38	13.80	22.59	23.26	23.63	18.22	16.39	16.29	13.34	13.64	12.58	14.22	7.35	8.71
MnO	2.07	2.84	2.20	2.32	2.84	2.97	2.71	2.45	2.97	2.71	2.58	2.84	2.84	2.97	1.29	1.03
MgO	2.98	4.94	3.78	3.81	4.28	4.81	4.86	4.41	4.26	4.16	4.81	4.69	4.10	4.13	1.13	0.17
CaO	26.58	27.70	26.44	31.76	25.05	21.97	24.21	26.72	28.12	28.12	31.62	30.50	33.16	28.54	28.40	3.64
Na ₂ O																
K ₂ O	1.25	0.14	0.33	0.22	0.23	0.13	0.12	0.00	0.16	0.51	0.14	0.36	0.40	0.40	2.75	9.20
P ₂ O ₅	5.94	6.37	6.94	9.85	5.13	3.02	4.03	7.01	6.58	6.67	9.60	6.46	7.29	5.48	9.17	3.05
SrO	0.79	0.67	0.67	0.74	0.56	0.54	0.48	0.61	0.75	0.58	0.78	0.85	0.85	1.57	0.68	0.19
Nb ₂ O ₅	0.46	0.35	0.19	0.22	0.11	0.12	0.35	0.23	0.22	0.33	0.15	0.08	0.05	0.04	0.00	0.00
LOI (1000 °C)	0.00	0.00	0.00	0.00	0.00	0.00	0.00	0.00	0.00	0.00	0.00	0.00	0.00	0.00	0.00	0.00
Total	67.55	69.52	57.84	64.55	63.16	58.49	62.56	62.18	62.33	63.34	64.88	63.97	64.66	62.75	78.54	89.51
ppm																
Ba																
Be	0	0	0	0	0	0	0	0	0	0	0	0	0	0	0	0
Cr	0	0	0	0	0	0	0	0	0	0	0	0	0	0	0	0
Ga	0	0	0	0	0	0	0	0	0	0	0	0	0	0	10	38
Hf	3.3	5	5.5	3.5	6.5	3.4	5	3.5	2.9	3.8	3	4.3	3.2	2.5	24	15.1
Li	0	0	0	0	0	0	0	0	0	0	0	0	0	0	0	0
Sc	0	0	0	0	0	0	0	0	0	0	0	0	0	0	0	0
Sn	0	0	0	0	0	0	0	0	0	0	0	0	0	0	0	0
Ta	0	0	0	0	0	0	0	0	0	0	0	0	0	0	0	0
Th	327.5	305.2	266.3	585.3	315.1	306	246	254.6	442.1	359.5	430.2	393.1	422.4	535	381.7	347.2
U	11.2	10	10.3	12.6	5.5	6.9	12	9.9	10.1	12.7	13.5	4.5	4.1	4.1	27.8	11.4
V	0	0	0	0	0	0	0	0	0	0	0	0	0	0	0	0
W	0	0	0	0	0	0	0	0	0	0	0	0	0	0	0	0
Zr	193	254	263	201	314	179	244	190	174	231	191	264	204	157	1293	819
La	2581.5	2438.3	2531.9	3086.6	2416	4228.6	2874.8	2685	4019.6	3405	2968.4	3442.3	3460.2	4822	856.3	1283.8
Ce	5534.1	5274	5456.6	6764.9	5119.3	7965.1	5698.4	5756.8	8290.6	6930.2	6326.9	7225.3	7270.7	9667.1	1274.9	1924.5
Pr	632.46	610.26	622.83	802.79	583.08	798.53	601.97	652.15	969.02	788.43	717.48	865.31	831.02	1147.2	123.18	190.18
Nd	2398.2	2277.2	2307.7	3125.1	2144	2519.5	2086.3	2374.6	3244	2727.2	2734.7	2921.5	3084.7	3839.2	416.1	621.3
Sm	369.9	327	345.6	530.9	313.8	281.7	264.3	347.1	456.9	391	431.4	414.2	433.8	527.8	100.6	100.3
Eu	112.8	94.3	102.2	162.3	88.8	71.2	71.8	101.2	131.7	112.5	128.1	117.6	121.7	146.4	54.6	37.4
Gd	275.7	228.1	252	402.3	215	160.5	169.7	244.9	315.7	271.5	330.5	274.4	295.2	348.5	252.3	127.9
Tb	39.05	31.65	35.95	57.9	28.76	20.56	22.32	35.05	43.34	38.24	49.21	38.06	41.22	47.84	79.33	26.25
Dy	210.1	174.8	196.2	322.1	164.9	108.2	122.1	191.2	238.6	216.9	293.8	215.9	234.2	263.7	556.8	153.1
Ho	36.7	32.9	36	58.5	30.3	20.1	22.5	34.3	43.9	39.7	54.6	40.2	43.7	49.1	104.4	27.5
Er	109.6	101.9	108.7	171.7	89.6	60.7	64.7	95.2	124.1	114.2	154.7	117.7	128.7	139.6	257.7	66.1
Tm	15.1	14.44	15.22	22.24	12.03	7.99	8.37	11.9	15.89	14.25	18.68	15.24	16.5	18.24	30.92	8
Yb	86.8	82	88.4	124.3	68.9	45.7	46.4	64.1	83.7	77.3	97.5	83	92	102.7	172.5	44.7
Lu	11.23	10.5	11.41	15.47	8.59	6.03	5.99	7.98	10.42	9.6	11.9	10.29	11.92	13.02	21.3	5.53
Y	1033.2	907.5	994.6	1645.7	830.3	554.8	620.1	907.6	1257.4	1164.5	1590.9	1209	1298.6	1436.5	2959	736
Total ¹	69.81	71.60	59.96	67.23	65.09	60.95	64.48	64.30	65.25	65.76	67.42	66.71	67.43	66.75	79.73	89.92

Table D.1: All whole-rock geochemistry data for each rock type.

D.2 Laser ablation data: Kangankunde and Tundulu apatite

Sample number	BM 1969 131	BM 1969 131	BM 1969 131	BM 1969 131	BM 1969 131	BM 1969 131	BM 1969 131	BM 1969 131	BM 1969 131	BM 1969 131	BM 1969 131	BM 1969 131	BM 1969 131	BM 1969 131	BM 1969 131	BM 1969 131	BM 1969 131	BM 1969 131	BM 1969 131	BM 1969 131	BM 1969 131	BM 1969 131	BM 1969 131	BM 1969 131
Point number	oa - 1	ob - 1	od - 1	od - 6	oc - 1	oc - 2	oc - 4	oc - 6	oe - 1	of - 1	og - 1	oa - 2	ob - 2	od - 2	od - 4	od - 5	oc - 3	oc - 5	oc - 7	oc - 8	oe - 2	of - 2	og - 2	
Core/Rim	c	c	c	c	c	c	c	c	c	c	c	r	r	r	r	r	r	r	r	r	r	r	r	r
Comments																								
²³ Na	928	3320	1427	2032	1031	1580	2200	2810	1840	1310	2020	4100	3860	3420	4260	2590	3210	3180	2800	3390	3810	2370	3230	
± ²⁴ Mg	49	180	31	95	37	310	650	170	440	120	500	260	260	110	190	280	150	440	110	270	310	240	150	
± ²⁸ Si	77	3300	132	169	85	198	108	23	198	39	136	33	44	44	139	540	128	38	20	58	270	47	48	
± ³⁹ K	14	440	8	9	12	27	16	3	40	4	21	2	17	9	10	160	19	8	2	14	120	5	11	
± ⁴⁷ Ti	5	56	15	13	5	8	6	11	16	9	17	4	2	57	23	26	107	7	6	9	4	28	9	
± ⁵⁵ Mn	5	9	5	6	5	6	8	13	6	5	5	7	8	34	6	14	24	7	16	5	4	7	7	
± ⁵⁶ Fe	940	17500	1298	1332	476	916	647	489	1007	362	750	670	570	434	1640	10100	861	573	487	677	1020	599	673	
± ⁷⁵ As	210	2900	43	51	81	91	72	23	71	36	92	47	57	37	290	3600	79	45	17	66	160	37	18	
± ⁸⁸ Sr	950	359000	1454	1670	1640	1317	1450	416	1680	600	1740	439	530	3500	2350	86000	31000	470	348	740	860	483	501	
± ⁸⁹ Y	130	61000	48	140	440	98	350	81	280	120	310	10	130	1600	480	27000	12000	120	42	200	180	52	13	
± ⁹⁰ Zr	0.9	35.4	0.1	1.4	0.9	1.0	3.6	11.9	1.6	1.4	2.7	13.2	14.1	18.4	9.5	8.4	7.8	12.6	10.8	9.4	8.4	4.1	7.0	
± ¹¹¹ Cd	0.5	9.6	0.3	0.5	0.4	0.5	2.5	0.9	1.0	0.5	1.1	1.5	1.6	1.2	1.9	1.6	1.0	2.3	1.8	1.6	0.8	1.5	1.1	
± ¹³⁷ Ba	5250	9510	4480	6100	4306	5820	7840	25400	6500	8200	5860	15180	13900	21550	10980	11100	13300	15500	26800	19000	13300	10900	14980	
± ¹³⁹ La	680	490	220	290	98	790	950	1200	640	660	770	820	1400	960	770	1100	1600	1900	1200	2200	1100	1900	800	
± ¹⁴⁰ Ce	71	453	102	265	155	328	452	670	352	464	386	358	790	1391	438	710	635	397	720	534	349	447	313	
± ¹⁴¹ Pr	6	33	6	11	3	26	57	100	40	63	60	38	170	93	28	71	50	61	120	48	23	49	41	
± ¹⁴⁶ Nd	819	1010	1560	855	1298	1240	906	101	1150	450	1620	69	230	161	540	438	535	128	82	263	356	560	180	
± ¹⁵³ Eu	49	330	210	56	71	120	58	38	100	260	5	130	16	42	59	84	72	37	99	89	130	78		
± ¹⁵⁷ Gd	0.19	0.40	0.46	0.46	0.23	-0.02	-0.13	0.13	0.02	-0.13	0.28	0.19	0.63	0.36	0.20	0.35	-0.22	0.36	-0.13	0.14	0.23	0.32	-0.04	
± ¹⁶³ Tb	0.19	0.56	0.21	0.33	0.29	0.33	0.41	0.39	0.25	0.16	0.27	0.27	0.37	0.36	0.28	0.36	0.26	0.56	0.25	0.27	0.29	0.37	0.30	
± ¹⁷⁰ Yb	244	265	487	529	301	343	264	117	490	137	337	106	112	92	447	490	278	109	118	156	262	188	126	
± ¹⁷⁵ Lu	30	57	32	41	52	18	20	9	55	19	16	4	49	10	35	110	40	11	5	20	54	35	13	
± ¹⁸² Hf	17	1259	6	54	25	27	230	882	59	32	95	770	1360	1075	820	120	566	809	928	704	653	270	419	
± ¹⁸⁸ Er	7	88	1	11	1	8	170	99	43	4	66	120	120	46	160	29	36	68	80	97	64	110	74	
± ¹⁹² Os	50	4410	24	241	85	124	860	3110	350	155	360	3040	4000	4020	2740	580	1845	2840	3140	2500	2270	820	1520	
± ¹⁹⁷ Ir	20	280	2	45	6	40	620	210	250	20	240	330	350	130	500	100	89	270	210	390	160	340	230	
± ²⁰² Pt	12	648	5	47	14	23	145	425	43	33	59	418	595	663	378	103	297	421	423	342	340	145	245	
± ²⁰⁷ Pb	4	42	0	9	1	7	98	38	28	5	37	42	47	37	58	20	13	23	24	46	29	54	28	
± ²¹¹ Pb	80	3600	33	297	84	157	740	2390	280	228	340	2520	3140	3980	2070	730	1587	2240	2300	1950	1830	650	1400	
± ²¹⁴ Pb	29	200	3	51	4	47	470	170	170	34	200	290	220	170	290	120	92	180	140	280	140	230	120	
± ²¹⁷ Pb	41	1371	21	156	44	89	360	852	167	149	155	880	1084	1414	752	393	641	813	831	704	692	300	607	
± ²²⁰ Rn	11	78	2	24	2	20	190	60	89	22	83	59	94	74	75	37	46	42	36	93	53	94	44	
± ²²³ Rn	15	410	8	54	17	36	113	257	60	57	54	253	326	444	231	150	199	252	266	211	208	94	188	
± ²²⁶ Rn	5	32	1	8	1	7	55	14	29	7	26	23	33	29	16	11	15	25	15	27	11	27	10	
± ²²⁸ Rn	41	923	26	136	48	109	270	608	153	167	148	638	754	1064	514	410	493	585	607	500	469	264	452	
± ²³¹ Rn	10	55	2	16	3	13	110	51	65	18	63	49	85	72	45	16	44	25	55	60	25	81	27	
± ²³² Rn	5	64	4	16	7	16	31	53	19	22	19	44	65	107	44	46	50	46	54	41	40	28	38	
± ²³⁵ Rn	1	4	0	2	0	1	10	6	5	2	6	4	10	9	2	3	5	2	6	4	1	5	3	
± ²³⁸ Rn	19	172	20	68	34	81	130	202	87	111	88	147	239	434	148	206	197	145	207	149	129	121	122	

Continued on next page . . .

Continued from previous page ...

Sample number	BM 1969 131	BM 1969 131	BM 1969 131	BM 1969 131	BM 1969 131	BM 1969 131	BM 1969 131	BM 1969 131	BM 1969 131	BM 1969 131	BM 1969 131	BM 1969 131	BM 1969 131	BM 1969 131	BM 1969 131	BM 1969 131	BM 1969 131	BM 1969 131	BM 1969 131	BM 1969 131	BM 1969 131	BM 1969 131	BM 1969 131
Point number	oa - 1	ob - 1	od - 1	od - 6	oc - 1	oc - 2	oc - 4	oc - 6	oe - 1	of - 1	og - 1	oa - 2	ob - 2	od - 2	od - 4	od - 5	oc - 3	oc - 5	oc - 7	oc - 8	oe - 2	of - 2	og - 2
Core/Rim	c	c	c	c	c	c	c	c	c	c	c	r	r	r	r	r	r	r	r	r	r	r	r
±	3	10	1	5	1	4	36	30	18	13	18	16	48	32	8	17	20	23	29	13	5	19	10
¹⁶⁵ Ho	3	17	3	9	5	11	18	24	12	16	13	12	27	51	16	27	23	15	25	18	13	17	12
±	0	1	0	1	0	1	4	4	2	2	2	1	5	3	1	2	2	2	4	1	1	2	2
¹⁶⁶ Ho	5	31	8	20	12	24	38	40	27	34	31	22	56	87	30	52	45	25	45	33	22	33	20
±	0	2	0	1	1	3	7	6	3	5	5	3	12	7	2	5	4	7	8	3	2	3	4
¹⁶⁹ Tm	1	4	1	3	2	3	6	4	4	4	4	2	6	8	4	6	5	3	4	4	3	4	2
±	0	0	0	0	0	0	1	1	0	1	1	0	1	1	0	1	0	1	1	0	0	0	1
¹⁷² Yb	7	32	10	21	12	20	42	20	27	26	32	13	33	38	26	33	34	16	22	23	18	24	17
±	0	3	1	2	1	3	4	3	3	4	5	2	7	3	2	3	2	3	3	4	1	1	4
¹⁷² Lu	1	5	2	3	2	3	7	3	5	4	5	2	5	5	4	5	5	3	3	4	3	4	3
±	0	1	0	1	0	1	1	0	1	1	1	0	1	0	0	0	1	1	1	1	0	0	1
²⁰⁸ Pb	70	93	92	102	96	87	98	137	112	88	105	90	83	161	95	95	126	95	121	87	92	107	100
±	3	15	3	5	4	6	15	39	5	4	6	5	10	11	5	4	8	12	30	6	6	5	9
²³² Th	31	612	31	132	59	95	590	580	290	115	300	407	890	806	813	322	835	630	563	539	686	298	470
±	10	50	6	26	5	16	270	110	180	14	180	48	210	57	62	18	49	240	99	68	87	83	170
²³⁸ Th	2.5	11.4	3.0	4.6	2.5	3.4	20.2	2.5	9.5	4.2	10.5	1.5	6.3	2.4	9.4	5.3	13.8	5.3	2.8	7.6	6.9	4.5	6.2
±	1.1	1.0	0.8	1.3	0.3	0.6	5.2	0.3	3.7	0.6	3.9	0.2	3.2	0.2	0.6	0.8	1.9	3.2	0.4	1.8	1.6	0.8	2.9

*M CL = Maroon luminescence under CL

Table D.2: Laser-ablation data for apatite from Kangankunde and Tundulu

Continued from previous page ...

Sample number Point number Core/Rim	NHAC	NHAC	NHAC	NHAC	NHAC	NHAC	NHAC	NHAC	NHAC	NHAC	NHAC	NHAC	NHAC	NHAC	NHAC	NHAC	NHAC	NHAC	NHAC	NHAC	NHAC	NHAC	NHAC	NHAC	NHAC	NHAC		
	3	4	5	6	11	12	14	15	17	18	19	23	25	26	28	34	1	2	8	13	16	27	29	30	31	32	33	
	c	c	c	c	c	c	c	c	c	c	c	c	c	c	c	c	r	r	r	r	r	r	r	r	r	r	r	
¹⁶⁹ Tm	15	11	26	16	19	16	20	18	26	23	20	18	26	21	20	21	26	17	39	20	24	34	25	19	28	30	31	
±	2	1	3	1	1	0	1	1	2	1	1	1	1	1	1	1	2	1	1	1	1	1	2	2	2	2	2	
¹⁷² Yb	65	51	128	79	96	111	108	111	131	121	106	94	128	130	94	118	100	101	190	78	132	155	115	85	117	147	146	
±	6	4	11	6	3	7	4	4	4	4	5	8	8	9	9	4	9	6	8	9	5	7	4	9	6	8	12	13
¹⁷² Lu	8	6	14	10	13	13	11	15	15	15	13	10	14	15	10	13	9	11	19	7	14	15	12	7	12	16	14	
±	1	0	1	1	1	1	1	1	2	1	1	1	1	1	1	1	1	1	1	1	1	1	1	1	1	1	2	
²⁰⁸ Pb	12	4	6	4	6	3	17	14	14	5	6	14	4	10	5	18	7	54	5	6	7	16	14	8	13	16	17	
±	1	1	1	1	1	1	1	1	1	0	1	1	1	1	1	2	1	18	1	1	1	1	2	1	1	1	2	
²³² Th	219	73	269	79	101	49	440	213	234	153	162	554	117	279	236	774	325	243	228	317	227	1230	1041	507	983	1252	1400	
±	13	5	10	3	6	7	17	7	14	7	17	54	5	27	21	54	9	28	11	11	12	28	99	41	54	66	150	
²³⁸ Th	6	10.1	11.8	13.1	18.0	16.0	10.0	31.8	14.9	17.4	18.2	13.3	21.6	24.8	9.1	27.8	6.3	18.2	43.5	7.9	13.1	41.9	31.2	17.4	45.2	44.9	33.3	
±	1	0.5	0.8	0.7	0.7	1.6	0.7	2.4	1.4	1.0	1.2	1.1	0.7	1.8	1.0	2.1	0.4	2.5	5.8	0.3	0.4	1.5	3.2	1.5	3.2	2.7	2.9	

*M CL = Maroon luminescence under CL

Table D.3: Laser-ablation data for apatite from Kangankunde and Tundulu

Back image: Sunset after at rainstorm at Songwe.



